Petrology, Mineralogy and Geochemistry of the Beattie Syenite and Country Rocks, Abitibi Greenstone Belt, Québec

by Julie E. Bourdeau

Thesis submitted to the

Faculty of Graduate and Postdoctoral Studies

In partial fulfilment of the requirements

For the M.Sc. degree in Earth Sciences

Department of Earth Sciences

University of Ottawa

© Julie E. Bourdeau, Ottawa, Canada, 2013

Abstract

The Beattie syenite is composed of a series of lenticular bodies of syenitic rocks, situated immediately north of the Porcupine-Destor fault zone in the town of Duparquet, approximately 32 km north of Rouyn-Noranda in the Abitibi Subprovince. The principal body is 3.3 km long and 470 m in width and is flanked by a series of smaller lenses to the south and northeast. The intrusion has been zircon dated at 2682±1Ma and 2682.9±1.1 Ma and hosted the major part of the Au-mineralization of the now defunct Beattie mine, which was an important producer of gold in the area from 1933 to 1956 (9.66 Mt at 4.88 g/t Au). A total of 5 petrographic units are defined here, on the basis of field relationships, macroscopic textures, petrology and mineralogy:

1- The porphyritic Beattie syenite unit is composed of 2% to 10% of tabular sub- to anhedral feldspar phenocrysts about 2 mm to 10 mm in size, set in a red feldspathic and aphanitic matrix. This unit can be strongly cataclastic with abundant hydrothermal minerals.

2- The equigranular magnetite-bearing syenite unit includes few feldspar phenocrysts, about 2 mm to 10 mm in a fine-grained matrix. It is characterized by unaltered titanite, epidote, hornblende porphyroblasts and is the only unit with actinolite replacing clinopyroxene.

3- The porphyritic Central Duparquet syenite unit contains between 2% - 25% of coarse equant euhedral feldspar phenocrysts, about 5 mm to 16 mm in size, in a red or sometimes grey aphanitic matrix.

4- The megaporphyritic syenite unit is composed of very coarse alkali feldspar phenocrysts, typically 1 cm to 6 cm across, in a red aphanitic matrix. The phenocrysts often form a glomeroporphyritic texture.

5- The lath syenite unit occurs as numerous $\sim$ m-width thin dykes, which cross-cut all other petrographic units. These dykes display a characteristic trachytic texture, as defined by the preferential alignment of alkali feldspar laths, which are typically 1 cm to 3 cm in a grey or red aphanitic matrix.

Petrology and geochemistry investigations revealed that the syenite intruded into the older 2720-2718 Ma volcanic Deguisier Formation and the $<$2687±2 Ma sediments of the Porcupine Group. Detailed geochemical analysis revealed that the Deguisier Formation is composed of three units, forming a complete tholeiitic suite. The Deguisier Formation is proposed here to have been produced in a volcanic arc setting.

Detailed petrological, mineralogical and geochemical studies indicate that, the syenite is part of the alkaline series and is metaluminous to peraluminous. The syenite intruded at shallow depths through a sequence of injections, yielding the five comagmatic units.

The syenite and country rocks were then subjected to a series of hydrothermal alterations and brittle deformation events, combined with metamorphism to the greenschist facies. The Au-mineralization in this region is attributed to the hydrothermal alteration with brittle deformation.

Sommaire

La syénite de Beattie est composée d'une série de corps lenticulaires syénitiques retrouvés immédiatement au nord de la zone de faille Porcupine-Destor dans le village de Duparquet, située approximativement 32 km au nord de Rouyn-Noranda dans la sousprovince de l'Abitibi. Le corps principal mesure 3.3 km de long et 470 m de largeur. Celui-ci est accompagné d'une série de lentilles plus petites au sud et au nord-est. L'intrusion à été U-Pb datée à 2682 $\pm$1 Ma et 2682.9 $\pm$1.1 Ma et a contenu une partie de la minéralisation aurifère à la mine Beattie; une des principales mines productrices d'or dans la région, de 1933 jusqu'à 1956 (9.66 Mt at 4.88 g/t Au). Un total de 5 faciès pétrographiques sont définis par leurs relations de terrain, pétrographie, minéralogie et textures macroscopiques:

1- Le faciès syénite porphyritique Beattie est composée d'entre 2 - 10% de phénocristaux tabulaires héteéro- à xenomorphes (2 - 10 mm) contenus dans une matrice feldspathique aphanitique rouge. Ce faciès contient plusieurs minéraux hydrothermaux et peut être fortement cataclastique.

2- Le faciès syénite à magnétite contient peu ou pas de phénocrystaux de feldspath (2 - 10 mm) dans une matrice a grains-fins. Ce faciès est charactérisé par de la titanite, epidote, des porphyroblastes d'hornblende et est le seul faciès a contenir de l'actinolite, qui remplace le clinopyroxène.

3- Le faciès syénite porphyrique Central Duparquet contient entre 2 - 25% de gros phénocristaux équigranulaires de feldspath (5 - 16 mm) dans une matrice aphanitique rouge ou parfois grise.

4- Le faciès syénite mégaporphyrique est composé de très gros phénocristaux de feldspath alkalin, 1 - 6 cm, contenus dans une matrice aphanitique rouge. Les phénocristes peuvent parfois former une texture glomérophyritique.

5- Le faciès syénite à lattes apparaît comme filons, mesurant quelques mètres d'épaisseur, qui recoupent tout les faciès pétrographiques. Les filons sont caractérisés par une forte texture trachytique définie par l'alignement préférentiel de lattes de feldspath alcalin (1 - 3 cm) contenus dans une matrice aphanitique rouge ou grise.

Suite à des études pétrologiques et géochimiques, la syénite aurait intruit dans les volcanites de la Formation de Deguisier (2720-2718 Ma) et les sédiments du Groupe de Porcupine ($<$2687$\pm$2 Ma). Les analyses géochimiques de la Formation de Deguisier ont devoilé qu'elle est composée de trois unitées, formant une suite tholéiitique complète. La Formation de Deguisier est proposée d'avoir été produite dans un contexte d'un arc volcanique.

L'étude des caractéristiques pétrographiques, minéralogiques et géochimiques de la syénite ont permis sa classification comme appartenant à la suite alkaline, et étant métalumieuse à peralumineuse. La syénite aurait intruit à de faibles profondeurs suite à une séquence d'injections qui ont produit les cinq faciès comagmatiques.

La syénite à et les roches encaissantes ont subit plusieurs séquences d'altération hydrothermales et de déformation cassante, combinées avec un métamorphisme au faciès schiste-vert. L'abondance de l'or dans la région est attribuée a l'altération hydrothermale combinée avec la déformation cassante.

Acknowledgements

Foremost thanks are given to my mentors André E. Lalonde (University of Ottawa), Jean Goutier (Ministère des Ressources naturelles) and Anthony D. Fowler (University of Ottawa) for their relentless patience, ongoing support and encouragement.

Many thanks are also given to Claude Dion (Ministère des Ressources naturelles) and Marc Legault (Ministère des Ressources naturelles) who provided the necessary documentation and maps for this project.

Thanks are given to Peter Jones (Carleton University) for performing all electron microprobe analyses and George Mrazek (University of Ottawa) for the preparation of thin sections.

Further thanks are given to Fred Archibald and the hard working people at Clifton Star Inc. and Osisko Mining Corporation for allowing access to the property, drill cores and providing unique documentation.

Thanks are also given to all my parents for their support, encouragement and delicious, delicious food.

To Ergong, my love and soul, that always kept me true and steady for this project as well as in life.

In memoriam André E. Lalonde

Author's note

Subjects and geological maps presented and discussed in this thesis may have been subsequently updated. To obtain more recent data or reports concerning the studied area in this thesis, please consult the Système d'information géominière du Québec (E-SIGEOM) at `http://www.mrn.gouv.qc.ca/english/products-services/mines.jsp`.

Measurements and symbols for rock- and ore-forming minerals

Measurements

All units in this thesis follow the metric system (International system of units). As such, photographs with scales are all in centimetres unless otherwise noted.

Almost all older measurements in previous work have been carried out in imperial units, which for the purpose of this thesis have been converted into metric units.

Values are reported in Canadian dollars unless otherwise stated.

Table 1 – Symbols for measurement units

mg	milligram	**μm**	micromillimetre
g	gram	**mm**	millimetre
kg	kilogram	**cm**	centimetre
t	metric tonne	**m**	metre
g/t	gram per tonne	**km**	kilometre
mL	millilitre	**%**	percent
ppm	parts per million (1.0 x 10^{-4}%)	**wt%**	weight percent
ppb	parts per billion (1.0 x 10^{-7}%)		

Symbols for rock- and ore-forming minerals

Several mineral species are contained in this thesis. To avoid confusion, symbols for rock forming minerals are those standardized by Kretz (1983)[1]. A list of the symbols and corresponding rock and ore forming minerals encountered in this thesis are listed below.

Table 2 – Symbols for rock-and ore-forming minerals

Act	Actinolite	**Ccp**	Chalcopyrite	**Mgt**	Magnetite
Ab	Albite	**Chl**	Chlorite	**Ms**	Muscovite
An	Anorthite	**Cz**	Clinozoisite	**Or**	Orthoclase
Ap	Apatite	**Ep**	Epidote	**Py**	Pyrite
Apy	Arsenopyrite	**Gn**	Galena	**Qtz**	Quartz
Cal	Calcite	**Hem**	Hematite	**Ttn**	Titanite
Cb	Carbonate minerals	**Hbl**	Hornblende		

[1]Kretz, R. (1983) Symbols for rock-forming minerals. American mineralogist, 68, 277-279.

Contents

List of Tables **xv**

List of Figures **xxii**

List of Acronyms **xxv**

1 Introduction **1**

1.1 Purpose of study 2

2 Historical background **4**

2.1 Mining history and ongoing activity 4

2.2 Environmental aspects 7

2.3 Literature review and previous work 10

3 Field and analytical methods **22**

3.1 Field methods 22

3.2 Description of the geological map 24

3.2.1 Limitations and errors 25

3.3 Microscopy 25

3.4 Electron microprobe 25

3.5 Geochemistry 26

3.5.1 Older analyses 26

3.5.2 SOQUEM Inc. 26

3.5.3 Gold Fields Resources Canada Ltd. 27

3.5.4 Cogema Canada Ltd. 27

3.5.5 Noranda Exploration Ltd. 28
3.5.6 MRNF and University of Ottawa 28
3.5.7 Osisko Mining Corporation 33
3.6 Feldspar staining 35

4 Geological setting **36**
4.1 Geology of the Superior Province 36
4.2 Geology of the Abitibi greenstone belt 37
4.2.1 Stratigraphic Framework 38
4.2.2 Intrusion Framework 41
4.2.3 Metallogenic events 42

5 Geology of the Duparquet area, Southwest Sector **44**
5.1 Stratigraphy 46
5.1.1 Kinojévis Group 48
5.1.2 Hébécourt Formation, Blake River Group 70
5.1.3 Porcupine Group and Mont-Brun Fromation, Kewagama Group 71
5.1.4 Duparquet Formation, Timiskaming Group 75
5.2 Intrusive framework 79
5.2.1 Gabbro 79
5.2.2 Quartz-feldspar porphyry 81
5.2.3 Beattie syenite 84
5.3 Structural geology 87
5.3.1 Structural evolution 87
5.3.2 Faults 88
5.4 Regional Metamorphism 92
5.5 Alteration 93
5.6 Economic geology, Au-mineralization of the Beattie syenite 93
5.6.1 Epithermal veins 94
5.6.2 Disseminated sulphides associated with alkaline intrusions 94
5.6.3 Ag-quartz veins 95

6 Petrography and mineralogy of the Beattie syenite 98

6.1 Overview of the Beattie syenite . . . 99

6.2 Chronology of the petrographic units . . . 103

6.3 Porphyritic Beattie syenite . . . 115

6.3.1 Phenocrysts . . . 117

6.3.2 Matrix . . . 124

6.3.3 Apatite . . . 125

6.3.4 Magnetite . . . 126

6.4 Equigranular magnetite-bearing syenite . . . 127

6.4.1 Large euhedral crystals . . . 128

6.4.2 Matrix . . . 135

6.4.3 Actinolite . . . 138

6.4.4 Magnetite . . . 144

6.4.5 Titanite . . . 144

6.4.6 Apatite . . . 145

6.5 Porphyritic Central Duparquet syenite . . . 146

6.5.1 Phenocrysts . . . 148

6.5.2 Matrix . . . 155

6.5.3 Apatite . . . 157

6.5.4 Magnetite . . . 157

6.6 Megaporphyritic syenite . . . 158

6.6.1 Phenocrysts . . . 160

6.6.2 Matrix . . . 160

6.6.3 Apatite . . . 161

6.7 Lath syenite . . . 162

6.7.1 Laths . . . 165

6.7.2 Matrix . . . 168

6.7.3 Apatite . . . 170

6.7.4 Magnetite . . . 170

7 Geochemistry **171**

7.1 Deguisier tholeiitic basalt . . . 174

7.1.1 Major and compatible trace elements . . . 178

7.1.2 Incompatible trace elements . . . 183

7.1.3 Rare earth elements . . . 185

7.2 Deguisier tholeiitic andesite to dacite . . . 187

7.2.1 Major and compatible trace elements . . . 191

7.2.2 Incompatible trace elements . . . 195

7.2.3 Rare earth elements . . . 197

7.3 Tholeiitic rhyolite . . . 199

7.3.1 Major and compatible trace elements . . . 201

7.3.2 Incompatible trace elements . . . 204

7.3.3 Rare earth elements . . . 205

7.4 Lanaudière komatiites and komatitic basalts . . . 207

7.5 Gabbro . . . 210

7.5.1 Major and compatible trace elements . . . 210

7.5.2 Incompatible trace elements . . . 214

7.5.3 Rare earth elements . . . 216

7.6 The Deguisier Formation . . . 218

7.6.1 Relationship between the gabbro and the Deguisier Formation . . . 218

7.6.2 Evolution and tectonic setting . . . 221

7.7 Beattie syenite . . . 226

7.7.1 Major and compatible trace elements . . . 237

7.7.2 Incompatible trace elements . . . 242

7.7.3 Rare earth elements . . . 243

7.7.4 Tectonic setting . . . 247

8 Hydrothermal alteration, deformation and metamorphism to the greenschist facies of the Beattie syenite **253**

8.1 Hydrothermal alterations, metamorphism to the greenschist facies and deformation petrography and mineralogy . . . 253

8.1.1 Hydrothermal alterations and metamorphism to the greenschist facies . 253
8.1.2 Deformation 293
8.2 Geochemistry of hydrothermal alteration and metamorphism to the greenschist facies 297
8.2.1 Au-mineralization 297
8.2.2 Regional metamorphism to the greenschist facies 323

9 Interpretations **348**

10 Conclusion **362**

References **377**

A Error calculation **378**
A.1 EMP errors 378

B Geological and outcrop maps **382**

C EMPA data **391**
C.1 Mineral targets 391
C.2 Raw data 414

D Geochemistry data **415**
D.1 Choice of loss-on-ignition cut-off 416

List of Tables

2.1 Operations at the Beattie and Donchester mine 9

2.3 Current equivalence of old geological terms 18

2.2 Exploration reports on Beattie 21

3.1 Analytical methods and detection limits (SOQUEM) 27

3.2 Analytical methods and detection limits (Gold Fields Canada) 28

3.3 Detection limits (Cogema) 28

3.4 Analytical methods, accuracy and detection limits of oxides (MRN prior to 2002) 29

3.5 Analytical methods, accuracy and detection limits of minor elements (MRN prior to 2002) 30

3.6 Analytical methods used and detection limits for oxides (MRN and U of O) . . 30

3.7 Analytical methods and detection limits of minor elements (MRN and U of O) 31

3.8 Analytical methods and detection limits of REE (MRN and U of O) 32

3.9 Analytical methods and detection limits of oxides (Osisko) 33

3.10 Analytical method and detection limits of minor elements (Osisko) 34

6.1 Range and modal composition of the porphyritic Beattie syenite unit 117

6.2 Microprobe analyses and chemical formulas of phenocrysts from the porphyritic Beattie syenite unit 121

6.3 Microprobe analyses and chemical formulas of matrix feldspar from the porphyritic Beattie syenite unit 124

6.4 Range of modal composition of the equigranular magnetite-bearing unit 127

6.5 Microprobe analyses and chemical formulas of large euhedral crystals from the equigranular magnetite-bearing and transition zone 130

6.6 Microprobe analyses and chemical formulas of matrix feldspars from the equigranular magnetite-bearing unit . . . 136
6.7 Microprobe analysis and chemical formulas of actinolite within the equigranular magnetite-bearing unit . . . 139
6.8 Microprobe analyses and formulas of titanite from the transition zone . . . 144
6.9 Range and modal composition of the porphyritic Central Duparquet unit . . . 146
6.10 Microprobe analyses and chemical formulas of phenocrysts from the porphyritic Central Duparquet unit . . . 151
6.11 Microprobe analyses and chemical formulas of matrix feldspars from the porphyritic Central Duparquet unit . . . 155
6.12 Range of modal composition of the megaporphyritic unit . . . 158
6.13 Range of modal composition of the lath syenite unit . . . 163
6.14 Microprobe analyses and formulas of laths form the lath syenite unit . . . 166
6.15 Microprobe analyses and chemical formulas of matrix feldspars form the lath syenite unit . . . 168

7.1 Source of geochemical analyses used in this thesis . . . 172
7.2 Major and trace element analyses for the Deguisier tholeiitic basalt . . . 175
7.3 CIPW normative mineralogy of Deguisier basalt samples without volatiles . . . 181
7.4 Incompatible and rare earth elements for the Deguisier basalt . . . 184
7.5 Chondrite normalizing values for incompatible trace elements . . . 184
7.6 Major and trace element analyses of the Deguisier tholeiitic andesite to dacite . . . 188
7.7 Mean major oxide composition of the basalt and andesite to dacite units . . . 191
7.8 CIPW normative mineralogy of the Deguisier andesite to dacite unit samples without volatiles . . . 194
7.9 Incompatible and rare earth elements for the Deguisier andesite to dacite . . . 195
7.10 Major and trace element analyses of the Deguisier tholeiitic rhyolite . . . 200
7.11 CIPW normative mineralogy of the Deguisier rhyolite . . . 203
7.12 Major and trace element analyses for the Lanaudière komatiites and komatitic basalts . . . 208

7.13 Comparison between the average geochemistry of the Deguisier basalt and the Lanaudière komatiite 209
7.14 Major and trace elements analyses of specimens of the gabbro 211
7.15 CIPW normative mineralogy for the gabbro 214
7.16 Comparison of REE properties between units of the Deguisier Formation and the gabbro 220
7.17 Major and trace element analyses of the Beattie syenite 227
7.18 Peraklaline, peraluminous and metaluminous definitions including boundaries for indexes 239
7.19 Alumina saturation and peralkaline indexes of the syenitic units 241
7.20 REE characteristics of the syenitic units 247

8.1 Range and modal composition of hydrothermal and metamorphic minerals . . . 255
8.2 Microprobe analyses and chemical formulas of carbonate minerals 261
8.3 Microprobe analyses and chemical formulas of sericite 270
8.4 Microprobe analyses and chemical formulas of albite 276
8.5 Microprobe analyses and chemical formulas of chlorite 279
8.6 Microprobe analysis and chemical formulas of epidote 288
8.7 Scaling factors and identification of immobile elements for the Deguisier basalt 299
8.8 Scaling factors and identification of immobile elements for the Deguisier andesite to dacite unit 302
8.9 Scaling factors and identification of immobile elements for the Deguisier rhyolite 305
8.10 Scaling factor and identification of immobile elements for the gabbro 308
8.11 Gold abundance in each of the Beattie syenite units 314
8.12 Scaling factors and identification of immobile elements for the porphyritic Beattie and Central Duparquet syenite units 315
8.13 Scaling factors and identification of immobile elements for the porphyritic Beattie, megaporphyritic and lath syenite units against the equigranular magnetite-bearing unit 319
8.14 Average gold concentration in the porphyritic Beattie unit 321
8.15 NORMAT normative mineralogy of the least-altered basaltic samples 326

8.16 NORMAT normative mineralogy of the Deguisier andesite to dacite unit 329
8.17 NORMAT normative mineralogy of the Deguisier rhyolite 332
8.18 NORMAT normative mineralogy of the gabbro 333
8.19 NORMAT normative mineralogy of the porphyritic Beattie syenite unit 334
8.20 NORMAT mineralogy of the equigranular magnetite-bearing unit 341
8.21 NORMAT mineralogy of the porphyritic Central Duparquet unit 342
8.22 NORMAT normative mineralogy of the megaporphyritic syenite unit 345
8.23 NORMAT normative mineralogy of the lath syenite unit 346

A.1 Measured weight percent of oxides in a feldspar 379
A.2 Calculated chemical oxides for the feldspar formula 380
A.3 Ternary percentages and errors of each end-member 381

List of Figures

2.1 Mines of the Beattie syenite 8

4.1 Terrane map of the Superior Province 37
4.2 Abitibi greenstone belt 39

5.1 Location of the study area within the Duparquet Township 45
5.2 Geological time scale of the Beattie study area 47
5.3 Aphanitic Deguisier tholeiitic andesite to dacite 50
5.4 Deguisier tholeiitic andesite to dacite with quartz and albite amygdules 50
5.5 Deguisier tholeiitic andesite to dacite with albite amygdules 51
5.6 Oligoclase feldspar microphenocrysts in a fine-grained matrix 52
5.7 Matrix of the Deguisier andesite to dacite 53
5.8 Photomicrographs of diverse minerals filling amygdules 54
5.9 Seemingly gradational contact between the Deguisier rhyolite and andesite to dacite units 55
5.10 Altered section with a diffuse transition back to less-altered Deguisier andesite to dacite 56
5.11 Colour and textural variations of the Deguisier tholeiitic rhyolite 58
5.12 Shape and compositional variation of amygdules within the Deguisier tholeiitic rhyolite 59
5.13 Feldspar phenocrysts in an outcrop of the Deguisier tholeiitic rhyolite 60
5.14 Feldspar phenocrysts and relicts of primary mafic crystals in the Deguisier tholeiitic rhyolite 61
5.15 Plagioclase microphenocryst cluster in the Deguisier rhyolite 62

5.16 Small embayed quartz phenocryst in the Deguisier tholeiitic rhyolite 62
5.17 Rhyolitic matrix with wavy sericite veins 63
5.18 Large zoned amygdule in the Deguisier tholeiitic rhyolite 64
5.19 Detailed map of a Deguisier rhyolite outcrop 66
5.20 Anastomosing sericite filled fractures in the Deguisier rhyolite 67
5.21 Contacts between the Deguisier tholeiitic rhyolite and Beattie syenite 68
5.22 Porcupine mudrock specimen from the Beattie mine 72
5.23 Polymict conglomerate of the Porcupine Group 73
5.24 Pitted Porcupine conglomerate in an outcrop 73
5.25 Porcupine polymict conglomerate transitioning to wacke 74
5.26 Contact between the Porcupine sediments and the Deguisier basalt 75
5.27 Duparquet Formation polymict conglomerate 76
5.28 Clasts of the Beattie syenite within the Duparquet conglomerate 77
5.29 Contact between the Beattie syenite and the Duparquet conglomerate 78
5.30 Specimen of the gabbro 81
5.31 Drill core specimen of the gabbro 82
5.32 Sharp contact between Beattie syenite and the gabbro 83
5.33 Contact between a Beattie syenite dyke and the Porcupine sediments 86
5.34 Name and location of major faults and shear zones in the Beattie area 91
5.35 Disseminated sulphides in the Porcupine sediments 95
5.36 Disseminated sulphides in the Beattie syenite 96
5.37 Sulphides in the Ag-Au quartz vein 97

6.1 Syenitic portions of the Beattie syenite 101
6.2 Detailed map of outcrop Beattie east 104
6.3 Detailed map of outcrop next to QC-393 N road 105
6.4 Detailed map of outcrop near Central Duparquet 2 mine 106
6.5 Transition between the equigranular magnetite-bearing and porphyritic Beattie syenite units 108
6.6 Gradational contact between the porphyritic Beattie and Central Duparquet units 109

6.7 Detailed map of outcrops near Central Duparquet 1 mine 110
6.8 Contact between the megaporphyritic and porphyritic Central Duparquet units 111
6.9 Contact between the porphyritic Beattie syenite and lath syenite units 112
6.10 Contacts of the lath syenite unit supporting additional brittle deformation and subsequent hydrothermal minerals 113
6.11 Detailed geological time scale developed to include units 114
6.12 Drill core specimen of the porphyritic Beattie syenite unit 116
6.13 Xenoliths in the porphyritic Beattie syenite unit 117
6.14 Subhedral phenocryst of the porphyritic Beattie syenite unit 118
6.15 Smaller-sized phenocrysts 119
6.16 Location of samples submitted for electron microprobe analysis 120
6.17 End-member composition of phenocrysts from the porphyritic Beattie syenite unit 123
6.18 Back scatter image of a phenocryst from the porphyritic Beattie syenite unit . . 123
6.19 End-member composition of matrix feldspars from the porphyritic Beattie syenite unit 125
6.20 Back scatter images of orthoclase and albite composing the matrix of the porphyritic Beattie syenite unit 126
6.21 The equigranular magnetite-bearing unit 128
6.22 Oscillatory zoning in a large euhedral crystal 129
6.23 End-member composition of large euhedral crystals from the equigranular magnetite-bearing unit and transition zone 132
6.24 EBS images of feldspar phenocrysts from the equigranular thin section 133
6.25 EBS image of a feldspar phenocryst from the transition zone 134
6.26 Thin section appearance of the equigranular magnetite-bearing unit 135
6.27 End-member composition of matrix feldspars in the equigranular magnetite-bearing unit and the transition zone 137
6.28 EBS image of orthoclase and albite composing the matrix of the equigranular sample 137
6.29 Actinolite replacing clinopyroxene 138
6.30 IMA classification of calcic amphiboles 141

6.31 EBS image of compositional variation in actinolite 142
6.32 EBS image of actinolite pseudomorphs 143
6.33 EBS images of titanite crystals from the transition zone between the equigranular and porphyritic Beattie units 145
6.34 Porphyritic Central Duparquet specimen taken from an outcrop 147
6.35 Porphyritic Central Duparquet in the Beattie-Donchester body 147
6.36 Euhedral perthitic phenocryst of the porphyritic Central Duparquet unit 149
6.37 Compositionally zoned phenocryst 150
6.38 Poor glomeroporphyritic texture in the porphyritic Central Duparquet unit . . 150
6.39 End-member composition of phenocrysts from the porphyritic Central Duparquet unit 153
6.40 EBS images of feldspar phenocrysts from the porphyritic Central Duparquet unit 154
6.41 End-member composition of albite from the porphyritic Central Duparquet unit 156
6.42 EBS image of orthoclase and albite composing the matrix of the porphyritic Central Duparquet unit 157
6.43 The megaporphyritic syenite unit 159
6.44 Phenocryst of the megaporphyritic unit. 160
6.45 Quarter of a glomerocryst of the megaporphyritic unit 161
6.46 The lath syenite unit in a drill core specimen 163
6.47 Hydrothermal sericitization followed by brittle deformation of the lath unit . . 164
6.48 Feldspar laths demonstrating a trachytic alignment 165
6.49 End-member composition of laths from the lath syenite unit 167
6.50 Perthite feldspar lath 167
6.51 End-member composition of matrix feldspar from the lath syenite unit 169
6.52 Feldspathic matrix of the lath syenite unit 170

7.1 Jensen cation plot of the Deguisier basalt 178
7.2 TAS and alkaline classification of the Deguisier basalt analyses 180
7.3 Basalt classification using CIPW normative mineralogy 183
7.4 Chondrite-normalized incompatible trace element patterns of the Deguisier basalt 185
7.5 Chondrite normalized REE patterns for the Deguisier basalt unit 186

7.6 Jensen cation plot of the Deguisier andesite to dacite unit 192
7.7 TAS and alkaline classification of the Deguisier andesite to dacite analyses . . . 193
7.8 Chondrite-normalized incompatible trace element pattern of the Deguisier andesite to dacite unit 196
7.9 Chondrite normalized REE patterns for the Deguisier andesite to dacite unit . 197
7.10 Jensen cation plot of the Deguisier rhyolite 201
7.11 Analyses of the Deguisier rhyolite unit illustrated in the TAS classification scheme 202
7.12 Chondrite normalized incompatible trace element pattern for the Deguisier rhyolite 204
7.13 Chondrite normalized REE pattern of the Deguisier rhyolite 206
7.14 Jensen cation plot of the Lanaudière komatiite and komatitic basalt 209
7.15 Jensen cation plot of all samples of the gabbro 212
7.16 TAS and alkaline classification of the gabbro 213
7.17 Chondrite normalized incompatible trace element pattern of the gabbro 215
7.18 Chondrite normalized REE patterns of the gabbro 216
7.19 Chondrite-normalized incompatible trace element pattern for the Deguisier Formation including the gabbro 219
7.20 Chondrite-normalized incompatible trace element pattern for the Deguisier Formation including the gabbro 220
7.21 Jensen cation plot of all the Deguisier Formation samples 221
7.22 Tectonic discrimination of the Deguisier basalt 223
7.23 Tectonic discrimination of the Deguisier rhyolite 224
7.24 TAS classification of the Beattie syenite samples 238
7.25 Alkaline subdivision of the Beattie syenite 240
7.26 Peralkaline, perlauminous and metaluminous characterization for samples of the Beattie syenite 241
7.27 Averaged chondrite-normalized incompatible trace element pattern of all the syenitic units 243
7.28 Chondrite-normalized incompatible trace element pattern for individual units of the Beattie syenite 244
7.29 Chondrite normalized REE pattern of the Beattie syenite 245

7.30 Chondrite-normalized REE diagram of the Beattie syenite units 246
7.31 Pearce et al. (1984) tectonic discrimination diagrams for the Beattie syenite . . 249
7.32 Harris et al. (1986) tectonic discrimination diagram for the Beattie syenite . . . 251

8.1 Relicts of a mafic mineral and titanite 256
8.2 Calcite replacing actinolite 257
8.3 Cataclastite filled with carbonate minerals 258
8.4 Disseminated carbonate minerals in the feldspathic matrix 259
8.5 Core of phenocrysts replaced by carbonate minerals 260
8.6 Reactivated chlorite vein filled with clear albite and quartz with carbonate minerals at the centre 262
8.7 End-member compositions of carbonate minerals 263
8.8 Electron backscatter image of calcite replacing actinolite in the equigranular magnetite-bearing unit 264
8.9 Relict of primary mafic mineral occupied by ankerite 265
8.10 Images of a calcite target in a Qtz-Ab-Cb vein 265
8.11 Sericite in the western portions of the Beattie syenite 267
8.12 Anastomosing network of sericite-filled veinlets 268
8.13 Sericite in a primary mafic mineral relict 268
8.14 Phenocrysts partially replaced by sericite 269
8.15 EBS image of recrystallized muscovite at the contact with a transecting quartz, albite, carbonate minerals vein 273
8.16 Albite in the Beattie syenite 275
8.17 End-member compositions of albite 275
8.18 Thin and numerous black chamosite veins in a cataclastic carbonatized zone . . 278
8.19 Tension vein of chlorite refilled by quartz, albite and carbonate minerals which is transected by a quartz and carbonate minerals vein 283
8.20 Pyrite and arsenopyrite in the Beattie syenite 285
8.21 Magnetite crystal with inclusions of chalcopyrite, galena and pyrite. 286
8.22 Epidote in the equigranular magnetite-bearing unit 287
8.23 Electron backscatter image of epidote 289

8.24 Subhedral crystals of xenotime 290
8.25 Black slikenfibers of tourmaline in a D_2 shear fault 291
8.26 Hornblende porphyroblast in the equigranular magnetite-bearing unit 292
8.27 Secondary D_2 shear fault transecting the Beattie syenite 293
8.28 Fractures filled with pale green sericite 295
8.29 En-echelon chlorite filled tension fracture 295
8.30 Detailed map of South Beattie outcrop 296
8.31 Diagram of an isocon plot 298
8.32 Isocon diagram of the Deguisier basalt 300
8.33 Isocon diagram of the Deguisier andesite to dacite 303
8.34 Isocon diagram of the Deguisier andesite and dacite without samples D958238 and 91884 304
8.35 Isocon diagram of the Deguisier rhyolite 306
8.36 Enrichment-depletion diagram of the Beattie area rhyolite 307
8.37 Isocon diagram of the gabbro 309
8.38 Isocon diagram of the Au-mineralized gabbro 310
8.39 Elemental enrichments associated with Au-mineralization 312
8.40 Isocon diagram of the porphyritic Beattie syenite unit 316
8.41 Elemental variations between distal and ore samples from the porphyritic Beattie unit 317
8.42 Isocon diagram of the porphyritic Central Duparquet unit 318
8.43 Isocon diagram between porphyritic Beattie syenite and the equigranular magnetite-bearing units 320
8.44 Isocon diagram of the megaporphyritic unit 321
8.45 Isocon diagram of the lath syenite unit 322

9.1 Petrogenetic model of the Beattie area 360
9.2 Hydrothermal fluid evolution in the Beattie area 361

List of Acronyms

apfu Atoms per formula unit. 119, 140, 142, 149, 280

AAS Atomic absorption spectroscopy. 26, 27, 35

AGB Abitibi greenstone belt. 1, 37, 38, 41–43, 93, 249, 250, 252, 356

ASI Aluminum saturation index. 239, 241, 242

BDB Beattie-Donchester syenitic body. 100, 102, 103, 115, 118, 127, 129, 146–148, 165, 264, 352

CAB Island arc calc-alkaline basalt. 222, 223

CDB Central Duparquet syenitic body. 100, 102, 103, 115, 118, 146–148, 158, 264, 352

EBS Electron backscatter. 118, 119, 121, 123–126, 130, 132–134, 136, 137, 140–145, 148, 154–157, 165, 166, 168, 262–265, 270, 273, 281, 288, 289

EDS Energy-dispersive X-ray spectrometry. 129, 260, 288

EMPA Electron microprobe analysis. 117, 118, 128, 139, 148, 155, 165, 168, 256, 259, 260, 267, 274, 278, 287, 342, 346

FA-AAS Fire assay-atomic absorption spectroscopy. 27, 34

HREE Heavy Rare Earth Elements. 185, 196, 197, 205, 216, 223, 224, 242, 245, 251

IAT Island Arc Tholeiite. 222, 223

ICP Inductively coupled plasma. 28

ICP-AES Inductively coupled plasma atomic emission spectroscopy. 29, 33, 34

ICP-MS Inductively coupled plasma mass spectrometry. 29

IMA International Mineralogical Association. 139, 141, 269, 278, 287

LILE Large Ion Lithophile elements (K, Rb, Sr, Cs, Ba,[Li, Na, Be, Mg, Pb, Eu]). 184, 196, 205, 215, 222, 243, 309, 311

LLF and CF Larder Lake Fault and Cadillac Fault. 18, 38, 40–43, 92

LOI Loss on ignition. 27, 29, 33, 174, 175, 183, 184, 187, 188, 195, 199, 200, 203, 210, 211, 226, 227, 299, 311, 312, 318, 319, 323, 325, 416, 417

LREE Light Rare Earth Elements. 184, 185, 196, 197, 204, 205, 215, 216, 221, 224, 242, 245, 251

MER Ministère de l'Énergie et des Ressources. 16, 172

MORB Mid-oceanic ridge basalt. 183, 222–224

MRN Ministère des Ressources naturelles. 2, 3, 9, 22, 24, 25, 27, 28, 45, 98, 172, 174, 187, 199, 210, 226, 297

MRNF Ministère des Ressources naturelles et de la Faune. 17

NAA Neutron activation analysis. 26, 28

NEB North-eastern syenitic bodies. 100, 351

OIA Seamount alkalic basalt. 222, 223

OIT Seamount tholeiitic basalt. 222, 223

PDFZ Porcupine-Destor fault zone. 2, 10, 15–18, 38, 40–44, 46, 49, 69–71, 79, 84, 85, 87–89, 92, 93, 102, 115, 142, 146, 239, 254, 293, 294, 305, 313, 320–322, 352–356, 360, 362–364

PI Perakaline index. 239, 241, 242

QFP Quartz-feldspar porphyry. 79, 81–83, 87, 350, 359

REE Rare Earth Elements. 18, 29, 32, 185, 186, 197, 198, 205, 206, 215, 216, 218–220, 223, 224, 243, 245–248, 250–252, 288, 297, 349

SCB Small central syenitic bodies. 100, 242, 351

TAS Total alkalis vs silica diagram. 179, 180, 191, 193, 202, 212, 213, 237, 238, 416

UQAM Université du Québec à Montréal. 29, 172, 199

VAG Volcanic arc granite. 247, 248, 250, 252

VMS Volcanogenic massive sulphide deposits. 17, 37, 42, 93

XRF X-Ray Fluorescence. 26–28

Chapter 1

Introduction

Within Archean greenstone belts there exists a known spatial relationship between some sites of gold mineralization, major fault zones, younger clastic sediments in unconformable basins, and small alkali intrusions. Interestingly, work done by Colvine et al. (1988) demonstrates that approximately 25% of the Au-mineralization in the western Abitibi Greenstone Belt (AGB), located in the Superior Province, Canada, can be associated with syenites, syenite porphyries or felsic feldspar porphyries despite the minute fraction that these intrusions represent (4% of the lithologies encountered in the AGB). In particular, the association between gold mineralization and the small alkali intrusions has been the subject of numerous studies such as, but not limited to Cameron and Hattori (1987), Hodgson (1993), Robert (2001), Macdonald et al. (2005) and Legault and Lalonde (2009) in the AGB.

The Beattie syenite, a good example of this association, is located about 32 km north of the city of Rouyn-Noranda. It is accessible via Highway QC-101, north, then by taking route QC-393 west to the small town of Duparquet. This paved route is accessible all year round. The area is also accessible by float plane via Duparquet Lake, situated approximately 1.5 km to the south. Local airports with flights to major Canadian cities are located in Timmins and in Rouyn-Noranda.

The Beattie syenite is composed of a series of lenticular bodies and dykes. The largest one, in the west of the study area, measures 3.3 km long and a maximum of 470 m wide. It is flanked by 4 smaller bodies, two smaller ones immediately to the south, a larger one to the southeast and one further to the northeast.

The syenite can be divided into 5 petrologically unique units: 1) porphyritic Beattie syen-

ite, 2) equigranular magnetite-bearing syenite, 3) porphyritic Central Duparquet syenite, 4) megaporphyritic syenite, and 5) lath syenite. The Beattie syenite was U-Pb zircon dated to be 2682.9 ± 1.1 Ma (David et al., 2007) and 2681.5 ± 1 Ma (Mueller et al., 1996) for the megaporphyritic syenite unit.

Because of its strong association with gold mineralization, the Beattie syenite was the subject of intense study and exploration leading to the opening of the large Beattie gold mine in 1933 and subsequently the smaller Donchester mine, and Central Duparquet 1 and 2 mines. After 23 years of exploitation, the exhaustion of ore as well as other causes resulted in the termination of production in 1956. Unfortunately, many historical records associated with these mines have been lost. This is particularly true for the Beattie mine which was the object of a fire. Mineral exploration at the abandoned Beattie mine however continues to this day. A massive drilling campaign has been recently carried out by a joint venture of Clifton Star Resources Inc. and the Osisko Mining Corporation.

In the 1990s a project was launched by the Ministère de l'Énergie et des Ressources du Québec (now called the Ministère des Ressources naturelles (MRN)) to review and map the Duparquet-Destor region. Upon close examination of the syenite, the MRN decided the region merited additional research. Meanwhile, a Master's thesis by Pigeon (2003) at the University of Ottawa explored in detail the mineralogy, geochemistry and petrogenesis of a suite of syenitic rocks along the Porcupine-Destor fault zone (PDFZ) in Ontario. Seeing the need for a continued documentation of the syenites along the PDFZ in Québec, this M.Sc. project was launched in 2009 at the University of Ottawa, with the support and collaboration of the MRN.

1.1 Purpose of study

The first objective of this study is to execute a complete description of the petrology, mineralogy and geochemistry of the Beattie syenite, more specifically, to determine and map the petrological units present in the Beattie syenite by describing the mineralogy and mineral chemistry of the principal rock-forming minerals in these units, to outline the geochemical evolution of the igneous units and the postmagmatic alteration of the rocks at the site.

The second objective of this study is to characterize the geochemical properties of the country rocks. These geochemical analyses were subsequently used to establish a tectonic

environment and to outline the post-magmatic alteration shared between the Beattie syenite an the country rocks.

An important contribution of this project is the preparation of an up-to-date geological map prepared with modern numeric mapping and geo-location methods, utilizing both recent field, geochemical and drill core data. This map at a scale of 1/7 500 accompanies this thesis (in both English and French; see Appendix B) and can also be consulted in the E-sigeom database of the MRN at `http://www.mrn.gouv.qc.ca/english/products-services/mines.jsp`. This is the first geological map of the Beattie syenite incorporating all its various units.

Chapter 2

Historical background

2.1 Mining history and ongoing activity

The Beattie syenite is host to 5 major ore bodies which were exploited from the early 1930s to the late 1950s. They are, in order of magnitude: 1) North orebody, 2) A orebody, 3) Donchester deposit, 4) Central Duparquet 2, and 5) Central Duparquet 1. Additionally, within the Beattie mine vicinity, there are a number of smaller ore bodies which follow the northwestern flank of the syenite (see Figure 2.1).

The North orebody is the largest deposit located along the northwestern contact between the Porcupine sediments and the Beattie syenite. It measures a length of 352 m to 518 m, a width 35 m to 65 m, extending to a depth of 490 m and dipping at 90° (Davidson and Banfield, 1944; Graham, 1954) (see Figure 2.1). The A orebody is situated ∼150 m southwest of the North orebody. This inverted V-shaped deposit is found at a depth between 150 m to 244 m, pitching at 45° to the east. Further east is the Donchester deposit hosted within the Deguisier andesite to dacite and lath syenite dykes, 60 m south of the syenite contact. This deposit extends along a strike length of 730 m with an average width of 1.9 m, dipping steeply, extending to a depth of 380 m (Graham, 1954; Bevan, 2011). Continuing southeastward is the Central Duparquet 2 deposit (also called the Dumico deposit), with mineralized zones extending for a strike length of 400 m and an average width of 2.0 - 2.3 m (Graham, 1954; Bevan, 2011). Last is the Central Duparquet 1 deposit located approximately 2 km southeast of the Donchester shaft. The extent of this deposit was never fully determined as it underwent limited exploitation.

Mr. John Beattie, a prospector in whose honour the Beattie mine and syenite was named, is credited with the discovery of gold in the region. He first began prospecting in the vicinity of Lac Duparquet in 1910 where he initially found gold in veins within metabasalts[1] on a small island in Lac Duparquet. An assessment of ore quantities at this first locality revealed that insufficient gold was present to warrant mining. Mr. Beattie later turned his attention to the east of Lac Duparquet where he later discovered the Beattie syenite. In 1923 he staked the ground upon which the principal ore deposits (North and A orebodies) are situated. The following year, Mr. Beattie let an option on the ground to Victoria Syndicate, a subsidiary of the Mond Nickel Company. During that summer, substantial trenching was done but results were discouraging and the option was put on hiatus. Exploration work eventually resumed and small discoveries were made from time to time. In 1927 a second option on the ground was given to the Consolidated Mining and Smelting Company of Canada. From 1928 to 1930 further trenching was done, along with several thousand meters of diamond drilling on a silicified zone along the northern contact margin of the syenite. Results were again discouraging and the option was abandoned in 1930. In the fall of that year, trenching work done by Mr. Beattie led to the discovery of what is known today as the 'North orebody'. He shortly re-optioned on the porphyry to D.H. Angus who in turn reoptionned it to Ventures Limited. The discovery was afterwards thoroughly drilled and a shaft was sunk. During the excavation of the shaft another orebody was accidentally discovered and named the 'A orebody'. Ore reserves of the North orebody were first estimated at 4 500 000 t with grades of 4.25 g/t Au were outlined above the 150 m level (Banfield, 1940).

Beattie Gold Mines Ltd. was founded in December 1931 with the necessary funding from Ventures Limited and the Nipissing Mining Company. After considerable development work, both above and underground, the foundations for a concentrator with a capacity of 725 t per day were laid. Additionally, a road as well as a railway were constructed from La Sarre, a small lumber town 40 km to the north. In 1933, the village of Duparquet was connected to the electrical grid permitting the operation of the mill. Plans were also started to build a cyanide extraction plant, as the ore concentrate was still being shipped to Tacoma, Washington for final processing. With the completion of the cyanide plant in 1934, the daily average of ore

[1]Because the rocks are so lightly metamorphosed to the greenschist facies, except near major faults, and to conform with practice in the area, the prefix meta- is omitted from hereon.

processed increased to 1 090 t. In 1936 the largest ball mill in metallurgical practice in the world (at that time) was installed, providing the processing plant with secondary grinding capacity. The following year, a large roasting plant was erected to treat the concentrated ore prior to cyanidation, finally eliminating the need to ship the ore, at considerable cost, to Tacoma. Additionally, an internal shaft was sunk from the 5^{th} (244 m) to the 9^{th} (427 m) level and was later deepened to the 13^{th} level (610 m). In 1941, the owners of the Beattie mine acquired the Donchester mine site.

The Central Duparquet area was first staked by George Kellar in 1924. This property was never fully exploited, being divided along 18 continuous claims (Hallé, 1990). It was successively held by the Duparquet Mining Co. Ltd., the Dumico Gold Corporation and last the Central Duparquet Mines Ltd. (Graham, 1954). The Central Duparquet mine operations were divided between two shafts. The first, to the east, was sunk in 1928 to a depth of 50 m. The second, to the west, was dug in 1937 to a depth of 305 m. The extracted ore was sent and processed at the Beattie mill. Interestingly, gold extracted from first Central Duparquet mine was in a free state, contained in quartz and subordinate carbonate mineral veins, while gold in the second Central Duparquet mine was comparable to all the other deposits, that is, associated with disseminated pyrite and arsenopyrite. The second Central Duparquet shaft was also connected to the Donchester and Beattie mines on the 6^{th} underground level (see Figure 2.1).

The Donchester mine was accidentally discovered during exploration work while connecting the second Central Duparquet and Beattie shafts. Subsequently, the mine opened in 1946, when a major shaft was sunk to a depth of 455 m with a total of 9 levels. Most mining activity occurred between the 5^{th} and 9^{th} levels. All the extracted ore was processed at the Beattie mill. Additionally, both the Donchester and Beattie mine workings were connected on two of the underground levels (3^{rd} and 6^{th}).

On the 15^{th} of June 1943 the Beattie mine suffered a disastrous cave-in in the North orebody where an underground stope broke through the surface. This in turn generated an earthflow where an estimated 764 500 m^3 of varved clays (Eden, 1964) filled the open pit and penetrated the underground workings. Restoration of the mine started immediately but was only completed in 1950. In 1944 mining ceased at the second Central Duparquet mine. The Donchester mine soon followed in 1956 due to ore exhaustion. The following year, the

Beattie mine also closed because of low ore grades, fixed gold prices, rising costs and shortage of labour and supplies which were all accentuated during the war years. Production details can be consulted in Table 2.1. Only with the help of a government mining aid program (the Emergency Gold Mining Act) was the Beattie mine able to sustain its operations in the post-war years.

The total production at the Beattie mine is estimated at 28.9 million grams of Au extracted from 8.4 million tonnes of ore material (Bevan, 2008), for an average grade of 4.04 g Au/t. The Donchester mine itself produced an additional 5.8 million grams of Au, processed from approximately 1.2 million tonnes of ore (Bevan, 2008) averaging 4.66 g Au/t (see Table 2.1). As for the second Central Duparquet mine, it processed 6 441 tonnes of ore at concentrations averaging 3.02 g Au/t (Bevan, 2008). Estimates for the Central Duparquet property are 2.9 million grams of Au, contained in 514 000 - 574 196 tonnes of ore (Hallé, 1990) at a calculated average of 4.65 - 5.10 g/t. Values obtained by R.B. Graham in 1954 from the second Central Duparquet mine while in production varied between 5.14 to 9.60 g Au/t.

After the closures, the sites remained dormant until the 1980s, except for minor surface exploration work in 1966. In 1980, SOQUEM Inc. renewed exploration within the Central Duparquet mines area by conducting exploration work and taking numerous geochemical samples. Afterwards, in 1987, the owners of the property conducted trenching, channel cutting and diamond drilling. Results showed the existence of mineralized structures within the Beattie property and defined many new gold-bearing zones along fracture zones. Tailings were also reassessed for additional extraction. In 2007, Clifton Star Resources, a Québec city based Company, acquired the property. Since then a total several million dollars have been invested on additional drilling, bulk sample testing of the tailings, cleaning up the Beattie mine site, and additional infrastructure to support the ongoing exploration program. The most recent development includes a joint venture with Osisko Mining Corporation, started in January 2010 and ended on June 17^{th} 2011 (Dupéré et al., 2011).

2.2 Environmental aspects

The Beattie mill processed the ore using the method of roasting arsenopyrite followed by flotation and cyanidation. Once the ore was roasted, the arsenic in the form of arsenic trioxide

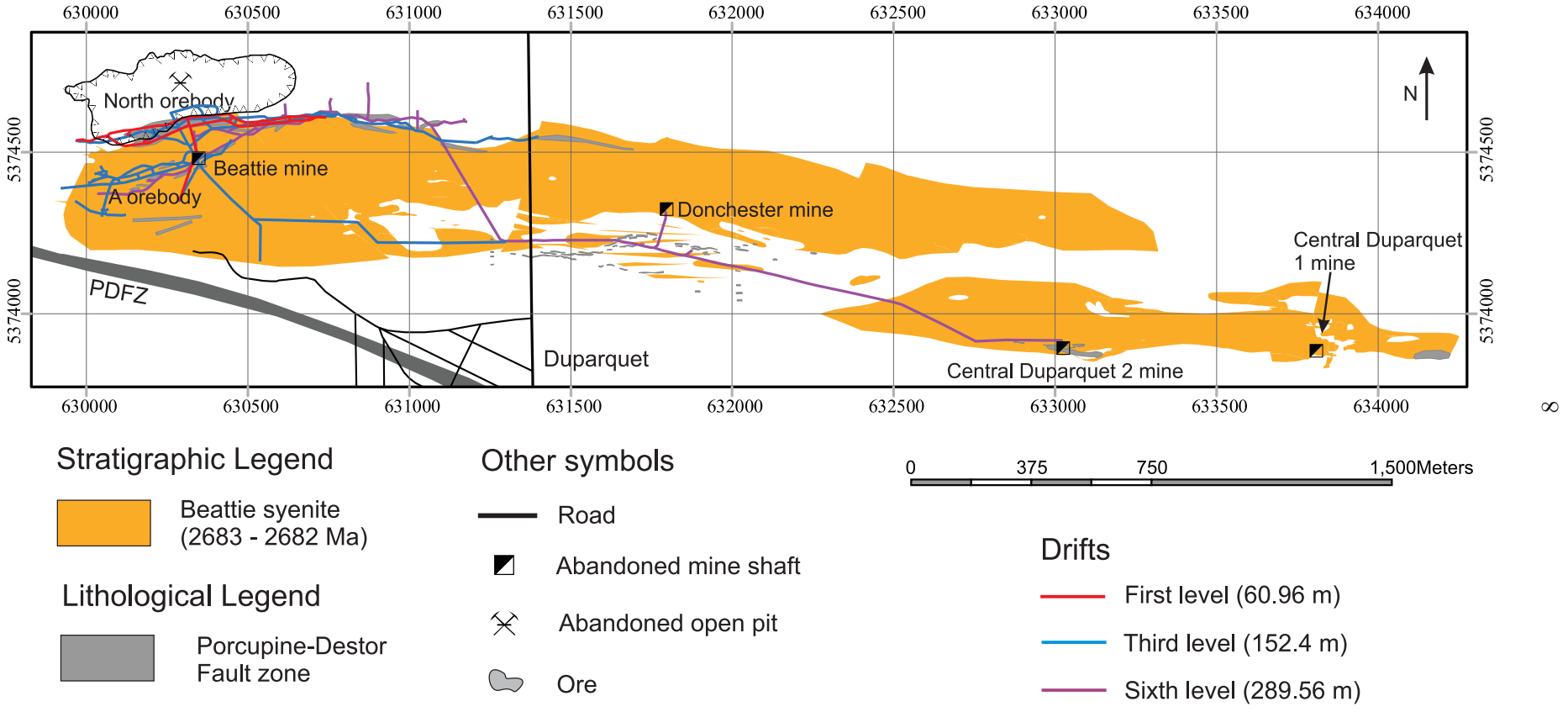


Figure 2.1 – Mines of the Beattie syenite. Included in this plan are the positions of historically exploited orebodies as well as the first, third and sixth level drifts.

Table 2.1 – Operations at the Beattie mine from May 1933 to April 1956 (Bevan, 2008). Data from 1943 to 1956 includes the ore processed from the Donchester mine.

Year	Tonnes milled	Grade g Au/t	Recovery %	g Au recovered	Net value ($)	Operating cost ($)	Net profit ($)
1933	131 512	7.129	74.98	702 876	582 234	389 281	183 953
1934	325 861	6.214	81.26	1 645 529	1 393 150	901 724	491 426
1935	395 315	5.672	76.99	1 725 589	1 625 947	1 013 050	612 897
1936	499 886	5.127	82.34	2 109 749	1 966 891	1 172 066	794 825
1937	526 639	4.918	79.38	2 054 882	1 994 486	1 219 941	774 545
1938	54 979	4.643	81.92	2 090 558	2 336 441	1351 836	984 605
1939	556 830	4.513	83.91	2 107 447	2 430 494	1 370 664	1 059 830
1940	517 454	4.753	81.87	2 222 779	2 720 831	1 404 676	1 316 155
1941	597 381	4.328	82.92	2 298 236	2 813 352	1 542 427	1 270 925
1942	596 582	3.734	89.95	2 011 431	2 463 310	1 544 330	918 977
1943	271 702	3.450	88.73	831 365	1 017 878	818 738	199 104
1944	113 035	4.180	87.78	414 889	507 946	922 360	-414 414
1945	Closed; clay slide June 16^{th} to Dec. 31^{th}, 1943 and Sept. 21^{th}, 1944 to June 30^{th}, 1946						
1946	97 451	3.676	77.56	277 754	310 325	555 200	-244 895
1947	221 625	5.459	84.56	1 009 992	1 128 635	1 546 988	-418 535
1948	419 119	4.263	86.89	1 551 752	2 316 164	2 049 533	166 631
1949	425 197	4.352	86.59	1 602 171	2 460 380	2 246 102	214 278
1950	553 746	3.779	84.35	1 764 314	2 743 165	2 417 086	317 079
1951	504 213	3.628	82.99	1 517 756	2 088 103	2 366 176	-278 073
1952	548 302	3.707	84.19	1 711 096	2 226 841	2 354 021	-127 080
1953	556 558	3.515	82.41	1 611 844	2 146 364	2 164 370	-18 006
1954	563 543	3.395	84.29	1 618 594	2 103 298	2 132 479	-29 181
1955	512 333	3.700	81.09	1 536 481	2 021 163	1 960 320	60 843
1956	91 127	3.621	97.42	321 423	415 101	400 700	14 401
Total	9 629 241	4.321	83.82	34 738 509	41 803 499	33 853 088	7 950 411

(As_2O_3) was collected. Approximately 2 250 tonnes of As_2O_3 were collected during the operation of the mill and the majority is contained on site in a large cement reservoir (Bevan, 2008). The rest is stored into metal and plastic drums inside 7 truck trailers on the property. A fence has been erected around the storage area encompassing the roaster and mill buildings, as requested by the MRN. A study on the possibility of arsenic contamination was performed by SNC-Lavalin for the owners. The conclusion was that any contamination is confined within the cement reservoir and containers. However, another study by the owners found the natural-overall arsenic levels within the local rocks and waters flowing to Lac Duparquet to be higher than the arsenic values inside the open pit, storage areas, the tailings pond, and Lac Duparquet (Bevan, 2008).

Monthly tests are being performed to measure the pH levels within the open pit and in the tailings pond by way of water monitors. The water pH within the tailings is generally between 8.7 and 9.5 (Bevan, 2008). This ensures the neutralization for the acidic effects generated by the sulphides.

2.3 Literature review and previous work

This section explores the previous work done by numerous authors as early as 1914. Considering the amount of exploration work done by exploration companies, Table 2.2 presents a chronological list of these reports in order to facilitate reading. Additionally, the reader can consult Table 2.3 which contains a list of historical lithological names with their current equivalence. Both tables can be found at the end of this section.

The first geological and topological reconnaissance publication of the Abitibi and Pontiac (including the Duparquet Township) was produced by A.E. Wilson in 1914. The publication is accompanied by a geological map illustrating the Duparquet township as composed of a small sedimentary lens surrounded by Kinojévis Group rocks (Abitibi volcanics). This lens, composed of slate and phyllite, starts on the north shore of Lac Duparquet and extends approximately 5 km to the east (strike: 100°). In 1918, Wilson published another geological report that included the Duparquet Township. It is important to note that neither reports nor the geological maps include the Beattie syenite.

In 1923, W.F. James reviewed the geological map of 1914, providing additional details regarding the western and southern areas of the Duparquet Township. However, his report did not include any additional information pertaining to the Beattie syenite.

Following was an article published by Douglas et al. (1924) which explored the possibility of continuation of the PDFZ in Québec. Seeing the continuation of geological structures, metamorphic conditions and porphyritic intrusions that are closely associated with gold mineralization, the authors strongly encouraged exploration in the Duparquet and Destor Townships.

In 1927, B.S.W. Buffam produced a complete map of the Duparquet township for the Geological Survey of Canada. This was the first to include the Beattie syenite, which measured a length of 4.8 km and a width of 1 km on the map. Included with this study was the first petrographic description of the syenite. A cursory account of the alteration minerals observed in thin section was also included. Buffam also documented the abundance of lath syenite dykes (small red porphyritic dykes) intruding the Kinojévis volcanic rocks (Keewatin rocks) and the Duparquet sediments (Timiskaming sediments). He further classified the Beattie syenite as pre-Timiskaming in age, which he deduced from the presence of syenitic blocks within the conglomerate. Buffam also reported the presence of the Lac Lépine syncline containing the

Duparquet sediments to the south.

Another geological reconnaissance by Cook et al. of the Geological Survey of Canada took place in 1931. The publication is accompanied by a geological map which also contains the Beattie syenite.

A revision of the northern half of the Duparquet township, completed by A.H. Lang in 1933, led to the production of a map and a report on the status of gold prospection in the Rouyn-Noranda and Matagami regions.

Following the discovery and beginning of operations at the Beattie mine, detailed geological work was conducted by J.J. O'Neill in 1933, 1934a and 1934b.

The first publication by O'Neill in 1933 includes the earliest detailed geological map of the Beattie mine site. This report established the age relationships between the regional rocks and introduces the term bostonite, a body located to the southeast of the Beattie mill which seems to include the lath syenite dykes, the Deguisier rhyolite and later, the quartz-feldspar porphyry located north of the Beattie syenite. O'Neill also provided the first size estimation of the syenite body, which measured 460 m wide and 700 m long, therefore restricting it to the Beattie mine site. After detailed field and petrographic observations, O'Neill concluded that the bostonite unit was a product of multiple intrusions and therefore hypothesized that the Beattie syenite would be similar. A structural analysis of the syenite body revealed 2 major and a minor set of cataclastic fractures which O'Neill classified as separate events. The first of the major sets possesses a strike of 080° with the second at 290°. The minor set was noted to have an orientation of 335° to 010° and 077° to 290°. When conducting petrographic work, O'Neill noted the presence of feldspar, hematite, to which he attributed the pink colouration of the syenite, and chlorite, calcite, sericite, titanite, biotite, epidote and minor tourmaline as alteration minerals. This assemblage led O'Neill to conclude that regional metamorphic conditions were of low- to medium-grade. In addition, he observed that the Au-mineralization was strongly associated with sulphide minerals (pyrite and arsenopyrite) which are abundant in the fractured zones. Associated with these zones are multiple pegmatitic and aplite veins, commonly observed in the North orebody. When mapping to the east, some confusion arose when a dyke of lath syenite (feldspar porphyry) was found in the Duparquet sediments, prompting the hypothesis that an injection of syenitic magma had occurred in the polygenetic Duparquet conglomerate. To supplement his hypothesis, O'Neill noted that there

was minimal deformation in the dyke when compared to rocks elsewhere in the region. This resulted in the misinterpretation of the syenite's age as post-Timiskaming.

In 1934a, O'Neill conducted additional field work, expanding the description of each rock unit. He classified the quartz-feldspar porphyry (bostonite) as younger with a similar composition as the syenite, only differing in texture, being chert-like when aphanitic. Further misclassifications include the gabbro as post-Timiskaming in age, concluded from a lack of major structural deformation. With continued exploration at the Central Duparquet mine shafts, O'Neill discovered the porphyritic Central Duparquet syenite unit, naming it the bostonite porphyry. O'Neill thought of joining it with the Deguisier rhyolite and syenitic lath dykes (bostonite) found at the Beattie mine site. Furthermore, he divided of the polygenetic conglomerate into 2 units: 1) the older, deformed and with syenitic clasts, and 2) the younger, undeformed and without the clasts. Syenitic clasts within the older unit were incorrectly interpreted as injections of syenitic magma into the conglomerate. O'Neill considered this magmatic injection to have accompanied the Au-mineralization. Metamorphic mineralogical additions include an added stage of silicification, a 3^{rd} generation of albite, with axinite in the vugs of the quartz-feldspar porphyry. From a mineralization point of view, O'Neill associated Au with the porphyritic Central Duparquet syenite unit (bostonite porphyry) and was the first to describe the existence of free gold associated with tetrahedrite, chalcopyrite and sphalerite in quartz veins at the first Central Duparquet mine.

In a brief report in 1934b, O'Neill developed a detailed description of the ore paragenesis in relationship with the hydrothermal minerals. In his descriptions he interprets the alteration to have begun with magnetite and chlorite, followed by pyrite then arsenopyrite (as it partially replaces pyrite), with the last two being associated with the Au-mineralization. The last stages of alteration consist of sericite followed by carbonate minerals and quartz. Finally, he also noted the presence of an erosional unconformity at the contact of the Kinojévis basalt with the Duparquet sediments.

In 1935 a report on the Beattie mine was written by C.H. Jr. Hopper. He suggested that the Beattie syenite was older than the Duparquet sediments, but maintained that the porphyritic Central Duparquet syenite unit (bostonite porphyry) intrusion was the youngest, associating it with the Au-mineralization. Hopper considered that another intrusion the 'grey syenite porphyry', a hydrothermally altered portion of the Beattie syenite, to have been the

source of mineralization at the Beattie mine. A structural study of the syenite body showed that it pitches 45° east and dies out at depth. The report indicated that the ore is hosted by andesite (as seen by pillows) with bands of sediments and trachyte. Hopper also divided the ore into several types: 1) vein breccia, 2) dyke breccia, 3) dark schist, 4) sericite platy type, 5) hydrothermally altered porphyritic Beattie syenite (Grey glass) and 6) hybrid. With the common occurrence of the hydrothermally-altered porphyritic Beattie syenite (grey glass), he hypothesized the mineralization occurred at shallow depths.

Another mine report was published by S.C. Davidson in 1938. He remapped the entire mine site and relogged several cores, providing additional details on the displacement along the main faults and shear zones and dividing the Porcupine sediments for correlation purposes. Davidson remarked that the Porcupine sediments are much more abundant underground and that there are pre- and post-ore faults.

In 1939, J. Tuttle (the mine superintendent) published in great detail his exploration of the spiral stoping system of the Beattie mine. He also discussed the operating costs and working conditions at both the open pit and the underground mine.

Several internal reports discussing the procedures and breakthroughs in ore extraction were produced in 1935; 1936a; 1936b; 1937; 1939 by Archibald et al.. In the latest published article in 1939, an account of laboratory experiments used in the ore separation were reported with great detail. Authors also discussed the difficulty in ore extraction due to the high arsenic content. Through experimentation, they argue about the possibility of doing experiments to see if Ag could be recovered as a byproduct.

In 1940, H.M. Bannerman recognized an association between the shear faults and the carbonated and silicified saturated zones. He was also the first to give a name to the polygenetic conglomerate, the Duparquet sediments.

After the opening of the underground workings, A.F. Banfield (1940) worked, as part of his Ph.D. thesis, to document in detail the geology of the syenite, its petrogenesis, structure, composition and economic implications by means of field work, chemical analyses and foremost underground documentation. First, he described the syenite as a comet shaped body possessing pitching 45° east. According to Banfield the syenite measures a length of 4.8 km and a maximal width of 460 m which progressively thins and fingers out. Banfield correctly reclassified the syenitic lens (bostonite porphyry) mentioned by O'Neill (1933) which hosts the

Central Duparquet mines as a separate lens of comparable size and shape as the lens hosting the Beattie and Donchester mines. Another important reclassification involves the Duparquet conglomerate (porphyry conglomerate) from O'Neill (1934a) as part of the Timiskaming, suggesting that the syenite is in fact pre-Timiskaming. This led Banfield to hypothesize two petrogenetic scenarios for the syenite: 1) it intruded into the Kinojévis (Keewatin) basalt or, 2) it intruded between the Kinojévis (Keewatin) basalt and already present Timiskaming sediments. However, much controversy remained as whether the syenite fragments found in the conglomerate were to be interpreted as clasts, or were resultant of a magmatic intrusion. In the end the second hypothesis prevailed. From the O'Neill (1933) hypothesis that the Beattie syenite was the product of multiple intrusive episodes, Banfield demonstrated it by employing petrographic and mineralogic means. This led to the recognition of several units and the proposition a common origin. These units are: 1) porphyritic Beattie syenite (Syenite porphyry) and 2) lath syenite (Lath porphyry) both in the vicinity of the Beattie mine, 3) porphyritic Central Duparquet syenite (Old porphyry), 4) megaporphyritic syenite (Plum porphyry) and 5) lath syenite (Porphyritic porphyry) encountered at the Central Duparquet 2 mine. With further observations of the contacts Banfield hypothesized that the time between these intrusive events was quite short. Mineralogically, Banfield noted a similarity between the Beattie syenite to a typical syenite with the exception of anorthoclase as the dominant feldspar. He also proposed a detailed sequence of alteration, starting with a potassic alteration (orthoclase dykes) which was followed by a silicification accompanied by the Au-mineralization, and finally a carbonatization. He further proposed that the Au-rich hydrothermal fluids originated from the intrusive syenitic magma body. While at the Beattie mine he reported that only 32% of the ore was associated with the syenite, while the remaining 68% was in the highly altered Porcupine sediments and Kinojévis pillow lavas. Having seen the proportions, he hypothesized that the mineralization resulted from selective replacement depending on the chemical and physical characteristics of the host rocks. These characteristics were also partially controlled by the Beattie fault, a vertical shear fault zone running parallel to the northern syenite contact. The timing of the Au-mineralization was thought to be post-Timiskaming, closely related to the syenite intrusion, despite observations at the Central Duparquet 2 mine where the ore crosses the megaporphyritic syenite unit (plum porphyry) and one lath syenite dyke (lath porphyry) at the Beattie mine. Banfield goes on describing each orebody associated with the Beattie

syenite and remarks that they are all of the disseminated pyrite type. Banfield provided a complete list of minerals associated with the Au-mineralization including: sulphur, pyrite, arsenopyrite, magnetite, ilmenite, native gold, electrum, chalcopyrite, molybdenite, galena, sphalerite, marcasite and an argentiferous arsenical mineral.

In 1944 S. Davidson and A.F. Banfield produced a revisited model of the Beattie Au-mineralization. The authors suggested that the ore deposit is closely associated with the brecciated Kinojévis (Keewatin) basalt, Porcupine sediments (Keewatin tuff) and syenite porphyry. Additional geochemical data were also provided and with them, new estimated revealing that 35% of the ore is in a free state, while the remaining 65% is associated with pyrite and arsenopyrite. Finally, after studying structural and mineralization aspects, the authors proposed that the mineralization is mesothermal or possibly epithermal.

A brief update of the Beattie mine production, structural geology and mineralogy was published a few years later by S. Davidson in 1948.

In 1954, B.R. Graham produced a geological map and report of the Hébécourt, Duparquet and Destor townships. The geological map included, at the time, the most comprehensive representation of the Beattie syenite, including several of its satellite intrusions. On the map, the syenite possesses a east-west orientation, measures a length of 4 km with a width between 305 - 460 m and a plunge of nearly 90°. Furthermore, in common with Banfield (1940), Graham accepted and elaborated on the syenite's division into units. They are (chronologically): 1) porphyritic Beattie syenite (porphyry syenite), 2) megaporphyritic syenite (plum syenite), and 3) lath syenite. He further subdivided this last unit into 2 sub-units: 1) the A set and 2) the B set on the basis that the A set are cut by B set dykes observed at the Donchester mine. Based upon detailed field observations Graham chronologically classified the syenite intrusion to have occurred simultaneously with the emplacement of the Timiskaming sediments and the lath syenite dykes. Graham also studied the structural geology, naming the local faults and concluding that there were 3 folding events with 2 main deformation events. The deformation events are: 1) pre-intrusive with abundant E-W shearing, and 2) post-intrusive with minimal NE or NW shearing. Further conclusions derived from structural studies were that the various regional porphyries were intruded into weakened zones created by the PDFZ. Following mineralogical observations of the volcanics, Graham concluded that the regional metamorphism corresponds to a low grade. He also discussed the abundance of alteration

minerals wherein: carbonate minerals dominate the regional mafic rocks, sericite is common in intrusive plutons and chlorite is usually found both in mafic and intermediate rocks. Finally, Graham provided a revision of the geology of the Beattie and Donchester mines.

As the Beattie, Donchester and Central Duparquet mines ceased their operations, so did the documentation. It wasn't until 1974 that P. Boivin wrote his Ph.D. thesis with the aim to review the petrography, stratigraphy, structure and metamorphism of the units in the Hébécourt, Duparquet and Destor townships. His most notable contributions were the characterization of the PDFZ as a reverse fault doubled with a dextral slip that was active over long periods, and the separation of the Kinojévis into 3 formations (chronologically): 1) felsic volcanics of the Hunter mine formation, 2) tholeiitic basalts and andesites of the Deguisier formation, and 3) mafic volcanics and porphyry of the Lac Lanaudière formation.

The next Ph.D. study was by M. Rocheleau in 1980 which focused on the stratigraphy and sedimentology of the Duparquet conglomerates and concluded that they were of fluvial origin.

Renewed economic interest in the Beattie syenite area started in the 1980s with several reports of exploration in the immediate and eastern areas of the Central Duparquet mines. These reports as well as many others can be consulted through the E-Sigeom (Examine) database at `http://www.mrn.gouv.qc.ca/english/products-services/mines.jsp` or can be acquired via SEDAR at `http://www.sedar.com/`.

In the 1990's the MER launched a project to update the geological map of the Destor and Duparquet townships. Consequently, from 1990 until 1994 J. Goutier and S. Lacroix, both MER geologists, conducted numerous field excursions. As a result, in 1992 a publication by J. Goutier and S. Lacroix presented a geochemical, petrological, structural and chronological classification of the townships. Based upon geochemical analyses of rocks form the area, Goutier and Lacroix produced the first classification of the Deguisier Formation concluding that it is composed of tholeiitic basalt and andesitic basalt, with sparse dacitic and rhyolitic tuffs. Furthermore, they subdivided the sediments into the Porcupine Group (north of the PDFZ) and the Kewagama Group (south of the PDFZ). Petrologically, they upheld the units composing the Beattie syenite, with the exception of the recombination of the two lath syenites divided by Graham (1954). Structurally, the presence of Porcupine sediments west of the syenite led Goutier and Lacroix to hypothesize that they were the result of late imbrication by dextral slip faulting. Older structural studies of the Porcupine sediments place it as younger

than the Blake River, however with recent U-Pb dating they correct it as post-Blake River (Davis, 2002). Goutier and Lacroix also resolved the confusion in age of the Beattie syenite by re-examining field relationships, placing it at the end of the Kinojévis, prior to the erosional unconformity leading to the Duparquet sediments. Finally, the authors proposed a tectonic paragenesis for rocks of the townships where: 1) the great folds (i.e., Abijévis syncline) were formed, followed by 2) local N-S extension occurred during the formation of the Duparquet basin. Next was 3) the regional compression of the region, followed by 4) dextral slip faulting that affected the PDFZ, and finally 5) the N-S compression with late NE-NW faulting.

In 1992, D. Beaudry conducted a structural study of the PDFZ between the towns of Duparquet and Destor. By observing the styles of deformation on both sides of the fault, D. Beaudry concluded that the PDFZ is the result of N-S shortening accompanied by folding and dextral slip faulting. The faulting in turn initiated the opening of the Duparquet basin.

Next, in 1996, Mueller et al. conducted the first U-Pb zircon dating of the Beattie syenite, specifically the megaporphyritic unit, which yielded an age of 2681.5 $\pm$1 Ma.

Several field excursion reports were subsequently published. The two most commonly cited are by J. Goutier (1996) and F. Robert (1997). Both guides contain detailed descriptions of the units of the Beattie syenite. The guide by Robert also presents the geological characteristics of syenite-associated disseminated gold deposits in the Abitibi, a precursor a subsequent paper by Robert (2001). In this article, Robert proposes a mineralization model of the ore bodies relative to the syenite intrusions. This model hypothesizes that the resulting ore bodies are different components part of a larger hydrothermal system which was centred on composite syenitic stocks.

In 2005, a publication from the MRNF by Legault et al. focused on the economic aspects along the PDFZ in Québec. Legault et al. (2005) provided a petrogenetic model and age estimations along with the recognition and division of 6 mineralization types. They are: 1) quartz and carbonate veins, 2) disseminated sulphides associated with porphyric intrusions, 3) epithermal veins, 4) silver-rich veins, 5) disseminated sulphides associated with bleaching, and 6) sulphides associated with volcanic massive sulphide (VMS) deposits.

In 2004 - 2005 a M.Sc. project was launched at the University of Ottawa in partnership with the MRNF. S. Patry initially accepted the project and conducted additional field work, collecting several samples for geochemical analyses and thin sections. Patry showed the dis-

tribution of selected major elements in the Beattie syenite and its associated host rocks using the software package MapInfo. He also demonstrated by using rare earth elements (REE) patterns that the Beattie syenite belonged to the calc-alkaline suite and thus likely originated from continental arc magmatism. These early findings were presented at the Geological Association of Canada (GAC-MAC) conference in Halifax in 2005 (Patry, 2005). Included with the presentation was a minor modification of the syenite units to which the megaporhyritic unit (plum porphyry from Banfield (1940); Graham (1954); Goutier and Lacroix (1992)) was renamed the glomeroporphyric unit. Unfortunately, Patry abandoned the project in 2005.

Next, in 2007, David et al. conducted another U-Pb zircon dating of the megaporphyritic unit, which yielded an age of 2682.9 ±1.1 Ma.

An article was published by Legault and Lalonde in 2009 in which they explored the existence of a relationship between the Au-mineralization and alkaline intrusions. The authors come to the conclusion that while not all syenites are hosts to Au deposits, the probability of mineralization increases with the proximity (< 2 km) to major fault zones such as the PDFZ and the Larder-Lake fault and Cadillac fault (LLF and CF). Legault and Lalonde (2009) also include a means to discriminate fertile from non-fertile intrusions. The characteristics of mineralized intrusions are: 1) small intrusion, size < 3 km^2, 2) elongated form with an E-W orientation, 3) porphyritic texture, 4) locally brecciated and 5) non-magnetic. Features for a sterile intrusion are: 1) a sub-circular form, 2) equigranular, trachytic texture, and 3) magnetic.

Last, another M.Sc. project with a focus on the Au-disseminated mineralization style was launched in 2011 at the Université du Québec à Montréal. Preliminary findings presented the GAC-MAC conference in St John in 2012 (Bigot, 2012) indicate that the metallic assemblage of the Beattie syenite is polyphased, consisting in 1) a primary phase enriched in iron-titanium, 2) several subsequent sulphidation phases, and 3) a late silica-enriched hydrothermal phase which remobilized gold and is marked by cataclasis.

Table 2.3 – Current equivalence of old geological terms

Author	**Year**	**Old terminology**	**Current equivalence**
Wilson, W.J.	1914	Abitibi volcanics	Kinojévis basalt
Wilson, W.J.	1914	Slate and phyllite	Duparquet polygenetic conglomerate and wacke

Buffam, B.S.W.	1925	Keewatin volcanics	Kinojévis basalt and gabbro
Buffam, B.S.W.	1925	Porphyry conglomerate	Duparquet polygenetic conglomerate and wacke
Buffam, B.S.W.	1925	Red feldspar porphyry*	Porphyritic Beattie syenite unit
Buffam, B.S.W.	1925	Small red porphyry dykes*	Lath syenite dykes
Buffam, B.S.W.	1925	Timiskaming conglomerate and arkose	Duparquet polygenetic conglomerate and wacke
Buffam, B.S.W.	1925	Timiskaming slate	Duparquet polygenetic conglomerate and wacke
Davidson, C.S.	1927	Speckled schist	A particular bed in the Porcupine sediments
O'Neill, J.J.	1932 - 1934	Augen porphyry	Highly schistose porphyritic Beattie syenite dykes intruding into Kinojévis basalt/Porcupine sediments
O'Neill, J.J.	1932 - 1934	Bostonite	Lath syenite dykes and Kinojévis rhyloite; porphyritic Beattie syenite unit (Beattie mine)
O'Neill, J.J.	1932 - 1934	Green rock, rhyolite, andesite, lath porphyry*	Kinojévis rhyolite
O'Neill, J.J.	1932	Green schists*, greenstone schist,	Kinojévis basalt
O'Neill, J.J.	1932	Hybrid porphyry*	Highly sheared (carbonate-sericite) porphyritic Beattie syenite dykes intruding into Kinojévis basalt/Porcupine sediments
O'Neill, J.J.	1932 - 1934	Keewatin schist*	Kinojévis basalt
O'Neill, J.J.	1932	Massive porphyry*	Porphyritic Beattie syenite unit
O'Neill, J.J.	1932	Porphyry schist*	Highly schistose poprhritic Beattie syenite unit dykes intruding into Kinojévis basalt/Porcupine sediments
O'Neill, J.J.	1932	Sericite schists*	Sericitized porphyritic Beattie syenite unit
O'Neill, J.J.	1932	Substitution porphyry*	Porphyritic Beattie syenite dykes intruding into Kinojévis basalt/Porcupine sediments
O'Neill, J.J.	1933	Porphyry conglomerate*	Duparquet polygenetic conglomerate
O'Neill, J.J.	1933	Rhyolite (seen in large Central Duparquet)	Kinojévis rhyolite
O'Neill, J.J.	1934	Schisted tuff	Porcupine sediments
O'Neill, J.J.	1934	Bostonite porphyry	Porphyritic Central Duparquet unit (east)
O'Neill, J.J.	1934	Serpentine porphyry	Both porphyritic Beattie syenite unit and Kinojévis rhyolite with abundant sericite
Hopper, C.H. Jr.	1935	Grey, altered, syenite porphyry	Heavily hydrothermally altered porphyritic Beattie syenite in the mine or Kinojévis rhyolite

Hopper, C.H. Jr.	1935	Grey glass	Heavily hydrothermally altered porphyritic Beattie syenite unit in the mine
Banfield, A.F.	1940	Grey massive	Heavily hydrothermally altered porphyritic Beattie syenite unit in the mine
Banfield, A.F.	1940	Porphyry conglomerate	Duparquet polygenetic conglomerate
Banfield, A.F.	1940	Felsite	Hydrothermally bleached Kinojévis basalt
Banfield, A.F.	1940	Older gabbro dykes	Gabbro
Banfield, A.F.	1940	Dumico old porphyry	Porphyritic Central Duparquet syenite unit
Banfield, A.F.	1940	Dumico plum porphyry	Megaporphyritic syenite unit
Banfield, A.F.	1940	Dumico porphyritic porphyry	Lath syenite dykes
Banfield, A.F.	1940	Syenite porphyry	Porphyritic Beattie syenite unit
Banfield, A.F.	1940	Coarse grained, red syenite porphyry	Porphyritic Beattie syenite unit
Banfield, A.F.	1940	Fine grained, red syenite porphyry	Porphyritic Beattie syenite unit
Banfield, A.F.	1940	Red, altered, syenite porphyry	Porphyritic Beattie syenite unit
Banfield, A.F.	1940	Grey altered syenite porphyry	Porphyritic Beattie syenite unit
Davidson, S., Banfield, A.F.	1944	Blue breccia	Hydrothermally altered and brecciated Kinojévis basalt
Davidson, S., Banfield, A.F.	1944	Breccia ore	Mineralized Kinojévis basalt
Graham, R.B.	1954	Syenite porphyry	Porphyritic Beattie syenite unit
Graham, R.B.	1954	Plum porphyry	Megaporphyritic syenite unit
Graham, R.B.	1954	Lath porphyry	Lath syenite dykes
Graham, R.B.	1954	Porphyritic porphyry	Lath syenite dykes
Graham, R.B.	1954	Porphyry conglomerate breccia	Duparquet polygenetic conglomerate
Patry, S.	2005	Glomeroporphyric unit	Megaporphyritic syenite unit

* = translated from French

Table 2.2 – Exploration reports on Beattie

Author	Year	Title	Company	E-Sigeom or other
Gagnon, P.	1981	Rapport de géochimie d'humus et de lithogéochimie: Projet Dalembert	SOQUEM Inc.	GM 37714
Praisé, JC.	1981	Rapport sommaire des travaux effectués sur le groupe GR10-15: Projet Duparquet, Canton Duparquet, Québec	Resources Gold Fields Canada Ltd.	GM 38945
Capus, G.	1988	Projet Porcupine-est: Rapport de fin de saison	Cogema Canada Ltd.	GM 48562
Halle, L.	1990	Campagne d'exploration 1989 - 1990	Exploration Fieldex Inc.	GM 49711
Bardoux et al.	1990	Compilation géologique, structurale et géophysique de la zone de faille Porcupine-Destor sur les propriétés Porcupine Ouest et Est canton d'Hébécourt de Duparquet	Cogema Canada Ltd.	GM 49436
Gadoury, M.	1995	Rapport de forages: Propriété Central Duparquet	Exploration Fieldex Inc.	GM 53555
Roy, P and Roy, F.	1997	Rapport des traveaux d'exploration effectués de la propriéte Duparquet	Exploration Maude lake Ltée	GM 56356
Archibald, F.T.	2008	2008 diamond drilling program	173714 Canada Inc.	GM 64140
Bevan, P.A.	2008	Technical report on Beattie-Donchester Gold mine property, Duparquet Township, Quebec	Clifton Star Resources	SEDAR
Bevan, P.A.	2009	Technical report on Beattie-Donchester Gold mine property, Duparquet Township, Quebec	Clifton Star Resources	SEDAR
Anonymous	2010	Diamond drill hole log, Dumico Project	173714 Canada Inc.	GM 65358
Bevan, P.A.	2011	Technical report on Donchester Gold mine property, Duparquet Township, Quebec	Clifton Star Resources	SEDAR
Rioux, L.	2011	Technical report on the Duparquet Properties (Beattie, Donchester, and Central Duparquet)	Osisko Mining Corporation and Clifton Star Resources	GM 65858

Chapter 3

Field and analytical methods

3.1 Field methods

Several older geological maps of the Beattie syenite were produced from the 1930s to 1950s, most notably of J.J. O'Neill in 1933 and by R.B. Graham in 1954. These maps are also accompanied by geological reports (see Chapter 2) which provide the rock descriptions. As a base for the update of the geological map produced in this thesis, the 1954 map produced by Graham was used. There are many more maps available, however most are unusable because of missing reference points (or coordinates), author(s), year, etc, and therefore serve only a qualitative purpose in this thesis.

The Beattie syenite was thoroughly mapped from 1990 to 1994 by J. Goutier, a geologist at the MRN by using both aerial photographs and GPS (UTM NAD 83) for greater accuracy. Outcrop data were recorded in the form of geofiches which were subsequently compiled in the ministry's geological database named E-Sigeom. This database can be accessed at the url: `http://www.mrn.gouv.qc.ca/english/products-services/mines.jsp`. The original geofiches are also kept at the Rouyn-Noranda office[1] and can be consulted upon request.

Field work continued in 2002 and 2003 by M. Legault, another geologist at the MRN who revisited and added detail to certain sections of the syenite, especially Au-mineralized areas. In 2004 S. Patry, a summer student hired by the MRN revisited most of the Beattie syenite outcrops, providing additional geofiches which were subsequently added to the Sigeom database. Field work was also performed by the author in 2008, 2009 and 2010. During

[1] 70 avenue Québec, Rouyn-Noranda (Québec), J9X 6R1

excursions all of the syenite was revisited with emphasis having been placed on the new clearings produced by Osisko Mining Corporation and Clifton Star Resources Inc. Positioning of the outcrops by M. Legault and S. Patry was recorded using a Garmin GPS38 GPS (UTM NAD 83) with an accuracy between ± 5 - 10 m. Positioning by the author was performed using a Garmin GPSMap 76 GPS (UTM NAD 83) with a presumed accuracy of ± 3 m.

In addition to geofiches, several syenitic and host rock samples were collected in 1990 and 1994 by Jean Goutier, in 2002 and 2003 by M. Legault, in 2004 by S. Patry, and finally in 2008 and 2010 by the author. The collected samples include every syenitic body encompassing almost every outcrop with multiple samples for the complex regions (see Appendix D for positions of samples collected for geochemistry). Collected samples were then cleaned of any surficial alteration with a diamond saw in preparation for geochemical analyses, as well as for the production of thin sections. A small portion of the specimen was additionally cut and kept in storage (Rouyn-Noranda or University of Ottawa) for future reference.

Furthermore, field data were obtained from SOQUEM Inc. This included geological maps and geochemical analyses. Numerous surveys in the eastern portions of the study area were conducted by P. Gagnon (1981). These surveys included soil and lithogeochemical sampling. Subsequently, detailed geological maps were constructed from both field and geochemical data and have been successfully georeferenced.

Geochemical analyses and detailed core logs were also obtained from Osisko Mining Corporation and Clifton Star Resources Inc. Positioning of geochemical samples was done with a Garmin GPSMap 76 GPS (UTM NAD 83) with an accuracy of ± 3 m. Drill holes were positioned (UTM NAD 83) by professional land surveyors with an accuracy of ± 5 cm. Azimuth, plunge and length of each bore hole was also recorded by the land surveyors and presented with the individual core descriptions. Detailed descriptions of each specimen were produced by several geologists from both Osisko and Clifton Star. As a result a total of 701 cores totalling a distance of 203.15 km were described. Additionally, photographs of core specimens ($\sim$ 50 m in each picture) were taken both under dry and wet conditions. The author was capable of consulting some of these cores to provide the dimension of depth. Cores produced prior to 1987 were not consulted, nor included in this thesis after several issues concerning their precise location arose. Since the termination of the partnership between Clifton Star and Osisko, core samples have been transferred to site of the old Beattie mill, at Duparquet, Québec and can

be consulted upon request.

Additionally, core logs from Cogema Canada Limited (Capus, 1988), Ressources minières Forbex Inc. (Hallé, 1990) and Exploration Fieldex Inc. (Gadoury, 1995) were included in the study. There is only one core specimen provided by Cogema and it falls far to the south east of the study area. The name of the geologist who carried out this description was regrettably not provided. Forbex produced a total of 10 cores principally in the east of the study area. Core descriptions were performed by L. Hallé, the author of the accompanying exploration report, who also recorded their azimuth, plunge and depth. Finally, Fieldex produced 6 bore holes also in the east. Cores were described by J. Gadoury, the author of the accompanying exploration report, who also recorded their azimuth, plunge and depth. All these cores were successfully repositioned with surface maps provided with the reports. They were subsequently georeferenced and included in the updated geological map.

3.2 Description of the geological map

A major component of this thesis relies on the production of an updated geological map of the Beattie syenite. As a result an accompanying geological map of the study area (in both English and French) can be found in Appendix B. This map can also be consulted or obtained through the E-Sigeom (Examine) database[2].

The original geological map was provided by the MRN which was based on the 1954 map produced by Graham. Expanding on it, recent geological field observations by J. Goutier (1990-1994), M. Legault (2002-2003), S. Patry (2004) and by the author (2008-2010) were added. Core logs from Fieldex (1995), Forbex (1990), Cogema (1988), including all of the Clifton Star and Osisko (1987-2010) (Archibald, 2008; Anonymous, 2010; Rioux, 2011) were also added to the map. Geochemical data from Banfield (1940), Davidson and Banfield (1944), SOQUEM (Gagnon, 1981), Gold Fields Resources Canada Ltée (Praisé, 1981), Cogema (Capus, 1988), MRN (1990-2004) (available through E-Sigeom), Clifton Star and Osisko (Rioux, 2011) and by the author (2009-2010) were also plotted.

All data were subsequently compiled using ArcGIS version 9.2 and more recently version 10.0. Existing roads, buildings (old mine operations including shafts) and the open pit were

[2] `http://www.mrn.gouv.qc.ca/english/products-services/mines.jsp`

added and left unmodified from the original MRN map.

3.2.1 Limitations and errors

The geological map of the Beattie syenite includes some older geochemical data obtained from private exploration companies. These data were corrected to the best possible fit using recent field observations and geochemical comparisons. However, some geochemical samples from SOQUEM Inc. as well as Gold Fields Resources Canada Ltd. could not be identified or their specific coordinates could not be retraced. These samples are included in Appendix D but have not been used in this thesis and the geological map.

3.3 Microscopy

Polished and conventional petrographic thin sections were examined using both reflection and transmission polarizing light microscopy using either a Nikon E600 or Olympus BX51 microscope. Photomicrography was done either with a Nikon E600 microscope equipped with a CoolPix 995 digital camera or an Olympus BX51 microscope with a QImaging digital photohead.

3.4 Electron microprobe

The chemical composition of several minerals were obtained by wavelength-dispersive X-ray spectrometry using the Camebax MBX electron probe microanalyser at Carleton University. Minerals analyzed include feldspars, sericite, actinolite, titanite, epidote, chlorite and carbonate minerals. The beam operating conditions on the instrument were 15 kV of bias voltage; 20 nA beam current and counting times from 15 to 60 seconds. Background measurements were made at 50% peak counting time on each side of the peak. Raw X-ray data were converted to elemental weight % (wt%) with the Cameca PAP matrix correction program. Oxide weight percents were calculated, assuming the most common valence state for the element analyzed. Analyses are accurate to 1-2% relative for major elements (>10 wt%), 3-5% relative for minor elements (0.5 to 5.0 wt%). Qualitative compositions were also obtained by energy-dispersive X-ray spectrometry on the same instrument to confirm mineral identifications and determine the presence or absence of major and trace elements prior to quantitative analysis.

3.5 Geochemistry

3.5.1 Older analyses

The first geochemical analyses of the Beattie syenite were published by A.F. Banfield in 1940. A total of 13 underground samples where analyzed from major oxides and occasionally Au, Ag, As and Cu. An additional 3 analyses of underground specimens were later published S.C. Davidson and A.F. Banfield in 1944. Analyses were conducted at the Beattie mill research centre by F.R. Archibald and P. Jacques. Alkali analyses were separately conducted by Ledoux & Co., New York. Only one sample of the Beattie ore was assessed Milton Hersey Co., in Toronto. Unfortunately, no quantitative accuracy errors or detection limits were provided with the analyses. With georeferenced maps of the underground workings (both of Beattie and Central Duparquet 2 mines), the author was successfully able to attribute coordinates for each analysis, within a reasonable margin of error ($\pm$ 10 m). These analyses were only utilized as a qualitative addition to this thesis as no sample of the mineralized ore can presently be obtained.

3.5.2 SOQUEM Inc.

A total of 103 lithogeochemical samples were published by P. Gagnon a geologist at SOQUEM Inc. in 1981. Analyses were performed at Métriclab of Ste-Marthe-sur-le-lac, Québec. The majority of major and minor elements were analyzed via atomic absorption spectroscopy (AAS), with the rest analyzed by X-ray fluorescence (XRF). Volatiles were either measured by weight loss after ignition or by gavimetric methods. Unfortunately, no detection limits were provided with these analyses and since then, the lab has gone out of business.

Numerous analyses of humus for As, Hg including Au were done at the X-ray Assay Laboratories Ltd. in Don Mills, Ontario. As and Au were analyzed by neutron activation (NAA) and Hg via a chemical method (CM). Au was also analyzed along with the lithological samples at Métriclab, Québec. To avoid confusion, only lithogeochemical values were kept in this project. As and Hg results have been included in Appendix D, but were not utilized. The accompanying Table 3.1 summarizes the methods and limited detection limits reported for the oxide or element concerned.

Table 3.1 – Analytical methods used and detection limits for SOQUEM Inc. (1981)

Oxide	Method	Detection limit	Element	Method	Detection limit
SiO_2	XRF		Ag	AAS	
Al_2O_3	AAS		As[1]	NAA	1 ppm
FeO	AAS		Au	AAS	
CaO	AAS		Co	AAS	
MgO	AAS		Cu	AAS	
Na_2O	AAS		Hg[1]	CM	10 ppb
K_2O	AAS		Ni	AAS	
MnO	AAS		Pb	AAS	
TiO_2	XRF		Zn	AAS	
P_2O_5	XRF				
H_2O	Gravimetric				
CO_2	Volume				
S	XRF				

[1]Humus samples, not kept in thesis

3.5.3 Gold Fields Resources Canada Ltd.

J. Praisé (1981) from Gold Fields Resources Canada Ltd. published in an exploration report deposited at the MRN (GM 39845) containing a total of 31 whole rock geochemical analyses. The samples analyzed were analyzed by X-ray Assay Laboratories Ltd. in Don Mills, Ontario. Additionally, a total of 127 samples were analyzed for Au and Ag, including 81 for Cu and Zn by Assayers Limited in Rouyn-Noranda, Québec. Samples analyzed for Au were completed using a combined fire assay-atomic absorption spectroscopy technique (FA-AAS). Ag, Cu, and Zn were analyzed by AAS. Whole rock samples were analyzed by XRF for a total of 10 oxide, 5 minor elements, loss-on-ignition (LOI) and CO_2. The accompanying Table 3.2 summarizes the methods and detection limits for the oxide or element concerned.

3.5.4 Cogema Canada Ltd.

G. Capus (1988) from Gogema Canada Ltd. deposited a report at the MRN (GM 48562). The exploration report includes the description of a single core specimen and a total of 23 analyses with major and minor elements (Ag, Au, Ba, Cr, Cu, Nb, Rb, Sr, Y, Zn, Zr) from rocks in the study area. Unfortunately, the report does not mention the geochemical laboratory where the analyses were performed, as well as the methods used. The only detection limits mentioned are shown in Table 3.3.

Table 3.2 – Analytical methods used and detection limits for Gold Fields Resources Canada Ltd. (1981).

Oxide	Method	Detection limit	Element	Method	Detection limit
SiO_2	XRF	0.01%	Ag	AAS	0.2 ppm
Al_2O_3	XRF	0.01%	Au	FA-AAS	7 ppm
Fe_2O_3	XRF	0.01%	Ba	XRF	10 ppm
CaO	XRF	0.02%	Cr	XRF	10 ppm
MgO	XRF	0.1%	Cu	AAS	1 ppm
Na_2O	XRF	0.1%	Rb	XRF	10 ppm
K_2O	XRF	0.01%	Sr	XRF	10 ppm
MnO	XRF	0.01%	Zn	AAS	0.5 ppm
TiO_2	XRF	0.01%	Zr	XRF	10 ppm
P_2O_5	XRF	0.01%			
LOI	Gravimetric	0.01%			
CO_2	Gravimetric	0.01%			

Table 3.3 – Detection limits for Cogema Canada Ltd. (1988).

Element	Detection limit
As	50 ppm
Au	5 ppb
Cu	1 ppm
Sb	5 ppm
W	10 ppm
Zn	1 ppm

3.5.5 Noranda Exploration Ltd.

A single analysis produced in 1991, with no accompanying report was provided by Noranda Exploration. Unfortunately, the exact original coordinates for this sample have been lost, and as a result are now only estimated. Consequently, this analysis was not used in this thesis.

3.5.6 MRNF and University of Ottawa

Prior to 2002 geochemical samples obtained by the MRN were analyzed at the Centre de Recherches Minérales du ministère de l'Énergie et des Ressources. A total of 14 samples including the syenite and host basaltic rocks located near or into the open pit of the Beattie mine were analyzed. Major elements were analyzed by XRF and minor elements with either inductively coupled plasma (ICP), XRF or by NAA. Tables 3.4 and 3.5 summarize the analytical methods used as well as the relative errors and detection limits in each case.

From 2002 thereon, analyses were performed by inductively coupled plasma atomic emis-

Table 3.4 – Analytical methods, accuracy and detection limits of oxides for the MRN at the Centre de Recherches Minérales du ministère de l'Énergie et des Ressources, prior to 2002.

Oxide	Method	Accuracy	Detection limit
SiO_2	XRF	0.9%	0.01%
Al_2O_3	XRF	4%	0.02%
Fe_2O_3	XRF	5%	0.1%
CaO	XRF	3%	0.02%
MgO	XRF	5%	0.1%
Na_2O	XRF	5%	0.1%
K_2O	XRF	3%	0.01%
MnO	XRF	14%	0.01%
TiO_2	ICP-AES	0.01%	
P_2O_5	XRF	8%	0.01%
LOI	Gravimetric	4%	0.1%
S	Gravimetric		0.01%
C	Gravimetric		0.01%

sion spectrography (ICP-AES) and by inductively coupled plasma mass spectrometry (ICP-MS) at Acme Labs in Vancouver, British-Columbia. A total of 55 sample were analyzed, of which 29 consist of syenitic rocks and 26 of host or other proximal rocks. These samples were analyzed for either or a combination of major, minor and trace elements. Additionally, an analysis shared by L. Bigot at the Université du Québec à Montréal (UQAM) was also processed by Acme Labs. The two following sections discuss the preparations, analysis and control methods for oxides, minor and REE used in this study.

Major elements

Samples were first crushed to 80% (passing a 2 mm mesh) to which 250 g of the sample was kept and once again pulverizing it to 85% (passing a 75 μm mesh). A 0.2 g sample is then taken and weighed in a graphite crucible and mixed with 1.5 g of $LiBO_2$ flux. It is then heated in a furnace for 30 minutes at 980°C. Once the mixture has cooled, it is dissolved in 5% HNO_3. Samples mixtures are then placed into an ICP-AES emission spectrograph (Varian 735) for the determination of the 18 major oxides and elements: SiO_2, Al_2O_3, Fe_2O_3, CaO, MgO, Na_2O, K_2O, MnO, TiO_2, P_2O_5, Cr_2O_3, Ba, Nb, Ni, Sr, Sc, Y and Zr. The LOI is determined by igniting a 1 g sample split at 950°C for 90 minutes and then measuring the weight loss. A summary of the oxides analyzed and their respective detection limits can be found in the accompanying Table 3.6.

Table 3.5 – Analytical methods, accuracy and detection limits of minor elements for the MRN at the Centre de Recherches Minérales du ministère de l'Énergie et des Ressources, prior to 2002.

Element	Method	Accuracy	Detection limit	Element	Method	Accuracy	Detection limit
Ag	NAA			Nb	XRF	30%	3 ppm
As	NAA			Nd	ICP-MS	20%	25 ppm
Au	NAA			Ni	ICP-MS	38%	1 ppm
B	ICP-MS			Pb	ICP-MS	23%	12 ppm
Ba	ICP-MS	8%	1 ppm	Pr	ICP-MS		10 ppm
Be	ICP-MS	24%	1 ppm	Rb	XRF	10%	3 ppm
Bi	NAA		3 ppm	Sc	ICP-MS	7%	1 ppm
Cd	ICP-MS	74%	2 ppm	Sm	ICP-MS	28%	2 ppm
Ce	ICP-MS	11%	3 ppm	Sr	XRF	4%	3 ppm
Co	ICP-MS	8%	2 ppm	Ta	XRF		3 ppm
Cr	ICP-MS	12%	1 ppm	Te	XRF		10 ppm
Cu	ICP-MS	13%	1 ppm	Th	XRF	30%	3 ppm
Dy	ICP-MS	50%	1 ppm	U	XRF	30%	3 ppm
Eu	ICP-MS	41%	1 ppm	V	ICP-MS	20%	2 ppm
Ga	XRF	15%	1 ppm	W	NAA		
La	ICP-MS	15%	2 ppm	Y	XRF	30%	3 ppm
Li	ICP-MS	14%	1 ppm	Zn	ICP-MS	15%	2 ppm
Mo	ICP-MS		4 ppm	Zr	XRF	30%	3 ppm

Controls include the incorporation of a blank sample placed first through all of the preparation stages. Additionally, for every 36 samples a duplicate is introduced to monitor the analytical precision. Finally, data undergoes a verification by a British Columbia certified assayer prior to being released.

Table 3.6 – Analytical methods used and detection limits for oxides for both the MRN and the University of Ottawa at Acme Labs in British Columbia, after 2002.

Oxide	Method	Detection limit	Element	Method	Detection limit
SiO_2	ICP-AES	0.01%	LOI	Gravity	0.1%
Al_2O_3	ICP-AES	0.01%	S	LECO	0.02%
Fe_2O_3	ICP-AES	0.04%	C	LECO	0.02%
CaO	ICP-AES	0.01%	Ba	ICP-AES	5 ppm
MgO	ICP-AES	0.01%	Ni	ICP-AES	20 ppm
Na_2O	ICP-AES	0.01%	Sc	ICP-AES	1 ppm
K_2O	ICP-AES	0.04%			
MnO	ICP-AES	0.01%			
TiO_2	ICP-AES	0.01%			
P_2O_5	ICP-AES	0.01%			
Cr_2O_3	ICP-AES	0.002%			

Minor and trace elements

Sample preparation involves a first crushing of the sample to 80% (passing a 2 mm mesh). Then a 250 g portion is taken and pulverized to 95% (passing a 100 μm mesh). Following, a 0.2 g sample is taken and weighed into a graphite crucible and mixed with 1.5 g of $LiBO_2$ flux. It is then heated in a furnace for 30 minutes at 980°C. Once the mixture has cooled, it is dissolved in 5% HNO_3. The solution is then shaken for 2 hours. A fraction of this solution is poured into a polypropylene test tube. Afterwards the solution is placed into an ICP-MS (Perlin-Elmer Elan 9000) for the determination of the following elements: Ba, Co, Cs, Ga, Hf, Nb, Rb, Sn, Sr, Ta, Th, Tl, U, V, W, Y, Zr, La, Ce, Pr, Nd, Sm, Eu, Gd, Tb, Dy, Ho, Er, Tm, Yb and Lu. The detection limits attributed to the individual elements can be found summarized in Tables 3.7 and 3.8.

A blank sample is incorporated first through all of the preparation stages. Additionally, for every 36 samples a duplicate is introduced to monitor the analytical precision. Finally, data undergoes a final verification by a British Columbia Certified assayer prior to being released.

Table 3.7 – Analytical methods, accuracy and detection limits of minor elements for the MRN and the University of Ottawa at Acme Labs in British Columbia, after 2002.

Element	Method	Detection limit	Upper limit	Element	Method	Detection limit	Upper limit
Au	ICP-MS	0.5 ppb	100 ppm	Pb	ICP-MS	0.1 ppm	10 000 ppm
Ag	ICP-MS	0.1 ppm	100 ppm	Rb	ICP-MS	0.1 ppm	10 000 ppm
As	ICP-MS	1 ppm	10 000 ppm	Sb	ICP-MS	0.1 ppm	2 000 ppm
Be	ICP-MS	1 ppm	10 000 ppm	Se	ICP-MS	0.5 ppm	100 ppm
Bi	ICP-MS	0.1 ppm	2 000 ppm	Sn	ICP-MS	1 ppm	10 000 ppm
Cd	ICP-MS	0.1 ppm	2 000 ppm	Sr	ICP-MS	0.5 ppm	50 000 ppm
Co	ICP-MS	0.2 ppm	10 000 ppm	Ta	ICP-MS	0.1 ppm	50 000 ppm
Cs	ICP-MS	0.1 ppm	10 000 ppm	Th	ICP-MS	0.2 ppm	10 000 ppm
Cu	ICP-MS	0.1 ppm	10 000 ppm	Tl	ICP-MS	0.1 ppm	1 000 ppm
Ga	ICP-MS	0.5 ppm	10 000 ppm	U	ICP-MS	0.1 ppm	10 000 ppm
Hf	ICP-MS	0.1 ppm	10 000 ppm	V	ICP-MS	8 ppm	10 000 ppm
Hg	ICP-MS	0.1 ppm	100 ppm	W	ICP-MS	0.5 ppm	10 000 ppm
Mo	ICP-MS	0.1 ppm	2 000 ppm	Y	ICP-MS	0.1 ppm	50 000 ppm
Nb	ICP-MS	0.1 ppm	50 000 ppm	Zn	ICP-MS	1 ppm	10 000 ppm
Ni	ICP-MS	0.1 ppm	10 000 ppm	Zr	ICP-MS	0.1 ppm	50 000 ppm

Table 3.8 – Analytical methods and detection limits of REE for the MRN and the University of Ottawa at Acme Labs in British Columbia, after 2002.

Element	Method	Detection limit	Upper limit
La	ICP-MS	0.1 ppm	50 000 ppm
Ce	ICP-MS	0.1 ppm	50 000 ppm
Pr	ICP-MS	0.02 ppm	10 000 ppm
Nd	ICP-MS	0.3 ppm	10 000 ppm
Sm	ICP-MS	0.05 ppm	10 000 ppm
Eu	ICP-MS	0.02 ppm	10 000 ppm
Gd	ICP-MS	0.05 ppm	10 000 ppm
Tb	ICP-MS	0.01 ppm	10 000 ppm
Dy	ICP-MS	0.05 ppm	10 000 ppm
Ho	ICP-MS	0.02 ppm	10 000 ppm
Er	ICP-MS	0.03 ppm	10 000 ppm
Tm	ICP-MS	0.01 ppm	10 000 ppm
Yb	ICP-MS	0.05 ppm	10 000 ppm
Lu	ICP-MS	0.01 ppm	10 000 ppm

3.5.7 Osisko Mining Corporation

A total of 232 samples where analyzed of which 148 were for major elements. All analyses were conducted at the ALS laboratories in Vancouver, British Columbia. Samples are first weighed, dried and finely crushed to 70% (passing a 2 mm, Tyler 9 mesh). A split up to 250 g is taken and pulverized to 85% (passing a 75 μm, Tyler 200 mesh). Testing of crushing efficiency is conducted on random samples. The obtained pulp is then submitted to be analyzed for major or minor elements, each detailed in the 2 following sections. For both types of analyses a blank sample was inserted at every 10^{th} analysis to monitor the analytical precision.

Major elements

A prepared sample of 0.20 g is mixed with 0.90 g of $LiBO_2$ flux and then fused in a furnace at 1000°C. Afterwards, the sampled is weighed to calculate the LOI. The result is cooled and dissolved in 100 mL of 4% of HNO_3 and 2% of HCl. The sample is then analyzed by ICP-AES (Agilent 700 series) with the results corrected for spectral inter-element interferences. The final oxide concentration is calculated from the measured elemental concentration. The accompanying Table 3.9 contains a summary of the oxides analyzed and their detection limits.

Table 3.9 – Analytical methods and detection limits of oxides for Osisko Mining Corporation at ALS laboratories, British Columbia.

Oxide	Method	Detection limit
SiO_2	ICP-AES	0.01%
Al_2O_3	ICP-AES	0.01%
Fe_2O_3	ICP-AES	0.01%
CaO	ICP-AES	0.01%
MgO	ICP-AES	0.01%
Na_2O	ICP-AES	0.01%
K_2O	ICP-AES	0.01%
MnO	ICP-AES	0.01%
TiO_2	ICP-AES	0.01%
BaO	ICP-AES	0.01%
Cr_2O_3	ICP-AES	0.01%
P_2O_5	ICP-AES	0.01%
LOI	Gravimetric	0.01%

Minor elements

Samples analyzed for minor elements are first digested with a nitric aqua regia solution in a graphite heating block. The resulting solution is diluted to 12.5 mL with deionized water, mixed and analyzed by ICP-AES (Agilent 700 series) with the results corrected for spectral inter-element interferences. It is important to note that this digestion method is effective to accurately isolate precious metals, metal sulphides, sulphates (except barite), phosphates and arsenides. However, major rock forming elements and more resistive metals are only partially dissolved. This implies that even though rock forming elements were detected, their actual concentrations are above those measured. Elements to which this effect is pronounced are Al, Ba, Be, Ca, Cr, Fe, K, La, Mg, Mn, Na, Sc, Sr, Th, Ti, U, V and W. As a result, these elements were excluded from this thesis. The following Table 3.10 gives the analytical method and detection limits for the elements that were kept. Whenever possible minor elements were converted from oxide percents to ppm by the author. These conversions were limited to Ba, Cr and Sr only when above the detection limit.

Table 3.10 – Analytical method and detection limits of minor elements for Osisko Mining Corporation at ALS laboratories, British Columbia.

Element	Method	Detection limit	Upper limit	Element	Method	Detection limit	Upper limit
Ag	ICP-AES	0.2 ppm	25 ppm	Mn	ICP-AES	5 ppm	50 000 ppm
As	ICP-AES	2 ppm	10 000 ppm	Mo	ICP-AES	1 ppm	10 000 ppm
B	ICP-AES	10 ppm	10 000 ppm	Ni	ICP-AES	1 ppm	10 000 ppm
Bi	ICP-AES	2 ppm	10 000 ppm	P	ICP-AES	10 ppm	10 000 ppm
Cd	ICP-AES	0.5 ppm	1 000 ppm	Pb	ICP-AES	2 ppm	10 000 ppm
Co	ICP-AES	1 ppm	10 000 ppm	S	ICP-AES	0.01%	10%
Cu	ICP-AES	1 ppm	10 000 ppm	Sb	ICP-AES	2 ppm	10 000 ppm
Ga	ICP-AES	10 ppm	10 000 ppm	Tl	ICP-AES	10 ppm	10 000 ppm
Hg	ICP-AES	1 ppm	10 000 ppm	Zn	ICP-AES	2 ppm	10 000 ppm

Gold analyses

All extracted cores were analyzed for Au at intervals of 1 meter on average. Results in function of depth are presented in the logs along with the core description. These analyses were conducted by FA-AAS (Varian AA 240FS). Sample preparation starts with a fusion with a mixture of lead oxide (PbO), sodium carbonate (Na_2CO_3), sodium tetraborate ($Na_2B_4O_7 \cdot 10H_2O$), silica and other reagents as required. It is then inquarted with 6 mg of gold-free

silver and cupelled to yield a metal bead. The bead is then digested in 0.5 mL of dilute HNO_3 in the microwave oven to which 0.5 mL of HCl in added. The solution is then diluted with 4 mL of de-mineralized water and analyzed by AAS against standards. With this method the detection limit for Au is 5 ppb with an upper detection limit of 10 000 ppb.

3.6 Feldspar staining

An initial staining of all the slabs was performed by S. Patry in 2004. However, when the project was reinitiated in 2009 the slabs had lost much of their colouration. Therefore in early 2010, representative samples were re-stained for potassic feldspar.

A total of 3 wide vessels were utilized. The first containing a mixture of 30.3 g of sodium cobaltinitrate ($Na_3Co(NO_2)_6$) dissolved in 50 mL of distilled water. The second containing distilled water, and in the third some hydrofluoric acid (HF) at a concentration of 48%. The staining procedure involved first dipping the sample in the hydrofluoric acid for a minute, then rinsing it for about 10 seconds in the distilled water and then finally gently dipping it in the colbaltinitrate solution for another minute. The samples were then left to dry prior to potassic feldspar counting and photography.

Chapter 4

Geological setting

4.1 Geology of the Superior Province

The Superior Province, which extends from northern Québec to eastern Manitoba, is invariably considered to be the nucleus of the North American continent. It is bounded to the north, west and east by Paleoproterozoic provinces and to the southwest by the Mesoproterozoic Grenville Province. The Province is characterized by Hadean to Mesoarchean continental tracts (4.3 to 2.8 Ga), Neoarchean oceanic terranes and Paleoproterozoic metasedimentary horizons (2.48 Ga) which overlie some of the Province's metagranites (Percival, 2007; O'Neil et al., 2008; Percival and Stott, 2010). The Province is regarded as a remnant of a continent that was fragmented in the Paleoproterozoic (Percival and Stott, 2010). Subsequent activity in the Proterozoic included limited rifting of the margins, the emplacement of numerous mafic dyke swarms, compressional reactivation, a large scale rotation around 1.9 Ga and a failed rifting event at 1.1 Ga (Percival, 2007).

In the past, the Superior Province was divided into subprovinces. Current progress now divides the Superior Province into terranes. Neoarchean oceanic terranes are identified by juvenile isotopic signatures, combined with a lack of Mesoarchean zircon inheritance. These oceanic terranes are dominantly characterized by greenstone-'granite' belts (Percival, 2007). In the Superior Province, examples of such terranes are the Oxford-Stull domain in the north, the western Wabigoon in the west, and the Wawa-Abitibi terrane in the southeast (see Figure 4.1). These greenstone-'granite' belts generally exhibit a record of oceanic floor, plateaux, island arcs and back arc environment settings (Thurston, 1994). Rocks formed in these oceanic

environments, particularly the Wawa-Abitibi terrane, are hosts to some of the largest VMS deposits of the Province.

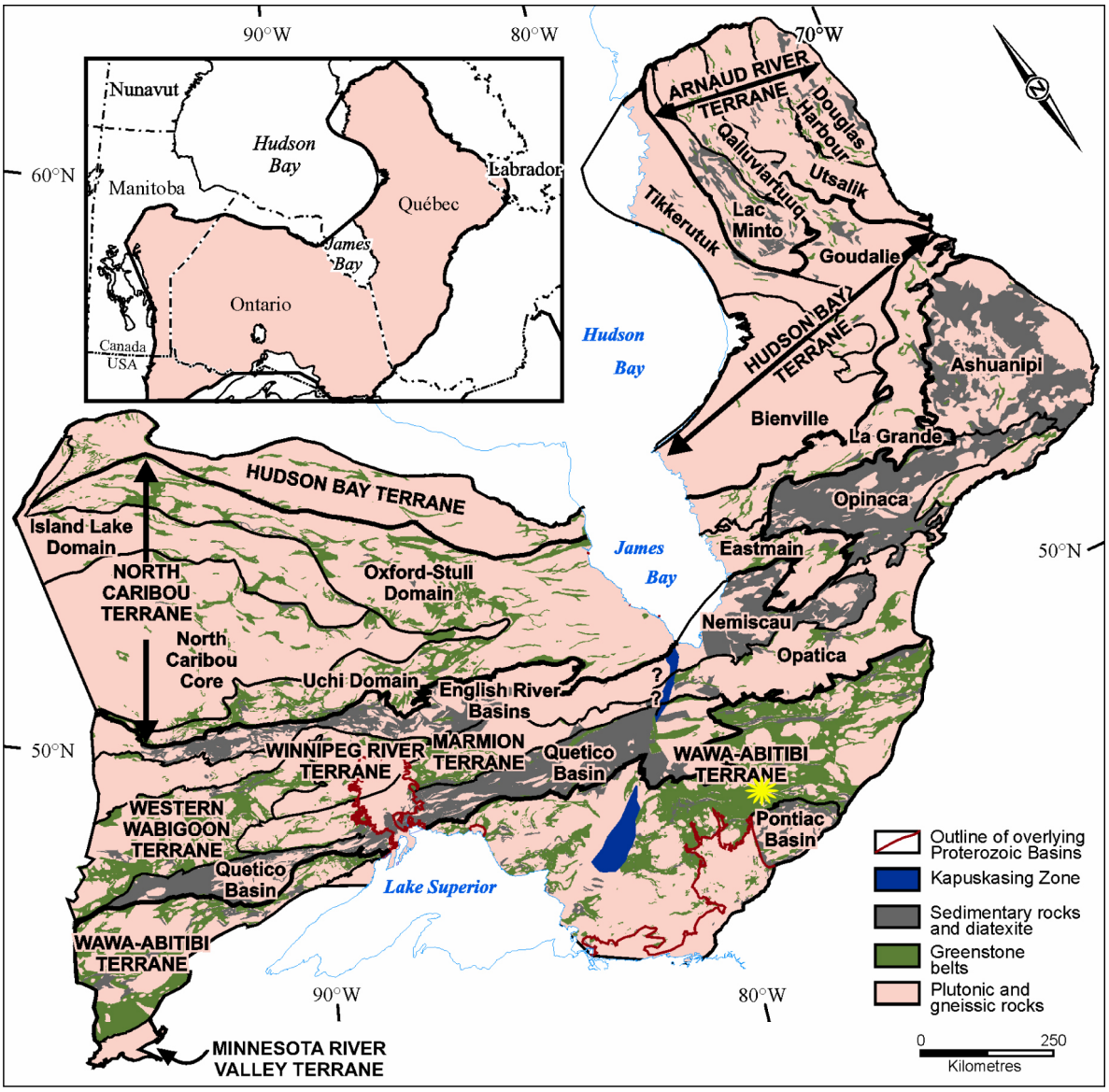


Figure 4.1 – Terrane map of the Superior Province. The yellow star is the approximate location of the Beattie syenite. Image taken and modified from Stott et al. (2010).

4.2 Geology of the Abitibi greenstone belt

Part of the Wawa-Abitibi terrane contains the Abitibi Subprovince, also known as the Abitibi greenstone belt (AGB) which is the largest greenstone belt in the world, covering a 310 × 720 km lozenge shaped area. It is bounded to the north by gnessic and intrusive rocks of

the Opatica Subprovince, to the south by sedimentary rocks of the Pontiac Subprovince and to the southeast by rocks of the Mesoproterozoic Grenville Province. To the west the AGB is interrupted by the north-northeast trending Kapuskasing structural zone, a west-dipping thrust of Paleoproterozoic age (see Figure 4.2).

4.2.1 Stratigraphic framework

The AGB possesses a coherent stratigraphy that was developed over a period of nearly 150 Ma (Goutier et al., 2010). The development of the belt has been divided into 8 distinct submarine volcanic episodes (2790 to 2640 Ma) which are locally separated by marine unconformities, commonly consisting of meta-sedimentary rocks[1] (Thurston et al., 2008). Additionally, numerous faults, intrusions and deformation zones cut across the AGB, however stratigraphic sections are generally well preserved. Temporal episodes found in the study area are individually described in the following paragraphs.

2723 - 2720 Ma episode

The 2723 - 2720 Ma episode (previously known as the Stoughton-Roquemaure assemblage) consists of mafic volcanic rocks with lesser intermediate to felsic volcanic rocks and komatiites. Rocks of this episode are widespread in the northern parts of the AGB (see Figure 4.2). To the north of the PDFZ there is no evidence of a discordance, whereas to the south of the LLF and CF, it is underlain by the 2770 - 2735 Ma episode, indicating a discordance of approximately 12 - 20 Ma (Ayer et al., 2005; Houlé et al., 2008).

2719 - 2711 episode

The most extensive portion of the 2719 - 2711 episode (previously known as the Kidd-Munro assemblage) extends approximately 450 km across the AGB, from the Kapuskasing Structural Zone in the west to the Grenville Province in the east (see Figure 4.2). Most occurrences are encountered along the northern margin of the Porcupine-Destor fault zone (PDFZ). The 2719 - 2711 episode is composed of the Kidd-Munro Assemblage in Ontario and of the upper Kinojévis assemblage in Québec. This episode, which was formerly considered to be a single

[1]Because the rocks are generally lightly metamorphosed to the greenschist facies and to conform with practice in the area, the prefix meta is omitted from hereon.

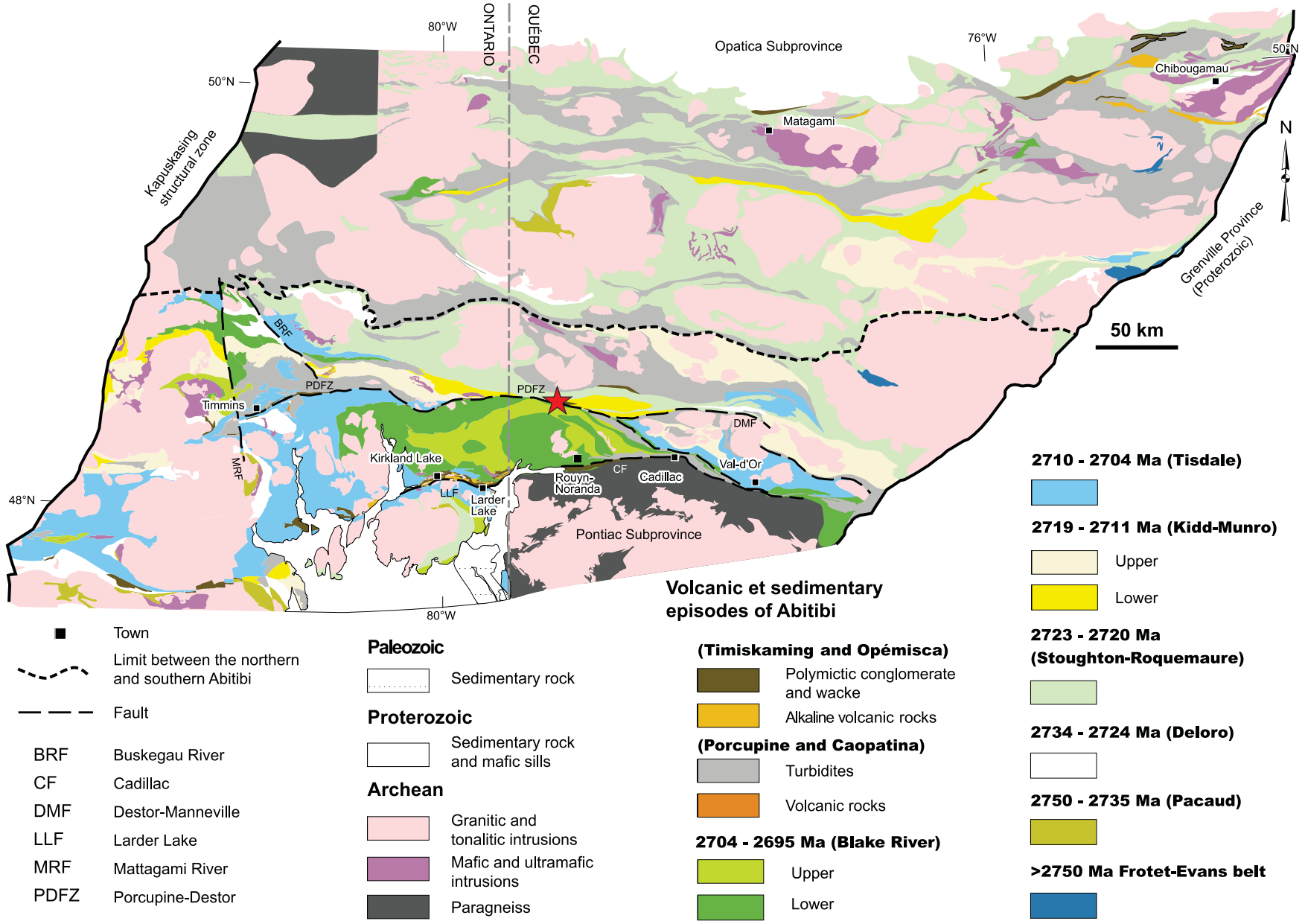


Figure 4.2 – Map of the Abitibi greenstone belt. The red star is the approximate location of the Beattie syenite. Image taken and modified from Goutier et al. (2010).

stratigraphic unit ranging from 2719 - 2711 Ma, has now been subdivided into a lower and upper assemblage.

The lower assemblage, ranging from 2719 - 2717 Ma in age (Houlé et al., 2008), is characterized by intermediate to felsic calc-alkaline volcanic rocks in Ontario and dominantly mafic tholeiitic rocks in Québec.

The upper assemblage ranges from 2717 - 2711 Ma in age (Houlé et al., 2008). It occurs north of the PDFZ and occupies a considerable portion of the study area. It consists of tholeiitic, komatiitic and calc-alkaline (2713 Ma) units with local occurrences of tholeiitic felsic volcanic rocks and minor, centimetre to metre scale, graphitic metasedimentary rocks.

2704 - 2695 episode

The 2704 - 2695 Ma episode (previously known as the Blake River assemblage) rocks occur principally between the PDFZ and the Cadillac fault (LLF and CF) with smaller portions occurring southwest of Kirkland Lake, in the Kamiskotia volcanic complex west of Timmins, and in the central part of the Swayze belt (see Figure 4.2). The Blake River group is the most important assemblage formed during this episode. The group is comprised of 4 stratigraphic intervals consisting of submarine volcanic and volcaniclastic sequences. The volcanic rocks are dominantly bimodal in composition (i.e., basalt, basaltic andesite, andesite versus rhyodacite, rhyolite) (Mercier-Langevin et al., 2011). Volcaniclastic units are commonly the result of flow fragmentation though some are pyroclastic in origin (Ross et al., 2007).

The first interval, 2704 - 2701.7 Ma, is associated with the formation of a tholeiitic lava plain with isolated felsic centres (Mercier-Langevin et al., 2011). Rocks of this first interval are found in the study area, south of the PDFZ.

The second interval, 2701.7 - 2699.3 Ma, is characterized by bimodal volcanism, the eruption of a large volume of vesicular andesites, and the continuation of the volcanic plain in the peripheries (Mercier-Langevin et al., 2011).

The third interval, 2699.3 - 2696.7 Ma, sees the continuation of andesitic volcanism, transitional to calc-alkaline and intermediate to felsic flow-domes accompanied by volcaniclastic rocks, developed over the tholeiitic lava plain (Mercier-Langevin et al., 2011).

The last interval, 2696.7 - 2695 Ma, is characterized by felsic volcanic rocks and mafic-intermediate volcaniclastic rocks (Mercier-Langevin et al., 2011).

Porcupine rocks

Porcupine rocks, ranging from 2690 - 2682 Ma, consists of wackes, siltstones and mudstones in widely distributed basins with lesser amounts of calc-alkaline felsic volcanic rocks, conglomerates and iron formations. Sequence divisions predominantly indicate distal submarine deposition by turbidity currents (Goutier and Lacroix, 1992; Ayer et al., 2005). In Timmins and in the area of Rouyn-Noranda, the observed contact between the Porcupine and the metavolcanic assemblages lacks a regolith or paleosol (Ayer et al., 2002) further supporting its deposition in a marine environment.

Timiskaming rocks

Timiskaming rocks range from 2682 - 2669 Ma, consist of the youngest of the supracrustal assemblages and the last of the unconformable successor basins. These rocks are primarily found near the long faults of the PDFZ and the LLF and CF as well as others further north. They are generally restricted to narrow corridors and consist of alluvial-fluvial conglomerates, sandstones, turbidites which are locally interlaced with alkaline to calc-alkaline volcanic rocks (Mueller et al., 1994). These were unconformably deposited on older metavolcanic and/or Porcupine rocks (Goutier and Lacroix, 1992; Ayer et al., 2005).

4.2.2 Intrusion Framework

Approximately one third of the AGB surface is composed of intrusive rocks. Spanning over 90 Ma, all of these intrusions can be divided as either 1) synvolcanic, or 2) syntectonic (Chown et al., 2002; Goutier and Melançon, 2010).

Synvolcanic intrusions

Synvolcanic intrusions are the oldest ranging from 2732 - 2696 Ma (Ayer et al., 2005; Goutier et al., 2010; Goutier and Melançon, 2010) and are therefore synchronous with the 2734 (Deloro assemblage) to 2695 Ma (Blake River assemblage) volcanic episodes. They occur predominantly near or in volcanic complexes as well as deeply eroded portions of the AGB. Importantly, this group predates most of the compressional strain. Consequently, the intrusions are relatively strongly deformed, being overprinted by regional schistosity and retrograded by

metamorphism (Chown et al., 2002) and locally they can be heavily hydrothermally altered. Compositionally, they may range from peridotite to granodiorite and are geochemically similar to their corresponding volcanic episodes (Ayer et al., 2005).

Syntectonic intrusions

Syntectonic intrusions range from 2711 - 2639 Ma (Ayer et al., 2005; Goutier et al., 2010; Goutier and Melançon, 2010) and are synchronous with major deformation periods in the AGB. Compared to the synvolcanic intrusions, syntectonic intrusions are generally less deformed and have magmatic foliations parallel or related to regional deformation. Many of these intrusions lie either adjacent to earlier intrusions, or within or near late southeast, or east-trending dextral strike slip deformation zones (i.e., PDFZ, LLF and CF). These intrusions have been subdivided into two groups based on geochronology and geochemistry: 1) the early intrusions (2711 - 2685 Ma (Ayer et al., 2005)) are characterized by tonalite, granodiorite, diorite and feldspar porphyries, and 2) the late intrusions (2684 - 2639 Ma (Ayer et al., 2005; Goutier et al., 2010)) which are generally smaller sized and typically consist of monzonite, syenite (e.g., the Beattie syenite), monzodiorite, granodiorite and granite.

4.2.3 Metallogenic events

Volcanic rocks across the entire stratigraphic sequence of the AGB are endowed with multiple world class economic metal deposits. These metals are found in either volcanic associated Cu-Zn-(Pb, Ag, Au) VMS deposits, magmatic Ni-Cu-(PGE) deposits and orogenic lode gold deposits. These deposits are however restricted to specific stratigraphic episodes.

VMS deposits tend to occur throughout the 2750 - 2735 Ma (Pacaud), 2734 - 2724 Ma (Deloro), 2723 - 2720 Ma (Stoughton-Roquemaure), 2719 - 2711 Ma (Kidd-Munro), 2710 - 2704 Ma (Tisdale) and 2704 - 2695 Ma (Blake River) volcanic-dominated episodes. Gold-rich VMS-styles seem to be concentrated to the youngest (i.e., 2704 - 2695 Ma (Blake River)) of the volcanic-dominated episodes.

As for the Ni-Cu-(PGE) mineralizations, they seem to be limited to the 2750 - 2735 Ma (Pacaud), 2723 - 2720 Ma (Stoughton-Roquemaure), 2719 - 2711 Ma (Kidd-Munro) and 2710 - 2704 Ma (Tisdale) volcano-stratigraphic episodes (Houlé and Lesher, 2010). Nonetheless, komatiites associated Ni-Cu-(PGE) deposits are restricted to the younger 2719 - 2711 Ma

(Kidd-Munro) and 2710 - 2704 Ma (Tisdale) volcanic-dominated episodes.

Last, the orogenic gold mineralization occurs in many assemblages and is structurally controlled. World-class deposits of this style are spatially and genetically associated to the PDFZ and the LLF and CF (Robert, 2001, 2012). Importantly, the emplacement of gold resulted from a long history of deformation and alteration. To permit Au-mineralization, there existed a long-lived auriferous hydrothermal system as well as an extensive plumbing system which was capable of ore concentration. Varied conditions though time resulted in diverse styles of gold mineralization (vein-type, disseminated, sulphide-rich), alteration mineralogy (ankerite, albite, sericite), ore minerals (pyrite, tellurides), and metals (Au, Ag, Cu, Mo, W) (Legault et al., 2005; Houlé et al., 2008). Disseminated-style gold deposits are spatially associated with quartz-monzonite to syenite intrusions in the AGB (Robert, 2001; Legault and Lalonde, 2009). These gold deposits, which include most found in the study area (i.e., Beattie, Donchester and Central Duparquet 2 deposits), generally occur within the intrusions or along their margins.

Chapter 5

Geology of the Duparquet area, Southwest Sector

The Duparquet area is located approximately 20 km east of the Ontario-Québec provincial border and 30 km north of Rouyn-Noranda. Geographically, the area is encompassed under the National Topographic System (NTS) as 32D11-0102, with an area of 256 km^2 (see Figure 5.1). Notably, the area contains the southeastern striking Porcupine-Destor fault zone (PDFZ) and immediately adjacent to the fault zone is the Beattie syenite. The studied area, hereon referred as the Beattie area, extends from 5373354 to 5375070 m N and 629273 to 636046 m E (UTM NAD 83, zone U17), covering a rectangular area of 10.55 km^2 as shown in Figure 5.1.

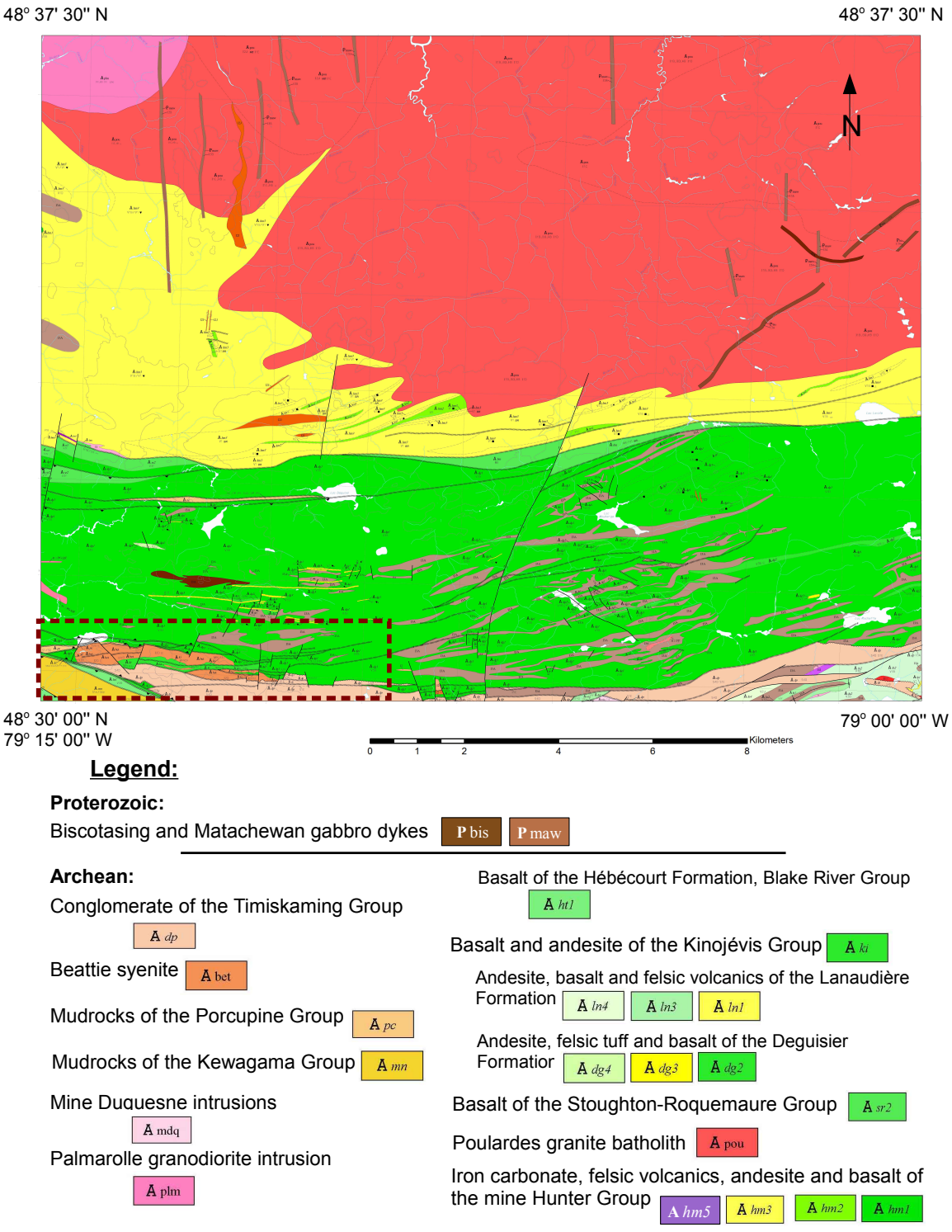


Figure 5.1 – Location of the study area within the Duparquet area. The area in the dashed rectangle indicates the extent of the study area, hereon referred as the Beattie area. Presented here is the official MRN geological map (prior to modifications within the dashed area) of the 32D11-0102, Duparquet area with a reduced and simplified legend. Geological map obtained and modified from Goutier and Beausoleil (2000).

5.1 Stratigraphy

A total of 2 major metavolcanic and 3 metasedimentary[1] groups are present in the Beattie area. The oldest volcanic group is the Kinojévis, with an estimated age of 2720 - 2718 Ma. This group is the equivalent of the Kidd Munro assemblage in Ontario. The youngest volcanic group is the Blake River estimated at 2703 - 2701 Ma (Mercier-Langevin et al., 2011). These 2 major groups are separated by the ESE trending PDFZ with the older Kinojévis located to the north and the younger Blake River to the south of the fault zone. The three sedimentary groups are the Kewagama (south of the PDFZ) dated between $< 2686 \pm 4$ Ma (Davis, 2002) and $> 2682 \pm 3$ Ma (Mortensen, 1993), the Porcupine (north of the PDFZ) dated at $< 2687 \pm 2$ Ma (Ayer et al., 2005) and the Timiskaming (north of the PDFZ) dated at $< 2679 \pm 3$ Ma (David et al., 2006). The Kewagama and Porcupine groups are quite peculiar, being chronologically and almost lithologically identical, but are separated by the PDFZ. Consequently, these two groups are divided into a northern and southern portion, hence the different names. The younger Timiskaming only occurs to the north of the PDFZ.

The structural orientation of both volcanic and sedimentary groups on both sides of the PDFZ is generally E-W. The stratigraphy on the northern side of the PDFZ indicates a southward younging of the units with near vertical dip varying between north and south for all groups. South of the PDFZ the stratigraphic top of the Blake River is also to the south with strong southwards inclinations. The younger Timiskaming Group lies unconformably over the Kinojévis Group where it occupies a southeastern striking syncline.

To facilitate reading, the stratigraphic groups are discussed in chronological order. Furthermore, a geological time scale with all the groups and events in the Beattie area is presented in Figure 5.2.

[1]Because the rocks are generally lightly metamorphosed to the greenschist facies (see Section 5.4), except near major faults, and to conform with practice in the area, the prefix meta is omitted from hereon.

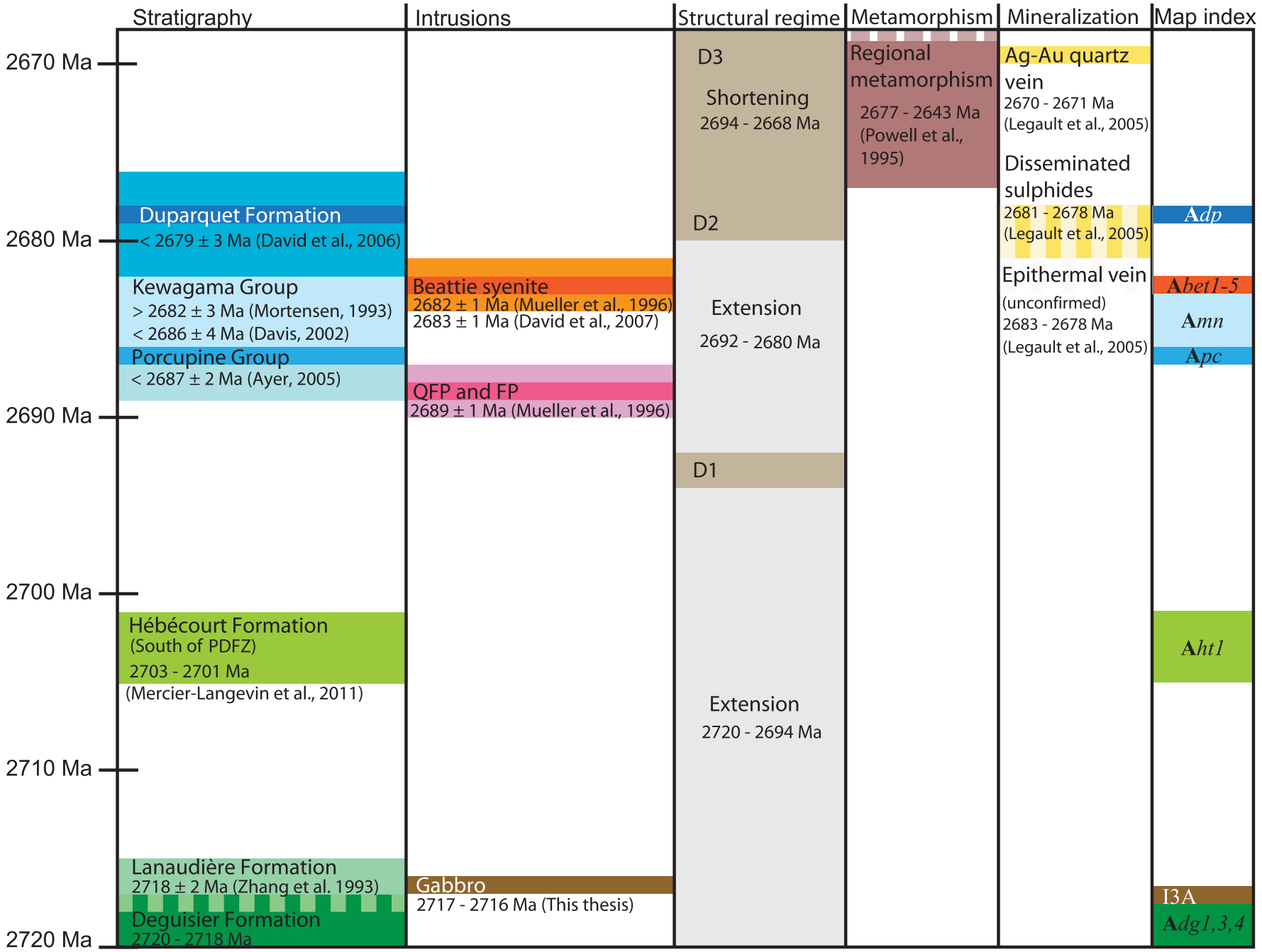


Figure 5.2 – Geological time scale of the Beattie study area.

5.1.1 Kinojévis Group

The oldest lithology in the Beattie area belongs to the Kinojévis Group. This group has been subdivided into 2 formations: 1) the Deguisier Formation, and 2) the Lanaudière Formation (Goutier and Lacroix, 1992). The older Deguisier Formation has an estimated age of 2720 - 2718 Ma and is the most abundant volcanic sequence in the Duparquet area as well as in the Beattie area. The younger Lanaudière Formation has been dated at 2718 ±2 Ma (Zhang et al., 1993) and only occurs underneath the Timiskaming sediments in the Beattie area (see Figure 5.1). This section will first focus on the Deguisier Formation and will be followed by the Lanaudière Formation.

Deguisier Formation, Kinojévis Group

The Deguisier Formation has an EW to NE-SW orientation with a thickness ∼5 km. It occurs as a monoclinal band with a southern polarity. Within the Duparquet Township, it is dominated by sequences of pillowed and massive basalts with thin horizons of hyaloclastites, lapilli tuff and chert between the flows. Lesser amounts of andesites, dacites, glomeroporphyritic basalt and rhyolite comprise the rest of the formation.

In the Beattie area, the Deguisier Formation units are chronologically (from base to top): the 1) tholeiitic basalt with a thickness between 100 - 200 m, the 2) tholeiitic andesite to dacite with a maximum thickness between 100 - 200 m, and the 3) rhyolite which attains a thickness $<$ 120 m, all of which are described individually below.

Before proceeding to the individual unit characteristics, the basalt and andesite to dacite units are indistinguishable from each other on the basis of petrography. This includes in outcrop, hand and drill core specimens as well as in thin section. The only way to distinguish them is with geochemical composition which is addressed in Chapter 7. Consequently, for the following section only, the descriptions of both the basalt and andesite to dacite units are merged.

Tholeiitic basalt and andesite to dacite units (**A***dg1* and **A***dg4*)

Both the basalt (**A***dg1*) and andesite to dacite (**A***dg4*) units occur as pillowed to massive volcanic flows. They are undoubtedly the most prevalent units of the Deguisier Formation

attaining a thickness ∼5 km in the Duparquet area. Both units form a large E-W striking band occupying the northern portions following the PDFZ divide. In the Beattie area, the basalt occupies the northern portions with an average thickness of 750 m. The andesite to dacite unit occupies the south with an average thickness of 150 m. North of the syenitic intrusion the basalt is frequently pillowed whereas the andesite to dacite between the syenitic lens is massive.

Field observations by the author were restricted to the immediate proximity of the Beattie syenite, observations of the andesite to dacite therefore dominate the following lithological, petrographic and structural discussions. Additionally, no thin section of the basalt was obtained, therefore the following thin section descriptions were obtained from Goutier and Lacroix (1992).

Field observations and hand-specimen petrography In numerous outcrops the Deguisier basalt and andesite to dacite units are dark coloured aphanitic rocks. The Deguisier basalt can readily be distinguished from all other rocks by its softness and aphanitic character. Colour varies in freshly broken fragments from dark grey to dark green. No pillows were found near the syenite, however they have been documented further north by Goutier and Lacroix (1992). The outcrops did not contain any visible amygdules, although they are found in drill core. In drill core, specimens of both basalt and andesite to dacite units are typically an aphanitic melanocratic rock as shown in Figure 5.3. Occasionally, amygdules are present with percentages varying between < 1 - $5\%_m$ (modal %). These amygdules measure between 0.05 - 0.8 cm across and are generally ellipsoid in shape due to subsequent deformation.

The amygdules near contacts zones are filled with quartz and occasionally albite which is preferentially found near albitic veins (see Figure 5.4). Away from the contact zones, the amygdules progressively become filled by albite as seen in Figure 5.5. In one instance, amygdules have been filled by orange-brown carbonate minerals and black chlorite. This specific occasion was found at a contact between the andesite to dacite unit and the Beattie syenite.

Thin-section petrography Regional mineralogical observations of the Deguisier basalt by Goutier and Lacroix (1992) report a composition of plagioclase, chlorite, epidote, quartz, opaques with accessory actinolite, carbonate minerals, prehnite-pumpellyite and stilpnome-

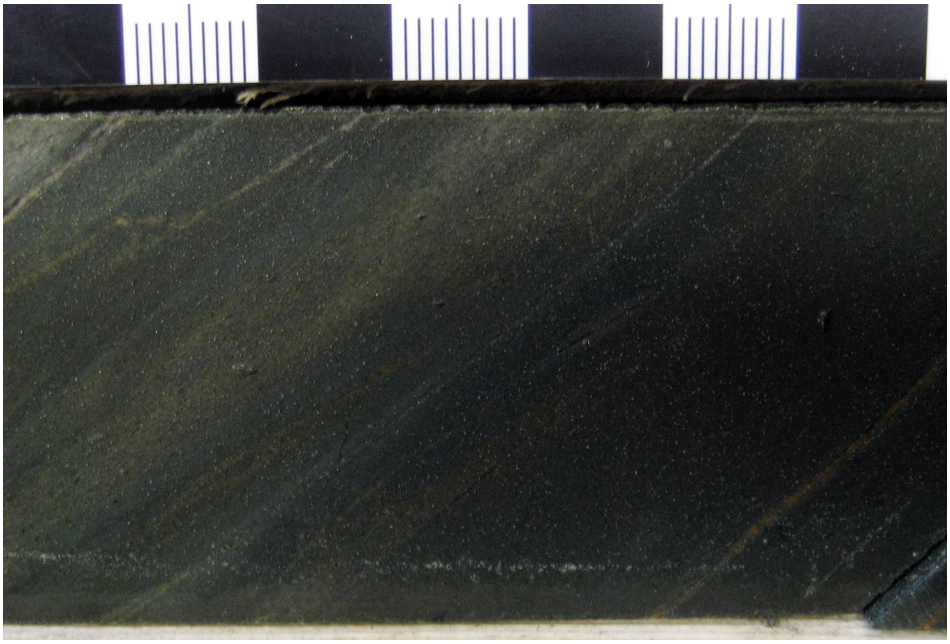


Figure 5.3 – Aphanitic Deguisier tholeiitic andesite to dacite. Colour bands denote an increase in schistosity caused by deformation near a contact with the Porcupine Group sediments. Drill core: B08-90, depth: 24.56 - 27.90 m.

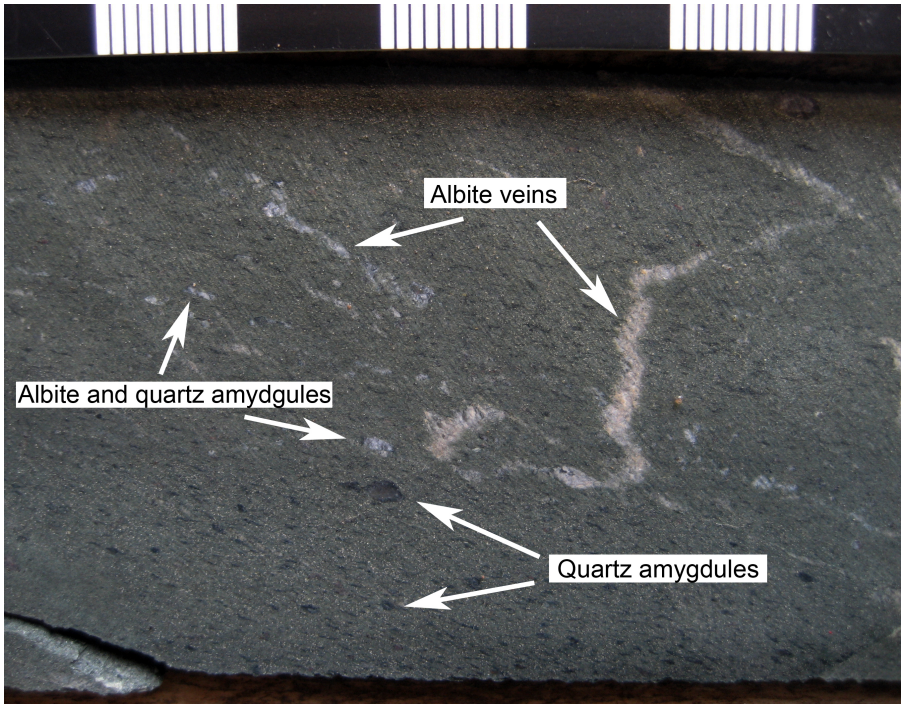


Figure 5.4 – Deguisier tholeiitic andesite to dacite with quartz and albite amygdules. Small (< 0.3 cm) quartz-filled amygdules (grey) are widespread. Accompanying quartz and albite amygdules (0.2 cm) are found in proximity of 0.2 cm wide albite vein (white). The ellipsoid shape of the amygdules results from localized deformation near the contact. Drill core: B08-73, depth: 18.20 - 21.30 m.

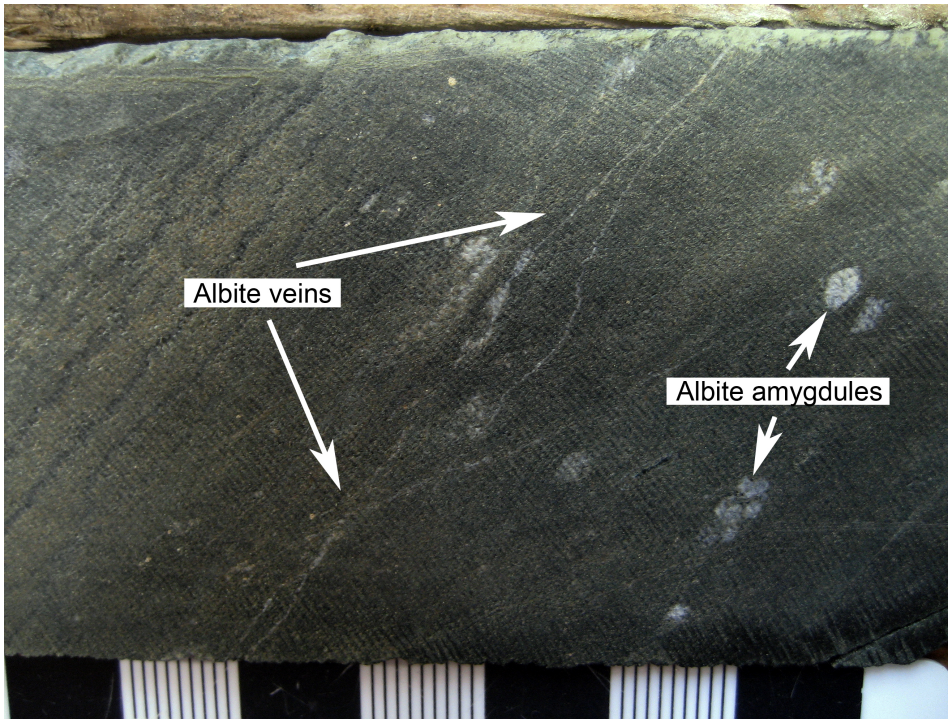


Figure 5.5 – Deguisier tholeiitic andesite to dacite with albite amygdules. The 0.5 cm albite filled amygdules (white) are on the right. These are accompanied by a thin ($<$ 0.1 cm) albite vein (white) diagonally crossing the drill core. Drill core: B09-26, depth: 4.5 - 8.00 m.

lane. Their descriptions also reflect a fine-grained matrix ($>$ 0.5 mm). Amygdules and plagioclase microphenocrysts were also noted in some of the thin sections. Furthermore, sericitization of the feldspars is variable (a few crystals to a near complete replacement) and many sections show evidence of carbonatization, pyritization and chloritization.

A thin section of andesite to dacite (based on geochemical results) of a specimen taken from near the contact with the Beattie syenite is composed of oligoclase (38%$_m$), epidote (25%$_m$), chlorite (18%$_m$), opaque minerals (7%$_m$), quartz (5%$_m$) with accessory hematite (2%$_m$), calcite (1%$_m$) and pyrite (trace). Minerals observed in thin section are very fine grained, varying between 2 - 0.025 mm. The largest crystals are euhedral microphenocrysts of sodic plagioclase that represent 1%$_m$ of the section. These vary between lath-shaped to equant crystals and do not define any igneous alignment (see Figure 5.6). The composition of a few feldspar phenocrysts was determined by the Michel-Lévy method to be An_{25}, therefore corresponding to oligoclase. These feldspar microphenocrysts are hosted in a very fine matrix of anhedral albite and quartz cut by anastomosing veinlets of epidote and chlorite. The epidote

is characterized by fine (0.05 mm) prismatic masses to columnar crystals. Inclusions of large epidote crystals (0.1 mm) occur in the cores of the plagioclase microphenocrysts (see Figure 5.6). Chlorite on the other hand appears as even smaller ($<$ 0.05 mm) aggregates of elongated crystals as seen in Figure 5.7. Sericitization of the feldspars is common, however the abundance and sizes of individual sericite crystals is unresolvable.

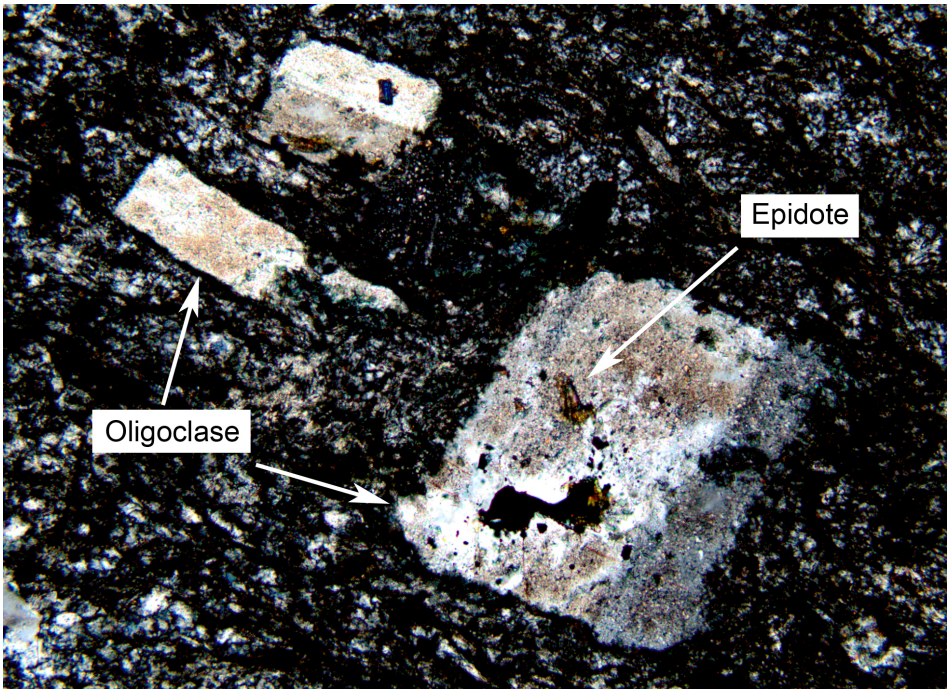


Figure 5.6 – Oligoclase feldspar microphenocrysts in a fine-grained matrix. Oligoclase crystals contain inclusions of epidote. Photomicrograph taken under crossed polars, FOV: 1.53 mm. Location: 632400E 5374053N.

The thin section contains $<$ 1%$_m$ ellipsoid amygdules. Amygdules were initially filled by chlorite. Subsequently, quartz and occasionally carbonate minerals filled their cores (see Figure 5.8).

Another thin section, of an andesite to dacite taken from a lens in between the Deguisier gabbro (north) and the Beattie syenite (south), was obtained. The intensity of shearing and alteration in this rock is quite evident, yielding a mineralogical composition of sericite (40%$_m$), carbonate minerals (30%$_m$), plagioclase (25%$_m$) with accessory quartz (2%$_m$) and opaque minerals (3%$_m$). All the feldspars show advanced sericitization, with only small (0.05 mm) fragmented remnants of the original plagioclase microphenocrysts. The engulfing sericite forms a continuous wavy network which overprints the entire rock. Rare, brittlely-deformed quartz-filled amugdules are present in this thin section and are depicted in Figure 5.8d. Carbonate

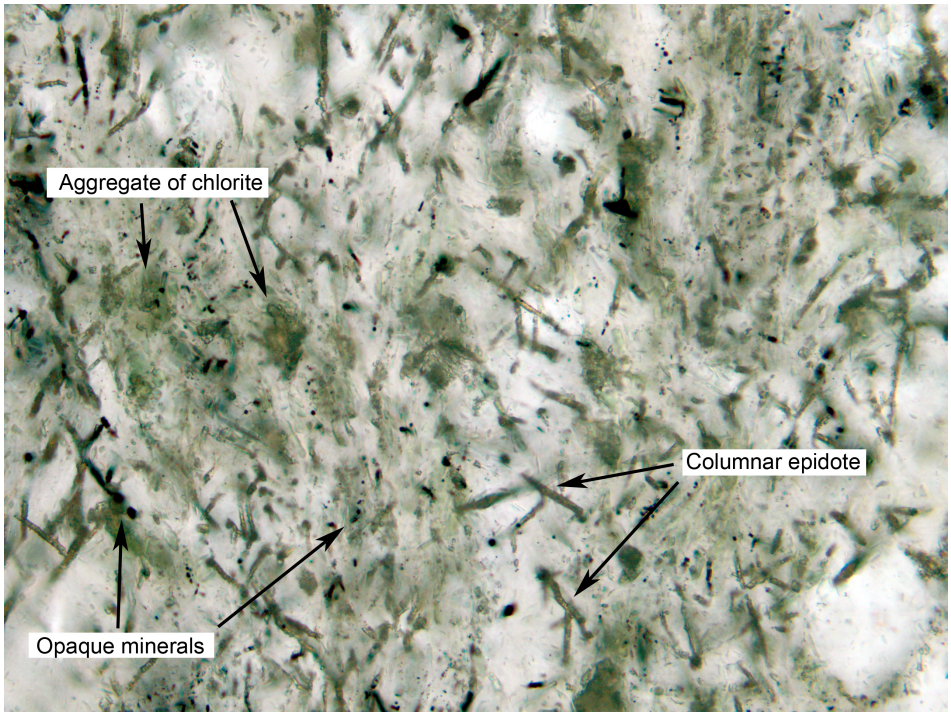
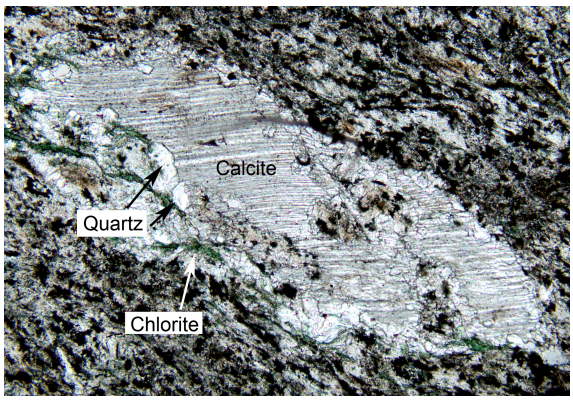


Figure 5.7 – Matrix of the Deguisier andesite to dacite. Beige-brown epidote is present as prismatic crystals measuring < 0.05 mm long. Green coloured chlorite occurs as aggregates measuring < 0.025 mm across. Small black anhedral opaque minerals are also disseminated through the matrix. All the crystals are hosted within the transparent feldspathic and quartz matrix. Photograph taken under plane polarized light, FOV: 0.25 mm. Location: 632400E 5374053N.

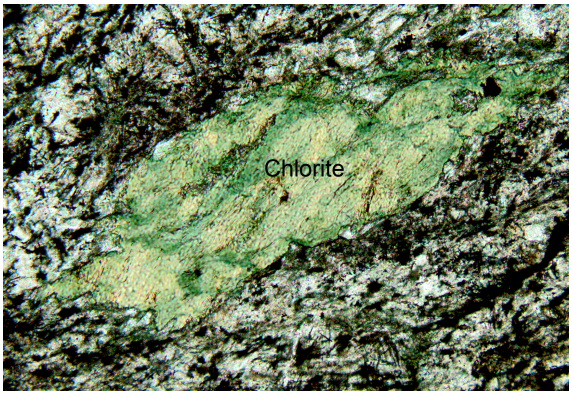
minerals occur both as an initial alteration and as late stage hydrothermal minerals along with skeletal sulphides.

Structural relationships Both units of the Deguisier Formation cannot be divided into structural domains because of their uniformity across the Duparquet Township. Structural studies by Goutier and Lacroix (1992) reveal that lava flows possess an E-W to NE-SW orientation with stratigraphic tops consistently to the south. Both basalt and andesite to dacite units were subject to several sequences of regional deformation which imparted a poorly developed, E-W striking schistosity dipping to the north. The intensity of this schistosity increases towards contacts. Sericitization, albitization, silicification and minor carbonatization also increase in contact zones (see Figure 5.4). Only one fold, corresponding to a monoclinal structure belonging to the northern flank of the Abijévis syncline, was documented by Goutier and Lacroix (1992).

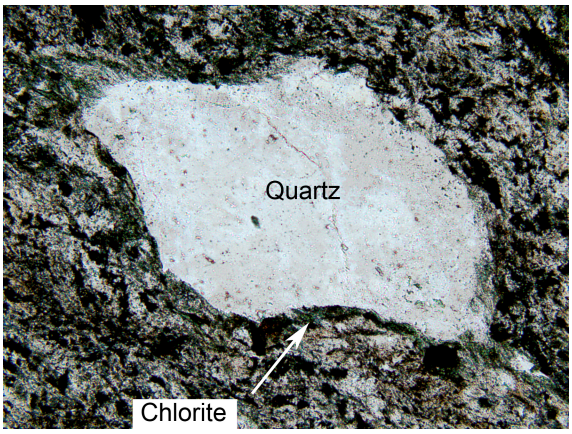
The Deguisier basalt and andesite to dacite units, which are oldest, are always cut by other



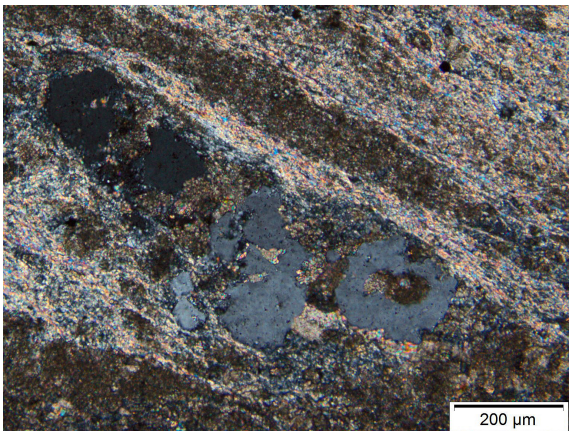
(a) Calcite in the interior of an amygdule with a rim of quartz and chlorite



(b) Chlorite entirely filling an amygdule



(c) Quartz in the interior of an amygdule with a rim of chlorite

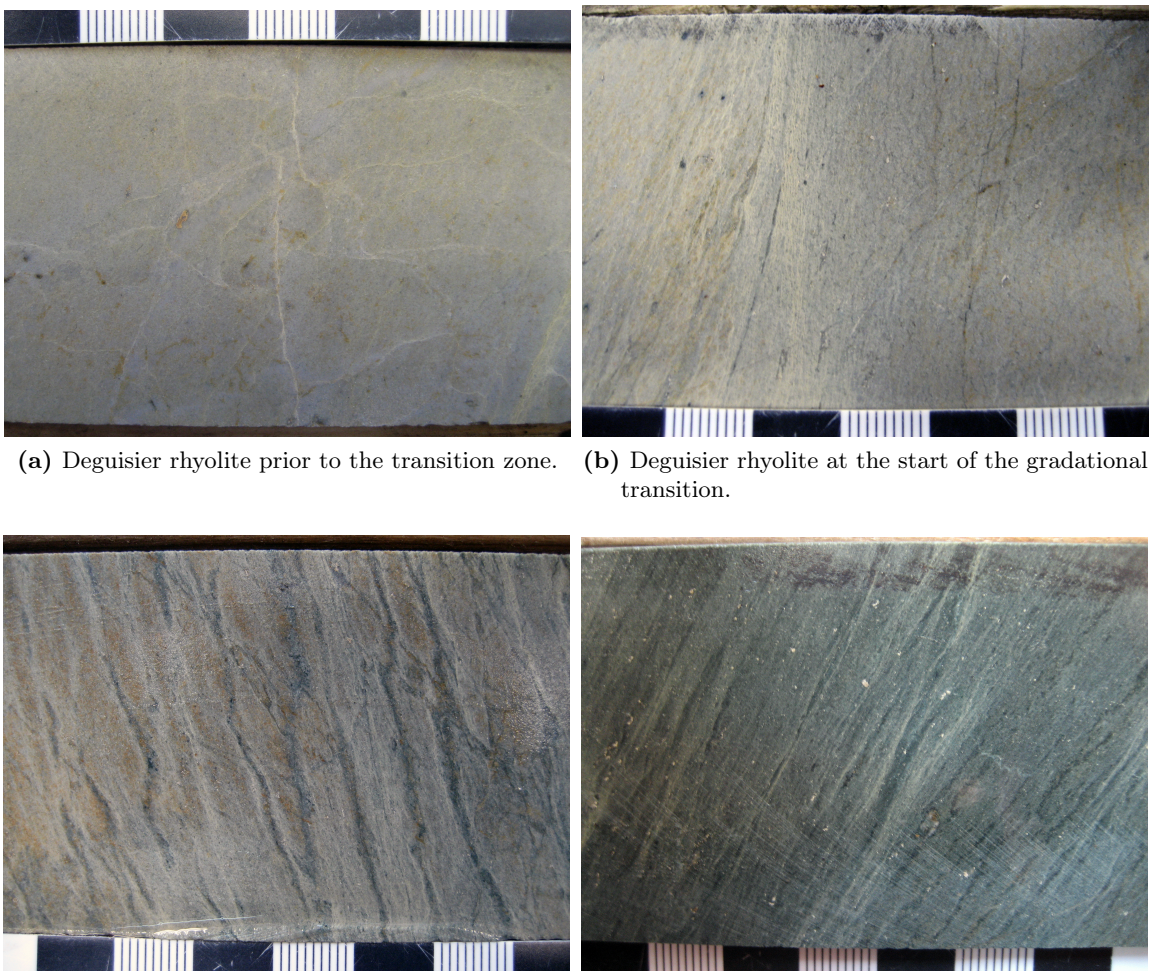


(d) Brittle deformation of a quartz-filled amygdule

Figure 5.8 – Photomicrographs of diverse minerals filling amygdules. Amygdules size for (a) is 1.95 mm, (b) is 1.44 mm, (c) is 1.14 mm and (d) is 0.8 mm across. First 3 photomicrographs taken under plane polarized light and last taken under crossed polars. Location (a), (b), (c): 632400E 5374053N and (d): 633146E 5373875N.

younger rocks. Schistosity is noted to increase at the contact zone, seen by the pronounced elongation, up to the brittle deformation of the amygdules (see Figures 5.4 and 5.8d). Both the basalt and andesite to dacite units generally become lighter coloured at the contact zones, imparting them with a grey colour. Contacts are sharp, but can appear as diffuse to gradational, chiefly caused by subsequent alteration (see Chapter 7) and deformation. Specifically, sharp contacts are noted between the basalt or the andesite to dacite units and the Beattie syenite, Porcupine sediments and Deguisier rhyolite. Contacts between the Deguisier Formation and the Porcupine sediments may at times appear diffuse, caused by lenses of dark wacke of similar appearance as the basalt or andesite to dacite units. At times, a gradational contact appears

between the andesite to dacite units and the Deguisier rhyolite, spanning a length between 1 - 5 m. These contacts, moving towards the andesite to dacite, demonstrate a progressive darker colour as well as a decrease in hardness as shown in Figure 5.9. After the gradational contact, there may be altered, pale coloured sections with a < 2 cm wide diffuse transition as shown in Figure 5.10. Both the gradational and diffuse transitions appear to be the result of subsequent alteration and deformation, obscuring the actual contact.



(a) Deguisier rhyolite prior to the transition zone.

(b) Deguisier rhyolite at the start of the gradational transition.

(c) Transition between the rhyolite and andesite to dacite units.

(d) Deguisier andesite to dacite at the end of the gradational transition.

Figure 5.9 – Seemingly gradational contact between the Deguisier rhyolite and andesite to dacite units. The contact extends for a length of 3 m and is caused by subsequent alteration and deformation. Drill core: B09-23, depth: 108.0 - 111.0 m.

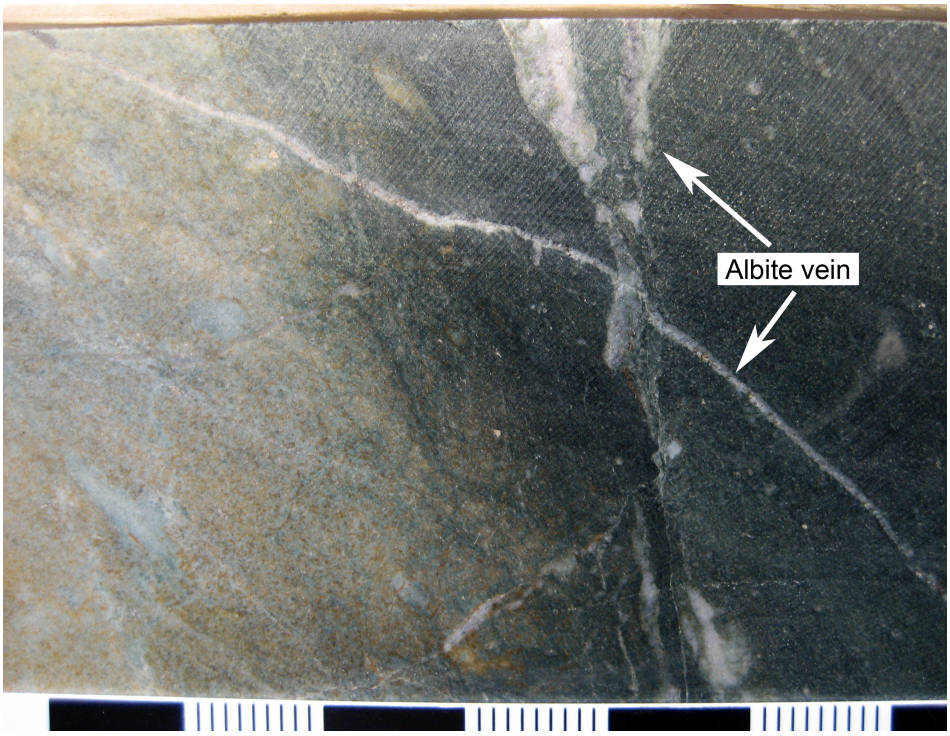


Figure 5.10 – Altered section with a diffuse transition back to less-altered Deguisier andesite to dacite. The alteration, denoted by its lighter colouration, is to the left, and the dark less altered Deguisier andesite to dacite is to the right. Crossing the contact are a few veins of albite (white). Drill core: B08-73, depth: 147.0 - 154.77 m.

Subalkaline rhyolite (A*dg3*)

The youngest unit of the Deguisier Formation is a subalkaline rhyolite. This rhyolite cuts both the Deguisier basalt and andesite to dacite units. In the Duparquet area, the rhyolite occurs as long E-W striking bands measuring $<$ 20 m thick and $<$ 2.65 km long. Clusters of rhyolitic bands occur in 2 separate instances. The first is located 3.5 km northeast of Duparquet. The second is located in the Beattie area, 400 m north of the town site.

Rhyolite in the Beattie area was first described and mapped by O'Neill (1933) partially under the name of bostonite (see Chapter 2). This name was upheld for years by many authors until its use was discouraged by Banfield (1940). Thereon, geological reports and maps referred to rhyolitic showings either as trachytic syenite dykes or as Deguisier basalt. The first use of the name rhyolite in the Beattie area was by Goutier (1996) during the geological revision of the area near the Central Duparquet mine 1. The rhyolite consists of two small showings north of the abandoned shaft of the Central Duparquet mine 1. Both showings are subcircular in shape and measure $<$ 20 m across. This rhyolite was not discussed nor included in the Goutier

and Beausoleil (2000) geological map due to its small size.

With recent field, drill core, petrographic and geochemical samples, new showings of rhyolite have been identified to the west, approximately 500 m southeast from the old Beattie mine shaft. These showings are irregular in shape, have a thickness of < 120 m and a length of < 240 m. The rhyolite previously mapped by J. Goutier has also been included in this thesis and accompanying geological map (see Appendix B).

At a large scale, the rhyolite appears heterogeneous which could be attributed to different sub-units composing it. Comparable studies by Moulton et al. (2011) of Kidd-Munro[2] rhyolites in the Prosser Township revealed a total of 5 sub-units, some of which closely match observations presented below (e.g., aphanitic vs porphyritic). Unfortunately, current data are insufficient to permit the division, characterization and mapping of different sub-units composing the Deguisier rhyolite. As such, causes for this heterogeneity remains an open question, pending future research. However, for the purpose of this thesis, the name rhyolite is used in a broad sense, grouping together all the variations encountered.

The following paragraphs explore in detail the lithological, petrographic and structural observations with emphasis on the western exposures.

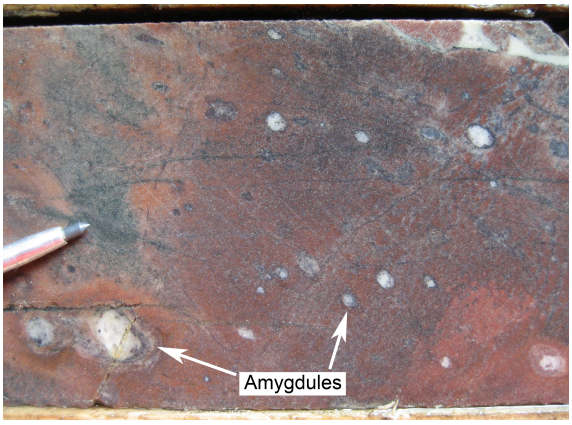
Field observations and hand-specimen petrography The identification of rhyolite in the field and in hand and drill core specimens is difficult because of the heterogeneous nature of this rock. However, there is a common property in all the varieties of rhyolite which is its great hardness compared to all other rocks in the study area. Frequently, the rhyolite appears massive, albeit commonly brecciated, with a white patina. Colour varies from beige to grey when relatively unaltered, but can also include orange, bright red, green and pink (see Figure 5.11). Local colour patterns are limited to a dominance of beige and grey in the western part of the area. All other colours observed lack a systematic variation and could therefore result from alteration.

Spherical to ellipsoid amygdules may be present in the relatively unbrecciated areas. These measure between < 0.1 - 2 cm and account for < 1 - $3\%_m$ of the rock. The amygdules are commonly filled by quartz with carbonate minerals, chlorite, albite and occasionally pyrite (see Figure 5.12). Generally, amygdules closer to contacts are quartz-dominated with lesser

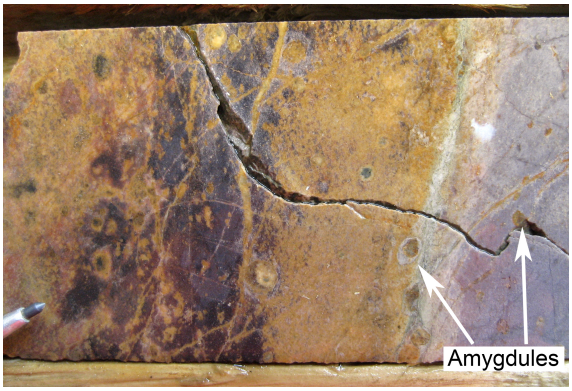
[2]equivalent to the Kinojévis Group in Québec



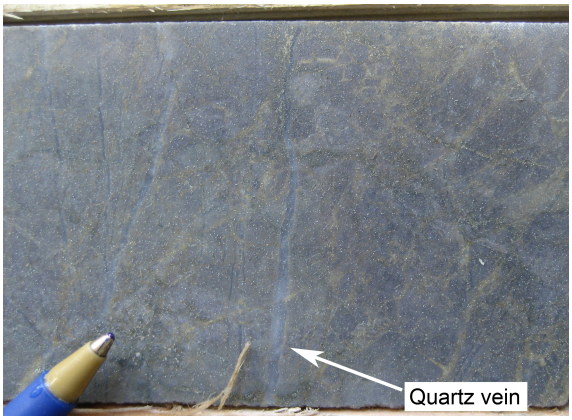
(a) Outcrop of reddish pink massive and non-amydular rhyolite. Location: 630902E 5374292N.



(b) Red amygdular rhyolite. Amygdules are filled with a rim of black chlorite and a core of white albite. Drill core: B09-103, depth: 3.00 - 9.13 m.



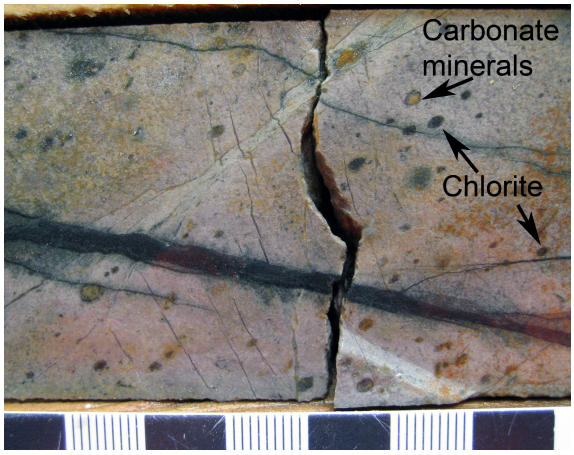
(c) Orange to grey amygdular rhyolite. The orange colouration is the result of local carbonatization. Drill core: B08-62, depth: 43.25 - 57.40 m.



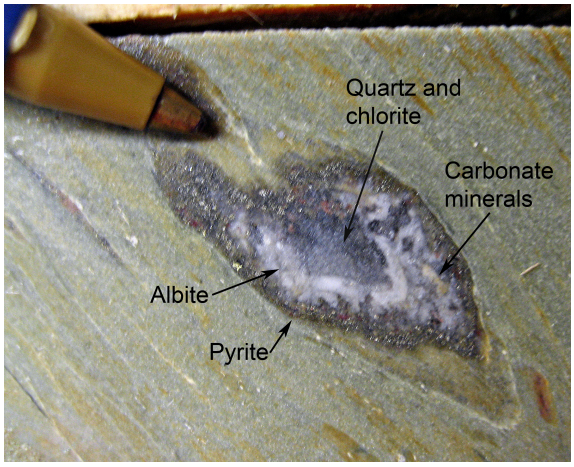
(d) Dark grey non-amygdular brecciated rhyolite. A late quartz vein transects the drill core specimen. Drill core: B09-88, depth: 40.00 - 47.00 m.

Figure 5.11 – Colour and textural variations of the Deguisier tholeiitic rhyolite.

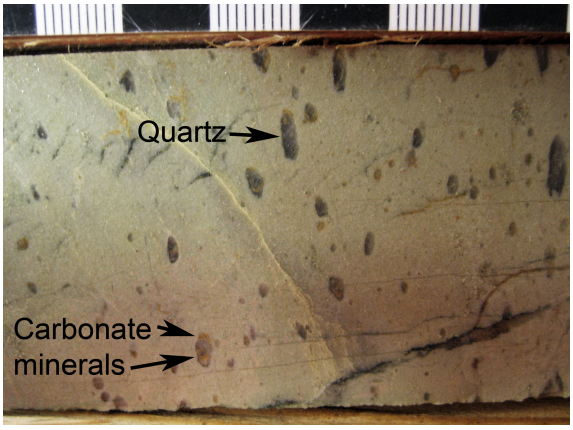
amounts of carbonate minerals, albite and chlorite. Amygdules away from contacts are chlorite-dominated with occasional quartz, albite and carbonate minerals. The mineral assemblage present in the amygdules is dependant on the alteration and therefore does not always demonstrate this particular spatial variation. Pyrite in the amygdules is rare and occurs only in the highly foliated, Au-mineralized sections. Zoning in the amygdules is common. However, there does not seem to be an exact established order with the exception of when pyrite is present. Such amygdules are surrounded by pyrite which has replaced the typical smooth amygdule border with an irregular one. Continuing towards the centre is a rim of white albite and beige carbonate minerals. The amygdule core is filled with either dark chlorite or grey quartz (see Figure 5.12b).



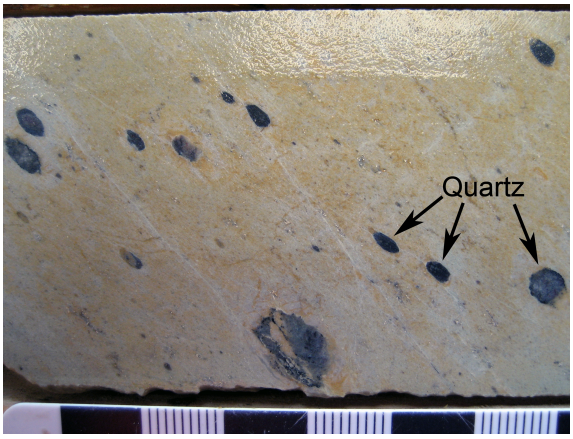
(a) Spherical amygdules filled with black chlorite and orange carbonate minerals. In a few amygdules is a chloritic rim surrounding a carbonate mineral heart. Drill core: B08-102, depth: 45.90 - 47.00 m.



(b) Large irregular amygdule. The edge is occupied by pyrite, followed by white albite and beige carbonate minerals. The heart of the amygdule is filled with a mixture of quartz and chlorite. Drill core: B08-102, depth: 79.50 - 85.50 m.



(c) Ellipsoid amygdules dominantly filled by quartz and occasionally accompanied orange carbonate minerals. Drill core: B08-102, depth: 79.50 - 85.50 m.



(d) Ellipsoid and irregular shaped amygdules filled by grey quartz. Drill core: B09-22, depth: 3.00 - 16.00 m.

Figure 5.12 – Shape and compositional variation of amygdules within the Deguisier tholeiitic rhyolite.

Uncommonly, the rhyolite contains visible feldspar phenocrysts. Their abundance and size increases eastwards in the western exposures, culminating in one outcrop containing a small cluster of them. This trend was also reflected in drill core specimens where phenocrysts also become visible progressing to the east. The feldspar phenocrysts are euhedral, prismatic, measure < 5 mm across and compose a maximum of $4\%_m$ of the drill core or outcrop. On average phenocryst values are $< 1\%_m$ in western outcrops (see Figure 5.13) and $< 2\%_m$ in drill core. In one instance, phenocrysts are accompanied by small relicts of primary mafic minerals

in a drill core. These relicts are composed of carbonate minerals measuring between 0.1 - 0.3 cm across and composing $<$ 1 - 3%$_m$ of the drill core (see Figure 5.14).

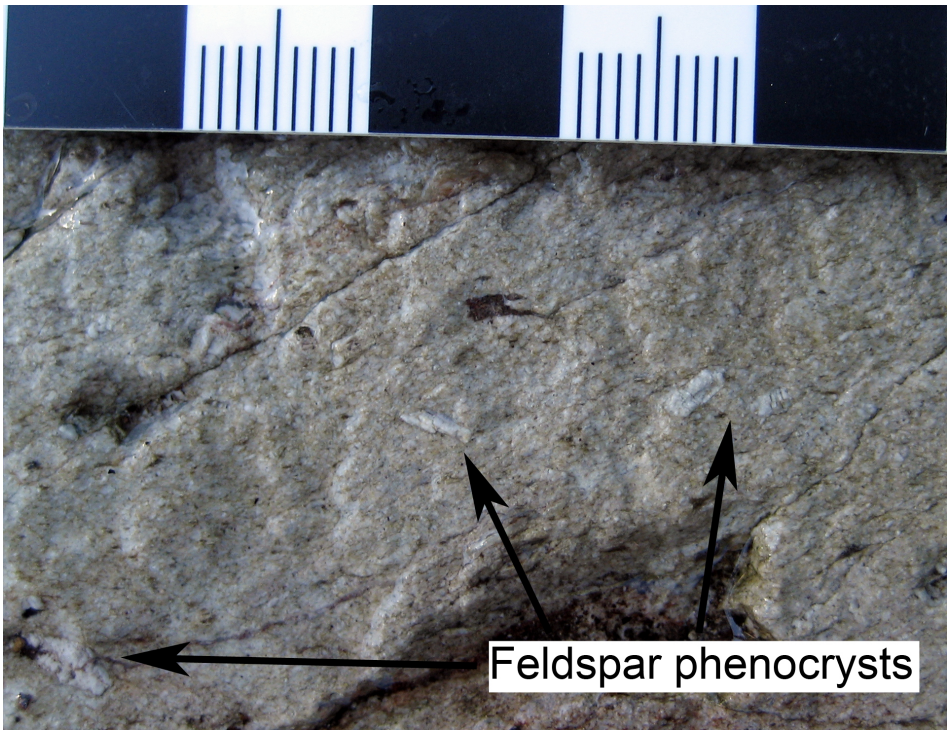


Figure 5.13 – Feldspar phenocrysts in an outcrop of the Deguisier tholeiitic rhyolite. Phenocrysts measure $<$ 5 mm across and compose 1%$_m$ of the rock. Location: 631096E 5374207N.

The rhyolite shows a slight colour banding in areas containing visible phenocrysts and primary mafic mineral relicts, clearly seen in Figure 5.14. Loosely aligned with this colour banding are the feldspar phenocrysts and the relicts of primary mafic minerals.

Thin-section petrography The modal mineralogy of the rhyolite unit was determined in a single thin section from the western exposure of the study area. The rhyolite is composed of quartz (44%$_m$), plagioclase (43%$_m$), sericite (10%$_m$) with accessory carbonate minerals (1%$_m$), apatite (1%$_m$), magnetite (1%$_m$) and trace chlorite and pyrite. Minerals observed in thin section were generally very fine grained, measuring between $<$ 0.01 - 0.2 mm. Microphenocrysts of quartz and plagioclase are very small, typically 0.2 - 2 mm across and represent a meagre 1%$_m$ of the rock, further adding to the difficulty of observing them in the field or in hand specimen. Quartz microphenocrysts generally demonstrate embayed characteristics (see Figure 5.16). Plagioclase microphenocrysts are commonly Carlsbad twinned and were deter-

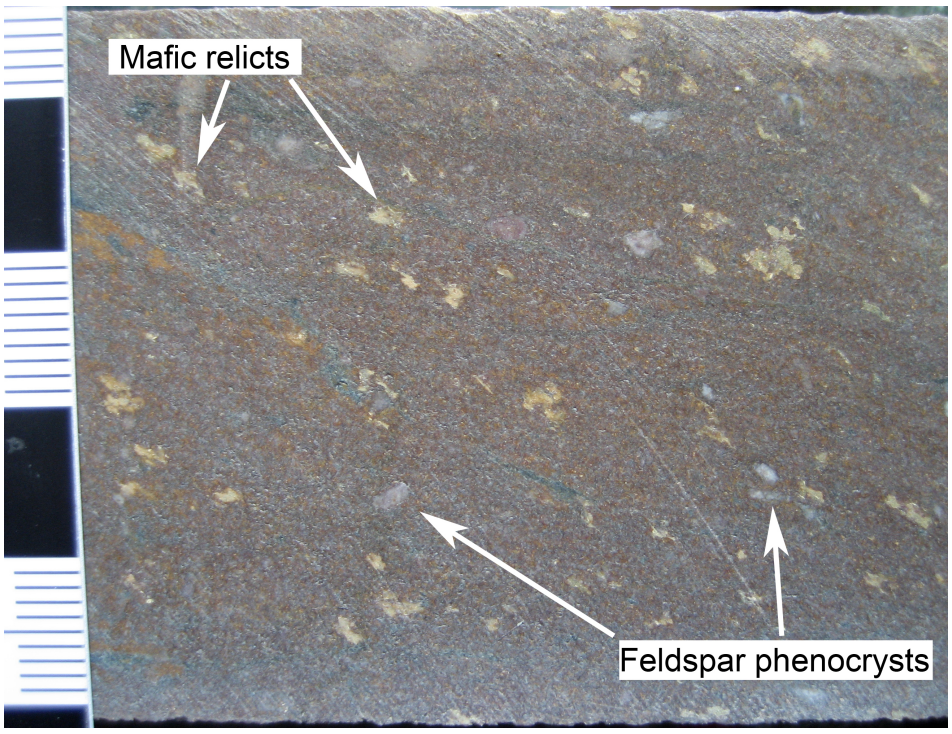


Figure 5.14 – Feldspar phenocrysts and relicts of primary mafic crystals in the Deguisier tholeiitic rhyolite. Phenocrysts are pale pink, measure < 3 mm and represent $2\%_m$ of the drill core specimen in a dark red aphanitic matrix. Relicts of primary mafic crystals are now replaced by beige carbonate minerals measuring < 3 mm across and representing $3\%_m$ of the drill core specimen. Coloured bands can be seen in the drill core specimen where feldspar phenocrysts are roughly aligned into a trachytic fabric. Drill core: B08-72, depth: 6.00 - 10.40 m.

mined by the Michel-Lévy method to be An_{20}, therefore corresponding to oligoclase. Feldspar microphenocrysts are commonly arranged in clusters, defining a poor glomeroporphyritic texture (see Figure 5.15). Single lath-shaped crystals represent the remainder of the plagioclase microphenocrysts. Both clusters and single plagioclase microphenocrysts are roughly aligned into a poor trachytic fabric.

The matrix of the rock is composed of a mixture of plagioclase, quartz and possibly alkali feldspar, producing an undulose extinction. This mixture appears as slightly radiating fibrous crystals with a diffuse margin which share a poor alignment as shown in Figure 5.17. The configuration is reminiscent of devitrification of a glassy matrix, possibly produced ensuing regional metamorphism and possibly alteration.

Subsequent to igneous crystallization, the feldspars were altered to sericite, characterized as a green anhedral mica. Sericite is present throughout the matrix as small anastomosing

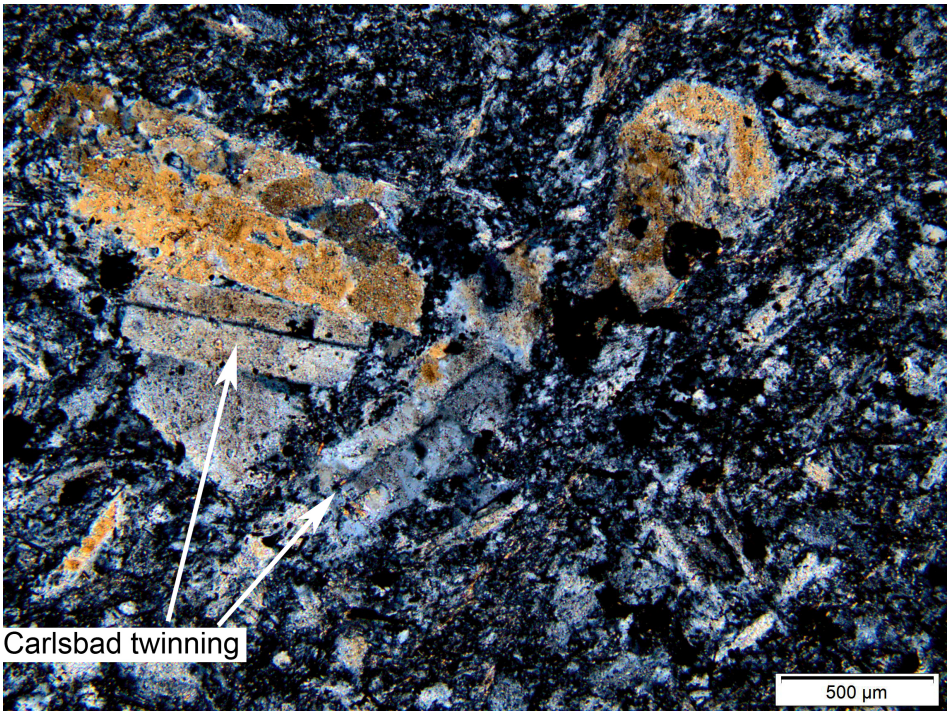
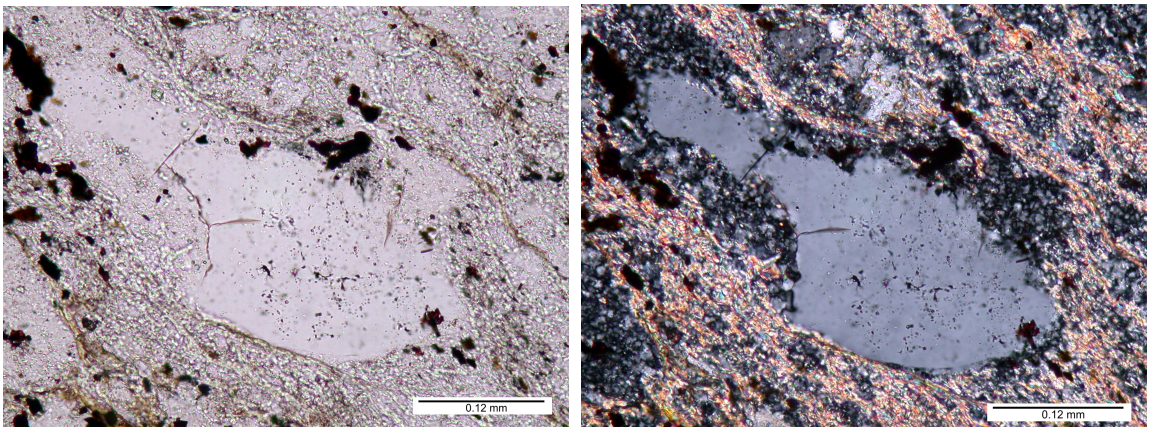


Figure 5.15 – Plagioclase microphenocryst cluster in the Deguisier rhyolite. These measure an average of 1 mm along their long section and define a poor glomeroporphyritic texture. Microphenocrysts are contained within a fine-grained (< 0.2 mm) feldspathic and quartz-rich matrix. Carlsbad twinning is also a common feature. Photomicrograph taken under crossed polars, FOV: 1.2 mm. Location: 630906E 5374295N.



(a) Small quartz phenocryst under parallel polars. **(b)** Small quartz phenocryst under crossed polars.

Figure 5.16 – Small embayed quartz phenocryst in the Deguisier tholeiitic rhyolite. FOV: 0.54 mm. Location: 630906E 5374295N.

networks of veins (see Figure 5.17). Locally, sericite is very abundant to the point of obliterating primary textures. On rare occasions, close to feldspar phenocrysts, crystals of carbonate minerals (< 0.2 mm) accompany the sericite.

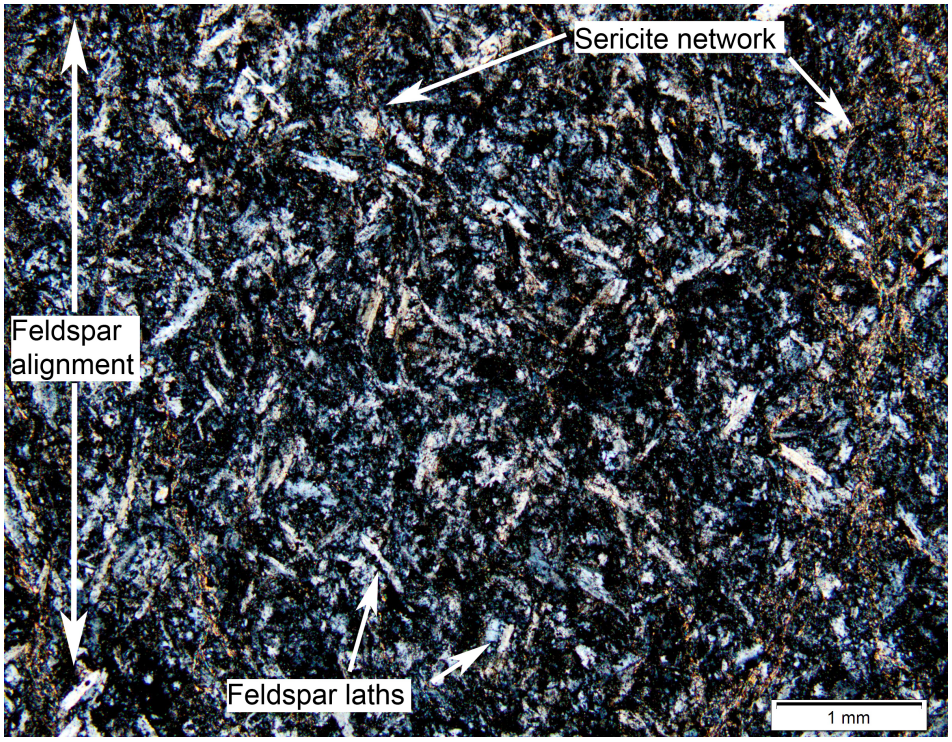


Figure 5.17 – Rhyolitic matrix with wavy sericite veins. Feldspars measure an average of 0.2 mm along their long axis. The approximate orientation of the feldspars is also shown by sericite, as illustrated by the arrows. Photomicrograph taken under crossed polars, FOV: 5 mm. Location: 630906E 5374295N.

Quartz also infiltrates the matrix as microcrystalline crystals ($<$ 0.01 mm), fills amygdules (see Figure 5.18), and accompanies chlorite in late veins.

Opaque minerals consist primarily of hematite with rare pyrite and magnetite. Hematite is found as extremely small crystals between $<$ 0.01 - 0.2 mm disseminated throughout the thin section, including the amygdules. Trace anhedral crystals of pyrite are also disseminated throughout the thin section as extremely fine crystals measuring $<$ 0.25 mm across.

Small relicts of zircon, titanite or monazite ($<$ 0.25 mm) are observed in thin section. Occasionally, their form remains, but whether those relicts were titanite, zircon or monazite is difficult to ascertain.

Other mafic mineral relicts are also observed in thin section. The original crystal outline is completely lost, replaced by irregular ellipsoid shaped structures. In these structures is a high concentration of anhedral to skeletal magnetite, quartz, occasional sericite and pyrite.

Amygdules are also observed in thin section. These are mineralogically zoned, complementing observations made in drill core. Amygdules of the thin section measure between 1 to

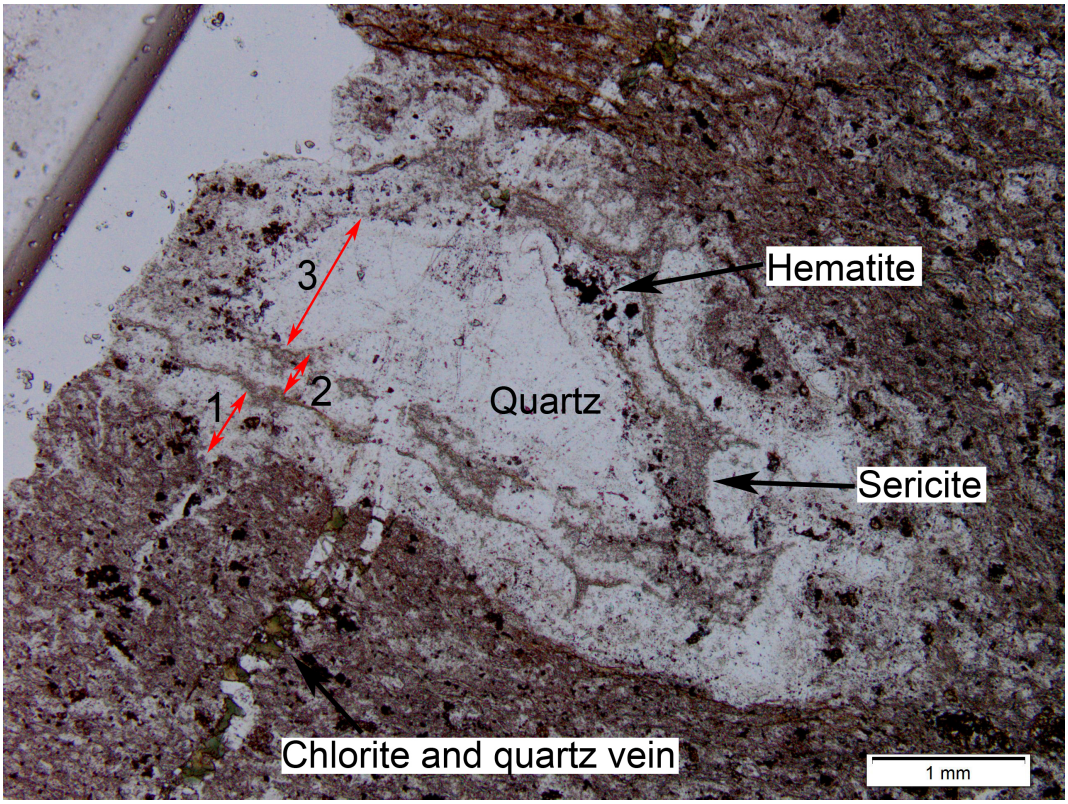


Figure 5.18 – Large zoned amygdule in the Deguisier tholeiitic rhyolite. The outer rim (0.2 mm) of the amygdule is composed of quartz (arrow 1 in illustration). Following is a rim (0.1 - 0.4 mm) of sericite, microcrystalline quartz and hematite (arrow 2 in illustration). The centre is composed entirely of quartz (arrow 3 in illustration) (1 mm). A late vein of quartz and chlorite cuts the first 2 rims, but merges with the centre. Photomicrograph taken under crossed polars, FOV: 5 mm. Location: 630906E 5374295N.

$>$ 3 mm across and represent $1\%_m$ of the rock. The area where the thin section was taken had all of its amygdules dominated by quartz. Thin section observations also showed that the amygdules are exclusively composed of quartz with the exception of the larger ones where quartz is accompanied by lesser amounts of sericite and magnetite (see Figure 5.18). Detailed observations of one of the larger amygdules revealed a complex, 3 stage, paragenesis. The first episode of crystallization consisted exclusively of quartz crystals (0.1 - 0.2 mm) which precipitated on the outer rim of the amygdule forming a uniform, 0.2 mm thick band. The second stage consisted of a sericite band, immediately followed by microcrystalline quartz and magnetite. This second stage infilled the amygdule further by 0.1 - 0.4 mm. The third and last stage was comprised of minor sericite deposition after which, a chlorite and quartz vein transected the amygdule, channelling fluids to the centremost part (1 mm) of the amygdule and completely filling it.

Structural relationships The Deguisier rhyolite cannot be divided into structural domains because of its limited exposure and overall uniformity within the study area. The rhyolite has petrographic textures indicative of a flow rather than an ignimbrite as there is neither widespread evidence of volcanic fragments nor welding in outcrop, drill core and thin section. Furthermore, the trachytic fabric observed in outcrops, drill core specimens and thin section also supports its emplacement as a volcanic flow. Further work is needed to determine with certainty if the exposed rhyolite was a volcanic flow or a dome. Concerning the heterogeneous nature of the rhyolite, a sequence of volcanic flows can potentially yield multiple textural and petrographic sub-units as demonstrated in rhyolitic flows of the Prosser Township (Moulton et al., 2011). To better demonstrate the heterogeneous nature and structural features of the rhyolite, Figure 5.19 provides a detailed perspective of an outcrop with accompanying photographs.

The general fabric in the Deguisier rhyolite, as displayed in the alignment of feldspar phenocrysts in an outcrop, is oriented E-W, although the top direction remains to be determined.

Subsequent regional deformation of the Deguisier rhyolite, locally imparted the rhyolite with a poorly developed E-W oriented schistosity. This schistosity pre-dates the emplacement of the Beattie syenite as rhyolite xenoliths found near the Central Duparquet 1 mine demonstrate a schistosity (Goutier, pers. comm., 2012). Afterwards, the E-W striking Donchester fault locally produced additional brecciation in the rhyolite located near the fault. Unlike the Deguisier basalt and andesite to dacite units, the rhyolite does not demonstrate any significant increase in schistosity or brecciation towards contacts.

Sericite locally fills the fractures created by brecciation. In one rare occasion, these fractures are anastomosing or arc-shaped with a secant of < 30 cm. Quartz amygdules occur throughout both the fractures and undisturbed rhyolite. The amygdules are near perpendicular to the orientation of the fractures. Caution should be exercised in these areas as the created pattern by the sericite-filled fractures have been mistaken as pillow structures (see Figure 5.20).

The rhyolite, in the Beattie area, occupies the top portions of the Deguisier Formation along with the andesite to dacite unit. However, the rhyolite is observed to cut across the andesite to dacite unit and is thus the youngest unit of the formation. Contacts between the two units are sharp, but may appear progressive, caused by subsequent alteration (see Figures

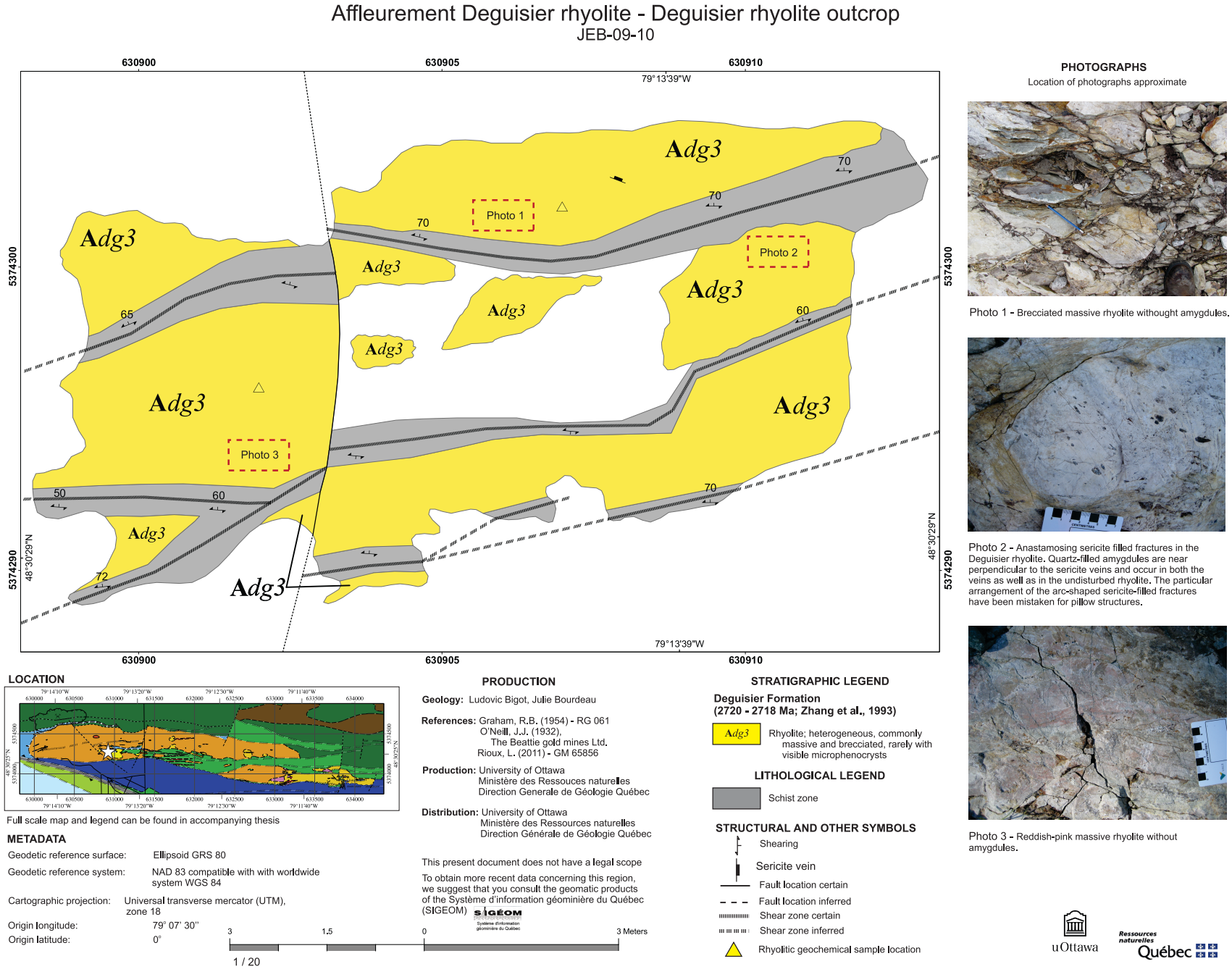
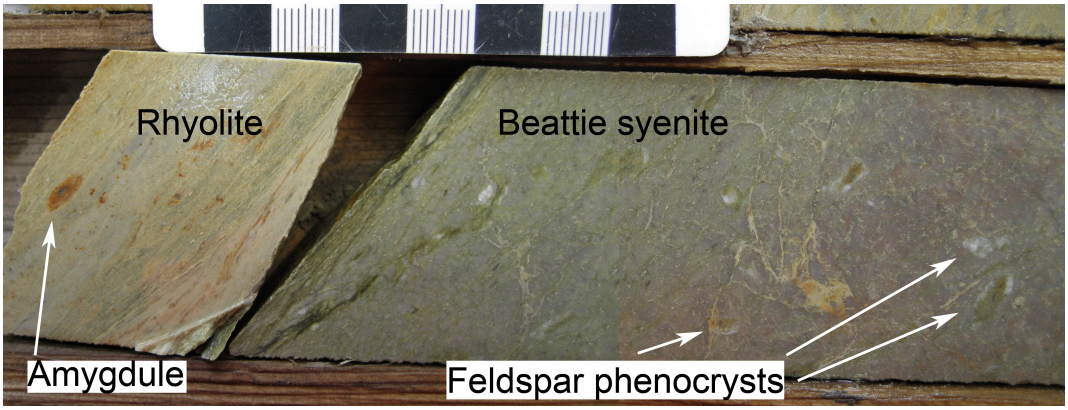


Figure 5.19 – Detailed map of a Deguisier rhyolite outcrop (JEB-09-10). Full resolution poster has been included in Appendix B.

5.9 and 5.10). Contacts with the Beattie syenite are sharp and exposed in numerous locations. Examples are presented in Figure 5.21.



Figure 5.20 – Anastomosing sericite filled fractures in the Deguisier rhyolite. Quartz filled amygdules are near perpendicular to the sericite veins and occur in both the veins as well as in the undisturbed rhyolite. The particular arrangement of the arc-shaped sericite-filled fractures have been mistaken for pillow structures. Location: 630906E 5374295N.



(a) Contact between the beige amygdular rhyolite (left) and the Beattie syenite (right) in a drill core specimen. Drill core: B08-102, depth: 85.50 m.



(b) Contact between massive grey rhyolite (left) and the red Beattie syenite (right) in a drill core specimen. Drill core: B09-85, depth: 15.30 m.

Figure 5.21 – Contacts between the Deguisier tholeiitic rhyolite and Beattie syenite.

Lanaudière Formation, Kinojévis Group

The Lanaudière Formation is located between the Deguisier Formation and the PDFZ. The formation is composed of basalts, komatiites, andesites and rhyolites (Goutier and Lacroix, 1992; Goutier, 1996). In the Beattie area, evidence of komatiites and komatitic basalts (as determined by geochemistry, see Chapter 7) was found unexpectedly in a drill core from Cogema Canada Ltd. (Capus, 1988)(drill core: PC-01, azimuth: 0° dip: 50° and depth: 199.46 m). The drill hole is located within the Duparquet conglomerate, 473 m southeast of the Central Duparquet 2 mine shaft. As such, volcanics of the Lanaudière Formation are encountered approximately 87 m beneath the Timiskaming sediments.

The author has never seen volcanics from the Lanaudière Formation, therefore the following lithological and structural descriptions are entirely based on Goutier (1996); Goutier and Lacroix (1992); Capus (1988).

Drill core observations and hand-specimen petrography Capus (1988) describes the drill core as successions of pillows and flow breccia horizons with minor spinifex horizons extending for < 7 m. Geochemically, the pillows and flow breccias have been associated with komatitic basalts, whereas komatiites are associated with the presence of spinifex horizons (see Chapter 7). Spinifex bearing areas are described as massive, fine grained to cryptocrystalline, and sporadically with pillows. The relative abundance of spinifex decreases when approaching a contact with the komatitic basalt (Capus, 1988).

Structural relationships Structural studies by Goutier and Lacroix (1992) reveal that the formation possess E-W to NE-SW orientation with stratigraphic tops principally to the south. Furthermore, the different lithologies come into contact with the PDFZ at an angle between 20° - 30° (Goutier and Lacroix, 1992). Deformation of the komatiites and komatitic basalts is heterogeneous. Near the PDFZ these rocks were transformed to carbonitized chlorite, talc and sericite schists (Graham, 1954). Further away from the fault, the intensity of deformation decreases where in the drill core pillow, flow breccia and spinifex textures have been preserved. Transecting shear faults are also common in areas away from the PDFZ. Such a fault noted in the drill core PC-01 (depth: 142 to 144 m) has transformed the komatitic basalt into a breccia infilled with chlorite, graphite and traces of pyrite (Capus, 1988).

The contact between the Deguisier and Lanaudière Formation is masked by the Timiskaming sediments and/or obscured by transecting faults (Goutier and Lacroix, 1992). However, in the Destor area, the start of the formation is marked by Lanaudière rhyolitic flows which rest onto basalts from the Deguisier Formation (Goutier, 1996).

5.1.2 Hébécourt Formation, Blake River Group (A *ht1*)

The Hébécourt Formation is one of the nine Formations belonging to the Blake River Group. U-Pb dating of zircon from a rhyolite of the Hébécourt Formation yielded an age of 2703 - 2701 Ma (McNicoll et al., ress). This formation occupies the most northerly extension of the Blake River Group. Within the Duparquet Township, the Hébécourt Formation is only found in the southwestern portion. Specifically, it is located south of the PDFZ, striking in the same direction as the fault. The formation is composed dominantly of basalt, but on the basis of physical volcanology combined with stratigraphical and geochemical data, Rogers (2010) identified 5 units in the area of Lac Hébécourt (located west of the Beattie area), that are: 1) the Hébécourt basalt, 2) Hébécourt basaltic andesite, 3) Hébécourt main rhyolite (Low-Ti), 4) Hébécourt main rhyolite (High-Ti) and 5) Hébécourt upper rhyolite. Of the five units, only the Hébécourt basalt occurs in the Beattie area. The unit occurs as a ESE striking, 400 m thick band of homogeneous basalt.

Field observations and hand-specimen petrography Lithological descriptions made by Goutier and Lacroix (1992) and Rogers (2010) describe the unit as composed of either massive or pillowed basalt. Individual pillows measure, on average, between 60 - 80 cm, contain $< 40\%_m$ of millimetre to centimetre size amygdules and possess thick selvages. Pillows are tightly packed with only a small amount of fine-grained, angular hyaloclastite inter-pillow material. Massive lavas are fine-grained to aphanitic basalt. They are non-vesicular and aphyric.

Thin-section petrography The Hébécout basalt unit is composed of plagioclase, actinolite, chlorite, epidote, quartz and opaque minerals (Goutier and Lacroix, 1992). Feldspar microphenocrysts measuring between 100-200 μm are rarely accompanied by olivine phenocrysts (Rogers, 2010). Groundmass crystals are generally very small, being irresolvable in some instances. Primary textures, when preserved, commonly demonstrate radial quench textures

along with some skeletal crystals of pyroxene which crystallized between plagioclase (Rogers, 2010).

Structural relationships The Hébécourt basalt unit is slightly deformed (Goutier and Lacroix, 1992). The deformation increases towards the PDFZ, wherein amygdules become increasingly stretched towards the fault zone. Furthermore, a slight foliation defined by a spaced cleavage cutting the bedding also becomes tighter towards the PDFZ. The increase in deformation progressively becomes so intense that basaltic rocks are transformed to a chloritic schist.

The changing polarity of the pillows and bedding reveal that the unit is part of an asymmetrical Z-fold. This fold is centred to the northwest of Lac Duparquet, strikes parallel to the PDFZ and plunges near vertically to the southeast (Goutier and Lacroix, 1992).

5.1.3 Porcupine Group (A*pc*) and Mont-Brun Formation, Kewagama Group (A*mn*)

Both the Porcupine and Kewagama Group sediments are lithologically and chronologically similar. They are however separated by the PDFZ resulting in the division into 2 separate groups. Consequently, the northern portion is occupied by the Porcupine Group and the south is part of the Kewagama Group.

In the Beattie area, the Kewagama Group is represented by the Mont-Brun Formation dated at $<$ 2686 $\pm$4 Ma by Davis (2002) and $>$ 2682 $\pm$3 Ma by Mortensen (1993). The Porcupine Group has been dated at $<$ 2687.2 $\pm$1.6 Ma by Ayer et al. (2005). Both the Porcupine and Mont-Brun sediments appear as thin elongated bands. One of these bands is immediately west of the syenite, north of the PDFZ (Porcupine) with another thicker one south of the PDFZ (Kewagama). Individual bands may reach apparent distances $>$ 10 km and a thickness $<$ 750 m.

Outcrops of the Porcupine sediments in the Beattie area are extremely rare and have only recently been excavated. As a result, the following paragraphs exploring the lithological and structural features are principally based from drill core observations. No thin section was ever produced, therefore the thin-section petrography is omitted.

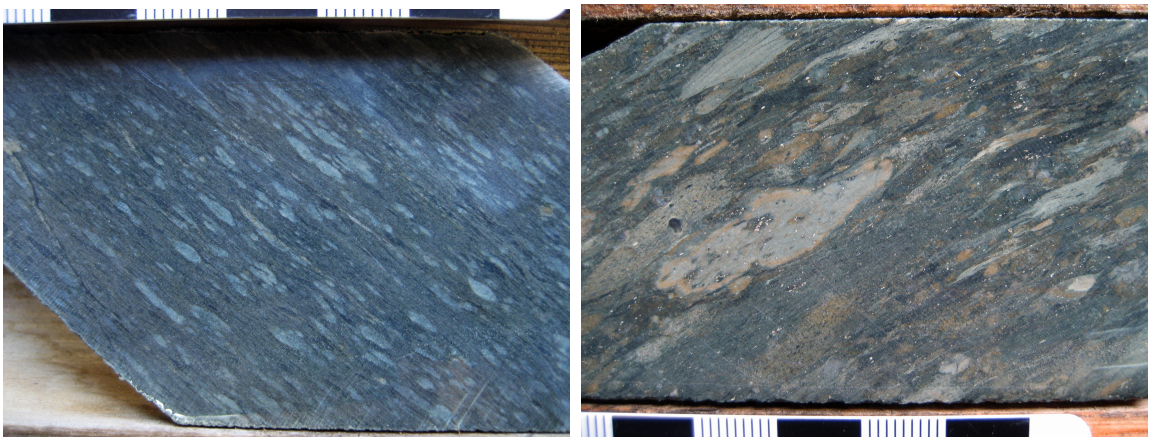
Field observations and hand-sample petrography Both groups have beds of wacke and mudrocks. Wackes form greenish-grey to dark grey beds measuring < 30 cm thick. Mudrocks on the other hand, are black to dark green fine grained rocks forming graded centimetre scale beds (see Figure 5.22).



Figure 5.22 – Porcupine mudrock specimen. Slight grading is best observed on the left. Specimen taken by Graham (1954) from the Beattie mine (exact location and depth unknown).

Uniquely, the Porcupine Group is also composed by a polymict conglomerate, with lens measuring < 10 m thick. The conglomerate is characterized by < 5 cm clasts of greenish chert, rhyolite and basalt (see Figure 5.23). All clasts have been subsequently elongated through deformation. Overall, clasts gradually increase in size progressing eastwards, obtaining a maximal length of 8 cm across. The Porcupine polymict conglomerate was also observed in a few outcrops. The surface of such outcrops contains sub- to centimetre pits caused by preferential weathering of clasts (see Figure 5.24). Furthermore, pits revealed the same elongation of the clasts as encountered in drill cores. Contacts between individual beds are generally normally graded. At other times, contacts between sediment types (i.e., conglomerate and wacke) are progressive, on the order of < 10 cm (see Figure 5.25).

Ultimately, the Porcupine sediments can be differentiated from the Duparquet conglomer-



(a) Conglomerate in drill located west, immediately next to the Beattie open pit. Clasts are well sorted, albeit very elongated. Drill core: B09-64, depth: 33.20 - 38.20 m.

(b) Conglomerate in core situated further east. Lighter coloured clasts are dominated by the local Deguisier rhyolite. Drill core: B08-73, depth: 9.00 - 18.20 m.

Figure 5.23 – Polymict conglomerate of the Porcupine Group. Lithic fragments measure < 5 cm. All fragments have been subsequently elongated with mafic clasts more so compared to felsic ones. Clasts demonstrate an increase in size from west (a) to east (b).

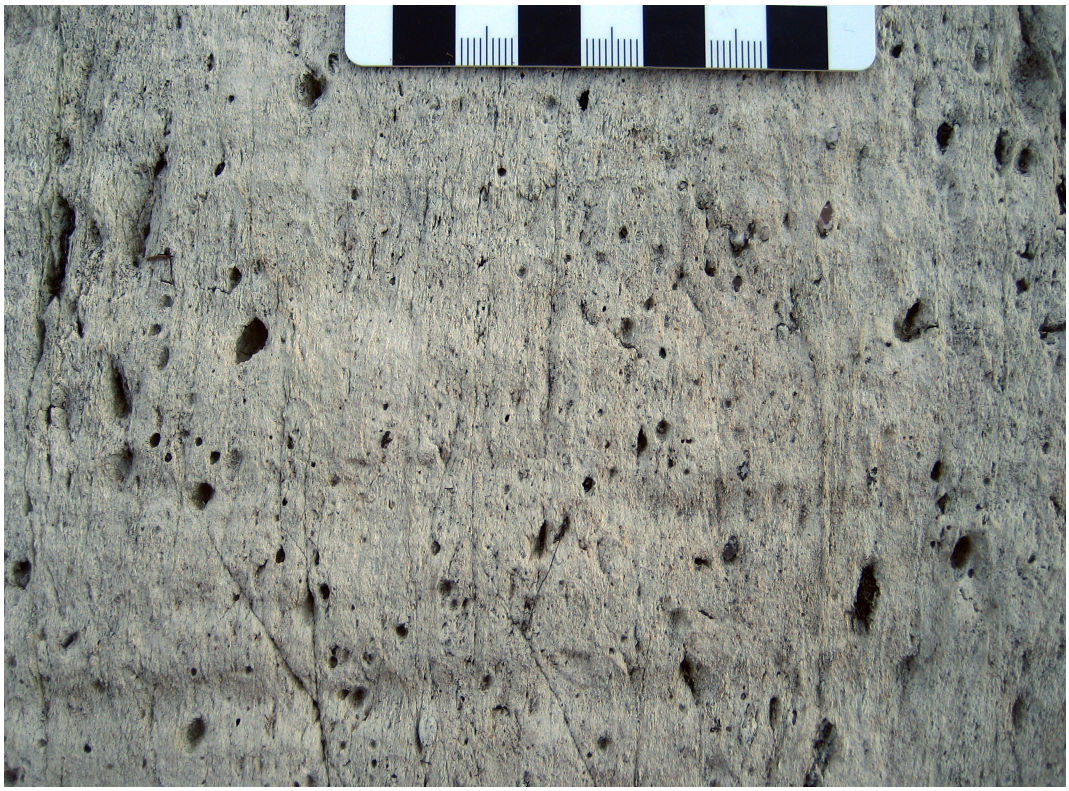


Figure 5.24 – Pitted Porcupine conglomerate in an outcrop. A general E-W elongation is reflected by the now weathered clasts and from the matrix. Location: 631001E 5374311N.

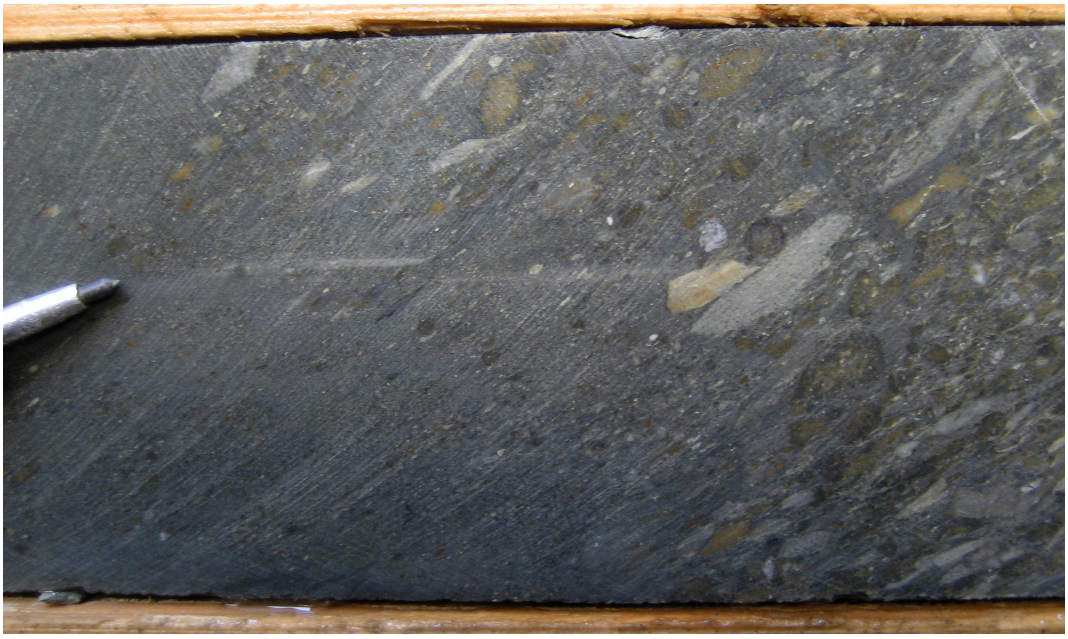


Figure 5.25 – Porcupine polymict conglomerate transitioning to wacke. The grey coloured wacke is to the left and the conglomerate is to the right. Drill core: B09-07, depth: 203.00 - 215.8 m.

ate by a smaller average clast size and by the absence of syenitic and jasper fragments.

Structural relationships Clasts of the Porcupine sediments have been flattened and now demonstrate an E-W elongation. This is readily seen in outcrop, where both clasts and the matrix appear flattened (see Figure 5.24). Structurally, the Porcupine and Kewagama Groups underlie the Blake River Group, yet two U-Pb zircon dates show that they are both younger than the Blake River Group.

Both groups have highly sheared upper and lower contacts. Additionally, they display polarity reversals, indicating folding in the unit (Goutier and Lacroix, 1992). Studies of an outcrop in the Duquesne mine area reveal that polarity reversals are resultant of SE trending folds. This particular outcrop is cut by numerous E-W to SE dextral faults, by a trending NE - SW fault set and by a NE striking crenulation cleavage dipping moderately to strongly southeast, associated to small Z-shaped folds (Lacroix and Landry, 1991). Progressing west, the deformation intensifies, marked by a stronger E-W foliation, cut by a NE cleavage which obliterated any primary structures (Goutier and Lacroix, 1992).

Contacts between the Porcupine sediments and the Deguisier basalt are sharp, measuring $<$ 1 cm across (see Figure 5.26). No evidence of a regolith or paleosol were found. At the

contact, the Deguisier basalt is pale in colour compared to its typical dark colour elsewhere. However, the colour variation only lasts approximately 50 cm.

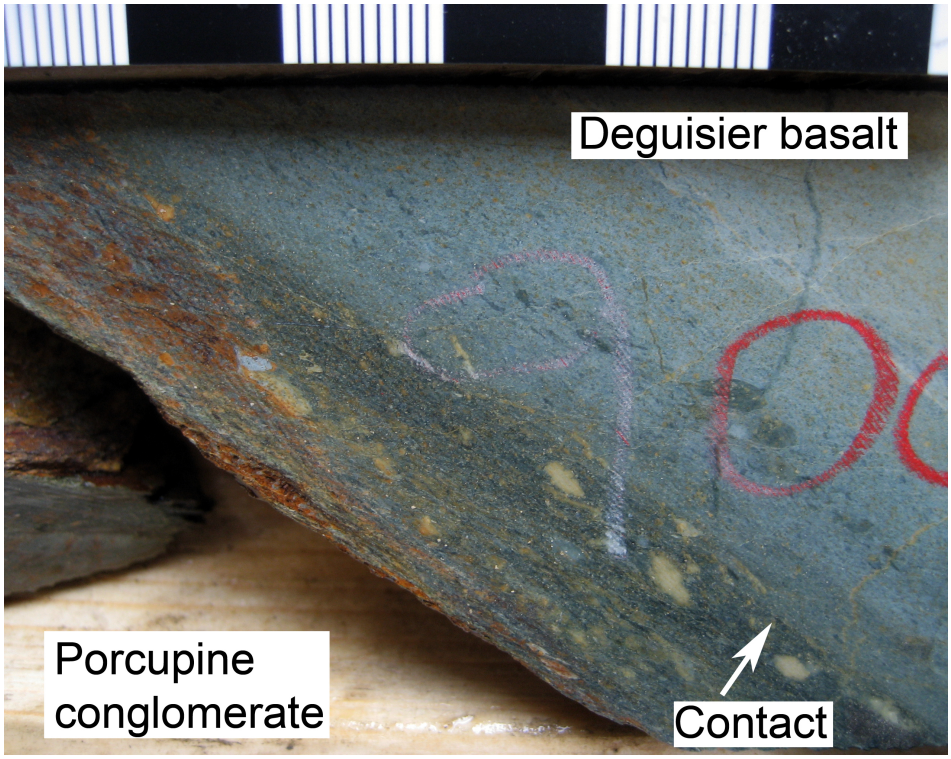


Figure 5.26 – Contact between the Porcupine sediments and the Deguisier basalt. The Porcupine sediments (left) have small fragments measuring < 0.4 mm across. The Deguisier basalt (right) on the other hand has a few elongated quartz filled amygdules. Following the contact, the Deguisier basalt is tan coloured, returning to a typical dark green colour after 50 cm.

5.1.4 Duparquet Formation, Timiskaming Group (A*dp*)

The Duparquet Formation consists of a polygenetic polymict conglomerate with subordinate wacke and mudstone. The formation belongs to the Timiskaming Group, having an age $<$ 2679 $\pm$3 Ma (David et al., 2006). It occupies the southern parts of the township as thin ($<$ 740 m), elongated ($>$ 7 km), E-W striking bands bounded by faults or resting unconformably on the Deguisier Formation, the Lanaudière Formation and the Beattie syenite.

Lithological description Most of the Duparquet Formation consists of a polymict conglomerate. Clasts are extraformational, ranging from cobbles to boulders ($<$ 1 cm - 1 m). Local clasts are an assortment from the Kinojévis Group (Deguisier and Lanaudière Forma-

tions), Beattie syenite and quartz feldspar porphyry. Distant clasts on the other hand are from granites and jasper bearing outcrops (see Figure 5.27). All clasts are hosted in a fine grained (sand to granule size), dark grey to green matrix probably composed from mafic fragments.



Figure 5.27 – Duparquet Formation polymict conglomerate. Clasts are extraformational ranging from granules to boulders. Location: 633897E 5373846N.

Wackes and mudstones also compose part of the formation. They are characterized by dark grey foliated lenses oriented parallel to the conglomerate lamination. Additionally, wacke lenses increase in abundance from the lower to the upper portions of the formation. Wackes in the inferior portions of the formation have parallel laminations, whereas in the upper portions they commonly display cross-lamination structures. Small clasts in the wacke and mudstone are the same lithic fragments composing the conglomerate (Goutier and Lacroix, 1992).

The Duparquet conglomerate can be distinguished from the Porcupine sediments by a larger average clast size and by the presence of syenitic and jasper fragments (see Figure 5.28).

Structural relationships The Duparquet Formation lies unconformably on older lithologies (Kinojévis volcanics, Beattie syenite and quartz feldspar porphyry) or is bounded by faults.

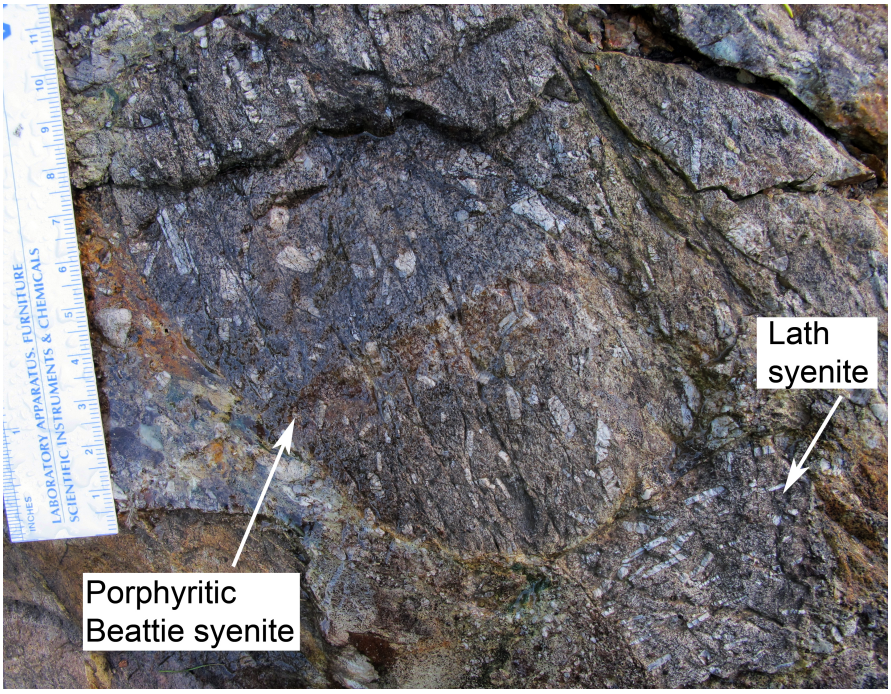


Figure 5.28 – Clasts of the Beattie syenite within the Duparquet conglomerate. The larger clast (centre) belongs to the porphyritic Beattie syenite unit, while the smaller clast (lower right) belongs to the lath syenite unit. Location: 634073E 5373919N.

Bedding orientation varies locally in the Formation. Succeeding sedimentation was a folding event which changed the orientation and angle of the bedding (Goutier and Lacroix, 1992). Subsequently, a foliation, characterized by a loosely spaced cleavage, transversely cuts the regional axial planes (Goutier and Lacroix, 1992). This foliation intensifies towards hinge zones also toward the southern and western edges of the formation. Flattened zones have the same transversal orientation as the foliation. Occasionally, deformed zones contain steeply plunging late minor Z-shaped folds. These minor folds overprint both the bedding and foliation. In the Beattie area, the foliation is defined by a crenulation cleavage, oriented southwest and inclined between 36° - 46° southwest (Goutier and Lacroix, 1992).

Contacts between the Duparquet Formation and older rocks are either sheared with a thickness spanning less than 1 cm across or are sharp. In one outcrop, a pristine contact between the Duparquet conglomerate and the Beattie syenite was observed. This contact is located at the eastern portion of the syenite and is characterized by a small fault. This fault separates the conglomerate from the syenite by a thin band of soft, schistose and partially altered material measuring 5 cm across (see Figure 5.29). The occurrence of the schistose material is the result of strata tilting, flattening and a differential contrast at the contact.

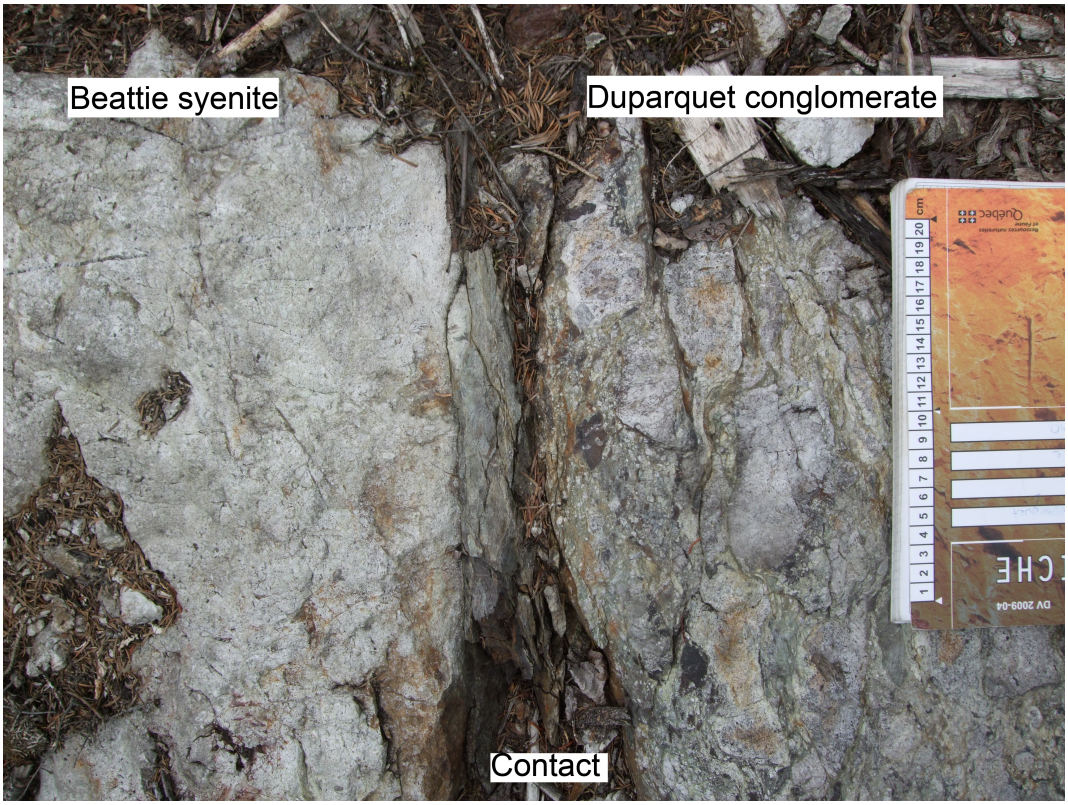


Figure 5.29 – Contact between the Beattie syenite and the Duparquet conglomerate. The Beattie syenite is to the left and the Duparquet conglomerate is to the right. This contact is the unconformity with shistose material associated with a differential contrast. Location: 634075E 5373913N.

5.2 Intrusive framework

A total of 3 major distinct intrusions occur in the Beattie and immediate area. They are, chronologically: 1) the gabbro, estimated at an age of 2717 - 2716 Ma (this thesis, see Section 7.6), 2) quartz-feldspar porphyry (QFP), U-Pb zircon dated at 2689.4 $^{+3.2}_{-2.9}$ Ma (Mueller et al., 1996), and 3) Beattie syenite, U-Pb zircon dated at 2682.9 ± 1.1 Ma (David et al., 2007) and at 2681.5 ± 1.0 Ma (Mueller et al., 1996). The oldest intrusion is classified as synvolcanic whereas the 2 younger ones are syntectonic. The gabbro intrudes into the units of the Deguisier Formation. As for the syntectonic intrusions they were in part emplaced in a klippen composed of fine grained sedimentary rocks as well as in massive or pillowed mafic volcanic rocks (Goutier, 1996). All intrusions are located north of the PDFZ. Furthermore, all are generally E-W striking, following the regional stratigraphic orientation.

To facilitate reading, the 3 intrusions are discussed in chronological order. Their chronological position with respect to the stratigraphy, metamorphism and Au-mineralization is illustrated Figure 5.2.

5.2.1 Gabbro (I3A)

The gabbro is deemed younger than the Deguisier Formation as indicated from geochemical investigations (see Section 7.6) combined with the multiple intrusive horizons that cut both the Deguisier and Lanaudière Formations. However, it is possible that there are younger gabbro horizons as documented in the eastern portions of the Duparquet area, therefore preventing its classification as a solely synvolcanic intrusion. Furthermore, Goutier and Lacroix (1992) reported that the intrusive gabbros sometimes correspond to diorites, therefore the name gabbro is only correct in a general sense. Gabbro intrusions occur as E-W striking, $<$ 300 m thick, irregular to tabular shaped masses. In the Beattie area, the gabbro occurs predominantly north, in contact with the Deguisier basalt. Occasionally, the gabbro comes into contact with the Beattie syenite and other units of the Deguisier Formation.

The following paragraphs address the lithological, microscopic properties and structural relationships of the gabbro with an emphasis on gabbro found near the Beattie syenite. Unfortunately, no thin section of the gabbro was obtained, therefore the following thin section descriptions are from Goutier and Lacroix (1992).

Field observations and hand-specimen petrography The gabbro, in the Beattie area, is a phaneritic mesocratic rock with crystal sizes < 0.3 mm across. Near contacts, the gabbro possesses a bright to pale green colour (see Figure 5.30), which gradually darkens to a deep shade of green (see Figure 5.31). The gabbro was also documented in drill core specimens taken at depth. Gabbro in core specimens is mesocratic with crystal sizes varying between $<$ 0.1 - 0.3 mm (see Figure 5.31).

Observations of the gabbro in the Duparquet area by Goutier and Lacroix (1992) report colour variations from mesocratic to melanocratic. Other regional observations describe the gabbro as ophitic to subophitic, with some pegmatitic zones in the thickest bodies (> 200 m).

Mineralogically, from both drill core and field observations, the gabbro is composed of plagioclase ($30\%_m$), pyroxene or amphibole ($40\%_m$), carbonate minerals ($10\%_m$) as well as accessory chlorite, talc ($2\%_m$) with trace hematite and chalcopyrite. Plagioclase crystals are typically pale green to grey, measuring < 0.3 cm across. Pyroxene or amphibole (depending on the alteration intensity) are dark to pale green also measure < 0.3 cm across. Alteration minerals consist of thin veins (< 0.1 cm) of black chlorite, carbonate minerals that stain the gabbro as small (0.1 cm) networks of orange coloured material and small (0.1 cm) masses of beige talc. Additionally, there are white albite veins (0.1 - 0.2 cm) (see Figure 5.31) which are occasionally accompanied by hematite and chalcopyrite ($<$ 0.1 - 0.2 cm).

Thin-section petrography Descriptions of gabbro thin sections from the region done by Goutier and Lacroix (1992) reveal that the mineralogical assemblage consists of plagioclase, pyroxene, amphibole, chlorite and opaques with accessory epidote, carbonate minerals and quartz. The preservation of the pyroxenes and feldspar sericitization is variable. Occasionally, cores of pyroxene crystals are rimmed by amphibole, whereas in other thin sections, pyroxene is completely replaced by amphibole and chlorite. Furthermore, exsolution was observed within the opaque minerals, suggesting that they are oxides (magnetite-ilmenite). Alteration minerals present in thin sections consist of carbonate minerals found in pyroxene cores, as well as chlorite and epidote.

Structural relationships The gabbro intrudes into units of the Deguisier and Lanaudière Formations. Akin to the Deguisier Formation, it cannot be divided into structural domains due



Figure 5.30 – Specimen of the gabbro. The mesocratic gabbro is composed of bright green crystals of amphibole (< 0.3 cm) with accompanying grey to pale green crystals of plagioclase (< 0.3 cm). Alteration minerals are beige talc (0.1 cm) and brown carbonate minerals (0.1 cm). Location: 633075E 5373870N.

to its uniformity across the Duparquet area. Since it occupies the same area as the Deguisier Formation, the gabbro was subject to the same general regional deformation events. As such, the gabbro has a poorly developed E-W striking, north-dipping schistosity. An exception is found in the area of the Central Duparquet 2 mine where the gabbro has been partially transformed into a schist.

A contact with the younger Beattie syenite was observed in a drill core specimen. The contact between the two is sharp as presented in Figure 5.32. Progressing toward the contact, over a distance of ∼1 m, the gabbro looses its dark green colour and becomes beige-brown. An increase in foliation, as observed at the surface, was comparatively minimal in drill core. Subsequent veins of black chlorite, brown carbonate minerals and white albite transect the contact (see Figure 5.32).

5.2.2 Quartz-feldspar porphyry

The QFP is the oldest of the syntectonic intrusions, located outside the Beattie area. The porphyry consists of trondhjemitic dykes or masses measuring < 4.6 km across and < 340 m thick. These dykes or masses appear in the middle of the Duparquet sediments, in proximity

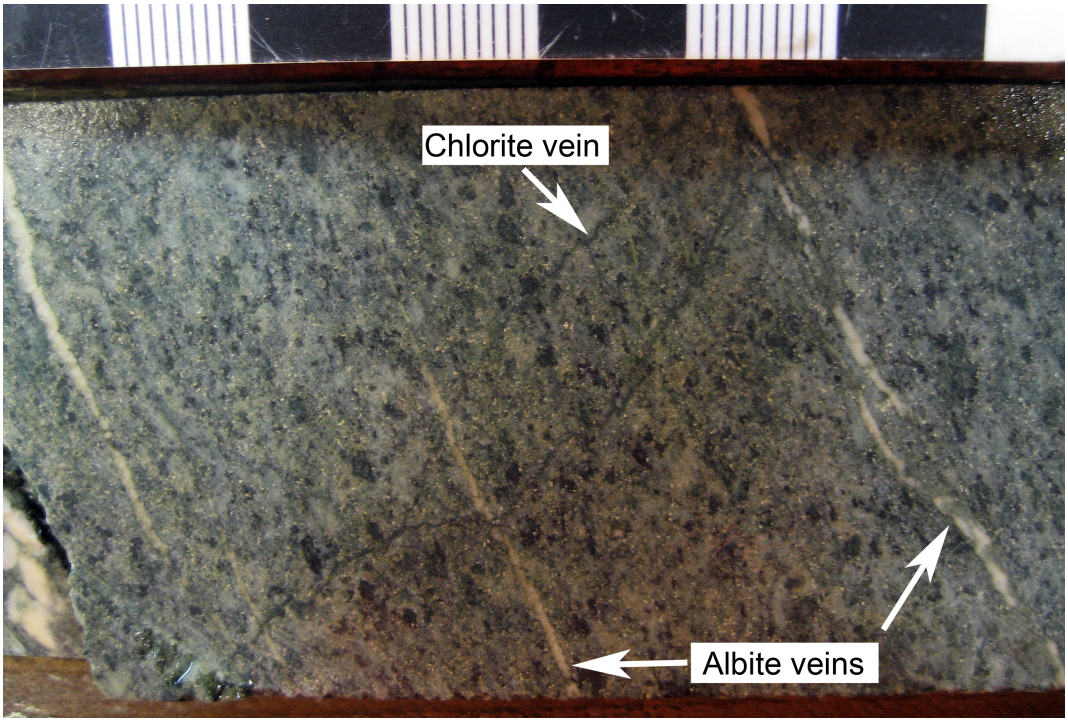


Figure 5.31 – Drill core specimen of the gabbro. The mesocratic gabbro is composed of dark green crystals of pyroxene or amphibole (< 0.3 cm) with accompanying grey to pale green crystals of plagioclase (< 0.3 cm). Alteration minerals consist of a dark green vein of chlorite. Subsequent veins of white albite transect the core. Drill core: B08-21, depth: 123.2 m.

to the Lac Lanaudière syncline, east of Lac Lanaudière, and in the area of the Duquesne mine. The closest occurrence of the QFP is located 500 m outside the Beattie area, or 2 km northwest from the town of Duparquet.

The author has never seen the QFP, therefore the following lithological, microscopic and structural descriptions are entirely based from Graham (1954) and Goutier and Lacroix (1992).

Field description and hand-sample petrography The QFP is characterized by large green plagioclase (1 - 4 mm) and quartz phenocrysts (< 1 - 10 mm) in a microgranular matrix. The abundance and size of the phenocrysts vary locally. Specifically, quartz phenocrysts decrease in size southwards. The QFP colour varies from grey, pink, green and yellow when fresh, to white and yellow-green when weathered.

Thin-section petrography The QFP is composed of plagioclase (20 - 40%$_m$), quartz (< 1 - 20%$_m$), sericite, chlorite (biotite), apatite (2 - 5%$_m$), with accessory calcite, epidote, pyrite

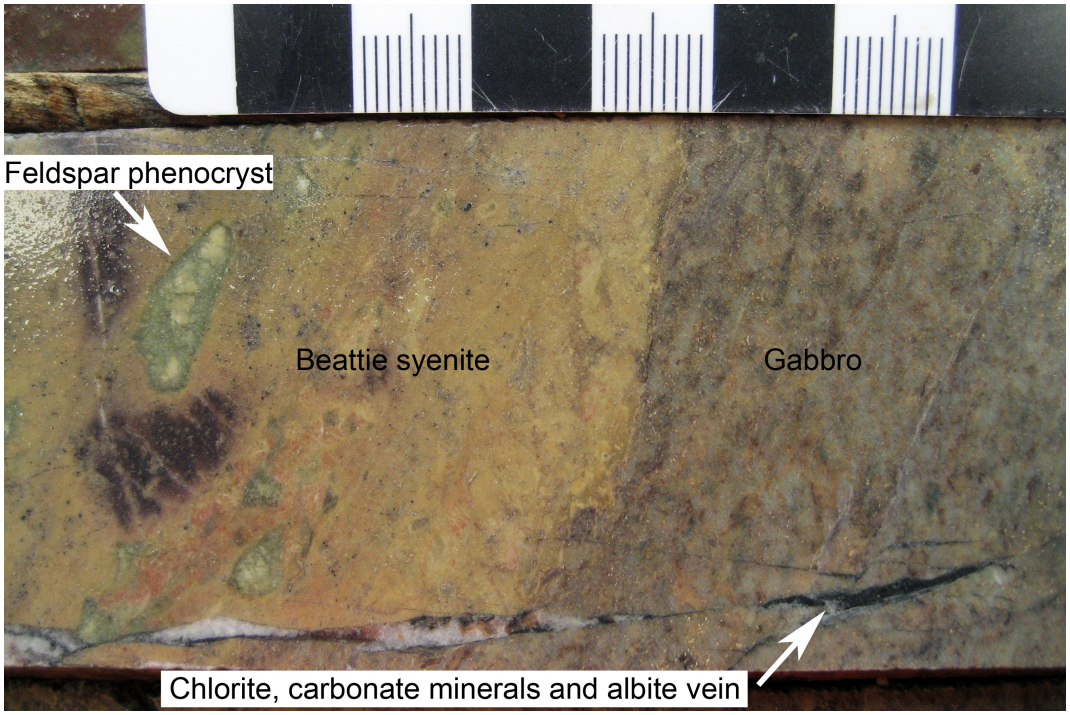


Figure 5.32 – Sharp contact between Beattie syenite and the gabbro. The younger Beattie syenite is to the left with a few sericitized feldspar phenocrysts (green to white). The gabbro is to the right, denoted by the beige-brown colouration as compared to the usual dark green. A subsequent vein of black chlorite, brown carbonate minerals and albite transect the contact. Drill core: B08-21, depth: 122.20 m.

and magnetite (Graham, 1954; Goutier and Lacroix, 1992). Euhedral plagioclase phenocrysts measuring between 0.25 - 4 mm across are the most abundant. However, the plagioclase phenocrysts are not always clearly visible as a result of intense sericitization and carbonatization. Accompanying plagioclase are lesser amounts of quartz phenocrysts measuring 4.5 mm across on average. Larger quartz phenocrysts are occasionally embayed or possess a lace-like crystalline edge. The matrix of the porphyry is composed of a fine grained mixture of quartz and sericite, measuring $<$ 0.02 mm with accessory apatite (0.5 - 0.2 mm), pyrite, calcite and magnetite. The only ferromagnesian mineral is biotite which is an accessory mineral. Biotite has generally been altered to small laths of chlorite (6 - 3 mm) with epidote, magnetite or sericite.

Structural relationships The QFP has been structurally emplaced at shallow depths (Goutier and Lacroix, 1992). Furthermore, U-Pb zircon dating classifies the pluton as a syntectonic intrusion.

5.2.3 Beattie syenite (A*bet1-5*)

The Beattie syenite is the youngest of the intrusions and one of the main focus of this study. This syenite appears as a number of elongated, E-W striking lens measuring $<$ 3.4 km long and $<$ 460 m thick. These lens are only found in the southwestern Duparquet area, north of the PDFZ, and have all been included into the Beattie study area. U-Pb zircon dating of the syenite yielded ages of 2682.9 $\pm$ 1.1 Ma (David et al., 2007) and 2681.5 $\pm$ 1.0 Ma (Mueller et al., 1996).

Very brief descriptions of the lithological, petrographic and structural observations are presented in the following paragraphs since Chapter 6 is dedicated to the igneous petrography and mineralogy, Chapter 7 to the chemistry and Chapter 8 to the hydrothermal alterations, metamorphism to the greenschist facies and deformation of the Beattie syenite.

Field observations and hand-specimen petrography Historically, the Beattie syenite had been subdivided into 3 different units by Banfield (1940) and 4 by Graham (1954) (see Section 2.3). In the course of this study, the units have been reclassified and divided into 5 distinct units. They are, chronologically (from oldest to youngest): 1) porphyritic Beattie syenite, 2) equigranular magnetite-bearing syenite, 3) porphyritic Central Duparquet syenite, 4) megaporphyritic syenite, and 5) lath syenite.

The Beattie syenite can be recognized by feldspar phenocrysts of variable size hosted within a generally red to brown aphanitic matrix. Depending on the unit, feldspar phenocrysts can measure between 0.2 - 6 cm across and compose between 1 - 50%$_m$ of the syenite. Regional metamorphism combined with hydrothermal alteration deeply affected the syenite in some areas. Specifically, there are anastomosing veins of green sericite locally transecting the syenite. Furthermore, there are also veins of albite, carbonate minerals, chlorite and quartz which occur in all the syenitic lenses.

Thin-section petrography The syenite is dominantly composed of orthoclase and albite. Accessory minerals are apatite, titanite and uniquely within the unaltered syenite unit, clinopyroxene relicts now replaced by actinolite and calcite. Secondary hydrothermal minerals in thin section can be quite abundant, including pale green sericite, carbonate minerals, chlorite, quartz and hematite. Additionally, hydrothermal pyrite, arsenopyrite and rarely chalcopyrite

which can also be associated with Au-mineralization, are also found in thin section.

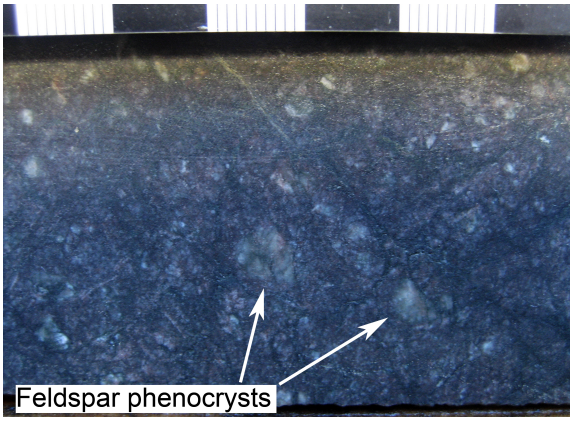
Structural relationships Structurally, the Beattie syenite is bounded by faults to both north and south. The syenite is dominated by pervasive E-W trending, secondary shear faults and series of conjugate shear and extension fractures. Their abundance and intensity dramatically increase towards the PDFZ.

Contacts between the Beattie syenite, Deguisier rhyolite and gabbro have already been addressed in Section 5.1.1.

The contact between the Beattie syenite and the Porcupine sediments is however quite peculiar. Specifically, the Beattie syenite intrudes into the sediments as 10 - 30 m long apophyse, initially described by Banfield (1940) as fingers radiating outwards. These dykes are abundant and intrude further into the Porcupine sediments as compared to the Deguisier basalt. The contact between the syenite and sediments is obscured by deformation and alteration. As such the contact appears as a progressive mixture of both syenite and sediments with no evidence of contact metamorphism, extending between 10 - 30 m, as measured from the centre of the syenite dyke (see Figure 5.33). At the centre, the syenite is massive with a deep red colour (see Figure 5.33a). Progressing outwards, the syenite becomes darker with occasional patches containing feldspar phenocrysts (see Figure 5.33b). The darker colour results from the darkening of the matrix to a darker reddish-black colouration likely caused by alteration. Furthermore, Banfield (1940) reported that the syenite can, at times, display a lighter colouration at this stage. At the contact the feldspar phenocrysts disappear (see Figure 5.33c). However, the exact location of the contact is difficult to ascertain as the phenocrysts become increasingly obscured due to deformation and alteration, which causes changes in phenocryst abundance, size and colour prior to the contact. From thereon, the rock becomes massive (see Figure 5.33d).



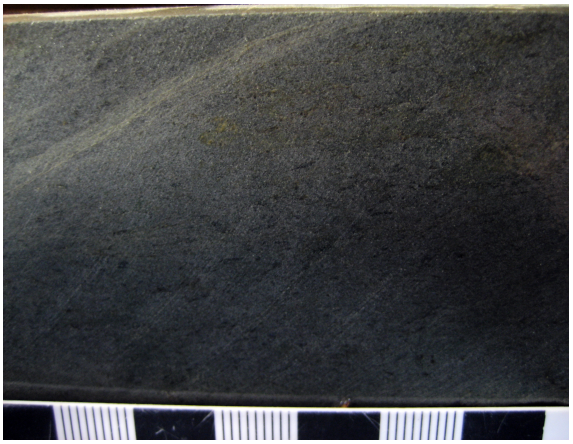
(a) Centre of the syenite dyke. The syenite appears massive with a dark-red colouration.



(b) Syenite dyke transitioning to Porcupine sediments after 14 m. The syenite becomes darker and supports lighter coloured feldspar phenocrysts.



(c) Approximate contact between the Beattie syenite and Porcupine sediments at 19 m. Feldspar phenocrysts disappear.



(d) Porcupine sediments after the contact with the Beattie syenite at ∼25 m.

Figure 5.33 – Contact between an intrusive Beattie syenite dyke and the Porcupine sediments. The above sequence of photographs were taken progressing downwards in a drill core. Drill core: B09-61, depth: 24.00 - 50.00 m.

5.3 Structural geology

Rocks of the Duparquet area have a complex history of deformation. It began with a long regime of extension, followed by several shorter-lived episodes of shortening and local extension. The succession of events are compiled in Figure 5.2. A discussion of current structural aspects of each unit have already been provided in the sections above. Consequently, the following focuses on the structural evolution of the Beattie area with additional descriptions of the local faults.

5.3.1 Structural evolution

Chronologically, the oldest structural regime recorded was one of extension, estimated to have occurred between 2720 - 2694 Ma (Legault et al., 2005). With this extensional event was the emplacement of the Kinojévis and Blake River Groups. After their emplacement, the structural regime changed to the first shortening event (D_1). This event produced large scale folds, found along the northern side of the PDFZ. The closest of these folds, the Abijévis syncline, is located in the neighbouring Destor Township. These folds tilted the older volcanic groups to the present southern polarity and imparted them with an E-W striking, south dipping schistosity (Goutier and Lacroix, 1992; Legault et al., 2005). Following D_1 was an N-S extensional period, from 2692 - 2680 Ma (Legault et al., 2005). The extension resulted in the creation of basins which were progressively filled by the Porcupine and Timiskaming Groups sediments. Furthermore, this extensional event facilitated the intrusion of the QFP and Beattie syenite plutons. Following the extension, after the Timiskaming Group sedimentation, was another shortening period (D_2). This period created the far-reaching PDFZ. Oblique dextral displacement by the PDFZ transported the Kewagama and Blake River Groups northwest (Goutier and Lacroix, 1992; Goutier, 1996). Later on, the D_2 event also created several dextral strike-slip, E-W striking faults transecting most lithologies. In the Beattie area these faults are the Beattie, Donchester and Central Duparquet faults. Displacement in these faults in turn affected the PDFZ (Goutier and Lacroix, 1992). However, these faults are not necessarily extensions of the PDFZ as they cover a broad age range. Specifically, some faults are clearly older and some younger than the Duparquet Formation. Near D_2 faults is an intense ENE-WSW to E-W schistosity. Finally, the last structural regime was another shortening event

(D_3). This last period affected all the units and older structures as they are cut by numerous conjugate faults. These faults either strike NE-SW or NW-SE and are equally divided between a dextral or senestral displacement.

5.3.2 Faults

The Beattie area contains numerous faults created during either the D_2 or D_3 shortening events. Older faults associated with D_2 are the PDFZ, Beattie, Donchester and Central Duparquet. Younger D_3 faults haven't been individually named since they propagate on a smaller scale and are numerous. Consequently, they are discussed together due to their importance in late stage Ag-quartz vein mineralization (see Section 5.6). To facilitate reading the characteristics of individual faults are discussed below in chronological order. Additionally, Figure 5.34 illustrates the location of each fault on a simplified geological map of the Beattie area.

Porcupine-Destor Fault zone

The most prominent fault in the Beattie area is the PDFZ. This fault transects the south-western portion of the study area and comports itself as a barrier, separating stratigraphic groups, north and south. The PDFZ rarely outcrops and has therefore been studied and measured from multiple boreholes. The fault strikes at 110° and dips at an angle between 50 - 80° south (Graham, 1954). Structural studies of the PDFZ reveals that it corresponds to a complex superposition of multiple faults which have had different displacements over several events (Goutier, 1996). The superposition of faults resulted in a large shear zone between 15 - 200 m thick. Intense shearing accompanied by hydrothermal alteration transformed the igneous rocks into mixed talc and chlorite schists with pervasive sericite, carbonate minerals and quartz (Graham, 1954). The schists originated from the Lanaudière komatiites, with some still demonstrating relict spinifex textures. Fault zone schists demonstrate evidence of ductile displacement and/or intense brecciation. Evidence of displacement was determined by a steep dipping stretching lineation, present in the upper portion of the fault. This lineation is parallel to the Blake River monocline, revealing that the fault moved vertically. Furthermore, this lineation is orientated eastwards, suggesting a dextral faulting style. Thus, the PDFZ is an inverse dextral-slip fault (Goutier and Lacroix, 1992).

Beattie faults

The Beattie faults occur as two, E-W striking, merging faults located north of the Beattie syenite. The southern Beattie fault is the longest, extending to a distance of 11 km. The fault begins with a SE-NW strike which gradually changes to E-W. Additional measurements delineate a shear zone between 120 to 180 m in width with a northern dip between 75° - 80° (Graham, 1954). This fault branches away from the PDFZ in the Hébécourt area, 4.8 km northwest of the Beattie mine shaft. Prior to entering the Duparquet area, this fault branches into 2 segments for a distance of 2.5 km before merging back together, 1.6 km west of the abandoned Beattie mine shaft. Thereon, the southern fault continues eastwards bounding most of the northern margin of the syenite. The northern Beattie fault branches away from the southern Beattie fault 3 km northwest from the abandoned Beattie mine shaft, in the Hébécourt area. This fault then extends for a distance of 5 km. The two faults merge together 520 m northeast of the abandoned Donchester mine shaft. Afterwards the faults continue on as smaller shear zones with a general E-W strike. Both faults have been offset in numerous locations by the younger D_3 faults.

Donchester fault

The fault branches away form the PDFZ approximately 1.88 km west from the abandoned Donchester mine shaft and follows an easterly strike. Progressing eastwards, between the syenitic lens, the fault is offset numerous times by the younger D_3 faults. Measurements in the Donchester mine area reveal that the fault dips near vertical to steeply north with a shear zone between 30 - 100 m across (Graham, 1954).

Central Duparquet fault

The Central Duparquet fault is found south of the Beattie syenite, into the Duparquet sediments. The fault branches away form the PDFZ at the southeastern corner of the town of Duparquet and continues, following an easterly strike with a steep southern dip (Graham, 1954). The Central Duparquet 1 and 2 mines are close to the fault which passes ∼100 m south of them. The Central Duparquet 2 mine studies attributed this fault as the main structural feature associated with the orebody (Graham, 1954). Good exposures of this fault near

the Central Duparquet 1 mine reveal that it is comprised of several sub-parallel shear zones, transected and subsequently offset by younger D_3 faults.

D_3 faults

D_3 faults are smaller (150 - 950 m long) strike-slip faults which are abundant throughout the Duparquet Township. Together they form networks of conjugate faults striking either NE-SW or NW-SE. Displacement within the faults are evenly divided between sinistral and dextral.

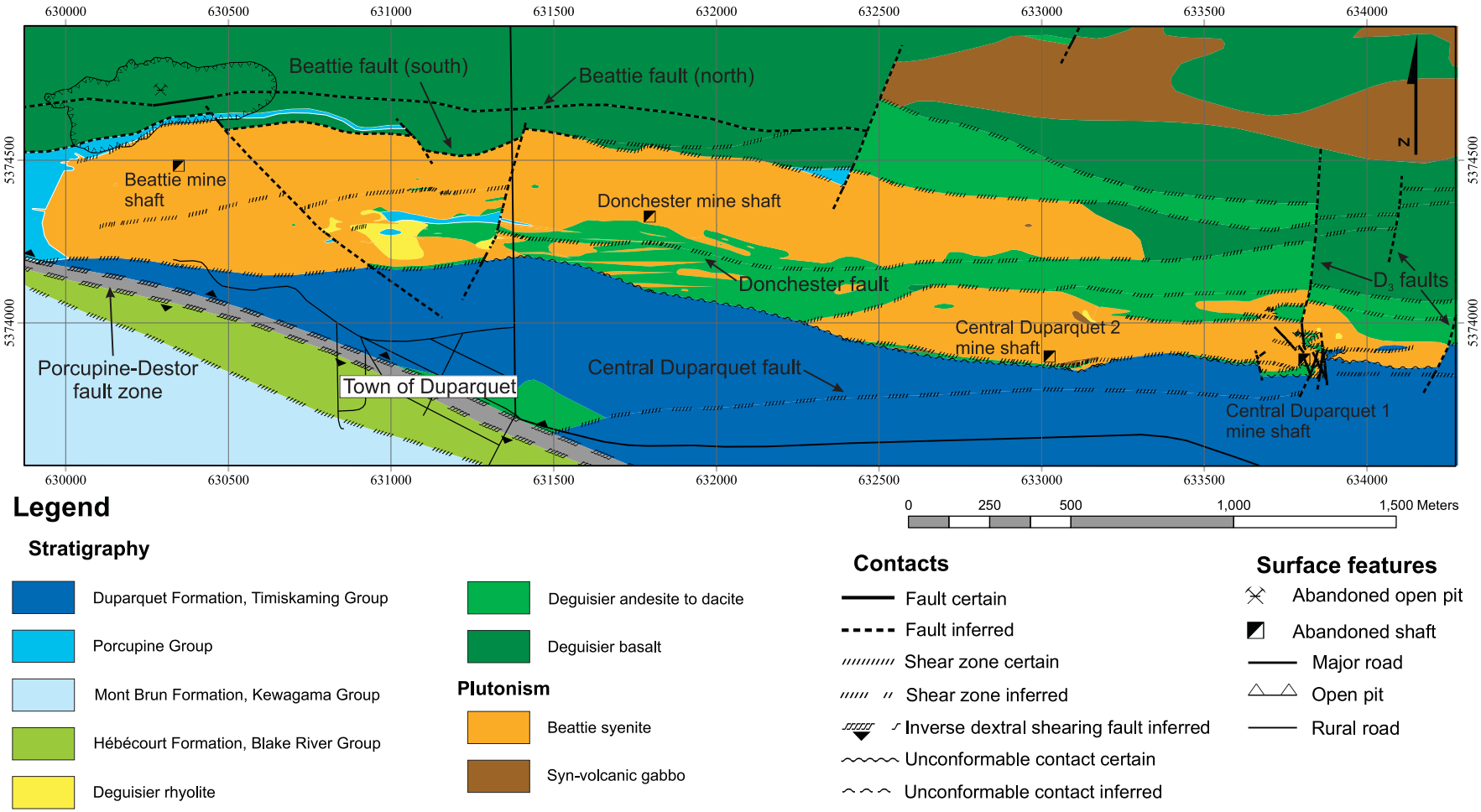


Figure 5.34 – Name and location of major faults and shear zones in the Beattie area. The geological map provided has been simplified and cropped. The complete and detailed geological map is found in Appendix B.

5.4 Regional Metamorphism

All rocks in the Duparquet Township have been metamorphosed to some degree. Fortunately, the metamorphic grade is very low, corresponding to the sub- to greenschist facies. As a result, igneous textures and structures have been preserved. Regional metamorphism postdates both the Duparquet Formation and most D_2 faults, as regional isograds overprints them both. Thus, the age span of regional metamorphism has been estimated between 2677 - 2643 Ma (Powell et al., 1995) (see Figure 5.2). Regionally, the metamorphic isograds are subparallel to the stratigraphy and structure, dipping shallowly to the north (Powell et al., 1995). Furthermore, thermobarometry performed by Powell et al. (1995) in Rouyn-Noranda, as well as 80 km west of the city, both yielded common metamorphic conditions of 220 MPa and 250°C.

Generally, common textures of metamorphic minerals in relatively undeformed syenitic rocks include pristine relicts of primary mafic phenocrysts and randomly oriented epidote crystals and amphibole porphyroblasts. Both textures suggest a static metamorphic environment. This same conclusion was obtained by Powell et al. (1995) based on observations in mafic rocks.

Foliations are practically non-existent in the sub- to greenschist facies. Where foliation exists, it is of a similar style and orientation to fabrics found in high strain zones (e.g., PDFZ). This foliation is produced by a weak alignment of metamorphic chlorite.

In the Beattie area, the metamorphic grade corresponds exclusively to the greenschist facies. This facies has been subdivided by Powell et al. (1995) into a lower 1) clinopyroxene-actinolite-epidote, and higher 2) actinolite-epidote subfacies. The sub-grades are separated by the complete replacement of igneous clinopyroxene phenocrysts by actinolite. From mineralogical observations in the Beattie syenite, phenocrysts have been completely replaced by actinolite (see Chapter 6). Therefore, the higher actinolite-epidote sub-facies corresponds to the metamorphic facies of the Beattie syenite and surrounding areas.

Near the PDFZ, metamorphic minerals in the Beattie area are quite scarce because of destabilization by CO_2 metasomatism. As a result, the metamorphic mineralogical assemblage is dominated by carbonate minerals, chlorite and epidote.

Retrograde metamorphism is common along the southern LLF and CF where metamorphic hornblende is partially replaced by actinolite, and oligoclase commonly has an albite rim

(Powell et al., 1995). This is not the case along the PDFZ which shows very little to no evidence of retrograde metamorphism.

5.5 Alteration

In all the Duparquet area the degree of alteration is generally low, with the exception of rocks located near D_2 shear faults and contacts (see Chapter 7). Near the faults and contacts, the alteration mineralogy is dominated by carbonate minerals, chlorite, sericite, pyrite, arsenopyrite and minor silicate minerals. All the D_2 faults as well as contacts carry the same geochemical alteration signature (see Chapter 7). Moving away from D_2 faults and contacts, the alteration decreases in a distance of < 50 m. Finally, alteration in the D_3 faults is almost exclusively confined to the fault, leaving the encasing rocks untouched.

Information on the nature and sequence of alteration minerals is greatly lacking in some aspects. As such, this thesis does have the goal of outlining the alteration of both the Beattie syenite and country rocks. Results are discussed in Chapter 9.

5.6 Economic geology, Au-mineralization of the Beattie syenite

The PDFZ constitutes the most conspicuous Au-mineralization features of the AGB. This single feature is associated with over 46 t Au in Québec and 2400 t Au in Ontario (Legault et al., 2005). Gold associated to the PDFZ was exploited at the Beattie, Donchester, Central Duparquet 2 mine.

A total of 6 different Au-mineralization styles along the PDFZ were recognized by Legault et al. (2005). They are chronologically: 1) sulphides associated to VMS, 2a) epithermal veins (synvolcanic), 3a) carbonate minerals and quartz veins, 2b) epithermal veins (synsedimentary), 4) disseminated sulphides associated with bleaching, 5) disseminated sulphides associated to a porphyry intrusion; subdivided to 5a) disseminated sulphides associated with calc-alkaline intrusions, and 5b) disseminated sulphides associated with alkaline intrusions, 3b) carbonate minerals and quartz veins, and finally 6) Ag-Au quartz veins.

Interestingly, 3 of these Au-mineralization styles occur in the Beattie area. The styles are the 2b) epithermal veins (synsedimentary), 5b) disseminated sulphides associated with alkaline intrusions, and 6) Ag-Au quartz veins. The first was exploited at the Beattie, Donchester and

Central Duparquet 2 mines, whereas the latter was exploited at the Central Duparquet 1 mine. Their temporal relationship with the stratigraphy and the intrusions is illustrated in Figure 5.2.

5.6.1 Epithermal veins

The oldest Au-mineralization style is exclusively found along the margins of the Duparquet basin (Legault et al., 2005). This mineralization style is characterized by microcrystalline quartz or chalcedony veins associated with carbonate minerals and sulphides. These veins often demonstrate colloform, crustiform bandings and cockade, comb textures (Legault et al., 2005). Elemental enrichments associated with this Au-mineralization style are Pb, Zn, Hg, Mo, Bi (± Cu) (Legault et al., 2005).

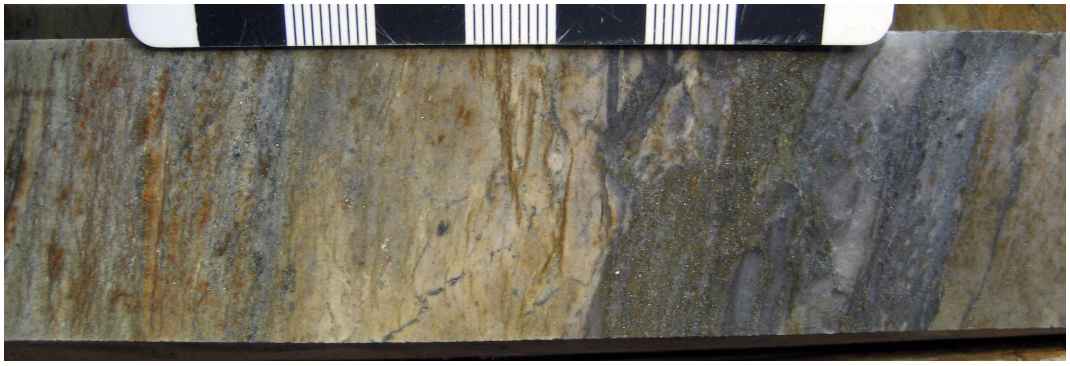
The veins are often folded and boudinaged, indicating that they are pre-D_2. Furthermore, the presence of fragments of these veins within the conglomerate indicates that they are synchronous with the opening of the Duparquet basin extending to the onset of sedimentation.

This Au-mineralization style has not yet been documented in the Beattie area. Furthermore, preliminary assessments at the contact between the Deguisier andesite to dacite and Duparquet sediments (south of the Donchester mine shaft) have not recorded any significant gold concentrations. However, with the Duparquet sediments dominating the southern portion of the Beattie area, there could be a potential for this type of Au-mineralization.

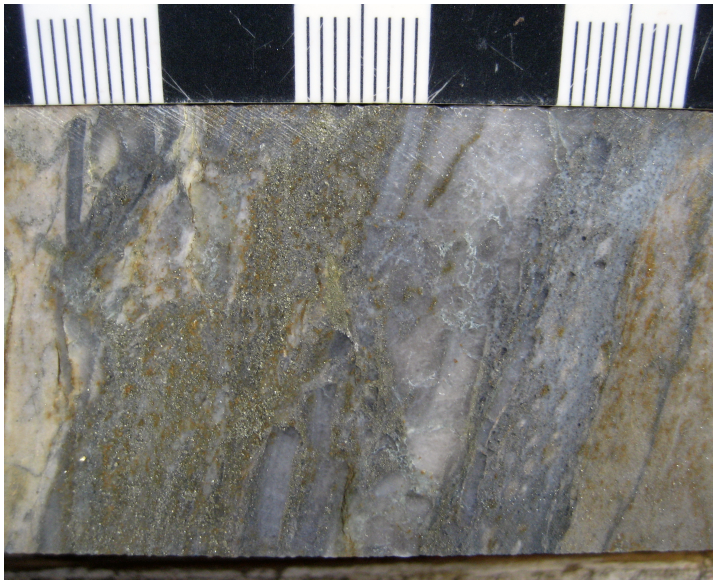
5.6.2 Disseminated sulphides associated with alkaline intrusions

The second Au-mineralization style postdates the syenitic intrusion. Thus, this mineralization is inferred to have occurred between 2681 - 2678 Ma (Legault et al., 2005). This style is demarked by finely disseminated (10 - 20$\%_m$) pyrite (0.07 - 0.3 mm) and arsenopyrite (0.01 - 0.04 mm) in E-W striking orebodies that are encased in silicified, albitized, sericitized and carbonitized zones (Banfield, 1940; Davidson and Banfield, 1944; Graham, 1954)(see Figures 5.35 and 5.36). As such, metallurgical and geochemical studies indicate an elevated Au/Ag ratio with corresponding high values of arsenic (Legault et al., 2005).

Interestingly, the mineralization is hosted in great part by the Porcupine sediments, Deguisier basalt and andesite to dacite unit. Mineralized zones observed in the Deguisier rhyolite on the other hand are rare with the exception of contacts between it and the Beattie syenite.



(a) Overview of a Au-mineralized zone in the Porcupine Group.



(b) Close-up on the most mineralized zone.

Figure 5.35 – Disseminated sulphides in the Porcupine sediments. Sulphides, dominantly pyrite and arsenopyrite are very fine grained and are accompanied by white albite, grey quartz and orange carbonate minerals. Drill core: B08-01, depth: 29.70 - 31.00 m.

Generally, from drill core observations along the southern margin of the syenite, mineralized zones in the Porcupine Group are wide and contain extremely fine sulphide crystals (see Figure 5.35), whereas other rocks support larger crystals which decrease in abundance within a few centimetres away from the mineralized zones (see Figure 5.36).

5.6.3 Ag-quartz veins

The Ag-Au quartz vein style is rare but very distinct. Gold is found in NW-SE striking, 100 m long, 30 cm wide quartz and carbonate tension veins found in syenite and gabbro near D_3 faults. Since their arrival was quite late (i.e., syn-D_3) with an age between 2670 - 2671 Ma

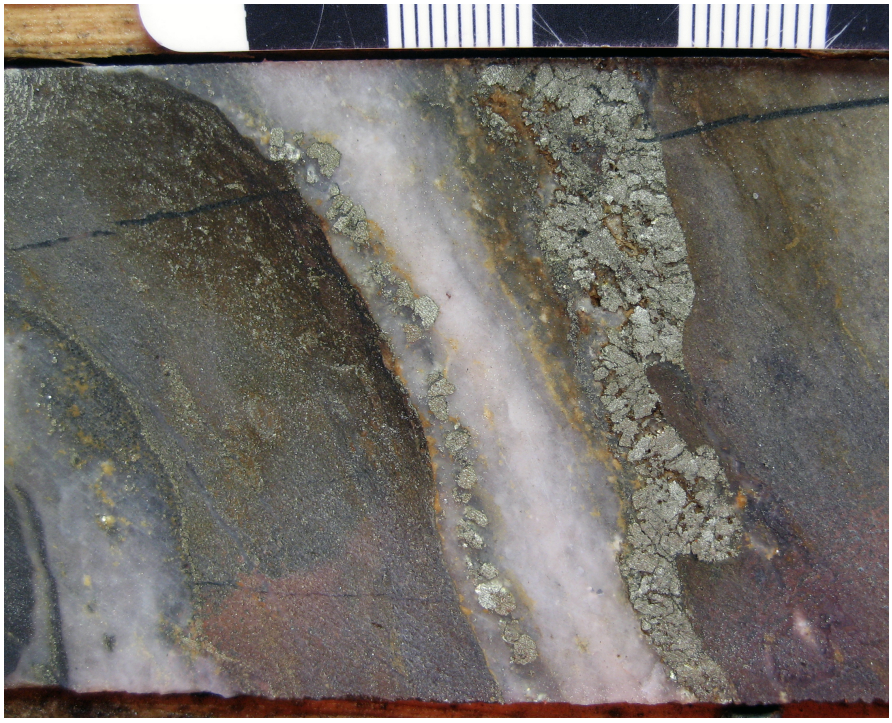
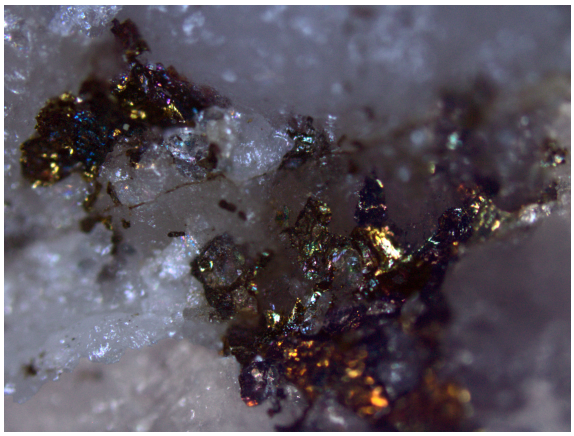


Figure 5.36 – Disseminated sulphides in the Beattie syenite. Sulphides, both pyrite and arsenopyrite, are larger and concentrated together. A vein of albite (white), quartz (grey) and carbonate minerals (tan to orange) transects the mineralization. Drill core: B09-103, depth: 6.00 - 6.30 m.

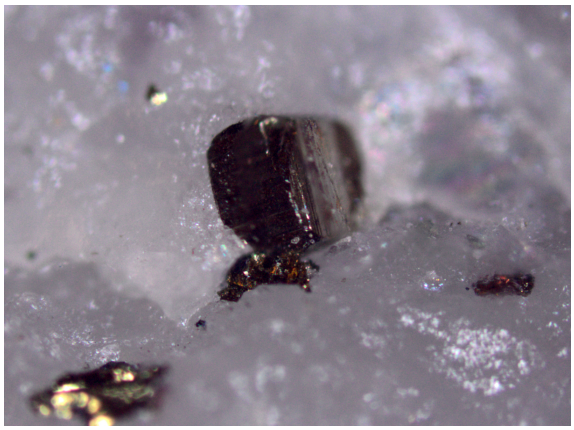
(Legault et al., 2005) they are not deformed and have minimal alteration (see Figure 5.2).

In these veins gold is in a free state and is accompanied by chalcopyrite, pyrite, tetrahedrite, arsenopyrite, sphalerite and galena. Their Au content is lower than 10 g/t with a low Au/Ag ratio produced by high concentrations of Ag. Additionally, these veins demonstrate an elemental enrichment in As, Cu, Zn, Pb, Sn and Hg (Legault et al., 2005).

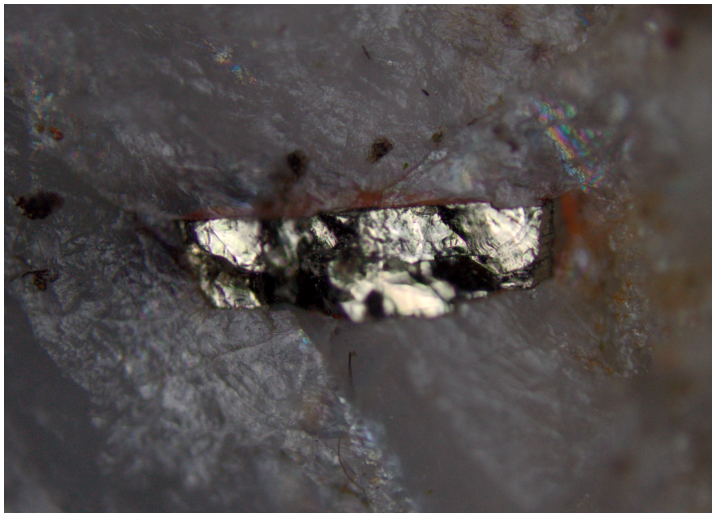
A hand sample collected by the author revealed chalcopyrite, pyrite and arsenopyrite contained in a quartz matrix as seen in Figure 5.37. The dominant sulphide minerals are anhedral chalcopyrite crystals, forming aggregates measuring 1.5 - 0.5 mm across. Very few crystals of pyrite were found. Pyrite is present as euhedral cubic crystals measuring $<$ 1 mm across. A satin-like grey sheen on the surface of the pyrite may be the result of an epitaxial overgrowth of tetrahedrite as seen in Figure 5.37b. Finally, a single 0.96 mm columnar crystal of arsenopyrite was observed in the sample.



(a) Oxidized anhedral chalcopyrite



(b) Cubic pyrite with a satin-like grey sheen, perhaps the result of epitaxial overgrowth of tetrahedrite.



(c) Columnar arsenopyrite.

Figure 5.37 – Sulphides in the Ag-Au quartz vein. The field of view for (a) is 4 mm across. Individual crystals measure (b) 0.75 mm and (c) 0.96 mm across. Photomicrographs taken under reflected light. Sample taken from a debris pile next to the Central Duparquet 1 mine shaft, location: 633807E 5373887N.

Chapter 6

Petrography and mineralogy of the Beattie syenite

A major objective of this thesis is to produce a complete petrographic and mineralogical description of the Beattie syenite. To achieve this objective, multiple excursions in the summers from 2008 to 2011 were conducted. Field observations performed by Jean Goutier (1990 - 1994) can be consulted at the MRN office[1] or through the database Sigeom[2]. A total of 73 thin sections were also collected in order to supplement field observations. Drill cores produced by Clifton Star Resources Inc. and the Osisko Mining Corporation were also consulted, albeit in a limited fashion. The drill cores observed were mostly located near or within the western occurrence of the Deguisier rhyolite. All information gathered through the different media were subsequently incorporated in the accompanying geological map of the Beattie syenite (see Appendix B).

The Beattie syenite contains a myriad of igneous, hydrothermal and greenschist facies metamorphic minerals. In addition, multiple episodes of brittle deformation have subsequently overprinted the syenite. For simplification purposes, this chapter will focus on igneous features encountered in the syenite and Chapter 8 will address the hydrothermal and greenschist facies minerals, the chemical changes produced the influx of Au-related fluids and the structural changes produced by brittle deformation. Since hydrothermal minerals are widespread in the syenite, and therefore inevitable in the following descriptions, their origin has been identified

[1] 70 avenue Québec, Rouyn-Noranda (Québec), J9X 6R1

[2] `http://www.mrn.gouv.qc.ca/english/products-services/mines.jsp`

to avoid confusion.

This chapter first provides an overview of the syenite with the establishment of the chronological order of the petrographic units, followed by a detailed description of each petrographic unit.

6.1 Overview of the Beattie syenite

The Beattie syenite is composed of 5 units, characterized on the basis of field relationships, petrography, mineralogy and textures. Chronologically, they are the: 1) porphyritic Beattie syenite, 2) equigranular magnetite-bearing syenite, 3) porphyritic Central Duparquet syenite, 4) megaporphyritic syenite, and 5) lath syenite.

The porphyritic Beattie syenite unit is the most abundant, encompassing 84.46% (inferred surface area) of the Beattie syenite. It is characterized by 2 - 10 mm sub- to anhedral feldspar phenocrysts contained in a red aphanitic matrix. Within the porphyritic Beattie syenite unit are lenses, with a gradational contact, of the equigranular magnetite-bearing unit, which corresponds to the least abundant unit, representing a meagre 0.16% (inferred surface area) of the syenite. The unit is distinguished by a lack of, or extremely few, feldspar phenocrysts. Additionally, this unit contains actinolite and metamorphic hornblende, unaltered titanite and magnetite, the latter rendering the unit magnetic. The porphyritic Beattie syenite unit transitions to the porphyritic Central Duparquet unit south-eastwards. This unit accounts for 12.69% (inferred surface area) of the syenite. It is characterized by 10 - 20 mm equant euhedral feldspar phenocrysts contained in a red or grey aphanitic matrix. Together, the porphyritic Beattie syenite and the porphyritic Central Duparquet units are the petrographic end-members of the syenite. Intruding as masses or dykes within the porphyritic Central Duparquet unit is the megaporphyritic syenite unit which represents 1.27% (inferred surface area) of the syenite. The unit is characterized by large 1 - 6 cm long feldspar phenocrysts, occasionally demonstrating a glomeroporphyritic texture, hosted in a pink to red aphanitic matrix. The lath syenite unit is youngest, occurring as dykes which transect all other syenitic units and representing 1.42% (inferred surface area) of the syenite. It is characterized by 1 - 3 cm long feldspar laths which display a strong trachytic texture.

The 5 units are divided among a number of lenticular bodies and dykes which comprise the

Beattie syenite. For simplification purposes, the lenticular bodies have been amalgamated into 4 large portions. They are, in order of magnitude, the: 1) Beattie-Donchester body (BDB), 2) Central Duparquet body (CDB) 3) North eastern bodies (NEB) and 4) Small central bodies (SCB). The division of the syenitic portions can be seen in Figure 6.1.

The BDB is composed of a large lenticular body, measuring a length of 3.4 km, a width of 460 m and occupying an area close to 1 km^2, and two smaller syenitic dykes which transect the Porcupine sediments to the west (see Figure 6.1). The BDB is host to the now abandoned Beattie and Donchester mines, hence the name. The great majority of this portion is composed by the porphyritic Beattie syenite unit. Occasionally, there are sub-circular lenses ($<$ 100 m across) of the porphyritic Central Duparquet unit. These lenses are found in the area of the Donchester mine and progressing eastwards. In addition the only outcrop of the equigranular magnetite-bearing syenite unit is found in the BDB. Finally, numerous E-W striking dykes of lath syenite unit are also found in the BDB.

The CDB is located south-east from the large BDB. It is separated from the BDB by $\sim$100 m of andesite to dacite of the Deguisier Formation. The CDB is composed of a single lenticular body measuring a length of 1.98 km and a width of 220 m. This body was host to the now abandoned Central Duparquet 1 and 2 mines, reflected in the name. Comparatively to the BDB this portion hosts four out of five petrographic units. To the west, the porphyritic Beattie syenite unit dominates which progressively transitions to the porphyritic Central Duparquet unit eastwards. Interestingly, the east also contains sub-circular to irregularly shaped lens of the megaporphyritic syenite unit. Finally, subsequent dykes of lath syenite unit are also found in the CDB.

The NEB is located northeast, separated from the BDB by 1.35 km of Deguisier basalt and andesite to dacite. This portion is comprised of 2 syenitic lens and a small dyke. Beginning west is a syenitic dyke measuring $<$ 2 m across, extending for a distance $>$ 110 m. Continuing eastwards, is the largest of the syenitic lens measures $\sim$500 m across and 60 m in width. It is accompanied by a smaller lens which measures $\sim$80 m across and 10 m wide. All 2 syenitic lens and dyke are composed exclusively by the porphyritic Beattie syenite unit.

The smallest of the syenitic portions is the SCB. This last one is comprised of 4 small lenticular bodies and a large number of transecting dykes. Most are separated from the BDB by the Donchester fault (see Section 5.3) and seem completely detached from the larger

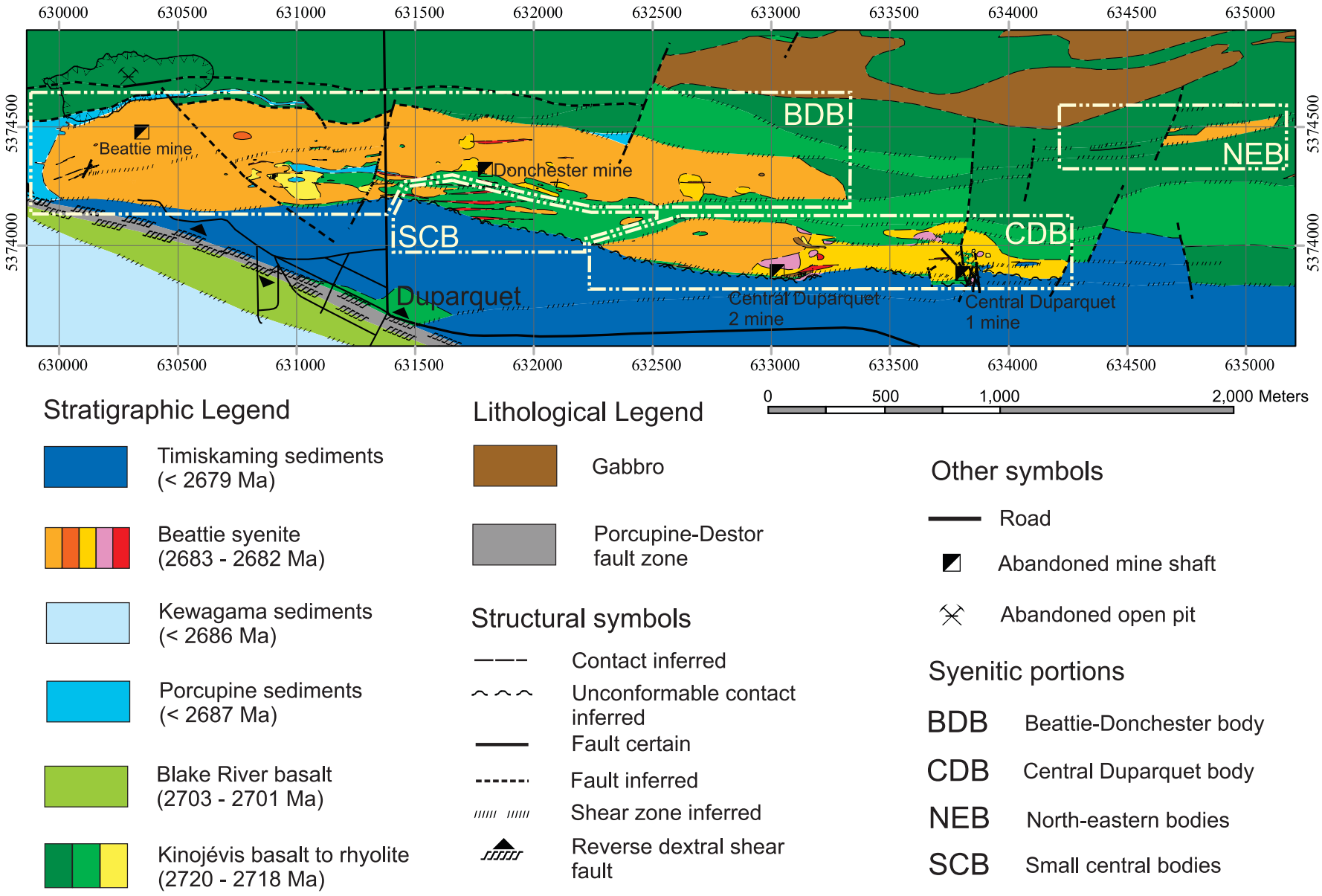


Figure 6.1 – Syenitic portions of the Beattie syenite. Syenitic dykes which transect the Porcupine sediments to the west (not shown) are also included in the BDB.

surrounding syenitic portions (i.e., BDB and CDB). They are located immediately between the BDB and the CDB. Beginning west, the first body measures 150 across and 40 m in width. Further east is the largest of the 4 bodies, measuring ∼220 m across and 20 m in width. Continuing east is a smaller lens which measures $<$ 100 m across and $<$ 30 m in width. The smallest lens measures ∼20 m across and $<$ 10 m in width. All 4 lenticular bodies are composed of the porphyritic Beattie syenite unit, whereas the transecting dykes are composed of the younger lath syenite unit.

Other unconfirmed syenitic lens were documented by Gagnon (1981) and Roy and Roy (1998), located further west and southwest. Those southwest are in relatively close proximity to the PDFZ (Roy and Roy, 1998), whereas those to the west are generally, in or near to the Duparquet polygenetic conglomerate (Gagnon, 1981). However, since these syenitic bodies fall far outside of the study area, they were not observed and documented in the scope of this thesis.

6.2 Chronology of the petrographic units

Contacts with the older Deguisier units are sharp and at times contain xenoliths. This is best illustrated in the detailed outcrop maps presented in Figures 6.2, 6.3 and 6.4. Furthermore, western contacts between the Porcupine sediments and the porphyritic Beattie syenite have already been addressed in Chapter 5.

The porphyritic Beattie syenite unit is presumed to be the oldest of the petrographic units since it is the most abundant and widespread of all units, contains less and smaller phenocrysts, and is intruded or cut by some of the other petrographic units (i.e., equigranular magnetite-bearing and lath syenite units).

Intruding the porphyritic Beattie syenite unit is the equigranular magnetite-bearing unit. The contact between the two is gradational, extending for $<$ 10 m and is characterized by a change from a grey equigranular syenite to a pink porphyritic one with the complete loss of amphiboles, titanite and magnetite crystals. The transition begins with a loss of the greenschist facies hornblende porphyroblasts (see Figure 6.5a). This first stage also sees an increase in size and abundance of feldspar phenocrysts (0.5 - 1 cm, 5 - 8%$_m$). Small fractures filled with either hydrothermal and/or metamorphic calcite and chlorite also appear. Continuing outwards, mid-way in the transition, the smaller actinolite crystals are lost and the feldspathic matrix changes to a pink colour (see Figure 6.5b). Additionally, the average size and abundance of phenocrysts continues to increase (0.5 - 1 cm, 10%$_m$). Magnetite and titanite are still visible, but magnetism steadily decreases in intensity. Furthermore, small scale metamorphic quartz, albite and carbonate minerals veins appear. Finally, at the last transition stage, the feldspathic matrix is pink and the syenite is porphyritic. Magnetite and titanite disappear and so does the rock's magnetism. The amount of brittle deformation increases further, to the multitude of tension fractures that are typical of the porphyritic Beattie unit.

The contact between the porphyritic Beattie and Central Duparquet units is also gradational. The transition between the two units is demarked by an increase in size and abundance, combined with a change in shape of phenocrysts (i.e., anhedral to euhedral, tabular to equant) (see Figure 6.6). The complete transition can be traced from $>$ 5 - 10 m in the BDB and close to $\sim$400 m in the CDB.

The megaporphyritic unit has been inferred to be younger than the porphyritic Central Du-

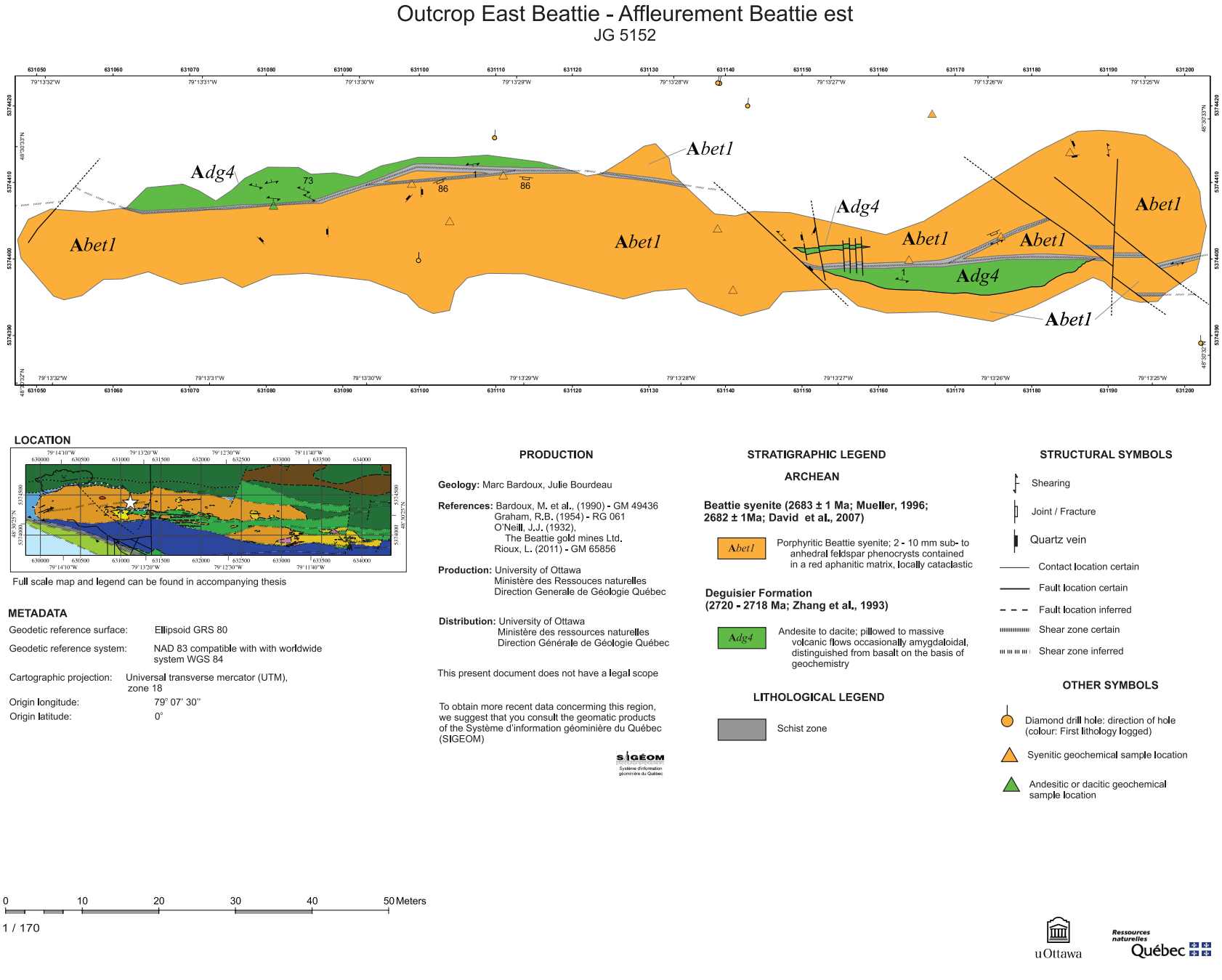


Figure 6.2 – Detailed map of outcrop Beattie east (JG 5152). Full resolution poster has been included in Appendix B.

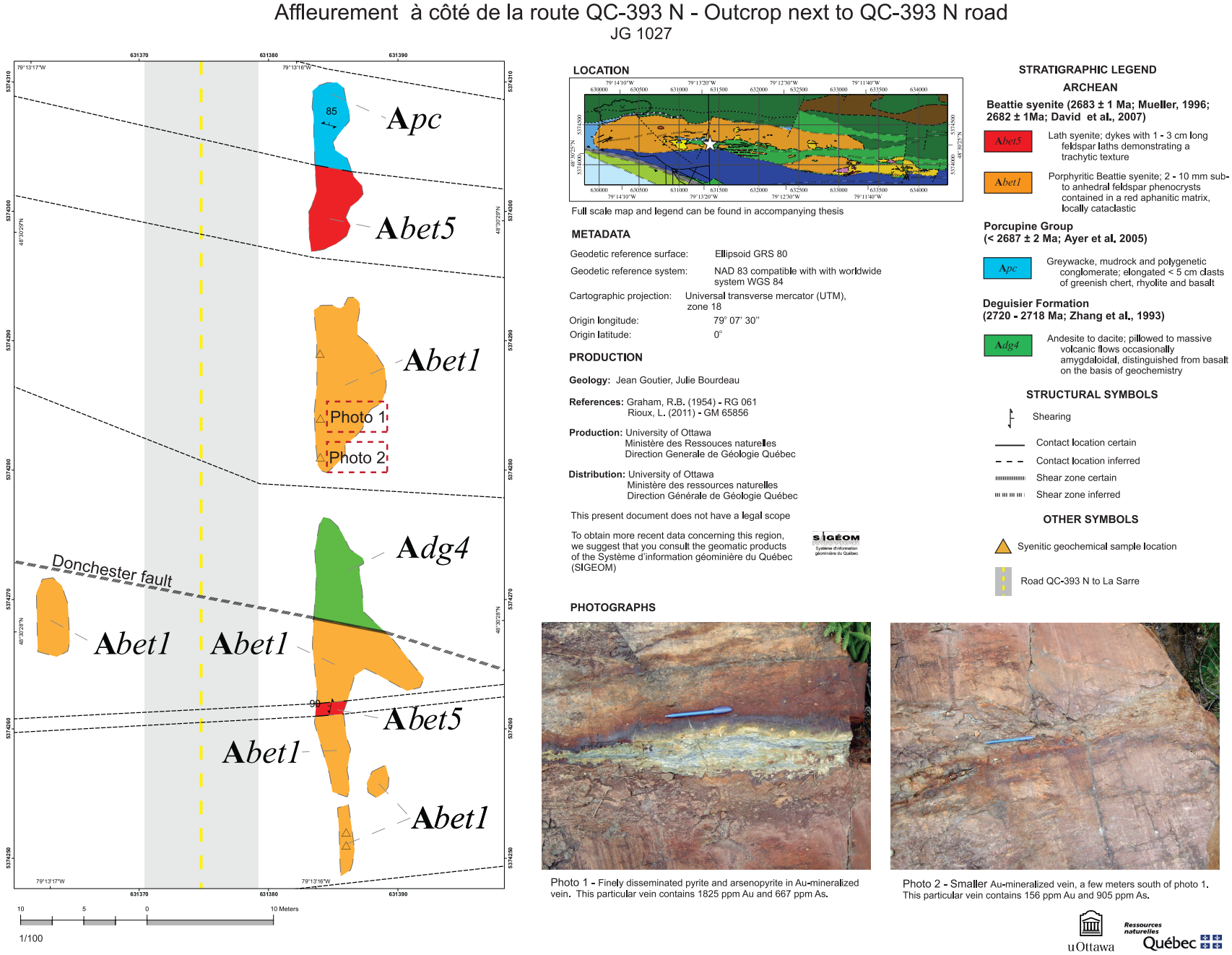


Figure 6.3 – Detailed map of outcrop next to QC-393 N road (JG 1027). Full resolution poster has been included in Appendix B.

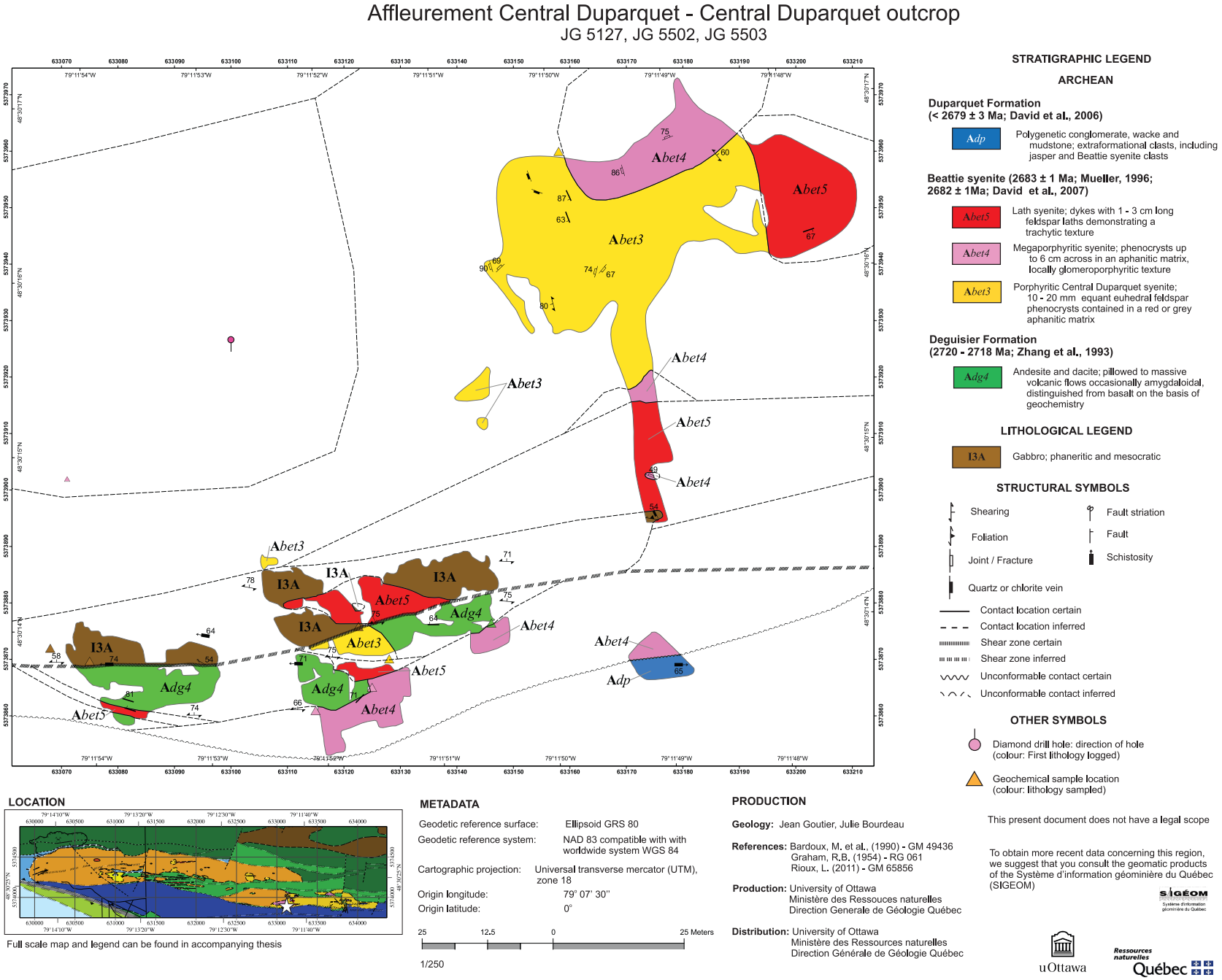
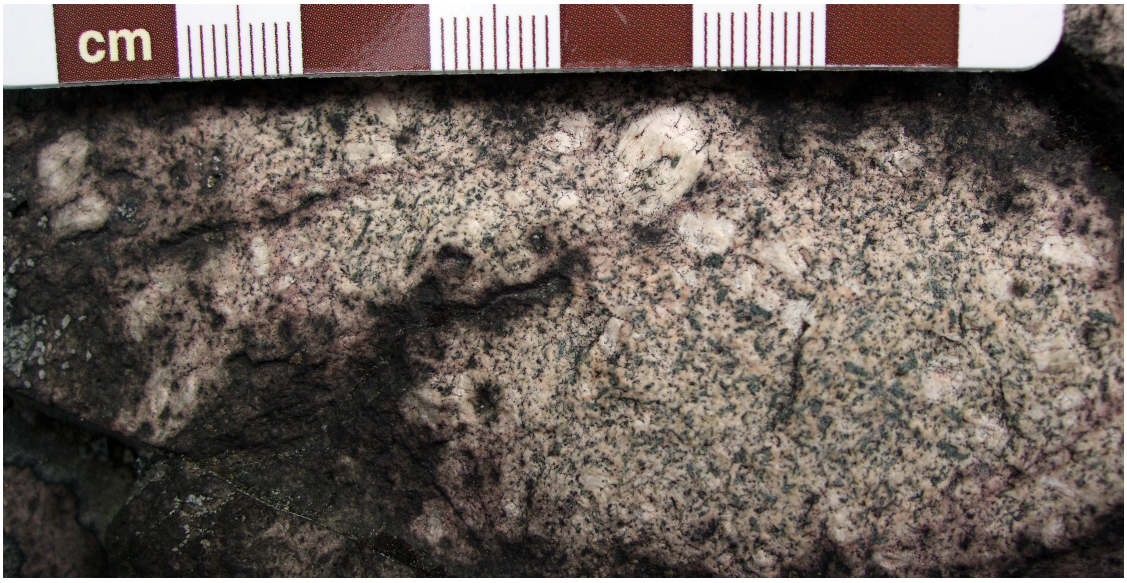


Figure 6.4 – Detailed map of outcrop near Central Duparquet 2 mine (JG 5127, JG 5502, JG 5503). Full resolution poster has been included in Appendix B.

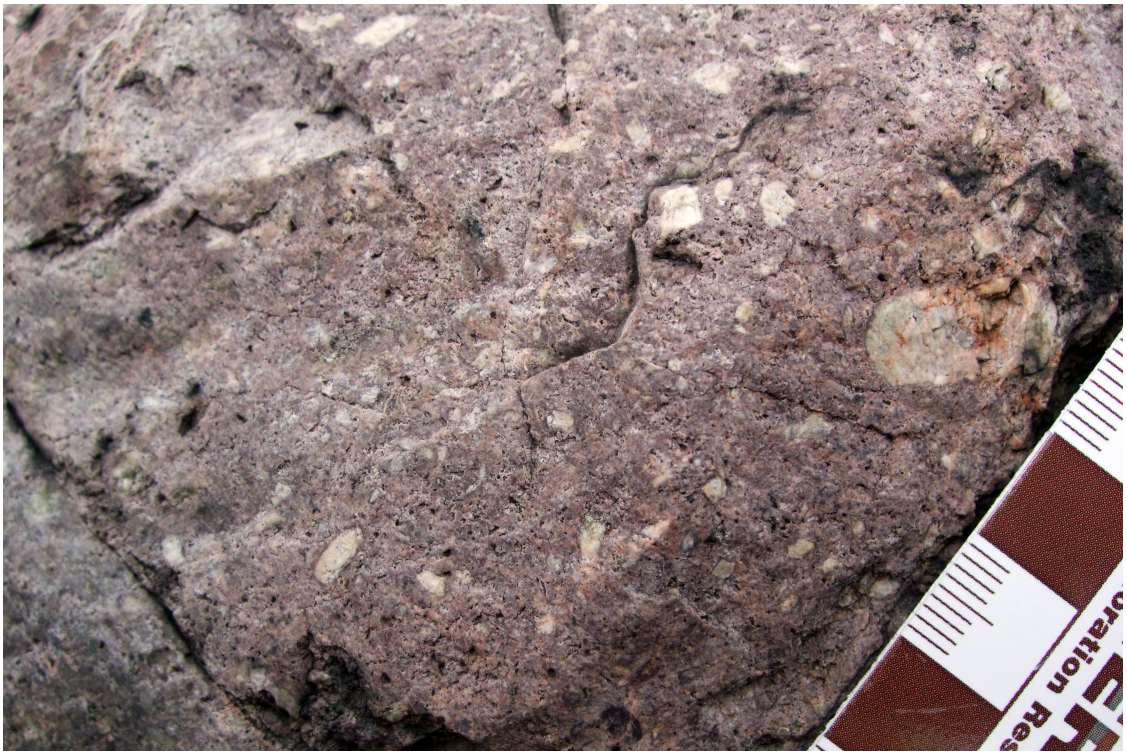
parquet unit. Field relationships have found that the megaporphyritic unit generally transects the porphyritic Central Duparquet unit as irregular masses. A detailed outcrop perspective is provided in Figures 6.4 and 6.7. These observations fall in line with the ones made by Banfield (1940) who described the unit as masses or dykes intruding into the porphyritic Central Duparquet unit. The contact between the megaporphyritic unit and Central Duparquet unit is generally sharp and occasionally gradational. Both types of contacts were also observed by Graham (1954). Towards the contact, the unit demonstrates a reduction in both size and abundance of phenocrysts. This phenocryst loss can give the appearance of a gradational contact, which is further obscured by the common red aphanitic matrix of both units (see Figure 6.8). Nonetheless, a sharp delineation between the two units has commonly been observed. The observation of a gradational contact indicates that the emplacement timing of the megaporphyritic unit was shortly after that of the porphyritic Central Duparquet unit.

Finally, the lath syenite unit is the youngest of the petrographic units as the dykes cut all other units and country rocks (see Figure 6.9). A detailed outcrop perspective of the field relationships is presented in Figure 6.3. On a finer scale, contacts between the lath syenite and other syenitic units or country rocks have occasionally been brittlely deformed and subsequently infiltrated by hydrothermal minerals (e.g., sericite, chlorite, pyrite and arsenopyrite) as presented in Figure 6.10.

To summarise, the porphyritic Beattie unit is the oldest petrographic unit closely followed by the equigranular magnetite-bearing and porphyritic Central Duparquet units. They were followed by the megaporphyritic and finally the lath syenite units. Figure 6.11 elaborates on the geological time scale, with the inclusion of the syenitic units.



(a) Increase in the size and abundance of white feldspar phenocrysts. This first transition stage is demarked by a loss of hornblende porphyroblasts. Location: 630739E 5374525N.



(b) Further increase in phenocryst size and abundance. This outermost transition stage demonstrates the complete loss in amphibole crystals and a change from grey to a pink feldspathic matrix. Location: 630806E 5374483N.

Figure 6.5 – Transition between the equigranular magnetite-bearing and porphyritic Beattie syenite units. Photographs are arranged progressing away from the centre of the unit, transitioning to the porphyritic Beattie syenite unit. The transition is denoted by a change to a pink coloured matrix, an increase in size and abundance of feldspar phenocrysts and a loss of amphiboles, titanite and magnetite crystals.

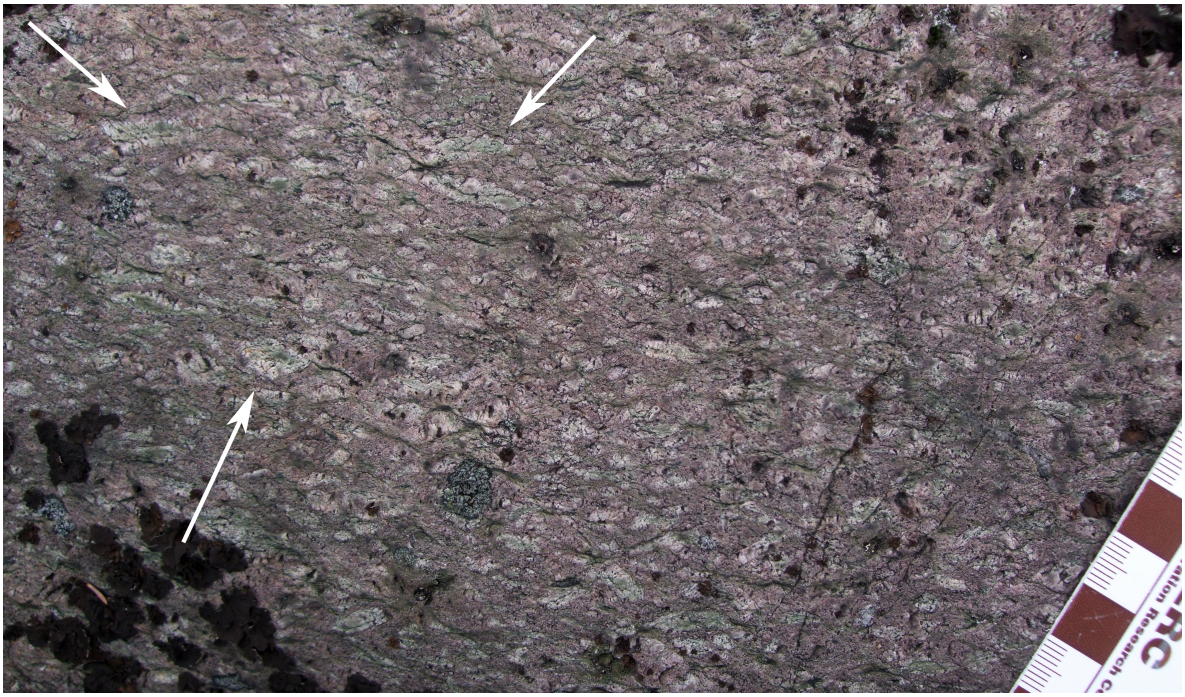


Figure 6.6 – Gradational contact between the porphyritic Beattie and Central Duparquet units. Larger phenocrysts (white arrows) become progressively dominant. Pale green, fractured phenocrysts are the result of a secondary D_2 shear fault $\sim$ 20 m south. Additionally, the outcrop is transected by numerous small green hydrothermal sericite in anastomosing veins. Location: 632440E 5373967N.

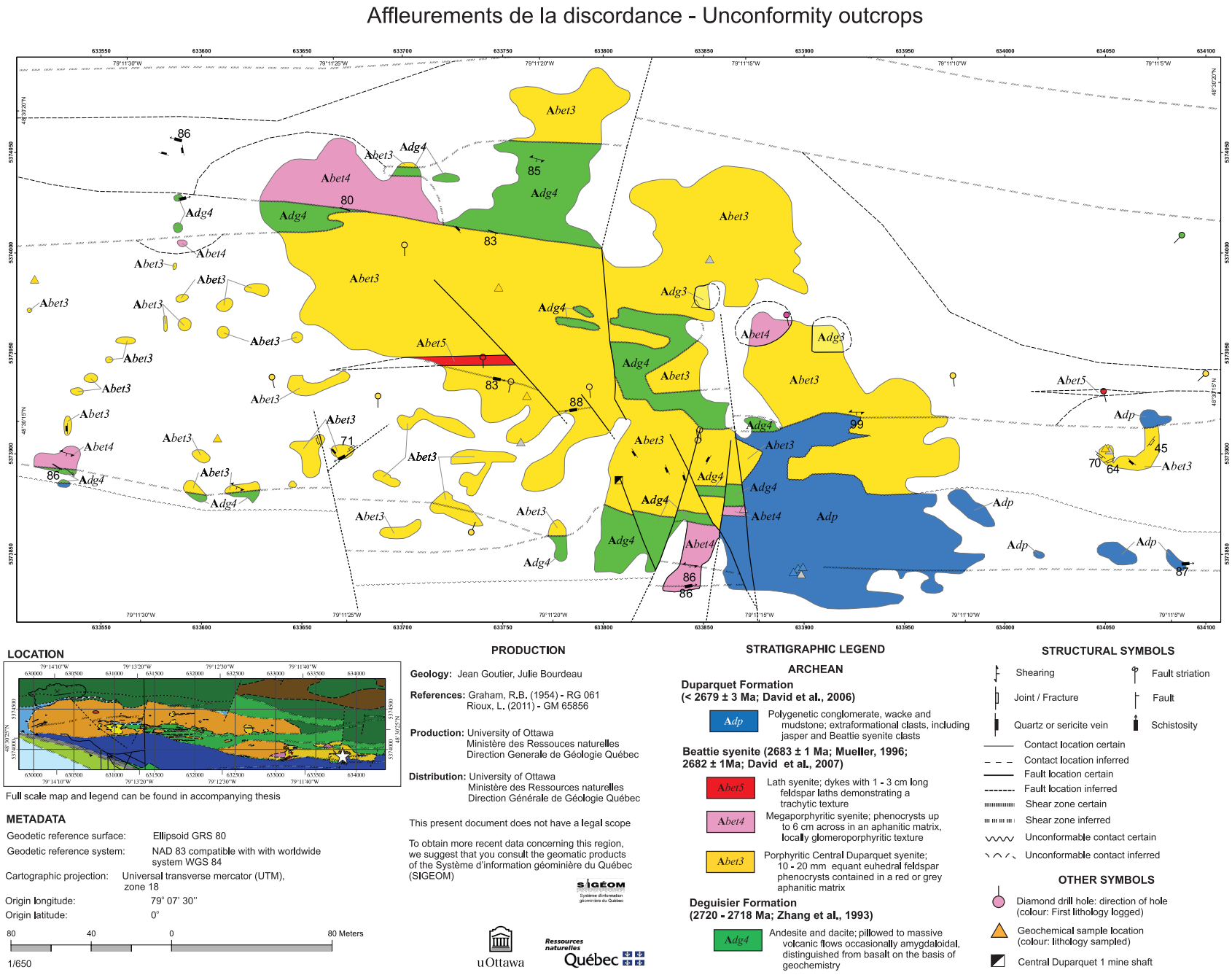


Figure 6.7 – Detailed map of outcrops near Central Duparquet 1 mine. Full resolution poster has been included in Appendix B.

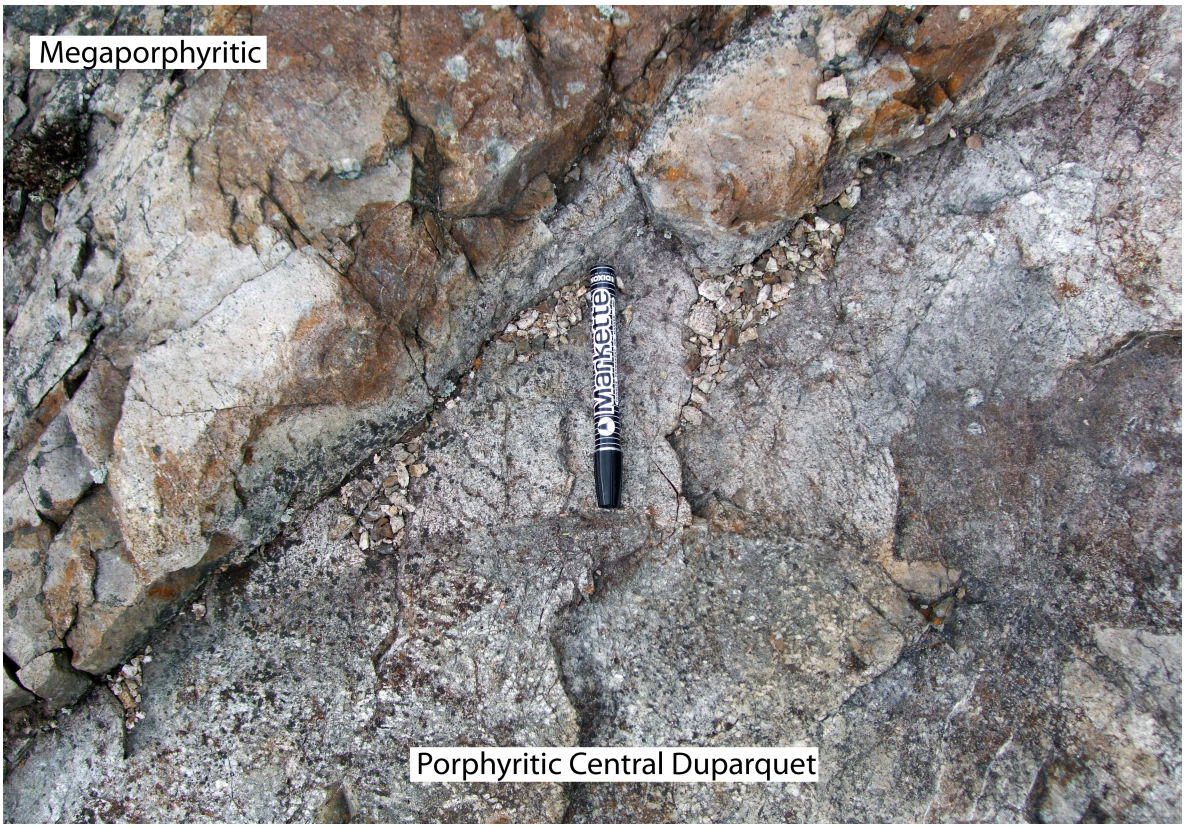


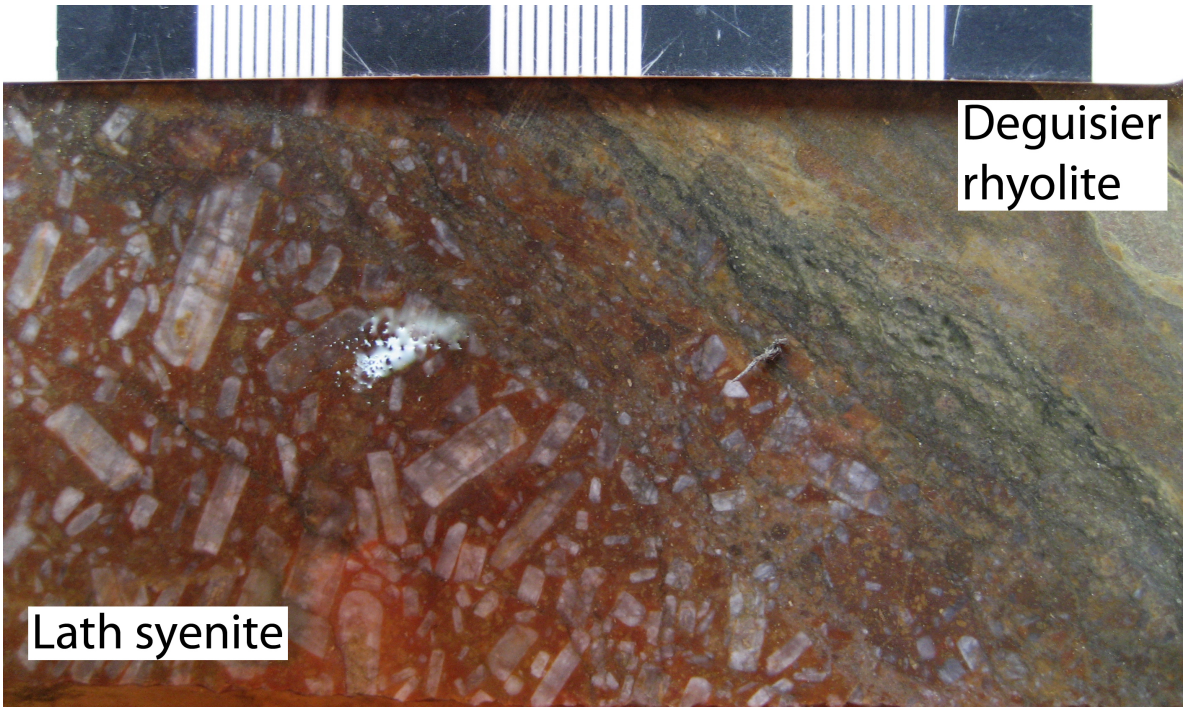
Figure 6.8 – Contact between the megaporphyritic and porphyritic Central Duparquet units. The megaporphyritic unit (above) demonstrates a loss in phenocrysts leading to the contact. The contact is sharp, pointed by the black tip of the marker. The porphyritic Central Duparquet (below) has smaller sized phenocrysts that appear right at the contact. Location: 633177E 5373955N.



Figure 6.9 – Contact between the porphyritic Beattie syenite and lath syenite units. The porphyritic Beattie syenite occupies the left portion and the lath syenite occupies the right portion of the photograph. The contact between the two is located at the "a" in markette. The contact was subsequently cut by a grey quartz vein. Location: 630802E 5374346N.



(a) Contact between the porphyritic Beattie syenite and lath syenite units. The contact has been brecciated and subsequently infiltrated by sericite as seen by the darker green colour. Additionally, late grey quartz veins cut the contact. Drill core: B09-87, depth: 84.65 m.



(b) Contact between lath syenite and Deguisier rhyolite. The contact, in darker colours, contains a mixture of hydrothermal chlorite and sulphide minerals. Drill core: B08-62, location: 57.92 m.

Figure 6.10 – Contacts of the lath syenite supporting additional brittle deformation and hydrothermal minerals.

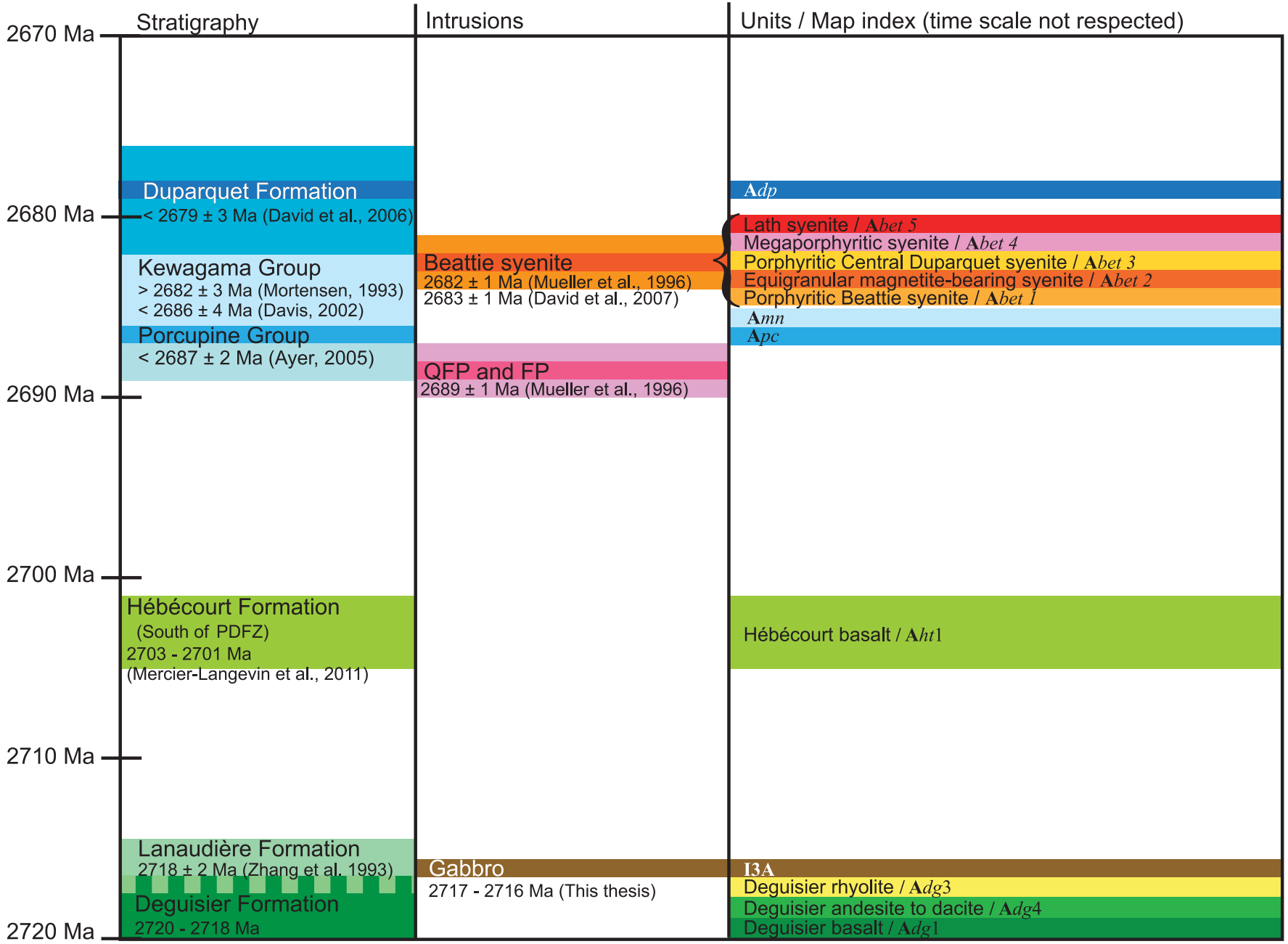


Figure 6.11 – Detailed geological time scale developed to include units.

6.3 Porphyritic Beattie syenite (A*bet1*)

The porphyritic Beattie syenite unit is the most abundant unit, encompassing 84.46% (inferred surface area) of the Beattie syenite. The unit dominates the western and northern portions of the syenite and covering an area approximately 3.4 by 0.5 km (in the BDB). To the west, the unit begins as an apophysis intruding into the Porcupine Group sediment (see Chapter 5 and accompanying geological map presented in Appendix B). Continuing eastwards, in the general area of the Beattie mine, the unit is transected by multiple shear faults, joints and fractures, caused by the unit's proximity to the PDFZ. Accompanying the deformation are a myriad of hydrothermal alterations and metamorphic minerals. Both the deformation and hydrothermal minerals decrease in abundance progressing eastwards. These features will be discussed in detail in Chapter 8.

The unit is characterized by white, red, pink to pale green, 2 - 10 mm, subhedral to anhedral feldspar phenocrysts in a pink to red aphanitic, feldspathic matrix (see Figure 6.12). Phenocrysts are loosely aligned together forming a poorly defined trachytic texture best observed in less deformed areas. Field measurements reveal that phenocrysts follow a general E-W strike, varying between 071 - 122°. Furthermore, phenocrysts are generally compositionally zoned in areas less brittlely deformed and increase in size and abundance eastwards. Specifically, western phenocrysts are anhedral, measure between 2 - 5 mm and compose 1 - $2\%_m$ of the rock, whereas eastern phenocrysts measure between 5 - 10 mm are generally subhedral and compose 5 - $10\%_m$ of the rock. Additionally, $1\%_m$ of eastern phenocrysts measure $\leq$ 2 cm across. Interestingly, there are a few areas where phenocrysts become larger and more abundant. Such areas are seemingly randomly distributed throughout the syenite (i.e., BDB and CDB) forming masses which may extend for a few meters to a decametre.

The unit contains large decametre scale xenoliths. They are commonly composed of the Deguisier andesite to dacite unit, the gabbro and rarely from the Deguisier rhyolite. These measure up to $<$ 25 m across (inferred through drill core and geochemical specimens). Most xenoliths are found in proximity to secondary D_2 shear faults and/or D_3 faults. This proximity between xenoliths and faults could be the product of rock heterogeneities, where competence contrasts between the syenite and the xenoliths could have facilitated the continuation of the faults.

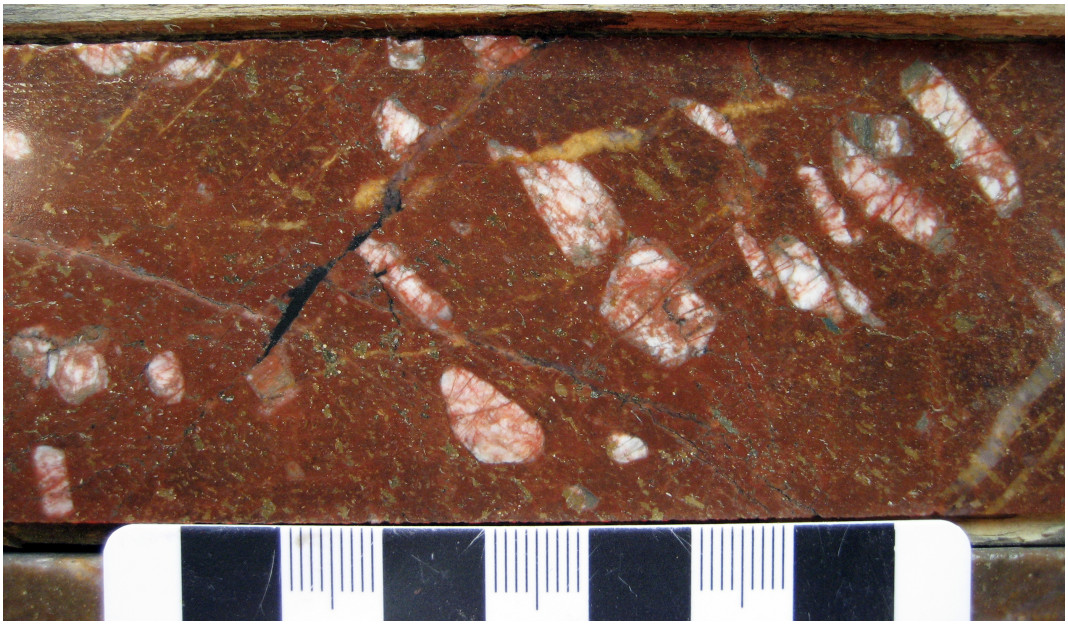
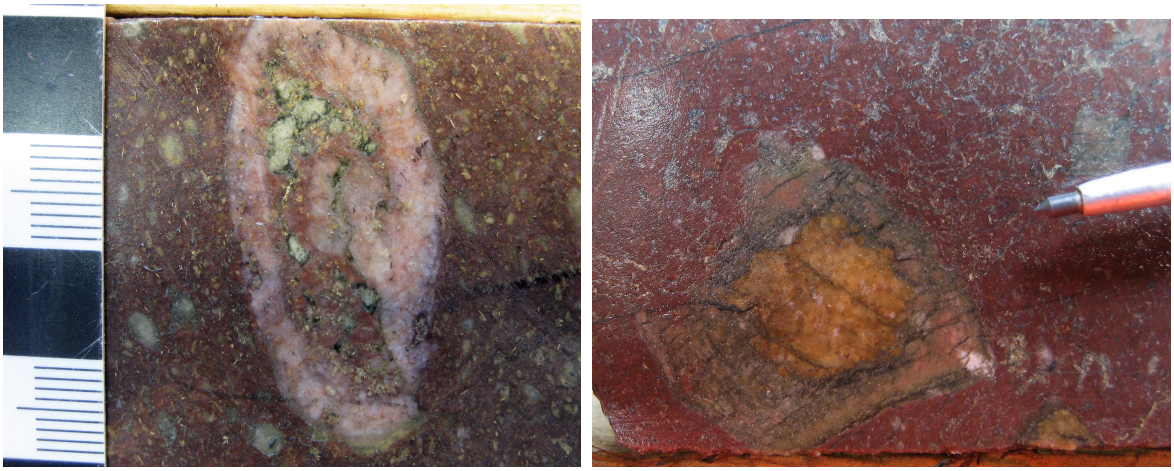


Figure 6.12 – Drill core specimen of the porphyritic Beattie syenite unit. White and red feldspar phenocrysts are contained in a red aphanitic matrix. Phenocrysts measure 1 cm, are sub- to anhedral. Additionally, a few phenocrysts have a thin rim of green sericite from subsequent hydrothermal alteration. Hydrothermal and greenschist facies veins of black chlorite, grey quartz along with white albite and beige-orange carbonate minerals transect the syenite. Drill core: B08-21, depth: 116 - 122.2 m.

The unit also contains small, 1 - 2 cm across, xenoliths. These occasionally served as nucleation centres onto which a rim (3 - 4 mm thick) of syenitic feldspar grew (see Figure 6.13). Xenoliths themselves consist of feldspars amalgamations, mixtures of feldspar and chlorite, or feldspar and carbonate minerals. All xenoliths demonstrate evidence of reaction with the syenite since all their edges have been rounded.

Igneous minerals composing the porphyritic Beattie syenite are dominantly orthoclase[3] and albite, constituting both phenocrysts and the aphanitic matrix, with trace amounts of magnetite and apatite. Albite can reliably be distinguished from orthoclase by lesser amounts of turbidity and a general lack of sericitization. The modal ranges of the unit, determined from microscopic observations is given in Table 6.1. In light of the high variability and number of minerals, a typical modal composition of the unit is also presented in Table 6.1. Both hydrothermal and greenschist facies minerals have not been included in the Table below.

[3]The structural state of alkali feldspar (i.e., orthoclase or microcline) has not been determined in this thesis. As such, the name orthoclase is used to designate potassium rich-feldspars.



(a) Xenolith composed of white and red feldspars and black chlorite. It was subsequently overgrown by pink feldspar from the syenite. Drill core: B09-85, depth: 15.30 - 25.60 m.

(b) Circular xenolith composed of beige carbonate minerals and small white feldspar. It was subsequently overgrown by pink feldspar from the syenite. Drill core: B08-102, depth: 3.60 - 12.40 m.

Figure 6.13 – Xenoliths in the porphyritic Beattie syenite unit. Both examples were observed in drill core specimens.

Table 6.1 – Range and modal composition of igneous minerals composing the porphyritic Beattie syenite unit. Ranges are based on 23 thin sections.

	Maximum ranges	Typical composition
Mineral	**Modal %**	**Modal %**
Orthoclase	2 - 52	34
Albite	30 - 56	34
Apatite	1 - 2	1
Magnetite	0 - 3	0

6.3.1 Phenocrysts

Both albite and orthoclase compose the sub- to anhedral feldspar phenocrysts. Commonly, albite will compose the phenocryst core which is surrounded by orthoclase. The opposite is also true, but rather infrequent (see Figure 6.14). The composition of albite, where present at the phenocryst core, was determined by the Michel-Lévy method to be between An_3 - An_{11}. This composition was subsequently verified via electron microprobe analyses (EMPA) (see below). Where orthoclase does compose the phenocryst core, it typically demonstrates perthitic exsolution and Carlsbad twinning. Altogether, phenocrysts measure 0.4 mm - 1.5 cm with rounded edges. Orthoclase or albite surrounding the core range from 0.1 - 0.3 mm thick. There are also smaller-sized phenocrysts (0.4 - 0.6 mm) which are entirely composed either of albite or orthoclase (see Figure 6.15).

The chemical composition of phenocrysts was verified using EMPA and complemented with

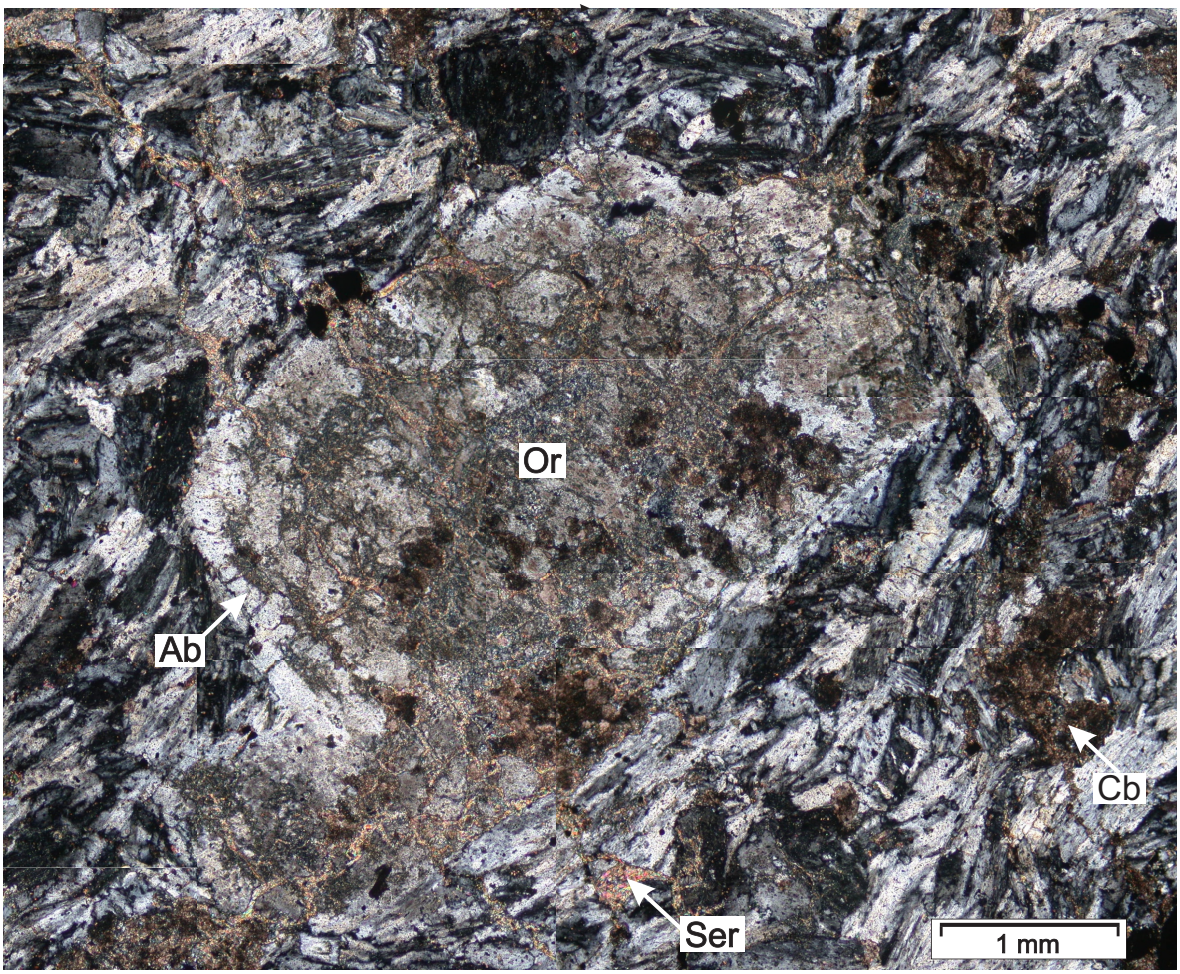


Figure 6.14 – Subhedral phenocryst of the porphyritic Beattie syenite unit. The core of the phenocryst is composed of sericitized orthoclase (Or) and is surrounded by clear albite (Ab). The phenocryst is hosted in a slightly radiating and fibrous feldspathic matrix composed of both orthoclase and albite. Altered carbonate minerals are disseminated in the feldspathic matrix. Photomicrograph taken under crossed polars. Location: 630963E 5374432N.

electron back-scatter (EBS) observations. As such, a total of 3 samples were submitted for EMPA. The westernmost sample, ZP-04-002, is located west in the BDB, 205 m south of the abandoned Beattie mine shaft. Next is sample ZP-04-042 which is located further east in the BDB, 517 m southeast from the Beattie mine shaft. The last sample, JG-5099-02 is located west in the CDB, 506 m west of the Central Duparquet 2 mine shaft. The exact locations of all samples submitted to EMPA can be viewed in Figure 6.16. Analyses were randomly selected within the crystals with additional analyses performed on unusual or distinct features. Both orthoclase and albite formulas have been calculated on an 8 oxygen basis. The composition and chemical formulas are presented in Table 6.2.

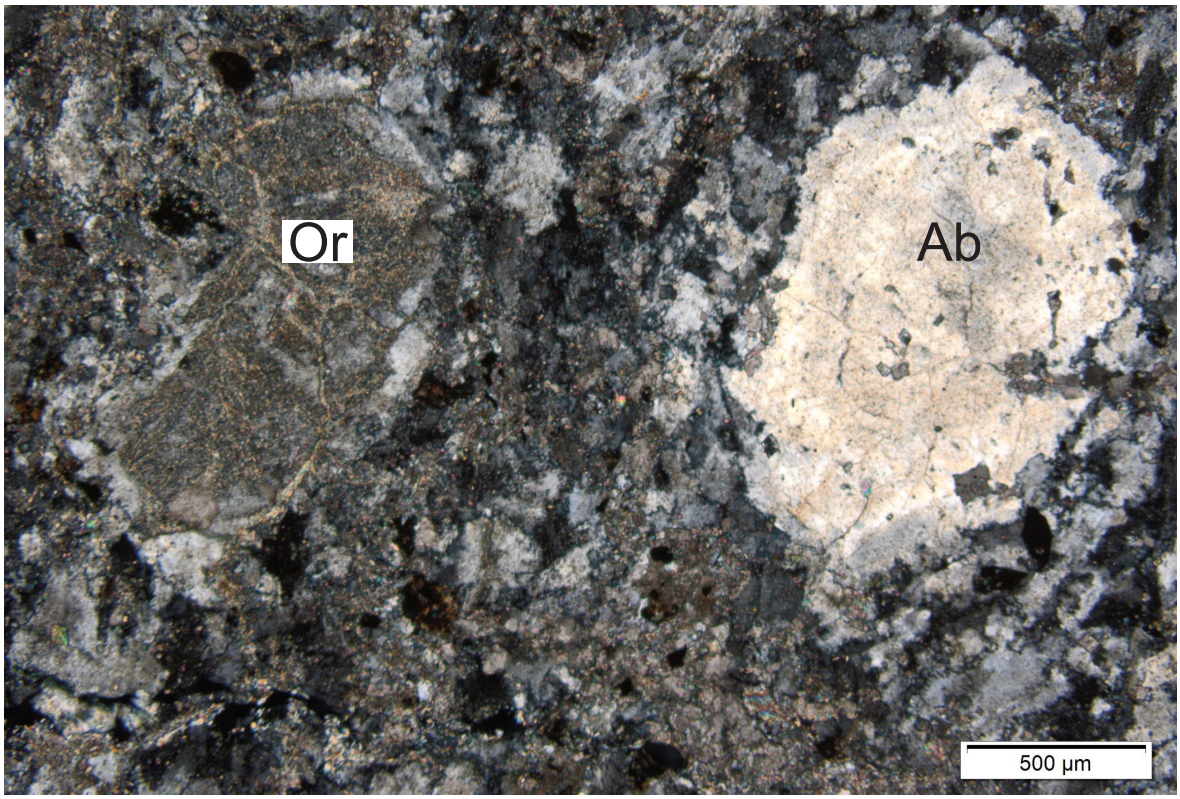
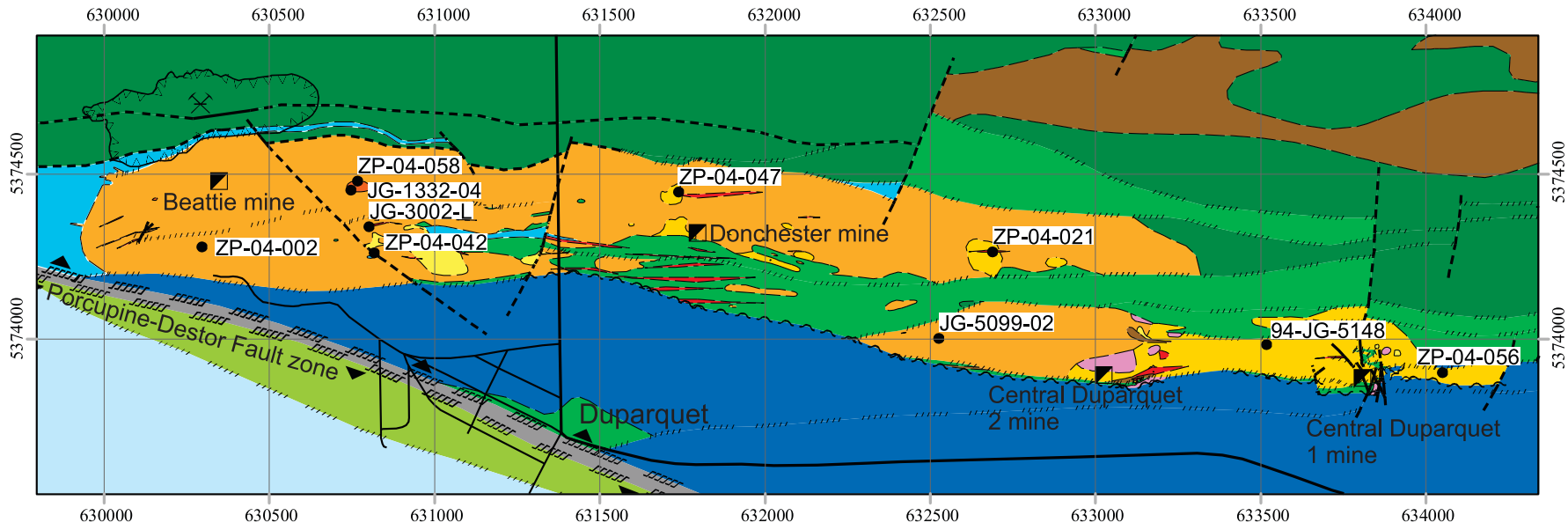


Figure 6.15 – Smaller-sized phenocrysts. They are almost entirely composed of either orthoclase (Or; left), now sericitized, or albite (Ab; right). Sericitization of the orthoclase phenocryst has obliterated primary igneous textures. Photomicrograph taken under crossed polars. Location: 630851E 5374575N.

The composition of orthoclase varies from 0.00 - 0.42 mol% An, 1.14 - 2.64 mol% Ab and the reminder 90.36 - 98.86 mol% Or. As for albite, the composition ranges from 0.00 - 0.53 mol% An, 0.45 - 2.57 mol% Or and 96.90 - 99.50 mol% Ab. A visualization of the feldspathic mol% end-member composition is presented in Figure 6.17.

Under EBS, phenocrysts either have an albite dominated core surrounded by orthoclase or are perthitic, blending almost perfectly with the matrix. The transition from the albitic core to orthoclase is rather jagged and uneven. In samples observed, the orthoclase surrounding the albite core measures between $<$ 0.1 - 0.4 mm and demonstrates a linear loss in Ba^{2+} towards the outer margins. This loss is observed in Figure 6.18 as a subtle decrease in luminosity where the brightest orthoclase, close to the core, contains 0.02 $\pm$ 0.00 atoms per formula unit (*apfu*) Ba^{2+} (analysis 2-3-3) and the darkest, at the edge, contains 0.01 $\pm$ 0.00 *apfu* Ba^{2+} (analysis 2-3-4). Perthitic phenocrysts display irregular exsolution textures and compositional zoning. Exsolved Ab-domains appear randomly, measure $<$ 50 μm, and are anhedral. As for



Stratigraphic Legend

- Timiskaming sediments (< 2679 Ma)
- Beattie syenite (2683 - 2682 Ma)
- Kewagama sediments (< 2686 Ma)
- Porcupine sediments (< 2687 Ma)
- Blake River basalt (2703 - 2701 Ma)
- Kinojévis basalt to rhyolite (2720 - 2718 Ma)

Lithological Legend

- Gabbro
- Porcupine-Destor fault zone

Structural symbols

- Fault certain
- Fault inferred
- Shear zone inferred
- Inverse dextral shear fault

Contact symbols

- Contact inferred
- Unconformable contact inferred

Other symbols

- Road
- Abandoned mine shaft
- Abandoned open pit
- Sample location and number submitted for electron microprobe analysis

Figure 6.16 – Location of samples submitted for electron microprobe analysis.

Table 6.2 – Microprobe analyses and chemical formulas of phenocrysts from the porphyritic Beattie syenite unit.

	Orthoclase					
	2-3-1	**2-3-3**	**2-3-4**	**2-5-2**	**2-7-2**	**2-7-4**
SiO_2	63.82 ± 0.45	62.72 ± 0.44	64.17 ± 0.45	64.68 ± 0.45	63.76 ± 0.45	64.24 ± 0.45
TiO_2	0.00 ± 0.00	0.00 ± 0.00	0.00 ± 0.00	0.00 ± 0.00	0.00 ± 0.00	0.00 ± 0.00
Al_2O_3	18.57 ± 0.13	18.62 ± 0.13	18.42 ± 0.13	18.70 ± 0.13	18.72 ± 0.13	18.90 ± 0.13
FeO	0.04 ± 0.03	0.22 ± 0.04	0.25 ± 0.04	0.11 ± 0.04	0.01 ± 0.00	0.20 ± 0.04
MgO	0.00 ± 0.00	0.00 ± 0.00	0.00 ± 0.00	0.00 ± 0.00	0.00 ± 0.00	0.00 ± 0.00
BaO	1.02 ± 0.07	1.04 ± 0.07	0.60 ± 0.06	0.69 ± 0.06	1.20 ± 0.07	0.40 ± 0.06
CaO	0.01 ± 0.00	0.08 ± 0.02	0.05 ± 0.02	0.00 ± 0.00	0.00 ± 0.00	0.00 ± 0.00
Na_2O	0.20 ± 0.02	0.23 ± 0.02	0.16 ± 0.02	0.12 ± 0.02	0.19 ± 0.02	0.18 ± 0.02
K_2O	15.79 ± 0.13	15.63 ± 0.13	15.73 ± 0.13	15.88 ± 0.13	15.69 ± 0.13	15.93 ± 0.13
Total	99.46	98.55	99.38	100.18	99.56	99.86
Chemical formula based on 8 oxygens						
Si^{4+}	2.98 ± 0.03	2.96 ± 0.03	2.99 ± 0.03	2.99 ± 0.03	2.98 ± 0.03	2.98 ± 0.03
Ti^{4+}	0.00 ± 0.00	0.00 ± 0.00	0.00 ± 0.00	0.00 ± 0.00	0.00 ± 0.00	0.00 ± 0.00
Al^{3+}	1.02 ± 0.01	1.04 ± 0.01	1.01 ± 0.01	1.02 ± 0.01	1.03 ± 0.01	1.03 ± 0.01
Fe^{3+}	0.01 ± 0.00	0.01 ± 0.00	0.01 ± 0.00	0.00 ± 0.00	0.00 ± 0.00	0.01 ± 0.00
Mg^{2+}	0.00 ± 0.00	0.00 ± 0.00	0.00 ± 0.00	0.00 ± 0.00	0.00 ± 0.00	0.00 ± 0.00
Ba^{2+}	0.02 ± 0.00	0.02 ± 0.00	0.01 ± 0.00	0.01 ± 0.00	0.02 ± 0.00	0.01 ± 0.00
Ca^{2+}	0.00 ± 0.00	0.00 ± 0.00	0.00 ± 0.00	0.00 ± 0.00	0.00 ± 0.00	0.00 ± 0.00
Na^{+}	0.02 ± 0.00	0.02 ± 0.00	0.01 ± 0.00	0.01 ± 0.00	0.02 ± 0.00	0.02 ± 0.00
K^{+}	0.94 ± 0.01	0.94 ± 0.01	0.94 ± 0.01	0.94 ± 0.01	0.93 ± 0.01	0.94 ± 0.01
$\sum/\Delta\sum$	4.99 ± 0.02	5.00 ± 0.02	4.97 ± 0.02	4.97 ± 0.02	4.98 ± 0.02	4.98 ± 0.02
Mol% end-member						
An:	0.05 ± 0.00	0.42 ± 0.10	0.26 ± 0.10	0.00 ± 0.00	0.00 ± 0.00	0.00 ± 0.00
Ab:	1.98 ± 0.19	2.18 ± 0.19	1.52 ± 0.19	1.14 ± 0.19	1.81 ± 0.19	1.69 ± 0.19
Or:	97.97 ± 1.49	97.40 ± 1.56	98.22 ± 1.58	98.86 ± 1.50	98.19 ± 1.50	98.31 ± 1.48

the compositional zoning, Ba^{2+}-enriched zones appear larger than Ab-domains, measuring $\sim$ 200 μm, but also appear randomly and are irregular in shape. Albite cores and exsolutions do not demonstrate any compositional variation. This can be observed from EBS images where albite remains a constant dark shade of grey (see Figure 6.18).

Table 6.2 Continued

	Orthoclase				Albite	
	42-4-1	**42-6-1**	**42-6-3**	**JG-5099-03**	**2-3-2**	**2-5-1**
SiO_2	64.41 ± 0.45	65.03 ± 0.46	63.09 ± 0.44	64.25 ± 0.45	67.11 ± 0.47	69.19 ± 0.48
TiO_2	0.00 ± 0.00	0.00 ± 0.00	0.00 ± 0.00	0.00 ± 0.00	0.00 ± 0.00	0.00 ± 0.00
Al_2O_3	19.32 ± 0.14	18.74 ± 0.13	19.49 ± 0.14	18.75 ± 0.13	19.86 ± 0.14	19.93 ± 0.14
FeO	0.26 ± 0.04	0.05 ± 0.03	0.15 ± 0.04	0.02 ± 0.00	0.12 ± 0.03	0.15 ± 0.03
MgO	0.00 ± 0.00	0.00 ± 0.00	0.00 ± 0.00	0.00 ± 0.00	0.00 ± 0.00	0.00 ± 0.00
BaO	0.75 ± 0.06	0.70 ± 0.06	1.33 ± 0.07	0.80 ± 0.02	0.09 ± 0.04	0.05 ± 0.05
CaO	0.00 ± 0.00	0.00 ± 0.00	0.00 ± 0.00	0.00 ± 0.00	0.11 ± 0.02	0.00 ± 0.00
Na_2O	0.22 ± 0.02	0.29 ± 0.02	0.25 ± 0.02	0.25 ± 0.01	11.20 ± 0.12	11.64 ± 0.12
K_2O	16.33 ± 0.13	16.25 ± 0.13	15.70 ± 0.13	15.97 ± 0.11	0.45 ± 0.02	0.32 ± 0.02
Total	101.29	101.06	100.01	100.05	98.96	101.28
Chemical formula based on 8 oxygens						
Si^{4+}	2.96 ± 0.03	2.99 ± 0.03	2.94 ± 0.03	2.98 ± 0.03	2.97 ± 0.03	2.99 ± 0.03
Ti^{4+}	0.00 ± 0.00	0.00 ± 0.00	0.00 ± 0.00	0.00 ± 0.00	0.00 ± 0.00	0.00 ± 0.00
Al^{3+}	1.05 ± 0.01	1.01 ± 0.01	1.07 ± 0.01	1.03 ± 0.01	1.04 ± 0.01	1.01 ± 0.01
Fe^{3+}	0.01 ± 0.00	0.00 ± 0.00	0.00 ± 0.00	0.00 ± 0.00	0.00 ± 0.00	0.00 ± 0.00
Mg^{2+}	0.00 ± 0.00	0.00 ± 0.00	0.00 ± 0.00	0.00 ± 0.00	0.00 ± 0.00	0.00 ± 0.00
Ba^{2+}	0.01 ± 0.00	0.01 ± 0.00	0.02 ± 0.00	0.01 ± 0.00	0.00 ± 0.00	0.00 ± 0.00
Ca^{2+}	0.00 ± 0.00	0.00 ± 0.00	0.00 ± 0.00	0.00 ± 0.00	0.01 ± 0.00	0.00 ± 0.00
Na^{+}	0.02 ± 0.00	0.03 ± 0.00	0.02 ± 0.00	0.02 ± 0.00	0.96 ± 0.01	0.97 ± 0.01
K^{+}	0.96 ± 0.01	0.95 ± 0.01	0.93 ± 0.01	0.95 ± 0.01	0.03 ± 0.00	0.02 ± 0.00
$\sum/\Delta\sum$	5.00 ± 0.02	4.99 ± 0.02	5.00 ± 0.02	4.99 ± 0.02	5.00 ± 0.02	5.00 ± 0.02
Mol% end-member						
An:	0.00 ± 0.00	0.00 ± 0.00	0.00 ± 0.00	0.00 ± 0.00	0.53 ± 0.10	0.00 ± 0.00
Ab:	2.01 ± 0.18	2.64 ± 0.19	2.36 ± 0.19	2.32 ± 0.10	96.90 ± 1.77	98.21 ± 1.68
Or:	97.99 ± 1.45	97.36 ± 1.45	97.64 ± 1.48	97.68 ± 1.26	2.57 ± 0.12	1.79 ± 0.11

Table 6.2 Continued

	Albite		
	2-7-1	**2-7-3**	**JG-5099-04**
SiO_2	69.57 ± 0.49	67.68 ± 0.47	68.90 ± 0.48
TiO_2	0.00 ± 0.00	0.00 ± 0.00	0.00 ± 0.00
Al_2O_3	19.58 ± 0.14	19.67 ± 0.14	19.84 ± 0.14
FeO	0.00 ± 0.00	0.23 ± 0.04	0.17 ± 0.02
MgO	0.00 ± 0.00	0.00 ± 0.00	0.00 ± 0.00
BaO	0.00 ± 0.00	0.08 ± 0.05	0.06 ± 0.02
CaO	0.01 ± 0.00	0.03 ± 0.02	0.09 ± 0.01
Na_2O	11.89 ± 0.12	11.49 ± 0.13	11.91 ± 0.14
K_2O	0.08 ± 0.01	0.33 ± 0.02	0.14 ± 0.01
Total	101.14	99.52	101.11
Chemical formula based on 8 oxygens			
Si^{4+}	3.00 ± 0.03	2.98 ± 0.03	2.98 ± 0.03
Ti^{4+}	0.00 ± 0.00	0.00 ± 0.00	0.00 ± 0.00
Al^{3+}	1.00 ± 0.01	1.02 ± 0.01	1.01 ± 0.01
Fe^{3+}	0.00 ± 0.00	0.01 ± 0.00	0.00 ± 0.00
Mg^{2+}	0.00 ± 0.00	0.00 ± 0.00	0.00 ± 0.00
Ba^{2+}	0.00 ± 0.00	0.00 ± 0.00	0.00 ± 0.00
Ca^{2+}	0.00 ± 0.00	0.00 ± 0.00	0.00 ± 0.00
Na^{+}	1.00 ± 0.01	0.98 ± 0.01	1.00 ± 0.01
K^{+}	0.00 ± 0.00	0.02 ± 0.00	0.01 ± 0.00
$\sum/\Delta\sum$	5.00 ± 0.02	5.01 ± 0.02	5.01 ± 0.02
Mol% end-member			
An:	0.05 ± 0.00	0.15 ± 0.09	0.41 ± 0.05
Ab:	99.50 ± 1.69	98.00 ± 1.87	98.82 ± 1.87
Or:	0.45 ± 0.11	1.85 ± 0.12	0.76 ± 0.06

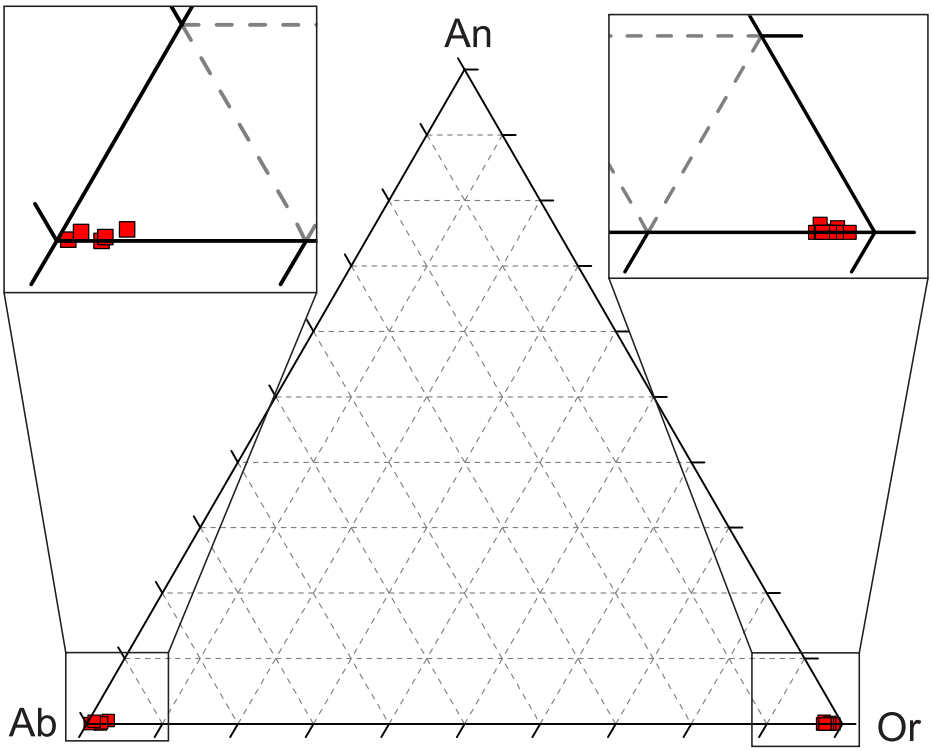


Figure 6.17 – End-member composition of phenocrysts from the porphyritic Beattie syenite unit. The 3 end members are: Or = orthoclase, An = anorthite, Ab = albite. Analyses are presented in mole %.

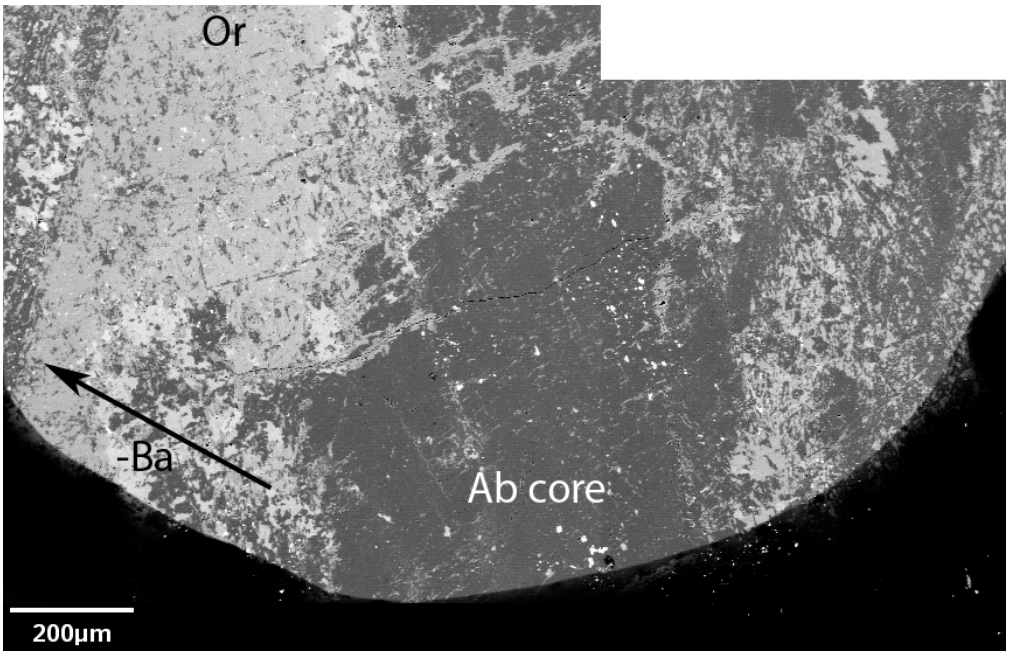


Figure 6.18 – EBS image of a phenocryst from the porphyritic Beattie syenite unit. Darker colours consist of albite (Ab), whereas lighter colours are orthoclase (Or). Additionally, the slight decrease in luminosity (direction of arrow) is caused by a reduction of Ba^{2+}. Sample: ZP-04-002, location: 630313E 5374277N.

6.3.2 Matrix

Following phenocrysts, feldspar crystals in the matrix measure 0.4 mm on average and demonstrate an undulose extinction, distorting optical measurements and preventing compositional determinations via the microscope (see Figure 6.14). The undulose extinction is the result of intermixing between albite and orthoclase as determined using EBS imaging. Crystals in the matrix appear as slightly radiating fibrous crystals with a diffuse to sutured margin. The configuration is reminiscent of devitrification of a glassy matrix. Turbidity and sericitization of orthoclase is not as pronounced in the matrix as in the phenocrysts.

A wide selection of crystals from the matrix were analyzed. Both orthoclase and albite formulas have been calculated on an 8 oxygen basis. The compositions and calculated chemical formulas of all matrix analyses is presented in Table 6.3.

Table 6.3 – Microprobe analyses and chemical formulas of matrix feldspar from the porphyritic Beattie syenite unit.

	Othoclase			Albite		
	2-1-1	**42-07-01**	**JG-5099-02**	**2-1-2**	**42-7-02**	**JG-5099-01**
SiO_2	63.87 ± 0.45	65.77 ± 0.46	65.04 ± 0.46	68.72 ± 0.48	69.89 ± 0.49	68.94 ± 0.48
TiO_2	0.00 ± 0.00	0.00 ± 0.00	0.00 ± 0.00	0.00 ± 0.00	0.00 ± 0.00	0.00 ± 0.00
Al_2O_3	18.99 ± 0.13	18.87 ± 0.13	18.50 ± 0.13	19.41 ± 0.14	19.95 ± 0.14	19.80 ± 0.14
FeO	0.71 ± 0.05	0.05 ± 0.03	0.03 ± 0.02	0.12 ± 0.03	0.06 ± 0.03	0.17 ± 0.01
MgO	0.00 ± 0.00	0.00 ± 0.00	0.00 ± 0.00	0.00 ± 0.00	0.00 ± 0.00	0.00 ± 0.00
BaO	0.38 ± 0.06	0.24 ± 0.05	0.17 ± 0.02	0.06 ± 0.04	0.06 ± 0.04	0.02 ± 0.00
CaO	0.28 ± 0.03	0.00 ± 0.00	0.00 ± 0.00	0.06 ± 0.02	0.12 ± 0.02	0.17 ± 0.01
Na_2O	0.54 ± 0.02	1.08 ± 0.03	0.23 ± 0.03	11.76 ± 0.12	12.00 ± 0.12	12.18 ± 0.15
K_2O	15.16 ± 0.12	15.56 ± 0.12	16.42 ± 0.11	0.14 ± 0.01	0.15 ± 0.01	0.14 ± 0.01
Total	99.93	101.57	100.40	100.27	102.23	101.40
Chemical formula based on 8 oxygens						
Si^{4+}	2.97 ± 0.03	2.99 ± 0.03	3.00 ± 0.03	3.00 ± 0.03	2.99 ± 0.03	2.98 ± 0.03
Ti^{4+}	0.00 ± 0.00	0.00 ± 0.00	0.00 ± 0.00	0.00 ± 0.00	0.00 ± 0.00	0.00 ± 0.00
Al^{3+}	1.02 ± 0.01	1.01 ± 0.01	1.00 ± 0.01	1.00 ± 0.01	1.01 ± 0.01	1.01 ± 0.01
Fe^{3+}	0.02 ± 0.00	0.00 ± 0.00	0.00 ± 0.00	0.00 ± 0.00	0.00 ± 0.00	0.00 ± 0.00
Mg^{2+}	0.00 ± 0.00	0.00 ± 0.00	0.00 ± 0.00	0.00 ± 0.00	0.00 ± 0.00	0.00 ± 0.00
Ba^{2+}	0.01 ± 0.00	0.00 ± 0.00	0.00 ± 0.00	0.00 ± 0.00	0.00 ± 0.00	0.00 ± 0.00
Ca^{2+}	0.01 ± 0.00	0.00 ± 0.00	0.00 ± 0.00	0.00 ± 0.00	0.01 ± 0.00	0.01 ± 0.00
Na^{+}	0.05 ± 0.00	0.10 ± 0.00	0.02 ± 0.00	0.99 ± 0.01	1.00 ± 0.01	1.02 ± 0.01
K^{+}	0.90 ± 0.01	0.90 ± 0.01	0.97 ± 0.01	0.01 ± 0.00	0.01 ± 0.00	0.01 ± 0.00
$\sum/\Delta\sum$	4.98 ± 0.02	5.00 ± 0.02	4.99 ± 0.02	5.00 ± 0.02	5.01 ± 0.02	5.03 ± 0.02
Mol% end-member						
An:	1.45 ± 0.16	0.00 ± 0.00	0.00 ± 0.00	0.27 ± 0.09	0.54 ± 0.09	0.76 ± 0.05
Ab:	5.06 ± 0.20	9.54 ± 0.29	2.08 ± 0.27	98.96 ± 1.72	98.64 ± 1.68	98.50 ± 1.93
Or:	93.49 ± 1.47	90.46 ± 1.33	97.92 ± 1.39	0.77 ± 0.06	0.82 ± 0.06	0.74 ± 0.05

Orthoclase composition ranges from 0.00 - 1.45 mol% An, 0.28 - 2.57 mol% Ab and 96.90 - 99.57 mol% Or. Albite composition varies from 0.27 - 0.76 mol% An, 0.74 - 0.82 mol% Or and 98.50 - 98.96 mol% Ab. A visualization of the feldspathic end-member compositions is presented in Figure 6.19.

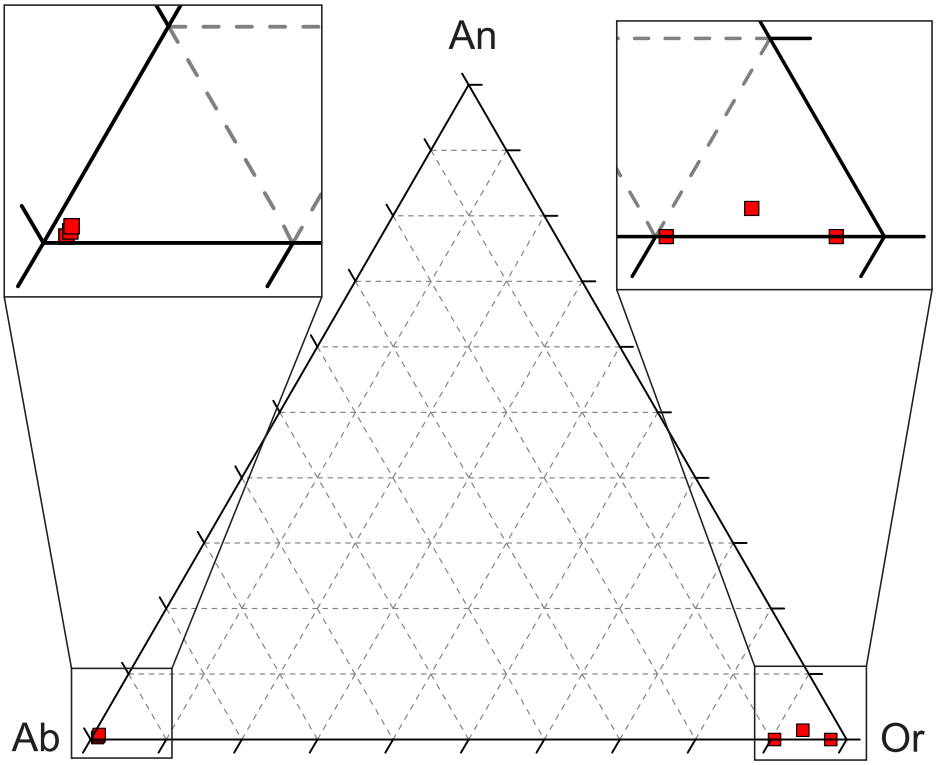


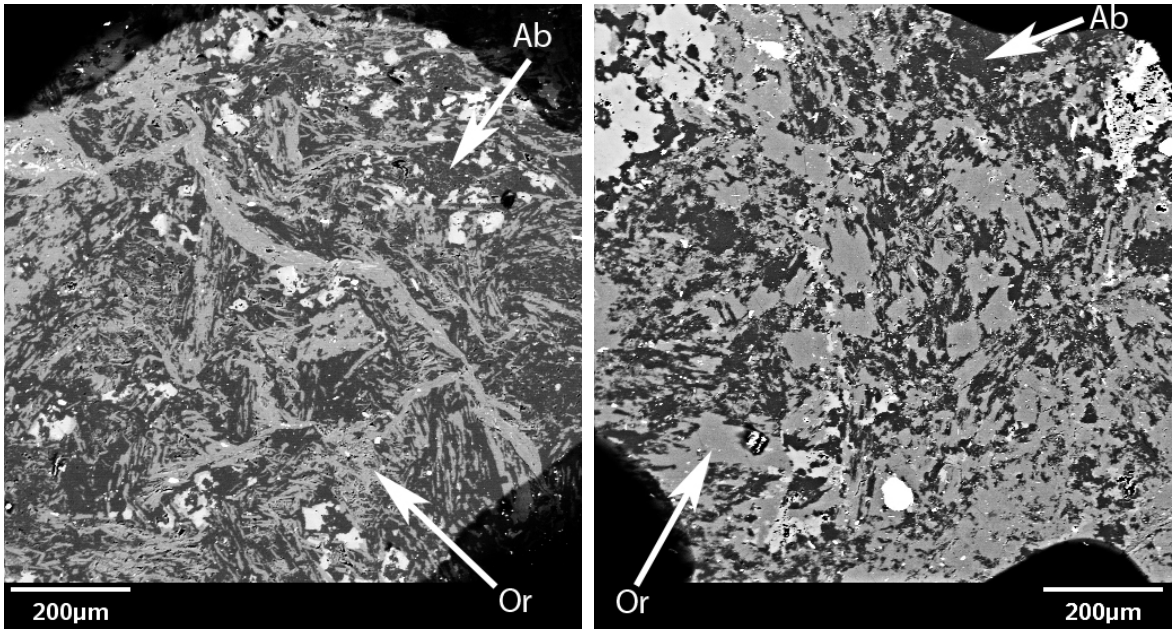
Figure 6.19 – End-member composition of matrix feldspars from the porphyritic Beattie syenite unit. The 3 end members are: Or = orthoclase, An = anorthite, Ab = albite. Analyses are presented in mole %.

From a compositional standpoint, matrix orthoclase is more Ab-variable compared to the phenocrysts. Additionally, albite demonstrates the least amount of compositional variability.

Both feldspars in the matrix are finely intermixed as small (< 200 μm) anhedral crystals (see Figure 6.20). Proportions of albite and orthoclase in the matrix are always near equal (determined from EBS observations and feldspar staining). Orthoclase occurs as thin blades or masses which may also be finely intermixed with hydrothermal sericite. This configuration of fine intermixed crystals explains the undulose extinction of the feldspathic matrix observed in thin section. Additionally, it also explains the Ab-variation as the matrix crystals seem to lack sufficient decomposition and therefore contain albite impurities.

6.3.3 Apatite

Euhedral to subhedral crystals of apatite measure between 0.1 - 0.4 mm across and are randomly distributed through the rock. Crystal margins have been slightly to moderately rounded. Larger crystals are commonly fractured, but do not show any displacement.



(a) Orthoclase occurs as thin blades with darker albitic masses. Sample: ZP-04-002, location: 630313E 5374277N.

(b) Both albite and orthoclase occur as anhedral crystals. Sample: JG-5099-02, location: 632525E 5374005N.

Figure 6.20 – EBS images of orthoclase and albite composing the matrix of the porphyritic Beattie syenite unit. The dark grey colours correspond to albite (Ab) and pale grey colours are orthoclase (Or) (and sericite).

6.3.4 Magnetite

Very little igneous magnetite was found. Magnetite occurs as subhedral crystals that are disseminated though the rock. These disseminated crystals typically have a thin (0.01 mm thick) reaction rim of hematite.

6.4 Equigranular magnetite-bearing syenite (A*bet2*)

The equigranular magnetite-bearing unit is one of the least abundant, representing a meagre 0.16% (inferred surface area) of the Beattie syenite, but is one of the most distinct units. It is exclusively found in the western portions of the BDB, appearing as E-W ellipsoid lens measuring $<$ 75 m across. Observations were obtained from a single large outcrop and from drill core specimens. This outcrop is found 420 m east from the abandoned Beattie mine shaft, and it is easily accessed and well exposed.

Compared to all the other units, the equigranular magnetite-bearing unit supports the least amount of brittle deformation and hydrothermal alteration, preserving almost all igneous textures. However this changes progressing outwards from the centre of the unit, transitioning to the porphyritic Beattie syenite unit where both deformation and alteration progressively increase.

At its centre, the rock consists of crystals of feldspars, amphiboles, titanite and magnetite, hosted in a grey feldspathic matrix (see Figure 6.21). The unit lacks or has very few sub- to anhedral white feldspar phenocrysts. Rather, the unit is non-porphyritic as opposed to all other units of the Beattie syenite. Where present, phenocrysts measure 1 - 3 mm and compose 2 - 10%$_m$ of the rock. Amphiboles are found as 0.2 mm actinolite crystals and as 4 mm hornblende porphyroblasts which together compose $<$ 10%$_m$ of the outcrop. The hornblende porphyroblasts will be addressed later in Chapter 8. The presence of magnetite renders the unit highly magnetic which is one of its key distinguishing features. The typical modal composition of the unit, as determined from thin section observations, is presented in Table 6.4. Hydrothermal and greenschist facies minerals were not included in the following table.

Table 6.4 – Range of modal composition of the equigranular magnetite-bearing unit. Ranges are based on 2 thin sections.

Mineral	**Modal %**
Orthoclase	37 - 39
Albite	36
Actinolite	5 - 10
Magnetite	10
Titanite	1 - 2
Crypto-mesoperthite	1
Apatite	1



Figure 6.21 – The equigranular magnetite-bearing unit. The unit is composed of white crystals of feldspar (1 - 3 mm), dark green 1 - 4 mm hornblende porphyroblasts, and small green prismatic, 0.2 mm crystals of actinolite in a grey feldspathic matrix. Location: 630783E 5374462N.

6.4.1 Large euhedral crystals

Large euhedral crystals are composed of albite, orthoclase and uniquely to the unit, crypto-mesoperthite. The distinction between albite and orthoclase can be made by increased sericitization and turbidity in orthoclase. These crystals measure ≤ 5 mm, show compositional zoning with one crystal demonstrating oscillatory zoning (see Figure 6.22). Cores are dominantly microperthitic and rarely albitic. In all cases, cores are surrounded by a crypto-mesoperthite rim (determined via EMPA see below) which appears virtually identical as albite surrounding an orthoclase core under the microscope. The rim measures $<$ 0.1 - 0.4 mm thick, is not turbid and appears as a sutured margin where the larger euhedral feldspar phenocrysts are in contact with the matrix.

Two samples were submitted for EMPA. Both originate from the single exposure of the unit

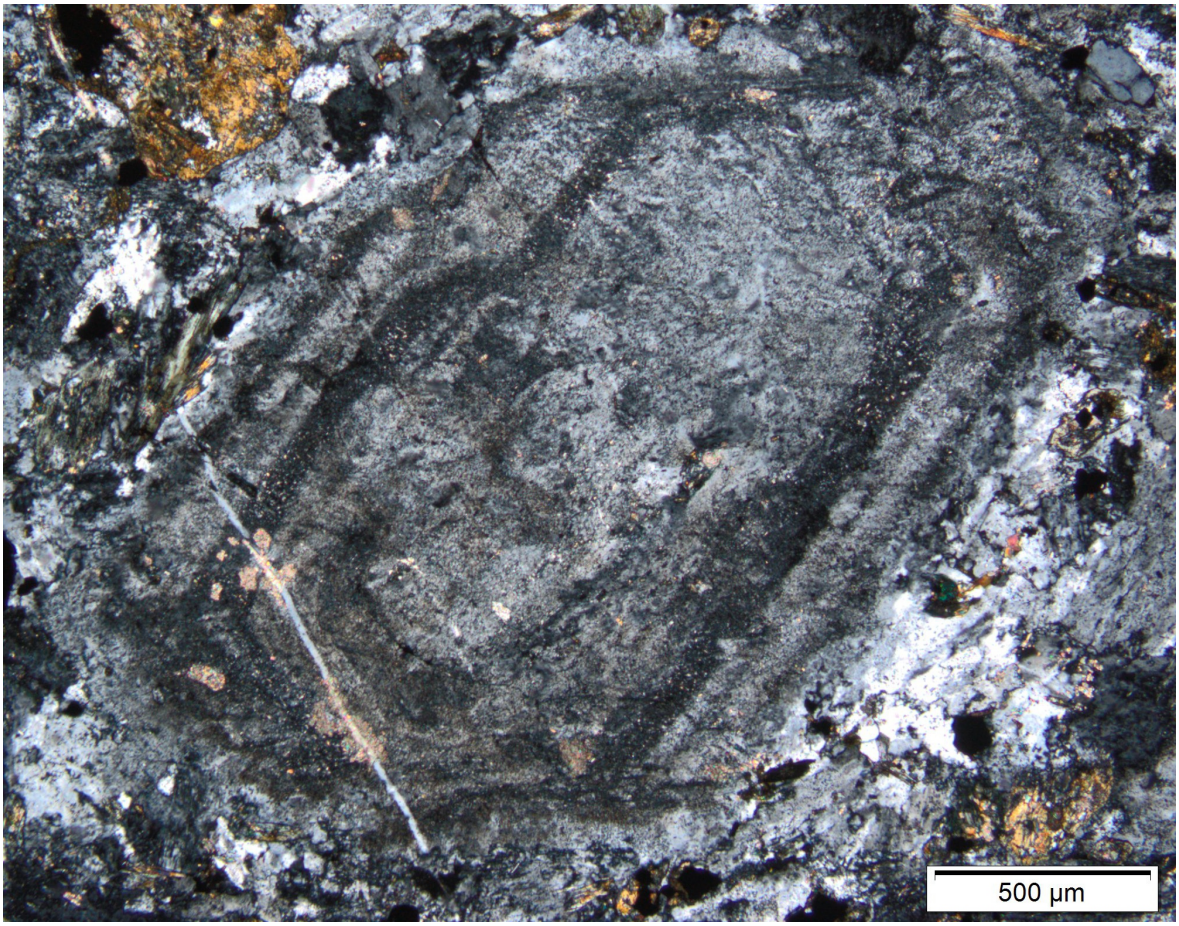


Figure 6.22 – Oscillatory zoning in a large euhedral crystal. The core of the crystal is composed of orthoclase demonstrating a microperthitic exsolution. A small vein transects the lower left portion of the crystal which is accompanied by small crystals of calcite. Photomicrograph taken under crossed polars. Location: 630767E 5374471N.

in the BDB. Unfortunately, the best representative sample for the unit was not available for analysis. Consequently, another sample, JG-1332-04 was chosen as an alternative, even though it begins to demonstrate minor porphyritic characteristics. Thin section JG-1332-04 is located close to the southwestern part of the unit and is henceforth referred as the equigranular sample. The second sample, ZP-04-58 is located north, at the beginning of the transition zone between the equigranular magnetite-bearing and porphyritic Beattie syenite units. Consequently, it is referred as the transition sample. The exact location of both samples can be viewed in Figure 6.16. Analyses were randomly selected within the crystals with additional analyses performed on unusual/distinct features. As for the crypto-mesoperthite, the analysis was complemented with several qualitative energy-dispersive X-ray spectrometry (EDS) analyses in order to confirm the chemical composition from several crystals. All feldspar formulas were

calculated on an 8 oxygen basis. The composition and chemical formulas are presented in Table 6.5.

Table 6.5 – Microprobe analyses and chemical formulas of large euhedral crystals from the equigranular magnetite-bearing and transition zone.

Orthoclase						
	Equigranular		Transition			
	JG-04-07	**JG-04-12**	**58-2-1**	**58-2-2**	**58-4-1**	**58-5-2**
SiO_2	64.79 ± 0.45	62.45 ± 0.44	63.99 ± 0.45	62.28 ± 0.44	63.71 ± 0.45	65.09 ± 0.46
TiO_2	0.00 ± 0.00	0.00 ± 0.00	0.00 ± 0.00	0.00 ± 0.00	0.00 ± 0.00	0.00 ± 0.00
Al_2O_3	18.72 ± 0.13	19.30 ± 0.14	18.83 ± 0.13	19.86 ± 0.14	19.11 ± 0.13	19.04 ± 0.13
FeO	0.08 ± 0.02	0.02 ± 0.02	0.09 ± 0.03	0.21 ± 0.04	0.21 ± 0.04	0.06 ± 0.03
MgO	0.00 ± 0.00	0.00 ± 0.00	0.00 ± 0.00	0.00 ± 0.00	0.00 ± 0.00	0.00 ± 0.00
BaO	1.07 ± 0.04	2.68 ± 0.05	0.70 ± 0.06	2.38 ± 0.09	1.53 ± 0.08	1.03 ± 0.07
CaO	0.00 ± 0.00	0.00 ± 0.00	0.04 ± 0.02	0.00 ± 0.00	0.00 ± 0.00	0.22 ± 0.02
Na_2O	0.16 ± 0.03	0.28 ± 0.03	0.50 ± 0.02	0.44 ± 0.02	0.21 ± 0.02	1.06 ± 0.03
K_2O	15.82 ± 0.11	14.76 ± 0.10	15.39 ± 0.12	14.35 ± 0.11	15.55 ± 0.12	15.38 ± 0.12
Total	100.64	99.49	99.56	99.53	100.33	101.87
Chemical formula based on 8 oxygens						
Si^{4+}	2.99 ± 0.03	2.94 ± 0.03	2.98 ± 0.03	2.92 ± 0.03	2.96 ± 0.03	2.97 ± 0.03
Ti^{4+}	0.00 ± 0.00	0.00 ± 0.00	0.00 ± 0.00	0.00 ± 0.00	0.00 ± 0.00	0.00 ± 0.00
Al^{3+}	1.02 ± 0.01	1.07 ± 0.01	1.03 ± 0.01	1.10 ± 0.01	1.05 ± 0.01	1.02 ± 0.01
Fe^{3+}	0.00 ± 0.00	0.00 ± 0.00	0.00 ± 0.00	0.01 ± 0.00	0.01 ± 0.00	0.00 ± 0.00
Mg^{2+}	0.00 ± 0.00	0.00 ± 0.00	0.00 ± 0.00	0.00 ± 0.00	0.00 ± 0.00	0.00 ± 0.00
Ba^{2+}	0.02 ± 0.00	0.05 ± 0.00	0.01 ± 0.00	0.04 ± 0.00	0.03 ± 0.00	0.02 ± 0.00
Ca^{2+}	0.00 ± 0.00	0.00 ± 0.00	0.00 ± 0.00	0.00 ± 0.00	0.00 ± 0.00	0.01 ± 0.00
Na^{+}	0.01 ± 0.00	0.03 ± 0.00	0.05 ± 0.00	0.04 ± 0.00	0.02 ± 0.00	0.09 ± 0.00
K^{+}	0.93 ± 0.01	0.89 ± 0.01	0.91 ± 0.01	0.86 ± 0.01	0.92 ± 0.01	0.90 ± 0.01
$\sum/\Delta\sum$	4.97 ± 0.02	4.98 ± 0.02	4.98 ± 0.02	4.97 ± 0.02	4.98 ± 0.02	5.01 ± 0.02
Chemical formula based on 8 oxygens						
An:	0.00 ± 0.00	0.00 ± 0.00	0.21 ± 0.10	0.00 ± 0.00	0.00 ± 0.00	1.08 ± 0.10
Ab:	1.51 ± 0.28	2.80 ± 0.30	4.70 ± 0.20	4.45 ± 0.21	2.01 ± 0.19	9.38 ± 0.29
Or:	98.49 ± 1.43	97.20 ± 1.39	95.10 ± 1.45	95.55 ± 1.38	97.99 ± 1.43	89.54 ± 1.38

The composition of orthoclase varies from 0.00 - 1.08 mol% An, 1.51 - 14.89 mol% Ab and 83.43 - 98.49 mol% Or. In addition, the composition for albite ranges from 1.16 - 4.66 mol% An, 1.67 - 9.16 mol% Or and 89.63 - 96.06 mol% Ab. A visualization of the feldspathic mol% end-member composition for all analyses is presented in Figure 6.23.

The feldspar nomenclature for the crypto-mesoperthite was performed with the aid of the optical microscope which revealed the absence of visible feldspar decomposition. The same observation was made via EBS images which revealed a lack of unmixing. However, considering the effects of metamorphism to the greenschist facies, feldspar decomposition would have been more than likely. The mol% end-member of the analysis results in the classification of this feldspar as a mesoperthite (see Figure 6.23). Consequently, the analyzed feldspar can be considered as a crypto-mesoperthite.

Large euhedral crystals in the equigranular thin section either have a mesoperthite or a perthitic orthoclase core (see Figure 6.24). Orthoclase in the mesoperthite core (analysis JG-

Table 6.5 Continued

	Orthoclase					
	Transition					
	58-5-3	**58-5-4**	**58-6-1**	**58-6-2**	**58-9-2**	**58-9-3**
SiO_2	62.97 ± 0.44	64.48 ± 0.45	60.44 ± 0.42	62.95 ± 0.44	64.82 ± 0.45	61.40 ± 0.43
TiO_2	0.00 ± 0.00	0.00 ± 0.00	0.00 ± 0.00	0.00 ± 0.00	0.00 ± 0.00	0.00 ± 0.00
Al_2O_3	19.61 ± 0.14	18.66 ± 0.13	18.17 ± 0.13	19.15 ± 0.13	19.32 ± 0.14	19.87 ± 0.14
FeO	0.28 ± 0.03	0.11 ± 0.03	0.19 ± 0.03	0.37 ± 0.04	0.02 ± 0.00	0.06 ± 0.03
MgO	0.00 ± 0.00	0.00 ± 0.00	0.00 ± 0.00	0.00 ± 0.00	0.00 ± 0.00	0.00 ± 0.00
BaO	1.62 ± 0.08	0.65 ± 0.06	1.71 ± 0.08	1.82 ± 0.08	1.45 ± 0.08	3.71 ± 0.11
CaO	0.00 ± 0.00	0.04 ± 0.02	3.22 ± 0.06	0.00 ± 0.00	0.00 ± 0.00	0.00 ± 0.00
Na_2O	0.37 ± 0.02	0.22 ± 0.02	0.20 ± 0.02	0.22 ± 0.02	0.55 ± 0.02	0.26 ± 0.02
K_2O	15.79 ± 0.13	16.63 ± 0.12	15.15 ± 0.12	15.96 ± 0.13	15.89 ± 0.13	15.09 ± 0.12
Total	100.64	100.78	99.08	100.47	102.04	100.39
Chemical formula based on 8 oxygens						
Si^{4+}	2.93 ± 0.03	2.98 ± 0.03	2.89 ± 0.03	2.94 ± 0.03	2.96 ± 0.03	2.90 ± 0.03
Ti^{4+}	0.00 ± 0.00	0.00 ± 0.00	0.00 ± 0.00	0.00 ± 0.00	0.00 ± 0.00	0.00 ± 0.00
Al^{3+}	1.08 ± 0.01	1.02 ± 0.01	1.02 ± 0.01	1.05 ± 0.01	1.04 ± 0.01	1.11 ± 0.01
Fe^{3+}	0.01 ± 0.00	0.00 ± 0.00	0.01 ± 0.00	0.01 ± 0.00	0.00 ± 0.00	0.00 ± 0.00
Mg^{2+}	0.00 ± 0.00	0.00 ± 0.00	0.00 ± 0.00	0.00 ± 0.00	0.00 ± 0.00	0.00 ± 0.00
Ba^{2+}	0.03 ± 0.00	0.01 ± 0.00	0.03 ± 0.00	0.03 ± 0.00	0.03 ± 0.00	0.07 ± 0.00
Ca^{2+}	0.00 ± 0.00	0.00 ± 0.00	0.17 ± 0.00	0.00 ± 0.00	0.00 ± 0.00	0.00 ± 0.00
Na^{+}	0.03 ± 0.00	0.02 ± 0.00	0.02 ± 0.00	0.02 ± 0.00	0.05 ± 0.00	0.02 ± 0.00
K^{+}	0.94 ± 0.01	0.98 ± 0.01	0.92 ± 0.01	0.95 ± 0.01	0.93 ± 0.01	0.91 ± 0.01
$\sum/\Delta\sum$	5.01 ± 0.02	5.01 ± 0.02	5.06 ± 0.01	5.01 ± 0.02	5.00 ± 0.02	5.01 ± 0.01
Chemical formula based on 8 oxygens						
An:	0.00 ± 0.00	0.20 ± 0.10	14.89 ± 0.34	0.00 ± 0.00	0.00 ± 0.00	0.00 ± 0.00
Ab:	3.44 ± 0.19	1.97 ± 0.18	1.67 ± 0.17	2.05 ± 0.19	5.00 ± 0.19	2.55 ± 0.20
Or:	96.56 ± 1.45	97.84 ± 1.50	83.43 ± 1.31	97.95 ± 1.47	95.00 ± 1.41	97.45 ± 1.44

Table 6.5 Continued

	Orthoclase	Albite				Anorthoclase
	Transition	Equigranular	Transition			Equigranular
	58-9-4	**JG-04-06r**	**58-5-1**	**58-6-3**	**58-9-1**	**JG-04-13**
SiO_2	64.44 ± 0.45	68.24 ± 0.48	66.23 ± 0.46	68.63 ± 0.48	70.30 ± 0.49	66.76 ± 0.47
TiO_2	0.00 ± 0.00	0.00 ± 0.00	0.00 ± 0.00	0.00 ± 0.00	0.00 ± 0.00	0.00 ± 0.00
Al_2O_3	18.88 ± 0.13	20.83 ± 0.15	21.67 ± 0.15	20.17 ± 0.14	20.89 ± 0.15	20.13 ± 0.14
FeO	0.15 ± 0.04	0.05 ± 0.01	0.45 ± 0.04	0.35 ± 0.04	0.10 ± 0.03	0.37 ± 0.02
MgO	0.00 ± 0.00	0.00 ± 0.00	0.00 ± 0.00	0.00 ± 0.00	0.00 ± 0.00	0.00 ± 0.00
BaO	1.14 ± 0.07	0.06 ± 0.02	0.15 ± 0.05	0.04 ± 0.00	0.06 ± 0.04	0.29 ± 0.03
CaO	0.00 ± 0.00	1.03 ± 0.02	0.25 ± 0.02	0.24 ± 0.02	0.35 ± 0.02	0.70 ± 0.02
Na_2O	0.25 ± 0.02	11.43 ± 0.14	10.24 ± 0.11	11.10 ± 0.12	11.13 ± 0.12	6.91 ± 0.10
K_2O	16.49 ± 0.13	0.31 ± 0.01	1.59 ± 0.03	0.49 ± 0.02	0.50 ± 0.02	6.61 ± 0.05
Total	101.35	101.94	100.59	101.01	103.33	101.77
Chemical formula based on 8 oxygens						
Si^{4+}	2.97 ± 0.03	2.94 ± 0.03	2.90 ± 0.03	2.97 ± 0.03	2.97 ± 0.03	2.95 ± 0.03
Ti^{4+}	0.00 ± 0.00	0.00 ± 0.00	0.00 ± 0.00	0.00 ± 0.00	0.00 ± 0.00	0.00 ± 0.00
Al^{3+}	1.03 ± 0.01	1.06 ± 0.01	1.12 ± 0.01	1.03 ± 0.01	1.04 ± 0.01	1.05 ± 0.01
Fe^{3+}	0.00 ± 0.00	0.00 ± 0.00	0.01 ± 0.00	0.01 ± 0.00	0.00 ± 0.00	0.01 ± 0.00
Mg^{2+}	0.00 ± 0.00	0.00 ± 0.00	0.00 ± 0.00	0.00 ± 0.00	0.00 ± 0.00	0.00 ± 0.00
Ba^{2+}	0.02 ± 0.00	0.00 ± 0.00	0.00 ± 0.00	0.00 ± 0.00	0.00 ± 0.00	0.01 ± 0.00
Ca^{2+}	0.00 ± 0.00	0.05 ± 0.00	0.01 ± 0.00	0.01 ± 0.00	0.02 ± 0.00	0.03 ± 0.01
Na^{+}	0.02 ± 0.00	0.95 ± 0.01	0.87 ± 0.01	0.93 ± 0.01	0.91 ± 0.01	0.59 ± 0.01
K^{+}	0.97 ± 0.01	0.02 ± 0.00	0.09 ± 0.00	0.03 ± 0.00	0.03 ± 0.00	0.37 ± 0.00
$\sum/\Delta\sum$	5.01 ± 0.02	5.02 ± 0.02	5.01 ± 0.02	4.99 ± 0.02	4.97 ± 0.02	5.01 ± 0.02
Chemical formula based on 8 oxygens						
An:	0.00 ± 0.00	4.66 ± 0.11	1.21 ± 0.10	1.16 ± 0.10	1.65 ± 0.10	3.32 ± 0.11
Ab:	2.25 ± 0.18	93.66 ± 1.82	89.63 ± 1.62	96.06 ± 1.76	95.53 ± 1.74	59.33 ± 1.22
Or:	97.75 ± 1.43	1.67 ± 0.06	9.16 ± 0.22	2.78 ± 0.12	2.83 ± 0.12	37.35 ± 0.62

04-07) has the same chemical composition as in the perthitic orthoclase (analysis JG-04-12). Furthermore, no significant Ba^{2+} variation was detected throughout the orthoclase-domains.

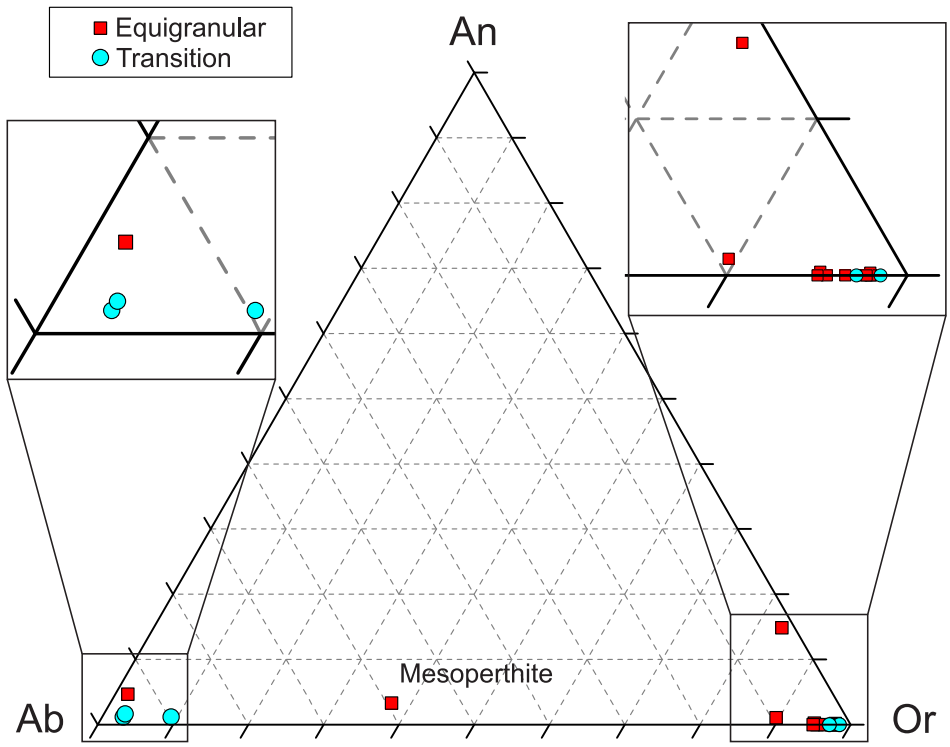
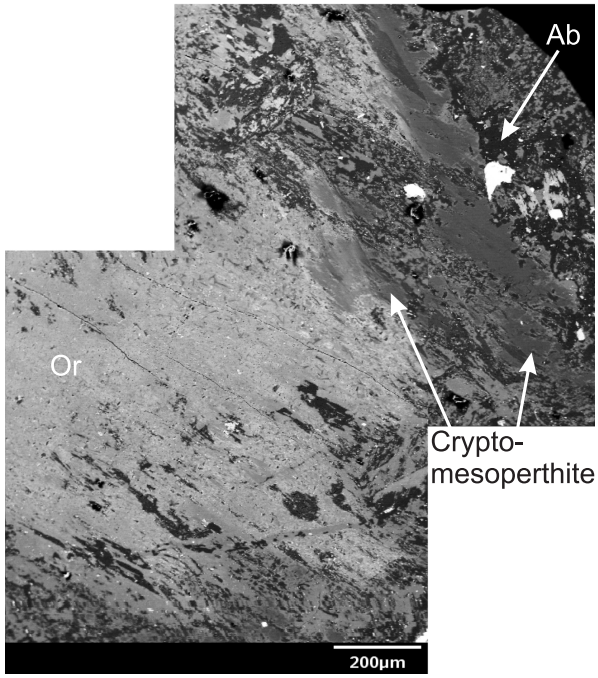


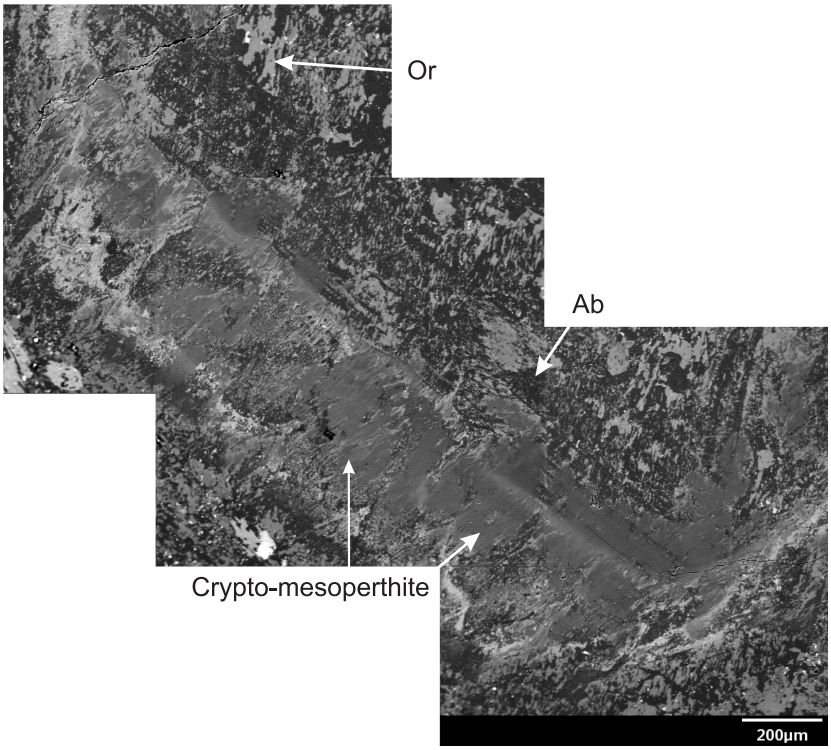
Figure 6.23 – End-member composition of large euhedral crystals from the equigranular magnetite-bearing unit and transition zone. The 3 end members are: Or = orthoclase, An = anorthite and Ab = albite. The analyses are presented in mole %.

Chemical variations indicate that albite has the highest An-enrichment measured (see Figure 6.23). This enrichment was however not perceived in both optical microscopy and EBS imaging. In all cases, the core is surrounded by a $<$ 0.1 - 0.4 mm thick band of crypto-mesoperthite. Upon close inspection of EBS images, there is evidence of compositional variation within the crypto-mesoperthite (see Figure 6.24). The compositional variations produce different shades of grey in the EBS images where the analysis is located in a lighter zone. This compositional variation does not affect the name given to the feldspar.

In the transition zone, phenocrysts are usually perthites which begin to demonstrate compositional zoning and have lost the crypto-mesoperthite rim. Furthermore, exsolution textures can be fine and erratic (see Figure 6.25). As such, exsolved orthoclase is occasionally found as small acicular to anhedral crystals. On the other hand, albite domains are irregularly-shaped with thin blades or surrounding masses of exsolved orthoclase. Additionally, feldspar decomposition may be incomplete, resulting in increased mol% of Ab for orthoclase and Or for albite (see Figure 6.25 and analysis 58-5-2). Towards the outer margins, orthoclase is compositionally zoned with decreasing amounts of Ba^{2+}. The zoning is best illustrated in Figure 6.25 where



(a) EBS image of a phenocryst with a perthitic orthoclase core surrounded by crypto-mesoperthite.



(b) EBS image of a phenocryst with a mesoperthite core surrounded by crypto-mesoperthite.

Figure 6.24 – EBS images of feldspar phenocrysts from the equigranular thin section. The lighter colours correspond to orthoclase (Or), the area demonstrating a progressive darkening belong to crypto-mesoperthite and the darkest is albite (Ab). Location: 630747E 5374454N.

the slight decrease in luminosity is directly correlated with the loss of Ba^{2+}. In this particular case, Ba^{2+} is at its highest concentration at the beginning of the outer rim with 0.07 ± 0.00 *apfu* Ba^{2+} whereas the outer part of the rim contains 0.02 ± 0.00 *apfu* Ba^{2+} (analyses 58-9-3 and 58-9-4). Furthermore, albite also demonstrates a slight An-enrichment which is reminiscent of the analysis performed in the equigranular thin section, but overall lacks compositional zoning. Drawing a parallel between both the equigranular magnetite-bearing and porphyritic Beattie units, the properties of the transition feldspar phenocrysts are truly a hybrid between the two.

Analysis 58-6-1 is unusually enriched in Ca^{2+}. This is the result of calcite contamination since the analysis has a very low compositional total and that thin acicular crystals of calcite are found in extremely close proximity to the location of the analysis (see Table 6.5).

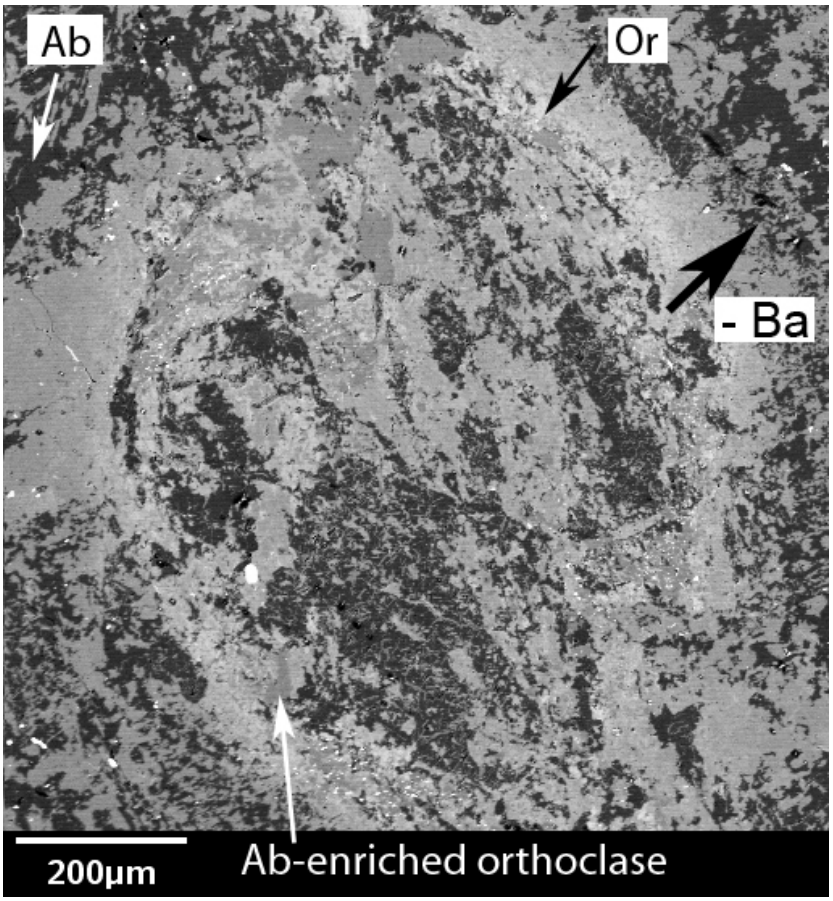


Figure 6.25 – EBS image of a feldspar phenocryst from the transition zone. Dark colours belong to albite (Ab), the slightly lighter are Ab-enriched orthoclase and the lightest is orthoclase (Or). Progressive compositional loss of Ba^{2+} is noted in the rim (large arrow) as a decrease in luminosity. Location: 630767E 5374481N.

6.4.2 Matrix

An intermix of both orthoclase and albite composes the matrix, producing an undulose extinction, similar to that observed in the porphyritic Beattie syenite unit. The difference between the porphyritic Beattie and the equigranular magnetite-bearing unit is that matrix feldspars are slightly larger and do not appear fibrous in the equigranular magnetite-bearing unit. Rather, feldspar crystals are anhedral and measure 0.4 - 0.8 mm (see Figure 6.26).



Figure 6.26 – Thin section appearance of the equigranular magnetite-bearing unit. Larger euhedral feldspars are contained in a feldspathic (grey) and actinolite (yellow) matrix. The larger crystals demonstrate compositional zoning with a turbid orthoclase core surrounded by clear crytpo-mesoperthite. Photomicrograph taken under crossed polars. Location: 630767E 5374471N.

Both feldspar analyses have been plotted on the feldspar ternary diagram, presented in Figure 6.28.

Albite and orthoclase composing the matrix of both the equigranular and transition occur as anhedral crystals in near equal proportions. This is a similar arrangement as the porphyritic Beattie syenite unit. However, feldspars appear uniformly distributed and orthoclase lacks

Table 6.6 – Microprobe analyses and chemical formulas of matrix feldspars from the equigranular magnetite-bearing unit.

	Orthoclase	Albite
	Equigranular	
	JG-04-20	**JG-04-19**
SiO_2	64.86 ± 0.45	68.50 ± 0.48
TiO_2	0.00 ± 0.00	0.00 ± 0.00
Al_2O_3	18.42 ± 0.13	19.84 ± 0.14
FeO	0.03 ± 0.02	0.26 ± 0.02
MgO	0.00 ± 0.00	0.00 ± 0.00
BaO	0.36 ± 0.03	0.05 ± 0.02
CaO	0.02 ± 0.01	0.58 ± 0.02
Na_2O	0.37 ± 0.03	12.13 ± 0.15
K_2O	15.77 ± 0.11	0.28 ± 0.01
Total	99.83	101.64
Chemical formula based on 8 oxygens		
Si^{4+}	3.00 ± 0.03	2.96 ± 0.03
Ti^{4+}	0.00 ± 0.00	0.00 ± 0.00
Al^{3+}	1.00 ± 0.01	1.01 ± 0.01
Fe^{3+}	0.00 ± 0.00	0.01 ± 0.00
Mg^{2+}	0.00 ± 0.00	0.00 ± 0.00
Ba^{2+}	0.01 ± 0.00	0.00 ± 0.00
Ca^{2+}	0.00 ± 0.00	0.03 ± 0.00
Na^{+}	0.03 ± 0.00	1.02 ± 0.01
K^{+}	0.93 ± 0.01	0.02 ± 0.00
$\sum/\Delta\sum$	4.98 ± 0.02	5.04 ± 0.02
Chemical formula based on 8 oxygens		
An:	0.10 ± 0.05	2.54 ± 0.10
Ab:	3.44 ± 0.28	96.01 ± 1.89
Or:	96.46 ± 1.42	1.46 ± 0.06

the bladed habit in the equigranular sample (see Figure 6.28). This configuration of finely intermixed feldspathic crystals would explain the slight Ab-enrichment, as albite crystals are always in close proximity. In both feldspars no compositional zoning was observed via EBS images (see Figure 6.28)

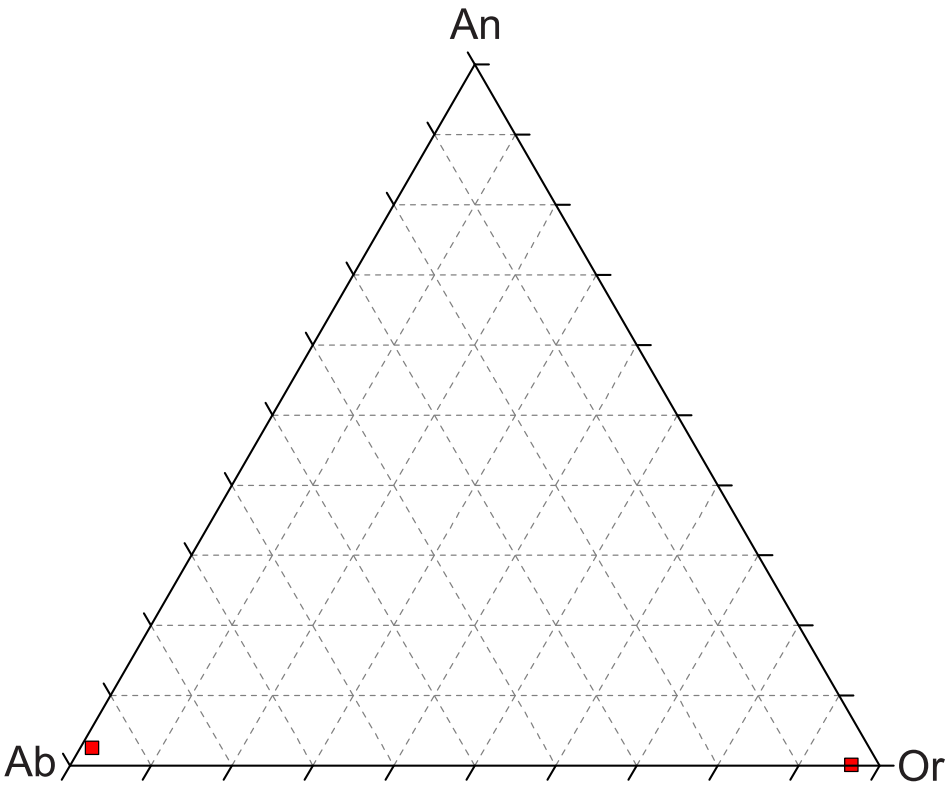


Figure 6.27 – End-member composition of matrix feldspars in the equigranular magnetite-bearing unit and the transition zone. The 3 end-members are: Or = orthoclase, An = anorthite and Ab = albite. Analyses are presented in mole %.

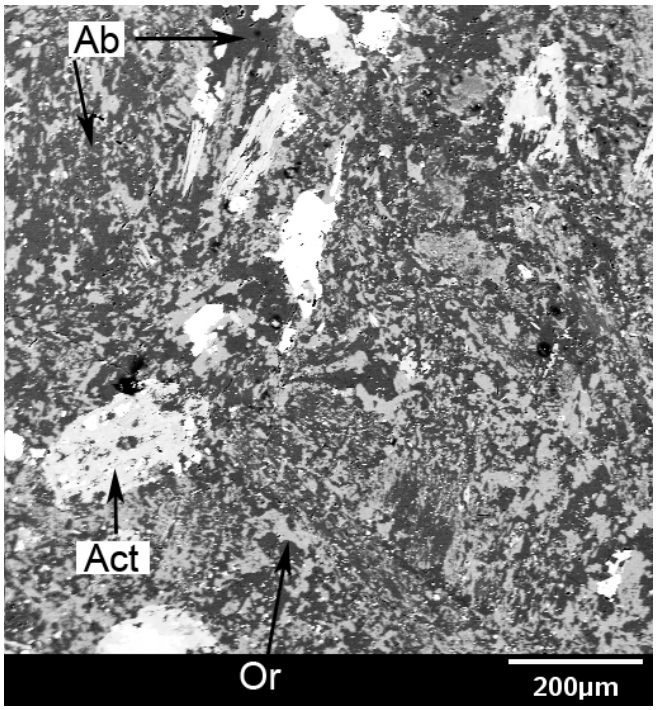


Figure 6.28 – EBS image of orthoclase and albite composing the matrix of the equigranular sample. The darker colours are attributed to albite (Ab), lighter ones belong to orthoclase (Or) and the lightest grey is actinolite (Act). Location: 630747E 5374454N.

6.4.3 Actinolite

Actinolite is considered to be a product of uralization and is therefore not part of the igneous mineralogical assemblage. Its habit and chemical composition are however reminiscent of the primary clinopyroxene it replaced. Consequently, actinolite has been kept as part of this chapter.

Actinolite is the dominant metamorphic ferromagnesian mineral only present in the equigranular magnetite-bearing unit. Crystals are pseudomorphs, measure 0.2 - 1.4 mm across, are pleochroic and appear fibrous (see Figure 6.29). Minor amounts of calcite, titanite, chlorite, hematite and magnetite also accompany actinolite in the clinopyroxene relict.

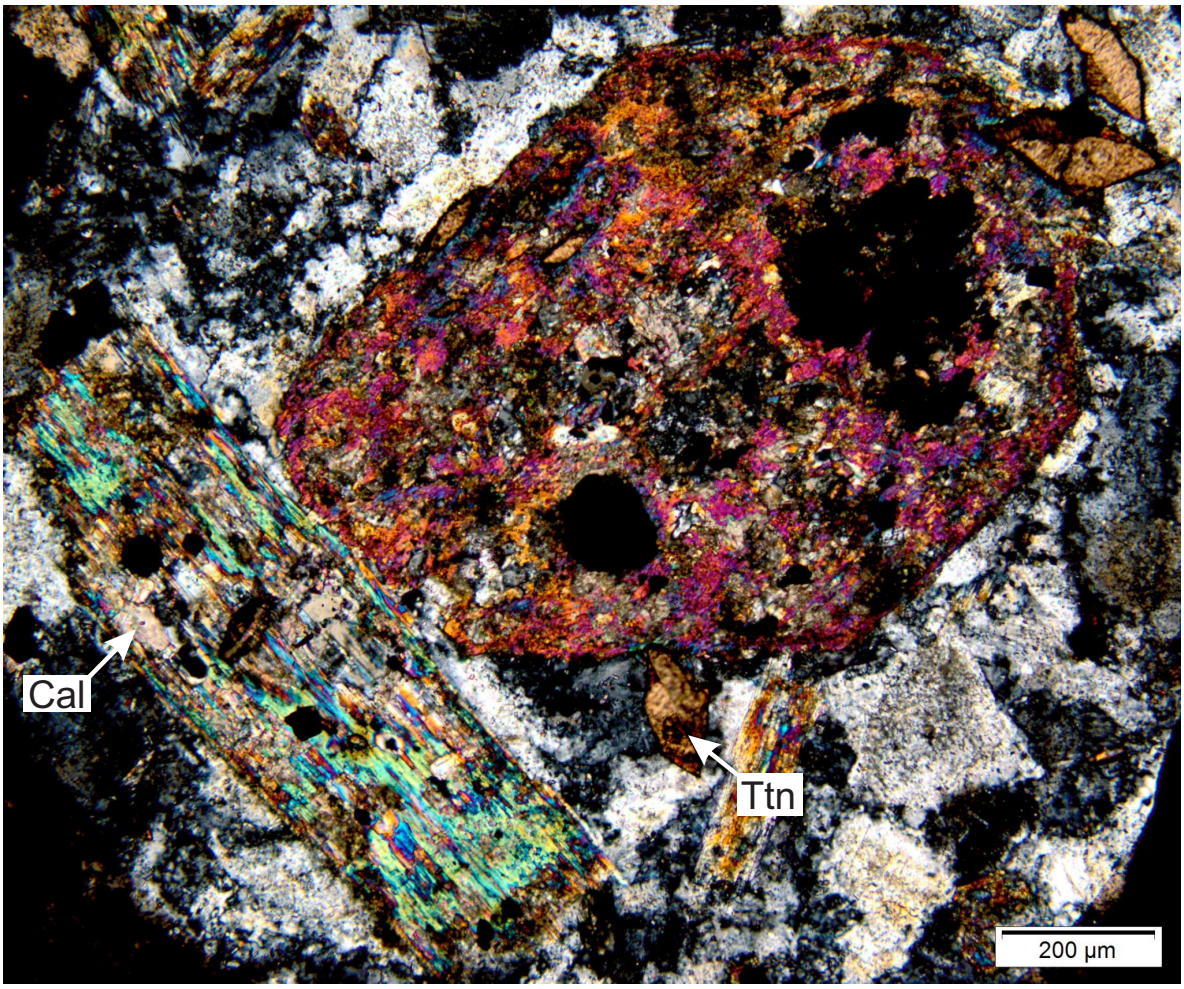


Figure 6.29 – Actinolite replacing clinopyroxene. The igneous shape of the clinopyroxene has been preserved. Actinolite is altering to calcite (Cal), chlorite (not seen), magnetite and hematite (opaques). Additionally, titanite crystals (Ttn) accompany actinolite. Photomicrograph taken under crossed polars. Location: 630747E 5374454N.

The chemical composition of actinolite was verified via EMPA. To this end, a total of 11 analyses on various crystals were performed. Estimations of Fe^{3+} were done by charge balance for the purpose of nomenclature. However, these estimations do not necessarily reflect the true Fe^{3+}-contents in a given environment (Schumacher, 1991). The resulting compositions and calculated formulas are presented in Table 6.7.

Table 6.7 – Microprobe analysis and chemical formulas of actinolite within the equigranular magnetite-bearing unit.

	JG-04-01	**JG-04-03**	**JG-04-04**	**JG-04-05**	**JG-04-09**	**JG-04-10**	**JG-04-11**
SiO_2	56.44 ± 0.40	57.09 ± 0.40	57.04 ± 0.40	53.71 ± 0.38	54.38 ± 0.38	54.01 ± 0.38	55.35 ± 0.39
TiO_2	0.00 ± 0.00	0.03 ± 0.00	0.01 ± 0.00	0.04 ± 0.00	0.03 ± 0.01	0.09 ± 0.01	0.02 ± 0.00
Al_2O_3	0.26 ± 0.02	0.90 ± 0.02	0.23 ± 0.01	1.19 ± 0.02	1.02 ± 0.02	1.13 ± 0.03	0.86 ± 0.02
Cr_2O_3	0.02 ± 0.01	0.04 ± 0.00	0.01 ± 0.00	0.03 ± 0.00	0.02 ± 0.02	0.01 ± 0.00	0.00 ± 0.00
FeO	9.03 ± 0.10	9.57 ± 0.11	8.78 ± 0.10	14.44 ± 0.13	11.57 ± 0.12	13.95 ± 0.13	11.88 ± 0.12
MnO	0.83 ± 0.04	0.83 ± 0.03	0.94 ± 0.03	1.16 ± 0.04	0.87 ± 0.04	1.06 ± 0.04	0.83 ± 0.03
MgO	17.59 ± 012	16.49 ± 0.12	17.91 ± 0.13	13.58 ± 0.11	15.63 ± 0.11	14.10 ± 0.11	15.63 ± 0.11
CaO	12.71 ± 0.10	12.22 ± 0.10	12.60 ± 0.10	12.70 ± 0.09	12.54 ± 0.10	12.30 ± 0.10	12.43 ± 0.10
Na_2O	0.37 ± 0.03	0.44 ± 0.02	0.35 ± 0.02	0.50 ± 0.02	0.43 ± 0.03	0.44 ± 0.04	0.45 ± 0.02
K_2O	0.14 ± 0.01	0.51 ± 0.01	0.09 ± 0.00	0.15 ± 0.00	0.10 ± 0.01	0.16 ± 0.01	0.08 ± 0.00
F	0.56 ± 0.06	0.44 ± 0.04	0.41 ± 0.04	0.25 ± 0.03	0.37 ± 0.05	0.31 ± 0.05	0.45 ± 0.04
Cl	0.01 ± 0.00	0.02 ± 0.00	0.02 ± 0.00	0.01 ± 0.00	0.00 ± 0.00	0.01 ± 0.00	0.00 ± 0.00
Total	97.94	98.58	98.38	97.76	96.98	97.57	97.98
H_2O	1.84	1.90	1.93	1.92	1.89	1.91	1.87
OH=F	0.24	0.19	0.17	0.11	0.16	0.13	0.19
OH=Cl	0.00	0.00	0.00	0.00	0.00	0.00	0.00
$\sum$	99.43	99.99	100.09	99.42	98.64	99.35	99.61
Chemical formula based on 13 cations							
Si^{4+}	8.04 ± 0.04	8.11 ± 0.04	8.05 ± 0.04	7.89 ± 0.04	7.91 ± 0.04	7.89 ± 0.04	7.97 ± 0.04
Al^{3+}	0.00 ± 0.00	0.00 ± 0.00	0.00 ± 0.00	0.10 ± 0.00	0.08 ± 0.00	0.11 ± 0.00	0.03 ± 0.00
$\sum$ **T**	8.04	8.11	8.05	8.00	8.00	8.00	8.00
Al^{3+}	0.00 ± 0.00	0.27 ± 0.00	0.04 ± 0.00	0.10 ± 0.00	0.09 ± 0.00	0.08 ± 0.00	0.11 ± 0.00
Ti^{4+}	0.00 ± 0.00	0.00 ± 0.00	0.00 ± 0.00	0.00 ± 0.00	0.00 ± 0.00	0.01 ± 0.00	0.00 ± 0.00
Fe^{3+}	0.00	0.00	0.00	0.00	0.00	0.00	0.00
Fe^{2+}	1.08	1.14	1.04	1.77	1.41	1.70	1.43
Mg^{2+}	3.74 ± 0.03	3.49 ± 0.03	3.77 ± 0.03	2.97 ± 0.03	3.39 ± 0.03	3.07 ± 0.03	3.35 ± 0.03
Mn^{2+}	0.10 ± 0.00	0.10 ± 0.00	0.11 ± 0.00	0.14 ± 0.00	0.11 ± 0.00	0.13 ± 0.00	0.10 ± 0.00
$\sum$ **C**	4.96	5.00	4.95	5.00	5.00	5.00	5.00
Na^{+}	0.06 ± 0.01	0.12 ± 0.01	0.10 ± 0.01	0.00 ± 0.00	0.04 ± 0.00	0.08 ± 0.01	0.08 ± 0.01
Ca^{2+}	1.94 ± 0.02	1.86 ± 0.02	1.90 ± 0.02	2.00 ± 0.02	1.96 ± 0.02	1.92 ± 0.02	1.92 ± 0.02
$\sum$ **B**	0.00	1.98	2.00	2.00	2.00	2.00	2.00
Na^{+}	0.04 ± 0.00	0.00 ± 0.00	0.00 ± 0.00	0.14 ± 0.01	0.08 ± 0.01	0.05 ± 0.01	0.04 ± 0.00
K^{+}	0.03 ± 0.00	0.09 ± 0.00	0.02 ± 0.00	0.03 ± 0.00	0.02 ± 0.00	0.03 ± 0.00	0.01 ± 0.00
$\sum$ **A**	0.07	0.09	0.02	0.17	0.09	0.08	0.06
O^{2-}	22.00	22.00	22.00	22.00	22.00	22.00	22.00
OH^{-}	1.75	1.80	1.81	1.88	1.83	1.85	1.80
F^{-}	0.25 ± 0.02	0.20 ± 0.02	0.18 ± 0.02	0.12 ± 0.01	0.17 ± 0.02	0.14 ± 0.02	0.20 ± 0.02
Cl^{-}	0.00 ± 0.00	0.00 ± 0.00	0.00 ± 0.00	0.00 ± 0.00	0.00 ± 0.00	0.00 ± 0.00	0.00 ± 0.00

The nomenclature and classification of the amphibole was done according to the current International Mineralogical Association (IMA) guidelines. A primary classification based on the occupancy of the **B**-sites, reveals that all amphiboles analyzed are members of the sodic-

Table 6.7 Continued

	JG-04-14	JG-04-18r	JG-04-21	JG-04-22
SiO_2	54.18 ± 0.38	53.18 ± 0.37	52.53 ± 0.37	55.11 ± 0.39
TiO_2	0.09 ± 0.01	0.09 ± 0.01	0.07 ± 0.01	0.03 ± 0.00
Al_2O_3	1.19 ± 0.03	1.64 ± 0.03	1.06 ± 0.02	1.02 ± 0.02
Cr_2O_3	0.00 ± 0.00	0.00 ± 0.00	0.01 ± 0.00	0.00 ± 0.00
FeO	11.71 ± 0.12	15.18 ± 0.14	14.49 ± 0.13	11.31 ± 0.11
MnO	0.90 ± 0.04	1.04 ± 0.04	1.28 ± 0.04	0.83 ± 0.03
MgO	15.55 ± 0.11	13.42 ± 0.11	13.45 ± 0.11	15.76 ± 0.11
CaO	12.67 ± 0.10	11.90 ± 0.10	12.16 ± 0.10	12.59 ± 0.10
Na_2O	0.33 ± 0.03	0.64 ± 0.04	0.35 ± 0.03	0.35 ± 0.02
K_2O	0.14 ± 0.01	0.20 ± 0.01	0.16 ± 0.01	0.12 ± 0.01
F	0.36 ± 0.05	0.21 ± 0.04	0.24 ± 0.04	0.38 ± 0.03
Cl	0.00 ± 0.00	0.01 ± 0.00	0.02 ± 0.00	0.00 ± 0.00
Total	97.12	97.50	95.80	97.49
H_2O	1.90	1.95	1.89	1.90
OH=F	0.15	0.09	0.10	0.16
OH=Cl	0.00	0.00	0.00	0.00
$\sum$	98.82	99.52	97.69	99.13
Chemical formula based on 13 cations				
Si^{4+}	7.88 ± 0.04	7.79 ± 0.03	7.84 ± 0.04	7.96 ± 0.04
Al^{3+}	0.12 ± 0.00	0.21 ± 0.00	0.16 ± 0.00	0.04 ± 0.00
$\sum$ **T**	8.00	8.00	8.00	8.00
Al^{3+}	0.08 ± 0.00	0.07 ± 0.00	0.03 ± 0.00	0.14 ± 0.00
Ti^{4+}	0.01 ± 0.00	0.01 ± 0.00	0.01 ± 0.00	0.00 ± 0.00
Fe^{3+}	0.00	0.17	0.09	0.00
Fe^{2+}	1.42	1.69	1.72	1.37
Mg^{2+}	3.37 ± 0.03	2.93 ± 0.03	2.99 ± 0.03	3.39 ± 0.03
Mn^{2+}	0.11 ± 0.00	0.13 ± 0.00	0.16 ± 0.00	0.10 ± 0.00
$\sum$ **C**	5.00	5.00	5.00	5.00
Na^{+}	0.03 ± 0.00	0.13 ± 0.01	0.06 ± 0.01	0.05 ± 0.00
Ca^{2+}	1.97 ± 0.02	1.87 ± 0.02	1.94 ± 0.02	1.95 ± 0.02
$\sum$ **B**	2.00	2.00	2.00	2.00
Na^{+}	0.07 ± 0.01	0.05 ± 0.01	0.05 ± 0.01	0.05 ± 0.01
K^{+}	0.03 ± 0.00	0.04 ± 0.00	0.03 ± 0.00	0.02 ± 0.00
$\sum$ **A**	0.09	0.09	0.08	0.07
O^{2-}	22.00	22.00	22.00	22.00
OH^{-}	1.83	1.90	1.88	1.83
F^{-}	0.17 ± 0.02	0.10 ± 0.02	0.11 ± 0.02	0.17 ± 0.02
Cl^{-}	0.00 ± 0.00	0.00 ± 0.00	0.01 ± 0.00	0.00 ± 0.00

calcic group. Specifically, the group boundaries are defined as $(Ca + Na)_B \geq 1.00$ and $Na_B < 0.50$ (Leacke et al., 1997). All analyses have a $(Ca + Na)_B$ between 1.98 - 2.00 and Na_B values of 0.00 - 0.13 *apfu*. Analyses also fulfil the optional clause that Ca_B is > 1.50, where values range from 1.86 - 2.00 *apfu*. The subdivision of the group into the individual species is illustrated in Figure 6.30. To this end, all amphibole analyses are actinolite. Unfortunately, 3 analyses plot outside the designated fields caused by Si^{4+} values greater than 8.0 *apfu*.

Actinolite crystals demonstrate a slight compositional variation. Figure 6.30 demonstrates 2 compositional clusters in the actinolite field. This variation is entirely the result of simple substitution between Fe^{2+} and Mg^{2+}, which is also reflected in EBS images. Figure 6.31

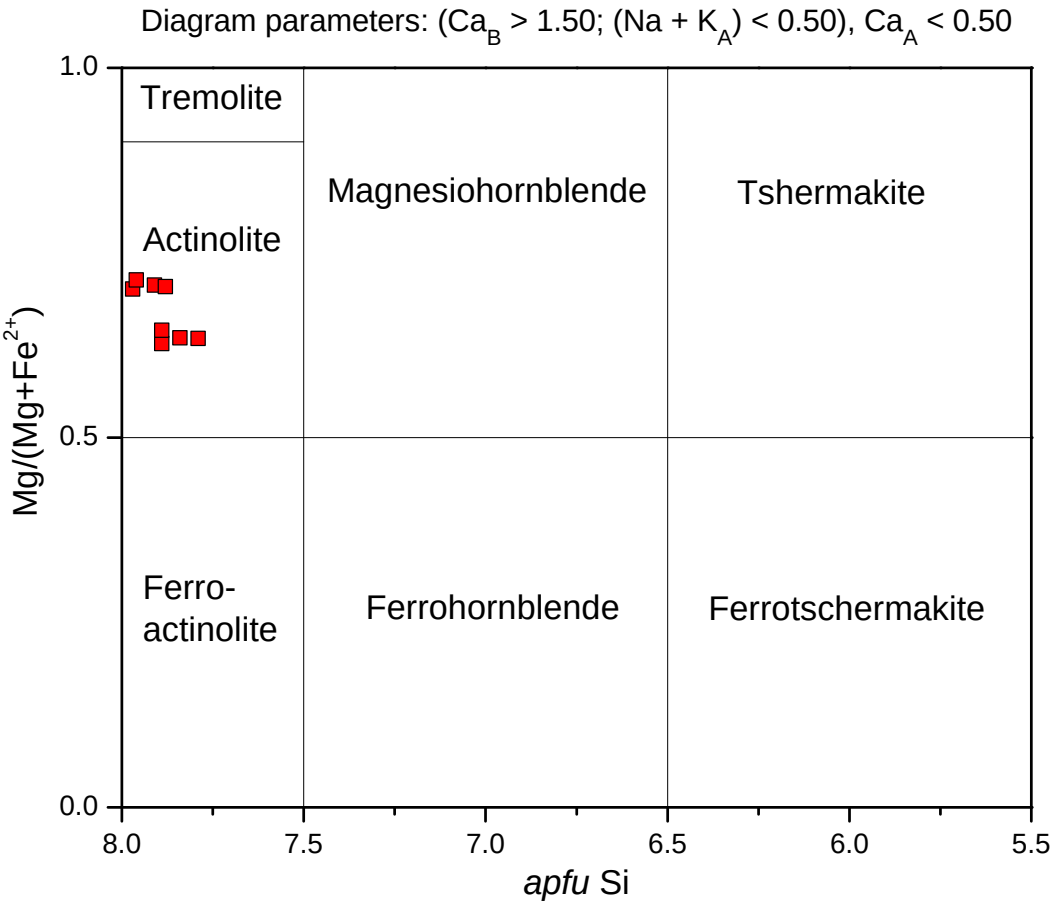


Figure 6.30 – IMA classification of calcic amphiboles. Nearly all analyses plot into the actinolite field. Three analyses plot slightly outside the field caused by excess Si^{4+}.

illustrates this substitution in which darker colours correspond to a dominance of Mg^{2+} and lighter colours are Fe^{2+}-enriched. Furthermore, EBS images reveal that the substitution occurs randomly throughout the crystals.

Actinolite crystals are metamorphic in origin, being part of the typical greenschist facies mineral assemblage (i.e., chlorite + albite + epidote ± quartz ± actinolite) and by replacing euhedral crystals of pyroxene (see Figure 6.32). Calcite accompanies actinolite as slender crystals found at the margins or in the pyroxene relicts. Subordinate amounts of titanite, quartz and oxide minerals also accompany actinolite (see Figure 6.32).

Possible primary pyroxene candidates given in literature are a titaniferous calcic clinopyroxene, aegerine or aegerine-augite (Moorhouse, 1959). Presuming actinolite analyses reflect the original mineralogy, the analyses contain high amounts of Ca^{2+} with very little Na^{+}. The dominance of Ca^{2+} is also supported by the abundance of calcite in and near the relict

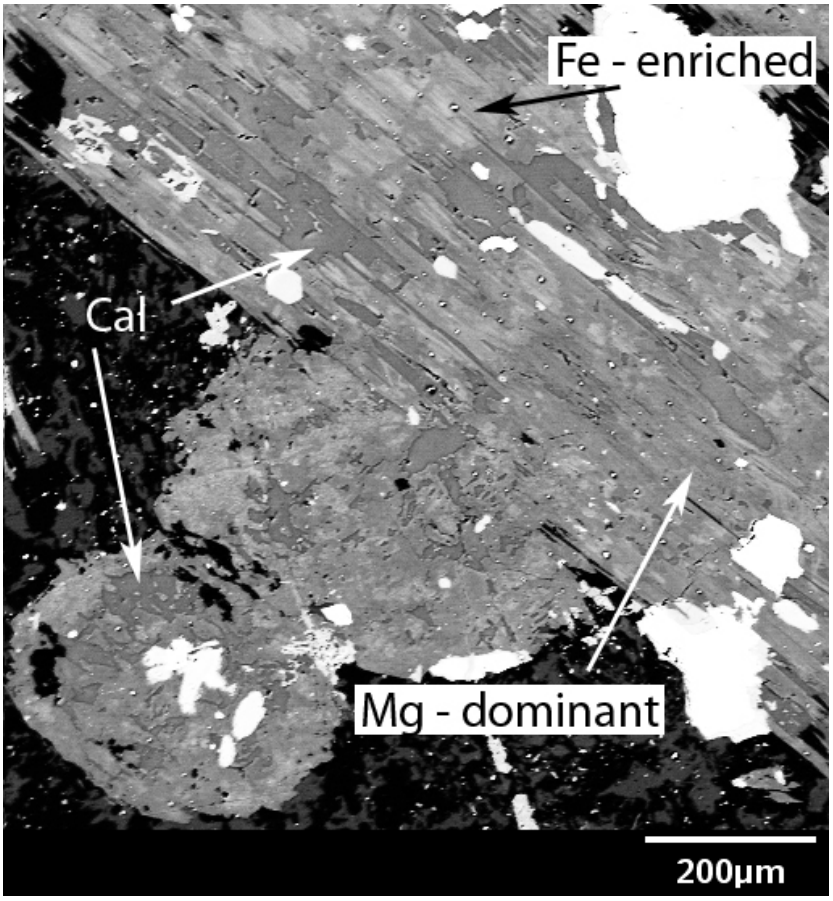


Figure 6.31 – EBS image of compositional variation in actinolite. Darker colours correspond to a dominance of Mg^{2+} and lighter colours are Fe^{2+}-enriched. Darker, lower relief crystals within actinolite is calcite (Cal). Location: 630747E 5374454N.

pyroxene. Such an abundance of Ca^{2+} therefore eliminates the candidature of aegerine and aegerine-augite, leaving calcic clinopyroxene. Augite therefore becomes a good candidate as chemical formulas of actinolite contain appreciable amounts of Fe^{2+} and Mg^{2+}. Upon closer inspection, amounts of Mg^{2+} outweigh Fe^{2+} with ratios near 2:1. Therefore diopside becomes a strong possibility. Diopside was also documented in similar syenitic plutons along the PDFZ by Pigeon (2003). Titanium is only present in small fractions in the actinolite analyses. Requirements for the addition of an adjectival modifier must be a quantity larger than 0.1 or 0.01 *apfu* (Morimoto, 1989). In all cases, Ti^{4+} values do not meet the necessary requirements. However, it should be noted that titanite crystals are often found in close proximity to the pyroxene relicts and oxides which also could accommodate Ti^{4+} are also found in and at the margins of the relicts (see Figure 6.32), therefore leaving the possibility for a titaniferous diopside. However, to remain cautious, the suggested igneous pyroxene will remain augite since

assumptions above are entirely based on a metamorphic equivalent, without detailed analyses and proportions of accompanying secondary minerals (i.e., calcite, titanite, oxides). The term augite here includes calcium-rich monoclinic pyroxenes.

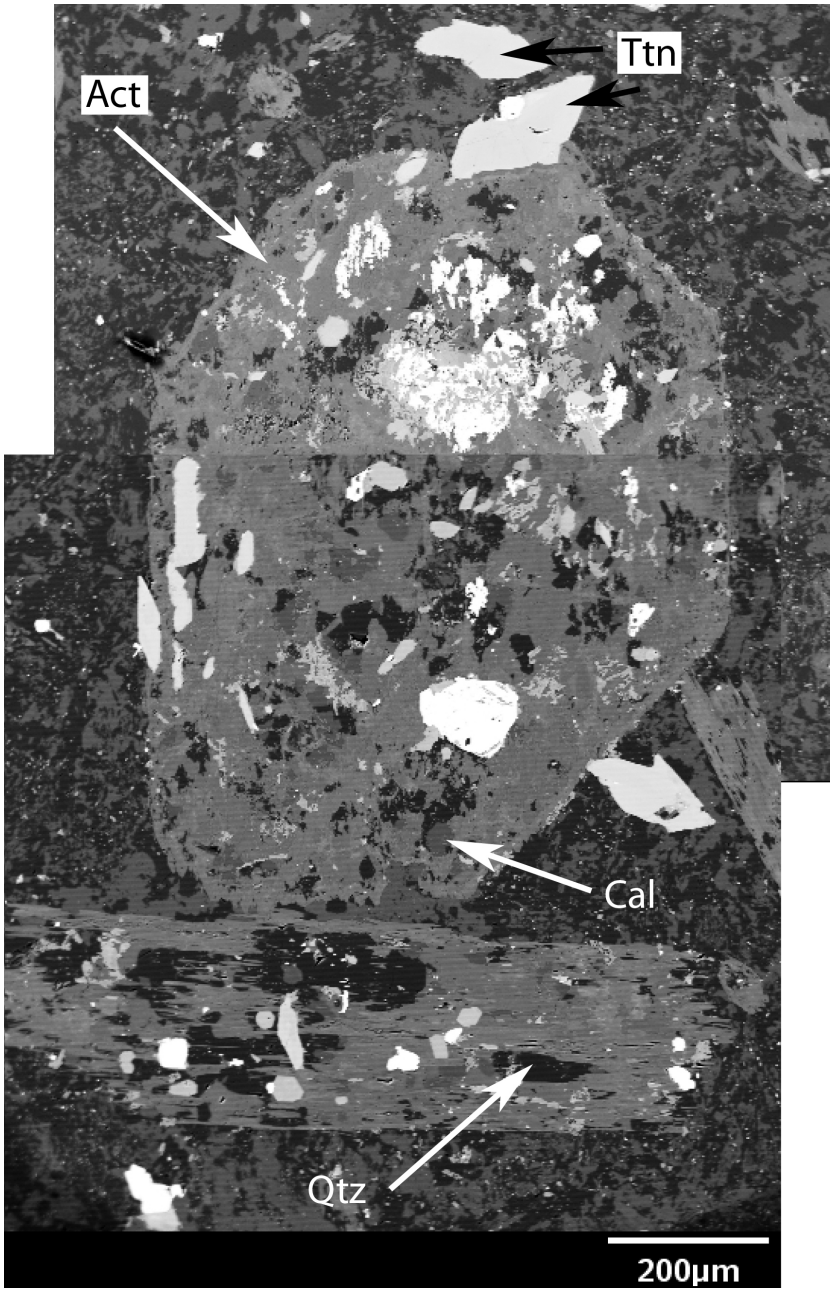


Figure 6.32 – EBS image of actinolite (Act) pseudomorphs. These are the same two crystals as presented in Figure 6.29. The actinolite is accompanied by titanite (Ttn), calcite (Cal) and quartz (Qtz). Location: 630747E 5374454N.

6.4.4 Magnetite

Euhedral magnetite crystals measure 0.1 - 0.2 mm across and are randomly distributed in the feldspathic matrix. A few anhedral crystals are also found in the clinopyroxene relicts, indicating that a small portion of magnetite is a product of alteration.

6.4.5 Titanite

Crystals are lamellar, euhedral, pleochroic and measure 0.1 - 0.6 mm in length. Titanite is randomly distributed though the rock and is not commonly altered. Occasionally, simple twinning is observed.

Two titanite crystals from the transition zone, encased in a phenocryst, were analyzed. The ensuing chemical formulas were calculated on 4 Si basis and subsequently renormalized to 1 Si. The composition and calculated formulas are presented in Table 6.8.

Table 6.8 – Microprobe analyses and formulas of titanite from the transition zone.

	58-7-1	**58-7-2**
SiO_2	29.83 ± 0.21	30.44 ± 0.21
TiO_2	35.31 ± 0.28	34.15 ± 0.27
Al_2O_3	1.54 ± 0.03	1.68 ± 0.03
FeO	2.05 ± 0.08	2.67 ± 0.08
MnO	0.03 ± 0.03	0.07 ± 0.01
MgO	0.00 ± 0.00	0.00 ± 0.00
CaO	28.19 ± 0.23	28.75 ± 0.23
Na_2O	0.07 ± 0.02	0.06 ± 0.00
K_2O	0.02 ± 0.01	0.02 ± 0.00
F	0.57 ± 0.07	0.31 ± 0.03
Cl	0.01 ± 0.00	0.00 ± 0.00
Total	97.61	98.15
H_2O	2.77	2.90
-OH=F	0.24	0.13
-OH=Cl	0.00	0.00
$\sum$	100.38	101.05
Chemical formula based on 4 Si		
Si^{4+}	1.00 ± 0.00	1.00 ± 0.00
Ti^{4+}	0.89 ± 0.00	0.84 ± 0.00
Al^{3+}	0.03 ± 0.00	0.03 ± 0.00
Fe^{2+}	0.06 ± 0.00	0.07 ± 0.00
Mn^{2+}	0.00 ± 0.00	0.00 ± 0.00
Mg^{2+}	0.00 ± 0.00	0.00 ± 0.00
Ca^{2+}	1.01 ± 0.00	1.01 ± 0.00
Ba^{+}	0.00 ± 0.00	0.00 ± 0.00
Na^{+}	0.00 ± 0.00	0.00 ± 0.00
K^{+}	0.00 ± 0.00	0.00 ± 0.00
F	0.09 ± 0.01	0.05 ± 0.01
Cl	0.00 ± 0.00	0.00 ± 0.00
OH	0.91	0.95

Both calculated chemical formulas presented in Table 6.8 correspond to a typical titanite. EBS images of the 2 crystals demonstrate compositional zoning, considered typical of titanites

(see Figure 6.33).

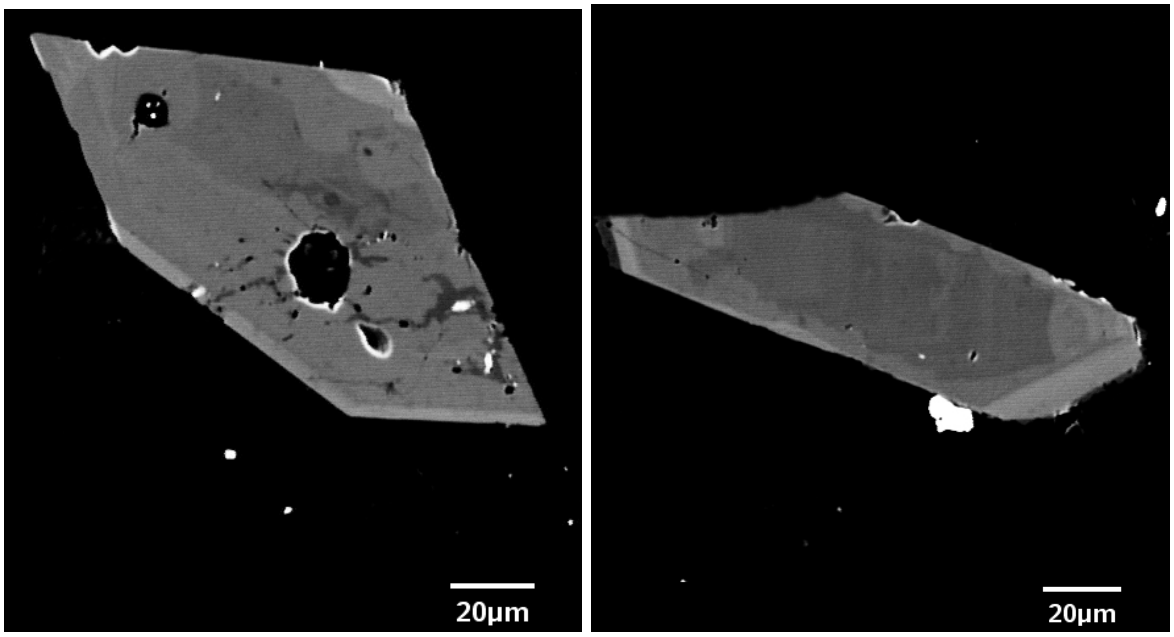


Figure 6.33 – EBS images of titanite crystals from the transition zone between the equigranular and porphyritic Beattie units. Both crystals are encased in a feldspar phenocryst. Additionally, both crystals are compositionally zoned. Location: 630767E 5374481N.

6.4.6 Apatite

Apatite is present as small sub- to euhedral crystals measuring 0.6 - 0.8 mm across. Larger crystals support a few fractures, but do not display any displacement nor any alteration.

6.5 Porphyritic Central Duparquet syenite (A*bet3*)

The porphyritic Central Duparquet syenite is the second most abundant unit, accounting for 12.69% (inferred surface area) of the Beattie syenite. The unit dominates the south and eastern portions of the Beattie syenite. It is characterized by sub-circular to ellipsoid bodies measuring $<$ 120 m across in the BDB. In the CDB the unit dominates the eastern portion, extending uninterrupted for a distance of 1.3 km.

The unit consists of white to pale green feldspar phenocrysts in a red to pink or grey feldspathic aphanitic matrix. The phenocrysts are euhedral, equant, measure between 10 - 20 mm and compose 15 - 25%$_m$ of the rock. Phenocrysts occasionally demonstrate compositional zoning and typically decrease in size towards contacts. Areas containing a large percentage of phenocryst demonstrate the beginnings of synneusis, expressed by a very poor glomeroporphyritic texture (see Figure 6.34). The unit also supports brittle deformation features and a myriad of hydrothermal alterations and greenschist facies minerals. However, both deformation and alteration are not as pervasive and abundant since the unit is located further away from the PDFZ.

Lenses of porphyritic Central Duparquet in the BDB are characterized by 10 - 20 mm euhedral feldspars. Phenocrysts are equant to prismatic in a dominantly grey matrix and are much less abundant (2 - 5%$_m$) than in the CDB (see Figure 6.35).

Igneous minerals in the porphyritic Central Duparquet unit are dominantly orthoclase and albite, composing both phenocrysts and the aphanitic matrix, with trace amounts of apatite and magnetite. Albite can be differentiated from orthoclase by lesser amounts of turbidity and a general lack of sericitization. The modal ranges of igneous minerals in the unit, determined from microscopic observations, are given in Table 6.9 along with a typical modal composition. Both hydrothermal and greenschist facies minerals have not been included in the Table below.

Table 6.9 – Range and modal composition of igneous minerals constituting the porphyritic Central Duparquet unit. Ranges are based on 9 thin sections.

	Maximum ranges	Typical composition
Mineral	**Modal %**	**Modal %**
Orthoclase	3 - 58	36
Albite	34 - 65	38
Apatite	Trace - 1	Trace
Magnetite	0 - 2	1

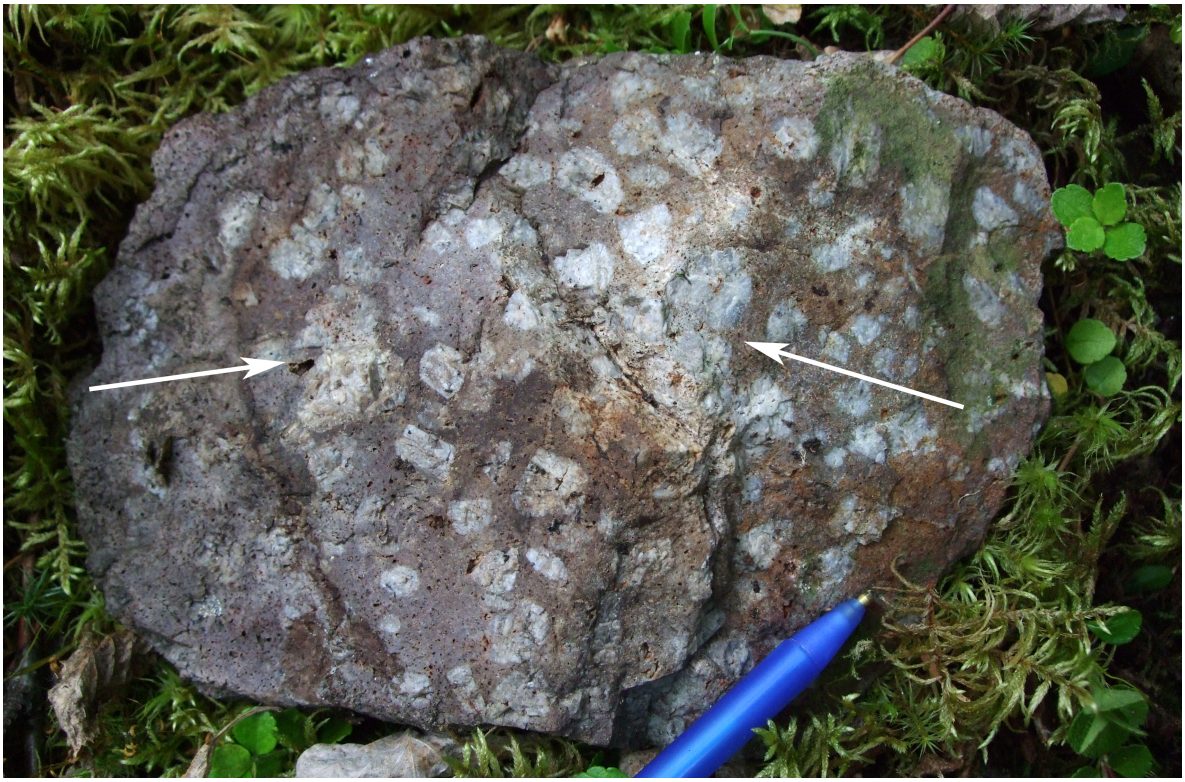


Figure 6.34 – Porphyritic Central Duparquet specimen taken from an outcrop. White feldspar phenocrysts (1 - 2 cm) are contained in a red aphanitic matrix. The white arrows demonstrate the very poor glomeroporphyritic texture. Location: 633240E 5373971N.



Figure 6.35 – Porphyritic Central Duparquet in the BDB. Phenocrysts are euhedral and measure, on average, between 1 - 2 cm, but are much less abundant than in the CDB. Location: 632878E 5374232N.

6.5.1 Phenocrysts

Both albite and orthoclase compose the sub- to euhedral phenocrysts. The core either is composed of orthoclase or albite. Orthoclase cores are commonly surrounded by more orthoclase as presented in Figure 6.36, or by albite (0.2 - 0.8 mm thick). Rarely, a phenocryst will have an albite core surrounded by orthoclase which are in turn surrounded by more albite (see Figure 6.37). The composition of albite in the core of phenocrysts was determined by the Michel-Lévy method to be between An_9 - An_{10}. The albitic composition was subsequently verified via EMPA (see below). Albite-only phenocrysts, measuring 5 - 10 mm across have also been rarely observed. Phenocrysts composed entirely of orthoclase are euhedral, equant to slightly tabular, measure up to 2.1 cm across and occasionally demonstrate perthitic exsolution (see Figure 6.36). At times, orthoclase phenocrysts demonstrate a very poor glomeroporphyritic texture (see Figure 6.38). Finally, in a special instance, a phenocryst transected by a metamorphic vein of quartz, albite and carbonate minerals, demonstrates faint tartan twinning.

The chemical composition of phenocrysts was the subject of further investigations using both EMPA and EBS imaging. A total of 3 samples were submitted for EMPA. The westernmost sample, ZP-04-047 is in the BDB, located 110 m northwest from the abandoned Donchester mine shaft. The next two samples are located in the eastern portion of the CDB. JG-94-5148 is located 307 m northwest from the abandoned Central Duparquet 1 mine shaft and ZP-04-056 is located 250 m east from the abandoned Central Duparquet 1 mine shaft. The exact locations of all samples submitted for EMPA can be viewed in Figure 6.16. Analyses were randomly selected within the crystals with additional analyses performed on distinct/unusual features. Both orthoclase and albite formulas have been calculated on an 8 oxygen basis. Chemical composition and calculated formulas are presented in Table 6.10.

The orthoclase end-member composition ranges from 0.00 - 0.31 mol% An, 1.08 - 2.85 mol% Ab and 97.15 - 98.92 mol% Or. As for albite, the composition varies from 0.19 - 0.28 mol% An, 0.61 - 0.72 mol% Or and 99.10 - 99.11 mol% Or. In all cases An-contents are negligible. A visualization of the feldspathic mol% end-member compositions is presented in Figure 6.39.

Phenocrysts either have an albite dominated core surrounded by orthoclase, are perthites or are perthitic orthoclase with an orthoclase overgrowth. The transition from the albite core

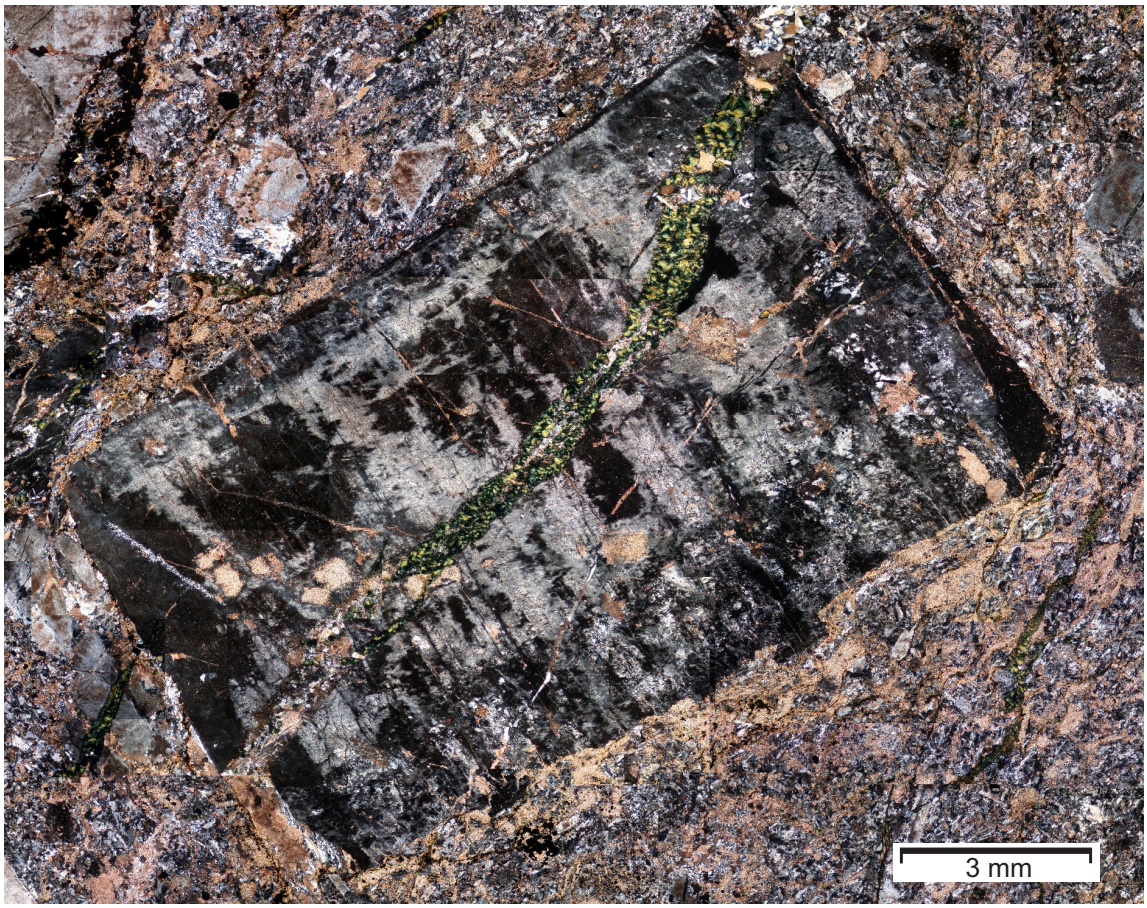


Figure 6.36 – Euhedral perthitic phenocryst of the porphyritic Central Duparquet unit. The phenocryst demonstrates two growth stages with the core displaying large perthitic exsolution textures and the second one displaying smaller perthitic exsolution textures. The phenocryst is contained in a sericitized matrix of hydrothermal origin. The matrix and phenocryst is cut by a vein containing hydrothermal green chlorite, colourless greenschist facies albite and beige carbonate minerals. Photomicrograph taken under crossed polars. Location: 631750E 5374450N.

to orthoclase is progressive with an increase of thin, massive to bladed orthoclase domains towards the outer margins (see Figure 6.40a). Orthoclase surrounding the albite core measures between $<$ 0.1 - 0.4 mm. Perthitic phenocrysts display irregular exsolution textures and are compositionally zoned (see Figure 6.40b). Exsolved Na-domains appear randomly but are occasionally aggregated together into 0.1 - 0.4 mm across irregular patches. As for compositional zoning, it is solely manifest by Ba^{2+} which can reach concentrations up to 0.03 $\pm$ 0.00 *apfu* Ba^{2+}. Ba^{2+}-enriched zones resemble veins measuring $<$ 40 μm thick or small irregular patches 20 - 30 μm across and seem randomly distributed through the crystal. The variation in Ba^{2+} can be observed in Figure 6.40c. The lighter shades of grey correspond to Ba^{2+}-enriched zones,

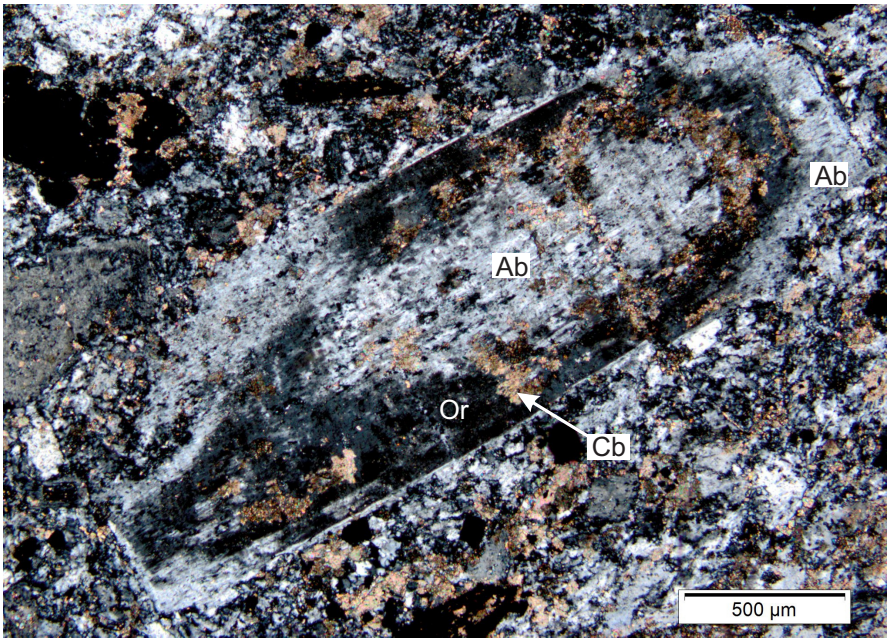


Figure 6.37 – Compositionally zoned phenocryst. The core is composed of albite (Ab) which is surrounded by orthoclase (Or) which are both surrounded by albite. Disseminated carbonate minerals (Cb) of hydrothermal origin also appear randomly in the feldspathic matrix and have a preference for orthoclase in the phenocryst. Photomicrograph taken under crossed polars. Location: 631597E 5374346N.

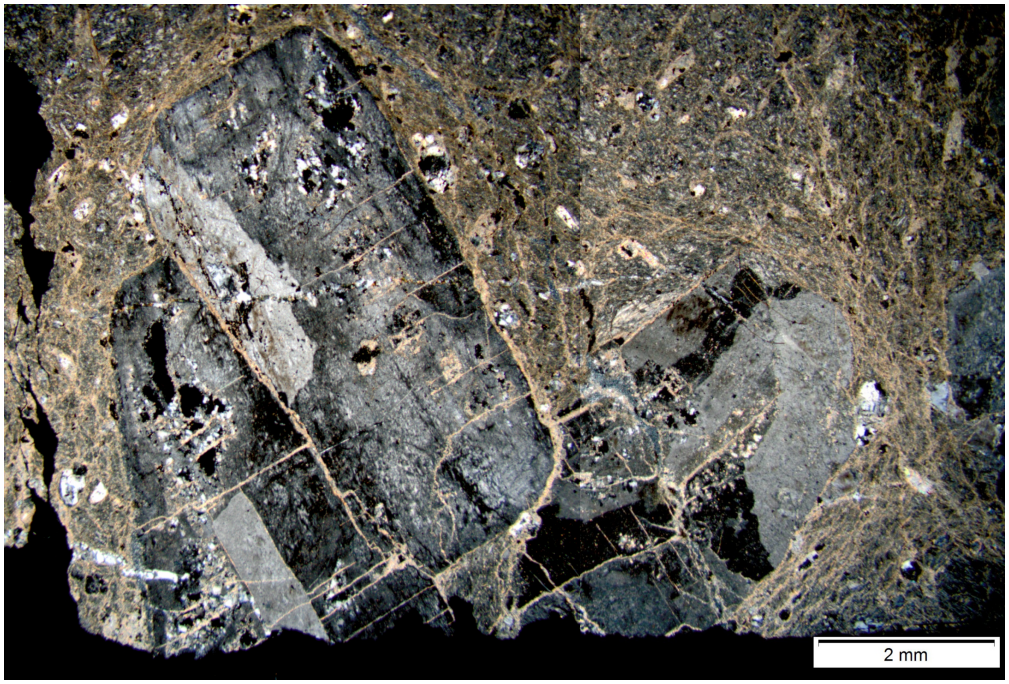


Figure 6.38 – Poor glomeroporphyritic texture in the porphyritic Central Duparquet unit. The phenocrysts are contained in a sericitized matrix produced by hydrothermal alteration. Photomicrograph taken under crossed polars. Location: 633897E 5373842N.

Table 6.10 – Microprobe analyses and chemical formulas of phenocrysts from the porphyritic Central Duparquet unit.

	Orthoclase					
	48-3-1	**48-3-2**	**48-6-1**	**48-8-1**	**47-2-1**	**47-2-2**
SiO_2	64.83 ± 0.45	63.63 ± 0.45	64.71 ± 0.45	64.22 ± 0.45	66.08 ± 0.46	65.46 ± 0.46
TiO_2	0.00 ± 0.00	0.00 ± 0.00	0.00 ± 0.00	0.00 ± 0.00	0.03 ± 0.02	0.02 ± 0.00
Al_2O_3	18.82 ± 0.13	18.70 ± 0.13	18.67 ± 0.13	18.88 ± 0.13	18.77 ± 0.13	19.17 ± 0.13
FeO	0.14 ± 0.04	0.07 ± 0.03	0.07 ± 0.03	0.01 ± 0.00	0.03 ± 0.00	0.17 ± 0.04
MgO	0.00 ± 0.00	0.00 ± 0.00	0.00 ± 0.00	0.00 ± 0.00	0.00 ± 0.00	0.00 ± 0.00
BaO	0.59 ± 0.06	0.60 ± 0.06	0.69 ± 0.06	0.54 ± 0.06	0.34 ± 0.05	0.66 ± 0.06
CaO	0.00 ± 0.00	0.00 ± 0.00	0.00 ± 0.00	0.06 ± 0.02	0.00 ± 0.00	0.00 ± 0.00
Na_2O	0.18 ± 0.02	0.16 ± 0.02	0.31 ± 0.02	0.16 ± 0.02	0.14 ± 0.02	0.17 ± 0.02
K_2O	15.87 ± 0.13	16.09 ± 0.13	15.86 ± 0.13	15.99 ± 0.13	16.93 ± 0.14	16.76 ± 0.13
Total	100.43	99.24	100.3	99.86	102.32	102.46
Formula calculated based on 8 oxygen						
Si^{4+}	2.99 ± 0.03	2.98 ± 0.03	2.99 ± 0.03	2.98 ± 0.03	3.00 ± 0.03	2.97 ± 0.03
Ti^{4+}	0.00 ± 0.00	0.00 ± 0.00	0.00 ± 0.00	0.00 ± 0.00	0.00 ± 0.00	0.00 ± 0.00
Al^{3+}	1.02 ± 0.01	1.03 ± 0.01	1.02 ± 0.01	1.03 ± 0.01	1.00 ± 0.01	1.03 ± 0.01
Fe^{3+}	0.00 ± 0.00	0.00 ± 0.00	0.00 ± 0.00	0.00 ± 0.00	0.00 ± 0.00	0.01 ± 0.00
Mg^{2+}	0.00 ± 0.00	0.00 ± 0.00	0.00 ± 0.00	0.00 ± 0.00	0.00 ± 0.00	0.00 ± 0.00
Ba^{2+}	0.01 ± 0.00	0.01 ± 0.00	0.01 ± 0.00	0.01 ± 0.00	0.01 ± 0.00	0.01 ± 0.00
Ca^{2+}	0.00 ± 0.00	0.00 ± 0.00	0.00 ± 0.00	0.00 ± 0.00	0.00 ± 0.00	0.00 ± 0.00
Na^{+}	0.02 ± 0.00	0.01 ± 0.00	0.03 ± 0.00	0.01 ± 0.00	0.01 ± 0.00	0.01 ± 0.00
K^{+}	0.93 ± 0.01	0.96 ± 0.01	0.93 ± 0.01	0.95 ± 0.01	0.98 ± 0.01	0.97 ± 0.01
$\sum/\Delta\sum$	4.97 ± 0.02	4.93 ± 0.02	4.99 ± 0.02	4.99 ± 0.02	5.00 ± 0.02	5.00 ± 0.02
Mol% end-member						
An:	0.00 ± 0.00	0.00 ± 0.00	0.00 ± 0.00	0.31 ± 0.10	0.00 ± 0.00	0.00 ± 0.00
Ab:	1.69 ± 0.19	1.49 ± 0.19	2.85 ± 0.19	1.49 ± 0.19	1.24 ± 0.18	1.52 ± 0.18
Or:	98.31 ± 1.49	98.51 ± 1.48	97.15 ± 1.45	98.20 ± 1.56	98.76 ± 1.50	98.48 ± 1.44

whereas darker grey zones do not support this enrichment. Furthermore, analyses 47-4-1 in an albitic core and 48-3-1 in a perthite demonstrate the same chemistry, therefore supporting near complete feldspar unmixing. Perthitic orthoclase phenocrysts are also compositionally zoned, both at the core and in the overgrowth. Exsolved Na-domains tend to increase in abundance towards the outer margins of the core. Overgrowths are composed of orthoclase, typically measure between 80 - 240 μm thick, almost evenly surrounding the core and attain a slightly larger thickness at the extremities (see Figure 6.40d). Zoning is once again produced by Ba^{2+} variations. At the core, zoning resembles that described for perthities above, however zoning in the overgrowth is progressive. Ba^{2+} is enriched at the beginning of the overgrowth and linearly decreases towards the margin.

Table 6.10 Continued

	Orthoclase					
	47-4-2	**47-5-1**	**47-5-2**	**47-7-1**	**47-7-2**	**56-3-1**
SiO_2	65.25 ± 0.46	65.25 ± 0.46	63.61 ± 0.45	64.65 ± 0.45	63.70 ± 0.45	66.17 ± 0.45
TiO_2	0.00 ± 0.00	0.00 ± 0.00	0.00 ± 0.00	0.00 ± 0.00	0.00 ± 0.00	0.00 ± 0.00
Al_2O_3	18.78 ± 0.13	18.48 ± 0.13	19.05 ± 0.13	18.44 ± 0.13	18.80 ± 0.13	18.64 ± 0.13
FeO	0.22 ± 0.04	0.00 ± 0.00	0.32 ± 0.04	0.11 ± 0.04	0.11 ± 0.03	0.00 ± 0.00
MgO	0.00 ± 0.00	0.00 ± 0.00	0.00 ± 0.00	0.00 ± 0.00	0.00 ± 0.00	0.00 ± 0.00
BaO	0.62 ± 0.06	0.69 ± 0.06	1.58 ± 0.08	0.66 ± 0.06	1.95 ± 0.09	0.11 ± 0.05
CaO	0.00 ± 0.00	0.00 ± 0.00	0.00 ± 0.00	0.00 ± 0.00	0.00 ± 0.00	0.00 ± 0.00
Na_2O	0.19 ± 0.02	0.19 ± 0.02	0.23 ± 0.02	0.19 ± 0.02	0.21 ± 0.02	0.23 ± 0.02
K_2O	16.33 ± 0.13	16.62 ± 0.13	16.31 ± 0.13	16.61 ± 0.13	15.92 ± 0.13	16.73 ± 0.13
Total	101.39	101.23	101.1	100.66	100.7	101.88
Formula calculated based on 8 oxygen						
Si^{4+}	2.99 ± 0.03	3.00 ± 0.03	2.95 ± 0.03	2.99 ± 0.03	2.97 ± 0.03	3.00 ± 0.03
Ti^{4+}	0.00 ± 0.00	0.00 ± 0.00	0.00 ± 0.00	0.00 ± 0.00	0.00 ± 0.00	0.00 ± 0.00
Al^{3+}	1.01 ± 0.01	1.00 ± 0.01	1.04 ± 0.01	1.00 ± 0.01	1.03 ± 0.01	1.00 ± 0.01
Fe^{3+}	0.01 ± 0.00	0.00 ± 0.00	0.01 ± 0.00	0.00 ± 0.00	0.00 ± 0.00	0.00 ± 0.00
Mg^{2+}	0.00 ± 0.00	0.00 ± 0.00	0.00 ± 0.00	0.00 ± 0.00	0.00 ± 0.00	0.00 ± 0.00
Ba^{2+}	0.01 ± 0.00	0.01 ± 0.00	0.03 ± 0.00	0.01 ± 0.00	0.04 ± 0.00	0.00 ± 0.00
Ca^{2+}	0.00 ± 0.00	0.00 ± 0.00	0.00 ± 0.00	0.00 ± 0.00	0.00 ± 0.00	0.00 ± 0.00
Na^{+}	0.02 ± 0.00	0.02 ± 0.00	0.02 ± 0.00	0.02 ± 0.00	0.02 ± 0.00	0.02 ± 0.00
K^{+}	0.95 ± 0.01	0.97 ± 0.01	0.97 ± 0.01	0.98 ± 0.01	0.95 ± 0.01	0.97 ± 0.01
$\sum/\Delta\sum$	4.99 ± 0.02	5.00 ± 0.02	5.02 ± 0.02	5.01 ± 0.02	5.00 ± 0.02	4.99 ± 0.02
Mol% end-member						
An:	0.00 ± 0.00	0.00 ± 0.00	0.00 ± 0.00	0.00 ± 0.00	0.00 ± 0.00	0.00 ± 0.00
Ab:	1.74 ± 0.19	1.71 ± 0.19	2.10 ± 0.18	1.71 ± 0.18	1.97 ± 0.19	2.05 ± 0.18
Or:	98.26 ± 1.46	98.29 ± 1.44	97.90 ± 1.45	98.29 ± 1.44	98.03 ± 1.48	97.93 ± 1.43

Table 6.10 Continued

	Orthoclase				Albite	
	56-3-2	**56-5-1**	**56-5-2**	**56-7-1**	**48-3-3**	**47-4-1**
SiO_2	65.07 ± 0.46	63.97 ± 0.45	64.00 ± 0.45	65.50 ± 0.46	69.04 ± 0.48	69.95 ± 0.49
TiO_2	0.00 ± 0.00	0.00 ± 0.00	0.00 ± 0.00	0.00 ± 0.00	0.00 ± 0.00	0.00 ± 0.00
Al_2O_3	18.78 ± 0.13	20.20 ± 0.14	18.75 ± 0.13	18.38 ± 0.13	19.69 ± 0.14	19.70 ± 0.14
FeO	0.02 ± 0.00	0.31 ± 0.04	0.03 ± 0.00	0.00 ± 0.00	0.00 ± 0.00	0.08 ± 0.03
MgO	0.00 ± 0.00	0.00 ± 0.00	0.00 ± 0.00	0.00 ± 0.00	0.00 ± 0.00	0.00 ± 0.00
BaO	1.38 ± 0.08	0.33 ± 0.05	1.79 ± 0.08	0.20 ± 0.05	0.05 ± 0.00	0.06 ± 0.04
CaO	0.00 ± 0.00	0.00 ± 0.00	0.00 ± 0.00	0.00 ± 0.00	0.06 ± 0.02	0.04 ± 0.02
Na_2O	0.16 ± 0.02	0.15 ± 0.02	0.16 ± 0.02	0.12 ± 0.02	11.77 ± 0.12	11.83 ± 0.12
K_2O	16.28 ± 0.13	16.09 ± 0.13	16.16 ± 0.13	16.75 ± 0.13	0.11 ± 0.01	0.13 ± 0.01
Total	101.69	101.05	100.89	100.95	100.72	101.79
Formula calculated based on 8 oxygen						
Si^{4+}	2.98 ± 0.03	2.93 ± 0.03	2.97 ± 0.03	3.01 ± 0.03	2.99 ± 0.03	3.00 ± 0.03
Ti^{4+}	0.00 ± 0.00	0.00 ± 0.00	0.00 ± 0.00	0.00 ± 0.00	0.00 ± 0.00	0.00 ± 0.00
Al^{3+}	1.01 ± 0.01	1.09 ± 0.01	1.03 ± 0.01	0.99 ± 0.01	1.01 ± 0.01	1.00 ± 0.01
Fe^{3+}	0.00 ± 0.00	0.01 ± 0.00	0.00 ± 0.00	0.00 ± 0.00	0.00 ± 0.00	0.00 ± 0.00
Mg^{2+}	0.00 ± 0.00	0.00 ± 0.00	0.00 ± 0.00	0.00 ± 0.00	0.00 ± 0.00	0.00 ± 0.00
Ba^{2+}	0.02 ± 0.00	0.01 ± 0.00	0.03 ± 0.00	0.00 ± 0.00	0.00 ± 0.00	0.00 ± 0.00
Ca^{2+}	0.00 ± 0.00	0.00 ± 0.00	0.00 ± 0.00	0.00 ± 0.00	0.00 ± 0.00	0.00 ± 0.00
Na^{+}	0.01 ± 0.00	0.01 ± 0.00	0.01 ± 0.00	0.01 ± 0.00	0.99 ± 0.01	0.98 ± 0.01
K^{+}	0.98 ± 0.01	0.94 ± 0.01	0.96 ± 0.01	0.98 ± 0.01	0.01 ± 0.00	0.01 ± 0.00
$\sum/\Delta\sum$	4.99 ± 0.02	4.99 ± 0.02	5.00 ± 0.02	4.99 ± 0.02	5.00 ± 0.02	4.99 ± 0.02
Mol% end-member						
An:	0.00 ± 0.00	0.00 ± 0.00	0.00 ± 0.00	0.00 ± 0.00	0.28 ± 0.09	0.19 ± 0.09
Ab:	1.47 ± 0.18	1.40 ± 0.19	1.48 ± 0.19	1.08 ± 0.18	99.11 ± 1.72	99.10 ± 1.71
Or:	98.53 ± 1.47	98.60 ± 1.48	98.52 ± 1.48	98.92 ± 1.45	0.61 ± 0.06	0.72 ± 0.06

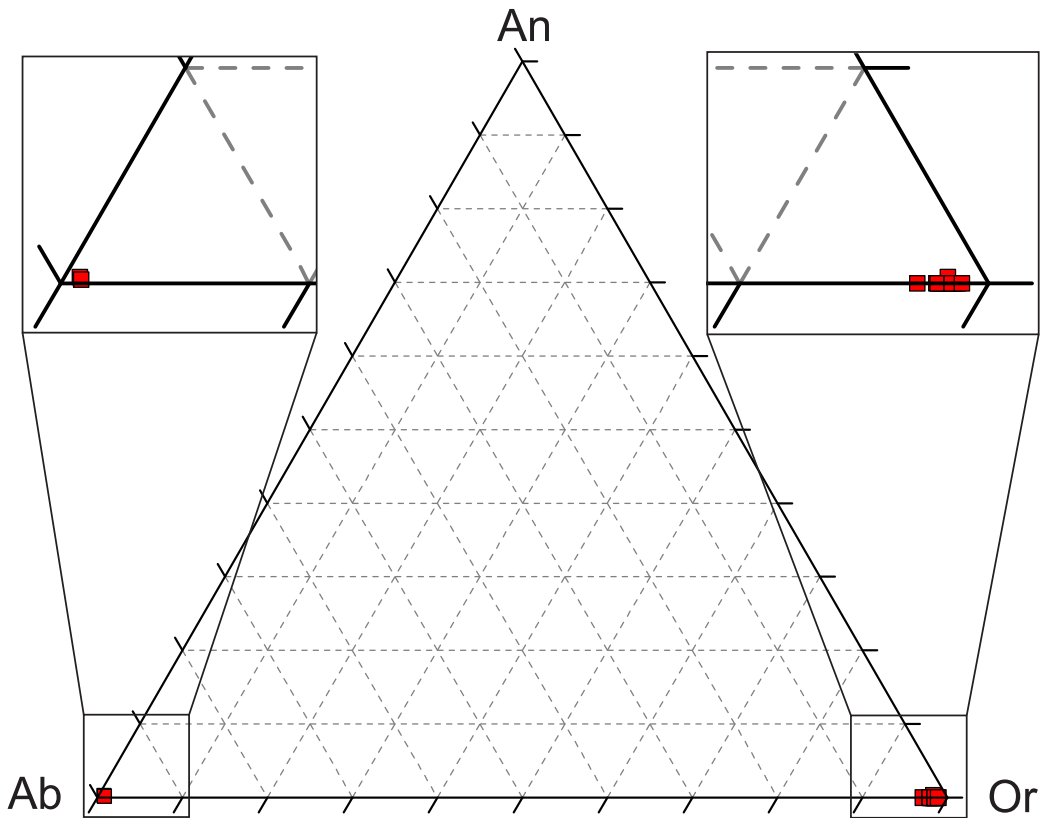
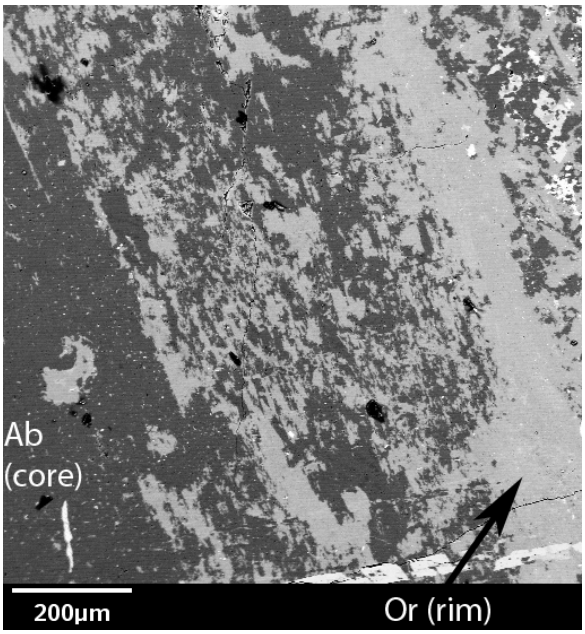
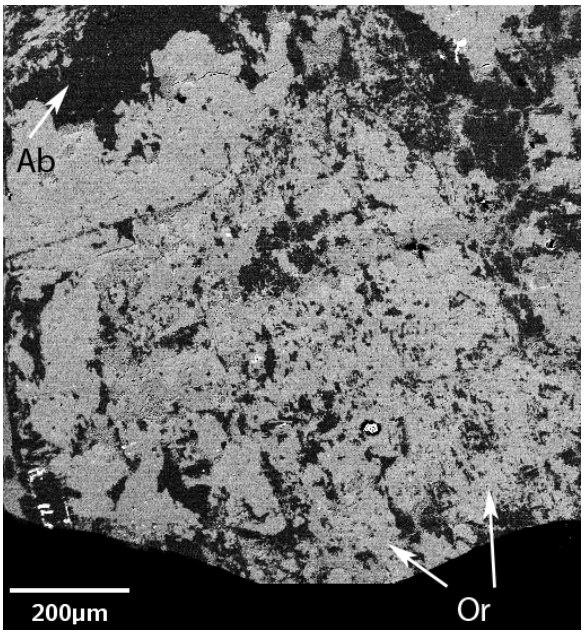


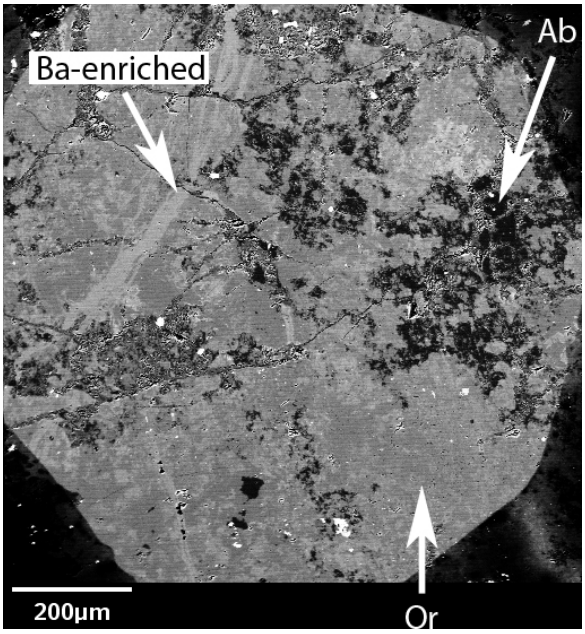
Figure 6.39 – End-member composition of phenocrysts from the porphyritic Central Duparquet unit. The 3 end-members are: Or = orthoclase, An = anorthite and Ab = Albite. Analyses are all presented in mole %.



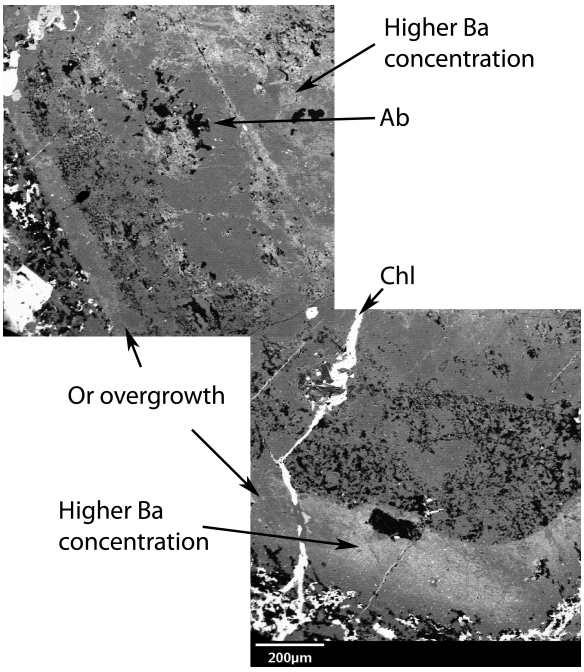
(a) Albite core surrounded by orthoclase. Sample: ZP-04-047, location: 631871E 5374373N.



(b) Perthitic phenocryst. Sample: JG-94-5148, location: 633517E 5373987N



(c) Inside a perthite phenocryst with Ba^{2+}-enriched veins and patches (light grey). Sample: ZP-04-056, location: 634050E 5373903N.



(d) Perthitic orthoclase phenocryst with and orthoclase overgrowth. Both core and overgrowth have Ba^{2+}-enriched zones (light grey). Sample: ZP-04-047, location: 631871E 5374373N.

Figure 6.40 – EBS images of feldspar phenocrysts from the porphyritic Central Duparquet unit. Dark grey colours correspond to albite (Ab), lighter grey to orthoclase (Or) and the lightest to hydrothermal chlorite (Chl).

6.5.2 Matrix

Following the phenocrysts, the feldspar crystals in the matrix are anhedral and demonstrate an undulose extinction, distorting optical measurements. The undulose extinction is the result of fine intermixing between albite and orthoclase (determined via EBS images, see below). The crystals measure between $\leq$ 0.002 - 0.4 mm and appear as slightly radiating fibrous crystals with diffuse to sutured margins. This crystalline configuration is once again reminiscent of devitrification of a glassy matrix. Turbidity and hydrothermal sericitization of orthoclase is generally not as pronounced in the matrix as it is in phenocrysts.

The composition of the matrix feldspars was also chemically verified via EMPA. Both orthoclase and albite chemical formulas were calculated on an 8 oxygen basis. The compositions and chemical formulas are presented in Table 6.11.

Table 6.11 – Microprobe analyses and chemical formulas of matrix feldspars from the porphyritic Central Duparquet unit.

	Orthoclase			Albite	
	48-5-2	**47-3-2**	**56-8-1**	**48-5-1**	**47-3-1**
SiO_2	64.44 ± 0.45	64.68 ± 0.45	64.87 ± 0.45	69.38 ± 0.49	70.00 ± 0.49
TiO_2	0.00 ± 0.00	0.14 ± 0.03	0.00 ± 0.00	0.00 ± 0.00	0.00 ± 0.00
Al_2O_3	18.58 ± 0.13	18.24 ± 0.13	18.62 ± 0.13	19.76 ± 0.14	19.82 ± 0.14
FeO	0.12 ± 0.03	1.15 ± 0.06	0.05 ± 0.03	0.09 ± 0.03	0.01 ± 0.00
MgO	0.00 ± 0.00	0.00 ± 0.00	0.00 ± 0.00	0.00 ± 0.00	0.00 ± 0.00
BaO	0.36 ± 0.06	0.30 ± 0.05	0.19 ± 0.05	0.00 ± 0.00	0.11 ± 0.04
CaO	0.00 ± 0.00	0.00 ± 0.00	0.00 ± 0.00	0.04 ± 0.02	0.03 ± 0.02
Na_2O	0.24 ± 0.02	0.22 ± 0.02	0.13 ± 0.02	11.95 ± 0.12	11.97 ± 0.12
K_2O	16.05 ± 0.13	16.67 ± 0.13	16.85 ± 0.13	0.10 ± 0.01	0.10 ± 0.01
Total	99.8	101.48	100.72	101.32	102.06
Formula calculated based on 8 oxygen					
Si^{4+}	2.99 ± 0.03	2.97 ± 0.03	2.99 ± 0.03	2.99 ± 0.03	3.00 ± 0.03
Ti^{4+}	0.00 ± 0.00	0.00 ± 0.00	0.00 ± 0.00	0.00 ± 0.00	0.00 ± 0.00
Al^{3+}	1.02 ± 0.01	0.99 ± 0.01	1.01 ± 0.01	1.00 ± 0.01	1.00 ± 0.01
Fe^{3+}	0.00 ± 0.00	0.04 ± 0.00	0.00 ± 0.00	0.00 ± 0.00	0.00 ± 0.00
Mg^{2+}	0.00 ± 0.00	0.00 ± 0.00	0.00 ± 0.00	0.00 ± 0.00	0.00 ± 0.00
Ba^{2+}	0.01 ± 0.00	0.01 ± 0.00	0.00 ± 0.00	0.00 ± 0.00	0.00 ± 0.00
Ca^{2+}	0.00 ± 0.00	0.00 ± 0.00	0.00 ± 0.00	0.00 ± 0.00	0.00 ± 0.00
Na^{+}	0.02 ± 0.00	0.02 ± 0.00	0.01 ± 0.00	1.01 ± 0.01	0.99 ± 0.01
K^{+}	0.95 ± 0.01	0.98 ± 0.01	0.99 ± 0.01	0.01 ± 0.00	0.01 ± 0.00
$\sum/\Delta\sum$	4.99 ± 0.02	5.01 ± 0.02	5.01 ± 0.02	5.01 ± 0.02	5.00 ± 0.02
Mol% end-member					
An:	0.00 ± 0.00	0.00 ± 0.00	0.00 ± 0.00	0.18 ± 0.09	0.14 ± 0.09
Ab:	2.22 ± 0.19	1.97 ± 0.18	1.16 ± 0.18	99.27 ± 1.71	99.32 ± 1.70
Or:	97.78 ± 1.48	98.03 ± 1.43	98.84 ± 1.44	0.55 ± 0.06	0.55 ± 0.06

The composition of orthoclase varies from 0.00 mol% An, 1.16 - 2.22 mol% Ab and 97.78 - 98.84 mol% Ab. Furthermore, the composition of albite ranges from 0.14 - 0.18 mol% An, 0.55 mol% Or and 99.27 - 99.32 mol% Ab. A visualization of the feldspathic mol% end-member composition is presented in Figure 6.41.

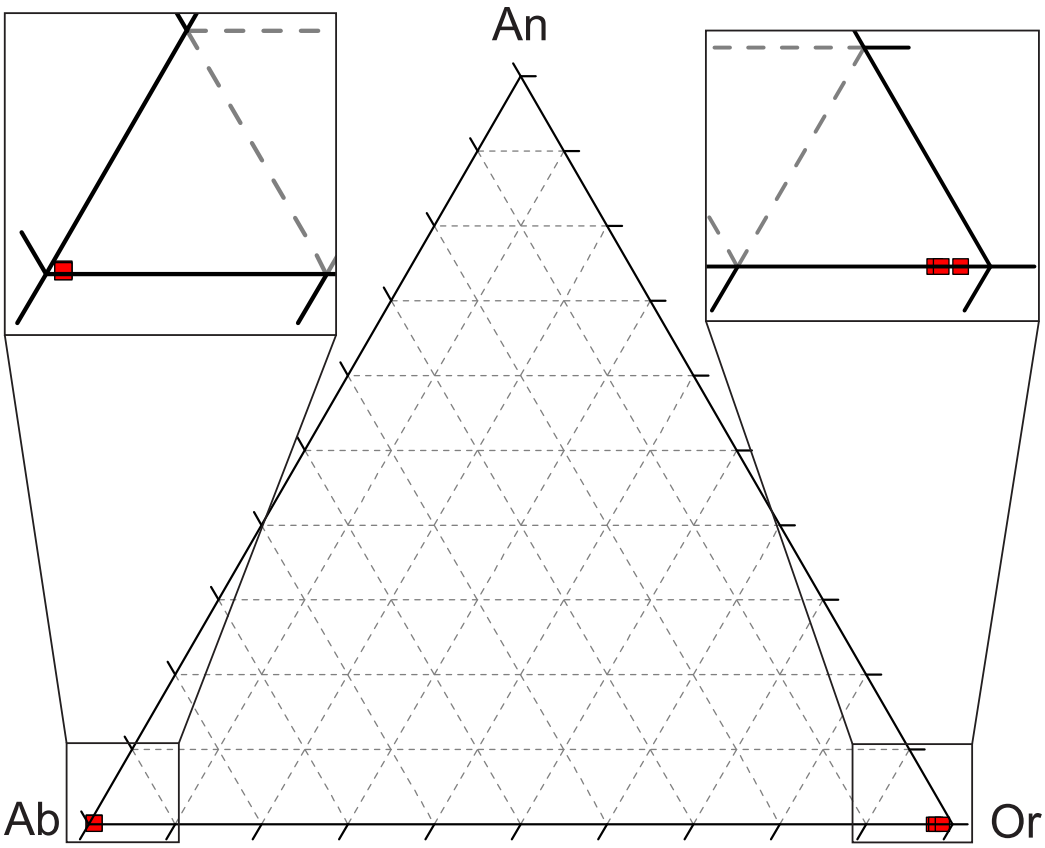


Figure 6.41 – End-member composition of albite from the porphyritic Central Duparquet unit. The 3 end-members are: Or = orthoclase, An = anorthite and Ab = Albite. Analyses are presented in mole %.

Both feldspars in the matrix have a constant chemical composition across all the samples, suggesting that feldspar unmixing was thorough for both albite and orthoclase. EBS observations reveal that the matrix is composed of a mixture of orthoclase, albite and subsequent hydrothermal sericite (see Figure 6.42). This finely intermixed arrangement does explain the undulose extinction of the matrix seen under the microscope. Orthoclase crystals appear as thin blades, as small prismatic crystals or as masses. Albite crystals are anhedral and measure < 200 μm long. Proportions of orthoclase and albite were nearly always equal which is in agreement with proportions determined via feldspar staining. In a single occasion, albite has been replaced by quartz, perhaps the result of local silica enrichment or subsequent infiltration and replacement as quartz veins are nearby.

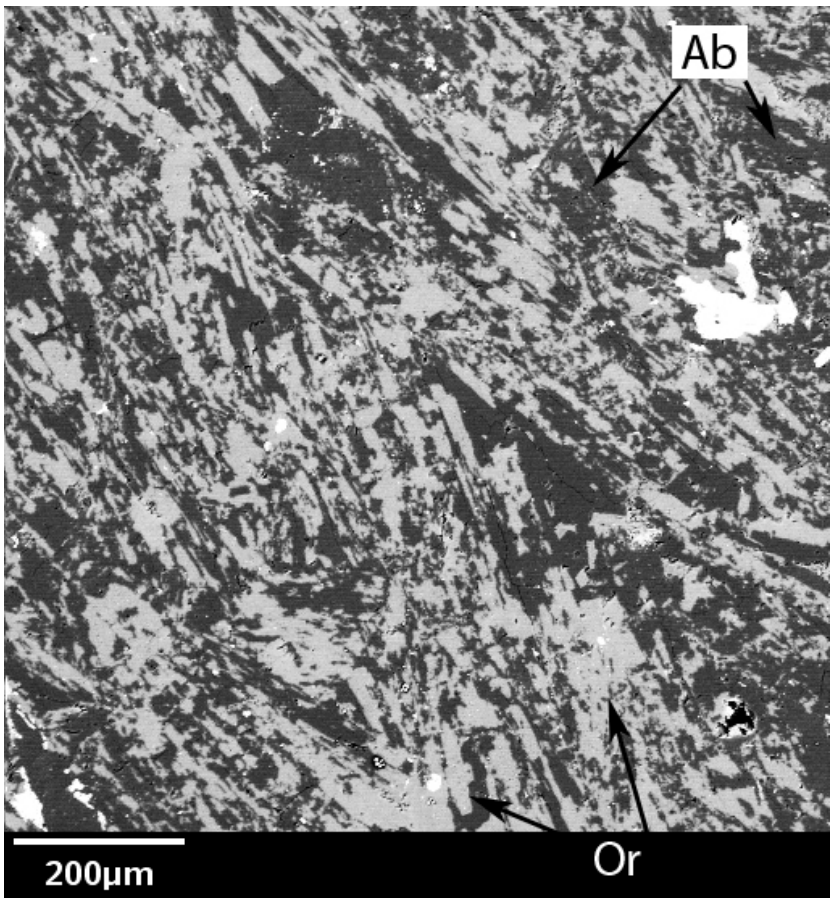


Figure 6.42 – EBS image of orthoclase and albite composing the matrix of the porphyritic Central Duparquet unit. Dark grey colours correspond to albite (Ab) and pale grey colours correspond to orthoclase (Or). Sample: JG-94-5148, location: 633517E 5373987N.

6.5.3 Apatite

Euhedral to subhedral crystals measure between 0.2 - 0.8 mm long and are randomly distributed though the rock. Crystal margins have occasionally been rounded. Larger crystals are commonly fractured, but do not show any displacement.

6.5.4 Magnetite

Igneous magnetite occurs as finely disseminated crystals which are anhedral and measure 0.2 mm across.

6.6 Megaporphyritic syenite (A*bet4*)

The megaporphyritic syenite unit is the second least abundant unit, representing 1.27% (inferred surface area) of the Beattie syenite. This unit is found as irregular to semi-circular shaped lens in the eastern portions of the CDB, occurring predominantly near or in contact zones with country rocks in the CDB. A hypothetical possibility is that the emplacement of the unit was facilitated by competence contrasts between the syenite and the country rocks. The largest megaporphyritic lens (180 m across) is found immediately north of the Central Duparquet 1 mine shaft. This occurrence continues at some depth (228.6 m) as this unit was observed underground by Banfield (1940). Progressing eastwards, there are several other pockets of the unit of smaller dimensions ($<$ 120 m across).

The unit is characterized by large white, beige to green feldspar phenocrysts in a pink to red aphanitic matrix (see Figure 6.43). The yellow to apple green colouration of the phenocrysts is a result of subsequent sericitization. These large anhedral to euhedral phenocrysts measure up to 6 cm across and compose between 5 - 20%$_m$ of the rock. Individual phenocrysts are tabular, compositionally zoned and share a poor E-W alignment. Locally, phenocrysts demonstrate a glomeroporphyritic texture. The unit is also transected by hydrothermal alterations and metamorphic minerals in veins. However, the abundance of hydrothermal and metamorphic minerals is much less than the porphyritic Beattie syenite unit.

Igneous minerals in the megaporphyritic unit consist dominantly of orthoclase, albite with trace amounts of apatite. Both orthoclase and albite constitute the phenocrysts and the matrix. Once again, albite can be differentiated from orthoclase by lesser amounts of turbidity and sericitization. The modal ranges of the unit, as determined from microscopic observations, along with a typical modal composition of the unit is presented in Table 6.12. Both hydrothermal and greenschist facies minerals have not been included in the table below.

Table 6.12 – Range of modal composition of the megaporphyritic unit. Ranges are based on 6 thin sections.

	Maximum ranges	Typical composition
Mineral	**Modal %**	**Modal %**
Orthoclase	10 - 80	41
Albite	12 - 74	38
Apatite	1	1



(a) Euhedral and tabular phenocrysts and glomerocrysts. Location: 633097E 5373909N.



(b) Glomeroporphyric texture. Location: 633173E 5373960N.

Figure 6.43 – The megaporphyritic syenite unit. Large, 1 - 6 cm, beige to white phenocrysts are hosted in an aphanitic pink to red matrix.

6.6.1 Phenocrysts

Both orthoclase and albite compose part of the phenocrysts and glomerocrysts. Euhedral phenocrysts are generally exclusively composed from a single to a few orthoclase crystals (see Figure 6.44). These phenocrysts measure between 4 mm - 5 cm and occasionally demonstrate perthitic exsolution. No compositional zoning change from the core to rim was observed. Albite on the other hand is found in smaller (0.2 - 1.6 mm) and a few sub- to euhedral phenocrysts. The composition of a few albite phenocrysts, using the Michel-Lévy method, was determined to be between An_4 - An_5. Glomerocrysts are composed of an amalgamation of both orthoclase and rarely albite phenocrysts (see Figure 6.45). Individual crystalline boundaries are occasionally difficult of ascertain because of subsequent hydrothermal sericitization.

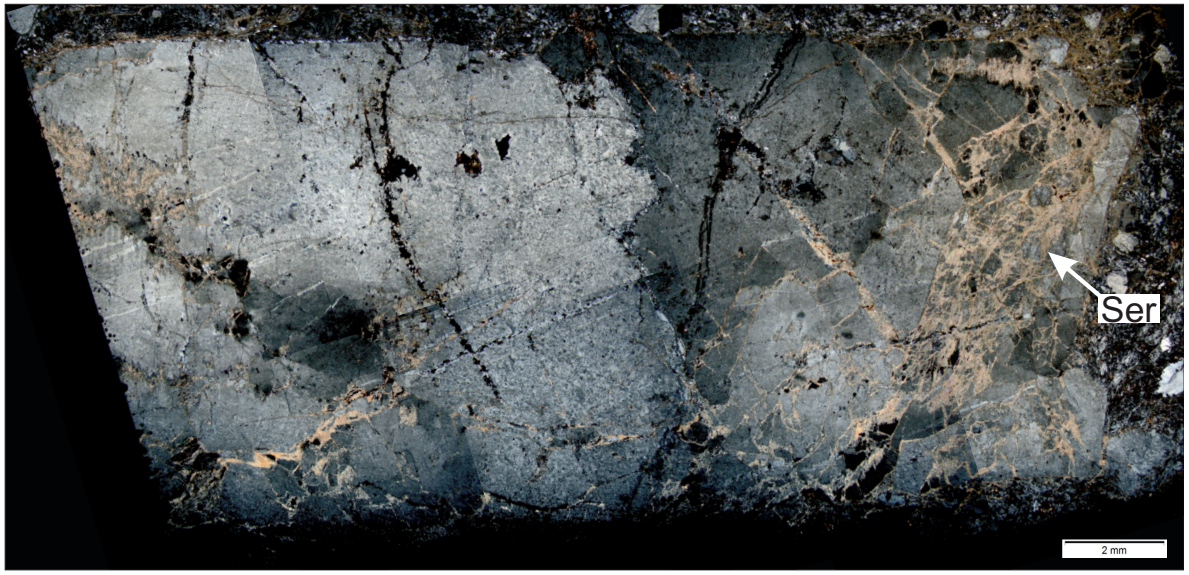


Figure 6.44 – Phenocryst of the megaporphyritic unit. The phenocryst is exclusively composed of orthoclase occasionally demonstrating fine perthitic exsolution. This phenocryst is composed of 2 individual crystals differentiated by their extinction angle. Veins of hydrothermal sericite (ser) cut the edge of the crystal. Photomicrograph taken under crossed polars. Location: 633897E 5373842N.

6.6.2 Matrix

The feldspathic matrix is composed of anhedral, slightly radiating, fibrous crystals measuring between 0.01 - 0.2 mm long with diffuse to sutured margins. The feldspathic matrix also demonstrates an undulose extinction which is the result of fine intermixing between albite and orthoclase. This crystalline arrangement is once again reminiscent of devitrification. Turbidity

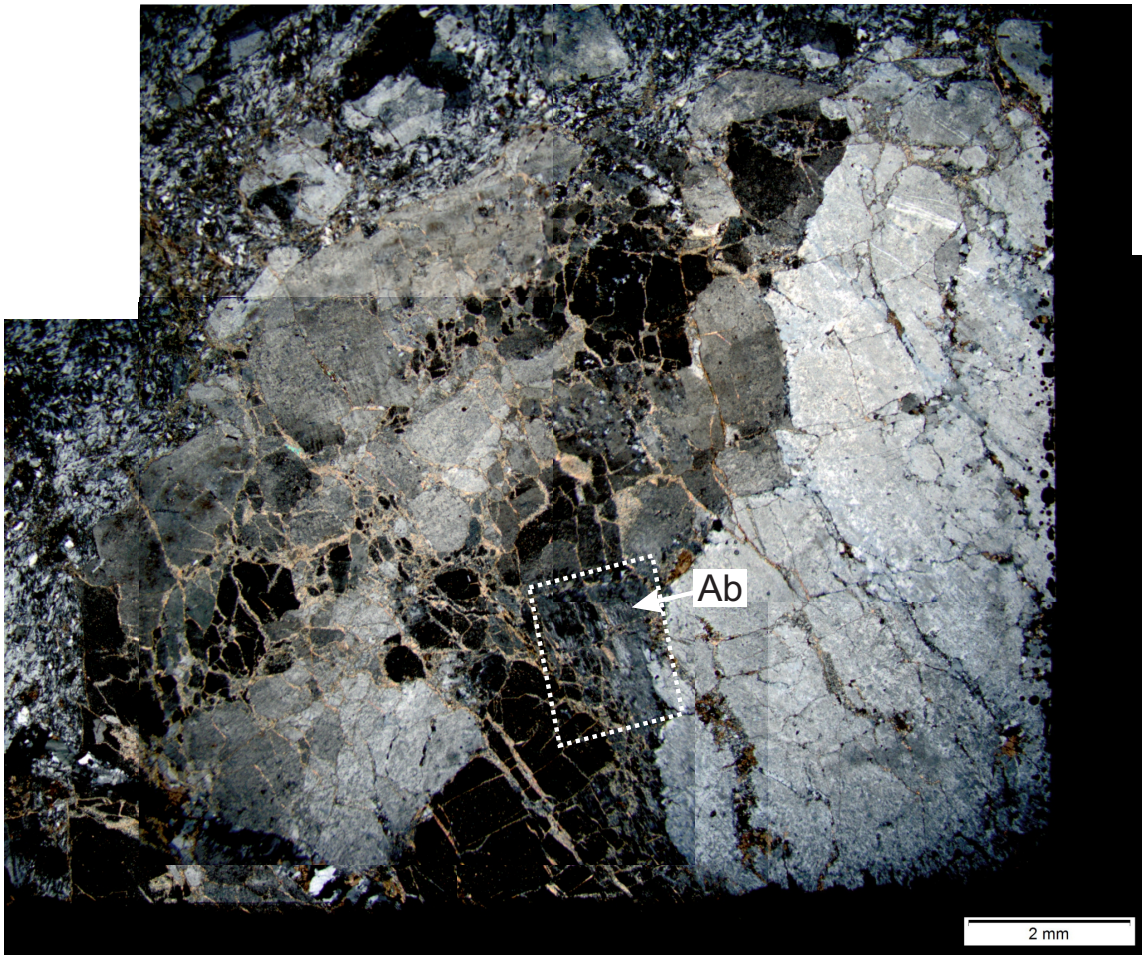


Figure 6.45 – Quarter of a glomerocryst of the megaporphyritic unit. The glomerocryst is composed of both albite (Ab) and orthoclase crystals differentiated by their extinction angle. A small albite crystal with albite polysynthetic twinning has been identified in the white dotted box. Veins of sericite transect the glomerocryst with a preference for boundaries between amalgamated crystals. Photomicrograph taken under crossed polars. Location: 634050E 5373903N.

and sericitization of orthoclase in the matrix is generally not as pronounced compared to phenocrysts.

6.6.3 Apatite

Sub- to euhedral, 0.2 - 0.4 mm long apatite crystals are randomly distributed though the rock. In one instance a small aggregation of a few apatite crystals was observed. Crystals margins may also be slightly rounded.

6.7 Lath syenite (A*bet5*)

The lath syenite is the youngest of the units, representing 1.42% (inferred surface area) of the Beattie syenite. The unit occurs as 1 - 65 m wide dykes transecting all other syenitic units and country rocks. All of the dykes strike between 070 - 096° or 260 - 276° with a near vertical dip. A large number of these dykes appear in the Deguisier andesite to dacite unit, in the proximity of the abandoned Donchester mine. These dykes have been successfully traced, with the help of drill core observations, for distances up to 450 m. Drill core observations confirm that the dykes continue near vertically at depth with a varying width, flexing as they continue deeper, at a large wavelength and small amplitude.

At first glance, the dykes are composed of large white (fresh) to brown or green (altered) euhedral feldspar laths contained in a grey or white (fresh) to red or green (altered) aphanitic matrix (see Figure 6.46). The feldspar laths are compositionally zoned, measure between 5 mm - 3 cm long and compose 20 - 50%$_m$ of the rock. Together the laths are evenly distributed throughout the dykes and form a strong trachytic texture. This trachytic texture shares the same strike as the dykes, indicating a magmatic flow along the dykes as they progressed. The abundance of laths varies locally, lacking a definite spatial pattern. This variation could be a characteristic of the individual dyke rather than the location. Furthermore, the dykes are transected by an assortment of hydrothermal and greenschist facies minerals and brittle deformation. The abundance of deformation and alteration varies locally, but is overall more abundant in the west. An example of a sericitized and brittlely deformed lath dyke is presented in Figure 6.47.

Dykes rarely contain xenoliths. Xenoliths consist of bright green chert (2 cm long) and basalt (10 cm long). All xenoliths have rounded edges and are aligned with the trachytic texture.

The lath syenite dykes are composed dominantly of orthoclase and albite with trace amounts of apatite and magnetite. Both laths and the aphanitic matrix are composed of albite and orthoclase. Albite can be differentiated from orthoclase by diffuse to clear albite polysynthetic twinning, and a general lack of turbidity and sericitization. The modal ranges of the unit are given in Table 6.13. In light of the high variability and number of minerals, a typical modal composition of the unit is also given in Table 6.13.

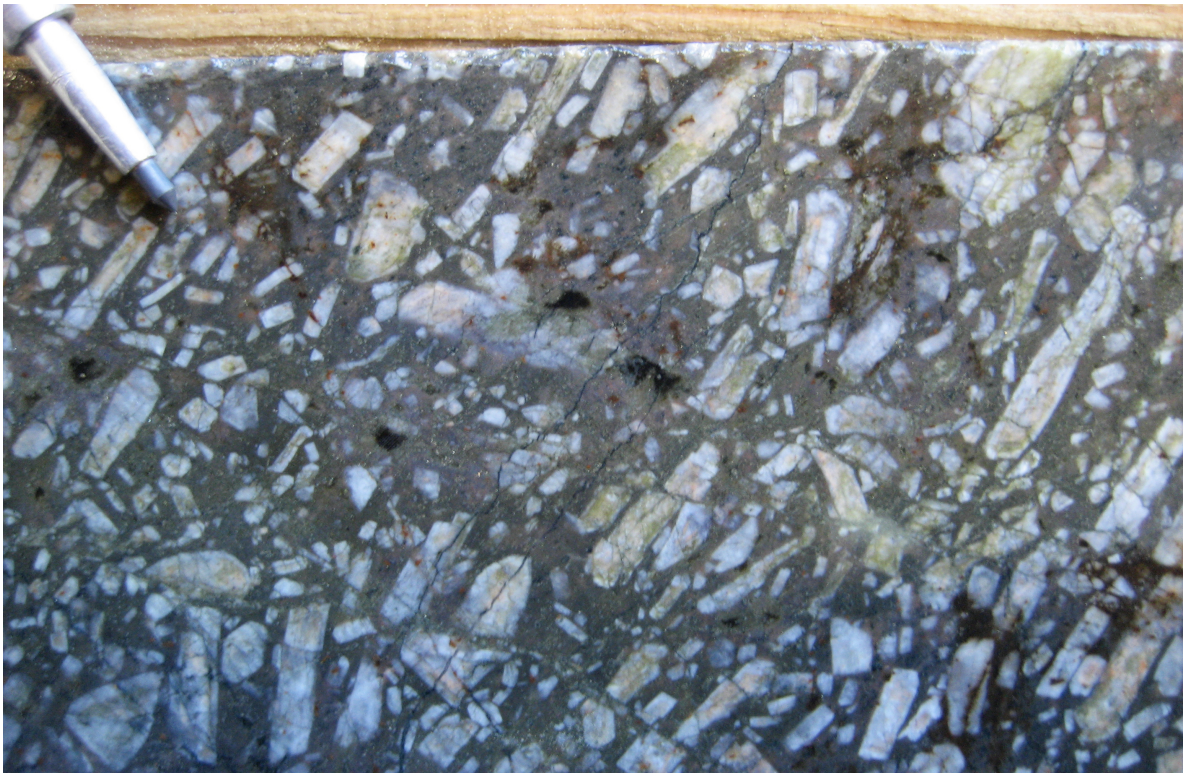


Figure 6.46 – The lath syenite unit in a drill core specimen. White feldspar laths are contained in a grey aphanitic matrix. A strong trachytic texture is evident. Subsequently some of the laths were sericitized, now demonstrating a pale green to yellow colour. Drill core: B09-06, depth: 63.00 - 68.30 m.

Table 6.13 – Range of modal composition of the lath syenite unit. Ranges are based on 6 thin sections.

	Maximum ranges	Typical composition
Mineral	**Modal %**	**Modal %**
Orthoclase	10 - 47	38
Albite	23 - 57	44
Apatite	1	1
Magnetite	0 - 3	0



Figure 6.47 – Hydrothermal sericitization followed by brittle deformation of the lath unit. Pale green sericitization of the matrix is seen as anastomosing veins in the matrix which were followed by the brittle deformation which fractured the laths. Location: 630800E 5374343N.

6.7.1 Laths

Laths are almost exclusively composed of orthoclase, at times demonstrating perthitic exsolution and Carlsbad twinning. In one instance, orthoclase laths also contain small inclusions of euhedral apatite. Albite on the other hand is rare, found only at the core of a few laths and surrounded by orthoclase. The composition of a few albite laths was determined by the Michel-Lévy method to be between An_5 - An_{12}, essentially corresponding to albite. Altogether, laths are euhedral and measure between 2 - 30 mm long. All laths align together to form a strong trachytic foliation (see Figure 6.48).

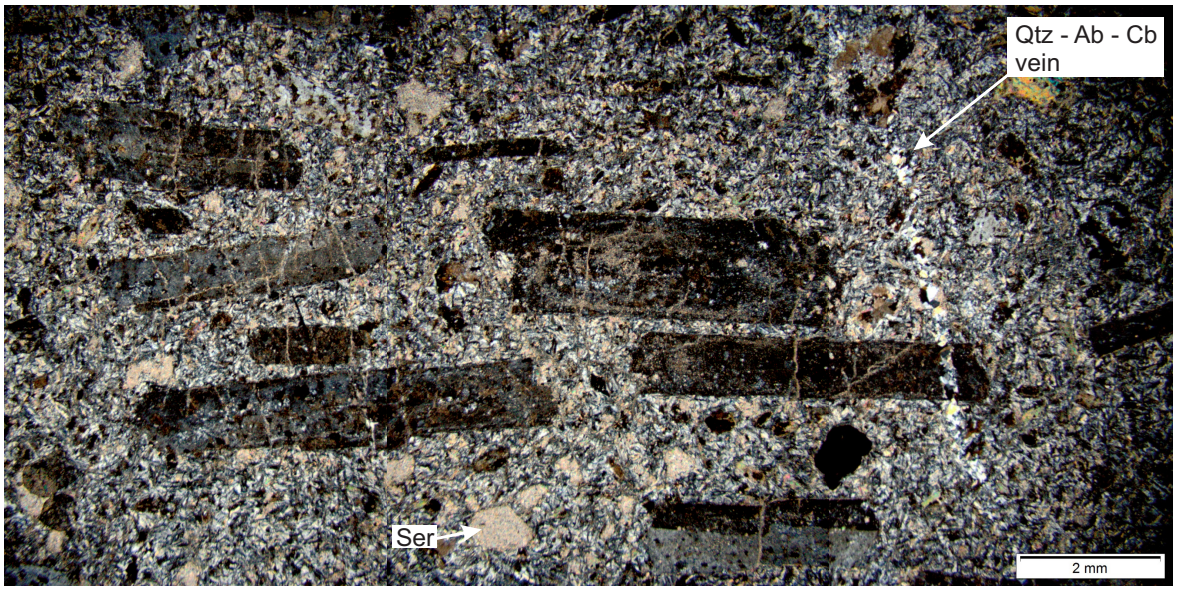


Figure 6.48 – Feldspar laths demonstrating a trachytic alignment. The laths are dominantly composed of orthoclase and are contained in a feldspathic matrix. Hydrothermal sericite (Ser) is also found in the matrix. A vein of quartz (Qtz), albite (Ab) and carbonate minerals (Cb) transect both the matrix and the laths. Photomicrograph taken under crossed polars. Location: 633125E 5373867N.

The chemical composition of the feldspar laths was investigated using EMPA and EBS imaging. Two samples were submitted for EMPA. Both are located in the BDB. The westernmost sample, JG-3002-L is located 473 m southeast from the abandoned Beattie mine shaft, whereas sample ZP-04-21 is located further east, 900 m east from the abandoned Donchester mine shaft. The exact locations of both samples submitted to EMPA can be viewed in Figure 6.16. Analyses were randomly selected within the crystals with additional analyses performed on unusual/distinct features. Both orthoclase and albite formulas were calculated on an 8 oxygen basis. The composition and calculated formulas are presented in Table 6.14.

Table 6.14 – Microprobe analyses and formulas of laths form the lath syenite unit.

	Orthoclase					Albite
	21-1-1*	**21-1-2**	**21-3-1**	**JG-3002-03**	**JG-3002-05**	**JG-3002-06**
SiO_2	66.03 ± 0.46	66.28 ± 0.46	65.48 ± 0.46	65.12 ± 0.46	64.19 ± 0.45	67.92 ± 0.48
TiO_2	0.00 ± 0.00	0.00 ± 0.00	0.00 ± 0.00	0.00 ± 0.00	0.00 ± 0.00	0.00 ± 0.00
Al_2O_3	18.50 ± 0.13	18.53 ± 0.13	18.35 ± 0.13	18.52 ± 0.13	18.99 ± 0.13	20.44 ± 0.14
FeO	0.00 ± 0.00	0.00 ± 0.00	0.03 ± 0.00	0.00 ± 0.00	0.37 ± 0.02	0.43 ± 0.02
MgO	0.02 ± 0.01	0.00 ± 0.00	0.01 ± 0.01	0.00 ± 0.00	0.00 ± 0.00	0.00 ± 0.00
BaO	0.00 ± 0.00	0.15 ± 0.05	0.33 ± 0.06	0.46 ± 0.03	0.44 ± 0.03	0.03 ± 0.02
CaO	0.00 ± 0.00	0.00 ± 0.00	0.00 ± 0.00	0.00 ± 0.00	0.00 ± 0.00	0.14 ± 0.01
Na_2O	0.21 ± 0.02	0.18 ± 0.02	0.15 ± 0.02	0.20 ± 0.03	0.23 ± 0.03	11.73 ± 0.14
K_2O	16.25 ± 0.13	16.40 ± 0.13	16.20 ± 0.13	16.26 ± 0.11	15.85 ± 0.11	0.81 ± 0.02
Total	101.04	101.53	100.56	100.55	100.07	101.51
Chemical formula based on 8 oxygens						
Si^{4+}	3.01 ± 0.03	3.01 ± 0.03	3.01 ± 0.03	3.00 ± 0.03	2.97 ± 0.03	2.95 ± 0.03
Ti^{4+}	0.00 ± 0.00	0.00 ± 0.00	0.00 ± 0.00	0.00 ± 0.00	0.00 ± 0.00	0.00 ± 0.00
Al^{3+}	0.99 ± 0.01	0.99 ± 0.01	0.99 ± 0.01	1.01 ± 0.01	1.04 ± 0.01	1.04 ± 0.01
Fe^{3+}	0.00 ± 0.00	0.00 ± 0.00	0.00 ± 0.00	0.00 ± 0.00	0.01 ± 0.00	0.01 ± 0.00
Mg^{2+}	0.00 ± 0.00	0.00 ± 0.00	0.00 ± 0.00	0.00 ± 0.00	0.00 ± 0.00	0.00 ± 0.00
Ba^{2+}	0.00 ± 0.00	0.00 ± 0.00	0.01 ± 0.00	0.01 ± 0.00	0.01 ± 0.00	0.00 ± 0.00
Ca^{2+}	0.00 ± 0.00	0.00 ± 0.00	0.00 ± 0.00	0.00 ± 0.00	0.00 ± 0.00	0.01 ± 0.00
Na^{+}	0.02 ± 0.00	0.02 ± 0.00	0.01 ± 0.00	0.02 ± 0.00	0.02 ± 0.00	0.99 ± 0.01
K^{+}	0.95 ± 0.01	0.95 ± 0.01	0.95 ± 0.01	0.96 ± 0.01	0.94 ± 0.01	0.04 ± 0.00
$\sum/\Delta\sum$	4.97 ± 0.02	4.97 ± 0.02	4.97 ± 0.02	4.99 ± 0.02	4.98 ± 0.02	5.04 ± 0.02
Mol% end-member						
An:	0.00 ± 0.00	0.00 ± 0.00	0.00 ± 0.00	0.00 ± 0.00	0.00 ± 0.00	0.63 ± 0.05
Ab:	1.93 ± 0.19	1.64 ± 0.18	1.39 ± 0.19	1.84 ± 0.28	2.16 ± 0.28	95.05 ± 1.82
Or:	98.07 ± 1.46	98.36 ± 1.46	98.61 ± 1.48	98.16 ± 1.40	97.84 ± 1.41	4.32 ± 0.12

* Analysis performed without detection of BaO

End-member orthoclase compositions range from 1.39 - 2.16 mol% Ab, 97.84 - 98.61 mol% Or. Surprisingly none of the orthoclase analyses contain any detectable An. A visualization of the feldspathic mol% end-member composition is presented in Figure 6.49.

Feldspar laths are either perthite with compositional zoning or perthitic orthoclase. In perthite, albite preferentially occupies the core, whereas orthoclase is concentrated outwards (see Figure 6.50). Ab-domains occur as irregularly-shaped exsolutions which measure < 50 μm across. The transition from albite to orthoclase domains is progressive, with orthoclase domains becoming larger and abundant outwards. The progressive increase in orthoclase is also marked by compositional zoning. Specifically, orthoclase is enriched in Ba^{2+} from midway with a linear loss towards the outer margins. Analyses reveal that there is less Ba^{2+} in this unit comparatively to all the others. Nonetheless, this compositional zoning can be observed via EBS images where Ba^{2+}-enriched zones are lighter (see Figure 6.50). Perthitic orthoclase laths on the other hand lack any compositional zoning, thus appearing uniform, and contain no significant Ba^{2+}-enrichments.

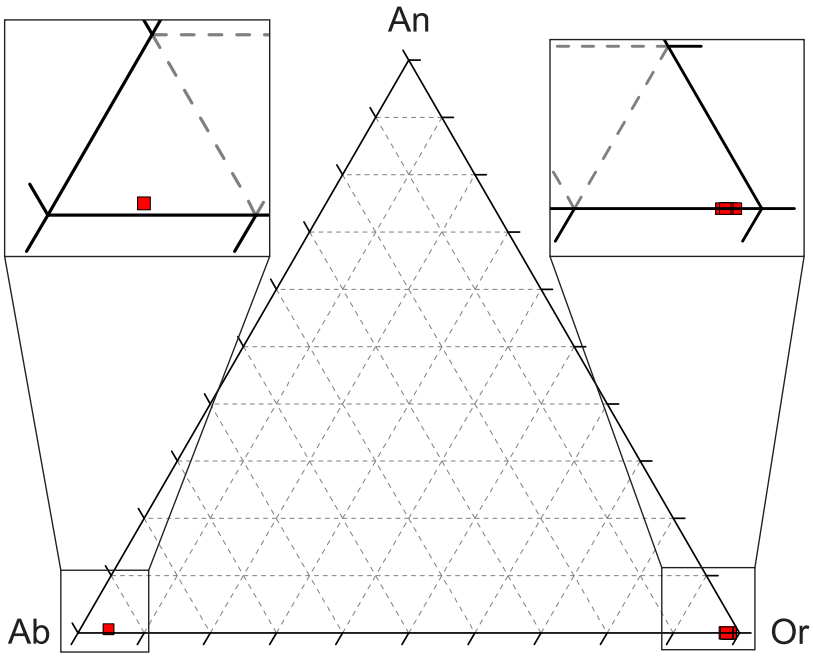


Figure 6.49 – End-member composition of laths from the lath syenite unit. The 3 end-members are: Or = orthoclase, An = anorthite and Ab = albite. Analyses are presented in mole %.

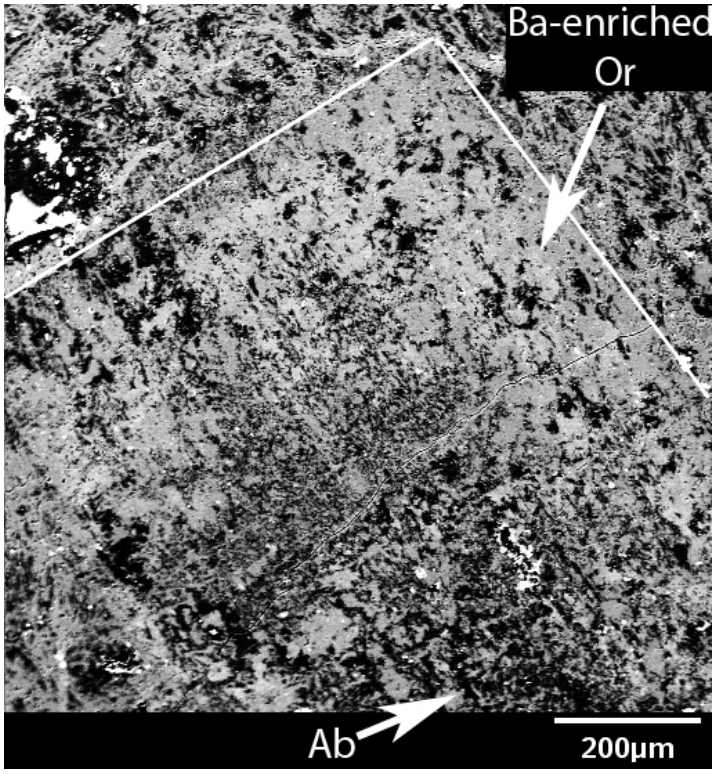


Figure 6.50 – Perthite feldspar lath. Albite (Ab) preferentially occupies the core, whereas orthoclase (Or) dominates the outer margins. The edge of the lath has been demarked by the white lines. Compositional zoning (Ba^{2+}) is also denoted by a progressive darkening of orthoclase towards the outer margin. Sample: JG-3002-L, location: 630958E 5374397N.

6.7.2 Matrix

The matrix is composed of intermixed albite and orthoclase, yielding an undulose extinction. Crystals are anhedral measure 0.2 mm across and appear as slightly radiating fibrous crystals with a diffuse margin. These features hint once again as a result of devitrification of a glassy matrix.

The chemical composition of the feldspathic matrix was also investigated via EMPA. Feldspar formulas were calculated on an 8 oxygen basis. The compositions and chemical formulas are presented in Table 6.15.

Table 6.15 – Microprobe analyses and chemical formulas of matrix feldspars form the lath syenite unit.

	Orthoclase	Albite	
	JG-3002-02	**21-9-1**	**JG-3002-01r**
SiO_2	65.30 ± 0.46	71.19 ± 0.50	68.62 ± 0.48
TiO_2	0.00 ± 0.00	0.00 ± 0.00	0.00 ± 0.00
Al_2O_3	18.56 ± 0.13	18.04 ± 0.13	19.67 ± 0.14
FeO	1.09 ± 0.03	0.48 ± 0.04	0.34 ± 0.01
MgO	0.00 ± 0.00	0.00 ± 0.00	0.00 ± 0.00
BaO	0.00 ± 0.00	0.04 ± 0.00	0.00 ± 0.00
CaO	0.00 ± 0.00	0.03 ± 0.02	0.02 ± 0.00
Na_2O	1.49 ± 0.02	10.93 ± 0.12	12.29 ± 0.15
K_2O	14.11 ± 0.10	0.16 ± 0.01	1.05 ± 0.02
Total	100.58	100.86	101.99
Chemical formula based on 8 oxygens			
Si^{4+}	2.99 ± 0.03	3.07 ± 0.03	2.97 ± 0.03
Ti^{4+}	0.00 ± 0.00	0.00 ± 0.00	0.00 ± 0.00
Al^{3+}	1.00 ± 0.01	0.92 ± 0.01	1.00 ± 0.01
Fe^{3+}	0.03 ± 0.00	0.01 ± 0.00	0.01 ± 0.00
Mg^{2+}	0.00 ± 0.00	0.00 ± 0.00	0.00 ± 0.00
Ba^{2+}	0.00 ± 0.00	0.00 ± 0.00	0.00 ± 0.00
Ca^{2+}	0.00 ± 0.00	0.00 ± 0.00	0.00 ± 0.00
Na^{+}	0.13 ± 0.00	0.91 ± 0.01	1.03 ± 0.01
K^{+}	0.82 ± 0.01	0.01 ± 0.00	0.06 ± 0.00
$\sum/\Delta\sum$	4.97 ± 0.02	4.93 ± 0.02	5.07 ± 0.02
Mol% end-member			
An:	0.00 ± 0.00	0.15 ± 0.10	0.09 ± 0.00
Ab:	13.83 ± 0.50	98.80 ± 1.83	94.60 ± 1.81
Or:	86.17 ± 1.32	0.95 ± 0.06	5.32 ± 0.13

End-member albite compositions range from 0.09 - 0.15 mol% An, 0.95 - 5.32 mol% Or and 94.60 - 98.80 mol% Ab. A visualization of the feldspathic mol% end-member composition is presented in Figure 6.51.

The composition of orthoclase in the matrix is more Ab-enriched compared to phenocrysts. EBS observations reveal that matrix feldspars are finely intermixed together, with the occasional addition of hydrothermal carbonate minerals and sericite. Orthoclase crystals are anhedral, appearing as masses or thin wavy blades. Albite crystals on the other hand are an-

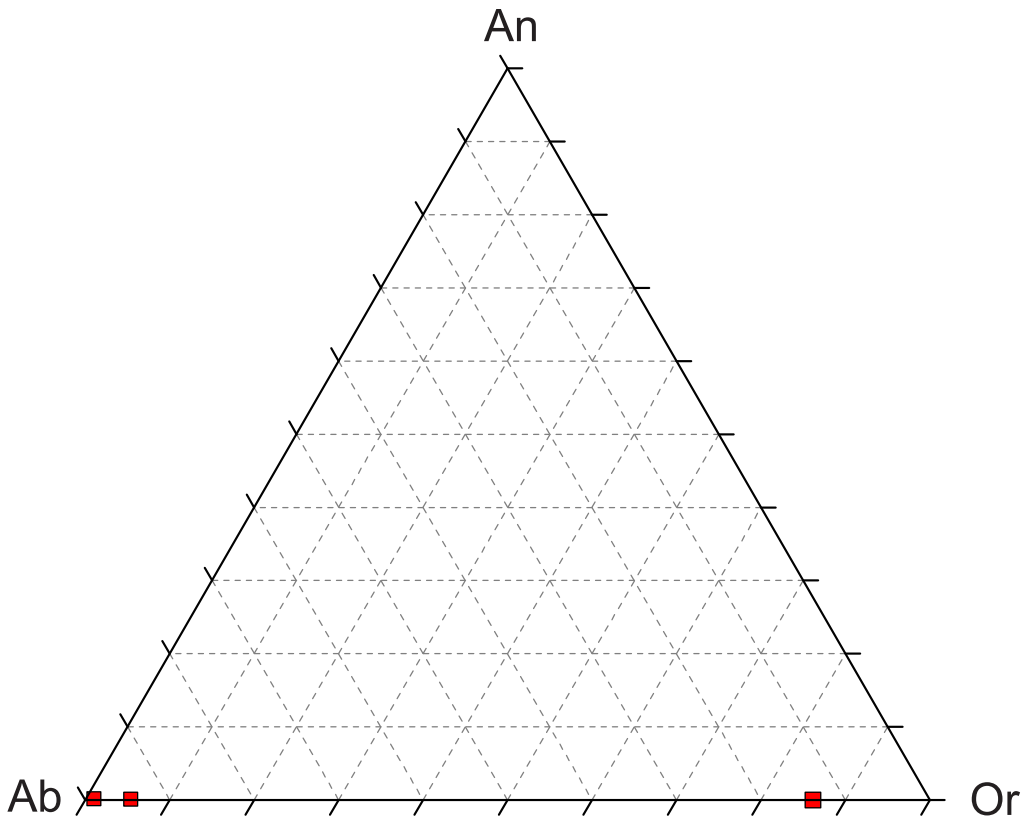


Figure 6.51 – End member composition of matrix feldspar from the lath syenite unit. The 3 end-members are: Or = orthoclase, An = anorthite and Ab = albite. Analyses are presented in mole %.

hedral and measure between 10 - 50 μm across. Generally, orthoclase is the dominant matrix feldspar, attaining a maximum ratio of 3:1 over albite. At its minimum, orthoclase and albite proportions are nearly equal (see Figure 6.52). Albite contamination is likely the cause for the Ab-enrichment of the analysis, stemming from incomplete feldspar decomposition.

Uniquely to the lath unit, albite has the highest Or-concentration, up to 5.32 mol% Or. This enrichment is sustained both in phenocrysts and in the matrix. Additionally, albite demonstrates a distinctive Fe^{3+}-enrichment, which can either be the result of impurities or material which has exsolved upon cooling. Together, both Or and Fe^{3+}-enrichments are deemed the product of incomplete feldspar exsolution. The incomplete exsolution could be the result of reduced autometamorphism, where the thin dykes ($<$ 25 m thick on average) would not have retained a significant amount of latent heat and would have therefore cooled quickly compared to the other syenitic units. This hypothesis is further weighed by the relatively smaller size and overall massive habit of the matrix crystals compared to the other units. Furthermore,

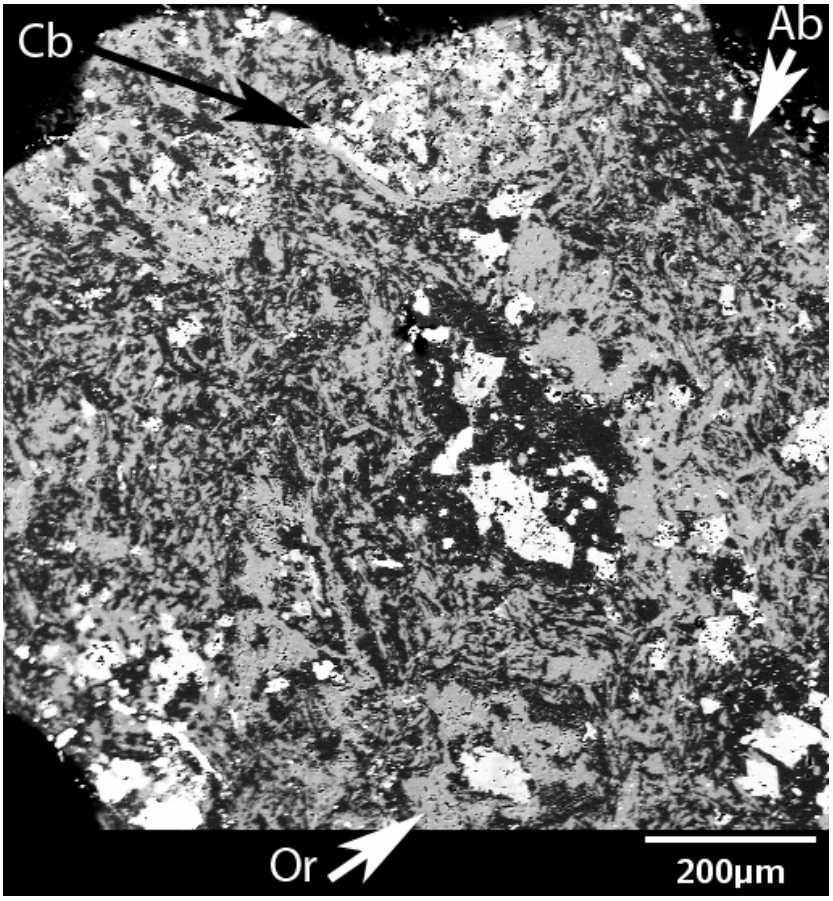


Figure 6.52 – Feldspathic matrix of the lath syenite unit. Both light grey orthoclase (Or) and dark albite (Ab) are anhedral, occurring as masses to thin wavy blades. The brightest grey belongs to hydrothermal carbonate minerals. Sample: JG-3002-L, location: 630958E 5374397N.

petrographic observations overall attribute less hydrothermal activity to the unit, limiting further exsolution.

6.7.3 Apatite

Sub- to euhedral crystals of apatite measure between 0.1 - 0.2 mm. They are randomly distributed though the rock and occasionally have rounded edges. In one instance, small 0.2 mm equant to hexagonal euhedral crystals of apatite preferentially occurred in feldspar laths.

6.7.4 Magnetite

Igneous crystals are found disseminated though the rock as extremely fine crystals measuring 0.02 mm on average.

Chapter 7

Geochemistry

A major goal of this project is to determine the geochemical nature of the Beattie syenite and country rocks. To achieve this goal, two main objectives will be addressed. They are: 1) to characterize whole rock, using major and trace elements and, 2) to use this geochemical information in the determination of the tectonic setting.

In order to fulfill the objectives a total of 490 geochemical samples are used in this Chapter. Of these, 243 are from the Beattie syenite while the remainder are from the country rocks. Geochemical analyses were performed by both commercial and governmental laboratories. Their source is chronologically presented in Table 7.1. Furthermore, all geochemical analyses have been amalgamated and can be consulted in Appendix D.

The two oldest sets of geochemical analyses, performed by Banfield (1940) and Davidson and Banfield (1944), were not used in this chapter because of their antiquity. They did however contribute to the characterization of the Beattie mine Au-mineralization, explored later in Chapter 8. Analyses done by SOQUEM Inc. are problematic. First, is the attribution of a large margin of error in the positioning of the samples (± 20 m). Second, the samples analyzed did not include a description of the rock. Third, some samples were not found on the map provided with the exploration report. Consequently, a total of 16 samples of this data set were excluded from this chapter, but are included and highlighted in the database. Geochemical analyses by Gold Fields Resources Canada Ltd. were all from the northeast portion of the Beattie area. Samples provided by this company were included because of the geological simplicity of the sector, lower levels of hydrothermal alteration and because samples positions were well documented. However, rock descriptions were not included with

the exploration report. As a result, 2 chemically anomalous samples were discarded from the analysis and discussion, but were included and highlighted in the database. Geochemical analyses by Cogema Canada Ltd. were performed on a drill core (number: PC-01) starting at a depth of 84.9 m. These analyses were kept as they present the only evidence of komatiites and komatitic basalts in the Beattie area, even though they do not represent the surficial geochemical characteristics sought in this chapter. All geochemical data from the MRN (1990 - 2009) were positioned and described with great accuracy. As a result, these analyses were kept. Only one sample was provided from Noranda Exploration Ltd. This sample did not include a location and was consequently rejected, but is also included in the database. Numerous samples were graciously provided by the Osisko Mining Corporation. These were well located and provided with rock descriptions. Accordingly, they are included in this chapter. One analysis was provided by L. Bigot, a student at the UQAM and was also utilized. Finally, geochemical samples taken by the author are also included in this chapter.

Table 7.1 – Source of geochemical analyses used in this thesis.

Year	Company, institution or source	Number of samples
1940	Banfield	13
1944	Davidson and Banfield	3
1980	SOQUEM Inc.	126
1981	Gold Fields Resources Canada Ltd.	31
1988	Cogema Canada Ltd.	23
1990	MER	6
1991	Noranda Exploration Ltd.	1
1994	MER	6
2002	MRN	3
2003	MRN	21
2004	MRN	24
2009	MRN	6
2010	Osisko Mining Corporation	232
2010	UQAM	1
2010	University of Ottawa	8

This chapter includes numerous tables of geochemical data in order to separate analyses that are deemed to be the best available representatives from the remainder of the database. Furthermore, to avoid confusion, the data are always arranged starting west and progressing eastwards. Any conflicting samples were further organized from north to south.

With the establishment of the geochemical database, this chapter pursues the main objec-

tives by following the chronological order of units established earlier in the thesis (see Chapter 5). First discussed are the individual units of the Deguisier Formation, Lanaudière Formation, followed by the gabbro. Following is a small section regrouping all the units of the Deguisier Formation. This section serves to establish links between individual units and to propose a tectonic setting. Ordinarily one should expect a discussion of the geochemical characteristics of the Hébécout Formation, however there were no geochemical samples from it in the Beattie area. Furthermore, the Hébécourt Formation was recently the subject of a M.Sc. thesis by Rogers (2010). Henceforth, the results will not be repeated, and the reader should consult his thesis if desired. The last section will focus on the Beattie syenite.

Unfortunately, there was a lack of geochemical data for the Porcupine Group sediments and most of the samples for the Duparquet Formation consisted of polymict clasts. Thus, the geochemical characteristics of the sedimentary units of the Beattie area has been omitted.

7.1 Deguisier tholeiitic basalt

The Deguisier basalt occupies the northern portion of the Beattie area and is the oldest lithology of the area. Initial geochemical classifications were done by Gélinas et al. (1976). An update by Goutier and Lacroix (1992) followed, based upon approximately 20 samples. Recent renewal in geological reconnaissance led to 51 new basaltic samples being analyzed.

Methodology

Representative samples were obtained from Osisko Mining Corporation, MRN and Gold Fields Resources Canada. Extra screening was necessary since all basaltic samples were provided via private companies and therefore not examined by the author. To recognize and classify severely altered samples the following rules were used: 1) samples must have a LOI $< 10\%$[1], 2) samples must not be clasts within the Duparquet polymict conglomerate, and 3) oxide values must not deviate extensively from the norm set by all other basaltic samples. Special emphasis was placed on high Fe_2O_{3T} values denoting pyrite, K_2O which is extremely mobile, and CaO combined with LOI which indicates carbonate minerals.

As a result, a total of 10 samples were considered significantly altered. These samples were excluded from all sections below. The remaining least altered samples are presented in Table 7.2. For reasons discussed at the beginning of this chapter, samples by SOQUEM Inc. are only used for the alteration geochemistry characterization found in Chapter 8. A complete list of all basaltic samples is found in Appendix D.

Prior to being used for plots and calculations, major and trace elements were corrected for LOI and are therefore on a 'dry' basis unless otherwise specified.

[1]A detailed discussion justifying the choice of LOI cut-off can be found in Appendix D

Table 7.2 – Major and trace element analyses of least-altered specimens of the Deguisier tholeiitic basalt. Major oxides are presented in wt% and trace elements are all given in ppm with the exception of Au which is given in ppb. Analyses presented have not been corrected for LOI.

Sample	**D958053**	**D958056**	**D958103**	**D958057**	**2003031998**	**D958236**	**3258**	**3261**
Institution	Osisko	Osisko	Osisko	Osisko	MRN	Osisko	GFRC	GFRC
Year	2010	2010	2010	2010	2003	2010	1981	1981
SiO_2	48.20	47.20	48.60	45.80	48.93	50.40	48.70	49.50
TiO_2	1.73	1.33	1.49	1.62	1.74	1.43	1.42	1.30
Al_2O_3	13.35	14.15	13.20	14.50	13.72	15.60	14.20	14.00
Fe_2O_3t	14.85	14.15	15.40	17.45	15.29	12.40	14.50	13.80
MnO	0.34	0.20	0.22	0.22	0.19	0.25	0.33	0.25
MgO	3.74	7.40	6.16	6.74	5.79	4.82	5.04	5.83
CaO	8.28	9.21	9.35	8.20	7.80	8.98	8.61	9.57
Na_2O	2.64	2.40	1.67	1.08	3.41	1.52	1.50	2.29
K_2O	0.05	0.21	0.15	0.11	0.04	0.07	0.05	0.17
P_2O_5	0.15	0.10	0.08	0.11	0.13	0.07	0.11	0.11
[a]CO_2	—	—	—	—	—	—	1.50	1.60
[a]S	0.14	0.04	0.09	0.02	0.04	0.16	—	—
[b]LOI	6.73	3.57	3.67	4.16	2.60	4.10	4.62	3.93
Total	100.06	99.92	99.99	99.99	99.64	99.64	99.08	100.75
Ag	< 0.2	< 0.2	< 0.2	< 0.2	—	< 0.2	0.80	0.80
As	7	39	54	10	—	2	—	—
Au	< 5	< 5	12	< 5	—	< 5	14.00	10.00
Ba	*2866*	—	—	—	34	—	130.00	180.00
Bi	< 2	< 2	< 2	< 2	—	< 2	—	—
Cd	< 0.5	< 0.5	< 0.5	< 0.5	—	< 0.5	—	—
Ce	—	—	—	—	—	—	—	—
Co	41	35	29	45	—	48	—	—
Cr	*136.84*	*205.26*	—	—	*109.47*	*205.26*	460.00	600.00
Cs	—	—	—	—	—	—	—	—
Cu	105	117	96	126	—	118	—	—
Dy	—	—	—	—	—	—	—	—
Er	—	—	—	—	—	—	—	—
Eu	—	—	—	—	—	—	—	—
Ga	20	< 10	< 10	< 10	—	< 10	—	—
Gd	—	—	—	—	—	—	—	—
Hf	—	—	—	—	—	—	—	—
Hg	< 1	< 1	< 1	< 1	—	< 1	—	—
Ho	—	—	—	—	—	—	—	—
La	—	—	—	—	—	—	—	—
Lu	—	—	—	—	—	—	—	—
Mo	< 1	< 1	< 1	< 1	—	< 1	—	—
Nb	—	—	—	—	—	—	—	—
Nd	—	—	—	—	—	—	—	—
Ni	47	56	29	40	77	77	—	—
Pb	< 2	< 2	< 2	< 2	—	< 2	—	—
Pr	—	—	—	—	—	—	—	—
Rb	—	—	—	—	—	—	< 10	—
Sb	< 2	—	< 2	—	—	< 2	—	—
Sc	—	—	—	—	46	—	—	—
Se	—	—	—	—	—	—	—	—
Sm	—	—	—	—	—	—	—	—
Sn	—	—	—	—	—	—	—	—
Sr	*1352.95*	—	—	—	231	*169.11*	110.00	70.00
Ta	—	—	—	—	—	—	—	—
Tb	—	—	—	—	—	—	—	—
Th	—	—	—	—	—	—	—	—
Tl	< 10	< 10	< 10	< 10	—	< 10	—	—
Tm	—	—	—	—	—	—	—	—
U	—	—	—	—	—	—	—	—
V	—	—	—	—	—	—	—	—
W	—	—	—	—	—	—	—	—
Y	—	—	—	—	35	—	—	—
Yb	—	—	—	—	—	—	—	—
Zn	112	66	80	110	—	87	—	—
Zr	—	—	—	—	87	—	70.00	50.00

RCFC *Resources Gold Field Canada*

[a] *Not included in totals* [b] *Loss on ignition at 1000° C*

< Red *Values below detection limit* *Blue* *Values calculated from oxides*

Table 7.2 Continued

Sample	**3951**	**3691**	**3694**	**3287**	**D958309**	**D958310**	**3679**	**3292**
Institution	GFRC	GFRC	GFRC	GFRC	Osisko	Osisko	GFRC	GFRC
Year	1981	1981	1981	1981	2010	2010	1981	1981
SiO_2	46.60	47.00	47.60	48.20	47.90	47.50	46.10	49.70
TiO_2	1.72	1.65	1.64	1.66	1.87	1.91	1.81	2.17
Al_2O_3	12.40	13.20	12.80	13.90	12.70	12.60	13.90	14.10
Fe_2O_3t	13.30	12.40	16.80	11.90	17.10	16.75	14.50	12.60
MnO	0.17	0.22	0.25	0.25	0.22	0.21	0.28	0.20
MgO	6.57	5.47	6.35	4.11	5.43	5.72	6.06	4.71
CaO	7.35	8.50	7.84	7.34	8.59	9.76	8.73	6.84
Na_2O	2.10	2.91	1.61	2.62	2.53	1.22	1.89	3.14
K_2O	0.11	0.21	0.08	1.60	0.08	0.03	0.04	0.62
[a]CO_2	5.00	5.70	0.50	5.70	—	—	3.10	3.00
[a]S	—	—	—	—	0.11	0.02	—	—
[b]LOI	9.85	9.23	3.77	8.62	3.37	3.37	6.85	6.62
Total	100.31	100.92	98.89	100.34	99.97	99.24	100.3	100.87
Ag	1.50	1.40	1.30	1.50	< 0.2	< 0.2	1.40	1.10
As	—	—	—	—	< 5	< 5	—	—
Au	21.00	21.00	14.00	302.00	5	5	21.00	14.00
Ba	210.00	210.00	180.00	250.00	—	—	190.00	410.00
Bi	—	—	—	—	< 2	< 2	—	—
Cd	—	—	—	—	< 0.5	< 0.5	—	—
Ce	—	—	—	—	—	—	—	—
Co	—	—	—	—	33	33	—	—
Cr	420.00	400.00	420.00	360.00	—	—	—	310.00
Cs	—	—	—	—	—	—	—	—
Cu	91.00	83.00	96.00	—	83	92	97.00	110.00
Dy	—	—	—	—	—	—	—	—
Er	—	—	—	—	—	—	—	—
Eu	—	—	—	—	—	—	—	—
Ga	—	—	—	—	< 10	< 10	—	—
Gd	—	—	—	—	—	—	—	—
Hf	—	—	—	—	—	—	—	—
Hg	—	—	—	—	< 1	< 1	—	—
Ho	—	—	—	—	—	—	—	—
La	—	—	—	—	—	—	—	—
Lu	—	—	—	—	—	—	—	—
Mo	—	—	—	—	< 1	< 1	—	—
Nb	—	—	—	—	—	—	—	—
Nd	—	—	—	—	—	—	—	—
Ni	—	—	—	—	43	41	—	—
Pb	—	—	—	—	3	< 2	—	—
Pr	—	—	—	—	—	—	—	—
Rb	—	—	—	30.00	—	—	—	—
Sb	—	—	—	—	< 2	< 2	—	—
Sc	—	—	—	—	—	—	—	—
Se	—	—	—	—	—	—	—	—
Sm	—	—	—	—	—	—	—	—
Sn	—	—	—	—	—	—	—	—
Sr	90.00	120.00	130.00	90.00	*676.48*	*1099.27*	60.00	100.00
Ta	—	—	—	—	—	—	—	—
Tb	—	—	—	—	—	—	—	—
Th	—	—	—	—	—	—	—	—
Tl	—	—	—	—	< 10	< 10	—	—
Tm	—	—	—	—	—	—	—	—
U	—	—	—	—	—	—	—	—
V	—	—	—	—	—	—	—	—
W	—	—	—	—	—	—	—	—
Y	—	—	—	—	—	—	—	—
Yb	—	—	—	—	—	—	—	—
Zn	140.00	131.00	140.00	—	94	96	131.00	206.00
Zr	80.00	90.00	90.00	90.00	—	—	90.00	140.00

RCFC *Resources Gold Field Canada*

[a] *Not included in totals* [b] *Loss on ignition at 1000° C*

< Red *Values below detection limit* *Blue* *Values calculated from oxides*

Table 7.2 Continued

Sample	**3669**	**3668**	**3665**	**3666**	**3667**
Institution	GFRC	GFRC	GFRC	GFRC	GFRC
Year	1981	1981	1981	1981	1981
SiO_2	48.10	48.40	46.00	48.90	48.20
TiO_2	2.80	1.82	1.60	1.89	1.77
Al_2O_3	12.80	13.20	12.10	13.70	12.40
Fe_2O_3t	16.70	15.50	17.50	15.80	17.10
MnO	0.21	0.23	0.45	0.27	0.23
MgO	4.12	4.22	4.43	4.89	4.77
CaO	5.99	6.31	7.85	5.60	6.37
Na_2O	1.92	1.43	1.00	2.75	3.48
K_2O	1.09	1.40	0.20	0.08	0.86
P_2O_5	0.17	0.15	0.16	0.15	0.14
[a]CO_2	2.70	4.80	5.40	2.40	2.00
[a]S	—	—	—	—	—
[b]LOI	5.70	8.39	9.93	6.39	4.39
Total	99.6	101.05	101.22	100.42	99.71
Ag	1.40	1.30	2.00	1.40	1.20
As	—	—	—	—	—
Au	165.00	82.00	521.00	—	412.00
Ba	450.00	360.00	170.00	200.00	310.00
Bi	—	—	—	—	—
Cd	—	—	—	—	—
Ce	—	—	—	—	—
Co	—	—	—	—	—
Cr	250.00	380.00	270.00	380.00	520.00
Cs	—	—	—	—	—
Cu	149.00	158.00	88.00	92.00	123.00
Dy	—	—	—	—	—
Er	—	—	—	—	—
Eu	—	—	—	—	—
Ga	—	—	—	—	—
Gd	—	—	—	—	—
Hf	—	—	—	—	—
Hg	—	—	—	—	—
Ho	—	—	—	—	—
La	—	—	—	—	—
Lu	—	—	—	—	—
Mo	—	—	—	—	—
Nb	—	—	—	—	—
Nd	—	—	—	—	—
Ni	—	—	—	—	—
Pb	—	—	—	—	—
Pr	—	—	—	—	—
Rb	30.00	30.00	—	—	< 10.00
Sb	—	—	—	—	—
Sc	—	—	—	—	—
Se	—	—	—	—	—
Sm	—	—	—	—	—
Sn	—	—	—	—	—
Sr	40.00	110.00	50.00	40.00	210.00
Ta	—	—	—	—	—
Tb	—	—	—	—	—
Th	—	—	—	—	—
Tl	—	—	—	—	—
Tm	—	—	—	—	—
U	—	—	—	—	—
V	—	—	—	—	—
W	—	—	—	—	—
Y	—	—	—	—	—
Yb	—	—	—	—	—
Zn	163.00	84.00	87.00	109.00	103.00
Zr	140.00	90.00	100.00	110.00	90.00

RCFC *Resources Gold Field Canada*
[a] *Not included in totals*
[b] *Loss on ignition at 1000° C*
< Red *Values below detection limit*

7.1.1 Major and compatible trace elements

General classification

Deguisier basaltic rocks are classified using a ternary diagram known as the Jensen cation plot (Jensen, 1976). The plot uses oxides for the apices, represented by cation percent of Al, Fe_{tot} + Ti, and Mg which are generally "immobile" under "mild" alteration regimes. In addition to providing a general classification, the Jensen cation plot also divides the subalkaline rocks into calc-alkaline and tholeiitic series. Basaltic samples have been plotted on the Jensen diagram and are presented in Figure 7.1.

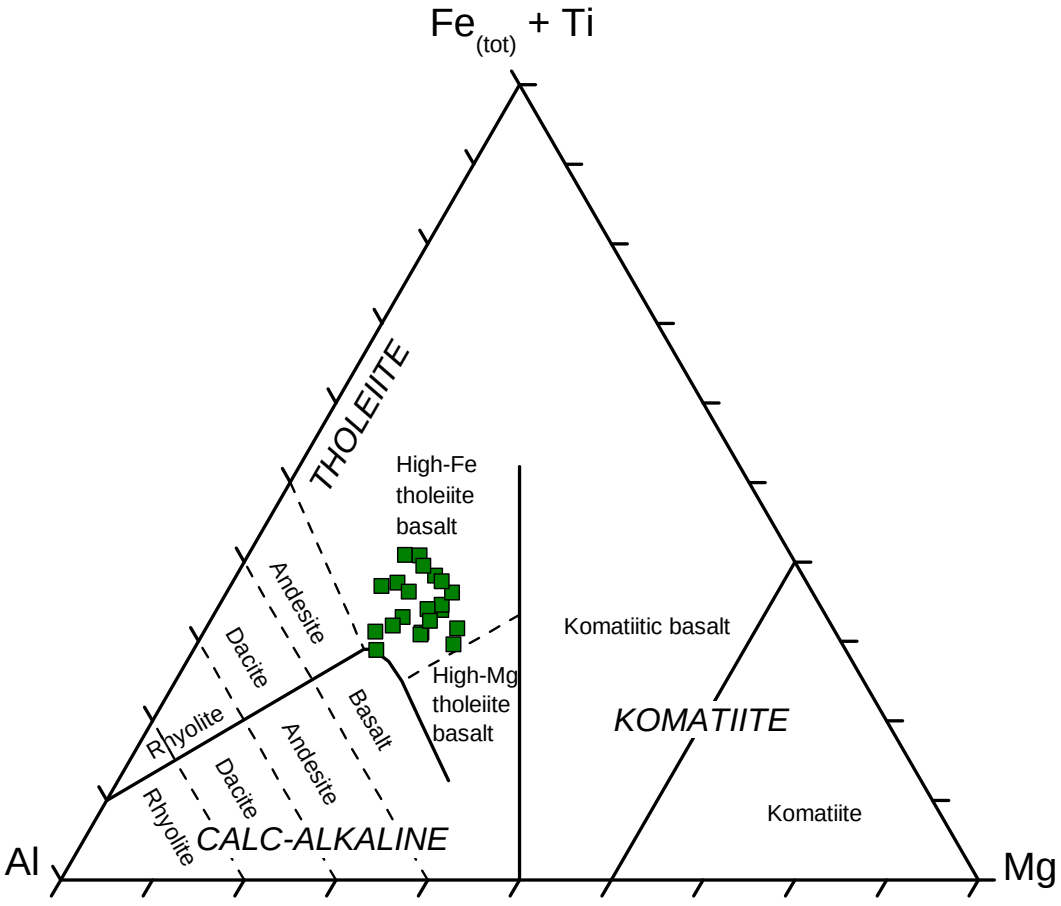


Figure 7.1 – Jensen cation plot of the Deguisier basalt.

Basaltic samples plot within the high-Fe tholeiitic field regardless their relative alteration intensity. Only one sample comes into contact with the boundary between the calc-alkaline and the tholeiitic series. As such, the Deguisier basalt is considered part of the tholeiitic series. This conclusion is also supported from findings by Gélinas et al. (1976) and Goutier

and Lacroix (1992).

The selected, least-altered, basaltic samples also still demonstrate most of their original (i.e., volcanic and unaltered) chemical characteristics. This can be observed in the widely used total alkalis ($Na_2O + K_2O$) against silica (TAS) diagram for volcanic rocks of Le Maitre et al. (1989) where basaltic samples generally fall within the basaltic compositional field with a few samples crossing into the basaltic-andesite field (see Figure 7.2). Included in this classification is the division of the alkaline and subalkaline fields following the subdivision trend defined by Irvine and Baragar (1971). Figure 7.2 demonstrates that the $Na_2O + K_2O$ values of the Deguisier basalt plot well into the subalkaline field. Altered samples were also plotted using this diagram (not shown), but most plotted in the alkaline field. This alkali enrichment is uniquely attributed to unusually high amounts of K_2O which reinforces the need for extra alteration discrimination. Nonetheless, the fact that the selected least-altered samples fall within the relevant field of Figure 7.2 is good evidence that locally the hydrothermal alteration/regional metamorphism was isochemical at the hand-sample scale.

CIPW norm

The CIPW norm is a useful method to obtain the normative mineralogy of a volcanic rock through its chemistry. It also makes it possible to classify a rock through the calculated pseudo-mineralogical assemblage. However, it should be noted that the modal mineralogy obtained via this calculation is qualitative especially with Archean rocks which have been subjected to various degrees of hydrothermal alteration and regional metamorphism to the sub- to greenschist facies. Uniquely, the CIPW norm allows a glimpse into the modal basaltic mineralogy which is crucial since most samples were not accompanied by thin sections.

Several norm parameter adjustments were made prior to calculating the normative mineralogical assemblage. First, the amount of ferrous iron was not measured. Therefore a ratio (Fe_2O_3/FeO) of 0.2 as recommended by Middlemost (1989) was assumed for all samples. Volatiles such as CO_2 and S were also excluded because both are a reflection of subsequent hydrothermal activity. Originally volatiles were included in the calculations, but high amounts of CO_2 resulted in high contents of normative calcite and anomalous corundum. The inclusion of sulphur on the other hand resulted in the presence of pyrite in the norm. The recalculation of the samples without the volatiles in effect reduces the hydrothermal alteration signature.

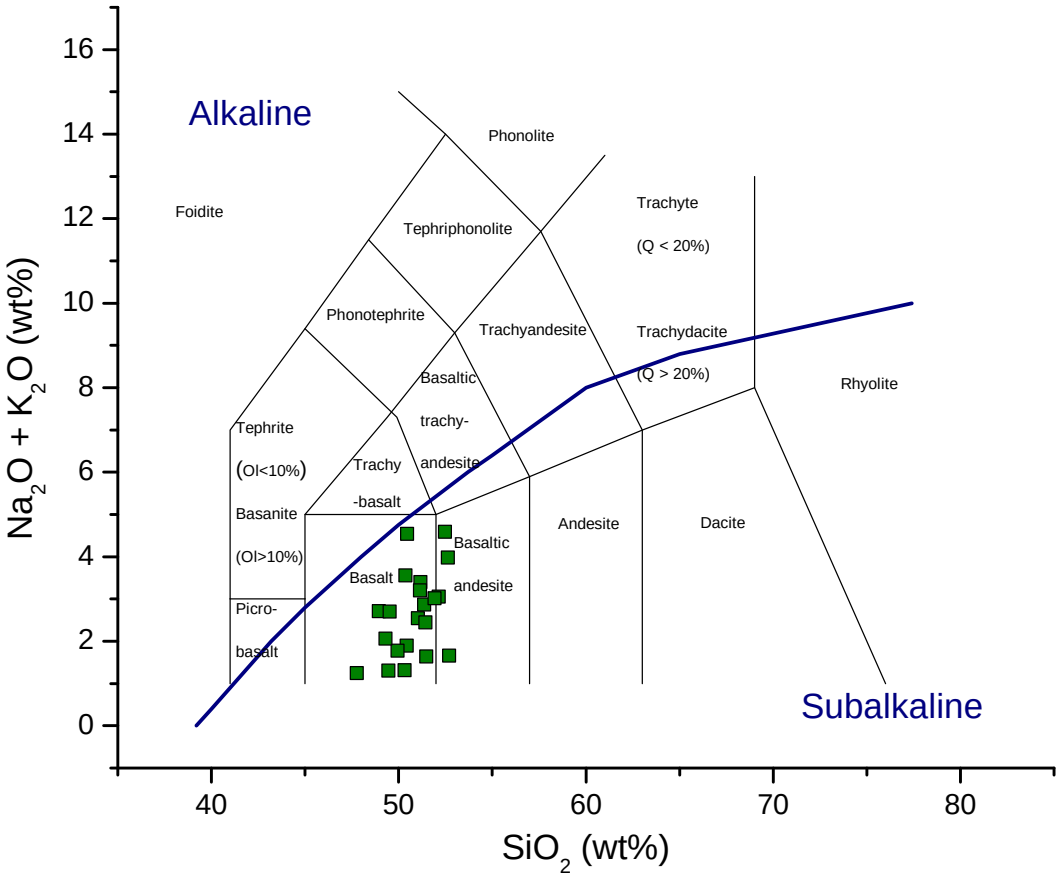


Figure 7.2 – Analyses of the Deguisier basalt unit illustrated in the TAS classification scheme for volcanic rocks of Le Maitre et al. (1989). Also shown in the figure is the dividing boundary for alkaline and subalkaline volcanic rocks (blue line) of Irvine and Baragar (1971).

As a result, the calculated basaltic modal mineralogy is presented in Table 7.3. The norm was calculated using a spreadsheet written by Kurt Hollocher (Union College, New York), found at the following web address: `www.neiu.edu/~kbartels/norm3.xls`.

The CIPW normative mineralogy without volatiles reveals that most samples are quartz normative tholeiitic basalts. Only 2 samples contain between 1.01 - 2.31 wt% normative olivine, while the remainder carries between 0.49 - 11.88 wt% normative quartz. None of the samples contain any nepheline or other feldspathoids. Furthermore, the exclusion of the volatiles also resulted in the elimination of anomalous corundum.

Parallels drawn between the normative mineralogy and the basalt are entirely based from andesite petrographic observations since both the basalt and andesite are petrographically similar (see Section 5.1.1). From thin sections, microscopic quartz was only observed in amygdules, suggesting that SiO_2 may either be of hydrothermal origin or mobilized during regional

Table 7.3 – CIPW normative mineralogy of Deguisier basalt samples without volatiles. Volatiles excluded are CO_2 and S. Normative mineralogy is presented in weight %. A ratio (Fe_2O_3/FeO) of 0.2 as recommended by Middlemost (1989) was assumed for all samples.

Sample	D958053	D958056	D958103	D958057	2003031998	D958236	3258
Quartz	6.63	—	6.26	5.13	0.49	11.88	10.16
Plagioclase	50.79	49.91	44.39	46.09	53.1	51.21	47.78
Orthoclase	0.3	1.3	0.95	0.71	0.24	0.41	0.3
Diopside	15.18	15.33	15.52	4.84	13.74	7.57	9.07
Hypersthene	18.7	23.94	25.01	34.35	24.08	22.1	24.99
Olivine	—	2.31	—	—	—	—	—
Ilmenite	3.57	2.66	2.98	3.27	3.46	2.87	2.89
Magnetite	4.67	4.31	4.7	5.36	4.63	3.8	4.51
Apatite	0.37	0.25	0.19	0.28	0.32	0.16	0.28
Zircon	—	—	—	—	—	—	0.01
Chromite	0.03	0.04	—	—	—	0.04	0.1
Total	100.24	100.05	100	100.03	100.06	100.04	100.09

Table 7.3 Continued

Sample	3261	3951	3691	3694	3287	D958309	D958310	3679
Quartz	4.52	6.09	2.09	6.91	3.47	3.16	8.12	4.21
Plagioclase	48.88	46.83	51.77	43.81	48.06	46.73	41.41	49.12
Orthoclase	1.06	0.71	1.36	0.53	10.4	0.47	0.18	0.24
Diopside	16.78	10.55	17.32	9.34	12.98	16.26	16.57	11.76
Hypersthene	21.7	27.46	19.68	30.51	17.45	24.06	24.41	26.04
Olivine	—	—	—	—	—	—	—	—
Ilmenite	2.58	3.65	3.46	3.32	3.48	3.72	3.84	3.72
Magnetite	4.18	4.32	3.96	5.19	3.8	5.21	5.13	4.55
Apatite	0.25	0.37	0.32	0.37	0.35	0.44	0.42	0.35
Zircon	0.01	0.01	0.01	0.01	0.01	—	—	0.01
Chromite	0.13	0.09	0.09	0.09	0.07	—	—	—
Total	100.09	100.08	100.06	100.08	100.07	100.05	100.08	100

metamorphism. Plagioclase is the dominant normative feldspar which was also reflected in thin section. There are variable amounts of normative orthoclase, considered uncommon in basalts (Moorhouse, 1959) and not observed in thin section. Orthoclase is therefore likely resultant of the CIPW norm limitations because hydrous portions are excluded. Consequently, the potassium forming orthoclase should in fact be attributed to biotite. However, no biotite was found in thin section due to subsequent hydrothermal alteration and regional metamorphism. Rather, from regional mineralogical observations performed by Goutier and Lacroix (1992), potassium is now presumed to be found in stilpnomelane. Normative oxides within the basalt are dominated by magnetite (3.70 - 5.36 wt%) closely followed by ilmenite (2.58 - 3.87 wt%). There is no normative hematite present based on the calculations, but the mineral is present in some thin sections. Accessory amounts of normative chromite and zircon are also present in both the calculation and in thin section, with the exception of apatite which has not been observed in thin section.

Table 7.3 Continued

Sample	3292	3669	3668	3665	3666	3667
Quartz	5.24	9.27	10.28	11.37	7.58	—
Plagioclase	52.7	42.48	41.08	40.49	51.8	48
Orthoclase	3.9	6.97	9.04	1.3	0.53	5.44
Diopside	9.24	5.07	4.53	9.35	1.86	13.47
Hypersthene	20.15	24.8	25.98	28.04	29.03	22.86
Olivine	—	—	—	—	—	1.01
Ilmenite	4.43	5.75	3.78	3.38	3.87	3.57
Magnetite	3.91	5.23	4.92	5.64	4.94	5.28
Apatite	0.42	0.42	0.37	0.42	0.37	0.35
Zircon	0.03	0.03	0.01	0.01	0.01	0.01
Chromite	0.07	0.06	0.09	0.06	0.06	0.12
Total	100.09	100.08	100.08	100.06	100.05	100.11

Gélinas et al. (1976) first reported chemical variations in the Deguisier basalt when progressing southwards, towards the stratigraphic top. These variations include a decrease in FeO_{tot}, SiO_2 and an increase in MgO, Al_2O_3 with no changes in TiO_2. Furthermore, Goutier and Lacroix (1992) reported that the level of SiO_2 saturation of the basalts is considered as silica-saturated with half of the analyses being olivine normative and the other half being quartz normative.

CIPW normative analyses can be utilized to determine the SiO_2 saturation level using the classification scheme proposed by Thompson (1984). Three ternary diagrams representing normative proportions of nepheline (and other feldspathoids), olivine, diopside, hypersthene and quartz are used to plot variations between nepheline-olivine-diopside, olivine-diopside-hypersthene and diopside-hypersthene-quartz. The first ternary diagram (left) corresponds to a silica-undersaturated basalt (alkali-basalts), in which samples are nepheline, feldspathoids and olivine normative. The second (middle) corresponds to a silica saturated basalt (olivine tholeiite) and are olivine and hypersthene normative. The last diagram (right) represents a silica-oversaturated rock (quartz tholeiite or high-Mg andesite) and is quartz and hypersthene normative. The resulting SiO_2 saturation plot from the normalized basaltic mineralogy is presented in Figure 7.3.

Basaltic samples in the Beattie area are silica-oversaturated with the majority of the samples plotting in the quartz tholeiite ternary portion. Only 2 samples plot in the olivine tholeiite portion. However, these analyses should not be considered as sole representatives of the Deguisier basalt and therefore localities outside the Beattie area may be silica-saturated as reported by Goutier and Lacroix (1992). Further investigations failed to find a link between the location of a sample and amount of quartz or olivine as Gélinas et al. (1976) reported.

Overall, normalized analyses are loosely clustered at the junction between the tholeiitic olivine and the quartz tholeiitic basalt fields indicating that the level of quartz saturation is low to moderate.

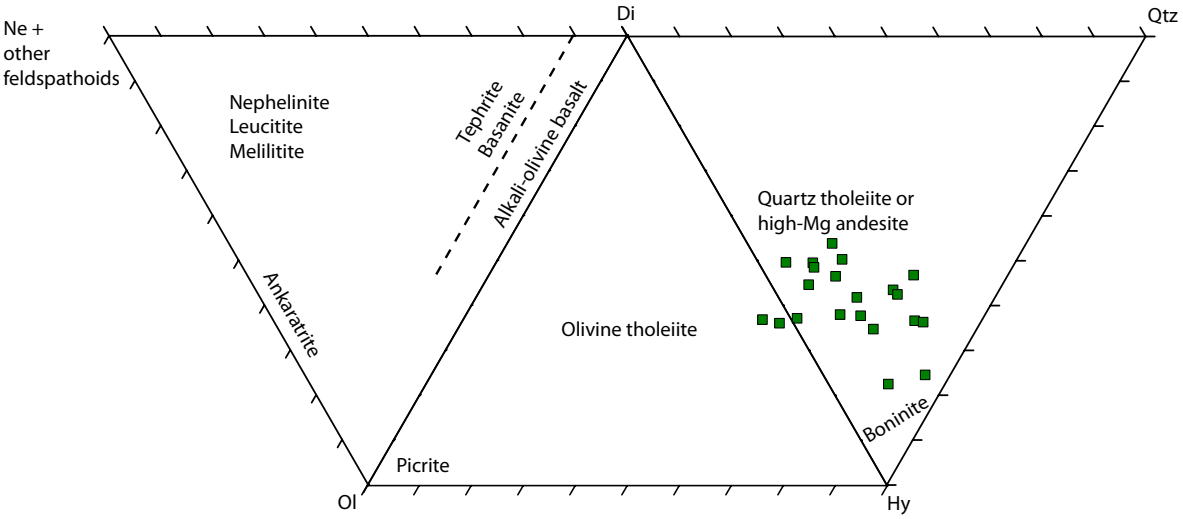


Figure 7.3 – Basalt classification using CIPW normative mineralogy. Classification diagram obtained from Thompson (1984). Normative minerals utilized are nepheline (Ne) - olivine (Ol) - diopside (Di), olivine (Ol) - diopside (Di) - hypersthene (Hy), or diopside (Di) - hypersthene (Hy) - quartz (Qtz).

7.1.2 Incompatible trace elements

Normalized incompatible trace element diagrams are a method of grouping trace elements and normalizing them with respect to a primitive composition. Typical normalizing factors used are those of a primitive mantle, a mid-oceanic ridge basalt (MORB), or a chondrite meteorite. For basalts, commonly used normalizing values are those of chondrites as they provide a measure of what the primitive bulk Earth concentrations are presumed to have been. These values have been provided by McDonough and Sun (1995), listed in Table 7.5. Only two analyses were measured for incompatible elements, and one of them is unfortunately largely incomplete. They are presented in Table 7.4. A further complication arises in the near complete sample 2003031938 which was analysed with a quartz vein. The presence of quartz will not affect the overall distribution of the incompatible elements, as the crystalline structure does not permit incompatible element substitution, but will result in a dilution of the incompatible elements. Furthermore, the sample was not analyzed for major elements and therefore a correction for LOI was not possible. Nevertheless, this represents the only available data. The resulting

normalized pattern is presented in Figure 7.4.

Table 7.4 – Incompatible and rare earth elements for the Deguisier basalt. Concentrations of the different elements are given in ppm. Only sample 2003031998 has been corrected for LOI.

Sample	2003031998	2003031938		2003031998	2003031938
Ba	0.003	1569.50	**Eu**	—	2.08
Th	—	2.4	**Gd**	—	6.99
Nb	—	10.4	**Tb**	—	1.19
La	—	21.3	**Dy**	—	6.85
Ce	—	51.7	**Y**	36.04	44.6
Pr	—	6.99	**Ho**	—	1.56
Nd	—	34.1	**Er**	—	4.02
Sm	—	6.9	**Tm**	—	0.65
Zr	89.58	140.6	**Yb**	—	3.8
Ti	17916.36	—	**Lu**	—	0.57
Hf	—	4.2			

Table 7.5 – Chondrite normalizing values for incompatible trace elements. Values presented are those of McDonough and Sun (1995). Concentrations of the different elements are given in ppm.

Element	**Concentration**	**Error (%)**	**Element**	**Concentration**	**Error (%)**
Ba	2.41	10	**Eu**	0.056	10
Th	0.029	15	**Gd**	0.199	10
Nb	0.24	15	**Tb**	0.036	10
La	0.237	10	**Dy**	0.246	10
Ce	0.613	10	**Y**	1.57	10
Pr	0.093	10	**Ho**	0.055	10
Nd	0.457	10	**Er**	0.160	10
Sm	0.148	10	**Tm**	0.025	10
Zr	3.82	10	**Yb**	0.161	10
Ti	440	10	**Lu**	0.025	10
Hf	0.103	10			

The normalized incompatible trace element pattern of the Deguisier basalt first reveals a slight decreasing trend ($[La/Yb]_{cn} = 3.8$) with a slight enrichment of light rare earth elements (LREE) with a negative Nb anomaly. Further investigations also revealed that large-ion lithophile element (LILE) (not shown) are also enriched compared to chondritic values. However, caution should be exercised with LILE Ba as it is highly variable. Least-altered samples contain an average of 437.41 ppm Ba (n = 15) which when normalized to the chondritic value yields a ratio of 181.5. The least-altered ratio is much smaller compared to sample 2003031938. As such, Ba is not to be considered as an immobile element for basalt.

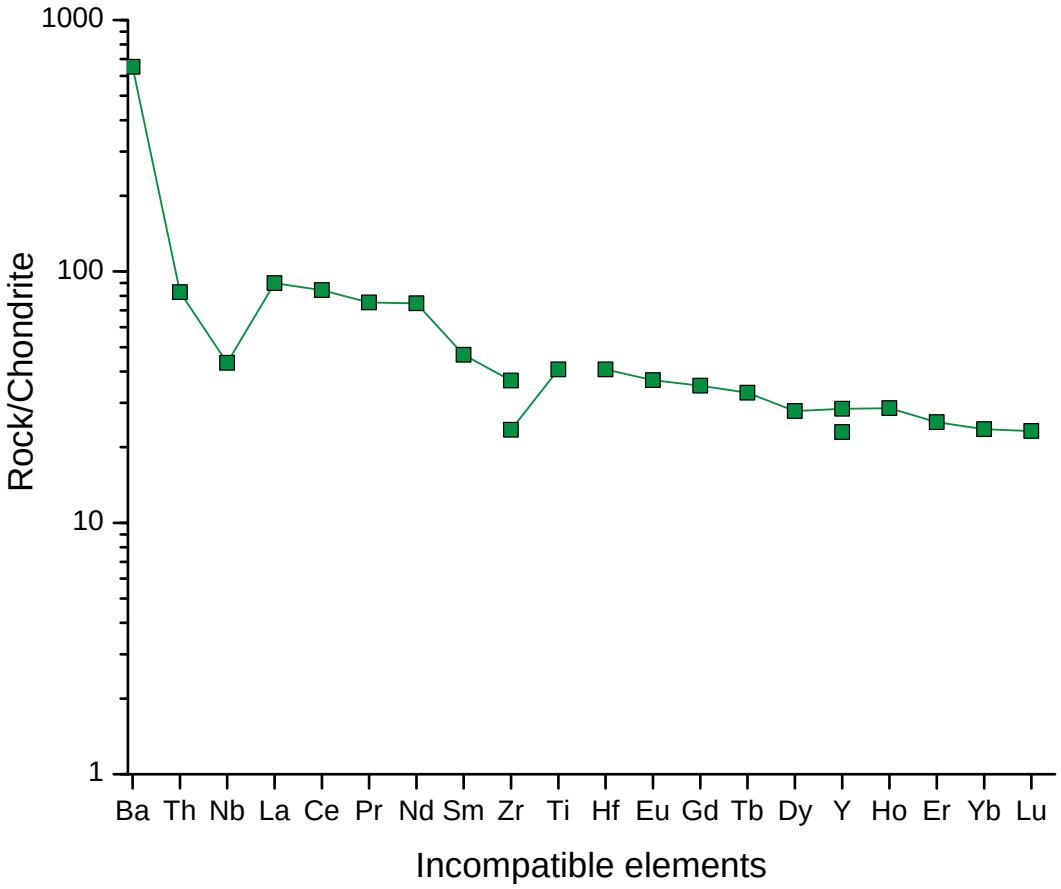


Figure 7.4 – Chondrite-normalized incompatible trace element patterns of the Deguisier basalt. Normalizing factors are those of McDonough and Sun (1995) presented in Table 7.5.

7.1.3 Rare earth elements

REE are a very useful and concise method to characterize the nature of a rock. Only a single sample of the Deguisier basalt was analyzed for REE (see Table 7.4). This sample was unfortunately analysed with a quartz vein, but as previously explained the resulting normalized REE will not affect the overall distribution of the REE, rather the presence of quartz in the sample will result in the dilution of the REE elemental concentrations. The sample was chondrite-normalized using values given by McDonough and Sun (1995) listed in Table 7.5. The resulting chondrite-normalized pattern is presented in Figure 7.5.

The obtained $\sum$REE is 148.7 ppm. The chondrite-normalized pattern reveals a slight enrichment of light rare earth elements (LREE) over heavy rare earth elements (HREE) ($[La/Lu]_{cn} = 3.94$). The $[La]_{cn}$ value is 89.9 while the $[Lu]_{cn}$ value is 22.8. The Eu/Sm value is of 0.30 indicating a very small negative Eu anomaly. Amplitude measurements on its

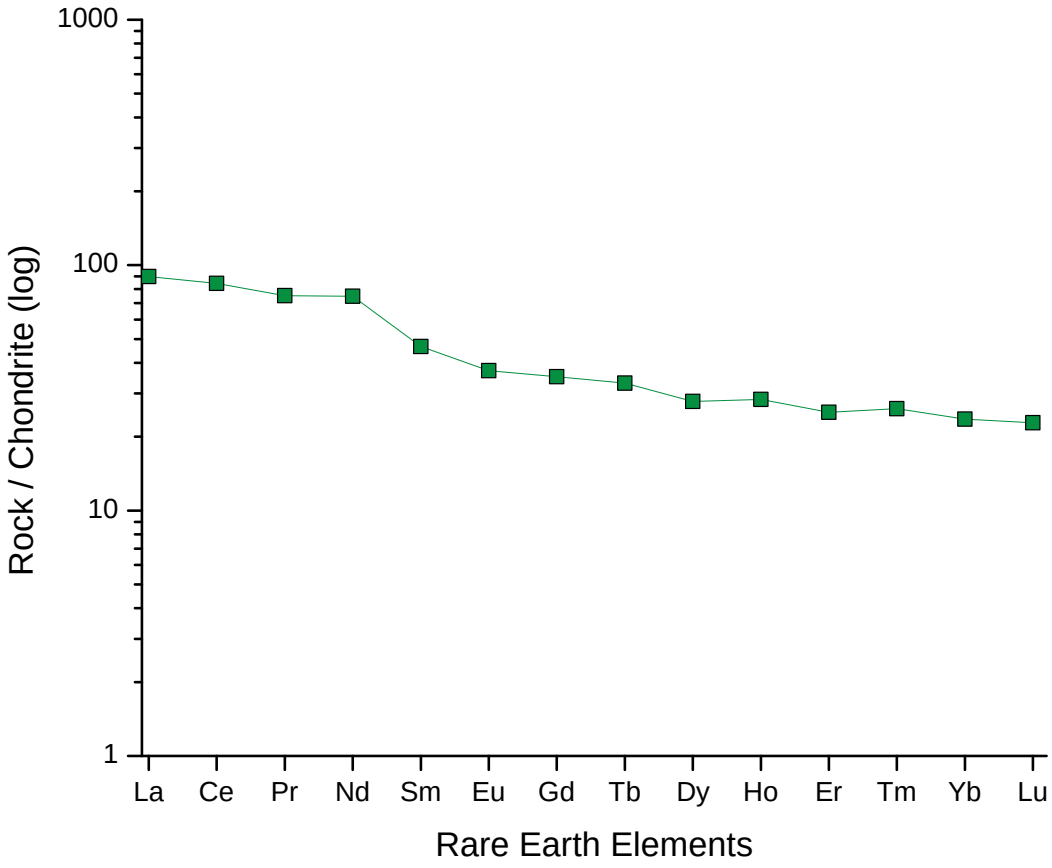


Figure 7.5 – Chondrite normalized REE patterns for the Deguisier basalt unit. Normalizing factors are those of McDonough and Sun (1995) listed in Table 7.5.

extent, $[Eu/Eu^*]_{cn}$ equals 0.9, [2] therefore revealing that it is a very small negative anomaly.

The basaltic REE contents carries the signature of a tholeiite. Literature values for tholeiitic basalts give a $\sum$REE between 15.2 - 322 ppm, $[La/Lu]_{cn}$ of 0.5 - 7.6 and a Eu/Sm value between 0.16 - 0.55 (Henderson, 1984). A comparison between the values from the unit and those obtained from the literature reveal that the Deguisier basalt values are located in the middle of ranges given in literature.

[2] Eu* is the value obtained at the Eu position by straight line interpolation between the plotted points for Sm and Gd.

7.2 Deguisier tholeiitic andesite to dacite

The Deguisier andesite to dacite unit is found in proximity and in contact with the Beattie syenite lenses. Initial geochemical investigations were done by Gélinas et al. (1976). A brief geochemical update was subsequently presented by Goutier and Lacroix (1992). Lately, a total of 62 samples were analyzed, after a renewed economic interest in the area. With these new data, an in depth exploration of the geochemical characteristics is now possible.

Methodology

Representative samples from the Deguisier andesite to dacite unit were obtained from Osisko Mining Corporation and the MRN. Extra screening was required since all andesitic to dacitic samples were not examined by the author. Rules for the recognition and subsequent exclusion of the most altered samples are that: 1) samples must have a LOI $< 10\%$[3], 2) samples must be free of quartz veins, and 3) oxide values must not extensively deviate from the norm set by all other samples. Particular attention was given to oxides such as Fe_2O_3, indicating pyrite, and K_2O which is extremely mobile. Almost all andesitic to dacitic samples come from close proximity ($<$ 50 m) to the Beattie syenite or to D_2 faults, resulting in greater elemental fluctuations. A greater amount of variability was therefore expected and tolerated in the selection criteria.

A total of 8 samples are considered severely altered and were excluded from all sections below. The least-altered samples employed for the remainder of the section are presented in Table 7.6. For reasons discussed in the introduction of this chapter samples provided by SOQUEM Inc. were excluded. A complete list of all andesitic to dacitic samples is provided in Appendix D.

Prior to being used for plots and calculations, major and trace elements were corrected for LOI and are therefore on a 'dry' basis unless otherwise specified.

[3]A detailed discussion justifying the choice of LOI cut-off can be found in Appendix D

Table 7.6 – Major and trace element least-altered specimens of the Deguisier tholeiitic andesite to dacite. Major oxides are presented in wt% and trace elements are all given in ppm with the exception of Au which is given in ppb. Analyses presented have not been corrected for LOI.

Sample	**2003031903**	**D958224**	**D958195**	**D958198**	**D958228**	**D958227**	**D958226**
Institution	MRN	Osisko	Osisko	Osisko	Osisko	Osisko	Osisko
Year	2003	2010	2010	2010	2010	2010	2010
SiO_2	63.07	63.90	60.40	59.60	66.20	59.50	61.10
TiO_2	0.86	1.19	1.20	1.20	1.16	1.23	1.46
Al_2O_3	8.31	11.25	10.95	11.65	10.80	11.65	13.70
Fe_2O_3t	5.33	6.21	6.35	8.50	5.00	6.44	7.39
MnO	0.32	0.17	0.14	0.24	0.22	0.21	0.14
MgO	3.04	1.18	1.03	1.44	0.61	1.02	1.43
CaO	5.86	4.12	2.59	4.40	4.45	5.67	3.58
Na_2O	0.68	4.16	4.99	5.71	2.14	3.40	3.31
K_2O	3.59	0.97	1.07	0.59	2.25	1.76	2.23
P_2O_5	0.31	0.34	0.32	0.39	0.37	0.40	0.57
[a]CO_2	8.65	—	—	—	—	—	—
[a]S	1.33	0.02	0.03	0.04	< 0.01	< 0.01	< 0.01
[b]LOI	8.10	5.78	6.31	6.53	6.06	7.55	6.26
Total	99.47	99.27	95.35	100.25	99.26	98.83	101.17
Ag	1.2	< 0.2	< 0.2	< 0.2	< 0.2	< 0.2	< 0.2
As	223.7	17	13	8	4	8	11
Au	819.6	5	9	5	5	5	5
Ba	252	*268.69*	—	*179.13*	447.83	447.83	447.83
Bi	0.3	< 2	< 2	< 2	< 2	< 2	< 2
Cd	0.1	< 0.5	< 0.5	< 0.5	< 0.5	< 0.5	< 0.5
Ce	42.8	—	—	—	—	—	—
Co	10.6	12	11	11	4	9	10
Cr	—	—	—	3	< 1	< 1	< 1
Cs	1	—	—	—	—	—	—
Cu	15.4	119	54	—	—	—	—
Dy	5.98	—	—	—	—	—	—
Er	3.74	—	—	—	—	—	—
Eu	1.66	—	—	—	—	—	—
Ga	14.5	< 10	< 10	< 10	< 10	< 10	< 10
Gd	6.17	—	—	—	—	—	—
Hf	4.5	—	—	—	—	—	—
Hg	0.66	< 1	< 1	< 1	< 1	< 1	< 1
Ho	1.25	—	—	—	—	—	—
La	20.4	—	—	—	—	—	—
Lu	0.51	—	—	—	—	—	—
Mo	9.1	< 1	< 1	< 1	< 1	< 1	< 1
Nb	9.9	—	—	—	—	—	—
Nd	26	—	—	—	—	—	—
Ni	1.2	3	< 1	< 1	< 1	3	3
Pb	6.9	< 2	6	4	< 2	3	< 2
Pr	5.6	—	—	—	—	—	—
Rb	73.9	—	—	—	—	—	—
Sb	3.5	< 2	< 2	< 2	< 2	< 2	< 2
Sc	11	—	—	—	—	—	—
Se	1.2	—	—	—	—	—	—
Sm	5.8	—	—	—	—	—	—
Sn	< 1	—	—	—	—	—	—
Sr	87.6	*169.12*	—	*253.68*	*169.12*	*169.12*	*169.12*
Ta	0.6	—	—	—	—	—	—
Tb	1.3	—	—	—	—	—	—
Th	1.4	—	—	—	—	—	—
Tl	0.4	< 10	< 10	< 10	< 10	< 10	< 10
Tm	0.59	—	—	—	—	—	—
U	1	—	—	—	—	—	—
V	54	—	—	—	—	—	—
W	21.8	—	—	—	—	—	—
Y	38.2	—	—	—	—	—	—
Yb	3.6	—	—	—	—	—	—
Zn	34	81	58	71	52	64	93
Zr	169.1	—	—	—	—	—	—

[a] *Not included in totals* [b] *Loss on ignition at 1000° C*

< Red *Values below detection limit* *Blue* *Values calculated from oxides*

Table 7.6 Continued

Sample	**D958230**	**D958233**	**D958253**	**D958256**	**D958235**	**D958247**	**D958272**	**D958273**
Institution	Osisko	Osisko	Osisko	Osisko	Osisko	Osisko	Osisko	Osisko
Year	2010	2010	2010	2010	2010	2010	2010	2010
SiO_2	64.30	59.90	57.60	63.30	59.80	59.90	54.10	63.50
TiO_2	0.97	1.45	1.33	1.67	0.89	1.34	1.67	1.36
Al_2O_3	9.34	13.35	11.95	13.65	14.30	11.50	13.00	12.55
Fe_2O_3t	6.18	7.80	11.10	8.61	8.59	6.34	9.30	6.98
MnO	0.18	0.11	0.23	0.16	0.11	0.31	0.25	0.15
MgO	1.28	1.01	2.66	1.28	4.63	0.72	1.16	0.92
CaO	5.20	4.00	4.31	1.70	3.24	5.60	5.01	3.03
Na_2O	1.81	6.54	2.49	4.22	2.89	2.57	2.46	1.65
K_2O	2.34	0.32	1.15	0.62	0.72	2.36	2.90	3.64
P_2O_5	0.29	0.38	0.43	0.50	0.25	0.29	0.18	0.40
[a]CO_2	—	—	—	—	—	—	—	—
[a]S	0.11	0.02	0.05	0.07	< 0.01	0.05	0.03	0.04
[b]LOI	8.41	3.83	6.49	3.17	3.70	8.17	9.60	6.88
Total	100.3	98.69	99.74	98.88	99.12	99.1	99.63	101.06
Ag	< 0.2	< 0.2	< 0.2	< 0.2	< 0.2	< 0.2	< 0.2	< 0.2
As	19	15	9	12	3	27	49	14
Au	< 5	6	< 5	< 5	< 5	< 5	< 5	< 5
Ba	*358.26*	—	*447.83*	*358.26*	*268.70*	*268.70*	*268.70*	*537.39*
Bi	< 2	< 2	< 2	< 2	< 2	< 2	< 2	< 2
Cd	< 0.5	< 0.5	< 0.5	< 0.5	< 0.5	< 0.5	< 0.5	< 0.5
Ce	—	—	—	—	—	—	—	—
Co	12	15	17	20	14	18	24	6
Cr	—	—	—	—	—	—	—	—
Cs	—	—	—	—	—	—	—	—
Cu	39	104	89	34	26	22	91	43
Dy	—	—	—	—	—	—	—	—
Er	—	—	—	—	—	—	—	—
Eu	—	—	—	—	—	—	—	—
Ga	< 10	< 10	< 10	< 10	< 10	< 10	< 10	< 10
Gd	—	—	—	—	—	—	—	—
Hf	—	—	—	—	—	—	—	—
Hg	< 1	< 1	< 1	< 1	< 1	< 1	< 1	< 1
Ho	—	—	—	—	—	—	—	—
La	—	—	—	—		—	—	—
Lu	—	—	—	—	—	—	—	—
Mo	< 1	< 1	2	< 1	< 1	< 1	< 1	< 1
Nb	—	—	—	—	—	—	—	—
Nd	—	—	—	—	—	—	—	—
Ni	2	6	4	45	17	3	7	1
Pb	3	< 2	3	< 2	< 2	< 2	< 2	< 2
Pr	—	—	—	—	—	—	—	—
Rb	—	—	—	—	—	—	—	—
Sb	< 2	< 2	< 2	< 2	< 2	< 2	< 2	< 2
Sc	—	—	—	—	—	—	—	—
Se	—	—	—	—	—	—	—	—
Sm	—	—	—	—	—	—	—	—
Sn	—	—	—	—	—	—	—	—
Sr	*169.12*	*169.12*	*253.68*	*169.12*	—	*169.12*	*169.12*	*169.12*
Ta	—	—	—	—	—	—	—	—
Tb	—	—	—	—	—	—	—	—
Th	—	—	—	—	—	—	—	—
Tl	< 10	< 10	< 10	< 10	< 10	< 10	< 10	< 10
Tm	—	—	—	—	—	—	—	—
U	—	—	—	—	—	—	—	—
V	—	—	—	—	—	—	—	—
W	—	—	—	—	—	—	—	—
Y	—	—	—	—	—	—	—	—
Yb	—	—	—	—	—	—	—	—
Zn	54	79	210	69	121	37	111	71
Zr	—	—	—	—	—	—	—	—
	[a]	*Not included in totals*			[b]	*Loss on ignition at 1000° C*		
	< Red	*Values below detection limit*			*Blue*	*Values calculated from oxides*		

Table 7.6 Continued

Sample	**D958301**	**35682**	**184153**
Institution	Osisko	MRN	MRN
Year	2010	1990	1994
SiO_2	60.50	54.90	62.04
TiO_2	1.41	1.61	1.62
Al_2O_3	12.70	13.00	12.66
Fe_2O_3t	9.22	10.80	8.41
MnO	0.14	0.21	0.19
MgO	1.22	2.43	2.09
CaO	2.02	5.87	4.25
Na_2O	2.27	2.68	4.33
K_2O	3.76	0.71	0.07
P_2O_5	0.39	0.44	0.50
[a]CO_2	—	—	—
[a]S	0.05	—	—
[b]LOI	6.32	5.94	2.98
Total	99.95	98.59	99.14
Ag	< 0.2	—	—
As	17	—	—
Au	< 5	—	—
Ba	*716.52*	273.00	76.00
Bi	< 2	—	—
Cd	0.5	< 2.00	< 2.00
Ce	—	38.00	48.00
Co	17	27.00	19.00
Cr	—	—	—
Cs	—	0.50	—
Cu	33	65.00	34.00
Dy	—	< 1	< 1
Er	—	—	—
Eu	—	3.10	< 1
Ga	< 10	17.00	14.00
Gd	—	5.00	—
Hf	—	5.70	—
Hg	< 1	—	—
Ho	—	0.90	—
La	—	16.00	22.00
Lu	—	0.56	—
Mo	< 1	4.00	4.00
Nb	—	9.00	10.00
Nd	—	< 25	—
Ni	< 1	39.00	39.00
Pb	< 2	< 12	< 12
Pr	—	< 10	—
Rb	—	20.00	< 3
Sb	< 2	—	—
Sc	—	31.00	33.00
Se	—	—	—
Sm	—	6.50	4.00
Sn	—	10.00	—
Sr	*253.68*	120.00	190.00
Ta	—	< 0.6	< 5
Tb	—	0.90	—
Th	—	< 1.10	< 3.00
Tl	< 10	—	—
Tm	—	0.80	—
U	—	0.50	—
V	—	130.00	142.00
W	—	—	—
Y	—	36.00	41.00
Yb	—	3.50	—
Zn	60	103.00	64.00
Zr	—	290.00	280.00

[a]	*Not included in totals*
[b]	*Loss on ignition at 1000° C*
< Red	*Values below detection limit*
Blue	*Values calculated from oxides*

7.2.1 Major and compatible trace elements

Field, drill core and thin section observations have all failed to distinguish the basalt from the andesite to dacite unit. Fortunately, this lack of differentiable features was not encountered with geochemistry. Notable differences between the two units have been found in 'immobile' TiO_2, P_2O_5 and Zr. Specifically, there is a loss in TiO_2 and an increase in P_2O_5 and Zr in the andesite to dacite unit. Other oxide decreases are noted when comparing Fe_2O_3t, MgO and CaO. To better perceive the distinctions, the normalized 'dry' averaged wt% oxide values samples from each unit are presented in Table 7.7.

Table 7.7 – Mean major oxide composition of the basalt and andesite to dacite units. Major oxides are all presented in wt% and Zr is in ppm.

	Basalt (n=21)	**Andesite-Dacite** (n=18)
SiO_2	50.77	65.21
TiO_2	1.83	1.41
Al_2O_3	14.23	12.88
Fe_2O_3t	15.90	8.25
MnO	0.26	0.21
MgO	5.66	1.73
CaO	8.41	4.48
Na_2O	2.27	3.47
K_2O	0.37	1.86
P_2O_5	0.14	0.40
Zr	100.34	262.75

n = number of averaged samples

General classification

The Deguisier andesitic to dacitic rocks are classified using the Jensen cation plot, presented in Figure 7.6.

In this diagram, the majority of samples extend from the tholeiitic andesite to the rhyolitic field. Only 2 samples diverge from the trend and plot in the calc-alkaline series. It should be noted that one of these samples is from a xenolith found within the Beattie syenite and the other is from a location adjacent to a contact (3 m) with the gabbro. The andesite to dacite unit is also considered part of the tholeiitic series.

These selected, least-altered, samples still demonstrate most of their apparent original chemical characteristics. This is best observed in the TAS diagram of Le Maitre et al. (1989) presented in Figure 7.7. Included in the TAS diagram is the division of the alkaline and subalkaline fields following the subdivision proposed by Irvine and Baragar (1971). Andesitic

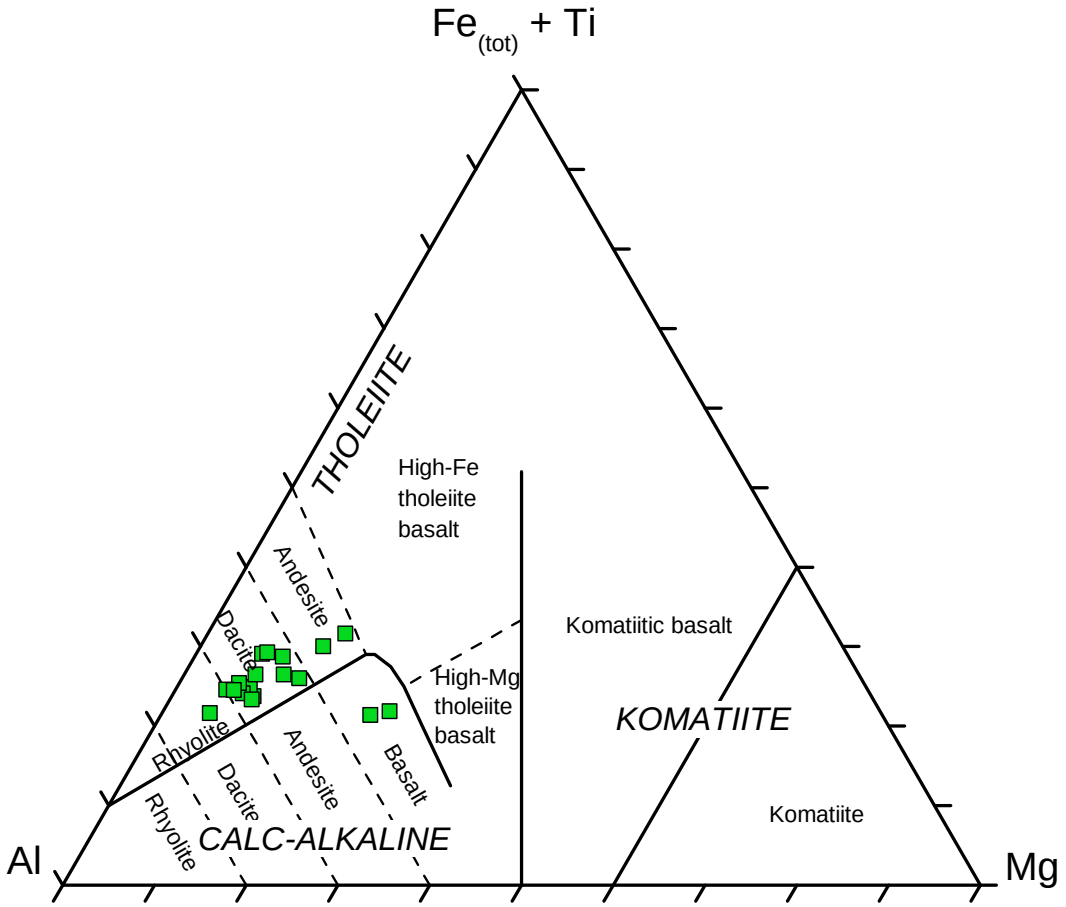


Figure 7.6 – Jensen cation plot of the Deguisier andesite to dacite unit.

to dacitic samples spread between both the andesite and dacite fields with all samples plotting in the subalkaline field. The majority of samples occupy the dacitic field and 4 samples are in the andesitic field. Only one sample possesses a slight enrichment in aklalies such that it plots in the trachydacite field.

CIPW norm

For a detailed discussion of the use and limitations of the CIPW norm, see the corresponding section within the Deguisier tholeiitic basalt. Similar to the basalt analyses, the amount of ferrous iron was not measured, therefore a ratio (Fe_2O_3/FeO) of 0.4 as recommended by Middlemost (1989) was assumed for all samples. This ratio was also kept for andesitic analyses since the average of SiO_2 is 65.21 wt%, plotting directly in the dacitic compositional field.

Volatiles in the area are known to be related to hydrothermal alteration (see Section 8.2.1).

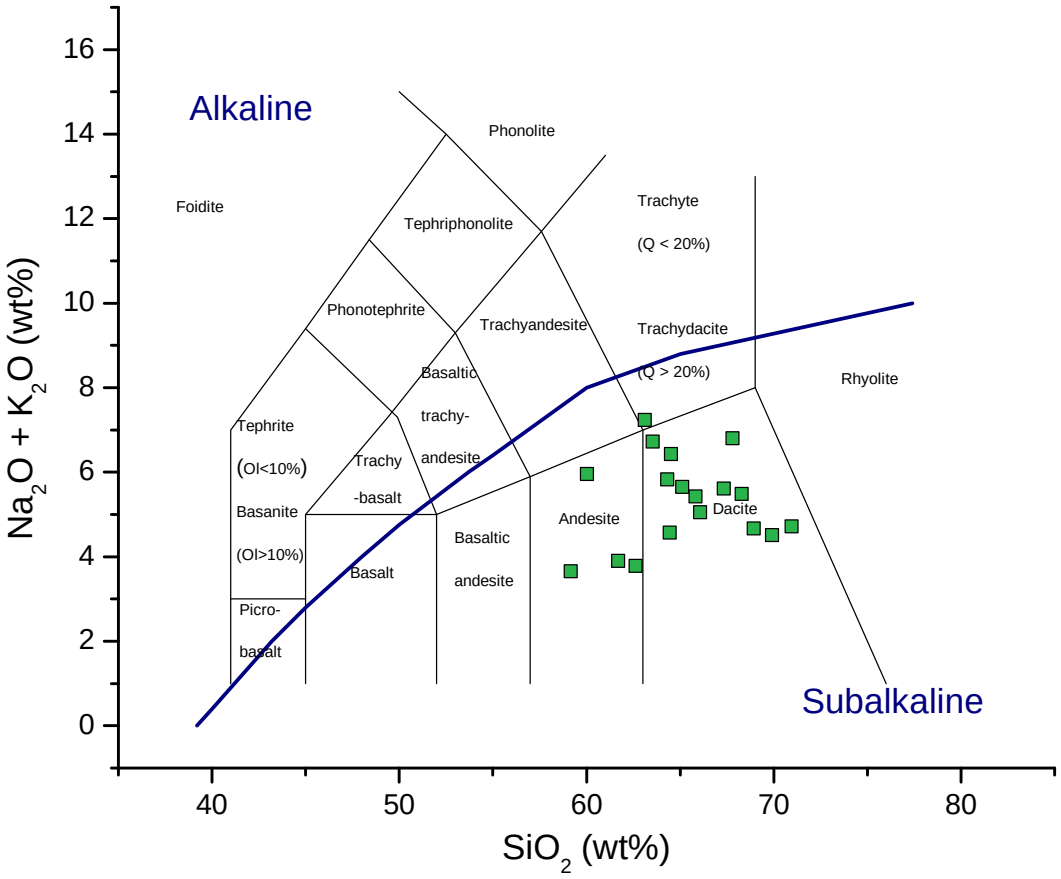


Figure 7.7 – Analyses of the Deguisier andesite to dacite unit illustrated in the TAS classification scheme for volcanic rocks of Le Maitre et al. (1989). Also shown in the figure is the dividing boundary for alkaline and subalkaline volcanic rocks (blue line) of Irvine and Baragar (1971).

For this reason, norm analyses were recalculated as volatile-free in an attempt to reduce the hydrothermal alteration signature. The resultant normative mineralogy is presented in Table 7.8.

The normative mineralogy of the andesite to dacite unit corresponds well to that of a typical mineralogical assemblage described in the literature. All samples are quartz-normative with amounts between 13.32 - 39.07 wt% norm. Thin section observations do not reveal any visible quartz crystals and therefore quartz is most likely a constituent of the fine-grained matrix. None of the samples contain any normative olivine or feldspathoids. However, a small amount normative corundum (0.68 - 4.32 wt%) was noted in a number of samples. This anomalous mineral is caused by local depletions of Ca which could not be corrected since CO_2 was not measured for many samples.

The dominant mineral in this unit is plagioclase which ranges from 16.25 - 65.11 wt%

Table 7.8 – CIPW normative mineralogy of the Deguisier andesite to dacite unit analyses calculated to be volatile-free. Normative mineralogy is presented in weight %. A ratio (Fe_2O_3/FeO) of 0.4 as recommended by Middlemost (1989) was assumed for all samples.

Sample	2003031903	D958224	D958195	D958198	D958228	D958227	D958226
Quartz	34.9	29.19	24.07	16.07	39.07	24.51	25.24
Plagioclase	16.25	47.65	52.49	56.6	33.72	44.11	44.64
Orthoclase	23.28	6.15	7.15	3.72	14.3	11.46	13.95
Corundum	—	—	—	—	—	—	0.68
Diopside	15.97	8.05	6.02	13.35	5.85	11.46	—
Hypersthene	3.62	1.83	2.72	1.57	0.68	—	6.64
Wollastonite	—	—	—	—	—	0.81	—
Ilmenite	1.79	2.43	2.56	2.45	2.37	2.56	2.94
Magnetite	3.39	3.87	4.15	5.29	3.12	4.1	4.54
Hematite	—	—	—	—	—	—	—
Apatite	0.79	0.86	0.83	0.97	0.93	1.02	1.39
Zircon	0.03	—	—	—	—	—	—
Total	100.02	100.03	99.99	100.02	100.04	100.03	100.02

Table 7.8 Continued

Sample	D958230	D958233	D958253	D958256	D958235	D958247	D958272
Quartz	37.32	13.39	26.22	32.3	26.37	27.91	18.61
Plagioclase	28.16	65.11	42.25	43.03	41.08	38.23	41
Orthoclase	15.13	2.01	7.33	3.84	4.49	15.42	19.15
Corundum	—	—	—	4.32	3.63	—	—
Diopside	12.2	10.17	0.65	—	—	9.59	7.39
Hypersthene	0.56	0.74	12.83	6.75	16.81	—	3.84
Wollastonite	—	—	—	—	—	1.26	—
Ilmenite	2.01	2.92	2.73	3.32	1.79	2.81	3.55
Magnetite	3.91	4.8	6.96	5.25	5.25	4.06	6.03
Hematite	—	—	—	—	—	—	—
Apatite	0.74	0.93	1.07	1.23	0.6	0.74	0.46
Zircon	—	—	—	—	—	—	—
Total	100.03	100.07	100.04	100.04	100.02	100.02	100.03

Table 7.8 Continued

Sample	D958273	D958301	35682	184153
Quartz	34.12	27.85	22.22	26
Plagioclase	28.27	28.89	47.84	53.92
Orthoclase	22.93	23.87	4.55	0.41
Corundum	1.39	2.23	—	—
Diopside	—	—	4.42	2.54
Hypersthene	5.26	7.6	9.7	7.59
Wollastonite	—	—	—	—
Ilmenite	2.75	2.87	3.32	3.21
Magnetite	4.32	5.74	6.81	5.1
Hematite	—	—	—	—
Apatite	1	0.97	1.11	1.2
Zircon	—	—	0.06	0.06
Total	100.04	100.02	100.03	100.03

norm. As a general observation, plagioclase phenocrysts are remarkably abundant and characteristic in andesites and dacites worldwide (Moorhouse, 1959). Thin section observations of the Deguisier andesite to dacite also revealed plagioclase phenocrysts. Orthoclase is also present as a normative mineral, but uncommon in andesites and dacites, unless occurring as

a xenocryst. The lack of orthoclase in thin sections further confirms that it is an abnormality. In this case, potassium in orthoclase should be attributed to biotite. This discrepancy arises from the limitations of the CIPW norm which excludes hydrous minerals. Both normative pyroxenes are normal constituents of andesites and dacites. Although a small percentage of the pyroxenes may also be attributed to hornblende. Ilmenite and magnetite are also normative minerals and have been observed as extremely small crystals part in the thin section groundmass. Other normal normative accessory minerals are hematite, apatite and zircon.

7.2.2 Incompatible trace elements

The andesitic to dacitic samples have been normalized with the chondritic values presented by McDonough and Sun (1995) (see Table 7.5). Older analyses performed in the 1990s were discarded due to their incompleteness, high detection limit and precision error. This eliminated all but 3 samples. Two samples are from xenoliths close to the Donchester mine shaft (samples: 2003031903 and 2003031930) and one is adjacent to a contact with the Beattie syenite (sample: 2004042821). Values are given in Table 7.9. A further complication arises in sample 2003031930 which was analyzed with a quartz vein. As previously explained, the presence of quartz will not affect the overall distribution of the incompatible elements, but will result in a dilution of the incompatible elements. Furthermore, sample 2003031930 was not analysed with major elements, therefore a correction for the LOI was not possible. Nonetheless, these analyses are the only available. The chondrite-normalized pattern is presented in Figure 7.8.

Table 7.9 – Incompatible and rare earth elements for the Deguisier andesite to dacite. Elemental concentrations are all given in ppm. Analyses presented, except for 2003031930 have been corrected for LOI.

Sample	2003031903	2004042821	2003031930		2003031903	2004042821	2003031930
Ba	275.44	951.41	102	**Eu**	1.81	0.58	0.66
Th	1.53	0.77	1.1	**Gd**	6.74	2.29	2.56
Nb	10.82	2.42	3.7	**Tb**	1.42	0.44	0.43
La	22.30	4.51	9.9	**Dy**	6.54	2.77	2.67
Ce	46.78	10.67	20.9	**Y**	41.75	13.09	17.4
Pr	6.12	1.46	2.52	**Ho**	1.37	0.56	0.59
Nd	28.42	7.15	12	**Er**	4.09	1.67	1.47
Sm	6.34	1.87	2.7	**Tm**	0.23	0.64	0.23
Zr	184.83	77.87	52	**Yb**	3.93	1.66	1.36
Ti	9400.08	10668.98	—	**Lu**	0.56	0.22	0.19
Hf	4.92	2.75	1.4				

All of the chondrite normalized samples demonstrate the same pattern with some variation

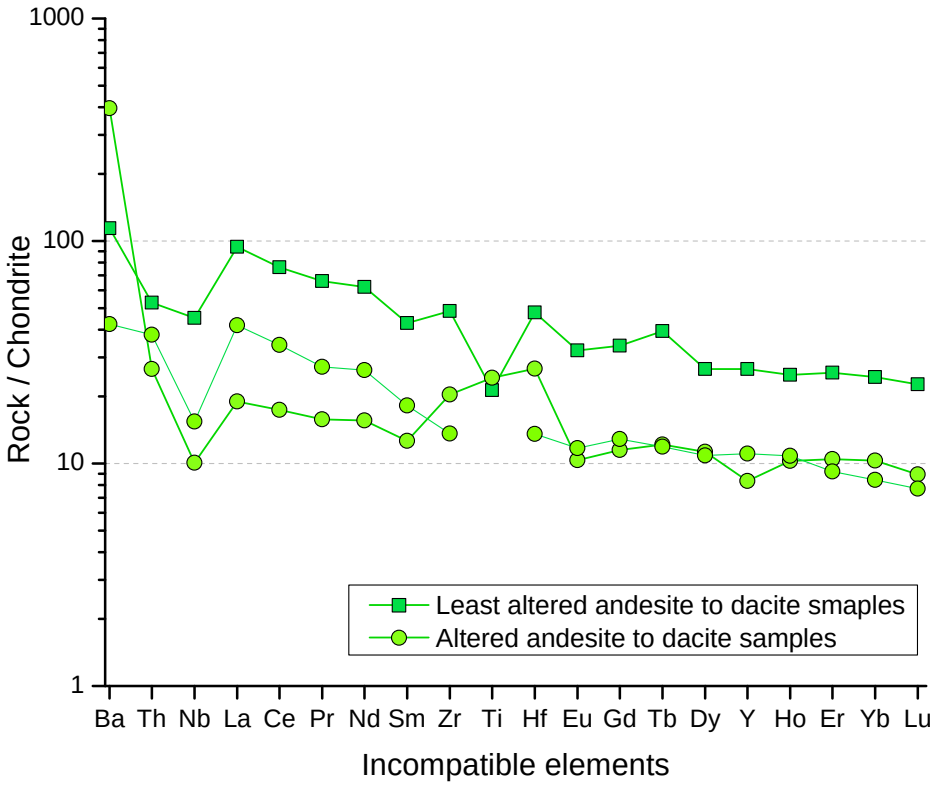


Figure 7.8 – Chondrite-normalized incompatible trace element pattern of the Deguisier andesite to dacite unit. Normalizing factors are those of McDonough and Sun (1995) presented in Table 7.5.

on the order of magnitude. Samples located away form the Beattie syenite and D_2 faults contain the same concentration as the most enriched sample (not shown, older discarded samples). Consequently, this sample (2003031903) is deemed to be the best representative of the unit. The least concentrated sample, La $<$ 20 times chondrite, is adjacent to a contact with the Beattie syenite. The middle range sample, La $<$ 40 times chondrite, was analyzed along with a quartz vein. Consequently, the effects of proximity to a contact as well as the inclusion of quartz in a sample resulted in a significant, $\sim$ 0.8 - 0.5 orders of magnitude, reduction of incompatible elements concentration.

The best representative normalized pattern reveals a slight decreasing trend ($[La/Yb]_{cn}$ = 3.85) with a slight enrichment of the LREE over the HREE. The pattern also holds a slight Nb anomaly which is in common with the pattern obtained for the Deguisier basalt. In addition, the pattern also demonstrates a slight negative Th anomaly, and a Zr and Hf positive anomaly. Investigations have revealed that LILE (not shown) are enriched compared to chondritic values. However a large discrepancy is observed with LILE Ba. This discrepancy was also observed

with the Deguisier basalt and is deemed the product of subsequent hydrothermal alteration where element Ba became mobile (see Section 8.2). Least-altered samples contain an average of 376.3 ppm Ba (n = 16) which yields a chondrite normalized ratio of 156.1, near the ratio obtained for the best representative sample.

7.2.3 Rare earth elements

The REE concentrations of the Deguisier andesite to dacite are presented in Table 7.9. Samples used are the same as previously presented in the incompatible trace elements section above. The samples have been chondrite-normalized using values given by McDonough and Sun (1995) listed in Table 7.5. The chondrite-normalized patterns are presented in Figure 7.9.

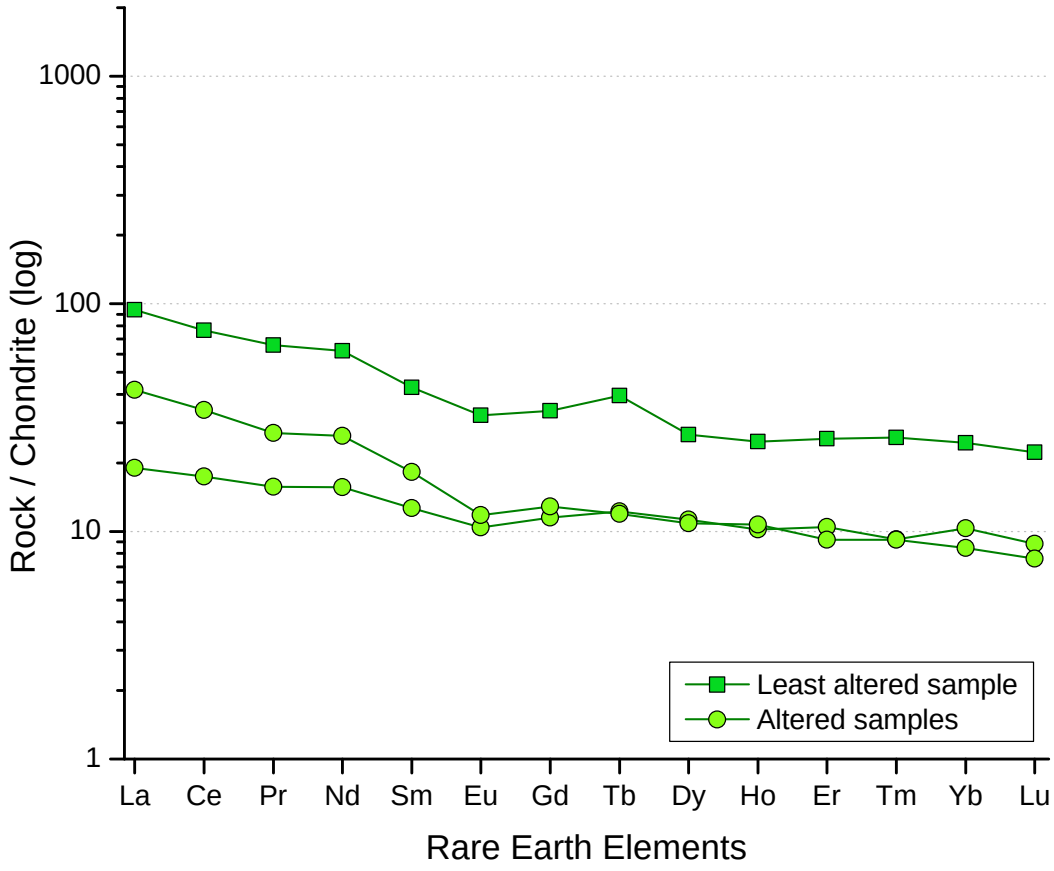


Figure 7.9 – Chondrite normalized REE patterns for the Deguisier andesite to dacite unit. Normalizing factors are those of McDonough and Sun (1995) listed in Table 7.5.

As previously discussed, the best representative sample (2003031903) of the unit possesses the highest concentration of REE. This sample has a $\sum$REE of 137.1 ppm. The chondrite-normalized REE pattern demonstrates an slight enrichment of the LREE over the HREE. The

$[La]_{cn}$ value is 94.1 while the $[Lu]_{cn}$ value is 22.3, yielding a ratio of $[La/Lu]_{cn}$ of 4.2. Eu/Sm value is of 0.29 indicating a very small negative Eu anomaly. This negative anomaly is also reflected in Figure 7.9. Amplitude measurements on its extent ($[Eu/Eu^*]_{cn}$) reveal that it is of 0.84, therefore a very small negative anomaly.

REE contents of the best representative sample carries the signature of a tholeiite. Literature values for tholeiitic andesites give a $\sum$REE between 25 - 178 ppm, $[La/Lu]_{cn}$ of 1.0 - 8.6 and a Eu/Sm value between 0.19 - 0.51 (Henderson, 1984). Values from the unit are generally located in the upper spectrum of literature ranges. Depleted samples are also within acceptable margins, but for reasons of their altered nature, they are not deemed to be appropriate representatives.

7.3 Tholeiitic rhyolite

Very little is known about the youngest volcanic unit of the Deguisier Formation. In particular there are no detailed geochemical studies in literature. The lack of existing literature along with the discovery of rhyolite in contact with the Beattie syenite suggests a need for a geochemical study. In order to achieve this, a total of 17 geochemical samples were used. Furthermore, a sample from a rhyolitic lens found further north, outside the study area, has been included for comparative purposes, due to the already limited number of analyses.

Methodology

Representative samples were obtained from Osisko Mining Corporation, MRN, L. Bigot (UQAM) and by the author. Rules employed to ascertain altered samples are: 1) measured oxides must not extensively deviate from the average set by other samples, and 2) samples must not have a LOI $> 3\%$[4].

Only a single sample from Osisko was considered altered. This sample possesses a very high SiO_2 and a LOI of 3.50%. Therefore this sample is excluded from all sections below. The remaining representative least-altered samples are listed in Table 7.10.

Additional samples were also provided by SOQUEM Inc., but for reasons previously discussed, these were only employed when characterizing the alteration geochemistry. A complete list of all Deguisier rhyolitic samples is presented in Appendix D.

Prior to being used for plots and calculations, major and trace elements were corrected for LOI and are therefore on a 'dry' basis unless otherwise specified.

[4]A detailed discussion justifying the choice of LOI cut-off can be found in Appendix D

Table 7.10 – Major and trace element least-altered specimens of the Deguisier tholeiitic rhyolite. Major oxides are presented in wt% and trace elements are all given in ppm with the exception of Au which is given in ppb. Analyses presented have not been corrected for LOI.

Sample	**05-A**	**JEB-10-09**	**D958143**	**D958379**	**D958269**	**94-00033**	**90-34311**[1]
Institution	UQAM	U of 0	Osisko	Osisko	Osisko	MRN	MRN
Year	2010	2010	2010	2010	2010	1994	1990
SiO_2	75.57	74.40	78.80	81.20	76.50	81.70	74.50
TiO_2	1.03	1.25	0.90	0.10	1.23	0.10	0.14
Al_2O_3	11.75	13.43	9.34	8.27	12.25	11.30	12.00
Fe_2O_3t	1.93	1.29	2.63	0.81	1.61	0.56	3.74
MnO	0.03	< 0.01	< 0.01	0.04	0.03	< 0.01	0.06
MgO	0.33	0.15	0.28	0.21	0.29	0.11	0.80
CaO	0.95	0.67	0.57	2.65	0.71	0.14	1.50
Na_2O	3.31	5.00	1.80	0.21	2.07	2.76	0.75
K_2O	3.01	2.09	3.46	2.10	3.14	2.27	3.44
P_2O_5	0.39	0.49	0.41	0.02	0.37	< 0.01	0.02
[a]**CO_2**	0.77	0.11	—	—	—	—	—
[a]**S**	< 0.02	< 0.02	< 0.01	< 0.01	0.03	—	—
[b]**LOI**	1.60	1.10	2.10	3.50	2.59	1.41	2.48
Total	99.9	99.88	100.3	99.11	100.79	100.37	99.43
Ag	0.3	< 0.1	< 0.2	< 0.2	< 0.2	—	—
As	15.1	5.5	8	2	26	—	—
Au	6.1	< 0.5	14	< 5	< 5	—	—
Ba	166	134	*79.13*	*447.83*	*358.26*	485	369
Bi	< 0.1	< 0.1	< 2	< 2	< 2	—	—
Cd	0.3	< 0.1	< 0.5	< 0.5	< 0.5	< 2	—
Ce	56.4	67.3	—	—	—	< 2	89
Co	6.5	3.2	3	< 1	7	66	4
Cr	—	*20.53*	—	—	—	3	—
Cs	1.7	1.4	—	—	—	—	—
Cu	78.7	55.4	106	10	70	< 1	13
Dy	6.38	7.33	—	—	—	3	3
Er	3.61	4.83	—	—	—	—	—
Eu	1.75	2.11	—	—	—	5	—
Ga	15.3	16.6	< 10	< 10	< 10	20	14
Gd	6.91	8.21	—	—	—	—	—
Hf	6.4	7.7	—	—	—	—	—
Hg	0.12	0.07	< 1	< 1	< 1	—	—
Ho	1.3	1.59	—	—	—	—	—
La	22.7	27.8	—	—	—	39	56
Lu	0.48	0.69	—	—	—	—	—
Mo	1	0.2	< 1	< 1	< 1	< 4	—
Nb	14	16.9	—	—	—	14	13
Nd	29.6	37.8	—	—	—	31	45
Ni	1.5	1.0	< 1	< 1	2	< 1	8
Pb	7.7	2.0	< 2	< 2	3	12	26
Pr	7.16	8.45	—	—	—	< 10	—
Rb	75	58.1	—	—	—	83	160
Sb	7	1.6	< 2	< 2	4	—	—
Sc	11	14.0	—	—	—	4	6
Se	< 0.5	< 0.5	—	—	—	—	—
Sm	6.73	7.96	—	—	—	< 2	8
Sn	3	2.0	—	—	—	10	—
Sr	150.5	148.3	—	—	—	88	70
Ta	0.9	1.0	—	—	—	< 5	—
Tb	1.14	1.29	—	—	—	—	—
Th	2.5	2.8	—	—	—	4	9
Tl	< 0.1	< 0.1	< 10	< 10	< 10	—	—
Tm	0.52	0.70	—	—	—	—	—
U	1.9	0.9	—	—	—	—	—
V	49	28.0	—	—	—	< 2	17
W	3.7	6.9	—	—	—	—	—
Y	36.3	44.7	—	—	—	50	37
Yb	3.3	4.63	—	—	—	—	—
Zn	26	9	32	11	24	28	60
Zr	244.2	289.9	—	—	—	175	150

[1] *Sample outside the Beattie area, from a northern rhyolitic lens*

[a] *Not included in totals* [b] *Loss on ignition at 1000° C*

< Red *Values below detection limit* *Blue* *Values calculated from oxides*

7.3.1 Major and compatible trace elements

General classification

The Deguisier rhyolite is classified using the Jensen cation plot, presented in Figure 7.10.

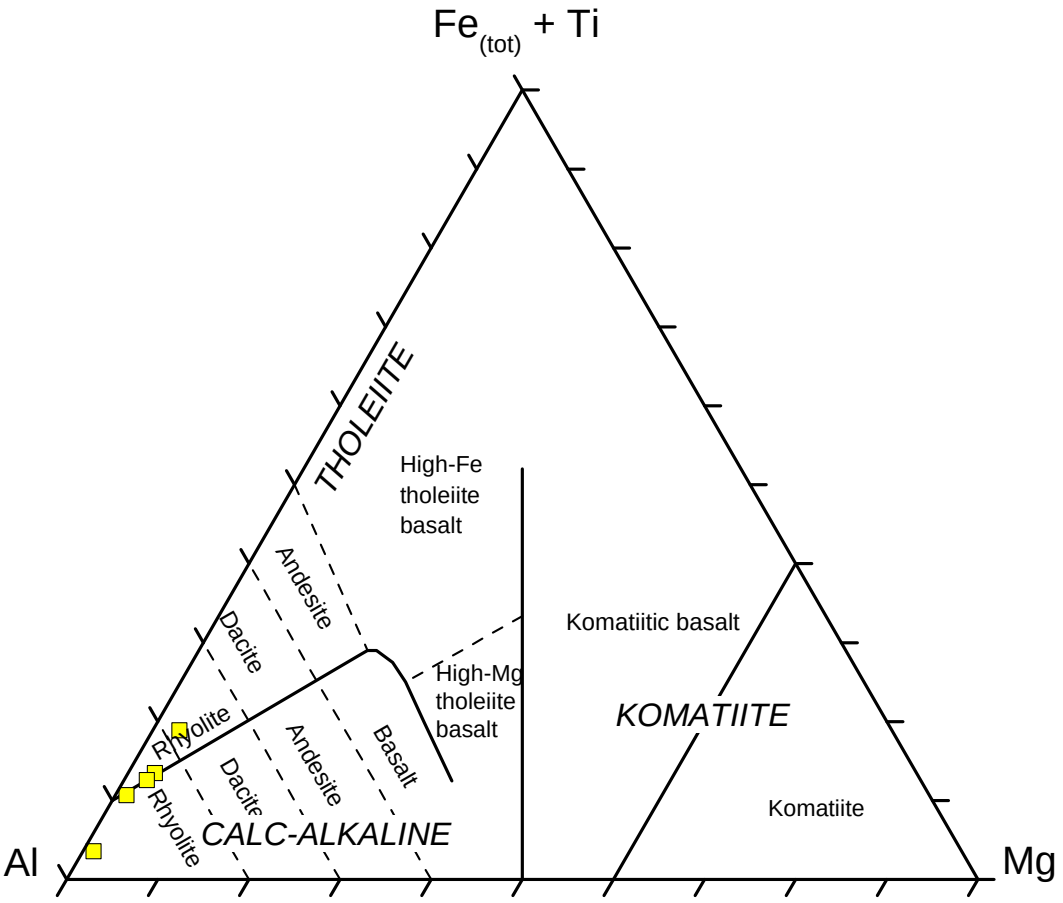


Figure 7.10 – Jensen cation plot of the Deguisier rhyolite.

Geochemical samples of the rhyolite demonstrate that they are at within the rhyolitic compositional field. Most analyses converge at the subdivision between the tholeiitic and calc-alkaline series, with one sample clearly part of the tholeiitic series and another as part of the calc-alkaline series. Further investigations of the magmatic affinity using a trace element diagram developed by Ross and Bédard (2009) also fail to attribute a specific series to the rhyolite. Specifically, samples span the tholeiitic to transitional field. Furthermore, the use of trace elements to define a magmatic affinity further restricts the number of available analyses to a total of 3, therefore invalidating any interpretations stemming from a lack of a sound statistical representation. The convergence in magmatic affinities is considered normal since

evidently the rhyolitic rocks are not in their pristine state. Nonetheless, since the rhyolite is considered to be related to both the basalt and andesite to dacite units, it can therefore be assumed that the rhyolite is from the same subalkaline trend.

Another general classification, using the TAS diagram of Le Maitre et al. (1989) demonstrates that all of the analyses also plot in the subalkaline rhyolitic field (see Figure 7.11). Included within the general classification is the division of the alkaline and subalkaline fields following the subdivision trend proposed by Irvine and Baragar (1971).

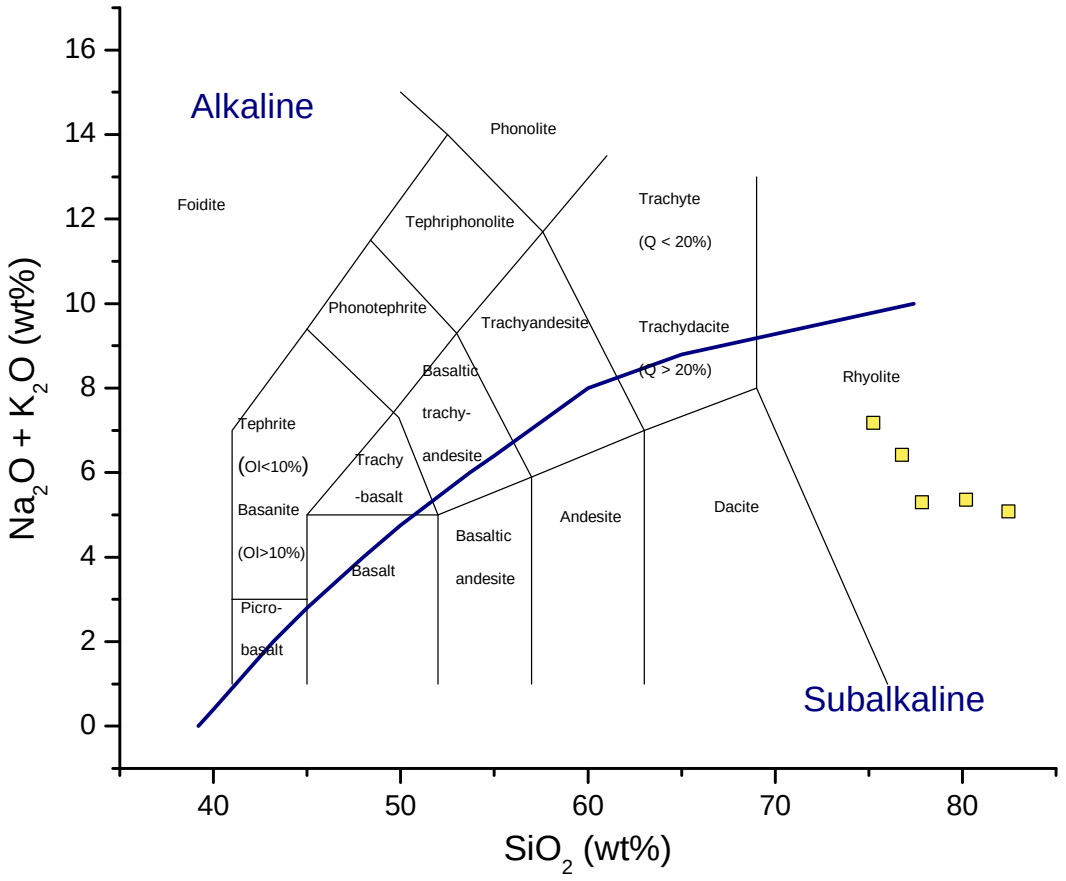


Figure 7.11 – Analyses of the Deguisier rhyolite unit illustrated in the TAS classification scheme for volcanic rocks of Le Maitre et al. (1989). Also shown in the figure is the dividing boundary for alkaline and subalkaline volcanic rocks (blue line) of Irvine and Baragar (1971).

CIPW norm

Results from the CIPW calculation are qualitative since the rhyolite has been subjected to hydrothermal alteration as well as regional metamorphism. Nonetheless, since only one thin section of the rhyolite was observed, the CIPW norm does provide an opportunity to explore

its mineralogical assemblage. Since the amount of ferrous iron was not measured, a Fe_2O_3/FeO ratio of 0.5 was assumed for all samples based on the recommendation of Middlemost (1989).

The rhyolitic samples contained low amounts of volatiles (< 2.59% LOI). Consequently, volatiles were included when calculating the norm. The resulting normative mineralogy is presented in Table 7.11.

Table 7.11 – CIPW normative mineralogy of the Deguisier rhyolite. Normative mineralogy is presented in weight %. A ratio (Fe_2O_3/FeO) of 0.5 as recommended by Middlemost (1989) was assumed for all samples.

Sample	05-A	JEB-10-09	D958143	D958269	94-00033
Quartz	48.17	38.18	55.63	52.47	57.04
Plagioclase	23.31	41.84	15.74	19.02	24.35
Orthoclase	17.97	12.47	20.86	18.91	13.53
Corundum	4.05	3.17	2.61	5.12	4.08
Hypersthene	0.82	0.37	0.72	0.75	0.36
Rutile	0.03	0.59	—	0.43	—
Ilmenite	1.92	1.27	1.75	1.56	0.19
Magnetite	—	—	1.27	—	0.41
Hematite	0.98	0.65	0.47	0.82	—
Apatite	0.9	1.16	0.97	0.88	0.02
Zircon	0.04	0.06	—	—	0.03
Pyrite	—	—	—	0.06	—
Calcite	0.83	0.06	—	—	—
Na_2CO_3	1	0.2	—	—	—
Total	100.02	100.02	100.02	100.02	100.01

The calculated normative mineralogy is typical of a rhyolitic mineralogical assemblage as confirmed in the literature. The mineralogy contains abundant normative quartz (38.18 - 54.04 wt%) which was distinguished as a few igneous crystals in thin section ($1\%_m$). The remaining normative quartz must therefore be a constituent of the feldspathic matrix as hypothesized in section 5.1. Other major normative mineral constituents are plagioclase (15.74 - 41.84 wt%) and orthoclase (13.53 - 20.86 wt%). Normative corundum, combined with potassium from orthoclase, should in fact be attributed to muscovite, now present as sericite. However, the limitations of the CIPW norm calculations excludes the possibility of any hydrous minerals. For this same reason, some of the hypersthene combined with corundum should be interpreted as biotite. Relicts of mafic minerals, now replaced by skeletal magnetite, quartz, occasional sericite and pyrite were observed in thin section. In terms of oxides, the rhyolite is ilmenite normative (0.19 - 1.92 wt%), with minor amounts of hematite (0.00 - 0.98 wt%) and occasionally magnetite (0.00 - 1.27 wt%). Accessory normative minerals are apatite, zircon and some calcite. Both oxides and accessory minerals were observed in thin section. Exceptions

are attributed to zircon which are now relicts and calcite which is of hydrothermal origin.

7.3.2 Incompatible trace elements

Normalizing factors employed are the chondritic values provided by McDonough and Sun (1995) (see Table 7.5). Although older analyses are typically discarded due to their incompleteness, high detection limit and precision error, the Deguisier rhyolite has only 3 samples which were analyzed for incompatible trace elements (samples: 05-A, JEB-10-09 and 94-00033). As such, the older analysis (sample: 94-00033) was kept. The chondrite-normalized pattern is presented in Figure 7.12.

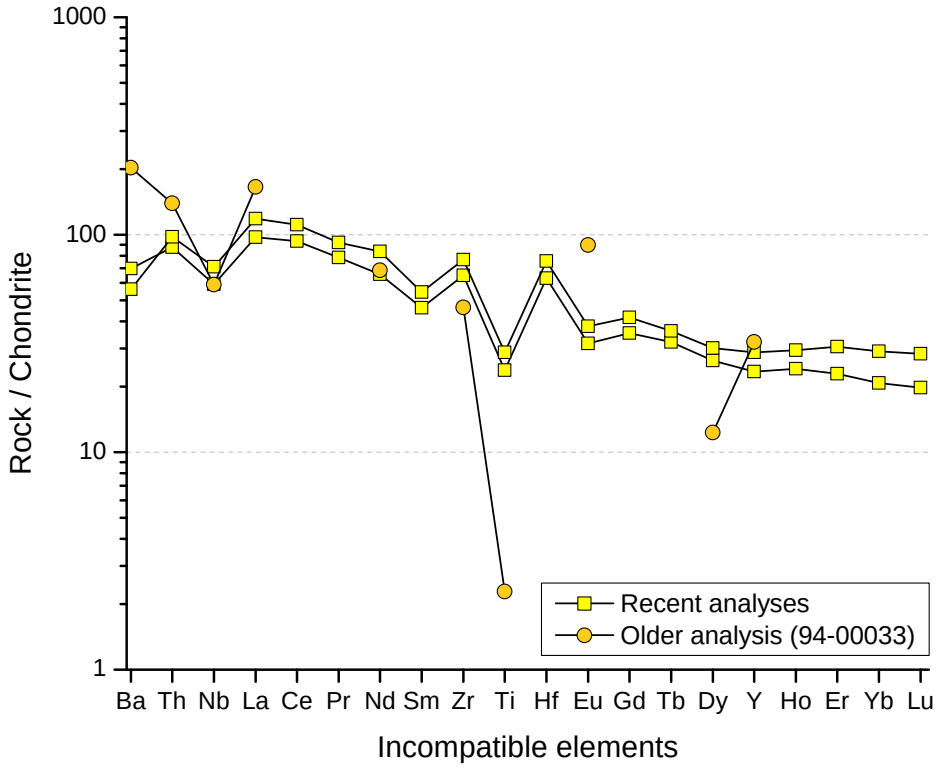


Figure 7.12 – Chondrite normalized incompatible trace element pattern for the Deguisier rhyolite. Normalizing factors are those of McDonough and Sun (1995) and are listed in Table 7.5.

Upon a first glance, the normalized incompatible trace element diagram is similar to that of the Deguisier basalt, and andesite to dacite unit. Specifically, the pattern possesses a slight decreasing trend ($[La/Yb]_{cn}$ = 4.67 - 4.08), LREE are enriched with again a negative Nb anomaly. Upon closer observations, the normalized pattern is remarkably similar to the one obtained for the andesite to dacite, where the pattern also holds a slight negative Th

anomaly, and a Zf and Hf positive anomaly. Further investigations reveal that LILE are also enriched compared to chondritic values (not shown). However, as opposed to the basalt and andesite to dacite units, the rhyolite demonstrates much less of a discrepancy concerning LILE Ba. Specifically, least-altered samples have an average of 268.1 ppm Ba (n = 5), which when chondrite normalized yields a ratio of 111.2, nearly midway between the normalized values presented in Figure 7.12.

Interestingly, Ti demonstrates the largest variation where one sample (94-00033) demonstrates a depletion. Comparisons between TiO_2 values, including those from SOQUEM Inc., do not reveal any pattern where values range from 1.34 - 0.10 wt%. The cause for this discrepancy is not known, but further observation reveal that the eastern sample 94-00033 also has very low concentrations of V (2 ppm) compared to western samples 05-A and JEB-10-09 (49.79 ppm and 28.31 ppm respectively). Further investigations reveal that eastern samples possess a higher concentration of Ba (average: 427.06 ppm, n = 2) compared to western samples (average: 162.2 ppm, n = 3). It is known that V can substitute for Ti, and that Ba is principally contained in feldspar or biotite (replacing K), suggesting that this eastern rhyolite underwent a larger amount of fractionation of Fe-Ti oxides compared to the western rhyolite.

7.3.3 Rare earth elements

A total of 3 samples were analyzed for REE. However, one of them was performed in the 1990s and was therefore excluded as it is largely incomplete, possesses a high detection limit and precision error. The 2 remaining samples that were utilized are JEB-10-09 and 05-A. Normalizing-chondrite values utilized are those of McDonough and Sun (1995) and are given in Table 7.5. The chondrite normalized pattern of the rhyolite is presented in Figure 7.13.

Overall, both chondrite-normalized samples are quite similar. The normalized pattern and slope is also similar to the one obtained for the Deguisier basalt and andesite to dacite units. The similarity of the slope is expected as the rhyolite is related to the other units of the Deguisier Formation (see Section 7.6).

Specifics of the rhyolite are a $\sum$REE between 150 - 183 ppm which is higher than the best representative sample of the andesite to dacite unit (137.1 ppm). The chondrite-normalized REE patterns demonstrates a very small preferential enrichment of LREE over HREE. $[La]_{cn}$ values range from 97.3 - 118.6 while $[Lu]_{cn}$ values range from 19.5 - 27.9, yielding $[La/Lu]_{cn}$

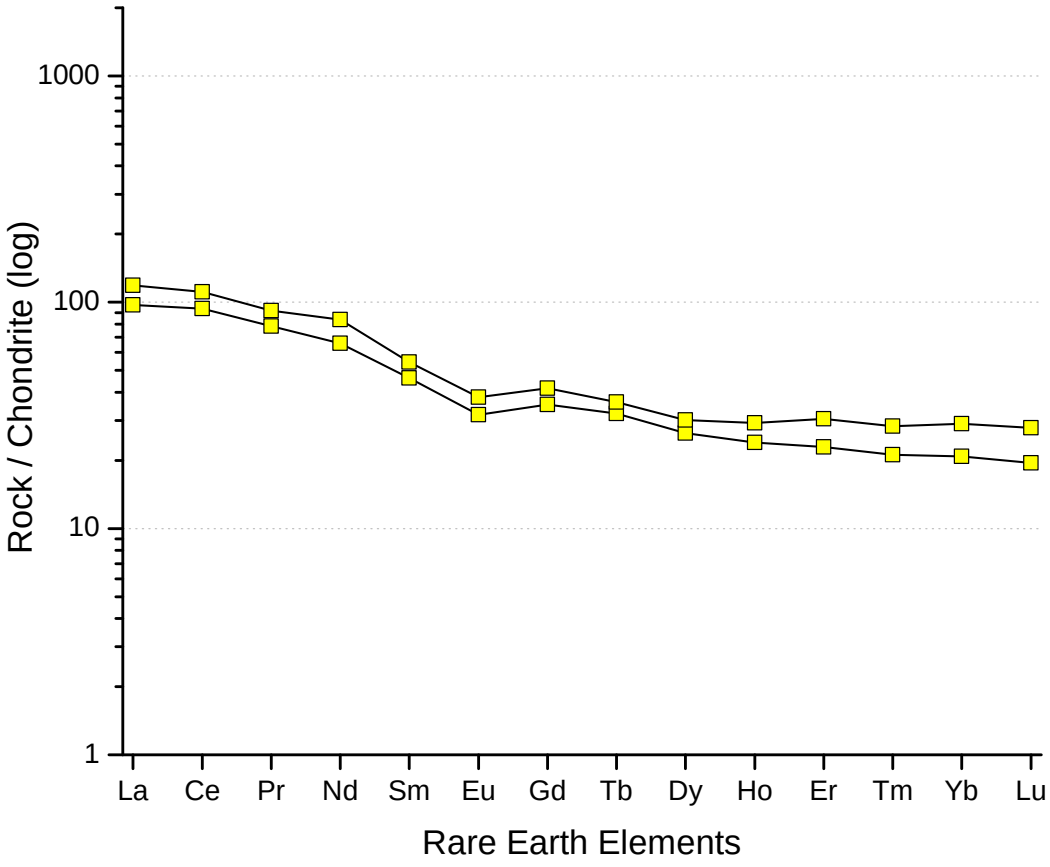


Figure 7.13 – Chondrite normalized REE pattern of the Deguisier rhyolite. Normalizing factors are those of McDonough and Sun (1995), listed in Table 7.5.

ratios between 4.25 - 4.99. A slight depletion in Eu can be directly observed from the normalized patterns. Measurements on the Eu anomaly reveal an Eu/Sm ratio between 0.26 - 0.27 revealing a small negative anomaly. The calculated extent of the anomaly ($[Eu/Eu^*]_{cn}$) reveal that it is on the order of 0.78 - 0.79. This small negative Eu anomaly could either be attributed to very limited plagioclase fractionation or to a high fO_2 or both (Henderson, 1984).

7.4 Lanaudière komatiites and komatitic basalts

Evidence of ultramafic lavas was unexpectedly found in a drill core from Cogema Canada Ltd. (Capus (1988), core: PC-01). The drill hole is located within the Duparquet conglomerate, 473 m southeast of the Central Duparquet 2 mine shaft and begins with polygenetic conglomerate followed by wacke, sandstone and mudrock. Mylonites tend to occur in proximity to, or at the contact between the Duparquet Formation and the Lanaudière Formation. The contact between the two is recorded at a depth of approximately 136 m (azimuth: 0.0°, dip: 50.0°). Following the contact are komatitic basalts and komatiites.

Details from the drill core log mention the presence of spinifex horizons extending for < 7 m. These rocks have a komatiitic composition. Komatitic basalts on the other hand are pillow lavas, flow breccias and include only minor spinifex texture.

A total of 13 geochemical samples were analyzed following the conglomerate-komatiite contact, up to a depth of 180 m. The unnormalized average SiO_2 is of 45.69 wt% and is accompanied by a strong marked depletions in alkalies, alumina and a marked increase in MgO in comparison to the basalts of the area. All geochemical samples are presented in Table 7.12. Altered or samples that correspond to a brecciated zone in the drill core log have been specially marked in the Table. A comparison using the average normalized oxide composition between the least-altered samples of the Deguisier basalt and Lanaudiète komatiites and komatitic basalts is presented in Table 7.13.

The least-altered samples were plotted on a Jensen diagram (see Figure 7.14) and demonstrate that the bulk of the samples are komatitic basalt in composition with a few crossing the boundary line into the komatiite compositional field. This marks the first evidence of Lanaudière komatiites and komatitic basalts located underneath the Duparquet sediments in the Beattie area.

Table 7.12 – Major and trace element analyses for the Lanaudière komatiites and komatitic basalts. Major oxides are presented in weight% and trace elements are all given in ppm except for Au which is given in ppb. Analyses presented have not been normalized.

Sample	**198811**	**198812**	**198813**	**198814**[1]	**198815**[1]	**198816**	**198817**	**198818**
Depth (m)	136.35	140	140.6	141.56	141.95	143.65	144.39	151.24
SiO_2	47.00	47.00	42.00	45.00	45.00	50.00	45.00	49.00
TiO_2	0.25	0.31	0.35	0.29	0.13	0.32	0.42	0.37
Al_2O_3	5.45	5.50	5.75	6.13	3.90	6.99	6.92	7.30
Fe_2O_3t	8.64	8.48	8.53	8.17	4.24	8.78	8.62	10.31
MnO	0.12	0.16	0.18	0.16	0.15	0.14	0.16	0.17
MgO	16.69	13.77	12.14	8.05	5.17	13.52	12.87	11.92
CaO	4.79	7.31	8.82	11.97	19.60	3.91	6.28	6.68
Na_2O	0.01	0.01	0.03	0.02	0.01	0.01	0.01	0.02
K_2O	0.01	0.01	0.01	0.01	0.01	0.01	0.01	0.01
P_2O_5	0.02	0.03	0.03	0.03	0.01	0.03	0.04	0.04
CO_2	—	—	—	—	—	—	—	—
S	—	—	—	—	—	—	—	—
LOI	—	—	—	—	—	—	—	—
Total	82.98	82.58	77.84	79.83	78.22	83.71	80.33	85.82
Ag	2.00	1.00	1.00	0.50	0.50	2.00	2.00	2.00
Au	3.00	3.00	5.00	3.00	10.00	3.00	3.00	15.00
Ba	2.00	3.00	5.00	7.00	6.00	3.00	2.00	4.00
Cr	1124.00	861.00	949.00	816.00	334.00	1319.00	1251.00	1366.00
Cu	48.00	51.00	50.00	103.00	164.00	55.00	39.00	80.00
Nb	5.00	3.00	2.00	1.00	1.00	5.00	4.00	3.00
Rb	25.00	25.00	25.00	25.00	25.00	25.00	25.00	25.00
Sr	21.00	23.00	40.00	80.00	144.00	8.00	22.00	35.00
Y	7.00	8.00	9.00	9.00	8.00	7.00	11.00	10.00
Zn	60.00	237.00	301.00	124.00	155.00	78.00	69.00	71.00
Zr	9.00	18.00	20.00	24.00	17.00	15.00	26.00	24.00

[1] = Samples in brecciated zone

Table 7.12 Continued

Sample	**198819***	**198820***	**198821**	**198822**	**198823**
Depth (m)	153.78	159.6	170.3	170.99	180.68
SiO_2	57.00	35.00	48.00	47.00	37.00
TiO_2	0.54	0.16	0.42	0.50	0.30
Al_2O_3	9.65	3.29	7.31	8.18	5.81
Fe_2O_3t	7.81	3.92	9.72	10.90	7.93
MnO	0.15	0.19	0.16	0.01	0.18
MgO	7.80	5.30	13.50	18.10	13.50
CaO	5.68	29.76	5.51	6.68	10.93
Na_2O	2.48	0.01	0.02	0.05	0.02
K_2O	0.03	0.01	0.01	0.01	0.02
P_2O_5	0.04	0.01	0.05	0.04	0.02
CO_2	—	—	—	—	—
S	—	—	—	—	—
LOI	—	—	—	—	—
Total	91.18	77.65	84.7	91.47	75.71
Ag	2.00	0.50	2.00	—	0.50
Au	3.00	3.00	3.00	—	1.00
Ba	13.00	6.00	3.00	—	6.00
Cr	497.00	350.00	1107.00	—	1694.00
Cu	75.00	19.00	63.00	—	64.00
Nb	3.00	1.00	5.00	—	4.00
Rb	25.00	25.00	25.00	—	25.00
Sr	67.00	213.00	21.00	—	108.00
Y	14.00	6.00	10.00	—	8.00
Zn	56.00	33.00	63.00	—	621.00
Zr	31.00	9.00	25.00	—	14.00

* = Altered samples

Table 7.13 – Comparison between the average normalized geochemistry of the Deguisier basalt (21 samples) and the Lanaudière komatiite (9 samples).

	Deguisier basalt	Komatiite
SiO_2	50.77	55.25
TiO_2	1.83	0.43
Al_2O_3	14.23	7.93
Fe_2O_3t	15.90	10.97
MnO	0.26	0.18
MgO	5.66	16.89
CaO	8.41	8.23
Na_2O	2.27	0.02
K_2O	0.37	0.01
P_2O_5	0.14	0.04

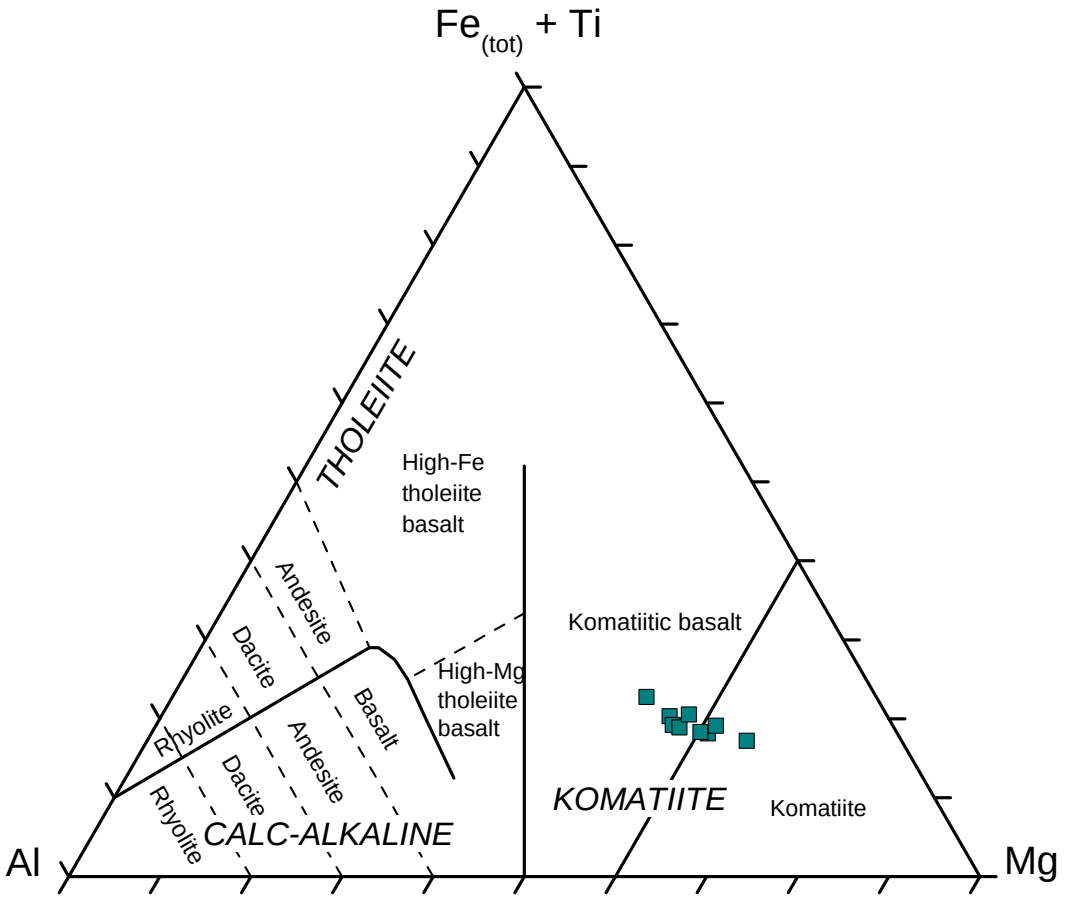


Figure 7.14 – Jensen cation plot of the Lanaudière komatiite and komatitic basalt.

7.5 Gabbro

The oldest plutonic rocks within the Beattie area belong to the gabbro. A few initial chemical properties were discussed by Goutier and Lacroix (1992). Since then 13 additional analysed samples were added to the database. This section will therefore serve as an update and will add detail to the geochemical characteristics of the gabbro.

Methodology

Representative samples were obtained from Osisko Mining Corporation, MRN, Gold Fields Resources Canada and by the author. Samples from SOQUEM Inc. once were again excluded, so that only 6 samples remain for the lithogeochemical investigation. Consequently, both least-altered and altered samples have been kept for discussion taking necessary precautions with altered samples will be taken and discussed where appropriate (see Table 7.14). Additionally, all gabbro analyses may be consulted in Appendix D.

Akin to the Deguisier units, the major and trace elements were corrected for LOI and are therefore on a 'dry' basis unless otherwise specified.

7.5.1 Major and compatible trace elements

General classification

Geochemical samples of the gabbro have been plotted in the Jensen cation plot and are presented in Figure 7.15. Although the plot is designed for volcanic rocks, it can be extended to plutonic rocks as long as one is certain that the materials represent liquid compositions. In general, small intrusions have not undergone much differentiation, and all evidence is that the small, $<$ 300 m thick, lens of gabbro in the Beattie area generally appear homogeneous (disregarding subsequent deformation and hydrothermal alteration).

Most gabbro samples plot in the high-Fe basaltic field which corresponds to the general volcanic equivalent of a gabbro. However, there is a large discrepancy into which compositional field the individual samples fall into. Proximal (altered) gabbro samples located at $<$ 50 m from the Beattie syenite and/or D_2 faults demonstrate the highest variability, whereas distant(least-altered) samples, located at $>$ 50 m, do not reflect this variation and plot in the high-Fe basaltic field. A more detailed discussion of this hydrothermal alteration characteristic

Table 7.14 – Major and trace elements analyses of specimens of the gabbro. Major oxides are presented in wt% and trace elements are all given in ppm with the exception of Au which is given in ppb. Analyses presented have not been corrected for LOI.

Sample	**2003031904****	**D958257**	**JG-5127-GW***	**2003031931***	**184109**	**3286**
Institution	MRN	Osisko	U of 0	MRN	MRN	GFRC
Year	2003	2010	2010	2003	1994	1981
SiO_2	44.94	49.10	43.12	—	41.50	47.70
TiO_2	1.64	1.57	0.41	—	1.18	1.40
Al_2O_3	15.52	11.60	12.39	—	11.90	13.50
Fe_2O_3t	12.04	13.70	6.67	—	13.44	15.10
MnO	0.18	0.21	0.11	—	0.19	0.20
MgO	2.01	4.03	6.81	—	5.77	6.47
CaO	5.08	5.96	8.46	—	7.99	8.47
Na_2O	0.46	3.33	0.20	—	1.52	2.79
K_2O	9.22	1.27	4.24	—	1.39	0.23
P_2O_5	0.47	0.15	0.04	—	0.07	0.12
[a]CO_2	7.07	—	16.93	—	—	0.50
[a]S	5.12	< 0.01	0.02	—	—	—
[b]LOI	8.50	3.10	17.20	—	14.20	3.00
Total	100.06	94.02	99.65	—	99.15	98.98
Ag	0.9	< 0.2	< 0.1	0.3	—	—
As	4986.6	2	54.1	9911.6	—	—
Au	3327.5	< 5	0.9	5562.9	—	—
Ba	420	*179.13*	318	418.4	49.00	140.00
Bi	0.2	< 2	< 0.1	< 0.1	—	—
Cd	< 0.1	< 0.5	< 0.1	< 0.1	< 2.00	—
Ce	74.6	—	7.6	12.6	14.00	—
Co	22	29	38.5	41.8	46.00	—
Cr	—	*136.84*	711.57	—	208.00	620.00
Cs	4.3	—	8.8	2.7	—	—
Cu	99.7	36	59.4	27.7	92.00	—
Dy	10.88	—	1.66	2.02	< 1.00	—
Er	6.11	—	0.97	1.24	—	—
Eu	2.83	—	0.44	0.58	< 1.00	—
Ga	25.7	< 10	11.5	19.9	15.00	—
Gd	10.5	—	1.44	1.41	—	—
Hf	8.2	—	0.8	2.4	—	—
Hg	0.58	< 1	0.04	2.66	—	—
Ho	2.18	—	0.32	0.41	—	—
La	35.1		3	5.3	3.00	—
Lu	0.91	—	0.14	0.16	—	—
Mo	4.3	< 1	0.2	7.9	—	—
Nb	18.9	—	1.2	3.1	4.00	—
Nd	51.4	—	4.7	7.6	—	—
Ni	2.9	24	57.5	46.1	75.00	—
Pb	11.9	< 2	0.8	23.2	< 12.00	—
Pr	10.16	—	0.99	1.6	< 10	—
Rb	170.9	—	174.4	97.7	43.00	—
Sb	12.7	< 2	0.9	19.3	—	—
Sc	24	—	31	—	42.00	—
Se	4.2	—	< 0.5	5.8	—	—
Sm	10.6	—	1.18	1.9	< 2.00	—
Sn	< 1	—	< 1	< 1	10.00	—
Sr	279.5	—	465.9	537.1	50.00	—
Ta	1.1	—	< 0.1	0.2	5.00	—
Tb	2.11	—	0.25	0.38	—	—
Th	2.5	—	0.4	0.5	< 3.00	—
Tl	0.8	< 10	0.2	1.3	—	—
Tm	0.93	—	0.14	0.19	—	—
U	1	—	0.1	1.2	—	—
V	120	—	156	333	323.00	—
W	92.9	—	0.5	82.6	—	—
Y	64.7	—	8.2	11.9	30.00	—
Yb	5.84	—	0.91	1.28	—	—
Zn	81	85	27	36	88.00	—
Zr	307.7	—	32.4	71.3	86.00	70.00

*****	*Altered samples*	******	*Sample from a xenolith*
GFRC	*Gold Fields Resources Canada*		
[a]	*Not included in totals*	[b]	*Loss on ignition at 1000° C*
< Red	*Values below detection limit*	*Blue*	*Values calculated from oxides*

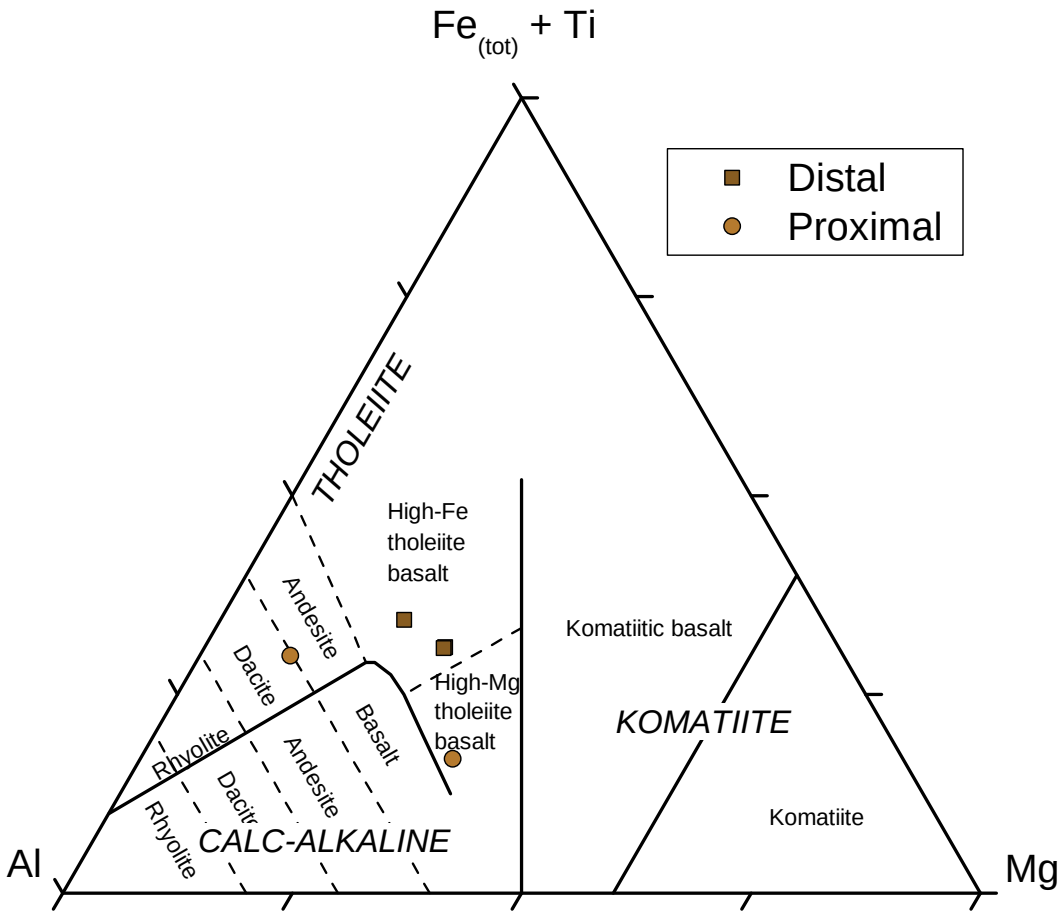


Figure 7.15 – Jensen cation plot of all samples of the gabbro. Distal samples are located $>$ 50 m to a contact with the Beattie syenite and/or a D_2 fault. Proximal samples are therefore located $<$ 50 m.

will be addressed later (see Section 8.2.1).

Another subjective method of classifying the gabbro lies in the use of the TAS diagram for plutonic rocks of Cox et al. (1979) which is presented in Figure 7.16. Gabbro samples generally plot within the gabbro field. Distinguishing between the least-altered (distal) from altered (proximal) samples, permits the observation that least-altered samples mostly plot in the gabbro field, whereas altered samples demonstrate an enrichment in silica and alkalies, and plot in other compositional fields.

The alkalinity of the gabbro is also illustrated in Figure 7.16, following the subdivision trend defined by Irvine and Baragar (1971). The majority of the samples are subalkaline with one exception. This particular gabbro sample was taken approximately 1 m from a contact zone and is thus not representative of the series since it underwent extensive hydrothermal

alteration.

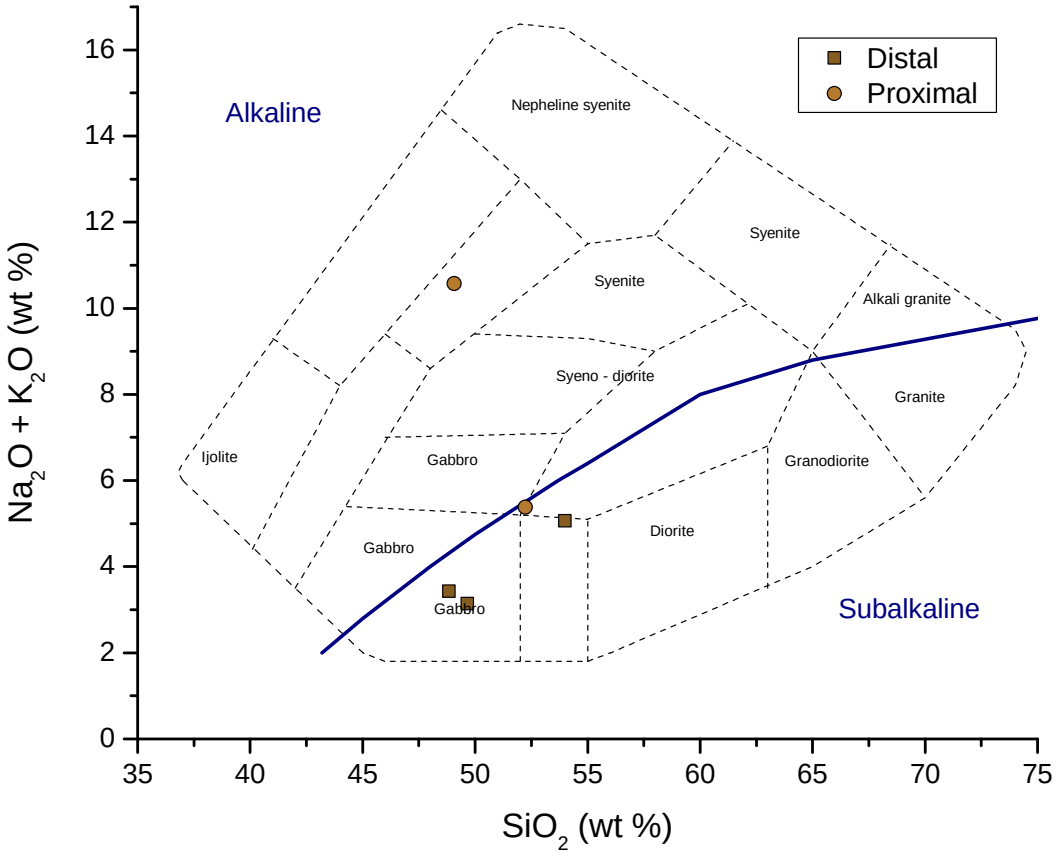


Figure 7.16 – Analyses of the gabbro illustrated in the TAS classification for plutonic rocks of Cox et al. (1979). Also shown in the figure is the alkaline vs subalkaline division (blue line) from Irvine and Baragar (1971). Distal samples are located $>$ 50 m from a contact with the Beattie syenite and/or a D_2 fault. Proximal samples are therefore located $<$ 50 m.

CIPW norm

Although it is unconventional to calculate the normative mineralogy of a plutonic rock, the CIPW norm offers a mineralogical assemblage that could not be determined due a lack of thin sections. The use and limitations of this calculation can be found in the corresponding Deguisier basalt section. Since the amount of ferrous iron was not measured, a Fe_2O_3/FeO ratio of 0.15 was assumed for all samples based on the recommendation of Middlemost (1989).

The calculated normative mineralogy of the least-altered samples is given in Table 7.15. All distal samples had very low concentrations of volatiles (i.e., S and CO_2) and hence were kept in the calculation.

Table 7.15 – CIPW normative mineralogy of the least-altered gabbro samples. Normative mineralogy is presented in weight %. A ratio (Fe_2O_3/FeO) of 0.15 as recommended by Middlemost (1989) was assumed for all samples.

Sample	D958257	184109	3286
Quartz	3.27	—	—
Plagioclase	45.83	41.03	49.62
Orthoclase	8.33	9.81	1.42
Diopside	14.63	17.49	12.57
Hypersthene	20.87	20.31	27.81
Olivine	—	5	0.80
Ilmenite	3.32	2.68	2.79
Magnetite	3.32	3.49	3.45
Apatite	0.39	0.19	0.3
Zircon	—	0.01	0.01
Chromite	0.03	0.04	0.13
Pyrite	0.02	—	—
Calcite	—	—	1.21
Total	100.01	100.05	100.11

All the samples are hypersthene normative, one is quartz normative while the remainder are olivine normative. Plagioclase is the dominant feldspar at $>$ 40 wt% norm. Normative pyroxenes are at nearly equal proportions between normative diopside and hypersthene. Orthoclase on the other hand is much less abundant and is considered an uncommon mineral in gabbros. Rather, orthoclase components should be interpreted as biotite. This discrepancy is caused by the CIPW norm calculation where hydrous components are omitted. For this same reason, hornblende is not present in the normative gabbro mineralogy. It stands to reason that some proportions of pyroxenes therefore belong to hornblende. All analyses are ilmenite and magnetite normative in nearly equal proportions. Accessory normative minerals are apatite, zircon, chromite. Both pyrite and calcite are subsequent hydrothermal additions.

7.5.2 Incompatible trace elements

Unfortunately, only 5 samples were analyzed for incompatible elements. Two of them, are older samples and were excluded since they are largely incomplete, have a high detection limit and precision error. From the 3 remaining samples, one originates from a xenolith within the Beattie syenite in the area of the Donchester mine (sample: 2003031904) and the other 2 are adjacent to a syenitic contact (sample: 2003031931 and JG-5127-GW). Nonetheless, these samples were retained and have been chondrite-normalized using McDonough and Sun (1995) values (see Table 7.5). The chondrite normalized pattern is presented in Figure 7.18.

The gabbro demonstrates the greatest variability of incompatible trace element concentra-

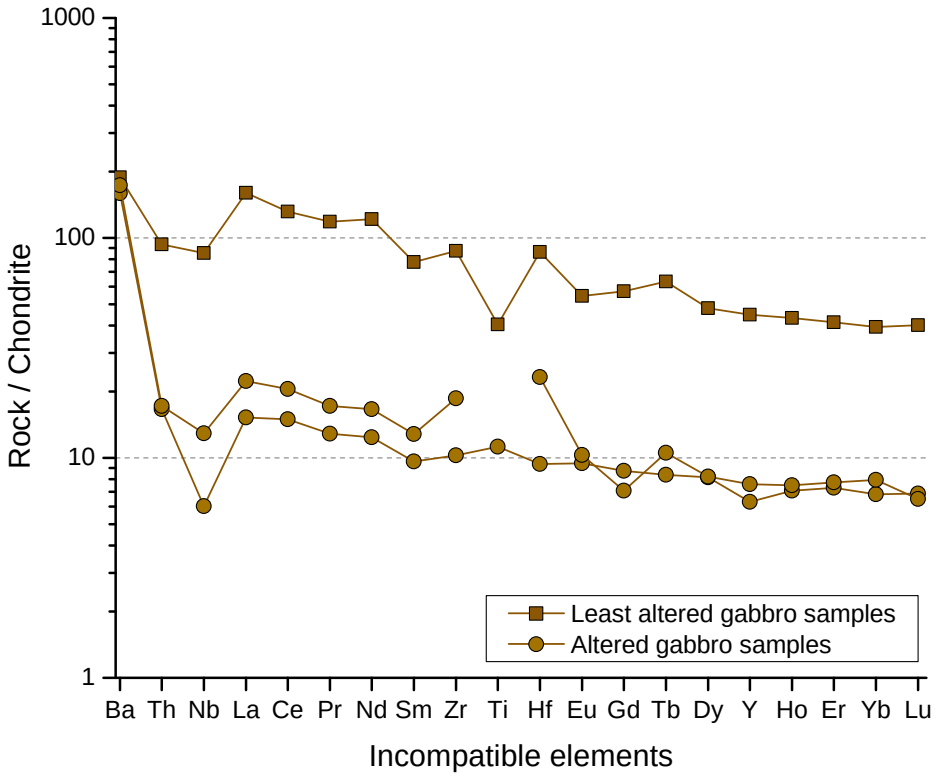


Figure 7.17 – Chondrite normalized incompatible trace element pattern of the gabbro. Normalizing values are those of McDonough and Sun (1995) listed in Table 7.5.

tions in the Beattie area. Nonetheless, this has not affected the pattern established by the unit (See Figure 7.17). The sample showing the highest abundance of REE is from a gabbro xenolith located in proximity of the Donchester mine (sample: 2003031904). The 2 depleted patterns, La $<$ 30 times chondrite, belong to gabbros adjacent to a syenitic contact. Both samples are located close to the Central Duparquet 2 mine shaft. Coincidentally, this same concentration variation is also reflected with the patterns of the Deguisier andesite to dacite. It stands to reason that the best representative gabbro REE pattern is the enriched sample since the andesite to dacite samples located away from the Beattie syenite and D_2 faults possessed the same concentration as the xenolith.

The best representative normalized gabbro sample demonstrates the same pattern as with all the units of the Deguisier Formation. Specifically, the normalized pattern demonstrates a slight decreasing trend ($[La/Yb]_{cn} = 4.1$), an enrichment of the LREE and a negative Nb anomaly. Additionally, LILE are enriched compared to chondritic values (not shown). The pattern also demonstrates a slight negative Th anomaly and positive Zr and Hf anomalies, akin to the Deguisier andesite to dacite and rhyolite units.

7.5.3 Rare earth elements

The same 3 incompatible trace elements samples were kept for REE. They have been chondrite-normalized using McDonough and Sun (1995) values (see Table 7.5). The chondrite normalized pattern is presented in Figure 7.18.

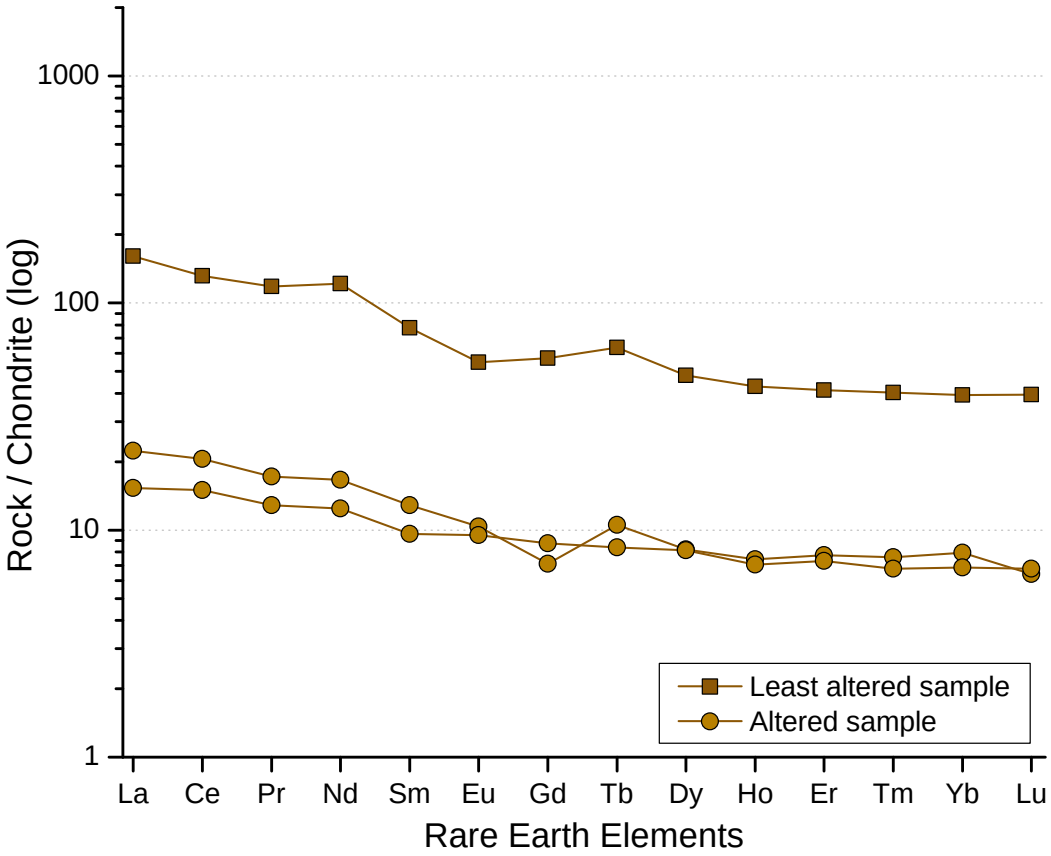


Figure 7.18 – Chondrite normalized REE patterns of the gabbro. Normalizing values are those of McDonough and Sun (1995) listed in Table 7.5.

The best representative gabbro sample has a $\sum$REE of 243 ppm. The chondrite-normalized patten demonstrates a very small enrichment of LREE over HREE. Measurements on this enrichment reveal that $[La]_{cn}$ value is 160.5 and $[Lu]_{cn}$ is 39.5, yielding $[La/Lu]_{cn}$ ratio of 4.1. Furthermore, the gabbro demonstrates a small negative Eu anomaly (see Figure 7.18). The ratio of Eu/Sm is of 0.27. The extent of the anomaly ($[Eu/Eu^*]_{cn}$) is 0.81, confirming a very small negative Eu anomaly.

The REE contents of the best representative gabbro sample carries the same subalkaline signature as demonstrated by the units of the Deguisier Formation. To reiterate, literature values for tholeiitic basalts are a $\sum$REE between 15.2 - 322 ppm, a $[La/Lu]_{cn}$ ratio of 0.5 -

7.6 and a Eu/Sm ratio between 0.16 - 0.55 (Henderson, 1984). The values obtained for the gabbro are within the mid-ranges of those given by literature. Altered samples on the other hand fall within the low ranges. The low-ranging values from these samples are expected as they were subjected to hydrothermal alteration.

7.6 The Deguisier Formation

The tholeiitic basalt, andesite to dacite and rhyolite units compose the Deguisier Formation. Their individual geochemical characteristics have already been addressed above. This now brings the possibility of exploring the chemical properties of the Formation as a whole. This section is 2-fold: 1) to the relationship(s) between the Formation and synvolcanic plutonism, and 2) to characterize of the evolution and the tectonic setting of the Formation.

7.6.1 Relationship between the gabbro and the Deguisier Formation

Little is known of the relationship, between the gabbro and the Deguisier Formation. Commonly, field relations and/or U-Pb zircon dating can used to establish temporal links, but neither of the lithologies have been dated. Consequently, other methods are required. In this particular case, comparisons between the trace elements patterns (i.e., REE and normalized incompatible trace element plots) are extremely useful. Concerns raised by alteration can be mitigated since alteration has only affected elemental concentrations and not their overall pattern.

The first comparison used is by comparing REE patterns. The chondrite normalized REE patterns of representative least-altered samples from each available unit have been combined with that of the gabbro. The comparison is presented in Figure 7.19.

Caution should be exercised when comparing the data in Figure 7.19 stemming from a limited number of samples. The variation in abundance is a result of alteration, but as previously mentioned, it has not affected the overall REE pattern. REE patterns are extremely similar to one another, holding the same subalkaline signature. Slopes ($[La/Lu]_{cn}$) and magnitudes of the Eu anomaly are additionally extremely similar. The exact values for comparative purposes have been listed in Table 7.16. This consistency holds well with the hypothesis that there exists a genetic relation between the gabbro and Deguisier Formation through the same parental magmatic source.

Another comparison can be made using the incompatible trace elements diagram. The best representative samples from each unit have been averaged (if possible) and are presented in Figure 7.20.

The chondrite normalized incompatible element patterns demonstrate a striking similarity.

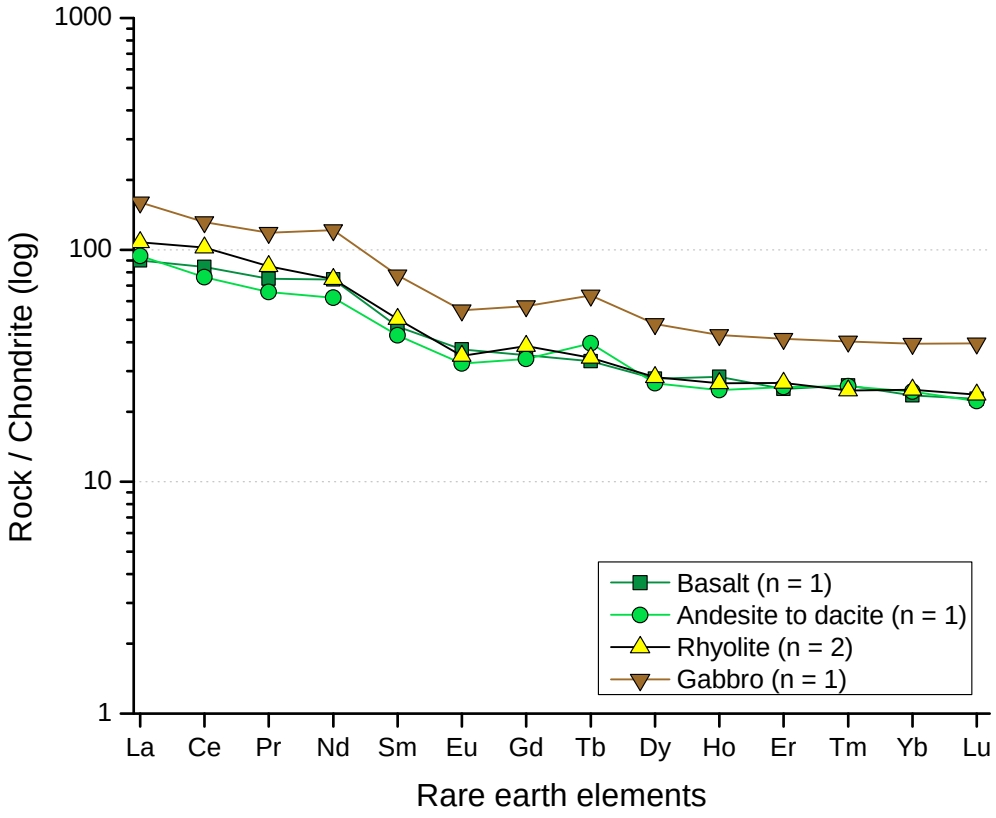


Figure 7.19 – Chondrite-normalized incompatible trace element pattern for the Deguisier Formation including the gabbro. Normalizing values are those of McDonough and Sun (1995) listed in Table 7.5.

The abundance variation observed in Ba is the result of subsequent hydrothermal alteration.

Both the REE and normalized incompatible trace element patterns support the hypothesis that the gabbro is likely related to the same parental magmatic source that produced the Deguisier Formation. Field relationships demonstrate lenticular bodies of gabbro alongside every unit of the Deguisier Formation. The gabbro also intrudes the 2718 ±2 (Zhang et al., 1993) Ma Lanaudière Formation supporting a post-chronous relationship with both the Deguisier and Lanaudière Formations. Abundance variations in the normalized incompatible trace element plot do not exhibit strong fractionation trends with respect to the Deguisier units. Furthermore, the normalized gabbro pattern possesses the same Zr and Hf enrichment only seen in the younger Deguisier Formation units. Consequently, the gabbro intruded immediately post-chronously with respect to the Deguisier and Lanaudière Formations. Therefore, the gabbro analyzed in the Beattie area can be classified as synvolcanic and constrained at an age between 2717 - 2716 Ma. Caution should however be exercised since there could be younger

Table 7.16 – Comparison of REE properties between units of the Deguisier Formation and the gabbro. Literature values for tholeiites have also been included from Henderson (1984).

Lithology	∑REE (ppm)	$[La/Lu]_{cn}$	Eu/Sm	$[Eu/Eu^*]_{cn}$
Basalt	148.7	3.94	0.30	0.91
Andesite to Dacite	137.1	4.2	0.29	0.84
Rhyolite	150.4 - 182.7	4.25 - 4.99	0.26 - 0.27	0.78 - 0.79
Gabbro	243	4.1	0.27	0.81
Tholeiites[1]	10 - 262	0.4 - 7.3	0.16 - 0.55	variable

[1] = Island arc and back-arc tholeiites

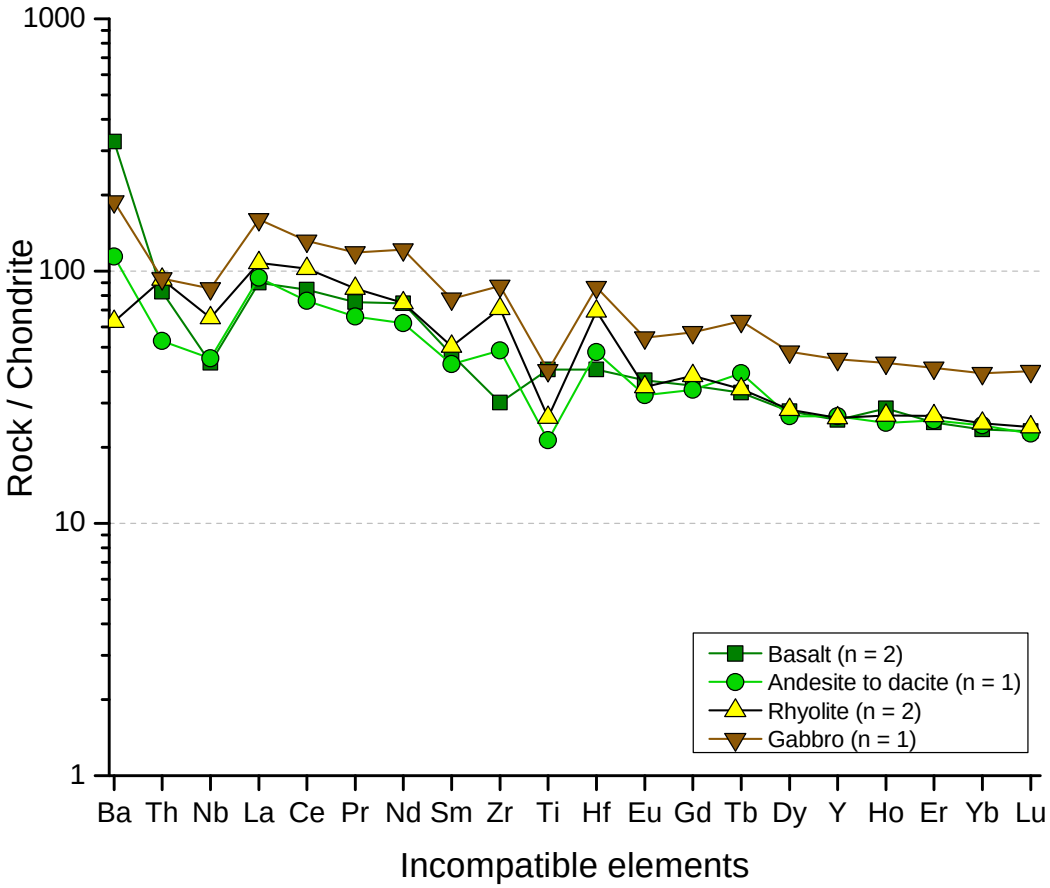


Figure 7.20 – Chondrite-normalized incompatible trace element pattern for the Deguisier Formation including the gabbro. Normalizing values are those of McDonough and Sun (1995) listed in Table 7.5.

gabbro intrusions in the area. Such examples have been documented in the eastern portions of the Duparquet area where gabbro lenses intrude into the younger Duparquet conglomerate (Goutier and Lacroix, 1992). These younger gabbro lenses have not been documented in the Beattie area, but considering the possibility of younger intrusions, the synvolcanic designation for the gabbro requires further testing.

7.6.2 Evolution and tectonic setting

The Deguisier Formation in the Beattie area is composed by a suite of volcanic tholeiitic rocks. The suite begins, to the north, with basalts extending to a thickness of approximately 600 m (0 m corresponding to the northern beginning of the Beattie area). They are overlain by andesite to dacite with a thickness of < 250 m. The andesites and dacites are accompanied by comparatively thin rhyolite lenses with a thickness of < 120 m. Together all the units form a complete tholeiitic suite from the basal basalts to the upper rhyolite. This is best illustrated with the Jensen cation plot presented in Figure 7.21.

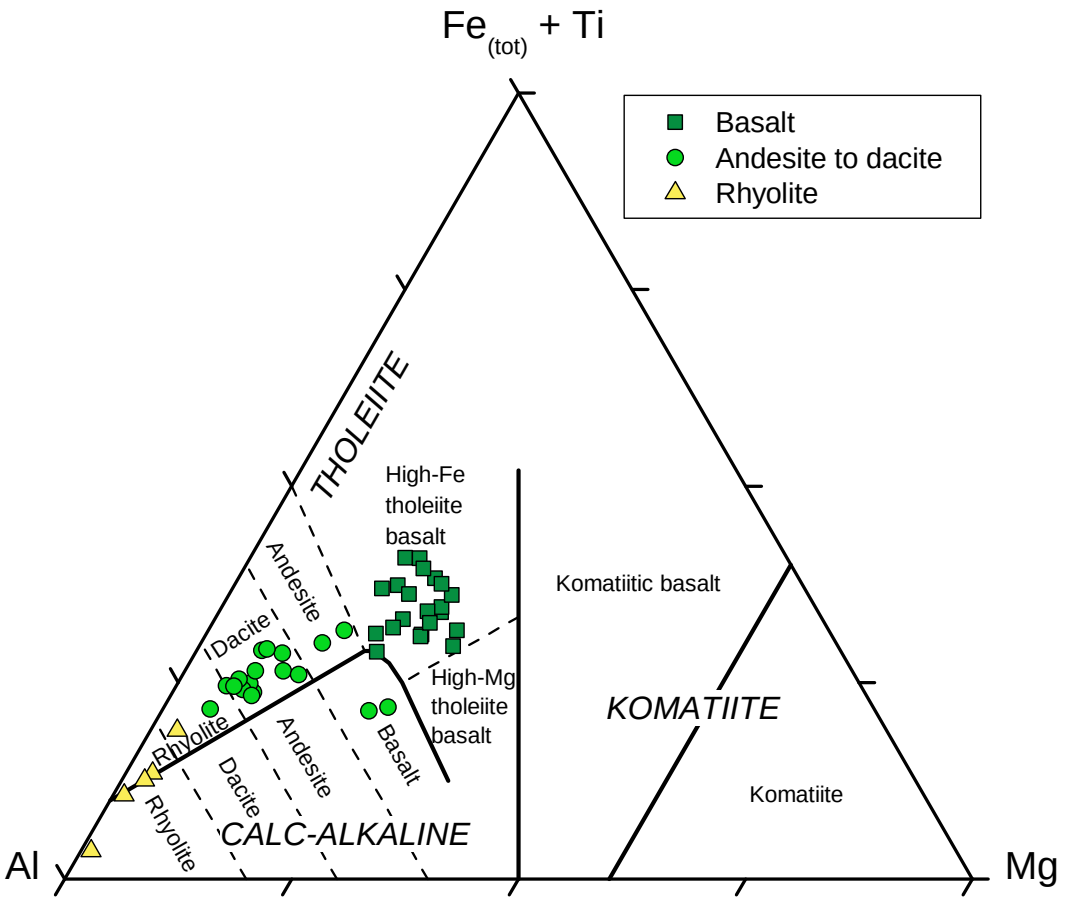


Figure 7.21 – Jensen cation plot of all the Deguisier Formation samples.

Further proof that the Deguisier basalt, andesite to dacite and rhyolite are part of the same tholeiitic suite is seen in the normalized incompatible trace elements plot presented in Figure 7.20. First and foremost, all the patterns exhibit the same gently decreasing trend with a slight enrichment of the LREE and a negative Nb anomaly. Another common element

is found in the LILE where values for each of the units are enriched compared to chondritic values.

The normalized incompatible trace element patterns of the Deguisier tholeiitic suite also presents sings of fractional crystallization. Specifically, the oldest of the units, the basalt, demonstrates a fairly flat pattern. The younger andesite to dacite unit pattern demonstrates a slight Th depletion and a Zr and Hf enrichment. This same elemental enrichment/depletion is again found in the youngest unit, the rhyolite. Progressing from the basalt to the rhyolite, the Th depletion and the Zr and Hf enrichment become accentuated, reflecting processes of fractional crystallization as the lavas of the Deguisier Formation evolved.

There exists numerous tectonic discrimination diagrams for rocks of basaltic to basaltic-andesitic composition. A diagram exploiting minor oxides will be used since most samples are incomplete and inconsistent in terms of trace elements analyzed. The amount of data available in the minor oxides will also help provide a clearer interpretation and will decrease any statistical error.

A diagram developed by Mullen (1983) permits the tectonic discrimination using basaltic samples. This diagram employs minor oxides: MnO, P_2O_5 and TiO_2 for the apices. Fortunately, these oxides have not been overly mobile during hydrothermal alteration combined with regional metamorphism (see Section 8.2). The diagram classifies the basalt into the MORB, island arc tholeiite (IAT), island arc calc-alkaline (CAB), seamount tholeiite (OIT) and seamount alkalic basalt (OIA). Limitations to this method of classification are that basaltic must contain between 45 - 54 wt% SiO_2. Field boundaries were empirically determined based on 507 published modern basalt analyses (Mullen, 1983). MnO and P_2O_5 have been scaled by a factor of 10 in order to expand the discrimination fields, although drawbacks include the amplification of the analytical error from 5 - 7%. Fortunately, this error amplification does not exceed the width of the fields. The resulting plot is presented in Figure 7.22.

Figure 7.22 demonstrates that the tectonic setting for the Deguisier basalt is divided between the MORB and IAT fields. Upon closer examination, the majority of the samples (64%) in the range plot distinctively in the IAT field. This division cannot bring a definite conclusion and only with the aid of the other units will it become clearer.

Unfortunately, discrimination diagrams for andesites and dacites are few. Furthermore, without major and minor elements, there is a lack of data. However, this lack is not encoun-

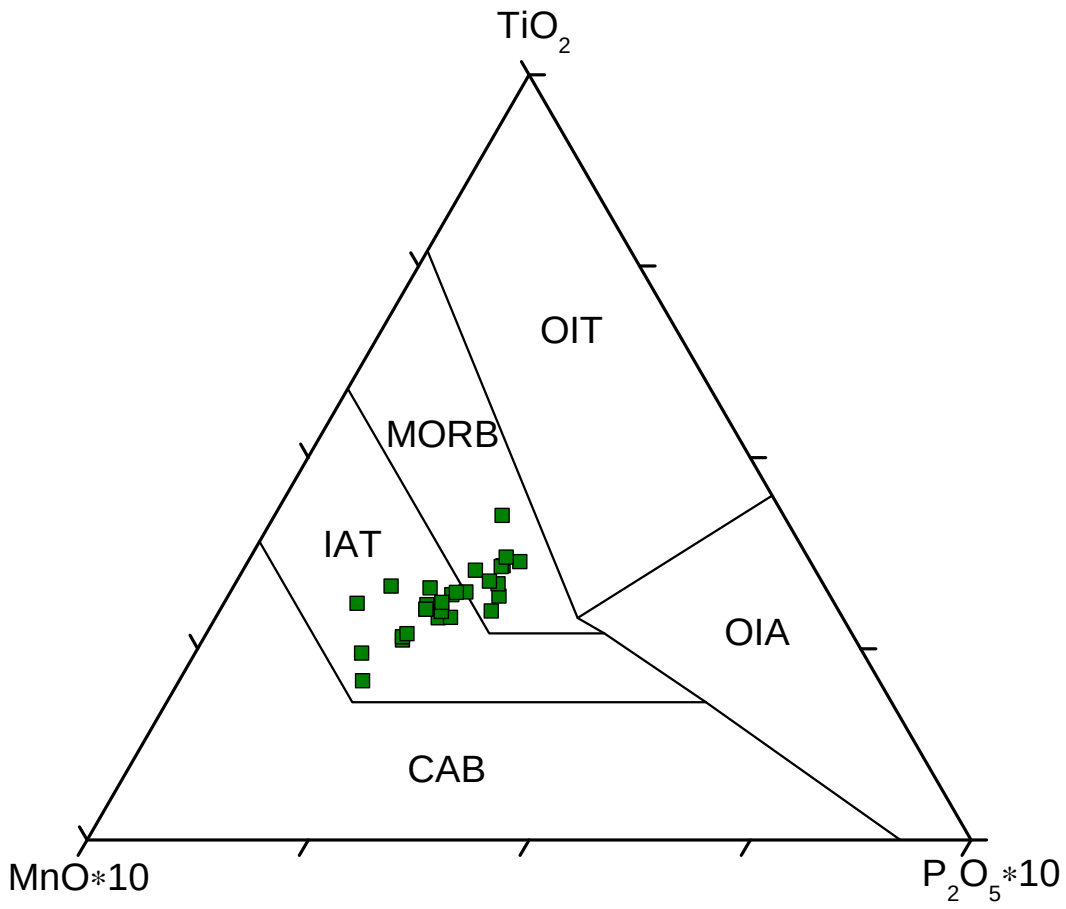


Figure 7.22 – Tectonic discrimination of the Deguisier basalt. the tectonic discrimination diagram was developed by Mullen (1983). Tectonic fields are mid-ocean ridge basalt (MORB), island arc tholeiite (IAT), island arc calc-alkaline (CAB), seamount tholeiite (OIT) and seamount alkalic (OIA).

tered with the rhyolite for which discrimination plots for granitic rocks can be used. While this is definitely not an ideal situation, rhyolitic samples can be used in granitic discrimination diagrams. In this case the Rb-Hf-Ta ternary diagram developed by Harris et al. (1986) is used. The results from both rhyolitic samples have been plotted in Figure 7.23.

Both rhyolitic samples plot in the volcanic arc field. This accords with the majority of basaltic samples. Nonetheless, it would be preferable to obtain additional supporting evidence.

REE can also be used to distinguish between tectonic settings and yield information about the magmatic source. Unfortunately in this case, REE patterns cannot easily distinguish between island arc, or ocean island tholeiite settings. However, it should be noted that ocean island arc tholeiites generally support lower HREE when compared to island arc. Nonetheless,

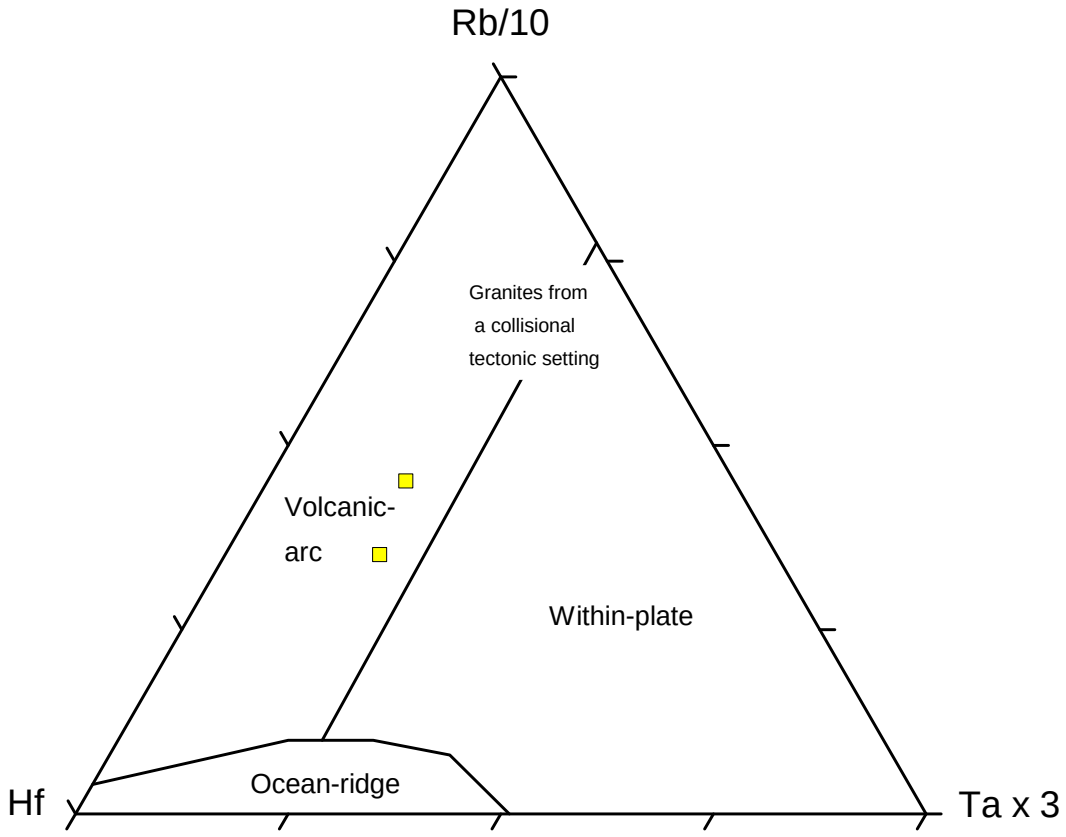


Figure 7.23 – Tectonic discrimination of the Deguisier rhyolite. Diagram from Harris et al. (1986).

comparisons between the Deguisier Formation REE ranges and that of island arc and back arc tholeiites are given in Table 7.16.

Values from the Deguisier Formation generally fall in the mid-ranges given in literature. The enrichment of LREE over HREE and a low variability in the HREE are common features in the island arc setting (Henderson, 1984). The lack of HREE variability is commonly attributed to garnet instability in the melt, therefore excluding the possibility of deep fractionation.

The agreement in trends allows the inference that the tectonic setting of the Deguisier Formation most likely corresponds to that of a volcanic island arc. Studies performed by Gélinas et al. (1976) also proposed a volcanic arc setting, but remained inconclusive as the MORB environment was also strongly considered. However, it should be noted that the normalized incompatible trace element patterns have negative Nb anomalies are unknown in E-MORB. Recently, studies confer a plume (extension) and a island arc (shortening) volcanic signature in the Kidd-Munro Group in Ontario (equivalent to the Kinojévis Group) (Ayer et al.,

2002). Consequently, the Deguisier Formation will be regarded as belonging to a volcanic arc tectonic setting.

Quaternary island arc volcanism may be dominated by basaltic rocks ($< 80\%$) (Winter, 2001). However, true basalts are generally subordinate in these arcs as a whole. Archean volcanism would on the other hand theoretically support a more basaltic composition since a greater heat flow would result in a higher degree of partial melting from its source. Current estimates of the Archean heat flow vary between 2 - 3 orders of magnitude higher than today (Lenardic, 1998; Eriksson et al., 2004). As such, it would have certainly played an important role in the origin of the formation. Subordinate andesite to rhyolite units, on the other hand, would not be an uncommon feature since quaternary volcanic arcs are known to contain both.

7.7 Beattie syenite

Initial geochemical classifications of the Beattie syenite were performed by Banfield (1940) and subsequently by Davidson and Banfield (1944). Afterwards, other studies have been published by Goutier and Lacroix (1992) and Legault et al. (2005). These studies focused primarily on the geochemical characteristics of the Au-mineralization. In contrast, the following will focus on the overall characterization of the Beattie syenite with an emphasis on compositional similarities or differences between the petrological units. This was accomplished using a total of 243 geochemical samples.

Methodology

Representative samples of the Beattie syenite were obtained from Osisko Mining Corporation, MRN, Gold Fields Resources Canada and by the author. In light of the plethora of samples from the private sector, they were submitted to additional screening in an attempt discriminate highly altered samples since some were not accompanied by adequate sample descriptions. Samples considered highly altered were determined via the following rules: 1) samples must not have been taken specifically for the characterization of Au-mineralization, 2) samples must not have been taken specifically for their alteration(s), 3) oxide values must not deviate extensively from the norm set by all least-altered syenitic samples (determined via petrographic observations), 4) samples must not contain $>$ 7-6% LOI[5] depending on the location and overall chemistry of the sample.

When sample descriptions were available, the discrimination of altered samples and/or Au-mineralized samples was primarily based on rules 1 and 2. Rules 3 and 4 on the other hand were strongly emphasized when samples were not accompanied by descriptions.

Samples considered altered were omitted from the following sections. The following Table 7.17 contains the least-altered geochemical samples that will be employed for the lithochemical analyses. Samples from SOQUEM Inc. were once again discarded for the following section. A complete list of all syenitic samples can be found in Appendix D.

Prior to being used for plots and calculations, major and trace elements were corrected for LOI and are therefore on a 'dry' basis unless otherwise specified.

[5]A detailed discussion justifying the choice of LOI cut-off is addressed in Appendix D

Table 7.17 – Major and trace element analyses of least-altered specimens of the Beattie syenite. Major oxides are presented in wt% and trace elements are all given in ppm with the exception of Au which is given in ppb. Analyses presented have not been corrected for LOI.

Porphyritic Beattie syenite unit

Sample	**D958002**	**D958004**	**2004042805**	**D958179**	**D958051**	**D958215**	**D958221**
Institution	Osisko	Osisko	MRN	Osisko	Osisko	Osisko	Osisko
Year	2010	2010	2004	2010	2010	2010	2010
SiO_2	64.60	58.20	60.62	63.40	59.00	55.70	60.10
TiO_2	0.43	0.48	0.26	0.41	0.54	0.53	0.51
Al_2O_3	13.60	14.65	17.77	12.80	16.70	15.25	16.40
Fe_2O_3t	4.60	4.98	3.10	5.29	5.44	5.00	5.76
MnO	0.03	0.19	0.07	0.10	0.15	0.09	0.21
MgO	0.44	1.08	0.76	0.56	0.65	1.15	0.24
CaO	1.21	3.18	2.60	1.48	1.96	2.68	0.46
Na_2O	0.65	0.88	3.91	0.81	2.34	1.49	4.51
K_2O	10.30	11.10	6.45	10.15	9.01	9.39	6.83
P_2O_5	0.29	0.33	0.10	0.25	0.28	0.28	0.24
[a]CO_2	—	—	2.57	—	—	—	—
[a]S	2.62	1.65	0.04	2.63	0.10	2.95	0.01
[b]LOI	2.38	4.09	3.90	3.97	3.70	6.01	3.31
Total	98.53	99.16	99.54	99.22	99.77	97.57	98.57
Ag	2	0.8	0.1	1.5	0.2	1.6	0.3
As	879	562	3.5	711	71	692	28
Au	6 230	3 060	5	5 690	185	3 870	16
Ba	*1880.87*	*2060.00*	2924.00	*1791.30*	*2686.96*	*1970.43*	*2239.13*
Bi	< 2	< 2	0.4	< 2	< 2	< 2	< 2
Cd	< 0.5	< 0.5	< 0.1	< 0.5	< 0.5	< 0.5	< 0.5
Ce	—	—	291.9	—	—	—	—
Co	8	11	3.1	10	8	9	7
Cr	—	—	—	—	—	—	—
Cs	—	—	2.6	—	—	—	—
Cu	21	18	4.1	25	25	17	19
Dy	—	—	4.99	—	—	—	—
Er	—	—	1.99	—	—	—	—
Eu	—	—	3.19	—	—	—	—
Ga	< 10	< 10	26.3	< 10	< 10	< 10	< 10
Gd	—	—	8.35	—	—	—	—
Hf	—	—	8.6	—	—	—	—
Hg	3	< 1	0.02	< 1	< 1	3	< 1
Ho	—	—	0.82	—	—	—	—
La	—	—	128.4	—	—	—	—
Lu	—	—	0.34	—	—	—	—
Mo	208	12	0.4	68	1	113	4
Nb	—	—	13.2	—	—	—	—
Nd	—	—	100.7	—	—	—	—
Ni	3	4	1	5	< 1	3	7
Pb	43	30	11	39	33	57	31
Pr	—	—	29.23	—	—	—	—
Rb	—	—	156.5	—	—	—	—
Sb	6	4	1	4	3	5	< 2
Sc	—	—	2	—	—	—	—
Se	—	—	< 0.5	—	—	—	—
Sm	—	—	14.8	—	—	—	—
Sn	—	—	< 1	—	—	—	—
Sr	*422.80*	*591.92*	637.80	*338.24*	*676.48*	*676.48*	*422.80*
Ta	—	—	0.3	—	—	—	—
Tb	—	—	1.2	—	—	—	—
Th	—	—	34.1	—	—	—	—
Tl	< 10	< 10	< 0.1	< 10	< 10	< 10	< 10
Tm	—	—	0.32	—	—	—	—
U	—	—	6.5	—	—	—	—
V	—	—	47	—	—	—	—
W	—	—	3.1	—	—	—	—
Y	—	—	27.5	—	—	—	—
Yb	—	—	2.13	—	—	—	—
Zn	107	56	40	58	49	160	64
Zr	—	—	328.6	—	—	—	—

[a] *Not included in totals* [b] *Loss on ignition at 1000° C*

< Red *Values below detection limit* *Blue* *Values calculated from oxides*

Table 7.17 Continued

Porphyritic Beattie syenite unit							
Sample	**JG-1332-01**	**2004042820**	**JG-1332-06**	**JG-1332-07**	**D958156**	**D958159**	**JG-1332-09**
Institution	U of 0	MRN	U of 0	U of 0	Osisko	Osisko	U of 0
Year	2010	2004	2010	2010	2010	2010	2010
SiO_2	57.24	58.32	58.19	56.92	55.30	61.60	57.99
TiO_2	0.58	0.56	0.55	0.54	0.52	0.53	0.56
Al_2O_3	16.82	16.64	16.55	16.41	15.70	18.70	16.70
Fe_2O_3t	5.85	5.39	5.35	2.52	4.83	3.66	5.54
MnO	0.09	0.09	0.11	0.07	0.13	0.03	0.11
MgO	1.73	1.84	1.42	0.80	0.64	0.30	1.58
CaO	3.06	2.77	3.51	7.05	4.44	0.26	3.52
Na_2O	5.69	5.36	5.78	4.69	5.48	4.24	5.60
K_2O	5.17	4.88	4.35	3.15	4.34	6.65	5.06
P_2O_5	0.35	0.31	0.30	0.32	0.32	0.14	0.33
[a]CO_2	2.09	1.95	2.42	5.61	—	—	1.80
[a]S	< 0.02	0.04	< 0.02	< 0.02	0.06	0.02	0.03
[b]LOI	2.70	3.00	3.20	7.30	5.58	1.80	2.20
Total	99.28	99.16	99.31	99.77	97.28	97.91	99.19
Ag	< 0.1	< 0.1	< 0.1	< 0.1	< 0.2	< 0.2	< 0.1
As	9.0	9.8	11.1	2.8	16	13	10.7
Au	0.5	1.3	0.5	0.5	14	7	0.5
Ba	3250.00	3100.00	3425.00	446.00	*3224.35*	*1701.74*	3543.00
Bi	0.3	0.1	0.2	0.1	2	2	0.5
Cd	0.1	0.1	0.1	0.1	0.5	0.5	0.1
Ce	255.9	266.2	271.9	272.9	—	—	263.8
Co	9.3	10.3	9.8	3.3	6	3	10.3
Cr	—	13.6	—	—	—	—	—
Cs	5.7	2.5	1.8	2.2	—	—	3.7
Cu	12.9	6.3	15.9	4.5	7	14	23.1
Dy	6.73	7.21	6.91	5.24	—	—	6.88
Er	3.01	3.06	3.01	2.04	—	—	2.93
Eu	4.28	4.47	4.45	4.32	—	—	4.55
Ga	23.3	27.8	23.1	24.5	< 10	< 10	23.8
Gd	13.59	12.6	13.35	12.59	—	—	13.79
Hf	8.8	9	8.8	8.6	—	—	9.0
Hg	< 0.01	0.03	0.07	< 0.01	< 1	< 1	0.02
Ho	1.16	1.1	1.14	0.88	—	—	1.17
La	120.7	125.5	125.1	128.3	—	—	120.2
Lu	0.43	0.43	0.42	0.38	—	—	0.43
Mo	0.2	0.7	0.2	< 0.1	< 1	< 1	0.2
Nb	13.3	12	13.5	13.8	—	—	13.6
Nd	111.4	117.3	112.0	113.2	—	—	114.1
Ni	6.9	7.7	6.1	2.0	2	2	6.2
Pb	22.7	24.7	43.2	6.3	38	11	17.3
Pr	28.33	30.04	29.53	29.85	—	—	29.01
Rb	128.6	96.3	75.4	104.4	—	—	114.3
Sb	0.8	0.8	0.5	0.5	< 2	< 2	1.2
Sc	8.0	7	7.0	7.0	—	—	8.0
Se	0.5	< 0.5	0.5	0.5	—	—	0.5
Sm	18.22	20.2	18.31	17.81	—	—	18.52
Sn	2.0	< 1	2.0	2.0	—	—	2.0
Sr	1769.00	1535.90	1302.00	312.30	*930.16*	*338.24*	1873.00
Ta	0.4	0.5	0.5	0.4	—	—	0.5
Tb	1.47	1.69	1.47	1.22	—	—	1.46
Th	25.8	29.7	25.0	25.0	—	—	24.8
Tl	0.6	< 0.1	< 0.1	< 0.1	< 10	< 10	0.3
Tm	0.43	0.45	0.42	0.35	—	—	0.42
U	7.0	7.2	6.7	4.8	—	—	6.9
V	98.0	99	97.0	90.0	—	—	97.0
W	1.4	3.5	3.8	9.7	—	—	0.5
Y	35.4	35.5	34.7	26.6	—	—	34.0
Yb	2.85	3	2.87	2.49	—	—	2.94
Zn	83	92	87	14	63	34	77
Zr	366.7	338.7	376.3	361.7	—	—	356.0
	[a]	*Not included in totals*		[b]	*Loss on ignition at 1000° C*		
	< Red	*Values below detection limit*		*Blue*	*Values calculated from oxides*		

Table 7.17 Continued

Porphyritic Beattie syenite unit								
Sample	**D958157**	**D958154**	**D958153**	**D958058**	**D958113**	**D958108**	**2009048666**	**D958109**
Institution	Osisko	Osisko	Osisko	Osisko	Osisko	Osisko	MRN	Osisko
Year	2010	2010	2010	2010	2010	2010	2009	2010
SiO_2	61.00	53.40	55.30	60.30	58.90	54.50	58.26	58.00
TiO_2	0.46	0.49	0.58	0.54	0.55	0.48	0.46	0.53
Al_2O_3	16.00	15.60	16.20	17.10	16.95	15.55	17.75	16.85
Fe_2O_3t	5.46	4.82	6.69	4.35	5.43	4.29	4.03	4.09
MnO	0.14	0.14	0.13	0.07	0.08	0.14	0.08	0.09
MgO	0.66	1.62	1.05	1.12	0.50	1.32	0.54	0.50
CaO	2.04	5.03	3.55	2.25	2.07	4.38	2.74	2.45
Na_2O	3.25	5.43	5.21	4.07	4.48	1.96	4.92	3.13
K_2O	5.96	4.32	4.77	6.21	5.12	8.67	6.64	8.00
P_2O_5	0.09	0.33	0.34	0.27	0.26	0.27	0.14	0.28
[a]CO_2	—	—	—	—	—	—	3.92	—
[a]S	0.10	0.07	0.15	0.03	0.85	0.03	0.18	0.35
[b]LOI	3.55	7.28	4.79	3.96	3.88	6.89	4.00	3.84
Total	98.61	98.46	98.61	100.24	98.22	98.45	99.56	97.76
Ag	< 0.2	< 0.2	< 0.2	< 0.2	0.3	< 0.2	< 0.1	0.3
As	21	15	33	18	44	17	5.8	98
Au	35	19	19	5	290	87	4 400	1 065
Ba	*1970.43*	*2239.13*	*2866.09*	*1791.30*	*2239.13*	*2149.56*	1967.00	*3045.22*
Bi	< 2	< 2	< 2	< 2	< 2	< 2	0.3	8
Cd	< 0.5	< 0.5	< 0.5	< 0.5	< 0.5	< 0.5	0.2	< 0.5
Ce	—	—	—	—	—	—	227.9	—
Co	5	7	7	5	9	5	7.3	8
Cr	—	—	—	—	—	—	—	—
Cs	—	—	—	—	—	—	1.9	—
Cu	27	34	23	18	18	7	7.4	25
Dy	—	—	—	—	—	—	5.45	—
Er	—	—	—	—	—	—	2.31	—
Eu	—	—	—	—	—	—	3.72	—
Ga	< 10	< 10	< 10	< 10	< 10	< 10	26.2	< 10
Gd	—	—	—	—	—	—	9.78	—
Hf	—	—	—	—	—	—	10.4	—
Hg	< 1	< 1	< 1	< 1	< 1	< 1	0.07	< 1
Ho	—	—	—	—	—	—	0.92	—
La	—	—	—	—	—	—	111.3	—
Lu	—	—	—	—	—	—	0.31	—
Mo	< 1	< 1	2	< 1	< 1	< 1	0.2	6
Nb	—	—	—	—	—	—	11.3	—
Nd	—	—	—	—	—	—	99.8	—
Ni	2	3	3	1	3	1	3.8	1
Pb	12	17	15	10	28	17	38.8	50
Pr	—	—	—	—	—	—	26.47	—
Rb	—	—	—	—	—	—	131.4	—
Sb	< 2	< 2	< 2	< 2	< 2	< 2	0.8	< 2
Sc	—	—	—	—	—	—	4	—
Se	—	—	—	—	—	—	< 0.5	—
Sm	—	—	—	—	—	—	15.15	—
Sn	—	—	—	—	—	—	2	—
Sr	*422.80*	*1691.19*	*1352.95*	*338.24*	*591.92*	*422.80*	757.50	*507.36*
Ta	—	—	—	—	—	—	0.4	—
Tb	—	—	—	—	—	—	1.26	—
Th	—	—	—	—	—	—	23.5	—
Tl	< 10	< 10	< 10	< 10	< 10	< 10	< 0.1	< 10
Tm	—	—	—	—	—	—	0.33	—
U	—	—	—	—	—	—	5.3	—
V	—	—	—	—	—	—	94	—
W	—	—	—	—	—	—	7.3	—
Y	—	—	—	—	—	—	29.8	—
Yb	—	—	—	—	—	—	2.11	—
Zn	72	34	46	67	64	55	87	55
Zr	—	—	—	—	—	—	389.1	—

[a] *Not included in totals* [b] *Loss on ignition at 1000° C*

< Red *Values below detection limit* *Blue* *Values calculated from oxides*

Table 7.17 Continued

Porphyritic Beattie syenite unit								
Sample	**2009048667**	**D958075**	**D958119**	**D958117**	**D958116**	**D958114**	**D958115**	**D958190**
Institution	MRN	Osisko	Osisko	Osisko	Osisko	Osisko	Osisko	Osisko
Year	2009	2010	2010	2010	2010	2010	2010	2010
SiO_2	55.58	58.80	59.00	57.90	58.40	55.40	57.40	58.50
TiO_2	0.51	1.25	0.31	0.47	0.42	0.57	0.54	0.58
Al_2O_3	17.16	13.15	18.35	15.70	12.80	16.60	16.35	17.75
Fe_2O_3t	4.67	7.75	5.91	5.34	4.71	5.42	5.20	3.95
MnO	0.12	0.17	0.17	0.17	0.16	0.12	0.13	0.05
MgO	0.83	0.84	0.47	0.59	1.37	0.97	0.34	0.60
CaO	4.13	3.26	0.55	2.49	5.40	3.09	4.16	4.21
Na_2O	4.81	5.31	1.25	3.07	3.15	4.34	3.29	4.05
K_2O	6.06	1.72	9.65	7.98	3.78	4.98	5.19	4.32
P_2O_5	0.30	0.41	0.02	0.27	0.26	0.32	0.31	0.30
[a]CO_2	5.20	—	—	—	—	—	—	—
[a]S	0.12	1.20	0.02	0.29	0.09	0.34	0.08	0.01
[b]LOI	5.30	7.02	3.64	4.87	7.74	5.25	4.76	4.90
Total	99.47	99.68	99.32	98.85	98.19	97.06	97.67	99.21
Ag	< 0.1	0.5	< 0.2	0.6	0.4	< 0.2	< 0.2	< 0.2
As	3.5	409	13	62	10	8	2	5
Au	26.7	14	18	220	< 5	17	6	15
Ba	2294.00	—	*1253.91*	*2686.96*	*5553.04*	*6538.26*	*4478.26*	*1343.48*
Bi	0.3	< 2	< 2	< 2	< 2	< 2	< 2	< 2
Cd	< 0.1	< 0.5	< 0.5	< 0.5	< 0.5	< 0.5	< 0.5	< 0.5
Ce	225.6	—	—	—	—	—	—	—
Co	8.0	18	3	9	8	13	7	2
Cr	—	—	—	—	—	—	—	—
Cs	2.2	—	—	—	—	—	—	—
Cu	15.3	66	27	22	2	35	11	69
Dy	6.18	—	—	—	—	—	—	—
Er	2.73	—	—	—	—	—	—	—
Eu	4.14	—	—	—	—	—	—	—
Ga	24.3	< 10	< 10	< 10	< 10	< 10	< 10	< 10
Gd	10.92	—	—	—	—	—	—	—
Hf	9.0	—	—	—	—	—	—	—
Hg	0.09	< 1	< 1	< 1	< 1	< 1	< 1	< 1
Ho	1.04	—	—	—	—	—	—	—
La	106.6	—	—	—	—	—	—	—
Lu	0.38	—	—	—	—	—	—	—
Mo	0.2	3	< 1	< 1	< 1	< 1	< 1	< 1
Nb	12.1	—	—	—	—	—	—	—
Nd	107.6	—	—	—	—	—	—	—
Ni	2.8	2	< 1	2	2	3	2	< 1
Pb	52.9	11	70	25	20	12	21	10
Pr	27.52	—	—	—	—	—	—	—
Rb	131.0	—	—	—	—	—	—	—
Sb	0.8	< 2	< 2	< 2	< 2	< 2	< 2	< 2
Sc	7	—	—	—	—	—	—	—
Se	< 0.5	—	—	—	—	—	—	—
Sm	16.83	—	—	—	—	—	—	—
Sn	2	—	—	—	—	—	—	—
Sr	781.10	*169.12*	*253.68*	*591.92*	*1099.27*	*761.04*	*591.92*	*507.36*
Ta	0.5	—	—	—	—	—	—	—
Tb	1.41	—	—	—	—	—	—	—
Th	26.5	—	—	—	—	—	—	—
Tl	< 0.1	< 10	< 10	< 10	< 10	< 10	< 10	< 10
Tm	0.40	—	—	—	—	—	—	—
U	5.8	—	—	—	—	—	—	—
V	106	—	—	—	—	—	—	—
W	9.5	—	—	—	—	—	—	—
Y	33.0	—	—	—	—	—	—	—
Yb	2.46	—	—	—	—	—	—	—
Zn	67	59	90	57	87	61	59	22
Zr	349.8	—	—	—	—	—	—	—
	[a]	*Not included in totals*			[b]	*Loss on ignition at 1000° C*		
	< Red	*Values below detection limit*			*Blue*	*Values calculated from oxides*		

Table 7.17 Continued

Porphyritic Beattie syenite unit							
Sample	**D958223**	**2004042804**	**2009048663**	**D958229**	**D958239**	**D958264**	**D958254**
Institution	Osisko	MRN	MRN	Osisko	Osisko	Osisko	Osisko
Year	2010	2004	2009	2010	2010	2010	2010
SiO_2	56.10	59.21	58.07	57.90	61.20	61.80	63.10
TiO_2	0.68	0.44	0.29	0.55	0.24	0.23	0.46
Al_2O_2	16.20	16.40	16.92	16.30	20.00	17.60	16.05
Fe_2O_3t	5.64	4.97	2.78	4.89	2.98	2.99	4.00
MnO	0.16	0.14	0.12	0.11	0.04	0.09	0.08
MgO	0.77	1.01	0.37	0.66	0.37	0.34	0.31
CaO	4.43	2.28	4.73	3.68	1.66	2.36	1.68
Na_2O	3.53	1.99	3.55	6.10	5.90	5.51	5.00
K_2O	6.29	9.81	7.49	4.16	3.29	4.59	5.18
P_2O_5	0.31	0.27	0.02	0.29	0.04	0.02	0.10
[a]CO_2	—	2.86	3.88	—	—	—	—
[a]S	0.17	0.37	0.74	0.02	0.04	0.07	0.01
[b]LOI	5.69	3.40	5.00	3.49	3.46	2.99	2.99
Total	99.8	99.92	99.34	98.13	99.18	98.52	98.95
Ag	< 0.2	0.2	0.3	< 0.2	0.3	< 0.2	< 0.2
As	13	48.9	101.1	16	15	4	4
Au	47	182.3	175.5	< 5	8	< 5	< 5
Ba	*3403.48*	2252.00	3368.00	*1880.87*	*1164.35*	*1433.04*	*1880.87*
Bi	< 2	0.9	2.3	< 2	< 2	< 2	< 2
Cd	< 0.5	< 0.1	0.5	< 0.5	< 0.5	< 0.5	< 0.5
Ce	—	345.7	289.1	—	—	—	—
Co	7	10.9	9.9	8	2	3	4
Cr	—	88.4	—	5	—	—	—
Cs	—	5.2	3.8	—	—	—	—
Cu	43	26.3	13.5	—	22	8	6
Dy	—	5.78	3.16	—	—	—	—
Er	—	2.14	1.21	—	—	—	—
Eu	—	4.43	2.58	—	—	—	—
Ga	< 10	26.3	26.6	< 10	< 10	< 10	< 10
Gd	—	11.08	6.04	—	—	—	—
Hf	—	9.9	12.7	—	—	—	—
Hg	< 1	0.24	1.63	< 1	< 1	< 1	< 1
Ho	—	0.86	0.50	—	—	—	—
La	—	157.5	157.9	—	—	—	—
Lu	—	0.31	0.18	—	—	—	—
Mo	< 1	2.6	5.3	< 1	< 1	< 1	< 1
Nb	—	16.3	13.3	—	—	—	—
Nd	—	131.6	101.9	—	—	—	—
Ni	2	24	1.3	5	< 1	< 1	< 1
Pb	13	41.2	79.9	61	12	51	11
Pr	—	35.16	30.33	—	—	—	—
Rb	—	172.6	148.4	—	—	—	—
Sb	< 2	1.4	2.8	< 2	< 2	< 2	< 2
Sc	—	6	< 1	—	—	—	—
Se	—	< 0.5	< 0.5	—	—	—	—
Sm	—	19.7	11.44	—	—	—	—
Sn	—	2	2	—	—	—	—
Sr	*591.92*	675.80	1331.10	*1183.83*	*253.68*	*507.36*	*422.80*
Ta	—	0.4	0.4	—	—	—	—
Tb	—	1.39	0.75	—	—	—	—
Th	—	31.5	31.3	—	—	—	—
Tl	< 10	< 0.1	0.2	< 10	< 10	< 10	< 10
Tm	—	0.31	0.19	—	—	—	—
U	—	6.4	12.8	—	—	—	—
V	—	104	73	—	—	—	—
W	—	22.8	15.6	—	—	—	—
Y	—	30.7	17.6	—	—	—	—
Yb	—	1.89	0.94	—	—	—	—
Zn	72	56	82	81	26	68	47
Zr	—	364.6	546.3	—	—	—	—
	[a]	*Not included in totals*		[b]	*Loss on ignition at 1000° C*		
	< Red	*Values below detection limit*		*Blue*	*Values calculated from oxides*		

Table 7.17 Continued

Porphyritic Beattie syenite unit							
Sample	**JG-5099-02**	**2004042815**	**2004042814**	**D958259**	**2004042811**	**3958**	**2004042799**
Institution	U of 0	MRN	MRN	Osisko	MRN	GFRC	MRN
Year	2010	2004	2004	2010	2010	1981	2004
SiO_2	59.80	57.95	56.37	62.50	57.45	55.20	56.07
TiO_2	0.45	0.56	0.51	0.52	0.53	0.67	0.56
Al_2O_3	17.89	15.94	15.32	18.60	16.15	15.00	15.90
Fe_2O_3t	4.08	5.39	4.74	2.50	4.36	5.46	5.37
MnO	0.09	0.11	0.14	0.03	0.07	0.18	0.13
MgO	0.82	0.70	1.71	0.51	0.68	1.59	1.14
CaO	1.54	3.73	4.69	1.90	6.15	6.00	5.51
Na_2O	2.63	5.22	4.87	7.65	6.22	7.24	5.49
K_2O	9.27	4.38	4.50	2.13	1.64	0.94	2.47
P_2O_5	0.15	0.34	0.27	0.10	0.29	0.33	0.35
[a]CO_2	1.21	3.52	5.95	—	4.70	5.90	6.35
[a]S	0.04	0.08	0.08	0.17	0.01	—	0.03
[b]LOI	2.50	4.70	6.40	2.69	5.90	6.93	6.80
Total	99.22	99.02	99.52	99.13	99.44	99.54	99.79
Ag	< 0.1	< 0.1	< 0.1	< 0.2	< 0.1	0.30	< 0.1
As	25.8	3.8	5.5	5	3.4	—	5.4
Au	34.5	< 0.5	1.9	26	0.6	21.00	< 0.5
Ba	4256.00	2973.00	2070.00	*537.39*	620.00	390.00	1194.00
Bi	0.5	0.2	0.4	< 2	< 0.1	—	1.0
Cd	< 0.1	< 0.1	< 0.1	< 0.5	< 0.1	—	< 0.1
Ce	298.7	250	227	—	263.4	—	263.2
Co	4.2	10	9.4	6	4.2	—	9.9
Cr	*20.53*	—	—	—	—	410.00	27.2
Cs	5.3	2	2.9	—	0.9	—	3.6
Cu	10.7	18.5	18	7	5.2	31.00	26.1
Dy	6.07	5.77	5.66	—	6.53	—	7.08
Er	2.80	2.36	2.24	—	2.76	—	—
Eu	4.02	4.19	3.7	—	3.97	—	4.36
Ga	25.7	24.2	24.1	< 10	25	—	27.1
Gd	12.40	11.72	10.44	—	11.96	—	12.09
Hf	8.4	8.9	8.2	—	10	—	9.7
Hg	0.15	0.06	0.12	< 1	0.03	—	80.00
Ho	1.08	0.93	0.92	—	1.04	—	1.12
La	150.8	118.4	112.5	—	124.9	—	122.4
Lu	0.42	0.37	0.37	—	0.44	—	0.42
Mo	0.6	0.4	1.1	< 1	0.4	—	0.4
Nb	14.4	11.8	11.8	—	12.6	—	12.7
Nd	112.9	111.3	96.4	—	110.7	—	115.70
Ni	9.4	3	5	3	3.4	—	3.1
Pb	38.5	16.2	21.4	4	26.7	—	77.3
Pr	31.63	27.76	24.96	—	28.43	—	29.27
Rb	183.0	105.1	121.5	—	67.3	20.00	69.9
Sb	0.8	0.7	0.8	< 2	0.6	—	2.0
Sc	4.0	7	6	—	7	—	8.0
Se	< 0.5	< 0.5	< 0.5	—	< 0.5	—	< 0.5
Sm	16.87	19.3	16.8	—	18.7	—	19.6
Sn	2.0	2	< 1	—	2	—	2.0
Sr	900.10	849.10	1116.20	*253.68*	484.90	220.00	869.80
Ta	0.5	0.5	0.5	—	0.4	—	0.3
Tb	1.28	1.46	1.38	—	1.53	—	1.64
Th	26.6	26.2	26.6	—	30.7	—	29.9
Tl	< 0.1	< 0.1	< 0.1	< 10	< 0.1	—	—
Tm	0.40	0.36	0.35	—	0.41	—	0.40
U	3.4	5.5	6.1	—	7.3	—	6.7
V	68.0	96	92	—	96	—	105
W	8.2	1.6	3	—	3.3	—	2.9
Y	32.6	30.5	30	—	35.1	—	38.6
Yb	2.86	2.67	2.42	—	2.85	—	2.83
Zn	67	55	47	14	33	40.00	49
Zr	368.9	300.6	312.4	—	369.3	300.00	349.3

GFRC *Gold Fields Resources Canada*

[a] *Not included in totals* [b] *Loss on ignition at 1000° C*

< Red *Values below detection limit* *Blue* *Values calculated from oxides*

Table 7.17 Continued

	Porphyritic Beattie syenite unit			Equigranular magnetite-bearing syenite unit		Porphyritic Central Duparquet unit		
Sample	**3280**	**3698**	**3284**	**JG-1332-04**	**90-34316**	**2004042817**	**90-34317**	**1990034318**
Institution	GFRC	GFRC	GFRC	U of 0	MRN	MRN	MRN	MRN
Year	1981	1981	1981	2010	1990	2004	1990	1990
SiO_2	61.00	58.30	56.10	58.52	59.90	57.26	58.19	59.00
TiO_2	0.54	—	—	0.54	0.53	0.53	0.47	0.52
Al_2O_3	15.60	17.40	16.50	16.75	16.60	16.25	16.44	15.90
Fe_2O_3t	6.42	5.44	5.85	5.15	5.07	4.92	3.75	3.38
MnO	0.08	0.10	0.14	0.12	0.11	0.12	0.10	0.10
MgO	0.85	0.77	0.87	1.54	1.53	0.72	1.14	1.17
CaO	2.26	3.02	5.06	3.86	3.06	4.41	2.94	3.17
Na_2O	3.78	5.22	6.35	5.67	5.36	6.04	4.29	4.49
K_2O	5.93	4.42	3.05	4.89	4.91	3.59	6.44	5.42
P_2O_5	0.29	0.35	0.39	0.30	0.29	0.28	0.11	0.16
[a]CO_2	1.50	2.40	4.20	0.99	—	4.77	—	—
[a]S	—	—	—	0.04	—	0.05	—	—
[b]LOI	3.23	3.93	5.39	1.70	1.19	5.40	5.13	4.90
Total	99.98	98.95	99.7	99.04	98.55	99.52	99	98.21
Ag	0.10	0.10	0.40	< 0.1	—	< 0.1	—	—
As	—	—	—	11.5	—	5.4	—	—
Au	157.00	28.00	21.00	< 0.5	—	1.3	—	—
Ba	2770.00	3400.00	2580.00	3255	3300	2432	1800.00	1800.00
Bi	—	—	—	0.7	—	< 0.1	—	10.31
Cd	—	—	—	< 0.1	< 2	< 0.1	< 2.00	< 2
Ce	—	—	—	264.7	220	254.5	204.00	196
Co	—	—	—	10.0	9	9.4	7.00	7
Cr	690.00	450.00	420.00	—	—	—	—	—
Cs	—	—	—	3.2	—	1.6	—	—
Cu	—	12.00	—	24.2	24	17.5	25.00	15
Dy	—	—	—	6.72	5	6.64	3.00	2
Er	—	—	—	3.06	—	2.74	—	—
Eu	—	—	—	4.49	2	4.15	< 1.00	2
Ga	—	—	—	26.1	27	26	27.00	24
Gd	—	—	—	13.65	—	11.58	60.06	54.69
Hf	—	—	—	9.6	—	9.9	—	—
Hg	—	—	—	0.03	—	0.09	—	—
Ho	—	—	—	1.17	—	1.04	—	—
La	—	—	—	123.9	134	122.8	126.00	126
Lu	—	—	—	0.44	—	0.45	—	—
Mo	—	—	—	0.2	< 4	0.6	< 4.00	< 4
Nb	—	—	—	13.7	3	11.1	8.00	7
Nd	—	—	—	113.7	74	108.7	75.00	94
Ni	—	—	—	3.6	11	3.3	10.00	7
Pb	—	—	—	34.8	56	23.4	65.00	34
Pr	—	—	—	29.98	64	28.1	27.00	12
Rb	100.00	80.00	60.00	105.2	100	83.7	150.00	120.00
Sb	—	—	—	0.9	—	2.8	—	—
Sc	—	—	—	7.0	7	6	4.00	5
Se	—	—	—	< 0.5	—	< 0.5	—	—
Sm	—	—	—	18.62	20	18.6	16.00	12
Sn	—	—	—	< 1.0	10	2	10.00	10
Sr	580.00	640.00	860.00	3038.0	3200	810.4	880.00	500.00
Ta	—	—	—	0.5	5	0.4	< 5.00	5
Tb	—	—	—	1.46	—	1.65	—	—
Th	—	—	—	27.9	7	29.2	14.00	21
Tl	—	—	—	0.2	—	< 0.1	—	—
Tm	—	—	—	0.42	—	0.41	—	—
U	—	—	—	6.6	—	6.1	—	—
V	—	—	—	95.0	115	89	87.00	90
W	—	—	—	5.7	—	3.6	—	—
Y	—	—	—	33.4	31	34.5	32.00	32.00
Yb	—	—	—	2.86	—	2.87	—	—
Zn	—	37.00	—	39	114	55	79.00	70.00
Zr	350.0	420.0	370.0	384.0	430	339.9	440.00	330.00

GFRC *Gold Fields Resources Canada*

[a] *Not included in totals* [b] *Loss on ignition at 1000° C*

< Red *Values below detection limit* *Blue* *Values calculated from oxides*

Table 7.17 Continued

Porphyritic Central Duparquet unit							
Sample	**2004042816**	**D958197**	**2009048662**	**2004042813**	**2004042812**	**D958248**	**D958249**
Institution	MRN	Osisko	MRN	MRN	MRN	Osisko	Osisko
Year	2004	2010	2009	2004	2010	2010	2010
SiO_2	57.62	57.10	55.07	53.77	60.53	64.50	58.70
TiO_2	0.60	0.51	0.53	0.62	0.42	0.59	0.59
Al_2O_3	16.72	17.60	16.99	16.55	15.10	17.20	17.70
Fe_2O_3t	4.29	4.92	4.56	5.52	4.02	3.26	3.58
MnO	0.12	0.14	0.12	0.15	0.14	0.04	0.12
MgO	0.90	0.84	1.61	1.41	1.07	0.58	0.69
CaO	3.79	3.70	4.56	4.30	4.87	1.00	2.17
Na_2O	5.20	5.08	6.20	4.60	6.49	3.14	4.94
K_2O	4.71	5.48	2.46	5.68	1.35	6.73	5.61
P_2O_5	0.35	0.14	0.28	0.20	0.22	0.20	0.21
[a]CO_2	4.37	—	6.41	5.95	5.32	—	—
[a]S	0.11	< 0.01	< 0.02	0.05	0.07	0.14	0.15
[b]LOI	5.10	5.41	7.30	6.50	5.60	2.86	4.16
Total	99.4	100.92	99.68	99.3	99.81	100.1	98.47
Ag	< 0.1	< 0.2	0.2	< 0.1	< 0.1	< 0.2	< 0.2
As	8	< 2	2.8	2.2	1.9	322	18
Au	1.6	< 5	1.5	1.7	1.3	24	6
Ba	1750	—	750	2834	554	*2149.56*	*2507.83*
Bi	< 0.1	< 2	0.8	0.3	1.5	< 2	< 2
Cd	< 0.1	< 0.5	0.3	< 0.1	< 0.1	< 0.5	< 0.5
Ce	262.5	—	212.0	286.1	200.5	—	—
Co	7.4	3	7.5	8.9	5.7	3	4
Cr	—	—	*20.53*	—	—	—	—
Cs	1.4	—	2.6	2.1	1.1	—	—
Cu	13.5	45	11.4	33	3.8	16	14
Dy	6.61	—	5.73	7.46	5.05	—	—
Er	2.71	—	2.62	2.88	1.98	—	—
Eu	4.37	—	3.95	4.43	3.39	—	—
Ga	26.1	< 10	24.1	27.7	20.6	< 10	< 10
Gd	12.57	—	10.13	12.61	9.11	—	—
Hf	9.7	—	9.5	10.3	7	—	—
Hg	0.02	< 1	0.04	0.13	0.11	< 1	< 1
Ho	1.04	—	0.97	1.17	0.83	—	—
La	127.2	—	103.6	144	96.3	—	—
Lu	0.43	—	0.37	0.42	0.31	—	—
Mo	0.7	< 1	0.4	0.6	1.1	< 1	< 1
Nb	12.2	—	11.8	13.7	9.1	—	—
Nd	115.4	—	98.1	115.2	88.2	—	—
Ni	5.1	< 1	2.1	2.7	4.3	2	< 1
Pb	12.8	12	50.0	25.2	7.5	12	28
Pr	28.84	—	25.66	30.13	22.08	—	—
Rb	108.2	—	77.9	137	54.4	—	—
Sb	0.5	< 2	1.0	0.9	0.5	4	4
Sc	8	—	7	5	6	—	—
Se	< 0.5	—	0.6	< 0.5	< 0.5	—	—
Sm	19.3	—	16.50	19.3	15.1	—	—
Sn	2	—	< 1	2	< 1	—	—
Sr	710.8	—	451.8	531.1	701.8	*422.80*	*761.04*
Ta	0.5	—	0.5	0.5	0.3	—	—
Tb	1.67	—	1.32	1.71	1.27	—	—
Th	27.1	—	25.8	33.3	21.8	—	—
Tl	< 0.1	< 10	< 0.1	< 0.1	< 0.1	< 10	< 10
Tm	0.42	—	0.40	0.43	0.34	—	—
U	4.9	—	5.3	5.4	5.1	—	—
V	100	—	106	132	65	—	—
W	10.5	—	4.0	7.4	11.5	—	—
Y	34.6	—	29.7	36.9	26.4	—	—
Yb	2.8	—	2.47	2.8	2.05	—	—
Zn	48	47	76	67	32	39	39
Zr	337.4	—	374.6	390.5	259.2	—	—
	[a]	*Not included in totals*		[b]	*Loss on ignition at 1000° C*		
	< Red	*Values below detection limit*		Blue	*Values calculated from oxides*		

Table 7.17 Continued

Porphyritic Central Duparquet unit							
Sample	**2009048664**	**2009048665**	**2004042808**	**2004042809**	**D958303**	**2004042810**	**D958277**
Institution	MRN	MRN	MRN	MRN	Osisko	MRN	Osisko
Year	2009	2009	2004	2010	2010	2004	2010
SiO_2	63.84	63.20	64.72	66.39	66.70	58.43	59.80
TiO_2	0.45	0.44	0.46	0.46	0.41	0.54	0.54
Al_2O_3	18.81	17.70	17.75	15.12	15.35	16.34	16.15
Fe_2O_3t	2.38	3.93	3.62	4.37	3.09	4.33	4.31
MnO	0.02	0.11	0.05	0.08	0.07	0.18	0.17
MgO	0.30	0.23	0.32	0.52	0.29	1.36	1.10
CaO	0.48	0.51	0.23	0.17	0.41	3.47	2.84
Na_2O	3.95	4.40	3.59	3.40	3.93	5.63	5.75
K_2O	8.06	6.95	7.61	5.67	6.51	4.02	4.03
P_2O_5	0.19	0.22	0.21	0.11	0.11	0.27	0.27
[a]CO_2	0.22	0.40	0.18	2.06	—	4.73	—
[a]S	0.09	0.12	0.03	0.11	0.34	0.36	0.31
[b]LOI	1.10	1.80	1.40	2.70	2.50	5.20	5.26
Total	99.58	99.49	99.96	98.99	99.37	99.77	100.22
Ag	< 0.1	< 0.1	< 0.1	0.4	0.2	< 0.1	0.2
As	4.0	6.1	4.1	16.2	34	5.2	7
Au	11.0	10.8	1.4	68.2	50	2.3	7
Ba	2022	2745	2108	2794	*3582.61*	1715	*2060.00*
Bi	0.2	0.4	0.2	0.5	< 2	0.4	2
Cd	0.2	< 0.1	< 0.1	2.3	< 0.5	< 0.1	< 0.5
Ce	191.5	228.1	277.7	230	—	263.6	—
Co	12.9	4.8	3.2	2.2	3	6.1	6
Cr	—	*13.68*	—	—	—	6.8	—
Cs	1.4	2.0	2.3	1.7	—	1.4	—
Cu	15.2	12.0	14.3	52.8	10	19.6	19
Dy	5.49	5.17	5.7	5.73	—	6.92	—
Er	2.27	2.13	2.3	2.19	—	2.73	—
Eu	3.40	3.97	3.93	3.28	—	4.09	—
Ga	26.2	23.6	29.3	25.2	< 10	25.1	< 10
Gd	9.13	10.22	10.59	9.16	—	11.38	—
Hf	10.8	9.5	10.8	10.8	—	10.3	—
Hg	0.03	0.19	0.16	6.39	2	< 0.1	< 1
Ho	0.86	0.85	0.92	0.86	—	1.13	—
La	90.6	108.2	121.8	109.5	—	121.9	—
Lu	0.28	0.28	0.32	0.34	—	0.41	—
Mo	0.1	0.3	0.8	0.5	< 1	0.9	< 1
Nb	16.7	14.5	15.5	12.3	—	11.6	—
Nd	86.7	109.3	112.5	92.1	—	109	—
Ni	3.0	2.6	2.8	2.5	2	3.5	3
Pb	21.0	17.2	16.4	34.3	59	18.1	15
Pr	22.48	27.55	29.37	24.33	—	28.5	—
Rb	171.8	133.6	172.8	127.4	—	90	—
Sb	1.0	2.7	2.5	9.9	< 2	0.9	—
Sc	3	4	3	4	—	7	3
Se	< 0.5	< 0.5	< 0.5	< 0.5	—	< 0.5	—
Sm	13.22	16.16	17.5	15.1	—	18.8	—
Sn	2	2	2	2	—	2	—
Sr	394.2	643.1	650.9	270.7	*338.24*	649.5	*676.48*
Ta	0.6	0.6	0.6	0.5	—	0.5	—
Tb	1.21	1.25	1.41	1.28	—	1.61	—
Th	22.9	17.9	21.9	25	—	29.1	—
Tl	< 0.1	< 0.1	< 0.1	< 0.1	< 10	< 0.1	< 10
Tm	0.31	0.31	0.34	0.34	—	0.43	—
U	3.8	3.9	5	5.7	—	6.7	—
V	58	63	47	59	—	91	—
W	7.4	14.6	21	17.6	—	5.6	—
Y	27.9	26.7	31.1	28.9	—	36.1	—
Yb	1.94	1.78	2.32	2.31	—	2.72	—
Zn	37	55	42	1084	92	55	57
Zr	416.5	354.1	379	343.7	—	330.9	—
	[a]	*Not included in totals*		[b]	*Loss on ignition at 1000° C*		
	< Red	*Values below detection limit*		*Blue*	*Values calculated from oxides*		

Table 7.17 Continued

	Megaporphyritic unit		Lath syenite unit	
Sample	**2002025869**	**2004042806**	**2003031914**	**2004042819**
Institution	MRN	MRN	MRN	MRN
Year	2002	2004	2003	2004
SiO_2	65.11	62.43	54.64	58.13
TiO_2	0.50	0.43	0.72	0.69
Al_2O_3	17.20	16.36	16.74	19.90
Fe_2O_3t	2.81	4.11	6.28	5.95
MnO	0.06	0.09	0.21	0.04
MgO	0.39	0.74	1.63	0.84
CaO	0.63	2.01	3.24	0.99
Na_2O	2.94	5.55	5.16	7.27
K_2O	7.17	4.49	3.97	2.72
P_2O_5	0.19	0.13	0.32	0.26
[a]CO_2	0.35	2.72	7.00	0.59
[a]S	0.22	0.01	0.05	0.04
[b]LOI	2.60	3.40	7.10	2.40
Total	99.6	99.74	100.01	99.19
Ag	—	< 0.1	< 0.1	< 0.1
As	—	4.3	11.7	< 0.5
Au	—	2	10.2	2.7
Ba	1997	1322	1781	2849
Bi	—	0.5	0.3	< 0.1
Cd	—	0.2	< 0.1	< 0.1
Ce	—	235.5	310	283.7
Co	—	5.4	10.7	5.5
Cr	—	—	—	—
Cs	—	1.7	2.2	3.3
Cu	—	13.5	102.9	94.2
Dy	—	5.64	9.18	9.15
Er	—	2.07	3.39	4.11
Eu	—	3.35	5.99	4.64
Ga	—	26.4	27.7	27.2
Gd	—	9.18	16.59	13.77
Hf	—	11.2	9.7	10.7
Hg	—	1.53	0.24	0.03
Ho	—	0.88	1.32	1.6
La	—	102.3	166.2	137
Lu	—	0.3	0.42	0.49
Mo	—	1	1	0.6
Nb	10.0	11	14.6	13.7
Nd	—	89	148.3	126
Ni	20.0	3.8	4.1	8.9
Pb	—	11.5	8.3	18.4
Pr	—	24.33	37.58	31.67
Rb	—	89.1	88.5	85.4
Sb	—	2.9	2.1	0.4
Sc	6.0	4	6	6
Se	—	< 0.5	< 0.5	< 0.5
Sm	—	15.2	23.6	20.6
Sn	—	2	< 1	2
Sr	559.0	535.2	720.4	508.3
Ta	—	0.3	0.7	0.6
Tb	—	1.32	2.31	2.08
Th	—	24	32.2	27.9
Tl	—	< 0.1	< 0.1	< 0.1
Tm	—	0.3	0.53	0.56
U	—	4.9	4.6	5
V	—	57	122	125
W	—	12.4	10.6	3.7
Y	28.0	29	45.4	51.2
Yb	—	1.97	3.2	3.36
Zn	—	50	80	25
Zr	452.0	347.8	383.5	370

[a] *Not included in totals*

[b] *Loss on ignition at 1000° C*

< Red *Values below detection limit*

7.7.1 Major and compatible trace elements

General classification

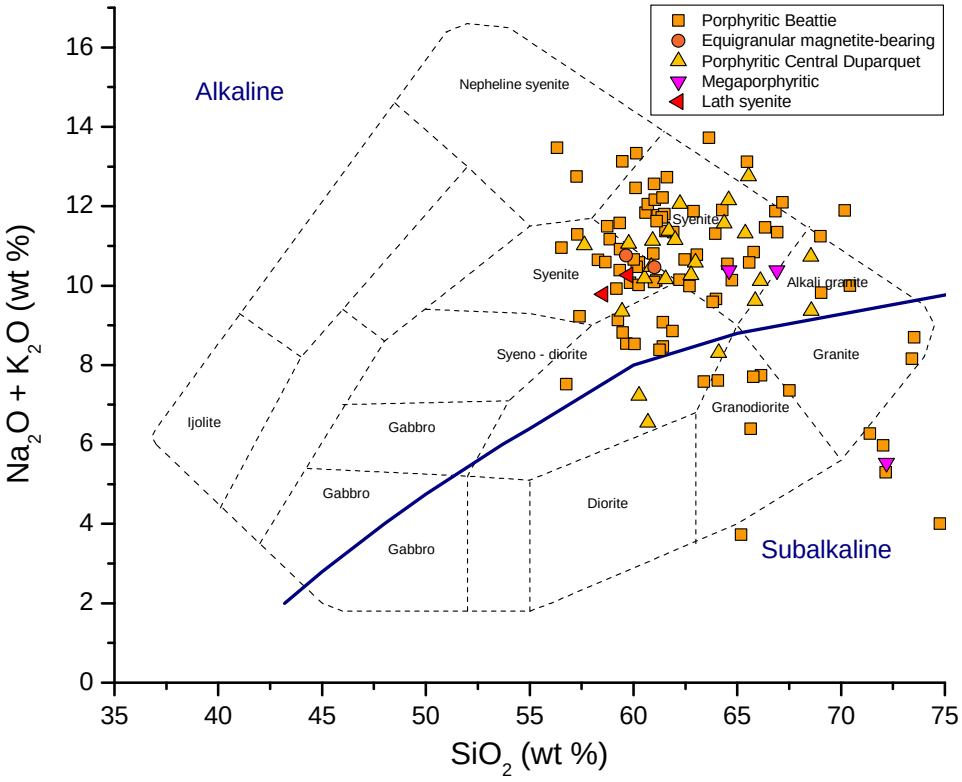
A general classification of the Beattie syenite was performed using the TAS diagram developed by Cox et al. (1979) for plutonic rocks. Figure 7.24a presents all geochemical samples, regardless of their alteration. In this Figure, all syenitic samples scatter close to, or plot within the syenite field. Figure 7.24b on the other hand presents the least-altered samples following additional screening and subsequent exclusion of altered samples. As a result, the exclusion of the heavily altered samples provide a much clearer perspective. Figure 7.24b demonstrates that least-altered samples plot distinctively within the syenite compositional fields with few analyses falling within the syeno-diorite (left), granodiorite (lower) and alkali-granite (right) fields.

Included with the classification TAS diagrams is the division of the alkaline and subalkaline affinities, following the trend defined by Irvine and Baragar (1971). Figure 7.24b demonstrates quite clearly that most of the analyses possess the necessary $Na_2O + K_2O$ values to be classified as alkaline. Only 3 analyses, 2 from the porphyritic Beattie syenite unit and 1 from the porphyritic Central Duparquet unit plot in the subalkaline field. Consequently, the Beattie syenite is considered part of the alkaline magmatic series.

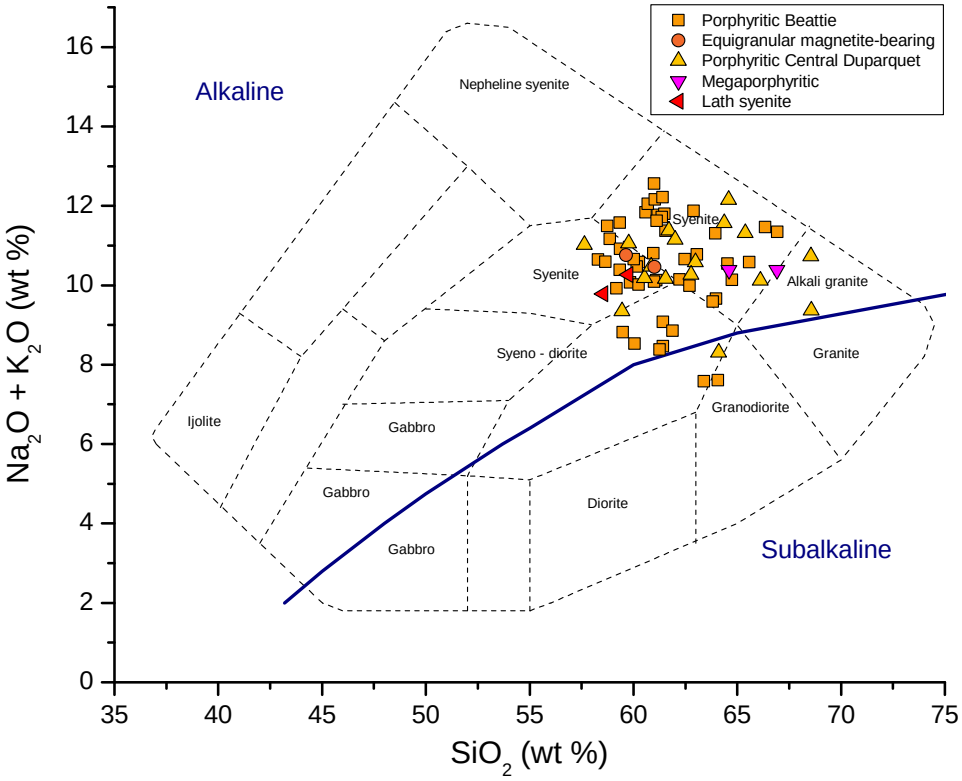
Magmatic series

Alkaline rocks can be further subdivided into the sodic (Na), potassic (K) and high potassic (High K) series. Divisions between sodic and potassic fields are those of Irvine and Baragar (1971), and the high potassic field is that of Middlemost (1975). The resulting subdivision plot for the Beattie syenite units is presented in Figure 7.25a.

Samples of the syenite are highly scattered, spanning from the Na- to the high K-series. The unit demonstrating the highest amount of variation is the porphyritic Beattie unit closely followed by the porphyritic Central Duparquet unit. This variability is likely caused by hydrothermal alteration associated with Au-mineralization which has dramatically increased K_2O concentrations, particularly in contact areas and/or in proximity to the D_2 faults (see Section 8.2). As evidence, Figure 7.25b presents all samples of the Beattie syenite, regardless of alteration. Upon closer inspection of Figure 7.25b altered samples clearly demonstrate an



(a) TAS classification of all syenitic samples



(b) TAS classification of the least-altered Beattie syenite samples

Figure 7.24 – TAS classification of the Beattie syenite samples. Samples illustrated in the TAS classification scheme for plutonic rocks of Cox et al. (1979). Also included in the diagram is the dividing boundary between the alkaline and subalkaline rocks (blue line) of Irvine and Baragar (1971).

overall enrichment of K_2O and a depletion of Na_2O. It should be noted that least-altered samples plotting in the high K-series were all located in proximity of major or secondary D_2 faults as well as in conjugate shear zones near the PDFZ. Consequently, these least altered samples plotting in the high K-series are the product of subsequent hydrothermal alteration and therefore do not represent the original magmatic series. In pursuing a solution, it can be noted that the equigranular magnetite-bearing syenite unit, which holds the least amount of hydrothermal alteration, is part of the K-series. Additionally, over half of the least-altered samples plot in the K-series. Consequently, but not conclusively, the Beattie syenite can be considered as part of the K-series.

Peraluminosity vs peralkalinity

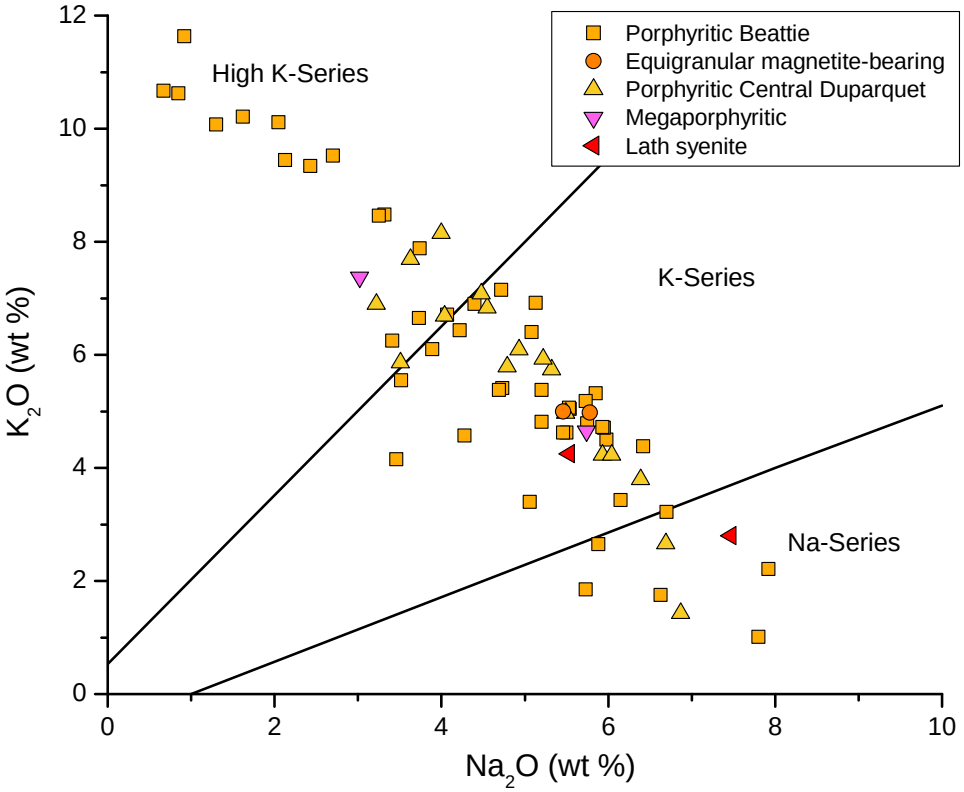
An additional method divides alkaline rocks into peralkaline, peraluminous and metaluminous fields. These fields were first defined by Shand (1927) and are separated by using the molar proportions of alkalis against alumina. The definition of individual fields and their respective indices are summarized in Table 7.18.

The peralkaline index (PI) defined as $(Na_2O + K_2O) / Al_2O_3$ is used to determine if rocks are peralkaline, based on whether PI > 1 or not. The aluminum saturation index (ASI), defined as $Al_2O_3 / (Na_2O + K_2O + CaO)$, is used to divide rocks into the peraluminous (PI > 1) and metaluminous (PI < 1) fields. The calculated indexes for the syenitic units are summarized and presented in Table 7.19 and illustrated in Figure 7.26.

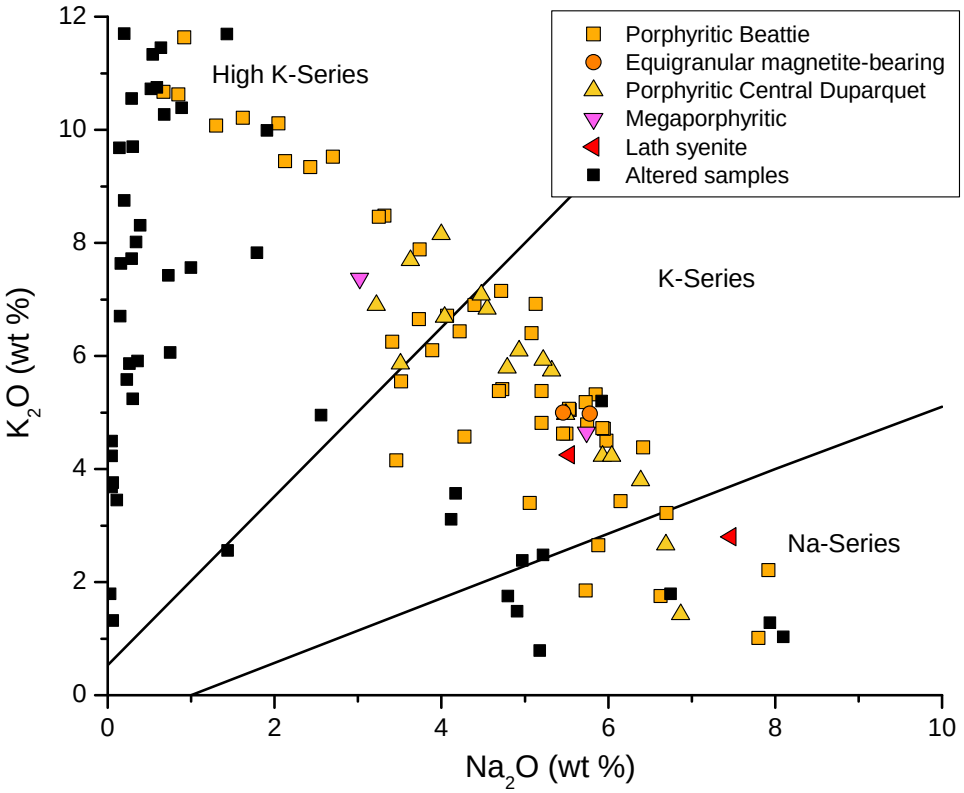
Table 7.18 – Peraklaline, peraluminous and metaluminous definitions including boundaries for indexes. Indexes are calculated in molar proportions.

Name	Definition
Peralkaline	$Al_2O_3 < (Na_2O + K_2O)$
Peraluminous	$Al_2O_3 > (Na_2O + K_2O + CaO)$
Metaluminous	$Al_2O_3 < (Na_2O + K_2O + CaO)$
Peralkalinity index	$(Na_2O + K_2O) / Al_2O_3$
Aluminum saturation index	$Al_2O_3 / (Na_2O + K_2O + CaO)$

Altogether least-altered samples of the Beattie syenite begin from the metaluminous field and cross into the peraluminous field (see Figure 7.26). Samples of the equigranular magnetite-bearing unit, along with a large cluster of samples from the porphyritic Beattie unit are metaluminous. Samples from the porphyritic Central Duparquet, megaporphyritic and lath



(a) Alkaline subdivision of the least-altered Beattie syenite samples



(b) Alkaline subdivision of all Beattie syenite samples

Figure 7.25 – Alkaline subdivision of the Beattie syenite. Original subdivision of the alkaline series was made by Irvine and Baragar (1971) with the addition of a high K-series by Middlemost (1975).

Table 7.19 – Alumina saturation and peralkaline indexes of the syenitic units.

Unit	Alumina saturation index	Peralkaline index
Porphyritic Beattie	1.41 - 0.82	0.96 - 0.64
Equigranular magnetite-bearing	0.98 - 0.92	0.87 - 0.85
Porphyritic Central Duparquet	1.29 - 0.91	0.88 - 0.72
Megaporphyritic	1.31 - 1.03	0.86 - 0.73
Lath syenite	1.26 - 1.06	0.76 - 0.75

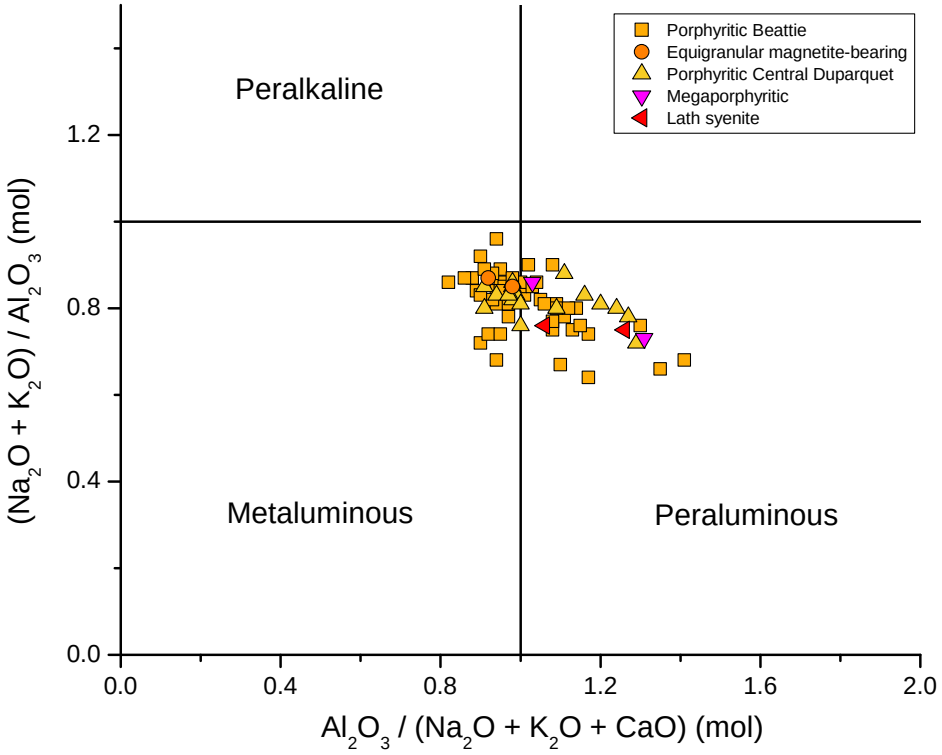


Figure 7.26 – Peralkaline, perlauminous and metaluminous characterization for samples of the Beattie syenite. Diagram obtained from Shand (1927).

units on the other hand are dominantly peraluminous.

The broadest ASI (1.41 - 0.82) belongs to the porphyritic Beattie unit extending into both the metaluminous and peraluminous fields. Only a single porphyritic Beattie sample strays close to the peralkaline field with a PI of 0.96. The remainder cluster at a PI between 0.80 - 0.90. The equigranular magnetite-bearing indexes demonstrate the least amount of variation. Both samples plot at the limit of the metaluminous field (ASI of 0.98 and 0.92). The porphyritic Central Duparquet unit also demonstrates a broad ASI (1.29 - 0.91) straddling both the metaluminous and peraluminous fields. Both megaporphyritic samples plot in the peraluminous field. These samples demonstrate a high ASI (1.31 - 1.03) and PI (0.86 - 0.73). Samples from the lath syenite unit are also peraluminous with an ASI between 1.26 - 1.06 and

a PI of 0.76 - 0.75.

The obtained indexes correspond well to the mineralogical assemblage of the syenite. Specifically, no feldspathoids were noted confirming that the Beattie syenite is not peralkaline. Rather, the feldspar-dominated syenite corresponds very well to a metaluminous to slightly peraluminous characterization. ASI variation encountered between the units could be the result from local alteration severity (i.e., sericitization) as this variation was not observed in the igneous mineralogical assemblage (see Chapter 6).

7.7.2 Incompatible trace elements

Older analyses performed in the 1990s were discarded due to their incompleteness, high detection limit and precision error. Only values from the least-altered samples with complete analyses were considered. As such, a total of 29 samples from all 5 syenitic units have been normalized to the chondritic values of McDonough and Sun (1995) presented in Table 7.5. In light of the high number of samples, averages from of each unit are presented together in Figure 7.27. A more detailed perspective of individual samples is presented in Figure 7.28.

The most prominent feature brought out in Figure 7.27 is that the averaged normalized samples from each unit all possess the same pattern. This feature is consistent with the hypothesis that all the units of the Beattie syenite are comagmatic. Very little concentration variation is observed between the units. This supports the concept that there was very little differentiation between the units. This hypothesis is reflected with major elements which all possess similar oxide and elemental concentrations. A small enrichment is noted in Sr of the equigranular magnetite-bearing unit. This discrepancy could have been produced by leaching in all other syenitic units during hydrothermal alteration as its behaviour is similar to Ca.

One sample (2009048663) from the porphyritic Beattie unit demonstrates an anomalous chondrite normalized pattern when compared to all others in Figure 7.28. This sample displays a strong depletion in HREE and is typical of samples analyzed in Au-mineralized and highly-altered areas. This particular sample was obtained at the edge of one of a small syenitic lens in the SCB, in close proximity to the Donchester fault (see Chapter 5). Consequently, this sample will be excluded from the discussion below.

Chondrite normalized patterns from each unit demonstrate a decreasing trend defined by a string enrichment of the LREE. The $[La/Yb]_{cn}$ values range from 56.6 to 27.8 for the

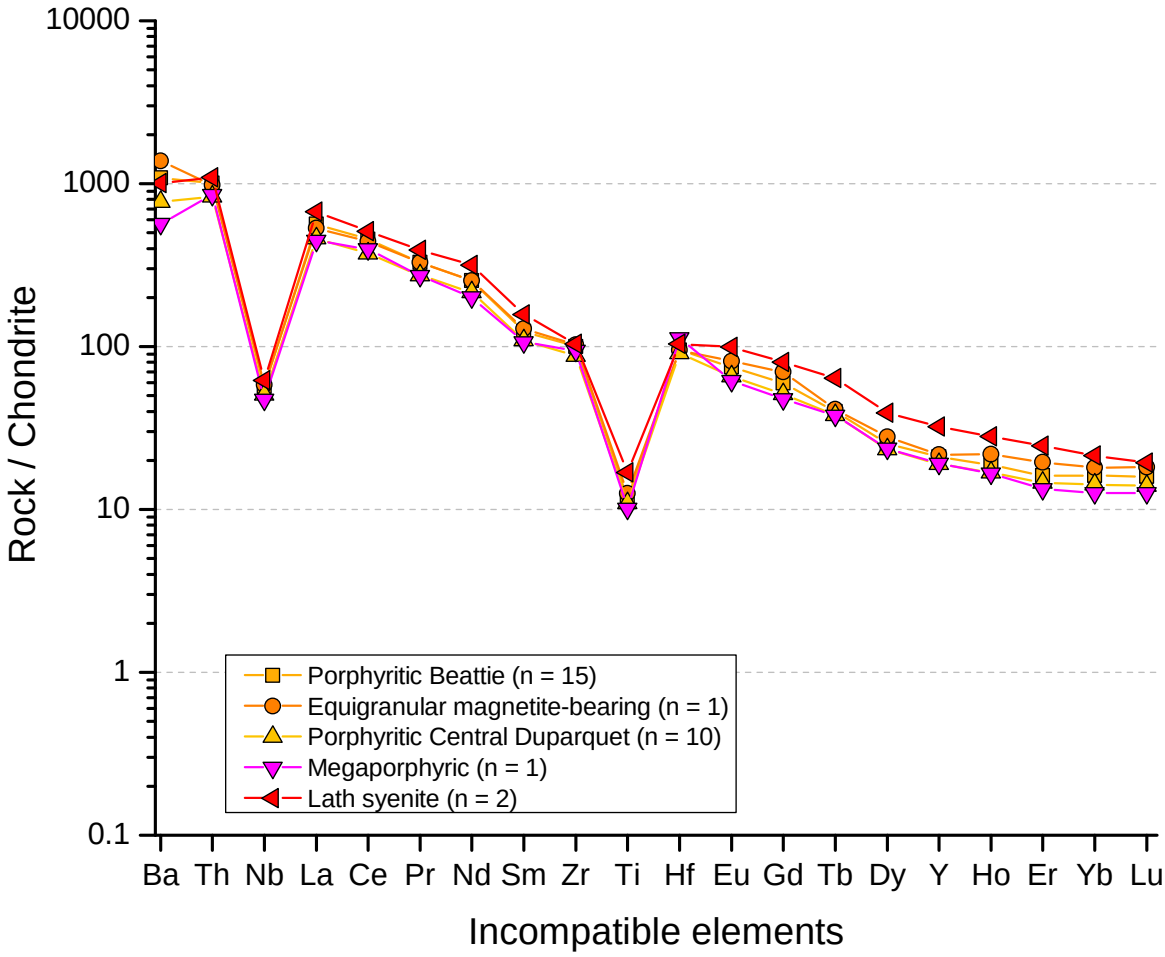
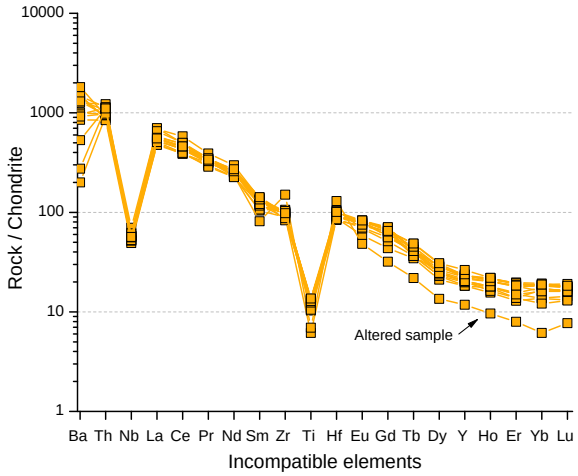


Figure 7.27 – Averaged chondrite-normalized incompatible trace element pattern of all the syenitic units. Normalizing factors are those of McDonough and Sun (1995) presented in Table 7.5. Here n = number of samples averaged.

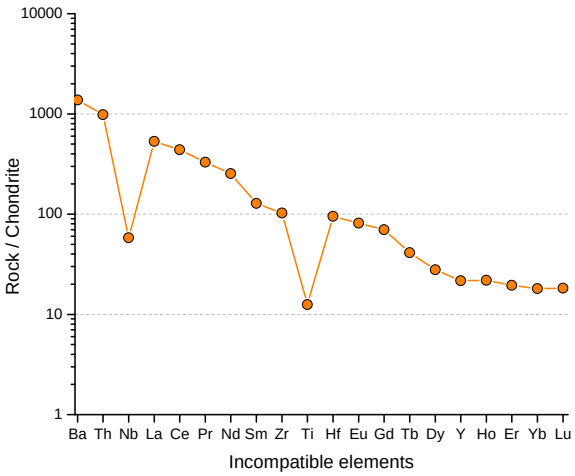
porphyritic Beattie unit, 29.4 for the equigranular magnetite bearing unit, 41.3 to 28.5 for the porphyritic Central Duparquet unit, 35.3 for the megaporphyritic unit and 35.3 to 27.7 for the lath syenite unit. Additionally, all the patterns for the units demonstrate a negative Nb anomaly. The implications for this anomaly will be discussed in Section 7.7.4. Further investigations revealed that LILE are also enriched compared to chondritic values (not shown). However, caution should be exercised with LILE element Ba as it is highly variable and therefore not considered as an immobile element for the Beattie syenite.

7.7.3 Rare earth elements

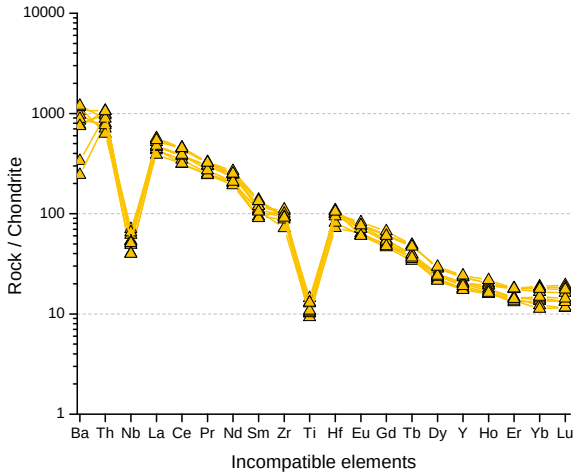
The REE concentrations of the least hydrothermally altered units have been included in Table 7.17. Analyses performed in the 1990s were excluded as they are incomplete, have a high



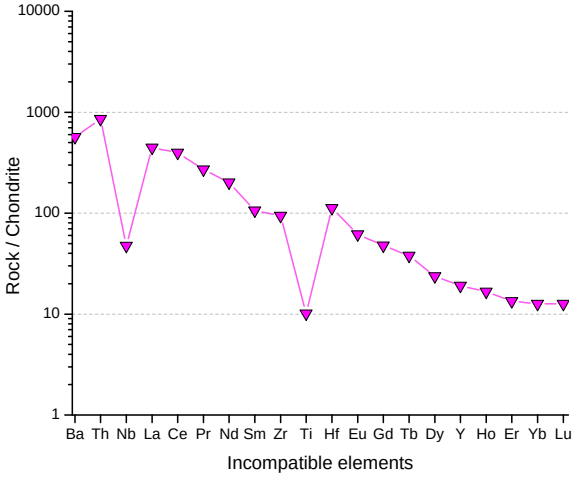
(a) Porphyritic Beattie syenite unit



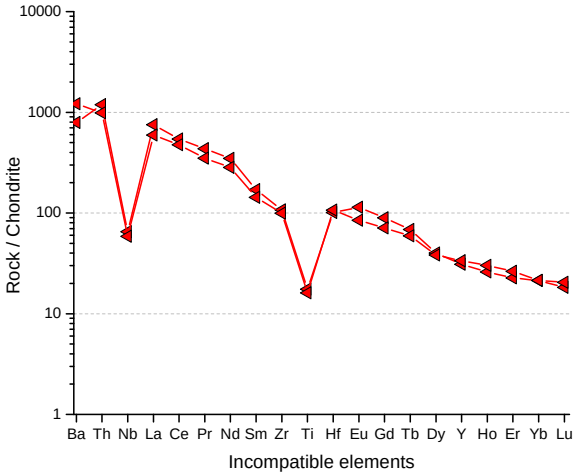
(b) Equigranular magnetite-bearing unit



(c) Porphyritic Central Duparquet unit



(d) Megaporphyritic syenite unit



(e) Lath syenite unit

Figure 7.28 – Chondrite-normalized incompatible trace element pattern for individual units of the Beattie syenite. Normalizing factors are those of McDonough and Sun (1995) presented in Table 7.5.

detection limit and precision error. As a result a total of 8 samples were excluded from this section, but can be consulted in Appendix D. Normalizing chondritic values used are those of McDonough and Sun (1995), given in Table 7.5. The chondrite-normalized samples of the Beattie syenite are given in Figure 7.29.

In light of the amount of samples, REE patterns have also been separated according to each unit and are presented in Figure 7.30.

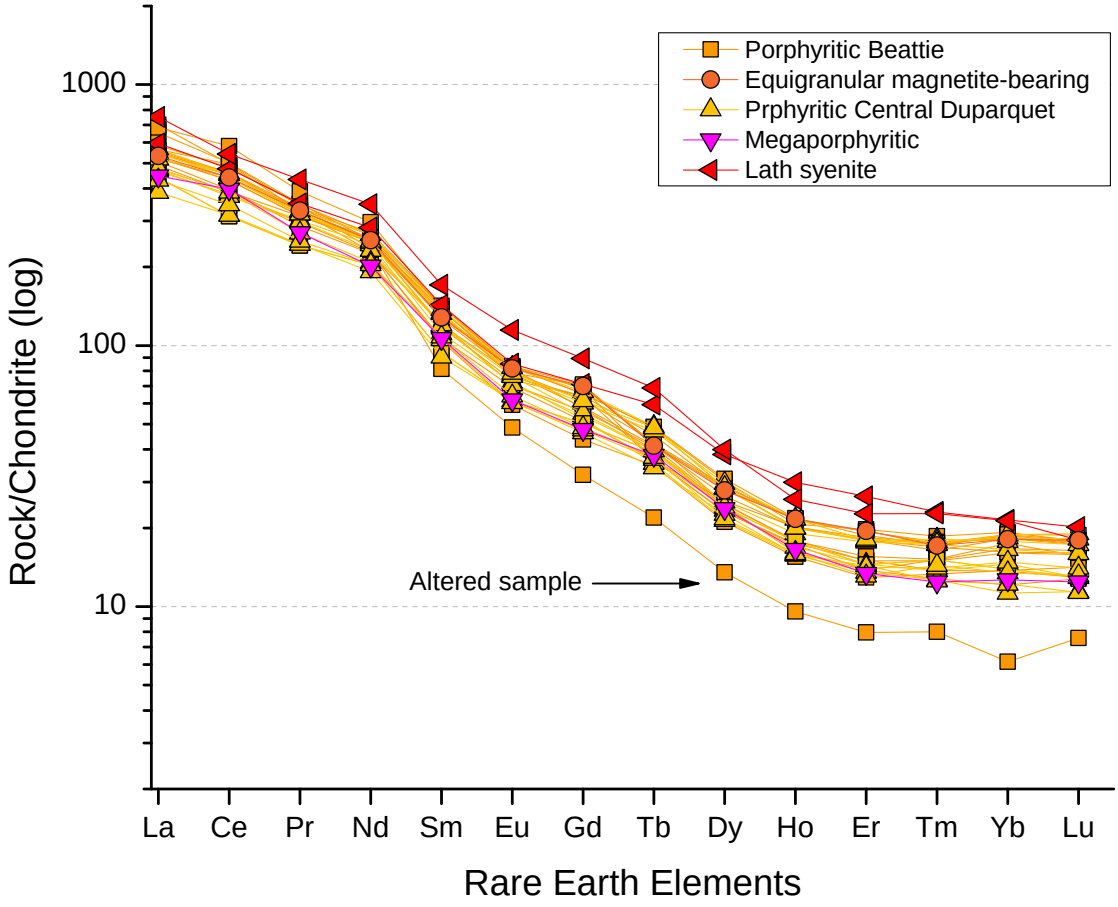
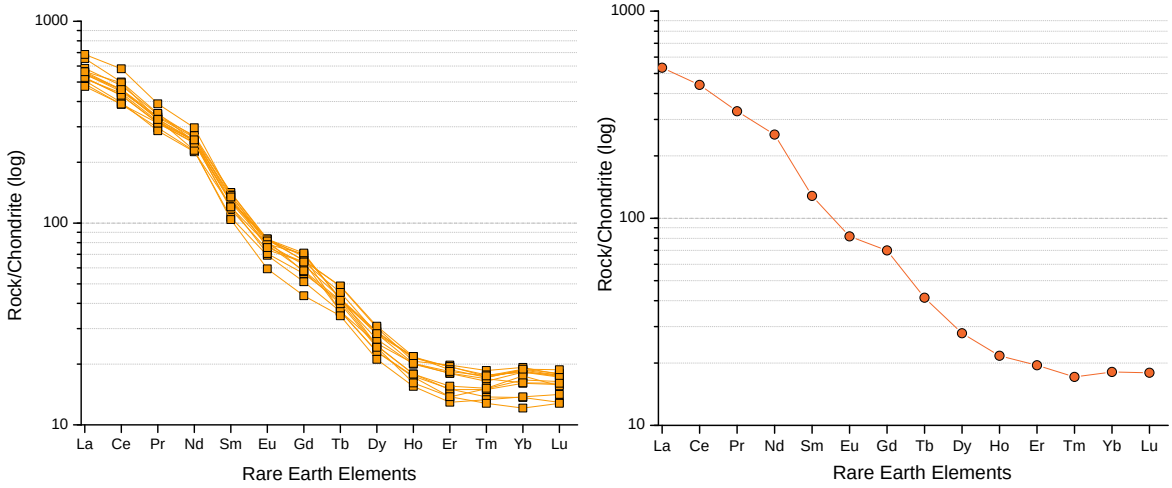


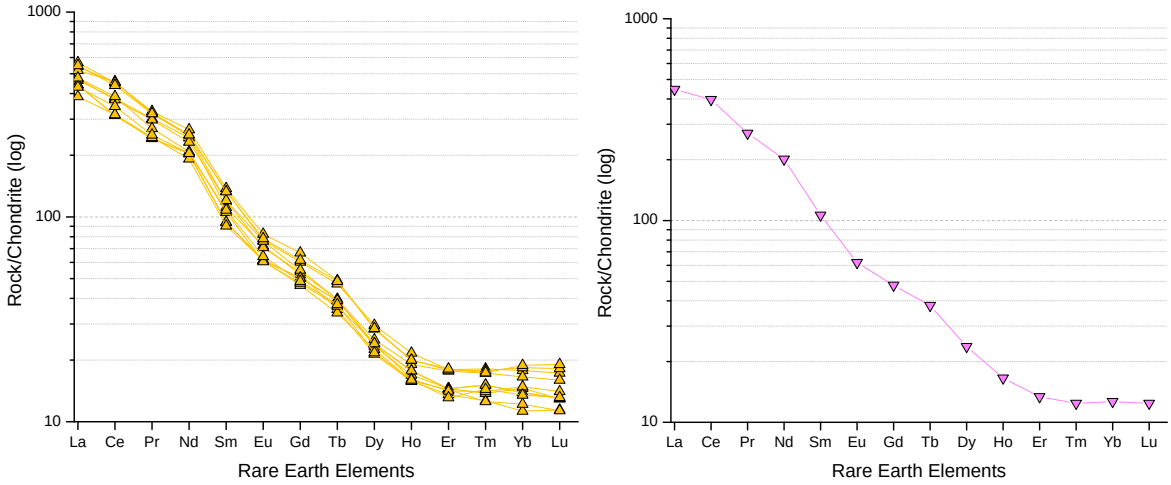
Figure 7.29 – Chondrite normalized REE pattern of the Beattie syenite. Normalizing factors are those of McDonough and Sun (1995), listed in Table 7.5. An altered sample (indicated by arrow) illustrates that concentration divergence exhibited in Au-mineralized and highly altered samples.

The REE patterns of all syenitic samples possess the same trend with a strong enrichment of LREE in which LREE>HREE. This similarity serves to reinforce the hypothesis that the units are comagmatic. The REE patterns do not demonstrate significant concentration variation between the majority of the units. The only exception is seen in a slight enrichment of the lath syenite with respect to all other units. This enrichment is expected since the lath unit is



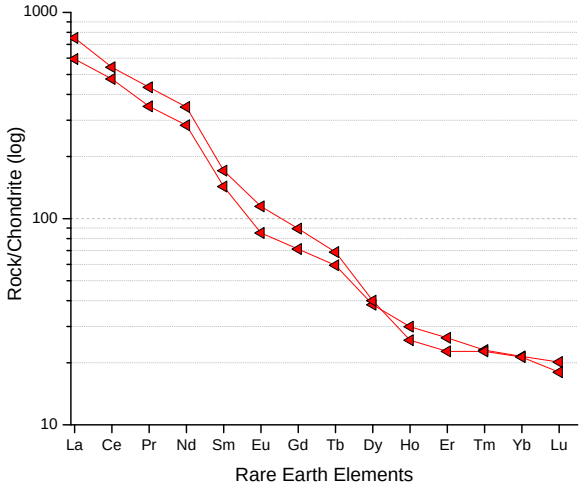
(a) Porphyritic Beattie syenite unit

(b) Equigranular magnetite-bearing unit



(c) Porphyritic Central Duparquet unit

(d) Megaporphyritic syenite unit



(e) Lath syenite unit

Figure 7.30 – Chondrite-normalized REE diagram of the Beattie syenite units. Normalizing factors are those of McDonough and Sun (1995), listed in Table 7.5. Altered and Au-mineralized samples have been excluded.

the youngest of the Beattie syenite. It is evident that there has been very little differentiation between the stages of emplacement when considering that the REE concentrations between the units are remarkably similar. This trend was also reflected in the normalized incompatible trace elements pattern (see Figure 7.27). Individual REE characteristics of each syenitic unit is presented in the following Table.

Table 7.20 – REE characteristics of the syenitic units.

Unit	$\sum REE$	$[La]_{cn}$	$[Lu]_{cn}$	$[La/Lu]_{cn}$	Eu/Sm	$[Eu/Eu^*]_{cn}$
Porphyritic Beattie	739 - 528 ppm	475.3 - 701.3	18.8 - 12.8	53.6 - 29.5	0.25 - 0.21	0.88 - 0.76
Equigranular magnetite-bearing	596 ppm	532.8	17.9	29.7	0.24	0.82
Porphyritic Central Duparquet	604 - 434 ppm	566.8 - 386.7	18 - 11.2	40.8 - 28.8	0.26 - 0.21	0.87 - 0.79
Megaporphyritic	508 ppm	446.6	12.4	36	0.22	0.8
Lath syenite	657 - 781 ppm	751.4 - 594.2	20.1 - 18	41.7 - 29.5	0.25 - 0.23	0.88 - 0.80

Detailed investigations of the characteristics of individual units reveal that the units possess a very small to no Eu anomaly. Archean syntectonic plutons do not typically possess a large negative Eu anomaly, whereas synvolcanic plutons will (Goutier, pers. comm., 2013). The lack of any significant Eu anomalies in all of the units could indicate that there was very limited fractionation, where plagioclase did not fractionate or that fO_2 remained high throughout the petrogenesis of the Beattie syenite (Henderson, 1984).

7.7.4 Tectonic setting

The first trace element discrimination diagrams providing a means of fingerprinting a tectonic setting for plutonic igneous plutons was produced by Pearce et al. (1984). These diagrams are based on variations of immobile trace element concentrations such as Rb, Y, Yb and Ta. Together, they can discriminate between volcanic arc granites (VAG), syn-collisional granites (syn-COLG), within plate granites (WPG) and ocean ridge granites (ORG). The behaviour of these elements and consequently the interpretation of the diagrams is not without warning. First and foremost, these diagrams are ideally meant to classify fresh, minimally altered, non-cumulate, non-porphyritic and non-aplitic plutonic rocks containing free visible quartz (Pearce et al., 1984).

Fortunately, the Beattie syenite does not demonstrate cumulate characteristics. However, the abundance of phenocrysts might be regarded as the beginning states of a cumulate. Nonetheless, the chemistry of the units do not reflect any evidence of a cumulate. Specifi-

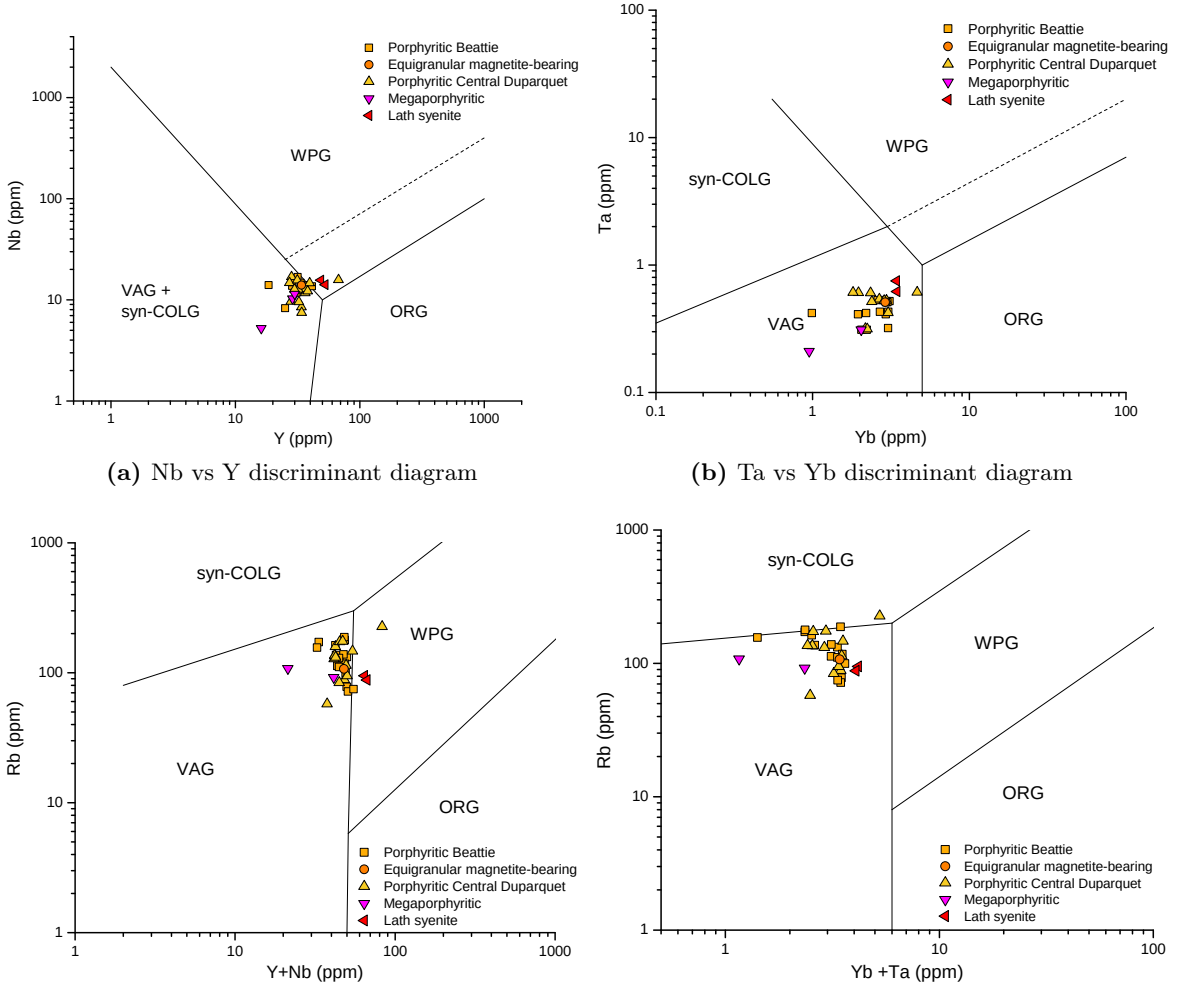
cally, all the units are syenitic in composition and possess similar characteristics. The only significant variance from this trend is encountered in the slight REE enrichment of the lath syenite unit. Overall, the Beattie syenite is characterized as porphyritic, however not all units are so (i.e., the equigranular magnetite-bearing unit). Finally, investigations using the CIPW normative mineralogy have classified the Beattie syenite as silica saturated.

Additional caution should also be exercised due to the behaviour of immobile trace elements in alteration regimes. The effects of hydrothermal sericitization are denoted by an enrichment of Rb. This elemental enrichment was particularly noted in areas of Au-mineralization. Furthermore, Rb tends towards depletion in chloritization and argillic alteration regimes. Elements such as Y and Nb demonstrate little variation during sericitization. However, Y is known to increase slightly at low temperature alteration such as chloritization (Jiang et al., 2005). A major exception to the relative element immobility is made when tourmalinization occurs, resulting in pervasive elemental depletion (Pearce et al., 1984).

Given that the syenite underwent both sericitization and chloritization, it stands to reason that the variations in Rb would be attenuated. This was also later confirmed via hydrothermal alteration studies (see Section 8.2.1). As for tourmalinization it is evident that it is the product of subsequent alteration as it is exclusively localized in secondary D_2 shear faults (see Chapter 8).

Given all these reasons, the tectonic setting trace element discrimination diagrams for all the units of the Beattie syenite is presented in Figure 7.31. Both altered and least-altered samples were utilized in the tectonic discrimination diagrams. Altered samples were included since they generally plot with the majority of the least-altered samples. However, large discrepancies are noted for heavily Au-mineralized samples.

The units of the Beattie syenite plot distinctively within the VAG field (see Figure 7.31). The only exceptions are found in Figure 7.31a and 7.31c in which the lath syenite crosses into the WPG field. This overlap is not concerning, especially when it is to such a low degree. Given that the lath syenite is the youngest of the units, a slight deviation, as an enrichment in Y would not be unusual. Nonetheless, the lath unit shares the same magmatic source as the other units. Therefore the lath unit is considered to be part of the same tectonic setting. Furthermore, the porphyritic units share the same field as the non-porphyritic equigranular magnetite-bearing unit, indicating that the concerns raised by Pearce et al. (1984) about



(a) Nb vs Y discriminant diagram

(b) Ta vs Yb discriminant diagram

(c) Rb vs (Y+Nb) discriminant diagram

(d) Rb vs (Yb+Ta) discriminant diagram

Figure 7.31 – Tectonic discrimination for the Beattie syenite. Diagrams are provided by Pearce et al. (1984). Discrimination fields are volcanic arc granite (VAG), syn-collisional granite (syn-COLG), within plate granite (WPG) and ocean ridge granite (ORG).

porphyritic plutons can be dismissed in the case of the Beattie syenite.

Additional warnings are given by Pearce et al. (1984) concerning Archean plutons. Differences between Phanerozoic and Archean conditions are: 1) higher Rb values, 2) slightly higher Y and Nb values, 3) a higher degree of partial melting, 4) a less fractionated mantle, and 5) a higher degree of crustal melting.

Results for the Beattie syenite demonstrate that even after a hypothetical enrichment of Rb, Y and Nb, the tectonic setting is not overly affected (see Figure 7.31). Geochemical studies of syntectonic AGB plutons do confirm a higher concentration of Rb (Feng and Kerrich, 1992) (referred by Feng and Kerrich as late-tectonic plutons), especially in zones of Au-mineralization

(see Section 7.6). Additionally, these syntectonic plutons reveal strongly fractionated REE patterns and marked Ta and Nb depletions (Feng and Kerrich, 1992), disproving Pearce et al. (1984) hypothesis of higher Archean Nb values. Finally, an enrichment in Y might also explain the crossing of the lath unit into the WPG field.

The Archean heat flow compared to today is assumed to have been 2 - 3 times higher (Eriksson et al., 2004). Consequently, partial melting of the mantle and crustal melting would have been significant factors in the initial magmatic production. Theoretically, a higher degree of partial melting and crustal contamination would result in the loss of a definite boundary between the syn-COLG and VAG fields due to higher Rb concentrations contained in the crust. Only in diagram 7.31d is the Beattie syenite close to the syn-COLG field. Yet studies of late-tectonic plutons in the AGB suggest that they may have been derived from low degrees of partial melting of a metasomatized depleted mantle (Feng and Kerrich, 1992).

As for the degree of mantle fractionation, current isotopic studies increasingly point to an early differentiation of the Earth, closely linked to the progressive accretion of the planet (Eriksson et al., 2004). Consequently, fractionation differences between a contemporary and Archean mantle should be less than that proposed by Pearce et al. (1984).

In light of the multiple warnings, a diagram by Harris et al. (1986) was employed to supplement the tectonic setting of the Beattie syenite. This ternary diagram is based on trace element (Hf, Rb, and Ta) distribution. Results for the units of the Beattie syenite are presented in Figure 7.32.

Both tectonic discrimination techniques support that the Beattie syenite has originated in a volcanic arc setting. However, the use of these diagrams is fraught with warnings and are ideally not suited for Archean plutonism. As such, other methods are required to determine the tectonic setting of the Beattie syenite.

The normalized incompatible trace element pattern of the Beattie syenite demonstrate a negative Nb anomaly. Studies on mineral/melt partition coefficients revealed that Nb strongly partitions (in decreasing order) into biotite, titanite, hornblende and to a lesser extent, clinopyroxene. Both biotite and hornblende are hydrous minerals and are absent from our syenitic mineralogical assemblage. Instead, the Beattie syenite contains clinopyroxene as the dominant ferromagnesian mineral, which is considered overall a rare occurrence in syenites (Moorhouse, 1959). As such the negative Nb anomaly is chiefly due to the absence of both hornblende

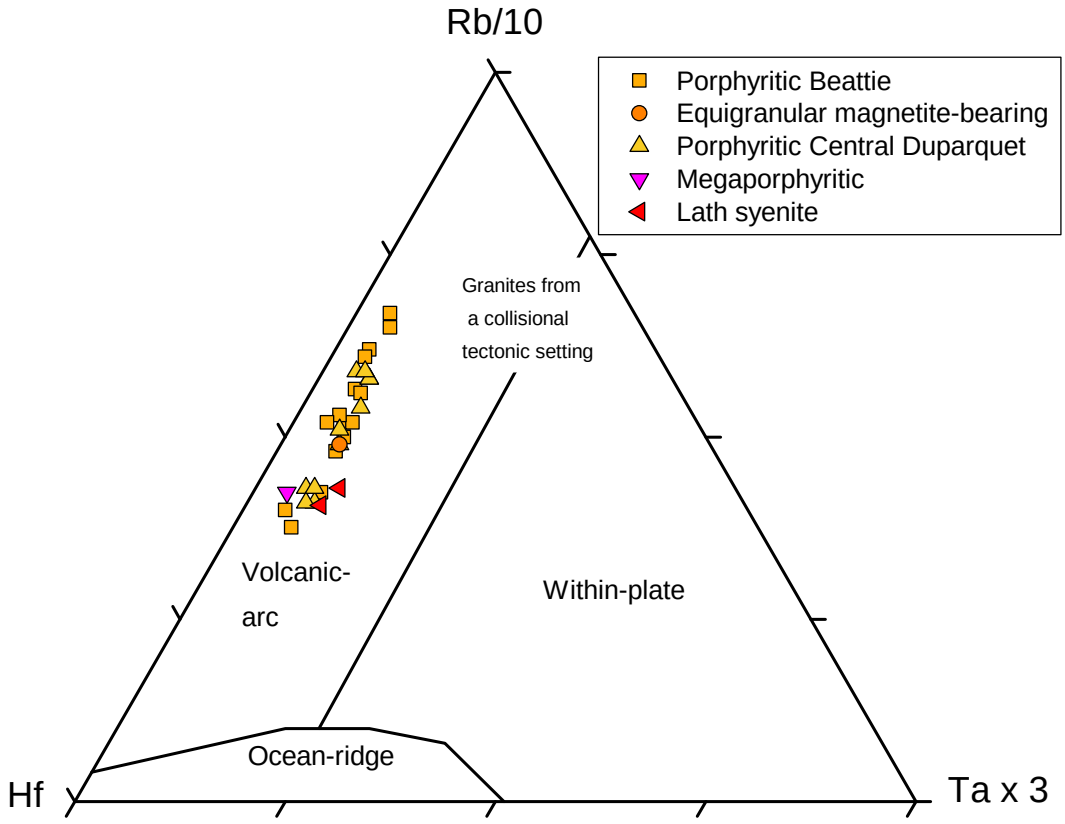


Figure 7.32 – Tectonic discrimination diagram for the Beattie syenite. Ternary diagram produced by Harris et al. (1986).

and biotite, which could be either due to the anhydrous nature of the primary melt, or that they were fractionated at depth. Given that syenites are typically anhydrous, when compared to granites, it would seem that the absence of hornblende and biotite is a reflection of the anhydrous nature of the primary melt. As such, the primary melt contained very little H_2O, much less than that of a typical syenite where hydrous minerals are common.

The strong depletion of the HREE compared to the LREE in the normalized REE patterns imply that garnet, which preferentially strongly partitions the HREE, was not at equilibrium at the time of melting. Consequently, the primary syenitic melt could not have originated from deep fractionation processes. Rather, the Beattie syenite was likely produced from crustal melting. Supplementing this hypothesis is the negative Nb anomaly, which is attributed to an anhydrous primary melt. Anhydrous melts are typically obtained by partial melting of the mantle or the lower crust. Since the REE characteristics preclude a deep fractionation process, it is logical that the Beattie syenite originated from the partial melting of the lower crust.

Current hypotheses on the origin of syntectonic plutons within the AGB all include a subduction related tectonic setting (Feng and Kerrich, 1992; Chown et al., 2002; Ayer et al., 2010). Recently there are 2 hypothetical scenarios considered for the generation of these plutons. Scenarios indicate that plutons are the result of: 1) successive accretion events with contamination of ancient, non-AGB crust or, 2) the progressive closure of oceanic basins accompanied by sediment subduction first to the north between the AGB and Opatica Subprovince and later to the south, between the AGB and Minnesota River Subprovince (Ayer et al., 2010).

The most likely of the scenarios suggested would be the successive accretion events with contamination of ancient, non-AGB crust. However, the Beattie syenite is hypothesized to have been produced from crustal melting, as opposed to crustal contamination. Unfortunately, any evidence of crustal contamination is unverified due to a lack of isotopic data. The second scenario involving sediment subduction seems unlikely, as subducting hydrous sediments would be at odds with the anhydrous nature of the primary syenitic melt.

In the Beattie area, the accumulation of the Porcupine followed by the Timiskaming sediments suggest that the area into which the syenite intruded was under an extensional setting. Core components of such settings include crustal thinning, heating and melting, all of which are consistent with both the incompatible trace elements and REE signatures of the Beattie syenite. To this end, the Beattie syenite is suggested to have originated in an extensional setting from crustal melting, rather than in a VAG setting.

Chapter 8

Hydrothermal alteration, deformation and metamorphism to the greenschist facies of the Beattie syenite

Following igneous crystallization, the Beattie syenite underwent events of hydrothermal alteration and deformation, both of which were later accompanied by regional metamorphism to the greenschist facies. Using all data established in the previous two chapters, this chapter is divided into two major parts. The first section focuses on the petrographic and mineralogical changes produced by hydrothermal alterations and regional metamorphism, followed by a brief description of changes produced by deformation. The second part focuses on the geochemical characteristics of the Au-mineralization and regional metamorphism of the Beattie syenite and country rocks.

8.1 Hydrothermal alterations, metamorphism to the greenschist facies and deformation petrography and mineralogy

8.1.1 Hydrothermal alterations and metamorphism to the greenschist facies

The syenite is transected or overprinted by an assortment of hydrothermal and greenschist facies minerals. Occasionally, these minerals are sufficiently abundant and fine, such that

they have locally (up to ∼decametre scale) changed the characteristics and physical properties of the syenite. In other instances, minerals filled tension fractures without interacting with the encasing syenite. Large scale observations reveal that hydrothermal minerals are more abundant in the western parts of the Beattie syenite in close proximity to the PDFZ, suggesting that the fracturing associated with the PDFZ likely enhanced hydrothermal fluid channelling. Greenschist facies minerals are best observed in the equigranular magnetite-bearing unit, since this unit supports the least amount of hydrothermal alteration and deformation. The large variety of hydrothermal and greenschist facies minerals is best discussed individually, in order of abundance as determined from macroscopic and microscopic observations. Hence, Table 8.1 provides individual mineral modal percentages observed on the microscopic scale. The following descriptions apply to all the petrographic units in varying degrees of extent, unless otherwise specified.

Table 8.1 – Range and modal composition of hydrothermal and metamorphic minerals in the Beattie syenite. Ranges are based on 23 thin sections for the porphyritic Beattie syenite, 2 for the equigranular magnetite-bearing, 9 for the porphyritic Central Duparquet, 6 for the megaporphyritic and 6 for the lath syenite units. All ranges and modal compositions are given in percent.

	Porphyritic Beattie		Equigranular	Central Duparquet		Megaporphyritic		Lath syenite	
Mineral	Maximum range	Typical composition	Typical composition	Maximum range	Typical composition	Maximum range	Typical composition	Maximum range	Typical composition
Carbonate minerals[2]	1 - 25	10	1	2 - 20	7	2 - 21	10	2 - 12	5
Sericite	2 - 30	15	—	1 - 22	13	3 - 15	7	10 - 30	10
Hematite	1 - 7	5	1	1 - 3	2	1 - 2	1	0 - 5	1
Albite	0 - 10	1	—	0 - 5	1	0 - 3	trace	0 - 1	trace
Chlorite	0 - 15	trace	0 - 2	0 - 1	0	0 - 1	0	0 - 5	1
Quartz	0 - 15	0	—	1 - 2	1	1 - 48	1	0 - 1	0
Pyrite[1]	0 - 2	0	—	0 - 2	trace	0 - 3	1	trace - 1	trace
Arsenopyrite[1]	0 - 3	0	—	0 - 2	trace	0 - 2	trace	trace - 1	trace
Chalcopyrite[1]	0 - trace	0	—	—	—	0 - trace	0	0 - trace	0
Magnetite	0 - 2	1	—	0 - 1	1	0 - trace	0	0 - 2	1
Epidote	—	—	0 - 1	—	—	—	—	—	—
Biotite	0 - trace	0	—	—	—	—	—	—	—
Fluorite	0 - trace	0	—	—	—	—	—	—	—
Xenotime	0 - trace	0	—	—	—	—	—	—	—
Tourmaline	0 - trace	0	—	—	—	—	—	—	—
Hornblende	—	—	0 - trace	—	—	—	—	—	—
Galena[1]	—	—	—	—	—	—	—	0 - trace	0
Barite	—	—	—	—	—	—	—	0 - trace	0

[1] Grouped together under sulphide minerals
[2] More abundant based on field observations

Carbonate minerals

Carbonate minerals are found as 0.01 - 1.2 mm crystals replacing primary mafic minerals and rarely titanite, as 0.01 - 0.3 mm disseminated crystals or as 0.1 mm - 1 cm crystals in transecting veins.

Throughout the syenite, primary mafic minerals have been replaced by calcite or ankerite (verified via EMPA, see below) with accompanying chlorite and hematite (see Figure 8.1). Partial replacement textures are best observed in the equigranular magnetite-bearing unit where calcite is found either at the margins or at the centre of actinolite crystals as presented in Figure 8.2. In all the other syenitic units, primary mafic minerals have been completely replaced with the preservation of their general shape. However, in areas demonstrating moderate to extensive deformation and hydrothermal alteration, the shape of the mafic relicts has commonly been obliterated.

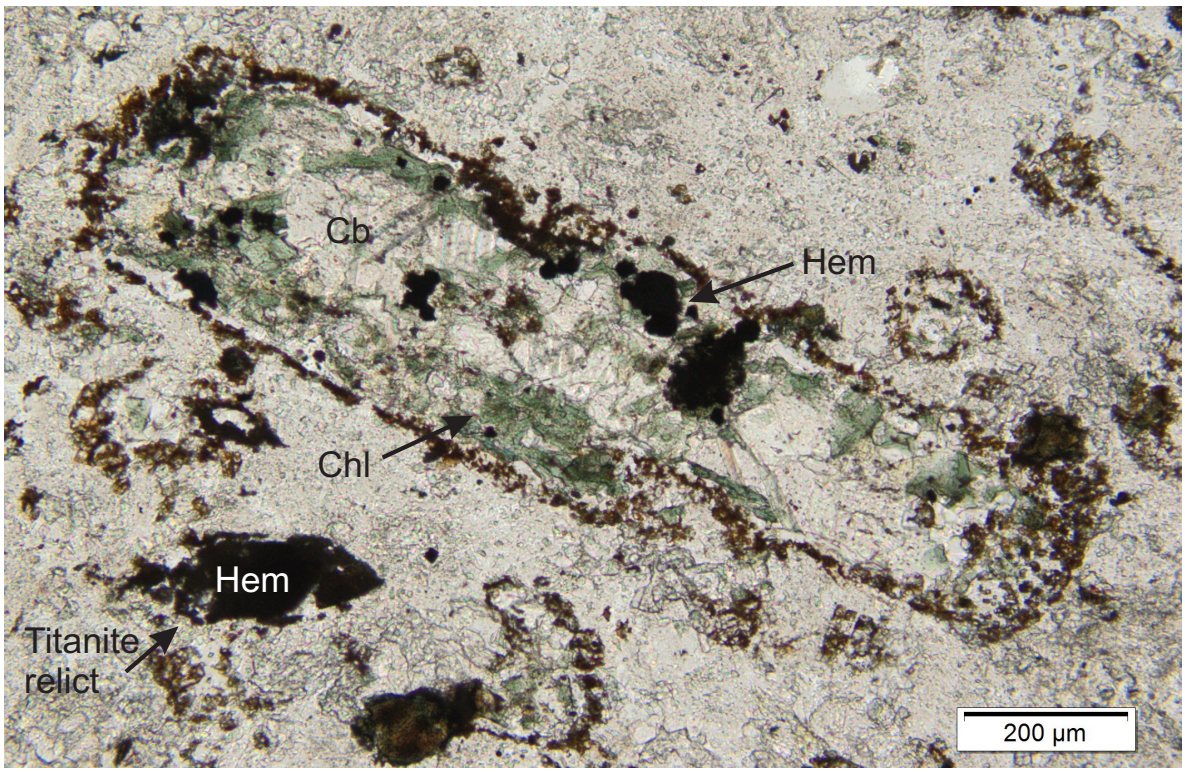


Figure 8.1 – Relicts of a mafic mineral and titanite. Minerals replacing the primary mafic mineral are carbonate minerals (Cb) at the centre, green chlorite (Chl) towards the margins and opaque hematite (Hem). Only hematite replaces the titanite relict which is located to the bottom left. Photomicrograph taken under plane polarized light. Location: 630652E 5374609N.

Carbonate minerals replacing primary titanite crystals is rare. In such cases, the titanite

relicts are dominantly composed of hematite and opaque clay materials, rarely with carbonate minerals found at their centre. The shape of the titanite relicts is commonly well preserved.

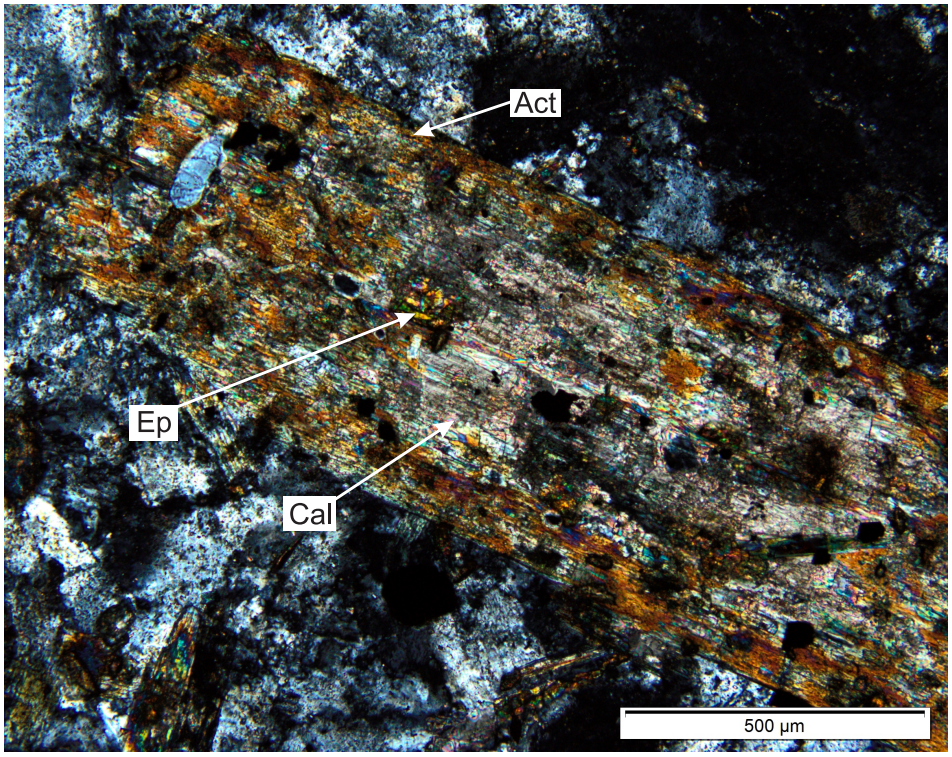


Figure 8.2 – Calcite (Cal) replacing actinolite (Act) in the equigranular magnetite-bearing unit. Calcite is accompanied by minor amounts of epidote (Ep), titanite, magnetite and hematite (opaques). Photomicrograph taken under crossed polars. Location: 630747E 5374454N.

Disseminated carbonate minerals occur throughout the syenite, but are best observed in cataclastic zones (see Figure 8.3). These zones form large E-W striking lenses measuring 1 - 10 m in length. Cataclasis resulted in the destruction of phenocrysts, and increased porosity, permitting the infiltration of carbonate-saturated solutions. This infiltration resulted in the current softened and orange-brown shades of the syenite. These lenses are typically encountered west of the abandoned Beattie mine shaft, although they have been observed up to midway between the Beattie and Donchester mine shafts. Fine-scale observations reveal that anhedral, disseminated carbonate crystals are evenly distributed throughout the rock. These crystals typically demonstrate advanced signs of alteration as presented in Figure 8.4, which explains the orange-brown shades of the carbonate-altered lenses. However, this alteration presented by these crystals also prevents their chemical determination. Further observations have found disseminated carbonate crystals in sericite veins. The crystals have been elongated

in the sense of the veins, indicating that disseminated carbonate minerals crystallized prior to sericite.



Figure 8.3 – Cataclastite filled with carbonate minerals. The cataclasis resulted in the destruction of feldspar phenocrysts and increased porosity, permitting the infiltration of carbonate-saturated solutions which changed the colour of the syenite to the current orange colour. Location: 630770E 5374365N.

Another rare form of disseminated carbonate minerals is expressed by the replacement of phenocryst or lath cores (see Figure 8.5). The amount of replacement varies between 40 - 80%$_m$ of the phenocryst, leaving a thin, millimetre sized rim of feldspar. The carbonatization of the phenocrysts is very local ($<$ 5 m) and is found in a few or all phenocrysts. Generally, these carbonatized areas are accompanied by a strong sericitization. This is observed by a green to grey coloured rim surrounding the phenocrysts, or more commonly, by a pale green matrix with pink patches, instead of the typical red colour.

Both disseminated and carbonate crystals in primary mineral relicts are temporally related as they share a similar size (0.1 - 0.6 mm), are typically altered and have been deformed by subsequent influx of sericite. The only minor difference is that crystals in primary mafic mineral relicts, phenocrysts or laths tend to be larger, measuring $\leq$ 1.2 mm across.

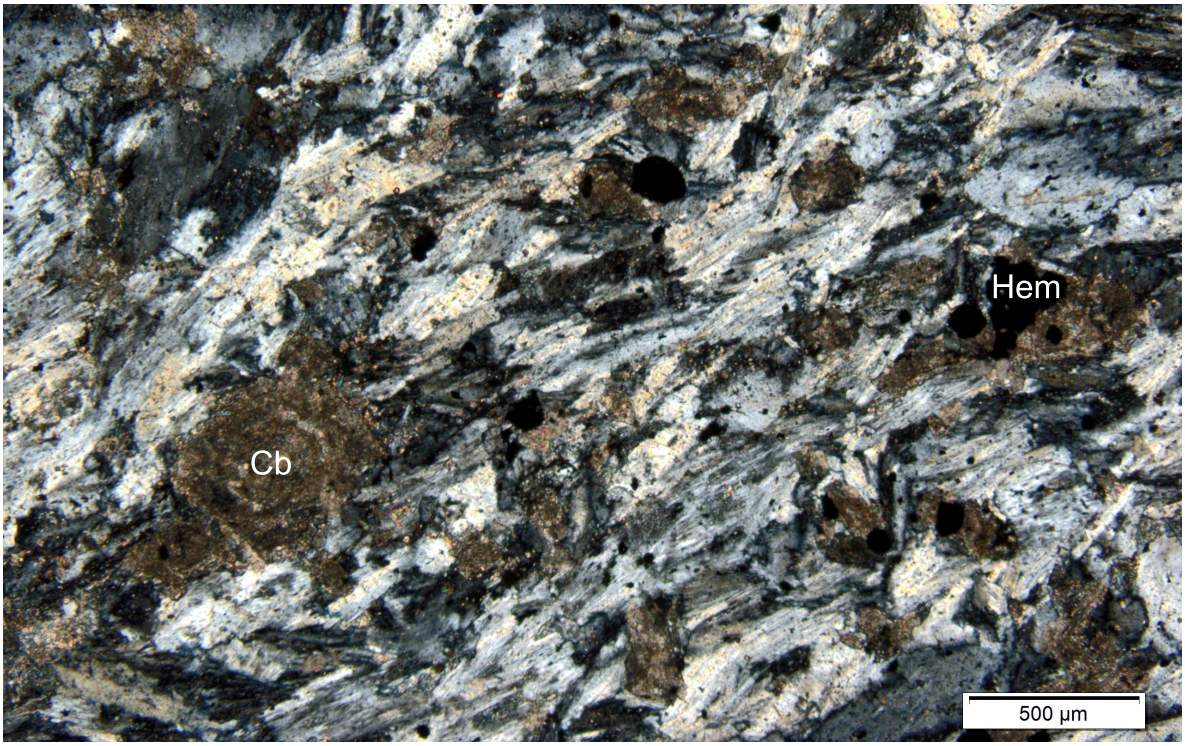


Figure 8.4 – Disseminated carbonate minerals (Cb) in the feldspathic matrix. Carbonate crystals are anhedral, evenly distributed though the matrix and demonstrate alteration, seen by a high turbidity. Photomicrograph taken under crossed polars. Location: 630963E 5374432N.

A later form of disseminated carbonate crystals is found in the equigranular magnetite-bearing unit where a few crystals are associated with metamorphic epidote, suggesting that a small portion (1 - 3%$_m$) of disseminated carbonate crystals may also be the product of subsequent metamorphism to the greenschist facies. These carbonate crystals can be set apart from the disseminated carbonate minerals by low amounts of alteration.

The oldest generation of carbonate minerals in veins occurs with albite, herein referred as Ab-Cb veins (see Figure 8.5). These veins measure between $<$ 1 mm - 3 cm across and only extend for short distances ($<$ 30 cm). Periodically, Ab-Cb veins occupy the central portions of pre-existing sulphide minerals veins in areas showing repeated brittle deformation and fluid injection. Slightly younger veins of quartz, albite and calcite to siderite (verified via EMPA, see below) $\pm$ dissolved, transported and recrystallized chlorite (Qtz-Ab-Cb veins) (see Figure 8.6) cut the Ab-Cb veins. The Qtz-Ab-Cb veins are slightly wider on average than the Ab-Cb veins ($<$ 5 cm wide). Both the Ab-Cb and Qtz-Ab-Cb veins are cut by quartz with lesser amounts of carbonate minerals veins (Qtz-Cb veins). Carbonate crystals in veins are beige-

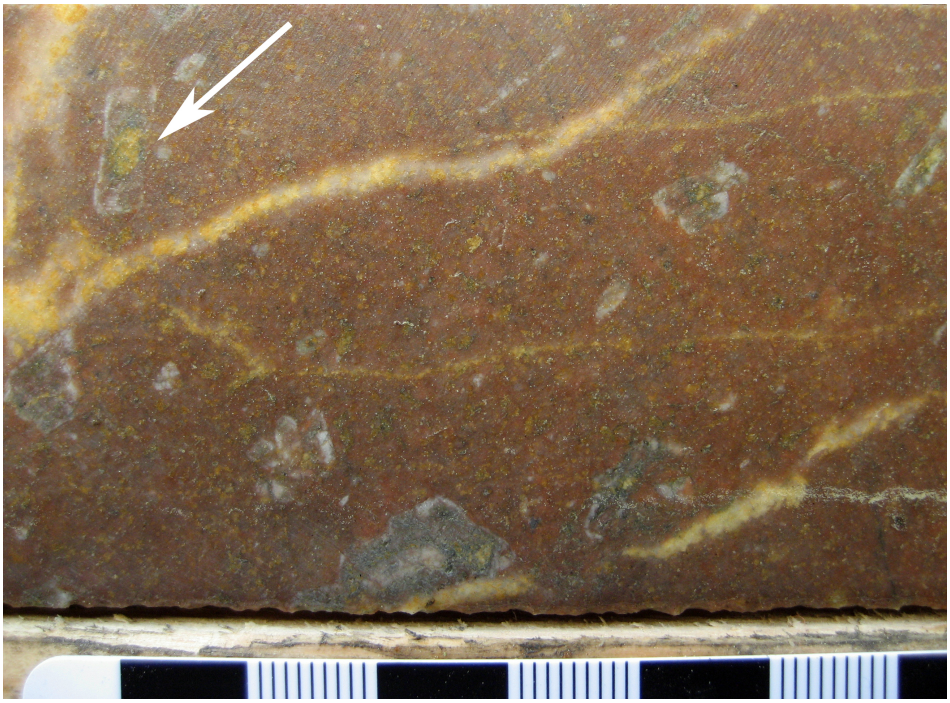


Figure 8.5 – Core of phenocrysts replaced by beige carbonate minerals (arrow). Feldspar phenocrysts are sub- to anhedral, measuring < 1 cm across. The drill core is also transected by carbonate minerals (orange-beige) and albite (white) filled veins. Drill core: B09-108, depth: 3.40 - 4.40 m.

orange in colour, measure $<$ 1 mm - 1 cm across, with the exception of the youngest generation of crystals in Qtz-Cb veins, which are euhedral and measure $<$ 1 cm across. In comparison to disseminated crystals, carbonate minerals in veins are subhedral, larger and demonstrate less alteration. Furthermore, rhombohedral cleavage and lamellar twinning are clearly seen in these crystals.

The chemical composition of carbonate minerals was subsequently verified via EMPA. A total of 10 analyses were performed on crystals in primary mafic mineral relicts and in Qtz-Ab-Cb veins. Disseminated carbonate minerals were not analyzed due to the advanced alteration demonstrated by the majority of crystals. It should therefore be noted that the analyses below are not representative for the disseminated carbonate minerals. All carbonate minerals were calculated on an 6 oxygen basis. The origin of the analysis, composition and chemical formula are presented in Table 8.2.

In addition to the standard detected elements, an appreciable amount of Sr^{2+} was also detected via EDS for analysis 47-9-1. While the Sr^{2+} is well below those of Fe^{2+} and Mg^{2+}, it is above the Mn^{2+} concentration. Additionally, small amounts of Mn^{2+} were detected in the

Table 8.2 – Microprobe analyses and chemical formulas of carbonate minerals.

	Beattie	Transition		Equigranular	Central Duparquet	
	42-1-1 Qtz-Ab-Cb vein	**58-1-1** Relict	**58-6-4** Relict	**JG-04-18** Relict	**47-9-1** Qtz-Ab-Cb vein	**56-6-1** Qtz-Ab-Cb vein
FeO	0.93 ± 0.06	0.26 ± 0.04	0.34 ± 0.04	0.15 ± 0.02	18.49 ± 0.24	52.96 ± 0.48
MnO	0.70 ± 0.06	1.69 ± 0.07	1.25 ± 0.07	0.40 ± 0.03	1.66 ± 0.07	1.67 ± 0.07
MgO	0.13 ± 0.02	0.21 ± 0.05	0.21 ± 0.00	0.06 ± 0.00	8.55 ± 0.09	4.81 ± 0.07
CaO	56.96 ± 0.40	55.53 ± 0.39	56.30 ± 0.39	51.79 ± 0.36	26.70 ± 0.21	0.42 ± 0.03
BaO	0.01 ± 0.00	0.07 ± 0.02	0.03 ± 0.02	0.00 ± 0.01	0.00 ± 0.00	0.03 ± 0.00
CO_2 (calc)	45.85	45.04	45.40	41.05	42.65	39.07
Total	58.74	57.77	58.49	52.59	55.39	59.90
Chemical formula based on 6 oxygens						
Fe^{2+}	0.03 ± 0.00	0.01 ± 0.00	0.01 ± 0.00	0.00 ± 0.00	0.53 ± 0.01	1.66 ± 0.01
Mn^{2+}	0.02 ± 0.00	0.05 ± 0.00	0.03 ± 0.00	0.01 ± 0.00	0.05 ± 0.00	0.05 ± 0.00
Mg^{2+}	0.01 ± 0.00	0.01 ± 0.00	0.01 ± 0.00	0.00 ± 0.00	0.44 ± 0.00	0.27 ± 0.00
Ca^{2+}	1.95 ± 0.01	1.94 ± 0.01	1.95 ± 0.01	1.98 ± 0.01	0.98 ± 0.01	0.02 ± 0.00
Ba^{2+}	0.00 ± 0.00	0.00 ± 0.00	0.00 ± 0.00	0.00 ± 0.00	0.00 ± 0.00	0.00 ± 0.00
C^{4+}	2.00	2.00	2.00	2.00	2.00	2.00
Mol% end-member						
Calcite:	98.43 ± 1.46	99.12 ± 1.45	99.02 ± 1.43	99.61 ± 1.42	50.35 ± 0.76	0.87 ± 0.06
Dolomite:	0.31 ± 0.05	0.52 ± 0.05	0.51 ± 0.05	0.16 ± 0.03	22.44 ± 0.37	13.82 ± 0.29
Siderite:	1.25 ± 0.08	0.36 ± 0.06	0.47 ± 0.06	0.23 ± 0.03	27.21 ± 0.50	85.32 ± 1.52
Mol% end-member including rhodochrosite						
Calcite:	97.50 ± 1.50	96.81 ± 1.50	97.33 ± 1.49	99.01 ± 1.45	49.13 ± 0.70	0.84 ± 0.05
Dolomite:	0.31 ± 0.05	0.51 ± 0.05	0.51 ± 0.05	0.16 ± 0.03	21.89 ± 0.37	13.45 ± 0.29
Siderite:	1.24 ± 0.08	0.35 ± 0.05	0.46 ± 0.05	0.22 ± 0.03	26.56 ± 0.50	83.05 ± 1.53
Rhodochrosite:	0.95 ± 0.08	2.33 ± 0.10	1.71 ± 0.10	0.60 ± 0.05	2.41 ± 0.11	2.65 ± 0.12

Table 8.2 Continued

	Central Duparquet	Lath syenite		
	56-6-2 Qtz-Ab-Cb vein	**21-2-1** Relict	**21-2-2** Relict	**21-4-1** Relict
FeO	54.22 ± 0.43	15.30 ± 0.21	21.94 ± 0.26	9.82 ± 0.18
MnO	0.84 ± 0.05	1.02 ± 0.06	0.34 ± 0.04	1.92 ± 0.08
MgO	4.44 ± 0.07	10.00 ± 0.10	4.20 ± 0.06	13.73 ± 0.11
CaO	0.53 ± 0.03	30.26 ± 0.24	30.66 ± 0.21	29.42 ± 0.24
BaO	0.03 ± 0.00	0.00 ± 0.00	0.00 ± 0.00	0.00 ± 0.00
CO_2 (calc)	39.01	44.67	42.30	45.29
Total	60.07	56.58	57.16	54.89
Chemical formula based on 6 oxygens				
Fe^{2+}	1.70 ± 0.01	0.42 ± 0.01	0.64 ± 0.01	0.27 ± 0.00
Mn^{2+}	0.03 ± 0.00	0.03 ± 0.00	0.10 ± 0.00	0.05 ± 0.00
Mg^{2+}	0.25 ± 0.00	0.49 ± 0.00	0.22 ± 0.00	0.66 ± 0.01
Ca^{2+}	0.02 ± 0.00	1.11 ± 0.01	1.14 ± 0.01	1.02 ± 0.01
Ba^{2+}	0.00 ± 0.00	0.00 ± 0.00	0.00 ± 0.00	0.00 ± 0.00
C^{4+}	2.00	2.00	2.00	2.00
Mol% end-member				
Calcite:	1.08 ± 0.06	53.92 ± 0.81	57.17 ± 0.81	52.36 ± 0.78
Dolomite:	12.60 ± 0.27	24.80 ± 0.40	10.90 ± 0.21	34.00 ± 0.50
Siderite:	86.32 ± 1.38	21.28 ± 0.40	31.93 ± 0.55	13.64 ± 0.30
Mol% end-member including rhodochrosite				
Calcite:	1.07 ± 0.05	53.16 ± 0.75	56.89 ± 0.72	50.98 ± 0.76
Dolomite:	12.43 ± 0.27	24.45 ± 0.41	10.84 ± 0.21	33.11 ± 0.51
Siderite:	85.16 ± 1.41	20.98 ± 0.40	31.77 ± 0.55	13.28 ± 0.30
Rhodochrosite:	1.34 ± 0.08	1.42 ± 0.09	0.50 ± 0.06	2.63 ± 0.11



Figure 8.6 – Reactivated chlorite (Chl) vein filled with clear albite (Ab) and quartz (Qtz) with carbonate minerals (Cb) at the centre. Photomicrograph taken under plain polarized light. Location: 634250E 5373925N.

analyses. Therefore, the mol% of rhodochrosite was also calculated and given in Table 8.2 as to include all pertinent end-member concentrations.

The mol% end-member composition reveals that carbonate minerals replacing primary mafic minerals range from nearly pure calcite, as seen in the equigranular magnetite-bearing unit and transition zone, to ankerite as seen in the lath syenite unit (see Table 8.2). The composition of carbonate minerals in Qtz-Ab-Cb veins varies from calcite to ankerite in the porphyritic Beattie unit and to siderite in the porphyritic Central Duparquet unit. The term ankerite here is used for carbonate minerals in which $Mg^{2+}/Fe^{2+} \leq 4{:}1$ (Deer et al., 1992). For visualization purposes the mol% end-member composition of all analyses are presented in Figure 8.7.

The compositional difference between carbonate minerals replacing primary mafic minerals can be explained by the resistance to hydrothermal alteration in the equigranular magnetite-bearing unit and adjacent transition zone compared to all the other petrographic units. Specifically, the lack of interaction between the incoming hydrothermal fluids and altering actinolite in the equigranular magnetite-beating unit would have prevented any variable enrichment in Fe^{2+}, Mg^{2+} or Mn^{2+}, therefore resulting in nearly pure calcite. This lack of interaction can also be observed via EBS where no compositional zoning was observed in calcite, reaffirming the chemical homogeneity demonstrated by the analyses (see Figure 8.8). As for the lath syenite

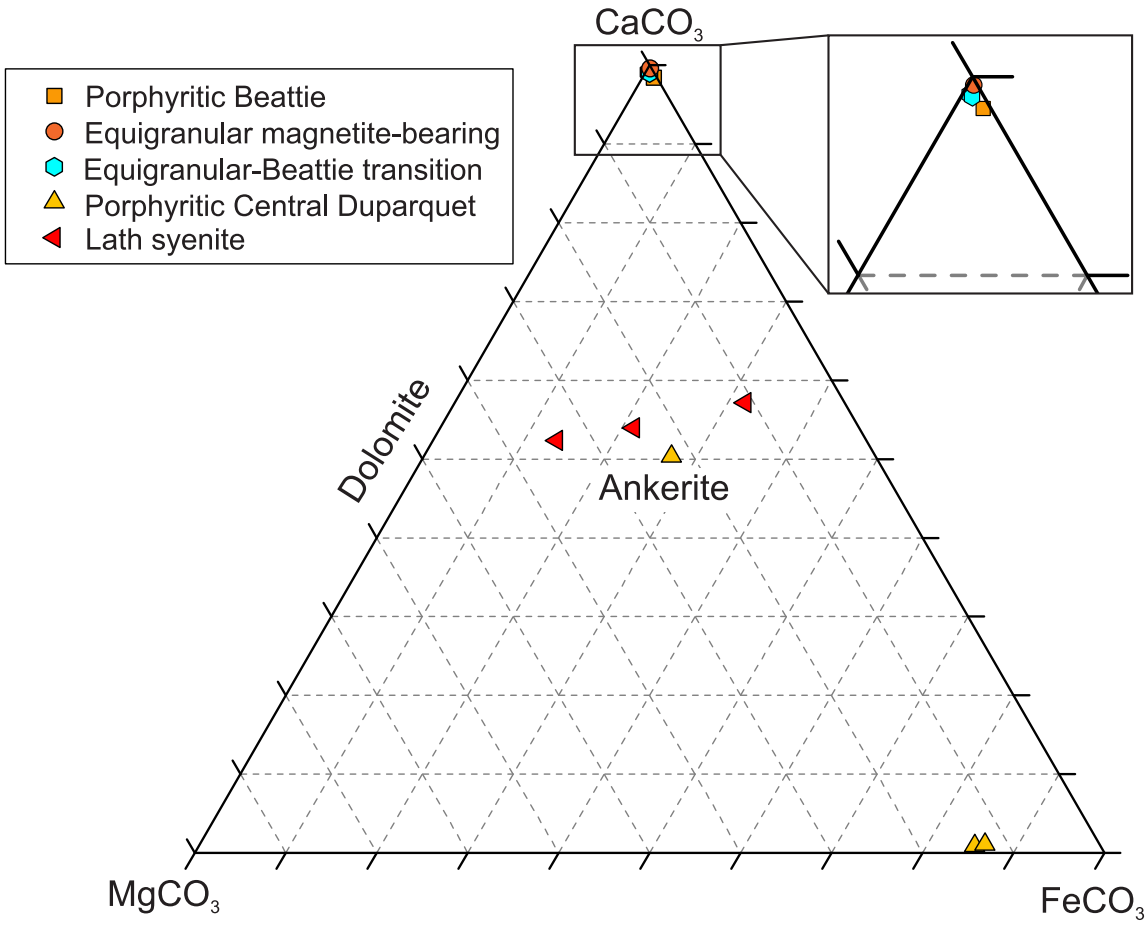


Figure 8.7 – End-member compositions of carbonate minerals. All analyses are presented in mole %.

unit, the interaction between the altering primary mafic minerals and the hydrothermal fluids produced cyclic enrichments of Fe^{2+}, Mg^{2+} and to a lesser amount Mn^{2+}. This interaction can be observed via EBS where carbonate minerals demonstrate pronounced compositional zoning as presented in Figure 8.9. Compositional zones in carbonate minerals are entirely caused by simple substitution of Fe^{2+}. Therefore, Fe^{2+}-enriched zones are lighter (analysis 21-2-2) and depleted zones appear darker, but also contain slightly more Mn^{2+} (analysis 21-2-1). These compositional zones are cyclic, starting from a dark Fe^{2+}-depletion, terminating in a lighter Fe^{2+}-enriched composition.

Compositional differences between carbonate minerals in transecting Qtz-Ab-Cb veins could be either caused by spatial or temporal compositional variations in hydrothermal fluids. The spatial compositional variation is best observed when combining all the chemical analyses,

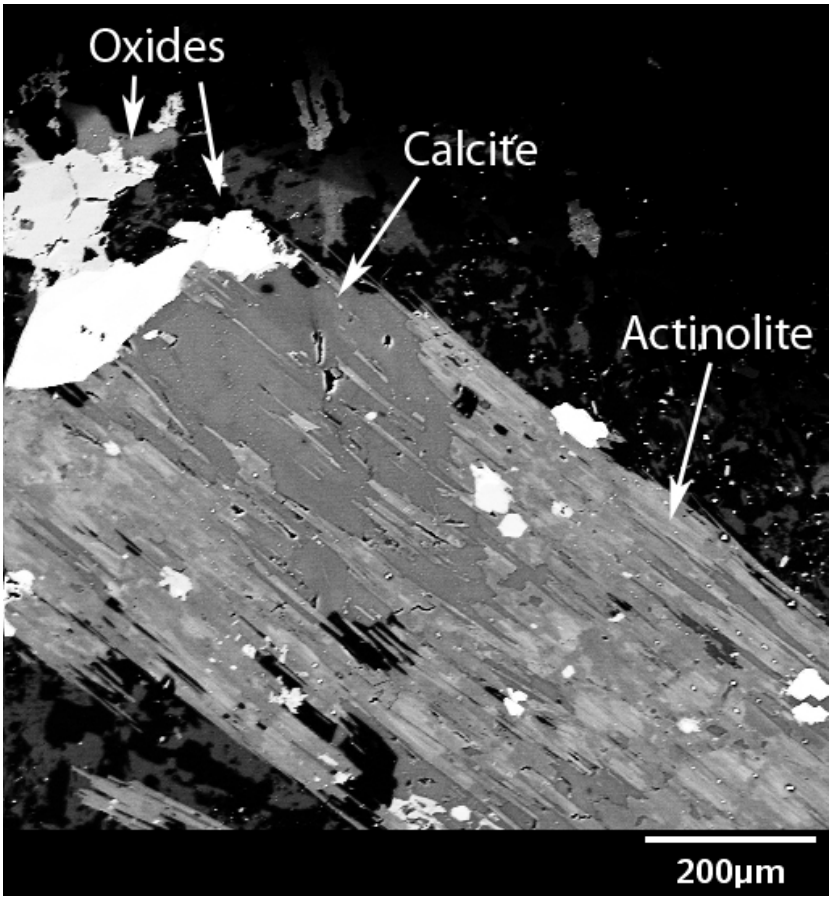
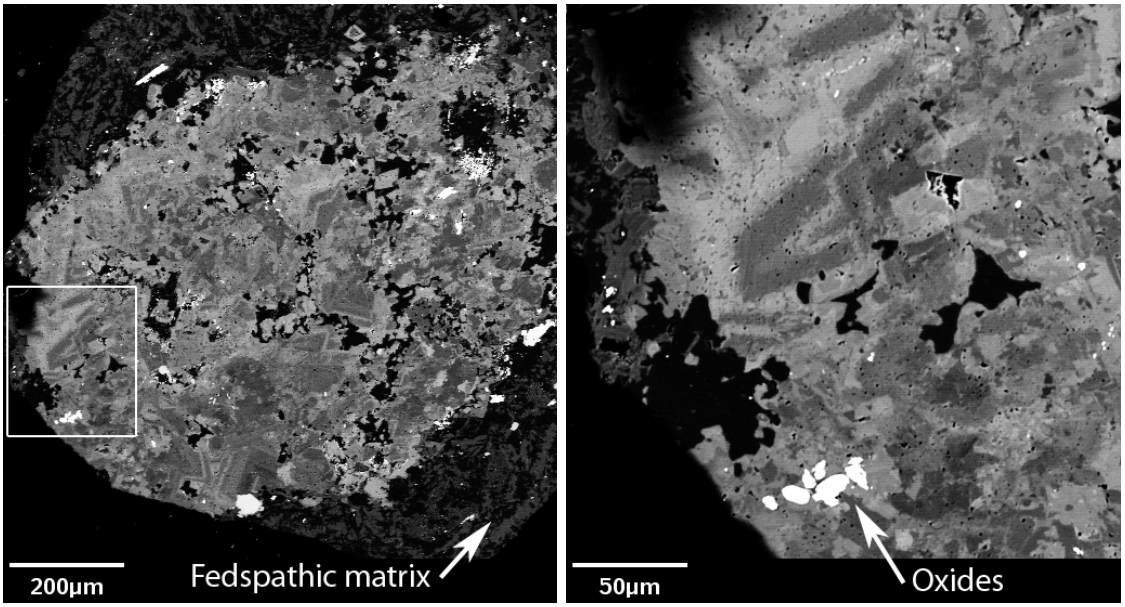


Figure 8.8 – EBS of calcite (uniform dark grey) replacing actinolite (heterogeneous medium to light grey) in the equigranular magnetite-bearing unit. No compositional zoning in calcite has been observed or measured. Sample: JG-1332-04, Location: 630747E 5374454N.

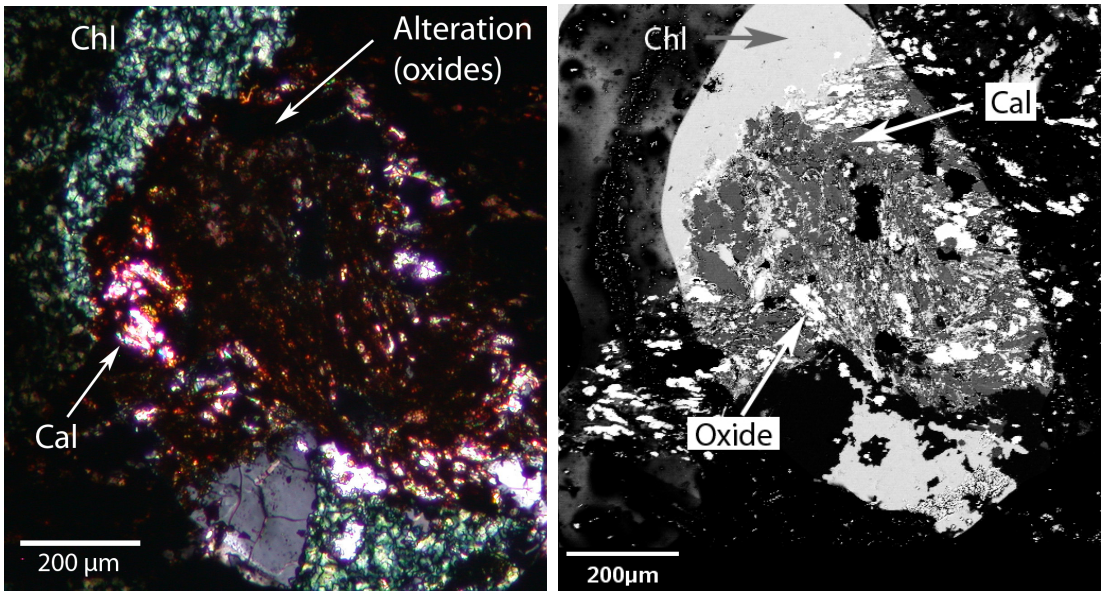
regardless of the petrographic unit. Specifically, analysis 42-1-1 which corresponds to calcite is located midway between the Beattie and Donchester mine shafts (see Figure 6.16), analysis 47-9-1 which corresponds to ankerite is located midway in the BDB, and finally analyses 56-6-1 and 56-6-2, both corresponding to siderite, are from the eastern margins of the CDB. As such, carbonate minerals in Qtz-Ab-Cb veins demonstrate a strong increase in Fe^{2+} and to a lesser extent Mg^{2+} when progressing from the west to the east. However, it should be noted that this trend remains hypothetical, due to a limited number of analyses. Compositional variations could have also been produced by multiple episodes of Qtz-Ab-Cb veining. The latter hypothesis is supported by a lack of compositional zoning in crystals, as observed via EBS and confirmed in analyses 56-6-1 and 56-6-2 which were both obtained from the same siderite crystal, regardless of heterogeneities observed in thin section (see Figure 8.10).



(a) Relict of a primary mafic mineral occupied by compositionally zoned ankerite. A close-up (white box) of the zonation is presented in (b).

(b) Close-up of compositionally zoned ankerite. Darker zones commonly compose the core, terminating in lighter zones towards the exterior.

Figure 8.9 – Relict of primary mafic mineral occupied by ankerite. The crystals demonstrate compositional zoning with a close-up presented in (b). Lighter zones are Fe^{2+}-enriched compared to the darker ones. Sample: ZP-04-021, location: 632690E 5374266N.



(a) Photomicrograph of a seemingly heterogeneous calcite target under the microscope, crossed polars.

(b) EBS image of the same calcite target.

Figure 8.10 – Images of a calcite target in a Qtz-Ab-Cb vein. Images of the target are under: (a) microscope, and (b) EBS. The seemingly heterogeneous calcite seen under the microscope lacks compositional zoning as demonstrated by EBS. Minerals identified are chlorite (Chl), calcite (Cal) and oxides. Sample: ZP-04-042, location: 630817E, 5374264N.

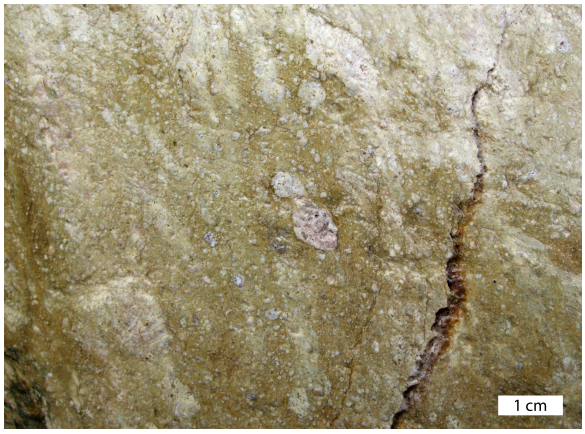
Sericite

Anhedral, pale-green to grey coloured sericite, is found in anastomosing veins of various widths and abundance as well as disseminated crystals.

Sericite veins occur throughout the syenite, but become smaller and less abundant eastwards. To the west, sericite veins measure between $<$ 1 mm - 5 cm wide, typically strike E-W or rarely N-S, and can be traced for several meters. The width and density of anastomosing veins is strongly dependent on the local extent of brittle deformation. At the maximum extent of deformation, sericite fills the cataclastite matrix, giving the rock a green colour. Remaining syenitic clasts have been relatively spared from sericitization (see Figure 8.11a). Progressing to slightly less deformed areas, sericite occurs as thin ($<$ 1 - 5 mm) and numerous veinlets (see Figure 8.11b). These areas are also typically accompanied by disseminated carbonate minerals. Finally, in the comparatively least deformed areas, sericite veins are large (1 - 5 cm) and less abundant (see Figure 8.11c).

On a finer scale, sericite crystals in veins/veinlets are pleochroic with diffuse margins and may rarely be accompanied by chalcopyrite and hydrothermal magnetite. The anastomosing veins form networks which preferentially transect the feldspathic matrix. Sericite in these networks tend to be almost entirely confined to the veinlets (see Figure 8.12), with the exception of when the veinlet(s) transect the orthoclase-rich portion of the phenocrysts. Sericite veinlets often transect carbonate minerals in relicts of primary mafic minerals and have deformed disseminated carbonate minerals, indicating that sericitization occurred after the crystallization of disseminated carbonate minerals. Uncommonly, the influx of sericite replaced carbonate minerals which occupied the relicts of primary mafic minerals (see Figure 8.13). The contour, size and distribution of the now sericite-filled relicts correspond to observations of actinolite crystals made in the equigranular magnetite-bearing syenite unit. The anastomosing veins of sericite are transected by both Ab-Cb and Qtz-Ab-Cb veins.

Disseminated sericite is locally observed replacing parts of the phenocrysts, imparting them with a rim or whole pale green colour (see Figure 8.14). As opposed to sericite in veins, disseminated sericite is found throughout the syenite. Sericite commonly replaces orthoclase, and to a lesser degree, albite as extremely small acicular crystals ($\leq$ 0.1 mm). This replacement is pronounced in phenocrysts where sericitization has often obliterated all igneous textures.



(a) Cataclastite filled with green sericite. The remaining syenitic clasts consist of pale coloured fragments. Location: 630795E 5374341N.



(b) Less deformed area showing fine and numerous veinlets of green sericite. Brittle deformation was powerful enough to obliterate feldspar phenocrysts. Location: 630789E 5374371N.



(c) Thicker and fewer anastomosing veins of green sericite in a less britally deformed area. The reduction in the extent of deformation permitted the preservation of small anhedral white feldspar phenocrysts ($<$ 1 cm). Location: 630789E 5374371N.

Figure 8.11 – Sericite in the western portions of the Beattie syenite. The width and number of veins is strongly dependent on the extent of local brittle deformation. The sequence of photographs are arranged in decreasing amount of deformation.

The composition of sericite was verified via EMPA. A total of 15 analyses were performed in anastomosing veins, in recrystallized crystals at a contact with a Qtz-Ab-Cb vein and in crystals that now occupy the relicts of primary mafic minerals. As for sericite in the lath syenite unit, crystals that have replaced carbonate minerals in relicts of primary mafic minerals were

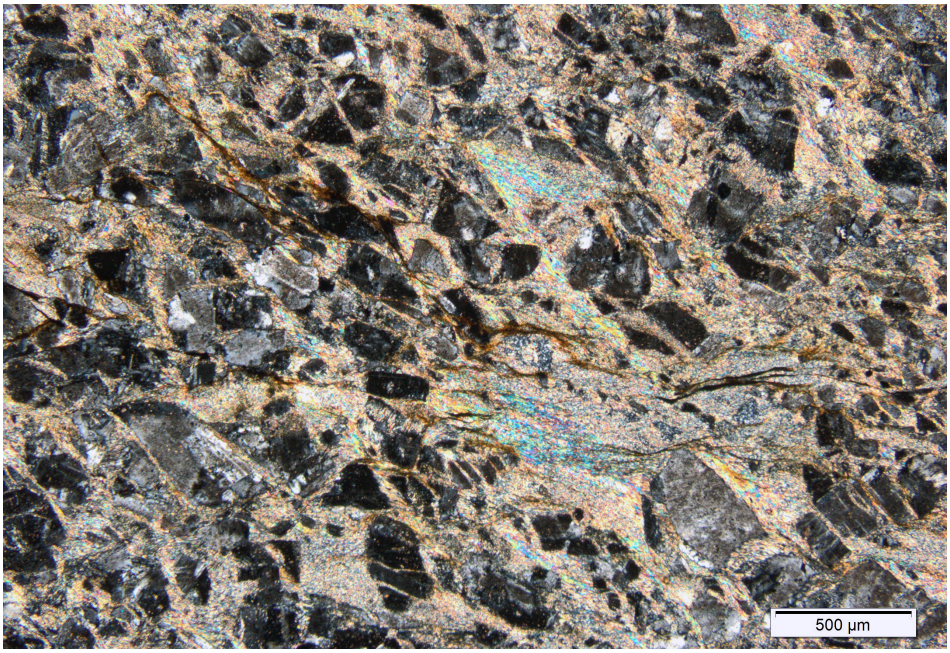


Figure 8.12 – Anastomosing network of sericite-filled veinlets. The sericite veinlets (yellow, blue) fill the cataclastite matrix, spearing the syenite clasts (black). Photomicrograph taken under crossed polars. Location: 632046E 5374145N.

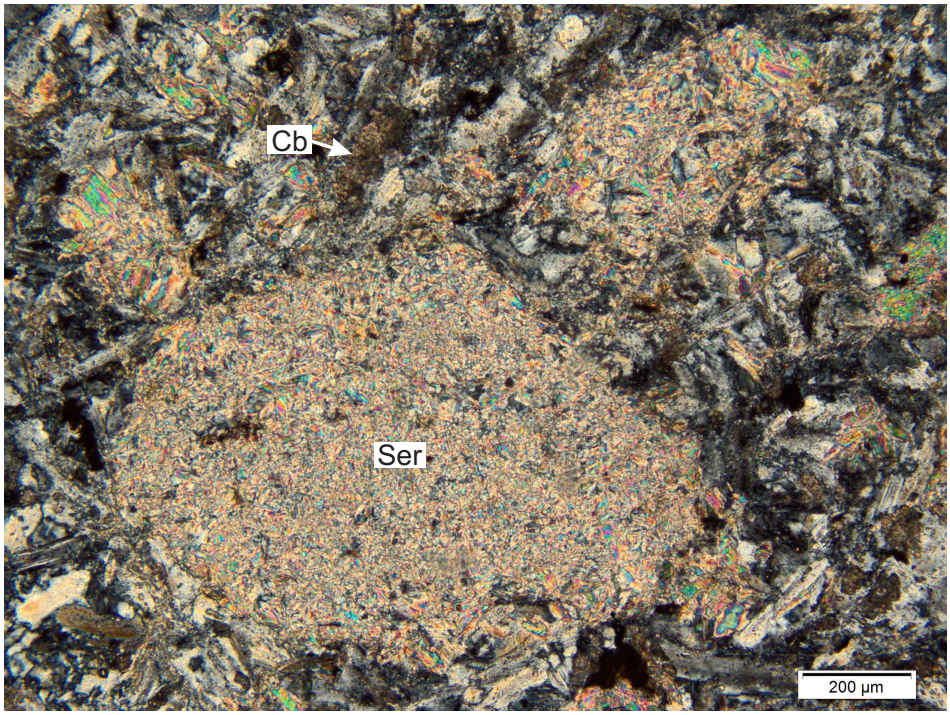


Figure 8.13 – Sericite in a primary mafic mineral relict. Sericite crystals (Ser) are anhedral with no definite boundaries. The sericite is hosted in the feldspathic matrix with disseminated crystals of carbonate minerals (Cb). Photomicrograph taken under crossed polars. Location: 633125E 5373867N.

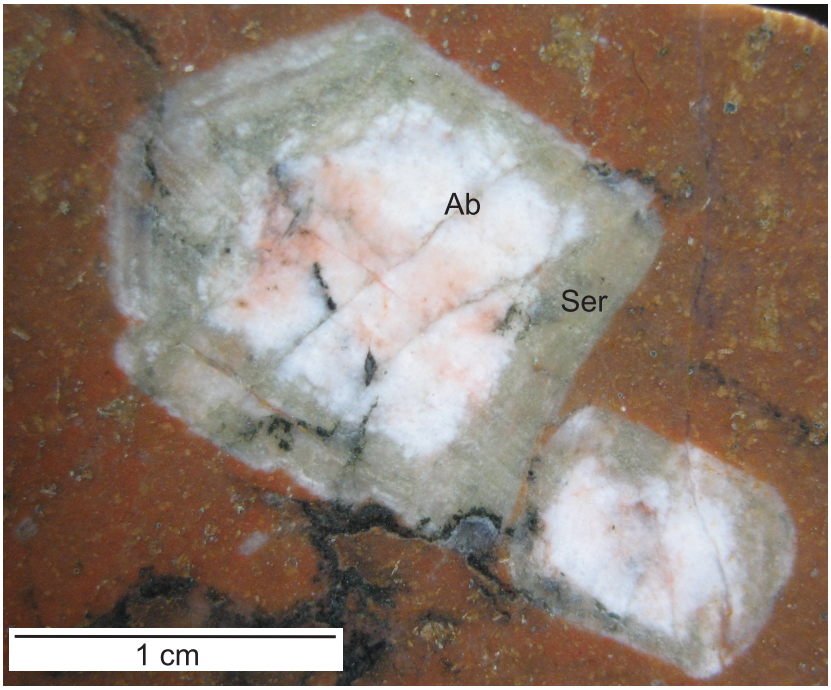


Figure 8.14 – Phenocrysts partially replaced by sericite (Ser). Disseminated sericite is replacing the orthoclase-rich portion of the phenocryst, leaving the albite (Ab) core surrounded by a green rim. Drill core: B09-22, depth: 62.00 - 72.75 m.

selected in order to avoid contamination as crystals outside the relicts were finely intermixed with carbonate minerals and opaques. Disseminated crystals were not analyzed due to their size. All sericite analyses were calculated on an 10 oxygen and 2 OH basis. The origin of the analyses, composition and calculated chemical formulas are presented in Table 8.3.

The classification and nomenclature of sericite was performed according to current IMA recommendations. Additionally, iron is only reported as Fe^{2+} since Fe^{3+} estimations in micas are notoriously inaccurate (Lalonde, pers. comm., 2011).

The mica group is subdivided into: 1) true micas, 2) brittle micas and 3) interlayer deficient micas. A true mica is defined if $\geq 50\%$ of **I** cations are monovalent (Reider et al., 1998), which is the case for the sericite formulas (see Table 8.3). The next necessary division is whether sericite is dioctahedral or trioctahedral. A mica is considered dioctahedral if it contains $<$ 2.5 octahedral cations (**M**) per formula unit, or trioctahedral if it contains $>$ 2.5 octahedral cations (Reider et al., 1998). All analyses presented are of dioctahedral micas since **M**-sites contain between 1.89 - 2.09 cations per formula unit. Finally, the species classification is made on the basis of ideal end-member compositions given in literature (Reider et al., 1998). Classification results have all analyses classified as muscovite. Adjectival modifiers in micas

Table 8.3 – Microprobe analyses and chemical formulas of sericite.

	Beattie			Central Duparquet		
	42-2-3	**42-5-1**	**JG-5099-05**	**48-1-1**	**47-1-1**	**47-1-2**
SiO_2	recrystallized	anastomosing	anastomosing	anastomosing	anastomosing	anastomosing
SiO_2	48.88 ± 0.34	47.40 ± 0.33	48.37 ± 0.34	47.43 ± 0.33	48.20 ± 0.34	54.14 ± 0.38
TiO_2	0.04 ± 0.02	0.34 ± 0.03	0.23 ± 0.01	0.40 ± 0.03	0.46 ± 0.03	0.21 ± 0.01
Al_2O_3	26.74 ± 0.19	28.83 ± 0.20	26.48 ± 0.19	29.78 ± 021	27.26 ± 0.19	24.42 ± 0.17
Cr_2O_3	0.01 ± 0.00	0.00 ± 0.00	0.03 ± 0.01	0.00 ± 0.00	0.02 ± 0.02	0.00 ± 0.00
FeO	7.12 ± 0.15	6.24 ± 0.14	5.01 ± 0.07	5.44 ± 0.13	6.84 ± 0.14	4.74 ± 0.11
MnO	0.05 ± 0.03	0.06 ± 0.02	0.02 ± 0.00	0.02 ± 0.00	0.00 ± 0.00	0.00 ± 0.00
MgO	1.52 ± 0.03	0.94 ± 0.03	2.74 ± 0.04	1.12 ± 0.03	1.97 ± 0.04	1.37 ± 0.03
BaO	0.15 ± 0.05	0.10 ± 0.05	0.32 ± 0.03	0.16 ± 0.05	0.28 ± 0.05	0.44 ± 0.02
CaO	0.00 ± 0.00	0.00 ± 0.00	0.00 ± 0.00	0.00 ± 0.00	0.00 ± 0.00	0.01 ± 0.00
Na_2O	0.05 ± 0.01	0.06 ± 0.02	0.06 ± 0.02	0.12 ± 0.02	0.08 ± 0.01	0.11 ± 0.01
K_2O	11.31 ± 0.10	11.48 ± 0.10	11.04 ± 0.08	10.81 ± 0.10	11.28 ± 0.10	12.95 ± 0.10
F	0.45 ± 0.06	0.34 ± 0.04	0.34 ± 0.05	0.47 ± 0.06	0.55 ± 0.05	0.40 ± 0.04
Cl	0.02 ± 0.01	0.00 ± 0.00	0.01 ± 0.01	0.01 ± 0.00	0.00 ± 0.00	0.01 ± 0.00
Total	96.34	95.79	94.67	95.75	96.94	98.81
Chemical formula based on 10 oxygens and 2 OH						
Ca^{2+}	0.00 ± 0.00	0.00 ± 0.00	0.00 ± 0.00	0.00 ± 0.00	0.00 ± 0.00	0.00 ± 0.00
Ba^{2+}	0.00 ± 0.00	0.00 ± 0.00	0.01 ± 0.00	0.00 ± 0.00	0.01 ± 0.00	0.01 ± 0.00
Na^{+}	0.01 ± 0.00	0.01 ± 0.00	0.01 ± 0.00	0.02 ± 0.00	0.01 ± 0.00	0.01 ± 0.00
K^{+}	0.99 ± 0.01	1.00 ± 0.01	0.97 ± 0.01	0.94 ± 0.01	0.98 ± 0.01	1.09 ± 0.01
$\sum$ I	1.00	1.02	0.99	0.96	1.00	1.11
Al^{3+}	1.50 ± 0.01	1.58 ± 0.01	1.49 ± 0.01	1.62 ± 0.01	1.48 ± 0.01	1.48 ± 0.01
Ti^{4+}	0.00 ± 0.00	0.02 ± 0.00	0.01 ± 0.00	0.02 ± 0.00	0.02 ± 0.00	0.01 ± 0.00
Cr^{3+}	0.00 ± 0.00	0.00 ± 0.00	0.00 ± 0.00	0.00 ± 0.00	0.00 ± 0.00	0.00 ± 0.00
Fe^{2+}	0.41 ± 0.01	0.36 ± 0.01	0.29 ± 0.00	0.31 ± 0.01	0.39 ± 0.01	0.26 ± 0.01
Mn^{2+}	0.00 ± 0.00	0.00 ± 0.00	0.00 ± 0.00	0.00 ± 0.00	0.00 ± 0.00	0.00 ± 0.00
Mg^{2+}	0.16 ± 0.00	0.10 ± 0.00	0.28 ± 0.00	0.11 ± 0.00	0.20 ± 0.00	0.14 ± 0.00
$\sum$ M	2.07	2.06	2.08	2.06	2.09	1.89
Si^{4+}	3.35 ± 0.03	3.35 ± 0.03	3.34 ± 0.03	3.23 ± 0.03	3.29 ± 0.03	3.58 ± 0.03
Al^{3+}	0.65 ± 0.01	0.75 ± 0.01	0.66 ± 0.01	0.77 ± 0.01	0.71 ± 0.01	0.42 ± 0.01
$\sum$ T	4.00	4.00	4.00	4.00	4.00	4.00
F	0.10 ± 0.01	0.07 ± 0.01	0.07 ± 0.01	0.10 ± 0.01	0.12 ± 0.01	0.08 ± 0.01
Cl	0.03 ± 0.00	0.00 ± 0.00	0.01 ± 0.00	0.01 ± 0.00	0.00 ± 0.00	0.01 ± 0.00
OH	1.90	1.93	1.92	1.90	1.88	1.92
$\sum$ OH	2.03	2.00	2.01	2.01	2.00	2.01
Name:	Ferrian-muscovite	Ferrian-muscovite	Ferrian-muscovite	Ferrian-muscovite	Ferrian-muscovite	Ferrian-muscovite

should only be used when an element exceeds 10% but does not surpass 50% of the respective site in the formula (Reider et al., 1998). The ferrian- adjectival modifier was applied to all analyses from the porphyritic Beattie syenite unit where Fe^{2+} represents between 14 - 20% of the **M**-site, to the first half of analyses from the porphyritic Central Duparquet unit where Fe^{2+} varies between 14 - 19%, and to all analyses from the lath syenite unit where calculated **M**-sites Fe^{2+} values range between 11 - 15%.

The difference between muscovite and ferrian-muscovite could not be distinguished via EBS observations. All appear as anhedral crystals, lacking compositional zoning. The lowest Fe^{2+} abundances (analyses 56-1-1 and 56-1-2) were obtained in recrystallized sericite at a

Table 8.3 Continued

	Central Duparquet					Lath syenite
	47-1-2	**56-1-1**	**56-1-2**	**56-2-1**	**56-2-2**	**21-3-2**
	anastomosing	recrystallized	recrystallized	anastomosing	anastomosing	replacing mafic
SiO_2	48.56 ± 0.34	49.06 ± 0.34	49.13 ± 0.34	49.52 ± 0.35	49.12 ± 0.34	46.37 ± 0.32
TiO_2	0.41 ± 0.02	0.30 ± 0.03	0.26 ± 0.03	0.22 ± 0.03	0.30 ± 0.01	0.16 ± 0.03
Al_2O_3	26.76 ± 0.19	30.91 ± 0.22	30.32 ± 0.21	30.15 ± 0.21	29.11 ± 0.20	31.68 ± 0.22
Cr_2O_3	0.02 ± 0.00	0.02 ± 0.02	0.00 ± 0.00	0.00 ± 0.00	0.00 ± 0.00	0.02 ± 0.00
FeO	6.99 ± 0.14	2.38 ± 0.09	2.45 ± 0.09	3.47 ± 0.10	3.28 ± 0.09	3.87 ± 0.11
MnO	0.02 ± 0.00	0.01 ± 0.00	0.02 ± 0.00	0.00 ± 0.00	0.05 ± 0.01	0.00 ± 0.00
MgO	1.84 ± 0.03	1.78 ± 0.03	1.77 ± 0.03	1.64 ± 0.03	1.52 ± 0.03	1.17 ± 0.03
BaO	0.22 ± 0.01	0.27 ± 0.05	0.25 ± 0.05	0.23 ± 0.05	0.35 ± 0.02	0.32 ± 0.05
CaO	0.00 ± 0.00	0.00 ± 0.00	0.02 ± 0.02	0.01 ± 0.00	0.04 ± 0.00	0.02 ± 0.00
Na_2O	0.08 ± 0.01	0.08 ± 0.01	0.10 ± 0.01	0.07 ± 0.01	0.11 ± 0.01	0.21 ± 0.02
K_2O	11.19 ± 0.10	11.58 ± 0.10	11.27 ± 0.10	11.35 ± 0.10	11.20 ± 0.10	10.61 ± 0.10
F	0.47 ± 0.04	0.94 ± 0.07	1.01 ± 0.07	0.81 ± 0.07	0.58 ± 0.04	0.51 ± 0.08
Cl	0.02 ± 0.00	0.00 ± 0.00	0.02 ± 0.00	0.00 ± 0.00	0.00 ± 0.00	0.00 ± 0.00
Total	96.58	97.33	96.62	97.49	95.66	94.93
Chemical formula based on 10 oxygens and 2 OH						
Ca^{2+}	0.00 ± 0.00	0.00 ± 0.00	0.00 ± 0.00	0.00 ± 0.00	0.00 ± 0.00	0.00 ± 0.00
Ba^{2+}	0.01 ± 0.00	0.01 ± 0.00	0.01 ± 0.00	0.01 ± 0.00	0.01 ± 0.00	0.01 ± 0.00
Na^{+}	0.01 ± 0.00	0.01 ± 0.00	0.01 ± 0.00	0.01 ± 0.00	0.01 ± 0.00	0.03 ± 0.00
K^{+}	0.98 ± 0.01	0.98 ± 0.01	0.96 ± 0.01	0.96 ± 0.01	0.97 ± 0.01	0.92 ± 0.01
$\sum$ I	1.00	1.00	0.98	0.98	0.99	0.96
Al^{3+}	1.47 ± 0.01	1.68 ± 0.01	1.68 ± 0.01	1.66 ± 0.01	1.64 ± 0.01	1.72 ± 0.01
Ti^{4+}	0.02 ± 0.00	0.02 ± 0.00	0.01 ± 0.00	0.01 ± 0.00	0.02 ± 0.00	0.01 ± 0.00
Cr^{3+}	0.00 ± 0.00	0.00 ± 0.00	0.00 ± 0.00	0.00 ± 0.00	0.00 ± 0.00	0.00 ± 0.00
Fe^{2+}	0.40 ± 0.01	0.13 ± 0.00	0.14 ± 0.00	0.19 ± 0.00	0.19 ± 0.00	0.22 ± 0.01
Mn^{2+}	0.00 ± 0.00	0.00 ± 0.00	0.00 ± 0.00	0.00 ± 0.00	0.00 ± 0.00	0.00 ± 0.00
Mg^{2+}	0.19 ± 0.00	0.18 ± 0.00	0.18 ± 0.00	0.16 ± 0.00	0.15 ± 0.00	0.12 ± 0.00
$\sum$ M	2.08	2.01	2.01	2.02	2.00	2.06
Si^{4+}	3.32 ± 0.03	3.26 ± 0.03	3.29 ± 0.03	3.29 ± 0.03	3.32 ± 0.03	3.17 ± 0.03
Al^{3+}	0.68 ± 0.01	0.74 ± 0.01	0.71 ± 0.01	0.71 ± 0.01	0.68 ± 0.01	0.83 ± 0.01
$\sum$ T	4.00	4.00	4.00	4.00	4.00	4.00
F	0.10 ± 0.01	0.20 ± 0.01	0.21 ± 0.01	0.17 ± 0.01	0.12 ± 0.01	0.11 ± 0.02
Cl	0.03 ± 0.00	0.00 ± 0.00	0.03 ± 0.00	0.00 ± 0.00	0.00 ± 0.00	0.00 ± 0.00
OH	1.90	1.80	1.78	1.83	1.88	1.89
$\sum$ OH	2.03	2.00	2.02	2.00	2.00	2.00
Name:	Ferrian-muscovite	Muscovite	Muscovite	Muscovite	Muscovite	Ferrian-muscovite

contact with a Qtz-Ab-Cb vein (see Figure 8.15). Recrystallization was deduced from thin section observations where a vein of pale green anhedral sericite is cut by a large Qtz-Ab-Cb vein. From < 3 mm towards the contact, sericite crystals are much larger, demonstrate a mica habit, lack pleochroism and the characteristic green colour. The compositional difference, by which recrystallized sericite has the lowest Fe^{2+}, suggests that recrystallization permitted Fe^{2+} exsolution. Exsolved Fe^{2+} was then segregated to the small oxides located nearby. Consequently this implies that the anhedral sericite in anastomosing veins did not have the necessary energy and/or time to exsolve Fe^{2+}, and therefore crystallization ensued immediately after infiltration.

Analyses of sericite replacing carbonate minerals in relicts of primary mafic minerals

Table 8.3 Continued

	Lath syenite		
	21-3-3	**21-7-1**	**JG-3002-04r**
	replacing mafic	replacing mafic	replacing mafic
SiO_2	47.64 ± 0.33	48.25 ± 0.34	47.03 ± 0.33
TiO_2	0.16 ± 0.03	0.23 ± 0.03	0.40 ± 0.02
Al_2O_3	29.80 ± 0.21	27.97 ± 0.20	29.27 ± 0.20
Cr_2O_3	0.01 ± 0.00	0.36 ± 0.03	0.00 ± 0.00
FeO	4.38 ± 0.11	5.51 ± 0.13	5.34 ± 0.07
MnO	0.01 ± 0.00	0.07 ± 0.03	0.00 ± 0.00
MgO	1.48 ± 0.03	1.77 ± 0.03	1.09 ± 0.02
BaO	0.27 ± 0.05	0.21 ± 0.05	0.15 ± 0.02
CaO	0.01 ± 0.00	0.00 ± 0.00	0.00 ± 0.00
Na_2O	0.16 ± 0.02	0.07 ± 0.01	0.10 ± 0.03
K_2O	10.72 ± 0.10	10.95 ± 0.10	11.13 ± 0.08
F	0.50 ± 0.08	0.41 ± 0.05	0.32 ± 0.05
Cl	0.01 ± 0.00	0.00 ± 0.00	0.00 ± 0.00
Total	95.12	95.81	94.83
Ca^{2+}	0.00 ± 0.00	0.00 ± 0.00	0.00 ± 0.00
Ba^{2+}	0.01 ± 0.00	0.01 ± 0.00	0.00 ± 0.00
Na^{+}	0.02 ± 0.00	0.01 ± 0.00	0.01 ± 0.00
K^{+}	0.93 ± 0.01	0.95 ± 0.01	0.98 ± 0.01
$\sum$ I	0.96	0.97	1.00
Al^{3+}	1.65 ± 0.01	1.54 ± 0.01	1.61 ± 0.01
Ti^{4+}	0.01 ± 0.00	0.01 ± 0.00	0.02 ± 0.00
Cr^{3+}	0.00 ± 0.00	0.02 ± 0.00	0.00 ± 0.00
Fe^{2+}	0.25 ± 0.01	0.31 ± 0.01	0.31 ± 0.00
Mn^{2+}	0.00 ± 0.00	0.00 ± 0.00	0.00 ± 0.00
Mg^{2+}	0.15 ± 0.00	0.18 ± 0.00	0.11 ± 0.00
$\sum$ M	2.06	2.07	2.05
Si^{4+}	3.25 ± 0.03	3.29 ± 0.03	3.24 ± 0.03
Al^{3+}	0.75 ± 0.01	0.71 ± 0.01	0.76 ± 0.01
$\sum$ T	4.00	4.00	4.00
F	0.11 ± 0.02	0.09 ± 0.01	0.07 ± 0.01
Cl	0.00 ± 0.00	0.00 ± 0.00	0.00 ± 0.00
OH	1.89	1.91	1.93
$\sum$ OH	2.00	2.00	2.00
Name:	Ferrian-muscovite	Ferrian-muscovite	Ferrian-muscovite

demonstrate very little compositional variation. All analyses are Fe^{2+}-enriched. This enrichment could result from the choice of the selected targets. However, it was determined from chemical analyses of actinolite that the likely igneous syenitic pyroxene was Ca-rich augite (in a broad sense, see Chapter 6). Therefore, Fe^{2+}-enrichment of sericite over Mg^{2+} could not have been entirely inherited from simple static replacement. This observation is further complemented by the observation that anastomosing veins of sericite transect every syenitic unit. Consequently, sericite originated in a dynamic rather than a static setting.

Finally, the green colouration of sericite is solely caused by Fe^{2+}-enrichment. This hypothesis is confirmed by the lack of other elements which could cause a green colouration, such as Cr^{3+}, and because colourless and non-pleochroic recrystallized sericite also possess the lowest

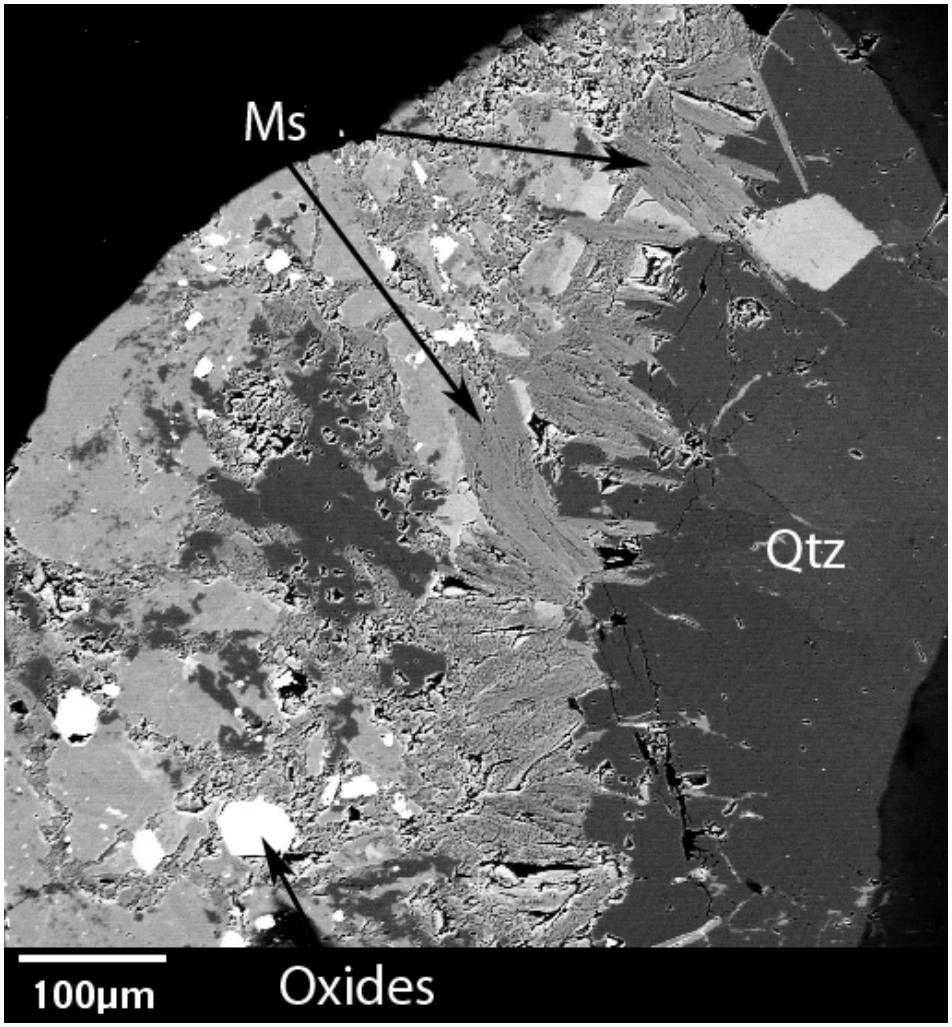


Figure 8.15 – EBS image of recrystallized muscovite at the contact with a transecting quartz, albite, carbonate minerals vein. Crystals of muscovite (Ms) are in contact with quartz (Qtz), and as opposed to all other sericite crystals, they are subhedral rather than anhedral. Furthermore, these crystals possess the least amount of Fe^{2+}. Sample: ZP-04-056, location: 634050E 5373903N.

amount of Fe^{2+}.

Hematite

Hematite is found as an alteration product of primary titanite, mafic minerals and magnetite. It can also occur as finely disseminated crystals or rarely as an overgrowth around pyrite.

Hematite is found as small anhedral crystals within and/or at the margins of titanite relicts, preserving the original form and twinning planes of titanite (see Figure 8.1). As for the mafic mineral relicts, hematite occurs as larger ($\leq$ 0.4 mm) anhedral crystals (see Figure 8.1). Additionally, hematite may also be found as a thin reaction rim (0.01 mm thick) around igneous magnetite.

Disseminated hematite crystals are anhedral, evenly distributed throughout the rock and measure between $<$ 0.01 - 0.1 mm across.

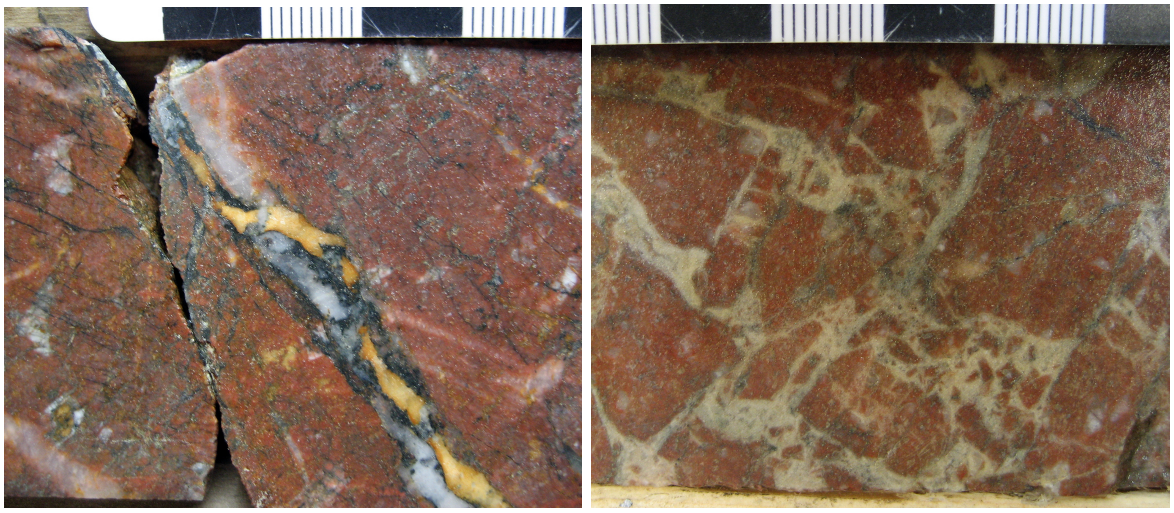
Albite

White anhedral albite always occurs in veins. Albite is found in both Ab-Cb and Qtz-Ab-Cb veins.

The oldest generation of albite is found in Ab-Cb veins (see subsection 8.1.1). Ab-Cb veins occupy the central portions of pre-existing sulphide minerals veins, indicating that Ab-Cb veins are post-Au-mineralization. This will be discussed in greater detail in subsection 8.1.1. Field relationships indicate that Ab-Cb veins are cut by Qtz-Ab-Cb veins (see Figure 8.16a). Albite is accompanied by subordinate amounts of beige carbonate minerals and is sometimes observed composing the matrix in brecciated D_2 shear zones (see Figure 8.16b). On a finer scale, albite crystals in both Ab-Cb and Qtz-Ab-Cb veins measure between 0.05 - 1 mm across, typically demonstrate polysynthetic twinning and are usually free of turbidity (see Figure 8.6). The compositions of a few albite crystals were determined by the Michel-Lévy method ranging from An_0 - An_6, nearly pure albite.

The average composition of albite in veins was confirmed by EMPA. Albite targets were selected in both Ab-Cb and Qtz-Ab-Cb veins. All formulas were calculated on an 8 oxygen basis. The origin, composition and chemical formulas are presented in Table 8.4.

The composition varies from 0.15 - 0.67 mol% An, 0.26 - 0.44 mol% Or and 99.07 - 99.57 mol% Ab. A visualization of the feldspathic mol% end-member compositions is presented in Figure 8.17.



(a) Beige albite and carbonate mineral vein cut by a subsequent quartz (grey), albite (white), carbonate minerals (beige) and chlorite (black) vein. The albite and carbonate minerals vein is slightly boudinaged. Drill core: B08-21, depth: 0.00 - 27.00 m.

(b) Albite accompanied by subordinate amounts of carbonate minerals composing the matrix of a brecciated D_2 shear zone. Drill core: B09-86, depth: 3.00 - 15.80 m.

Figure 8.16 – Albite in the Beattie syenite.

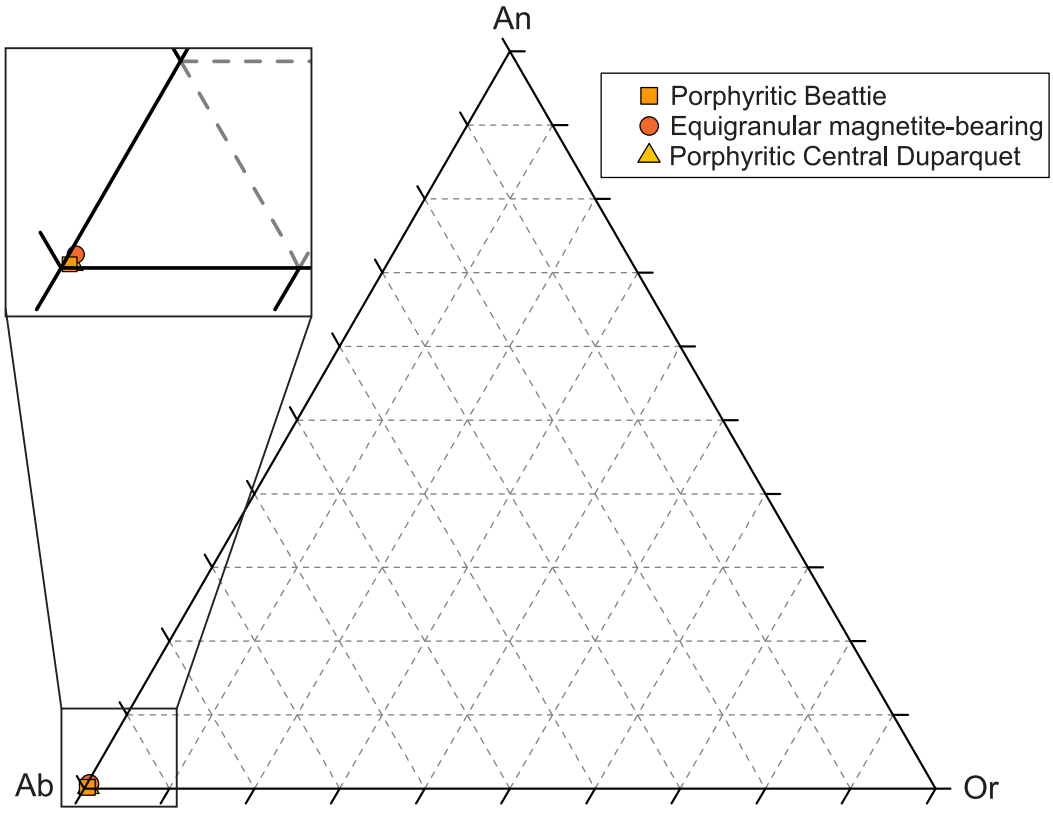


Figure 8.17 – End-member compositions of albite. All analyses are presented in mole %.

Table 8.4 – Microprobe analyses and chemical formulas of albite.

	Beattie	Equigranular	Central Duparquet
	42-3-01	**JG-04-08**	**56-4-1**
	Qtz-Ab-Cb	Ab-Cb	Qtz-Ab-Cb
SiO_2	69.96 ± 0.49	69.95 ± 0.49	69.44 ± 0.49
TiO_2	0.00 ± 0.00	0.00 ± 0.00	0.00 ± 0.00
Al_2O_3	19.76 ± 0.14	19.57 ± 0.14	19.70 ± 0.14
FeO	0.00 ± 0.00	0.04 ± 0.01	0.02 ± 0.00
MgO	0.00 ± 0.00	0.00 ± 0.00	0.00 ± 0.00
BaO	0.00 ± 0.00	0.00 ± 0.00	0.00 ± 0.00
CaO	0.03 ± 0.02	0.15 ± 0.01	0.04 ± 0.02
Na_2O	11.93 ± 0.13	12.34 ± 0.15	11.78 ± 0.12
K_2O	0.05 ± 0.01	0.05 ± 0.01	0.08 ± 0.01
Total	101.73	102.09	101.05
Chemical formula based on 8 oxygens			
Si^{4+}	3.00 ± 0.03	3.00 ± 0.03	3.00 ± 0.03
Ti^{4+}	0.00 ± 0.00	0.00 ± 0.00	0.00 ± 0.00
Al^{3+}	1.00 ± 0.01	0.99 ± 0.01	1.00 ± 0.01
Fe^{3+}	0.00 ± 0.00	0.00 ± 0.00	0.00 ± 0.00
Mg^{2+}	0.00 ± 0.00	0.00 ± 0.00	0.00 ± 0.00
Ba^{2+}	0.00 ± 0.00	0.00 ± 0.00	0.00 ± 0.00
Ca^{2+}	0.00 ± 0.00	0.01 ± 0.00	0.00 ± 0.00
Na^{+}	0.99 ± 0.01	1.03 ± 0.01	0.99 ± 0.01
K^{+}	0.00 ± 0.00	0.00 ± 0.00	0.00 ± 0.00
$\sum/\Delta\sum$	5.00 ± 0.02	5.02 ± 0.02	4.99 ± 0.02
Mol% end-member			
An:	0.15 ± 0.09	0.67 ± 0.05	0.19 ± 0.09
Ab:	99.57 ± 1.82	99.07 ± 1.93	99.37 ± 1.71
Or:	0.28 ± 0.06	0.26 ± 0.05	0.44 ± 0.06

The composition of albite in both Ab-Cb and Qtz-Ab-Cb veins demonstrates the least amount of compositional variation of all feldspars found in the Beattie syenite.

Chlorite

Dark green to black anhedral chlorite generally appears as small crystals replacing primary mafic minerals or in thin, $<$ 1 mm - 5 cm wide tension veins.

Pleochroic, green coloured chlorite crystals replacing primary mafic minerals are accompanied by carbonate minerals and hematite. Crystals measure $\leq$ 1.4 mm across, are turbid and anhedral (see Figure 8.1). In the equigranular magnetite-bearing unit, chlorite can display abnormal extinction patterns, likely caused by the incomplete alteration of actinolite. In areas demonstrating light hydrothermal alteration and deformation, chlorite crystals were subsequently dissolved and transported to nearby tension fractures. This process was observed in thin section where the chlorite crystals occupy fractures near mafic mineral relicts. Progressing to areas demonstrating moderate to extensive brittle deformation and hydrothermal alteration, chlorite has completely left the primary mafic mineral relicts and now occupy tension fractures, thereon referred to as chlorite-only veins. Chlorite crystals show evidence of additional dissolution and transportation by sericite veins, where chlorite crystals occupy their vein-centre, indicating that chloratization is pre- to syn-sericitization. Subsequently, many chlorite-filled tension fractures have been reopened and filled by Ab-Cb or Qtz-Ab-Cb veins (see Figure 8.6). In both Ab-Cb and Qtz-Ab-Cb veins, chlorite occupies the outer margins with clear, 0.1 - 0.2 mm across crystals radiating from the margins inwards. Occasionally, chlorite in these veins have been dissolved and transported along with the incoming fluids as some of the crystals are found at the vein-centre.

Interestingly, in rare instances, chlorite was observed replacing the cores of the feldspar phenocrysts in the same manner exhibited by carbonate minerals.

Chlorite was never observed to be finely disseminated throughout syenite. Rather, it only occurs in veins. The thickness and amount of chloritic veins is strongly dependent on the local extent of brittle deformation. Specifically, thin and numerous chlorite veinlets are found in cataclastic areas whereas larger veins are found in less deformed areas. Veinlets are often found in cataclastic carbonitized zones. These measure between $<$ 1 - 3 mm in thickness and either strike E-W or N-S (see Figure 8.18). Compared to sericite veins, chloritic ones are far less wavy and tend to terminate abruptly with a typical span of $\sim$10 cm, occasionally reaching a meter.



Figure 8.18 – Thin and numerous black chamosite veins in a cataclastic carbonatized zone. All chamosite veins strike E-W. The orange-brown colour of the syenite is caused by disseminated carbonate minerals. Additionally, a late centimetre thick quartz and carbonate mineral (white) vein cuts the outcrop. Location: 630135E 5374288N.

A total of 8 chlorite mineral analyses were performed to establish their chemical compositions and to identify the species. Selected crystals were found in Qtz-Ab-Cb veins, in a chlorite-only tension vein and in a sericite vein. All chlorite analyses were calculated on a 28 oxygen basis. The origin of the analyses, composition and chemical formulas are presented in Table 8.5.

The classification and nomenclature of chlorite group analyses were performed according to the current IMA recommendations. The chlorite group is subdivided into: 1) trioctahedral chlorite, 2) dioctahedral chlorite, 3) di, triotahedral chlorite, and 4) tri, dioctahedral chlorite. To perform this first classification, the proportion of occupied and unoccupied octahedral positions must be known. However, this cannot be known with only chemical data (i.e., EMPA). Furthermore, EMPA considers all iron as Fe_{tot}, without regard for Fe^{2+} and Fe^{3+}. As such, the attempt to attribute an end-member classification to the analyses will require a different approach. First, some assumptions must be made, notably that Fe^{tot} will be used

Table 8.5 – Microprobe analyses and chemical formulas of chlorite.

	Beattie				Central Duparquet	
	2-2-1	**42-2-1**	**42-2-2**	**JG-5099-06**	**48-2-1**	**47-8-1**
	Qtz-Ab-Cb	Qtz-Ab-Cb	Qtz-Ab-Cb	Chlorite vein	Sericite vein	Qtz-Ab-Cb
SiO_2	24.99 ± 0.17	23.42 ± 0.16	23.18 ± 0.16	27.37 ± 0.19	23.52 ± 0.16	25.29 ± 0.18
TiO_2	0.04 ± 0.02	0.03 ± 0.02	0.02 ± 0.00	0.03 ± 0.01	0.03 ± 0.00	0.04 ± 0.02
Al_2O_3	18.45 ± 0.13	19.25 ± 0.15	19.57 ± 0.16	18.32 ± 0.13	19.07 ± 0.13	16.21 ± 0.13
Cr_2O_2	0.00 ± 0.00	0.00 ± 0.00	0.00 ± 0.00	0.00 ± 0.00	0.00 ± 0.00	0.00 ± 0.00
FeO	34.8 ± 0.35	41.95 ± 0.42	42.54 ± 0.38	24.30 ± 0.19	40.97 ± 0.37	40.84 ± 0.37
MnO	0.13 ± 0.03	0.05 ± 0.03	0.15 ± 0.03	0.27 ± 0.03	0.00 ± 0.00	0.10 ± 0.03
BaO	0.03 ± 0.00	0.03 ± 0.00	0.07 ± 0.05	0.02 ± 0.00	0.00 ± 0.00	0.04 ± 0.00
MgO	10.15 ± 0.10	4.29 ± 0.06	3.59 ± 0.05	17.08 ± 0.12	4.98 ± 0.06	6.78 ± 0.07
CaO	0.06 ± 0.02	0.00 ± 0.00	0.00 ± 0.00	0.01 ± 0.00	0.01 ± 0.00	0.00 ± 0.00
Na_2O	0.03 ± 0.02	0.02 ± 0.02	0.00 ± 0.00	0.05 ± 0.03	0.03 ± 0.02	0.02 ± 0.02
K_2O	0.00 ± 0.00	0.01 ± 0.01	0.00 ± 0.00	0.02 ± 0.01	0.03 ± 0.01	0.00 ± 0.00
Cl	0.00 ± 0.00	0.00 ± 0.00	0.00 ± 0.00	0.02 ± 0.01	0.04 ± 0.01	0.00 ± 0.00
F	0.14 ± 0.03	0.00 ± 0.00	0.00 ± 0.00	0.11 ± 0.03	0.03 ± 0.03	0.09 ± 0.03
Total	88.82	89.06	89.11	87.57	88.70	89.42
Chemical formula based on 28 oxygens						
Si^{4+}	5.50 ± 0.04	5.35 ± 0.04	5.32 ± 0.04	5.71 ± 0.04	5.37 ± 0.04	5.72 ± 0.05
Al^{3+}	2.50 ± 0.02	2.65 ± 0.02	2.68 ± 0.02	2.29 ± 0.02	2.63 ± 0.02	2.28 ± 0.02
$\sum$ T	8.00	8.00	8.00	8.00	8.00	8.00
Al^{3+}	2.29 ± 0.02	2.54 ± 0.02	2.61 ± 0.02	2.34 ± 0.02	2.51 ± 0.02	2.05 ± 0.02
Ti^{4+}	0.01 ± 0.00	0.01 ± 0.00	0.00 ± 0.00	0.00 ± 0.00	0.01 ± 0.00	0.01 ± 0.00
Cr^{3+}	0.00 ± 0.00	0.00 ± 0.00	0.00 ± 0.00	0.00 ± 0.00	0.00 ± 0.00	0.00 ± 0.00
Fe^{2+}	6.41 ± 0.06	8.02 ± 0.08	8.16 ± 0.07	4.24 ± 0.03	7.83 ± 0.07	7.73 ± 0.07
Mn^{2+}	0.02 ± 0.00	0.01 ± 0.00	0.03 ± 0.01	0.05 ± 0.01	0.00 ± 0.00	0.02 ± 0.01
Mg^{2+}	3.33 ± 0.01	1.46 ± 0.02	1.23 ± 0.02	5.31 ± 0.04	1.70 ± 0.02	2.29 ± 0.03
Ca^{2+}	0.01 ± 0.00	0.00 ± 0.00	0.00 ± 0.00	0.00 ± 0.00	0.00 ± 0.00	0.00 ± 0.00
Ba^{2+}	0.00 ± 0.00	0.00 ± 0.00	0.01 ± 0.00	0.00 ± 0.00	0.00 ± 0.00	0.00 ± 0.00
Na^{+}	0.03 ± 0.01	0.02 ± 0.01	0.00 ± 0.00	0.04 ± 0.01	0.03 ± 0.01	0.02 ± 0.01
K^{+}	0.00 ± 0.00	0.01 ± 0.00	0.00 ± 0.00	0.01 ± 0.00	0.02 ± 0.00	0.00 ± 0.00
$\sum$ M	12.11	12.06	12.03	12.00	12.08	12.12
F^{-}	0.10 ± 0.02	0.00 ± 0.00	0.00 ± 0.00	0.07 ± 0.02	0.02 ± 0.02	0.06 ± 0.02
Cl^{-}	0.00 ± 0.00	0.00 ± 0.00	0.00 ± 0.00	0.01 ± 0.00	0.02 ± 0.00	0.00 ± 0.00
OH^{-}	7.90	8.00	8.00	7.92	7.96	7.94
$\sum$ OH	8.00	8.00	8.00	8.00	8.00	8.00
$x_\square$	-0.07	-0.04	-0.04	0.12	-0.05	-0.10
Name:	Chamosite	Chamosite	Chamosite	Clinochlore	Chamosite	Chamosite

as Fe^{2+} when calculating the chemical formula. Next, the vacancies ($x_\square$) in the normative chlorite formula (equation 8.1) are calculated in equation 8.2 (Zane and Weiss, 1998):

$$(R_x^{2+}R_y^{3+}\square_{12-x-y})^{VI}(Si_zR_{8-z}^{3+})^{VI}O_{20}OH_{16} \tag{8.1}$$

$$x_\square = 12 - \sum(R^{2+} + R^{3+} + R^{4+})^{VI} \tag{8.2}$$

The results have been included in Table 8.5. Next, it is necessary to specify the proportions between R^{2+} and R^{3+} + $\square$ in the octahedral sheet (see equation 8.1) (Zane and Weiss, 1998):

Table 8.5 Continued

	Central Duparquet	Transition zone
	47-8-2	**58-3-1**
	Qtz-Ab-Cb	Chlorite vein
SiO_2	26.02 ± 0.18	28.94 ± 0.20
TiO_2	0.05 ± 0.02	0.08 ± 0.03
Al_2O_3	15.51 ± 0.12	17.30 ± 0.14
Cr_2O_2	0.01 ± 0.00	0.01 ± 0.00
FeO	41.19 ± 0.37	21.28 ± 0.26
MnO	0.13 ± 0.04	0.26 ± 0.04
BaO	0.00 ± 0.00	0.00 ± 0.00
MgO	6.45 ± 0.07	19.53 ± 0.16
CaO	0.02 ± 0.00	0.04 ± 0.02
Na_2O	0.03 ± 0.02	0.01 ± 0.00
K_2O	0.00 ± 0.00	0.42 ± 0.02
Cl	0.00 ± 0.00	0.00 ± 0.00
F	0.08 ± 0.03	0.81 ± 0.06
Total	89.49	88.69
Si^{4+}	5.89 ± 0.05	5.94 ± 0.05
Al^{3+}	2.11 ± 0.02	2.06 ± 0.02
$\sum$ T	8.00	8.00
Al^{3+}	2.02 ± 0.02	2.13 ± 0.02
Ti^{4+}	0.01 ± 0.00	0.01 ± 0.00
Cr^{3+}	0.00 ± 0.00	0.00 ± 0.00
Fe^{2+}	7.79 ± 0.07	3.66 ± 0.04
Mn^{2+}	0.02 ± 0.01	0.05 ± 0.01
Mg^{2+}	2.17 ± 0.02	5.98 ± 0.05
Ca^{2+}	0.00 ± 0.01	0.01 ± 0.00
Ba^{2+}	0.00 ± 0.00	0.00 ± 0.00
Na^{+}	0.03 ± 0.01	0.01 ± 0.00
K^{+}	0.00 ± 0.00	0.22 ± 0.01
$\sum$ M	12.05	12.06
F^{-}	0.06 ± 0.02	0.53 ± 0.04
Cl^{-}	0.00 ± 0.00	0.00 ± 0.00
OH^{-}	7.94	7.47
$\sum$ OH	8.00	8.00
$x_\square$	-0.01	0.21
Name:	Chamosite	Clinochlore

Type 1; $x_{Mg} + x_{Fetot} \geq x_{Al} + x_\square$

Type 2; $x_{Mg} + x_{Fetot} < x_{Al} + x_\square$

where $x = apfu$

Following the calculations, all chlorite analyses belong to Type 1. Both the calculated R (sum of octahedral cations) and $x_\square$ correspond to the ranges of trioctahedral chlorite where R is between 10.0 - 12.00 and $x_\square$ is 2.0 - 0.00 (Bayliss, 1975; Bailey, 1988; Zane and Weiss, 1998). Analyses also demonstrate no overlap between chlorite subgroups, simplifying their classification. Finally, trioctahedral chlorite species are named based on the dominant divalent octahedral cation (Bailey, 1988). Analysed chlorite, with the exception of JG-5099-06 and 58-3-1, are Fe^{2+}-dominant and therefore belong to the chamosite end-member. Analysis JG-5099-06 and 58-3-1 is Mg^{2+}-dominant and is therefore part of the clinochlore end-member.

The final species names have also been included in Table 8.5.

Differences between chamosite and clinochlore could not be observed via EBS imaging as all selected crystals appear similar and lack compositional zoning. Investigations to uncover the compositional differences have found that the resulting chlorite chemistry is attributed to the local chemistry of the rock. Specifically, in the transition zone considered part of the equigranular magnetite-bearing unit, rocks have a normalized average Fe_2O_3/MgO[1] ratio of 3.32 (n = 2), comparatively to the porphyritic Beattie unit which has a ratio of 5.69 (n = 47) and the porphyritic Central Duparquet unit which has a ratio of 5.01 (n = 17). Consequently, since the transition zone has the lowest Fe_2O_3/MgO ratio, the crystallizing chlorite would have inherited from the abundance of Mg^{2+} (when compared to the other units) which resulted in clinochlore. Conversely, both the porphyritic Beattie and Central Duparquet units have greater amounts of Fe^{2+} in their rock chemistry which is directly reflected by the presence of chamosite. Clinochlore in the porphyritic Beattie unit (analysis JG-5099-06) is hypothesized to have resulted from a finer scale variation in the Fe_2O_3/MgO ratio. Specifically, a geochemical sample which yielded a ratio of 4.96 was taken at the location with the corresponding analysis. This ratio is slightly lower than the average for the unit and could have therefore resulted in the crystallization of clinochlore.

[1]Both Fe_2O_3 and MgO were relatively immobile during Au-mineralization, see section 8.2.1

Quartz

Quartz generally occurs in tension veins, rarely replaced the orthoclase core of a feldspar phenocrysts or replaced carbonate minerals in primary mafic mineral relicts.

There are at least two distinct generations of quartz in veins as deduced from field relationships. The oldest generation is found in $<$ 5 cm wide Qtz-Ab-Cb veins. Commonly, these veins have reopened chlorite-filled tension fractures, indicating prolonged activity among tension fractures. Chlorite occupies the outer margin, whereas quartz, albite and carbonate minerals, which occur in nearly equal proportions, are intermixed at the centre (see Figure 8.6). These veins are transected with minimal to no displacement by Qtz-Cb veins as presented in Figure 8.19. Qtz-Cb veins are dominantly composed of quartz with minor to trace amounts of carbonate minerals found at the centre of the veins. The Qtz-Cb veins can reach a thickness between 1 - 30 cm. In all cases quartz is translucent, grey (or white in outcrops) in colour. Crystals are typically anhedral, measure between 0.1 - 1.8 mm across and can demonstrate an undulatory extinction. Only in one instance were euhedral crystals of quartz observed in a vug created by the opening of a fissure.

Rarely quartz was observed in feldspar phenocrysts to replace the orthoclase core. Additionally, in one instance, quartz was observed to have replaced carbonate minerals in primary mafic mineral relicts. These crystals are anhedral and measure between 0.1 - 1 mm across.



Figure 8.19 – Tension vein of chlorite refilled by quartz, albite and carbonate minerals which is transected by a quartz carbonate minerals vein. The chlorite appears black in colour and is found at the margin of the vertical vein. A vertical chlorite filled tension vein is to the right. Quartz and albite appear as white anhedral crystals and are accompanied by a weathered patch of carbonate minerals (brown) at the centre of the vertical vein. The vertical vein is transected, with very little displacement, by the diagonal quartz and carbonate minerals (pale brown) vein. Location: 630313E 5374277N.

Sulphide minerals

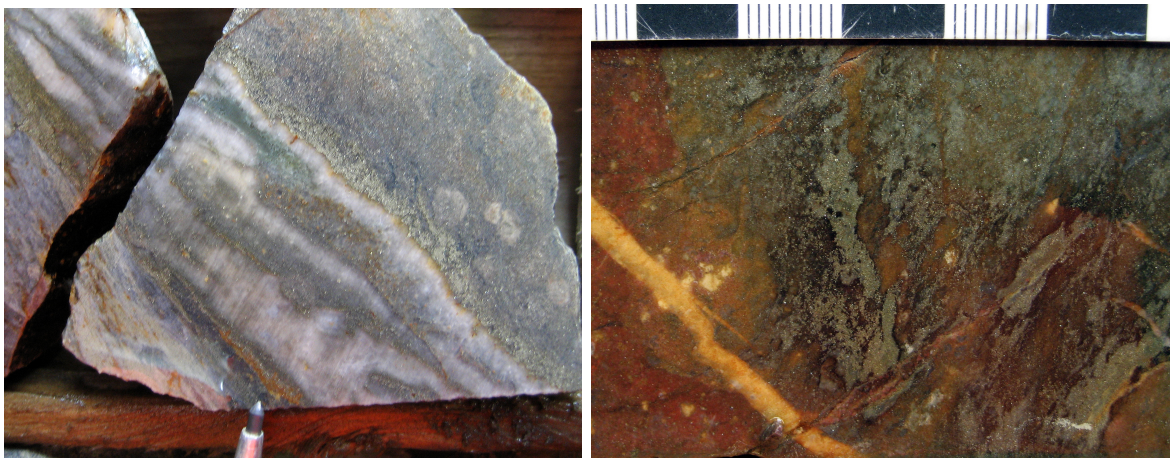
Sulphide minerals are the main source of Au-mineralization. Historically, this mineralization was found in brecciated and silicified zones where fine grained pyrite and arsenopyrite, the main sulphide minerals, rarely exceeded $10\%_m$ of mineralized zones (Davidson and Banfield, 1944). Unfortunately, underground workings permitting the observation of mineralized zones are not accessible as they were flooded after the closure of the mines. However, with the renewal of exploration in the area, drill cores provide a window into the habits and abundance percentages of sulphide minerals. Consequently, most of the macroscopic descriptions below have been sourced from drill core observations. Other accompanying sulphide minerals observed by the author are chalcopyrite and galena. Sulphur, ilmenite, native gold, electrum, sphalerite, marcasite, molybdenite and an argentiferous arenical mineral were also noted by Banfield (1940); Davidson and Banfield (1944); Graham (1954) but were not observed by the author.

Pyrite and arsenopyrite Pyrite and arsenopyrite appear as sub-millimetre size disseminated crystals in zones showing repeat brittle deformation and infiltration of hydrothermal fluids (see Figure 8.20a) and, at times, in contact zones. These zones often contain Ab-Cb veins at their centre. Both pyrite and arsenopyrite often crystallized at the outer margin of the veins. Progressing outwards, into the syenite, the concentration of sulphides decreases over the order of a few centimetres.

In rare occasions, both pyrite and arsenopyrite intrude into the syenite forming an irregular-shaped mass as presented in Figure 8.20b. These masses are often accompanied by quartz and overprint the pyrite and arsenopyrite veins, suggesting subsequent dissolution and transportation of pyrite and arsenopyrite by quartz.

The difference between pyrite and arsenopyrite is best observed in thin section. Specifically, pyrite crystals are slightly larger, between 0.01 - 0.4 mm across, than arsenopyrite crystals which measure between 0.001 - 0.2 mm across. Another distinction can be made with crystalline habits where pyrite generally appears as individual sub- to euhedral grains, whereas arsenopyrite crystals appear as rhombic-shaped and can demonstrate a skeletal habit. Arsenopyrite was also noted to occur as columnar crystals or as dendritic aggregates by (Davidson and Banfield, 1944).

Crystals of pyrite and arsenopyrite rarely have magnetite and chalcopyrite at their cores.



(a) Disseminated pyrite and arsenopyrite in a vein. Sub-millimeter size crystals are located on the outer margin of the vein and apparently exponentially decrease in abundance into the syenite. Drill core: B08-62, depth: 40.00 - 43.25 m.

(b) Mass of disseminated pyrite and arsenopyrite. The mass overprints the syenite and is accompanied by quartz. The mass is cut by a Ab-Cb vein (left). Drill core: B08-21, depth: 26.10 m.

Figure 8.20 – Pyrite and arsenopyrite in the Beattie syenite.

In other cases, they have been subsequently rimmed by magnetite or hematite. Additionally, in the megaporphyritic unit, some crystals demonstrate up to 2 distinct growth stages with inclusions of chalcopyrite or magnetite at their core.

Chalcopyrite Chalcopyrite was either observed at the core of pyrite and arsenopyrite crystals, in thin (< 5 mm) Qtz-Ab-Cb veins or rarely as independent crystals. Overall, chalcopyrite is closely associated with hydrothermal magnetite and less-so to with pyrite and arsenopyrite. At the core of pyrite and arsenopyrite, chalcopyrite inclusions are quite small, measuring 0.01 mm on average. In Qtz-Ab-Cb veins, chalcopyrite crystals are anhedral and measure between 0.005 - 2 mm across. These crystals are found at the vein-centre and are typically surrounded by anhedral hydrothermal magnetite. At times, these crystals seem to appear as inclusions in magnetite (see Figure 8.21). Finally, independent chalcopyrite crystals were only observed in the lath syenite unit where they measure between 0.005 - 0.05 mm across and occur in heavily sericitized zones.

Galena Galena was only found as small (0.002 mm) anhedral inclusions in magnetite, in a thin section from the lath syenite unit (see Figure 8.21).

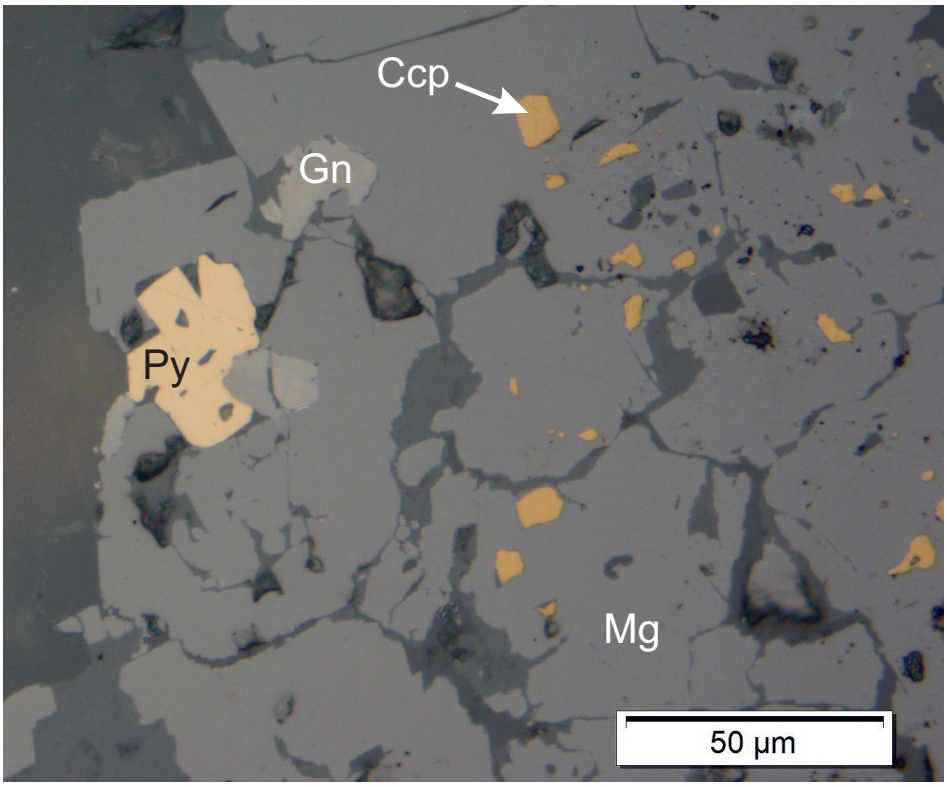


Figure 8.21 – Magnetite crystal (Mg) with inclusions of chalcopyrite (Ccp), galena (Gn) and pyrite (Py). Photomicrograph taken under reflected light. Location: 632690E 5374266N.

Magnetite

Very little hydrothermal magnetite was found. Magnetite dominantly appears as an even, $\leq$ 0.1 mm thick overgrowth around pyrite and arsenopyrite or at their core as subhedral crystals measuring $\leq$ 0.4 mm across. In one instance, larger crystals were located at the centre of a sericite vein. These larger magnetite crystals measure 0.02 - 0.8 mm across, are euhedral and contain inclusions of chalcopyrite and galena with barite at the outer margins (see Figure 8.21). In comparison, igneous magnetite will be found disseminated through the rock as small subhedral to anhedral crystals measuring 0.2 mm across. Most igneous disseminated magnetite crystals have been observed to possess a thin (0.01 mm thick) reaction rim of hematite.

Epidote

Epidote is unique to the equigranular magnetite-bearing unit. Crystals are pleochroic, sub- to euhedral, measure $\leq$ 0.2 mm and are almost always found near or within clinopyroxene relicts (see Figure 8.22). Epidote crystals are rarely found at the core of the large euhedral

feldspars. In larger epidote crystals, a single cleavage is occasionally visible. The determination of the chemical composition of epidote was first conducted on the basis of the optical sign and birefringence which indicated that the crystals correspond to epidote rather than clinozoisite. Their composition was subsequently confirmed via EMPA.

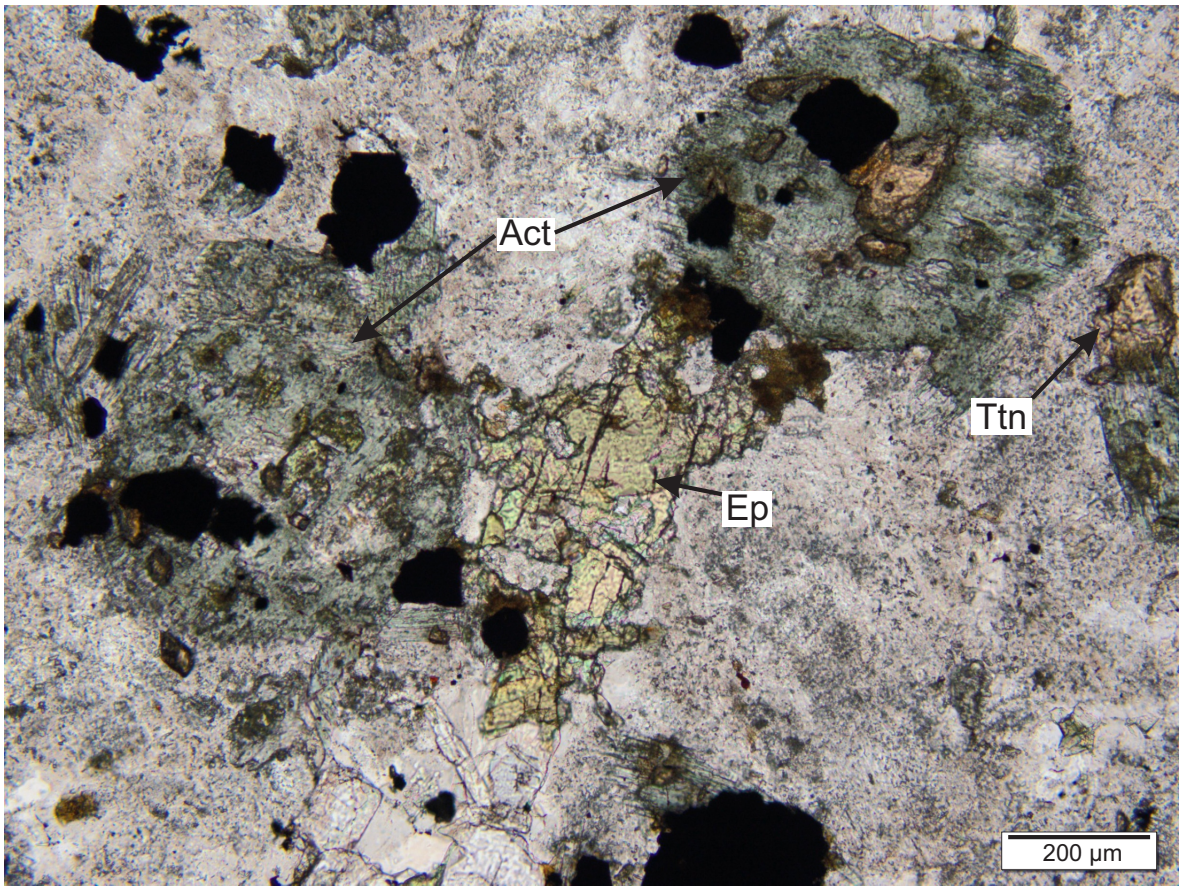


Figure 8.22 – Epidote in the equigranular magnetite-bearing unit. Pleochroic crystals of pale green epidote (Ep) are accompanied by darker green pleochroic actinolite. Minor amounts of titanite (Ttn) are also observed. Photomicrograph taken under plane polarized light. Location: 630747E 5374454N.

To ascertain the chemical composition of epidote, a total of 3 analyses were performed. Chemical formulas were calculated on a 12.5 oxygen basis. The compositions and calculated formulas are presented in Table 8.6.

The nomenclature of epidote minerals was adopted according to the current IMA recommendations (Armbruster et al., 2006). It is well known that there exists a complete solid-solution series between clinozoisite and epidote, therefore providing a means of calculating an end-member. The solid solution series can be simplified when comparing ratios of Al^{3+} and

Table 8.6 – Microprobe analysis and chemical formulas of epidote.

	JG-04-15	JG-04-16	JG-04-17
SiO_2	37.34 ± 0.26	37.32 ± 0.26	37.68 ± 0.26
TiO_2	0.61 ± 0.02	0.00 ± 0.00	0.03 ± 0.00
Al_2O_3	20.22 ± 0.14	20.38 ± 0.14	21.06 ± 0.15
FeO	14.44 ± 0.13	14.88 ± 0.13	14.21 ± 0.13
MnO	0.53 ± 0.03	0.32 ± 0.03	0.37 ± 0.02
MgO	0.07 ± 0.01	0.02 ± 0.01	0.02 ± 0.00
CaO	20.67 ± 0.14	21.25 ± 0.15	21.78 ± 0.15
Na_2O	0.05 ± 0.03	0.06 ± 0.03	0.00 ± 0.00
K_2O	0.00 ± 0.00	0.00 ± 0.00	0.01 ± 0.00
Total	93.99	94.24	95.15
Chemical formula based on 12.5 oxygens			
Si^{4+}	3.14 ± 0.03	3.13 ± 0.03	3.12 ± 0.02
$\sum$ **Z**	3.14	3.13	3.12
Al^{3+}	2.00 ± 0.02	2.02 ± 0.02	2.06 ± 0.02
Fe^{3+}	0.82 ± 0.01	0.85 ± 0.01	0.80 ± 0.01
Ti^{4+}	0.04 ± 0.00	0.00 ± 0.00	0.00 ± 0.00
$\sum$ **Y**	2.86	2.86	2.86
Mg^{2+}	0.01 ± 0.00	0.00 ± 0.00	0.00 ± 0.00
Fe^{2+}	0.00 ± 0.00	0.00 ± 0.00	0.00 ± 0.00
Mn^{2+}	0.04 ± 0.00	0.02 ± 0.00	0.03 ± 0.00
Ca^{2+}	1.86 ± 0.01	1.91 ± 0.02	1.93 ± 0.02
Na^{+}	0.01 ± 0.00	0.01 ± 0.00	0.00 ± 0.00
K^{+}	0.00 ± 0.00	0.00 ± 0.00	0.00 ± 0.00
$\sum$ **X**	1.92	1.95	1.96
Mol% end-member			
Cz	0.37 ± 1.94	1.89 ± 1.86	6.79 ± 1.97
Ep	99.63 ± 11.13	98.11 ± 10.66	93.21 ± 10.63

Fe^{3+}. Specifically, clinozoisite will have an ideal Al^{3+}:Fe^{3+} ratio of 3:0, whereas epidote will have a 2:1 ratio. To calculate the mol% end-member composition the following equations, employing the number of normalized cations, can be utilized:

$$X_{Cz} = \frac{Al^{3+} - 2}{Fe^{3+} + Al^{3+} - 2} \times 100 \tag{8.3}$$

$$X_{Ep} = \frac{Fe^{3+}}{Fe^{3+} + Al^{3+} - 2} \times 100 \tag{8.4}$$

Results show that the mol% end-member ranges from 93.21 - 99.63 mol% epidote. The complete ranges and associated errors are provided in Table 8.6.

Verifications via EDS revealed that epidote crystals lack significant amounts of REE. Minor substitution of Ca^{2+} for Mn^{2+} and Na^{+} occurs within the crystals, but have no effect on the epidote nomenclature. Very little to no Cr_2O_3 was detected, and from what was measured, the detection error matched the associated concentration.

EBS observations reveal slight compositional zoning within the crystals (see Figure 8.23).

This ever so slight luminosity variation has been investigated in analyses JG-04-16 (dark) and JG-04-17 (light). The variations from darker to lighter areas are noted in an increase in Al^{3+}, Ca^{2+} and a decrease in Fe^{3+} (see Table 8.6).

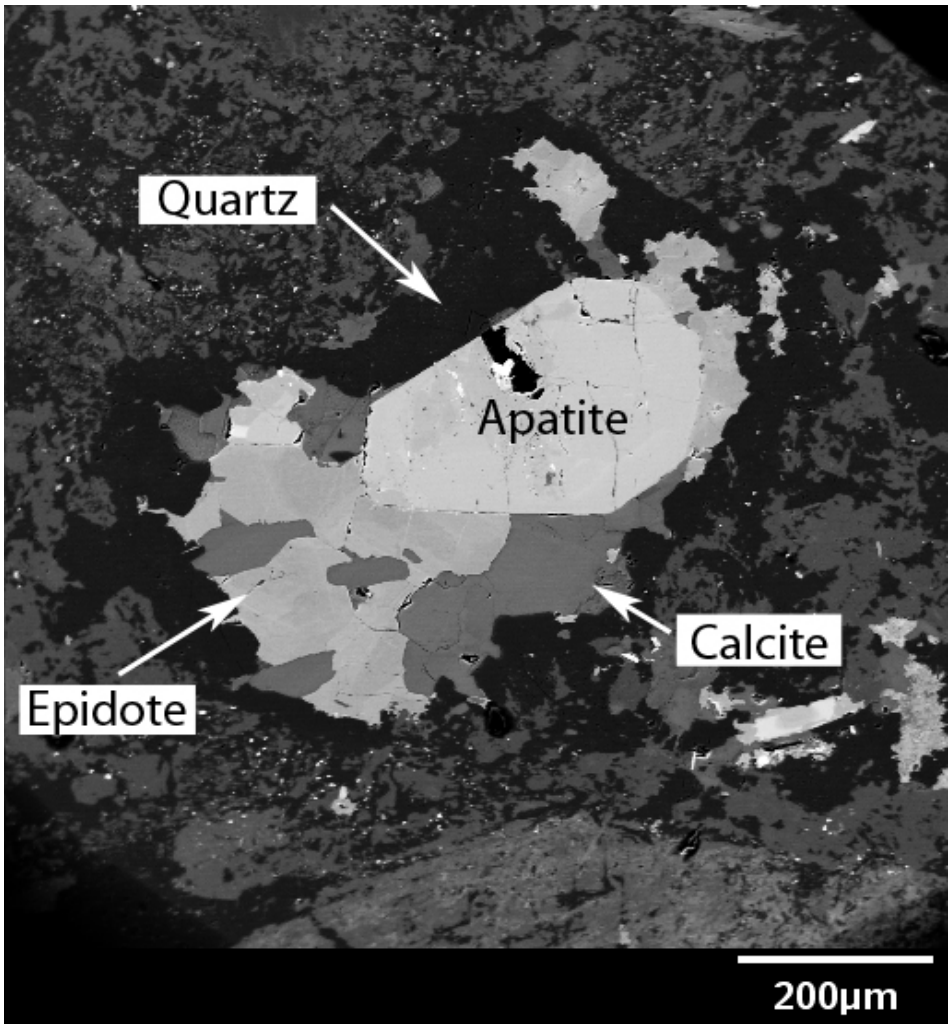


Figure 8.23 – EBS image of epidote. Slight compositional zoning is observed in epidote. The increase in luminosity is caused by an increase in Al^{3+}, Ca^{2+} and a decrease in Fe^{3+}. Location: 630747E 5374454N.

Biotite

Very few biotite crystals were observed located at the centre of a single sericite vein already intermixed with chlorite. Biotite crystals are subhedral, pleochroic, pale brown and ≤ 0.2 mm long.

Fluorite

Only a single small (0.08 mm) anhedral crystal of fluorite was found. This crystal was found in a small patch of quartz, opaque minerals and recrystallized sericite in a large vein of chlorite.

Xenotime

A few subhedral, ≤ 0.25 mm, crystals of xenotime were found in a transecting Qtz-Ab-Cb vein. The crystalline edges are slightly corroded as they appear with a orange-brown hue compared to the clear interior (see Figure 8.24).

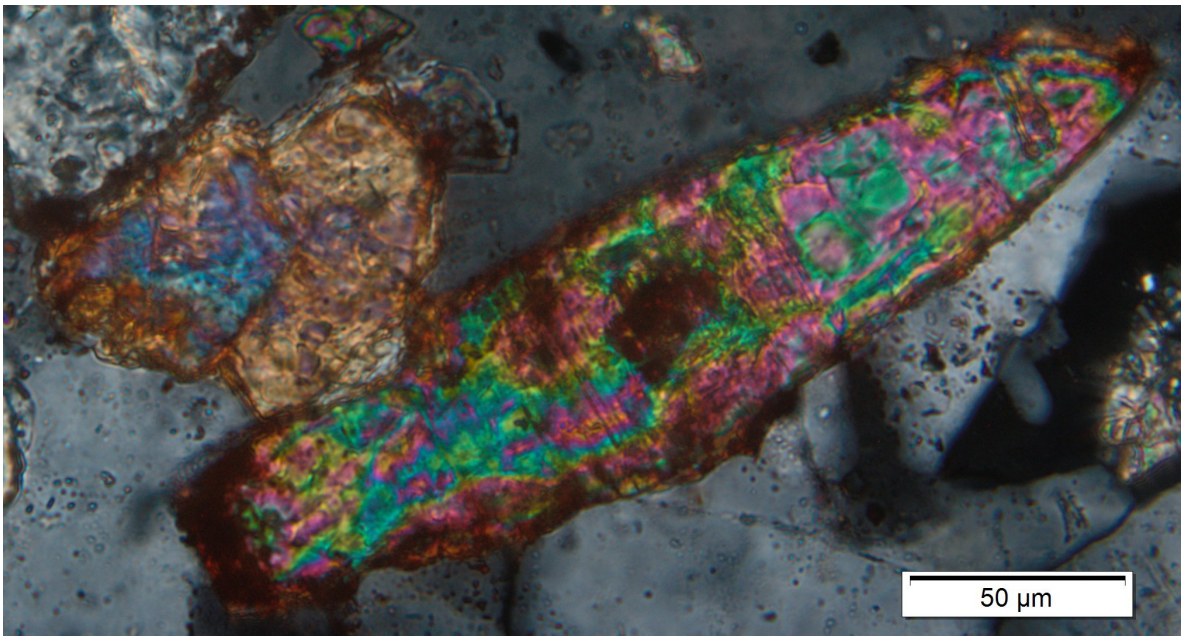


Figure 8.24 – Subhedral crystals of xenotime. Crystal contained in a transecting quartz, albite and carbonate minerals vein. Margins of the crystal are also slightly altered, demonstrating a brown hue compared to the clear interior. Photomicrograph taken under crossed polars. Location: 632652E 5374309N.

Tourmaline

Black tourmaline generally occurs as slikenfibers associated with D_2 shear zones (see Figure 8.25). Crystals are an acicular overgrowth which range from a few crystals to a complete covering of the rock, at times expressing ridge-in-groove lineations. Furthermore, tourmaline is also rarely observed in Qtz-Ab-Cb tension veins. Tourmaline crystals are typically anhedral and measure ≤ 0.15 mm across.



Figure 8.25 – Black slikenfibers of tourmaline in a D_2 shear fault. Location: 630301E 5374297N.

Barite

One of the rarest hydrothermal minerals is barite which consists of bright red anhedral crystals. The crystals are anhedral, measure < 0.01 mm across and are found at the centre of Qtz-Ab-Cb veins in zones of repeated brittle deformation, or at the margins of a hydrothermal magnetite crystals located at the centre of a sericite vein. Barite found in zones of repeated brittle deformation may be accompanied with pyrite and arsenopyrite.

Hornblende

Hornblende is also unique to the equigranular magnetite-bearing unit. The exact chemistry of the crystal could not be determined and the name hornblende is used in *sensu lato*, therefore as a calcic amphibole. Specific measurements for its determination as a calcic amphibole are that it is biaxial negative with a large 2V between 75 - 80°. This crystal is quite clearly a porphyroblast since it overprints the feldspathic matrix and surrounding clinopyroxene relicts. Therefore hornblende originated from regional metamorphism to the greenschist facies. The

porphyroblasts are anhedral, strongly pelochroic (forest green to brown) and measure 2 mm across on average. Figure 8.26 demonstrates such an example.

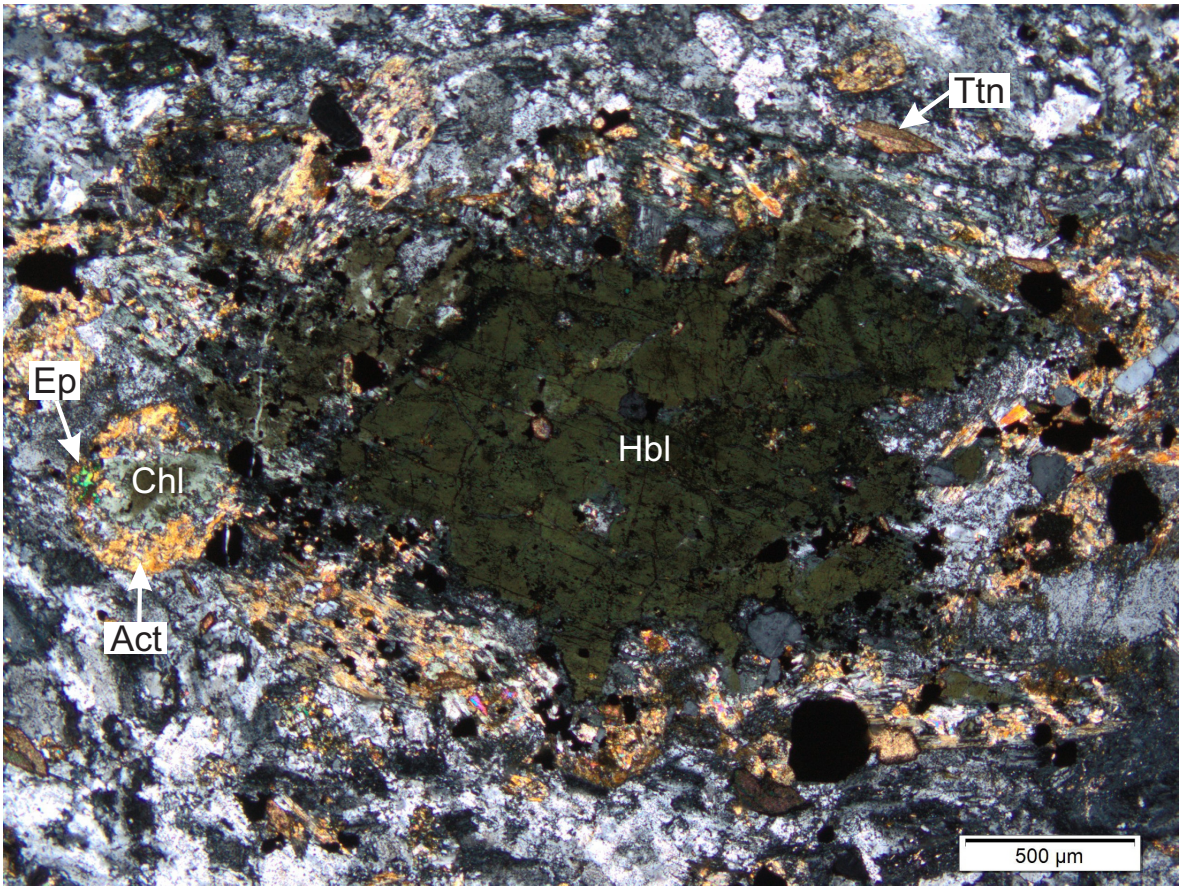


Figure 8.26 – Hornblende (Hbl) porphyroblast in the equigranular magnetite-bearing unit. The porphyroblast overprints the feldspathic matrix and surrounding clinopyroxene relicts. The clinopyroxene relicts are now composed of actinolite (Act) which is incompletely altered to calcite (not seen), chlorite (Chl) and opaques. A small crystal of epidote (Ep) is also observed in the clinopyroxene relict. Titanite crystals (Ttn) appear randomly through the rock. Photomicrograph taken under crossed polars. Location: 630767E 5374471N.

8.1.2 Deformation

After its initial emplacement, the syenite was transected by numerous generations of shear faults, strike-slip faults, joints and fractures. As previously mentioned, these features are rather abundant in the western portions of the unit, close to the PDFZ, and lessen progressing eastwards.

The largest structural features are secondary D_2 shear faults which transect the syenite and country rocks. These faults strike E-W, varying between 70 - 110°, and dip steeply south. Locally, fault contacts are often coated by tourmaline slikenfibers (see Figure 8.25). The presence of slikenfibers imply a slow aseismic creep (Twiss and Moores, 1992). The shear faults are also expressed by cataclastic zones which were later filled by a myriad of minerals and veins (discussed above), including Au-bearing pyrite and arsenopyrite (see Figure 8.27). These cataclastites can be recognized by an absence of phenocrysts, and numerous thin (< 1 cm) veins of pale green sericite and subordinate chlorite following the same strike.



Figure 8.27 – Secondary D_2 shear fault transecting the Beattie syenite. Location: 630952E 5374400N.

The secondary D_2 shear faults also affected the surrounding syenite, up to a distance of < 30 m, producing a series of conjugate shear and extension fractures. The conjugate shear

fractures measure between 1 - 5 cm across, have not, or have minimally disturbed the encasing rock, strike approximately in the same direction as the secondary D_2 shear faults, and dip at 45° from each other. Progressing eastwards, these fractures have been commonly filled with pale green sericite as presented in Figure 8.28. Where sericite is less abundant, shearing can be observed in the still identifiable phenocrysts that have been heavily fractured and elongated in the same sense of the shearing fractures. This illustrates that shear fractures have locally brittlely deformed the syenite with minimal to no displacement. The exact chronology of the conjugate shear fractures development could not be determined as they have interacted with each other and have been active for a protracted amount of time, caused by the continuous slow aseismic creeping nature of the D_2 shear faults which were in turn affected by the displacement episodes of the PDFZ. Extension fractures are often filled by chlorite in the western portions of the syenite. These fractures strike N-S and measure $<$ 1 cm in thickness. Some of the larger fractures were subsequently reopened and filled by Qtz-Ab-Cb veins. Most of these veins terminate simply by dying out or by branching and dying out. Interestingly, some of these veins terminate in a series of en-echelon fractures (see Figure 8.29).

Finally, NE-SW to NW-SE D_3 strike-slip faults and related Qtz-Cb filled tension veins, cut all previous features and structures (see Figure 8.28).

It should also be noted that the lath syenite unit has virtually escaped intense brittle deformation. The resulting deformation was generally caused by E-W conjugate shear and N-S extension fractures, rather than secondary D_2 shear faults. This is observed by a lack of cataclastic zones which have obliterated feldspar laths.

A detailed outcrop-scale perspective illustrating the interplay between the syenite and the structural features is presented in Figure 8.30.

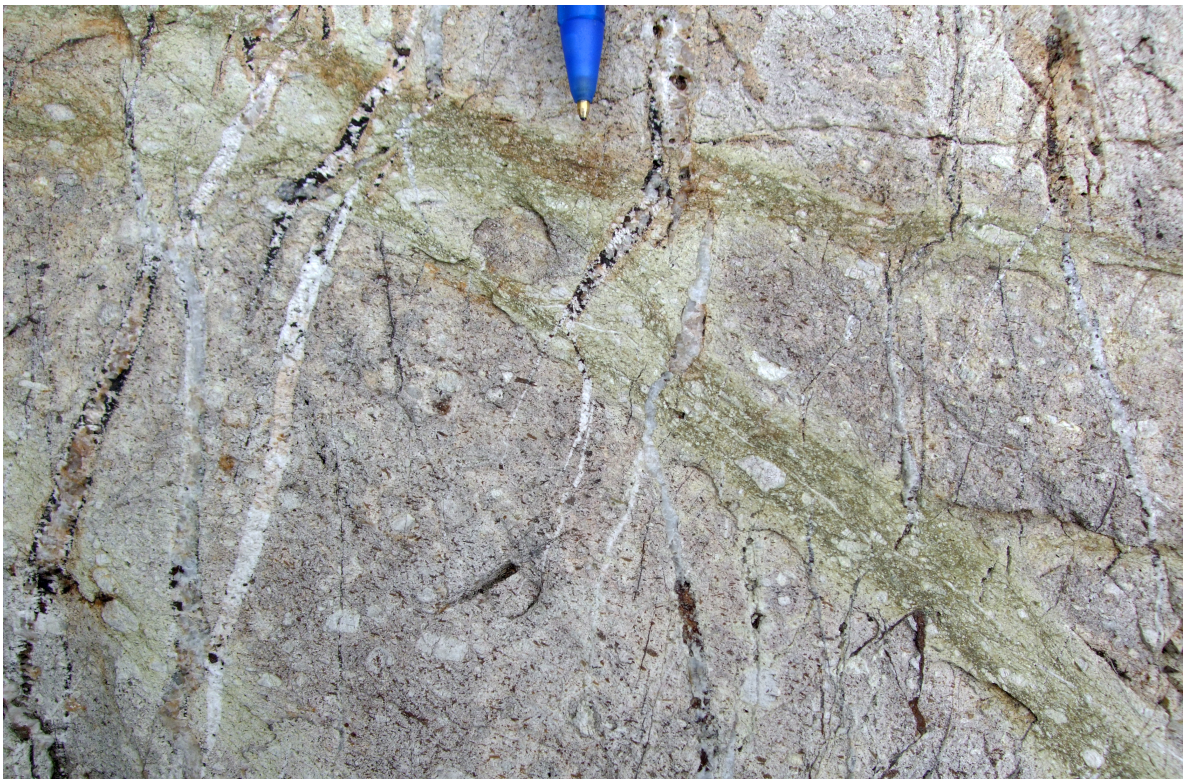


Figure 8.28 – Fractures filled with pale green sericite. Later developed white quartz and albite and weathered carbonate mineral veins cut the sericite veins. Location: 634050E 5373898N.



Figure 8.29 – En-echelon chlorite filled tension fracture. Location: 630313E 5374277N.

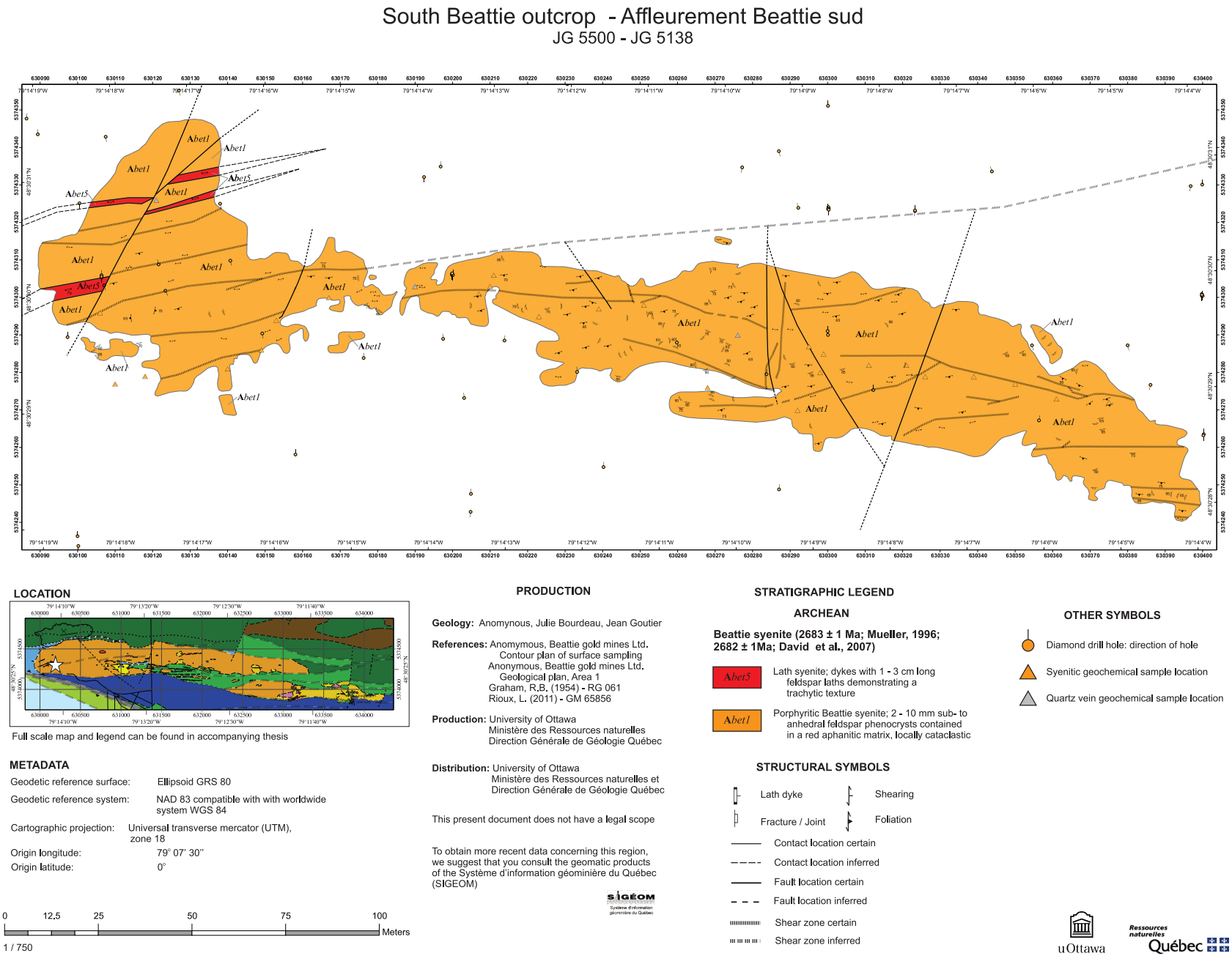


Figure 8.30 – Detailed map of South Beattie outcrop (JG 5500 - JG 5138). Full resolution poster has been included in Appendix B.

8.2 Geochemistry of hydrothermal alteration and metamorphism to the greenschist facies

For simplification purposes this section will proceed following the chronological order as established in Chapter 5.

8.2.1 Au-mineralization

Au-related hydrothermal alteration did have a noticeable effect in the Beattie area from a chemical standpoint. For country rocks, a first definitive Au-related alteration pattern was found in rocks near the Beattie syenite and D_2 faults. This relationship was therefore the subject of further investigations by employing isocon diagrams.

Isocon plots were developed by Grant (1986) as a means to plot a scaled unaltered sample against its altered equivalent. The isocon diagrams employ a scaling of the elements of which the scaling effect can be viewed in Figure 8.31. Elements demonstrating the least variation are considered 'immobile' and define the isocon slope which is usually approximately equal to one. The least mobile incompatible elements within greenstone belts are Zr, Y, Nb and the REE (MacLean and Barrett, 1993). Other least mobile elements, deduced from extremely low variability in the geochemical data, are TiO_2, Al_2O_3 and P_2O_5. It is important to note that experience has shown that these elements are conserved at the hand sample scale for regional metamorphism and mild alteration. However, intense alteration, such as hydrothermal carbonatization associated with ore deposits, may mobilize them. An isocon slope > 1 defines a loss in volume, as opposed to a slope < 1 which defines an increase. Consequently, elements plotting above the isocon line have been added to the rock (enrichment relative to a least-altered component), whereas elements plotting below the isocon slope have been removed (depleted relative to a least-altered component) (see Figure 8.31).

Unfortunately, margins of error for each element could not be provided with the diagrams since most analyses were not accompanied by their respective accuracies and in some cases, detection limits. Nonetheless, hydrothermal alteration signatures illustrated by the isocon diagrams are remarkably similar, regardless of lithology. As such, the need for elemental margins of errors is lessened.

To this end, data from SOQUEM Inc., Gold Fields Resources Canada Ltd., MRN, Osisko

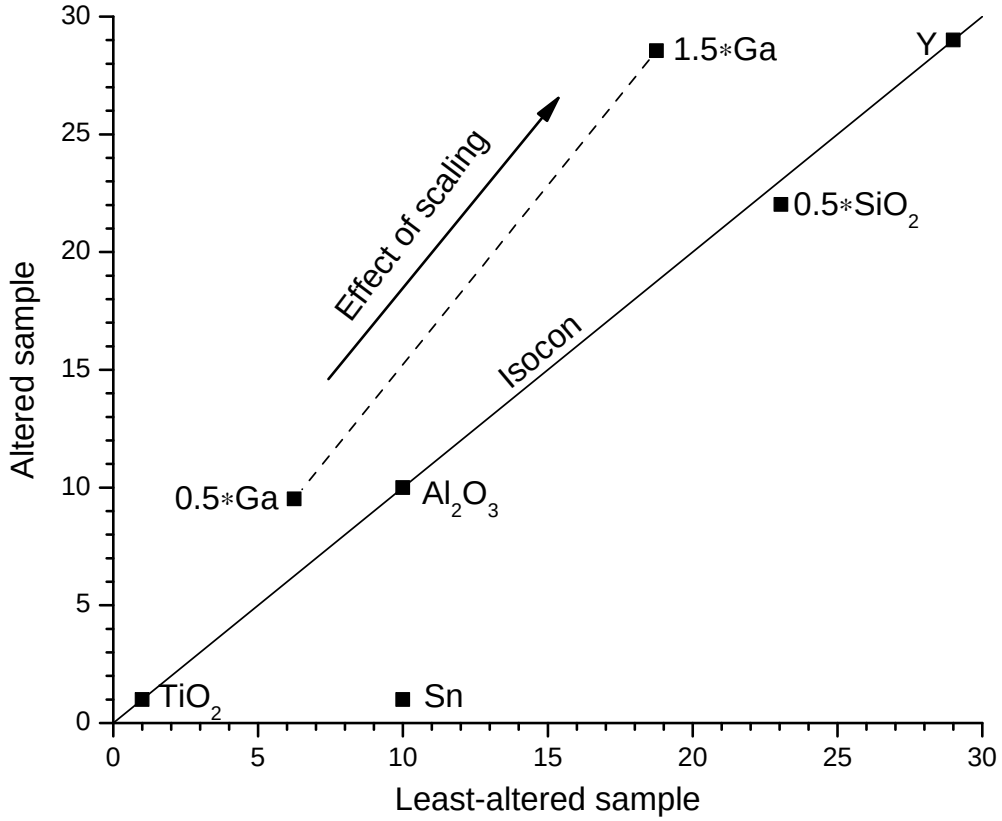


Figure 8.31 – Diagram of an isocon plot. The effect of scaling is illustrated by the dashed line for Ga. The isocon line is defined by 'immobile' elements TiO_2, Al_2O_3 and Y. Elements which plot above the isocon line indicate an enrichment (eg: Ga) whereas elements plotting below the line indicate a depletion (eg: SiO_2, Sn).

Mining Corporation and the author are all considered for the characterization of the Au-related hydrothermal alteration. The full dataset is presented in Appendix D.

Deguisier basalt

At a first glance, Au-mineralization seems closely related to contacts with the Beattie syenite as well as D_2 faults. In order to fully investigate this feature, the averages of proximal (< 50 m) to the contact with the syenite and D_2 faults were plotted against distal (> 50 m) basaltic samples. The specific scaling factors and elements used to define the isocon slope of the basalt are listed in Table 8.7 and the resulting isocon diagram is in Figure 8.32.

Table 8.7 – Scaling factors and identification of immobile elements for the Deguisier basalt.

Element	Scaling factor	Element	Scaling factor
SiO_2	0.5	**S**	60
Al_2O_3	1	**Ag**	9
Fe_2O_3t	1	**Au**	0.19
CaO	2.5	**Ba**	0.009
MgO	2.5	**Co**	0.19
Na_2O	3	**Cr**	0.05
K_2O	12	**Cu**	0.09
MnO	19	**Pb**	1
TiO_2	1	**Rb**	0.5
P_2O_5	4	**Sr**	0.09
LOI	3	**Zn**	0.1
CO_2	3	**Zr**	0.28
Immobile elements	**P_2O_5, TiO_2, Al_2O_3, Zr**		

The isocon plot of the Deguisier tholeiitic basalt demonstrates a pronounced enrichment in CO_2, Au, S and K_2O. Other notable elemental enrichments are in Rb, Co, Ag and volatiles (LOI). Elemental depletions are encountered in Sr and to a lesser degree in MgO and Fe_2O_3. This almost exact ore signature is encountered at the Holloway mine (Ropchan, 2000), although the elemental enrichments obtained for the Deguisier basalt are not as pronounced as those at the Holloway mine. This is caused by a greater distance from known Au-mineralized deposits in the Beattie area. Nonetheless, this enrichment trend in proximity of the Beattie syenite as well as D_2 faults illustrates that contacts and faults did play a role in channelling the Au-hydrothermal fluids.

The enrichment in CO_2 and K_2O is likely resultant in part to metasomatism. The increase in CO_2 is revealed in the presence of carbonate minerals. The increase in K_2O is attributed to sericite, present in small quantities in samples (subsequently verified using NORMAT calculations, see section 8.2.2).

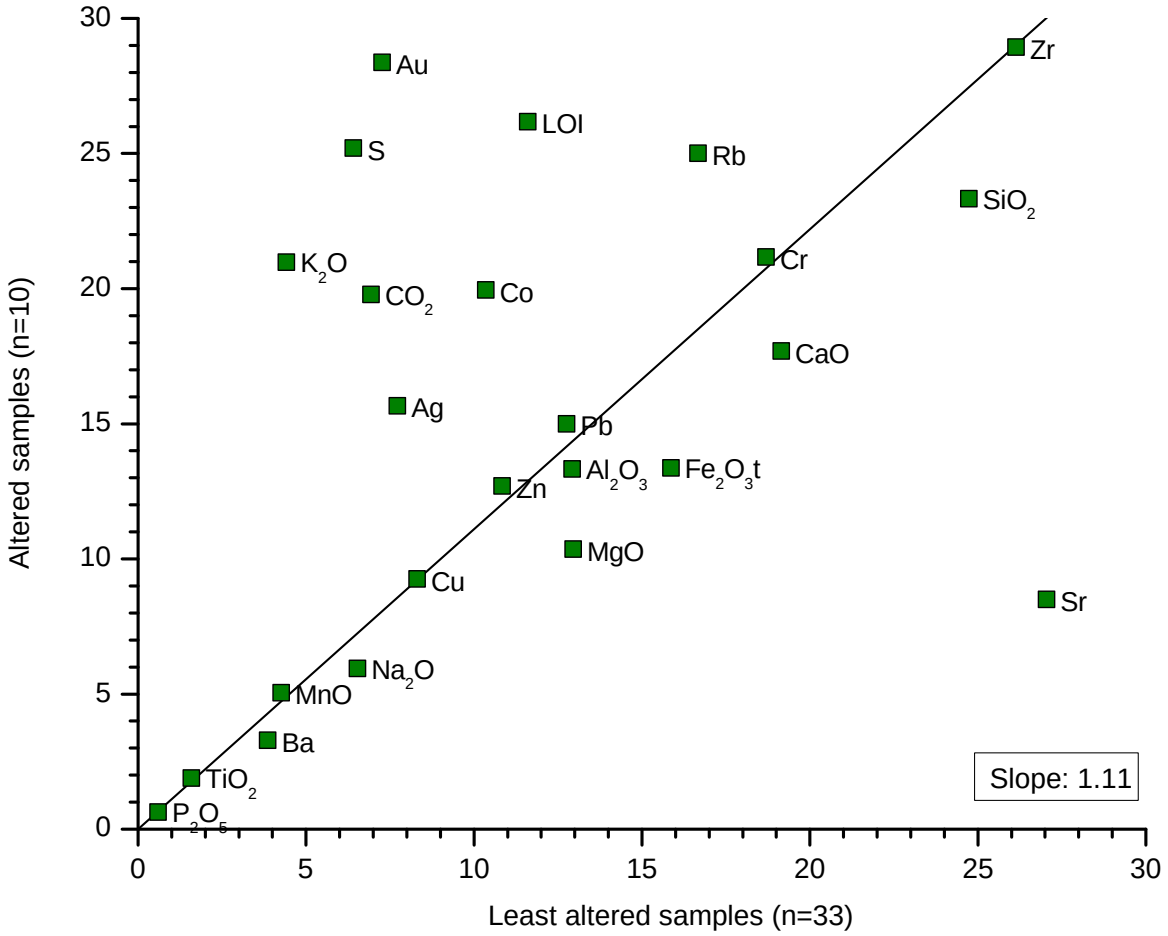


Figure 8.32 – Isocon diagram of the Deguisier basalt. Here distal (least-altered samples) are samples located $>$ 50 m from the Beattie syenite and D_2 faults and $>$ 30 m from contact with other lithologies. Proximal samples (altered samples) are located at distances $<$ 50 or 30 m. Analyses have been averaged with n corresponding to the number of averaged samples.

Deguisier andesite to dacite

The andesite to dacite unit also demonstrates the same characteristic alteration patterns in proximity to the contacts with the Beattie syenite as well as D_2 faults. This unit is bounded to the north and south by the Beattie syenite intrusion. Furthermore, the Donchester fault, one of the 3 major D_2 faults of the area, transects the unit. Both of these features provide a great opportunity to characterize the Au-mineralization effects within the Deguisier Formation.

Unfortunately, Zr which is considered to be an immobile element, could not used to define the isocon. This is caused by a lack of samples and because a severely altered sample (2004042821) contained only 70.8 ppm Zr. Such a low concentration resulted in a pronounced skewing of the average. For this reason, Al_2O_3 was chosen as a substitute since it has been measured for each and every sample and is therefore statistically better for the isocon determination. The immobile elements and scaling factors used for this unit are presented in Table 8.8.

To determine the effects of Au-mineralization near the fault and/or contact, samples were separated on the basis of their proximity. Proximal samples are located $<$ 10 m away from the features and distal samples are located $>$ 10 m. The first isocon plot, presented in Figure 8.33, demonstrates the enrichment-depletions between these 2 sets of samples.

Proximal against distal samples illustrate a strong enrichment in As, Rb, S and K_2O. Elemental depletions are encountered for Sn, Ni, Th, Mo and Zr. Interestingly, Au is located below the isocon indicating a concentration loss.

The same statistical effect noted for Zr is now found with Au. Specifically, two of the distal samples contain 2480 ppm Au (sample D958238 from Osisko) and 442 ppm Au (sample 91884 from SOQUEM) with the remainder of the samples (n = 34) average at 5.30 ppm Au. Unfortunately, this anomaly cannot be statistically tested stemming from a lack of data. Consequently, the last available option was to exclude these two samples. The resulting isocon plot of the proximal against distal samples without this enriched sample is presented in Figure 8.34.

The Au-mineralization pattern in proximity to the contact with the syenite and/or D_2 faults becomes clear without the enriched samples. Note, there is a very strong elemental enrichment in As, Au, Rb, S and K_2O. Elemental depletions are encountered in Sn, Ni, Th

Table 8.8 – Scaling factors and identification of immobile elements for the Deguisier andesite to dacite unit.

Element	Scaling factor		Element	Scaling factor	
	Proximal against distal[1]	Au-mineralization[2]		Proximal against distal[1]	Au-mineralization[2]
SiO_2	0.45	0.45	**Cu**	0.1	0.1
Al_2O_3	1	1	**Ga**	1	1
Fe_2O_3t	0.85	0.85	**Hg**	0.6	0.7
CaO	5	5	**Mo**	6	5.5
MgO	6.5	6.5	**Nb**	0.8	0.8
Na_2O	4.5	4.5	**Ni**	1	1
K_2O	8	8	**Pb**	3	3
MnO	80	80	**Rb**	0.2	0.2
TiO_2	1	1	**Sb**	8.6	8.6
P_2O_5	1	1	**Sc**	0.6	0.6
LOI	3.5	3.5	**Sm**	2	2
CO_2	2.5	3	**Sn**	1	1
S	100	100	**Sr**	0.1	0.1
Ag	35	35	**Th**	10	10
As	0.4	0.4	**V**	0.15	0.15
Au	0.1	0.3	**Y**	0.7	0.7
Ba	0.05	0.05	**Yb**	5	5
Co	0.85	0.85	**Zn**	0.1	0.1
Cr	0.1	0.1	**Zr**	0.098	0.098
Immobile elements[1]	**P_2O_5, TiO_2, Nb, Al_2O_3**				
Immobile elements[2]	**P_2O_5, TiO_2, Nb, Al_2O_3**				

and Zr.

This enrichment pattern is quite similar to the one obtained for the basalt unit and reinforces that contacts of the Beattie syenite as well as D_2 faults are the chief mineralized features, having also recorded the mobilization of Au-related elements. Thus, the Au-mineralization is structurally controlled rather than being directly associated with plutonism. However, to exercise caution, the single enriched samples could indicate another mineralization control by which the andesite to dacitic rocks would have been a more suitable host. This hypothesis will be tested later, in subsection 8.2.1.

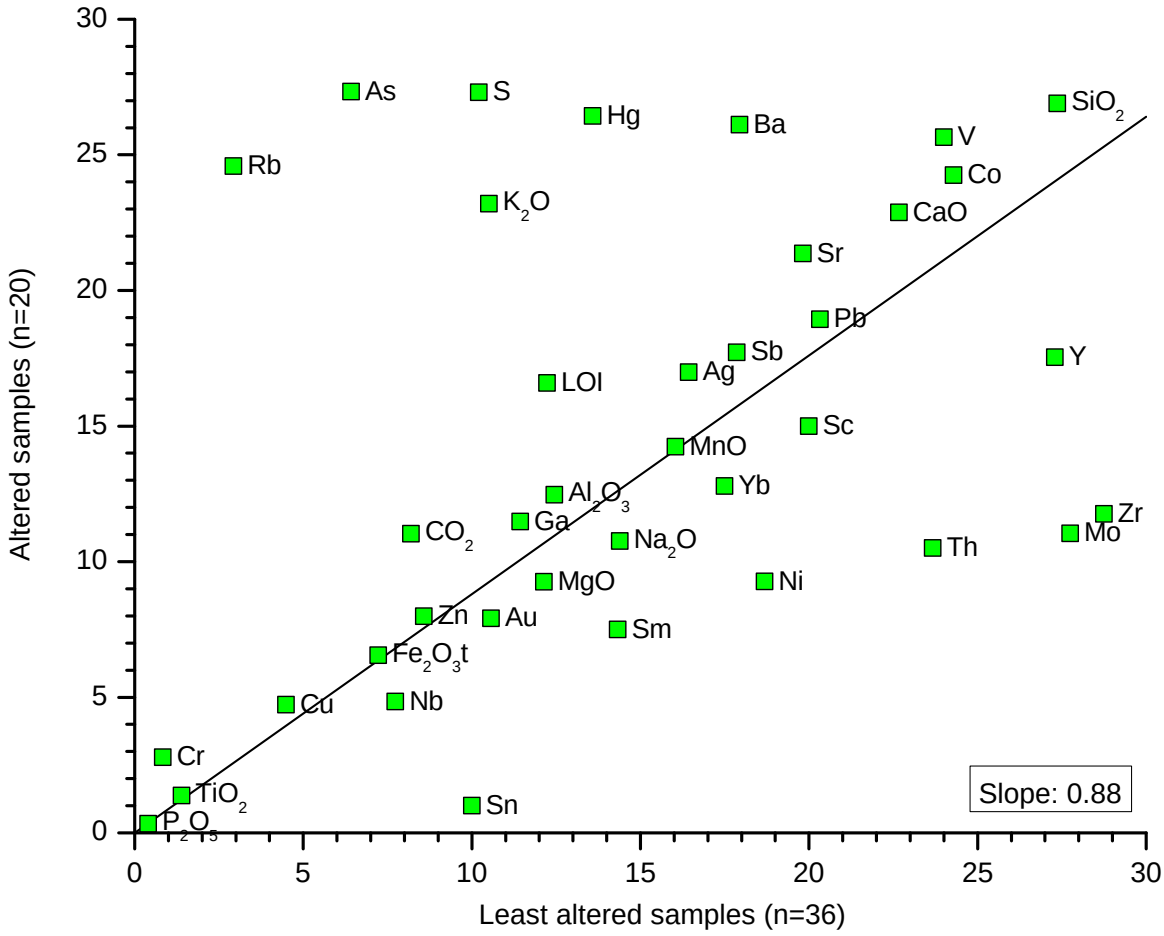


Figure 8.33 – Isocon diagram of the Deguisier andesite to dacite. Here distal samples are located $>$ 10 m from a contact with the Beattie syenite and/or a D_2 fault and proximal samples are located $<$ 10 m. Additionally, n = number of averaged samples.

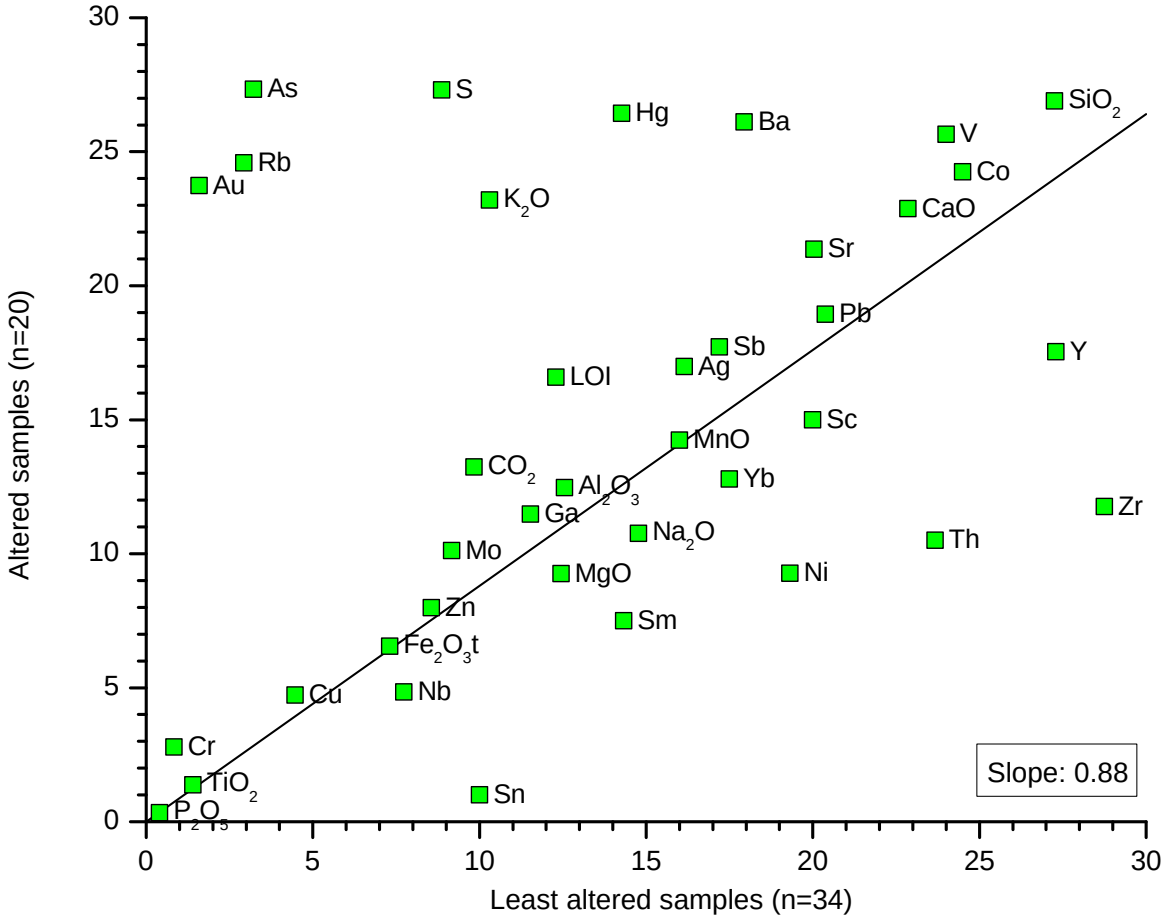


Figure 8.34 – Isocon diagram of the Deguisier andesite and dacite without samples D958238 and 91884. Here distal samples are located $>$ 10 m from a contact with the Beattie syenite and/or a D_2 fault and proximal samples are located $<$ 10 m. Additionally, n = number of averaged samples.

Deguisier rhyolite

In the case of the rhyolite there is a lack of altered samples, not enough to create an isocon diagram. Fortunately, a sample from a northern rhyolitic lens (sample: 90-34311, chemistry given in Chapter 7) permits its comparison to the rhyolite of the Beattie area. In this case, the northern rhyolite sample represents unaltered rhyolite as it is located away from the influence of the PDFZ and D_2 faults. The resulting isocon diagram should be interpreted lightly as a single sample is not a good statistical representation. The scaling factors are presented in Table 8.9 and the resulting plot is presented in Figure 8.35.

Table 8.9 – Scaling factors and identification of immobile elements for the Deguisier rhyolite.

Elements	Scaling factor	Elements	Scaling factor
SiO_2	0.3	**Ga**	1
Al_2O_3	1	**Nb**	1
Fe_2O_3t	3	**Nd**	0.5
CaO	10	**Ni**	2
MgO	10	**Pb**	1
Na_2O	3	**Rb**	0.1
K_2O	3	**Sc**	1
MnO	100	**Sm**	1
TiO_2	1.5	**Sr**	0.1
P_2O_5	1	**Th**	2
LOI	4	**V**	1
Ba	0.09	**Y**	0.6
Ce	0.2	**Zn**	0.4
Co	1	**Zr**	0.1
Cu	0.1		
Immobile elements	**P_2O_5, TiO_2, Nb, Y**		

Elemental differences present a significant enrichment in Co, Na_2O and Cu in the Beattie area rhyolites. Unfortunately, a comparison between the elemental enrichment or depletion of Au, Ag, As and S is not possible due to lack of data. Elements demonstrating a pronounced depletion are Pb, Ni and Zn. The specific reasons for the relative depletion of these elements could be due to slight compositional differences between rhyolites of different sequences in the Deguisier Formation. Comparing both rhyolites does not seem to yield a specific trend and variations are quite small. To illustrate, an enrichment-depletion diagram is presented in Figure 8.36.

The relative variability between the northern sample and those from the Beattie area is small. The largest enrichment is in SiO_2 which is 2.89 wt% greater in the Beattie area comparatively to the north. The greatest depletion is observed in Fe_2O_3t which is -2.14 wt%

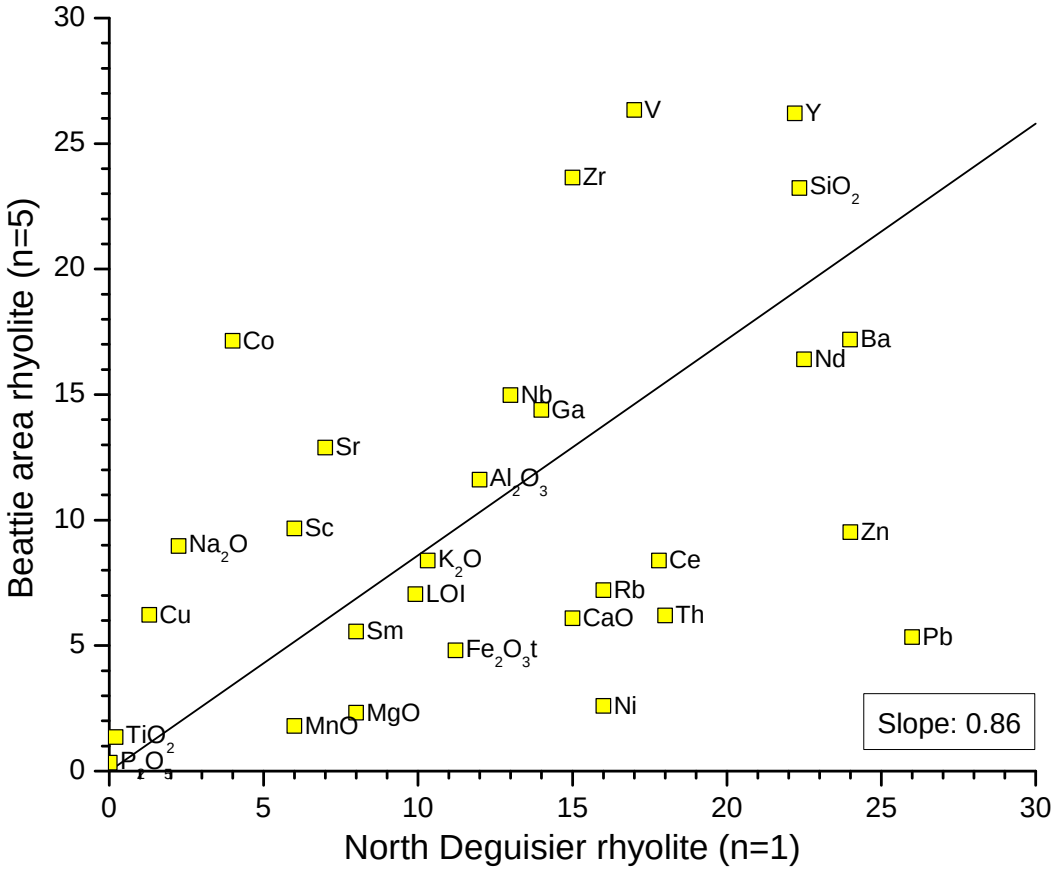


Figure 8.35 – Isocon diagram of the Deguisier rhyolite. Here rhyolite from the northern area (sample: 90-34311) is plotted against averaged rhyolite from the Beattie area. N = number of averaged samples.

lower. Such low variability in the samples is quite revealing. Specifically, that although the rhyolite was exposed to the same hydrothermal alteration which strongly affected the basalt and andesite to dacite units, the rhyolite seems to have resisted major chemical changes.

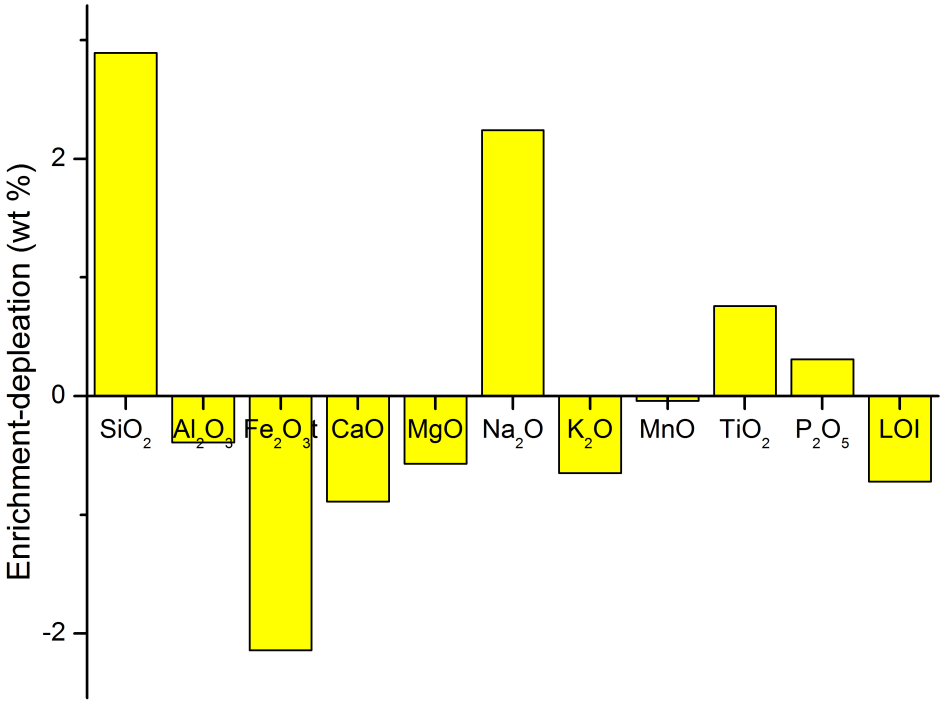


Figure 8.36 – Enrichment-depletion diagram of the Beattie area rhyolite. The averaged samples of the rhyolite (n = 5) have been normalized to a sample of northern rhyolite (sample: 90-34311).

Gabbro

Scaling factors employed for the gabbro are listed in Table 8.10. The resulting isocon diagram of average proximal (< 50 m) against distal (> 50 m) gabbro samples is presented in Figure 8.37.

Table 8.10 – Scaling factor and identification of immobile elements for the gabbro.

Element	Scaling factor		Element	Scaling factor	
	Proximal against distal[1]	Au-mineralization[2]		Proximal against distal[1]	Au-mineralization[2]
SiO_2	0.5	0.5	**Cu**	0.3	0.3
Al_2O_3	1	1	**Ga**	1	1
Fe_2O_3t	1	1	**Hg**	0.11	0.11
CaO	1	1.5	**Mo**	2	2
MgO	2	2	**Nb**	2	2
Na_2O	5	5	**Ni**	0.2	0.25
K_2O	6	2.9	**Pb**	1	1
MnO	20	20	**Rb**	0.15	0.2
TiO_2	1	1	**Sb**	1	1
P_2O_5	1	1	**Sc**	0.6	0.6
LOI	3	3	**Sm**	2	2
CO_2	5.5	4	**Sn**	1.5	1.5
S	22	5	**Sr**	0.01	0.01
Ag	20	20	**Th**	3	3
As	0.009	0.0037	**V**	0.085	0.08
Au	0.029	0.006	**Y**	0.1	0.1
Ba	0.06	0.025	**Zn**	0.1	0.075
Co	0.1	0.6	**Zr**	0.1	0.1
Cr	0.04				
Immobile elements[1]	**TiO_2, Nb, Al_2O_3, Y**				
Immobile elements[2]	**TiO_2, Nb, Al_2O_3, Y**				

Some discrepancies are noted with the 'immobile' elements that are used to define the isocon slope. This is chiefly caused by a limited number of samples combined with an altered sample which strays from the norm set by the other altered samples. Nonetheless, the elemental enrichments/depletions have not been affected.

The isocon plot of the gabbro demonstrates a pronounced enrichment in Au, As, S, CO_2, K_2O, Rb and Ba. Smaller increases are also denoted in Sb, Hg, Mo, Sm and Sr. The only element demonstrating a pronounced loss is Sn.

The pronounced enrichment in K_2O and Ba is likely the result of intense sericitization of the feldspars and CO_2 is the result of carbonatization. Both of these alteration minerals have been documented in thin sections by Goutier and Lacroix (1992).

Again the marked elemental enrichments are comparable to those obtained for the Deguisier

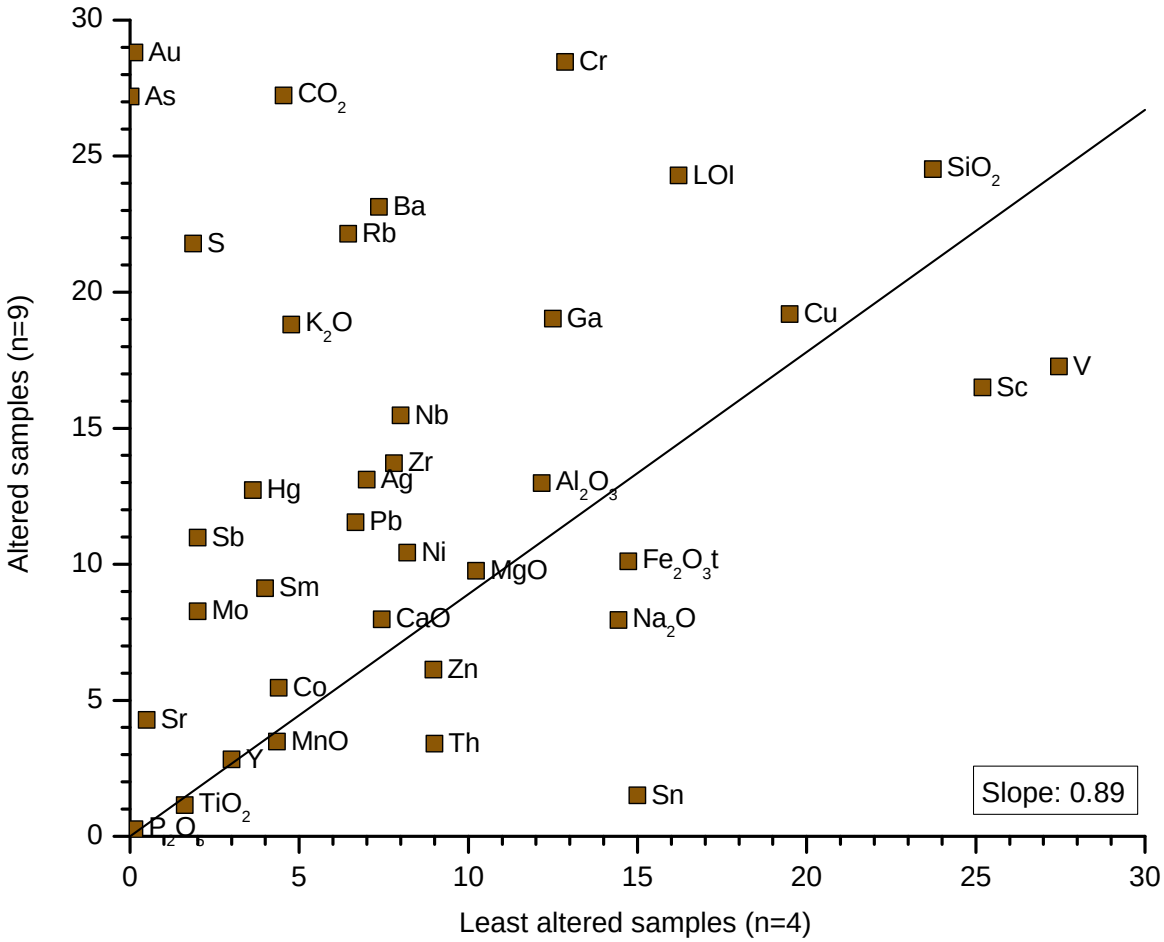


Figure 8.37 – Isocon diagram of the gabbro. Here distal (least-altered samples) are located at distances $>$ 50 m from the Beattie syenite and D_2 faults. Proximal samples (altered samples) are therefore located at distances $<$ 50 m.

basalt and andesite to dacite units. The increase in these enriched elements is much more pronounced than the basalt or andesite to dacite units, caused by the selection of 2 Au-mineralized samples next to the Donchester mine. In light of this, the 2 samples are plotted in another isocon diagram to focus specifically on the Au-mineralization signature. The scaling factors are presented in Table 8.10 and the resulting isocon diagram is presented in Figure 8.38.

The Au-mineralized isocon diagram demonstrates a significant enrichment of As, S, Au, K_2O, CO_2, Sb and Mo. This sheds light on the nature of the mineralizing fluids where Au was accompanied by S, As and to a lesser extent Mo and Sb. Hydrothermal fluids responsible for mineralization were sulphur-rich with elevated concentrations of Au, LILE and As. This same type of alteration and presumably Au-mineralization fluids were encountered at the Holloway

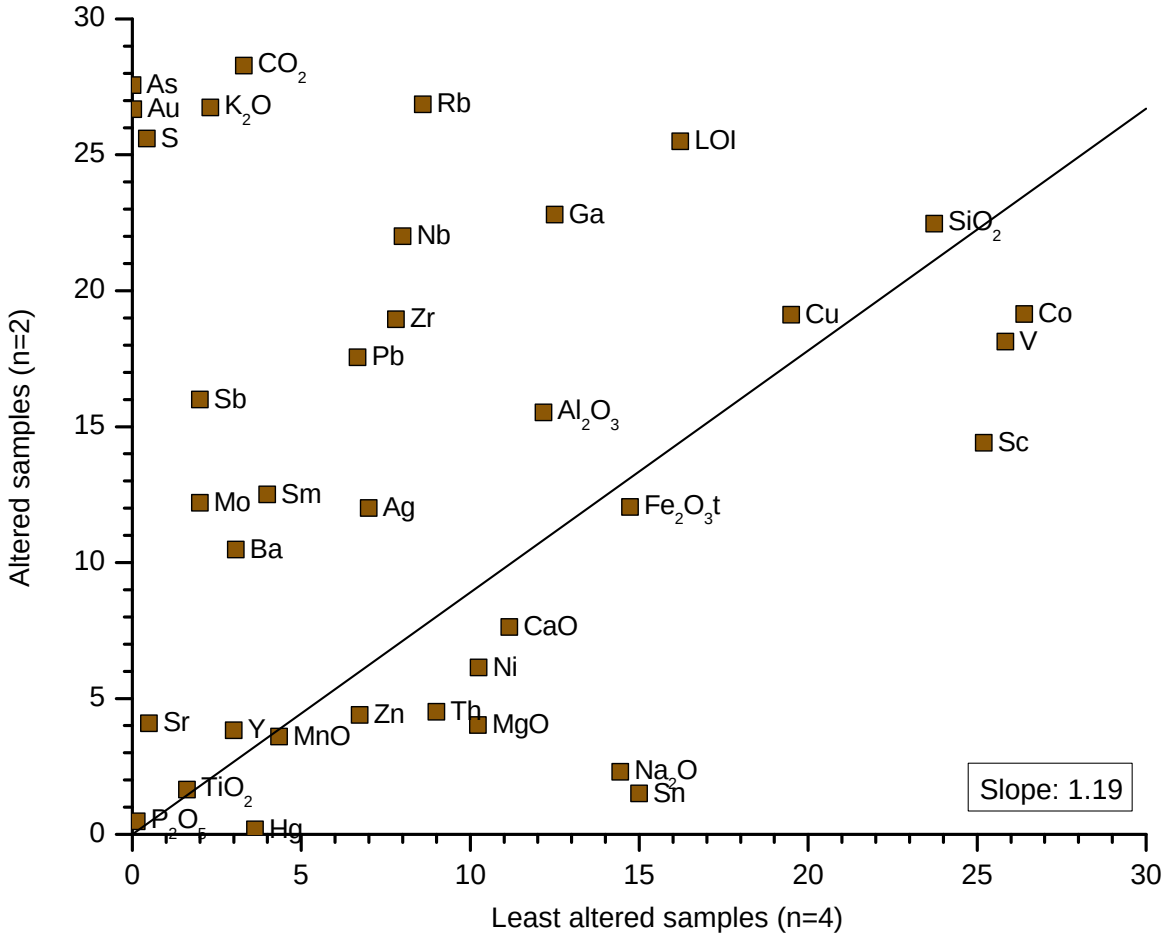


Figure 8.38 – Isocon diagram of the Au-mineralized gabbro. Here distal (least-altered samples) are located at distances > 50 m from the Beattie syenite and D_2 faults. Au-mineralized samples are both xenoliths within the Beattie syenite, in close proximity to the Donchester mine. Representative Au-mineralization samples are 2003031904 and 2003031931.

mine, where Ropchan et al. (2002) reported the exact same enrichment patterns.

Gold mineralization in the Deguisier Formation

Before proceeding on to the Au-related chemical characteristics of the Beattie syenite, it is important to review and combine the characteristics of the Deguisier Formation as a whole.

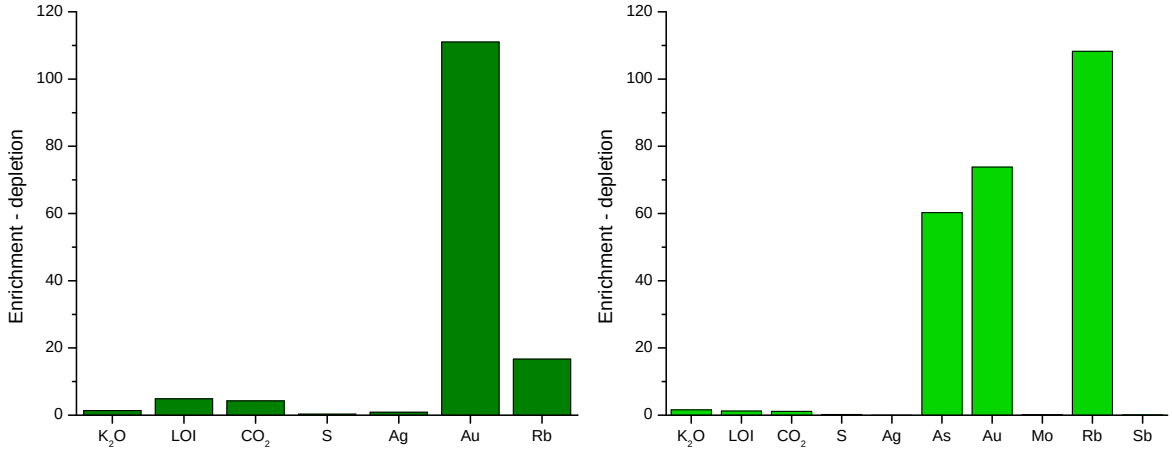
Disseminated style Au-mineralization within each of the units has already been established to be related to the proximity of a contact to the syenite and/or D_2 faults. Gold is therefore structurally controlled rather than being directly associated with plutonism.

Generalizations can be made in regard to the intensity of mineralization between the basalt and andesite to dacite units. This is perceived at the Donchester mine where gold was entirely hosted in the andesite to dacite unit. Gold at the Beattie mine on the other hand was generally contained in the Porcupine sediments with lesser amounts in the adjacent basalt (north) and syenite (south).

To compare the amount of mineralization between the basalt and the andesite to dacite unit an elemental variation diagram, focusing on the previously established elements associated with the Au-mineralization is used. As such, the Figure 8.39 illustrates the average enrichment within the respective unit. The method employed to provide the comparison is, for the Deguisier basalt, the average elemental variations of proximal samples normalized to distal samples. However, the two distal samples in the andesite to dacite unit which were significantly enriched compared to all others (samples: D958238 and 91884) were dismissed for the time being.

From Figure 8.39, gold in the Deguisier Formation demonstrates a strong relationship with As, Rb and to a lesser extent, K_2O LOI, CO_2, Ag and Mo. The composition of the Au-bearing fluids are comparable to both in style and associated elements to the Holloway mine (Ropchan, 2000). Specifically, Au-mineralization of the country rocks can be defined as Au $>$ Ag with associated trace elements (As, Mo, Sb), LILE (K, Rb, $\pm$Ba) and volatiles (CO_2 and S). The association of Ba with Au-mineralization could be dependent on the lithology as basalts demonstrate a depletion (see Figure 8.32) compared to andesites and dacites which demonstrate an enrichment. Another element that could also be associated with the Au-mineralization is W. The relationship could not be established since the element was not commonly analyzed.

Unfortunately, comparisons with the gabbro cannot be made as there are too few samples



(a) Elemental enrichment pattern for the basalt unit. **(b)** Elemental enrichment pattern for the andesite to dacite unit.

Figure 8.39 – Elemental enrichments associated with Au-mineralization. The ordinate axis reads depletion. K_2O is given in wt%, LOI, CO_2 and S are given in %, Ag, As, Rb are in ppm and Au is in ppb. Proximal samples (Au-mineralized) have been normalized to distal samples (sterile). Proximal samples are located < 50 m to the Beattie syenite and/or a D_2 fault, and distal samples are located at distances > 50 m.

to make any statistically valid interpretations. Additionally, both Au-mineralized sample were purposefully taken for the Au-mineralization and therefore do not represent the overall characteristics of the lithology.

The rhyolite did not contain any appreciable amounts of gold with the exception of one sample. This general lack was also reflected in outcrops and drill cores where few mineralized sections have been found. Of the mineralized sections, contacts with the Beattie syenite are a favourite where the mineralized sections appear as thin bands of disseminated pyrite extending for < 1 cm (on average). Therefore, it seems that the rhyolite was not as susceptible to fracturing as the other units which in turn severely limited the infiltration of Au-related hydrothermal fluids.

Averaged gold grades in proximity to syenitic contacts and/or D_2 faults for the basalt is 0.15 g/t and of 0.08 g/t Au for the andesite to dacite. However, considering all mineralized samples, regardless of location, excluding samples with < 5 ppb Au and including andesitic to dacitic samples D958238 and 91884; the basalt has an average of 0.11 g/t and the andesite to dacite unit has 0.26 g/t Au. This serves to indicate that even though the andesite to dacite unit is not particularly more Au-enriched at the contacts with the syenite and/or D_2 faults, it holds more Au-mineralization potential. This is reinforced by the highly Au-enriched

samples (D958238 and 91884) located at the centre of the andesite to dacite unit and by the mineralization style at the Donchester mine, where gold was mined in the andesite to dacite unit (see Figure 2.1).

A similar favorability for ore deposition was noted at the Holloway mine (Ropchan, 2000). Bohlke (1988) demonstrated that rocks with a higher Fe/Mg ratio were more effective in precipitating gold from hydrothermal fluids. Specifically, rock containing a ratio > 4 are considered suitable hosts for gold mineralization (Jones, 1992). Deguisier basaltic rocks have a Fe/Mg ratio of 1.46 and andesitic to dacitic rocks have a ratio of 2.93. The ratio for the andesite to dacite unit is not as high as compared to the Holloway mine, but it may have played a role. The rhyolite possesses a Fe/Mg ratio of 6.65, but lacks any significant Au-enrichments with the exception of one sample (D958086 at 21 900 ppb Au). The higher Fe/Mg ratio may have helped in the precipitation of gold in the rhyolite unit, but the lack of fractures necessary for the channelling of fluids would have prevented any significant amount of gold mineralization.

Another factor to consider is the proximity of both the rhyolite and andesite to dacite units to the PDFZ. The rhyolite is located closer to the PDFZ but is surrounded by the syenite. Such an arrangement could have shielded the rhyolite from large strains, therefore reducing the extent of fracturing. The andesite to dacite unit, on the other hand, lacks such a syenitic 'shield'. Consequently, the andesite to dacite unit could have been exposed to higher strain rates which in turn created the necessary channels permitting the infiltration of Au-hydrothermal fluids.

A last factor to consider when comparing the rhyolite to the andesite to dacite units is the proximity of major or secondary D_2 shear faults to the units. The rhyolite is not transected by any D_2 shear faults, whereas the andesite to dacite is. The presence of a D_2 fault would have resulted in the creation of additional fracturing and therefore permitting the infiltration of Au-related fluids.

It has already been established that the basaltic and andesitic to dacitic rocks are indistinguishable in both field and thin sections. In this case, the geochemistry, specifically the determination of the Fe/Mg ratio, in addition to the location of the unit with respect to contacts with the Beattie syenite, D_2 faults and the PDFZ would be a valuable asset to identify potential gold-bearing zones.

Beattie syenite

Section 8.2.1 demonstrated that Au-mineralization is structurally controlled by D_2 faults and lithological contacts in rocks belonging to the Deguisier Formation. As such, the same classification of samples (i.e., distal vs proximal) was employed to determine if gold in the Beattie syenite is also structurally controlled. Detailed mapping of several outcrops of the Beattie syenite permits a greater resolution when classifying proximal and distal samples. Consequently, proximal (generally altered) samples are located at < 5 m from a D_2 shear fault and/or contact in outcrops that have been mapped in detail and < 15 m in areas without outcrops. Distal (least-altered) samples are located at distances > 5 m in outcrops and > 15 m in areas without outcrops. For this subsection only, data from Banfield (1940) was also included.

After a first detailed inspection, the porphyritic Beattie syenite unit is the most Au-mineralized unit of the syenite. A brief comparison between units is presented in Table 8.11. The plethora of porphyritic Beattie unit samples also allow for a detailed comparison between proximal and distal samples. Scaling factors employed for the isocon diagram are listed in Table 8.12.

Table 8.11 – Average gold abundance in each of the Beattie syenite units. Gold abundance is given in ppb.

Unit	**Proximal samples**		**All samples**	
Porphyritic Beattie	647.63	n=103	340.59	n=170
Equigranular magnetite-bearing	0.5	n=1	0.5	n=1
Porphyritic Central Duparquet	233.52	n=13	123.90	n=25
Megaporphyritic	272.2	n=3	272.2	n=3
Lath syenite	5.97	n=3	5.97	n=3
	n = number of samples			

The isocon diagram of the porphyritic Beattie syenite indicates that Au is strongly associated with As, S, Ag, W, Sb and Mo. The Ag/Au ratio for average proximal samples is of 2.08, although a Au-mineralized sample taken from the Beattie mine open pit (sample: 1990034237) possesses a ratio of 0.36. The enrichment pattern is similar to the one obtained for the Deguisier Formation and the Holloway mine (Ropchan et al., 2002). Elemental Au-mineralization differences between the Deguisier and Beattie syenite are denoted in lesser amounts of Rb, CO_2 and K_2O. Both CO_2 and K_2O demonstrate a slight enrichment, but

Table 8.12 – Scaling factors and identification of immobile elements for the porphyritic Beattie and Central Duparquet syenite units.

Element	Scaling factor		Element	Scaling factor	
	Beattie	Central		Beattie	Central
SiO_2	0.45	0.45	**Hf**	1	1
Al_2O_3	1	1	**Hg**	1	0.7
Fe_2O_3t	4	4	**Mo**	0.2	1
CaO	4.5	5	**Nb**	1	1
MgO	5	5	**Nd**	0.1	0.15
Na_2O	5	5.5	**Ni**	3	3
K_2O	4	3.8	**Pb**	0.8	0.8
MnO	100	100	**Rb**	0.25	0.2
TiO_2	2	2	**Sb**	3	4
P_2O_5	1	1	**Sc**	1.1	1.2
LOI	5	5	**Sm**	1	1
CO_2	5	4.5	**Sn**	5	5
S	30	80	**Sr**	0.02	0.02
Ag	20	20	**Th**	1	1
As	0.09	0.2	**U**	2	2
Au	0.04	0.12	**V**	0.1	0.1
Ba	0.01	0.01	**W**	1.5	1.6
Bi	10	10	**Y**	0.8	0.8
Cr	0.08	0.25	**Yb**	3.5	3.5
Cu	0.1	0.1	**Zn**	0.1	0.1
Ga	1	1	**Zr**	0.06	0.06
Immobile elements	P_2O_5, TiO_2, Nb, Zr				

Rb is depleted in the porphyritic Beattie syenite unit. The exact reason is not known but could be the result of selective precipitation, or related to the distance from the centre of the hydrothermal source.

The isocon diagram presented in Figure 8.40 also demonstrates elemental depletions for Na_2O and to a lesser degree Sr and Ba. The depletion in Na_2O reveals that albite, often observed at the centre of mineralized veins (e.g., Figure 8.20a), is not directly associated with Au-mineralization. The elemental depletion observed in Ba, combined with variations observed in the Deguisier Formation, reinforces that it is also not directly associated with Au-mineralization.

A qualitative comparison between distal porphyritic Beattie unit samples and that of the Beattie ore, as measured by Banfield (1940) provides an additional perspective of elemental variations observed in Au-mineralization. However, since there are so few elements provided, a simple variation diagram is presented in Figure 8.41 instead of an isocon diagram.

Figure 8.41 illustrates similar elemental enrichment or depletions as the isocon diagram presented in Figure 8.40. Once again the loss of Na_2O reinforces that albite is not associated

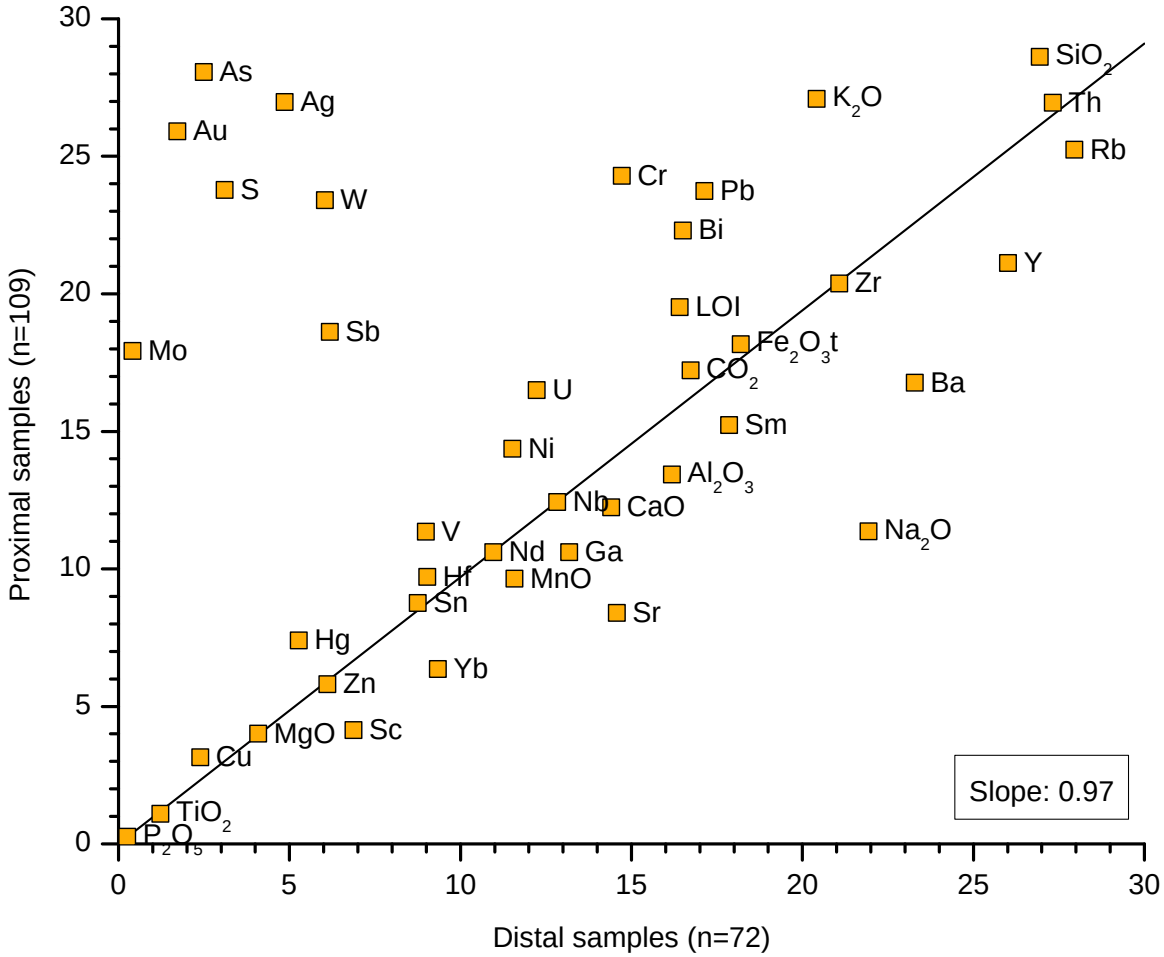


Figure 8.40 – Isocon diagram of the porphyritic Beattie syenite unit. Distal (least-altered) samples are located at distances > 5 m or > 15 m from D_2 shear faults and contacts (see text for explanation). Proximal (altered) samples are therefore located at distances < 5 m or < 15 m respectively.

with Au-mineralization. Slight increases in K_2O and S are typical and are consistent with Au-mineralization characteristics in the Deguisier Formation.

No isocon diagram was possible for the equigranular magnetite-bearing unit since it holds the least amount of hydrothermal alteration of all the Beattie syenite units.

Scaling factors for the porphyritic Central Duparquet unit are listed in Table 8.12 and the resulting isocon diagram of average proximal against distal samples is presented in Figure 8.42.

The isocon diagram of the porphyritic Central Duparquet unit reveals that Au is strongly associated with Mo, S, As and Hg. This marks the fist time that an enrichment was observed in Hg. Furthermore, Sb and W are not as strongly enriched in the porphyritic Central Duparquet

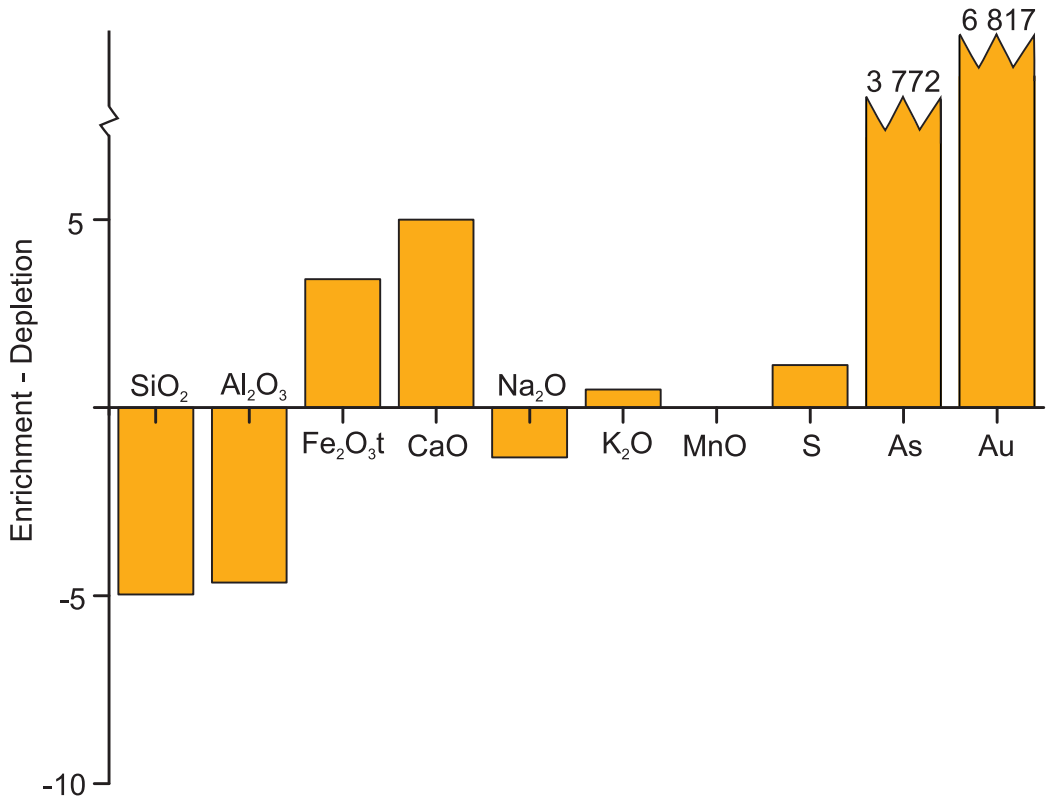


Figure 8.41 – Elemental variations between distal and ore samples from the porphyritic Beattie unit. SiO_2, Al_2O_3, Fe_2O_3t, CaO, Na_2O, K_2O and MnO are in weight %, S is in %, As in is ppm and Au is in ppb. The ore sample, provided from Banfield (1940) has been normalized to distal porphyritic Beattie syenite samples. Distal (least-altered) samples are located at distances $>$ 5 m or $>$ 15 m from D_2 shear faults and contacts (see text for explanation).

unit as they are in the porphyritic Beattie unit. The cause for these discrepancies could have been caused by slightly different sulphidation states in the area caused by an increase in distance from the hydrothermal source. This hypothesis is supplemented by different Ag/Au ratios, where averaged proximal (Au-mineralized) samples of the porphyritic Beattie unit have a ratio of 2.08 and those for the porphyritic Central Duparquet unit have a ratio of 1.28. Elements showing a pronounced depletion in the porphyritic Central Duparquet unit isocon diagram are Sn and Ga.

Before exploring the elemental variations of the last two syenitic units, an important comparison between the distal porphyritic Beattie syenite unit analyses against those of the equigranular magnetite-bearing unit is required since the megaporphyritic and lath syenite units lack distal samples. The equigranular magnetite-bearing unit was chosen to represent distal samples because the unit holds the least amount of hydrothermal alteration and defor-

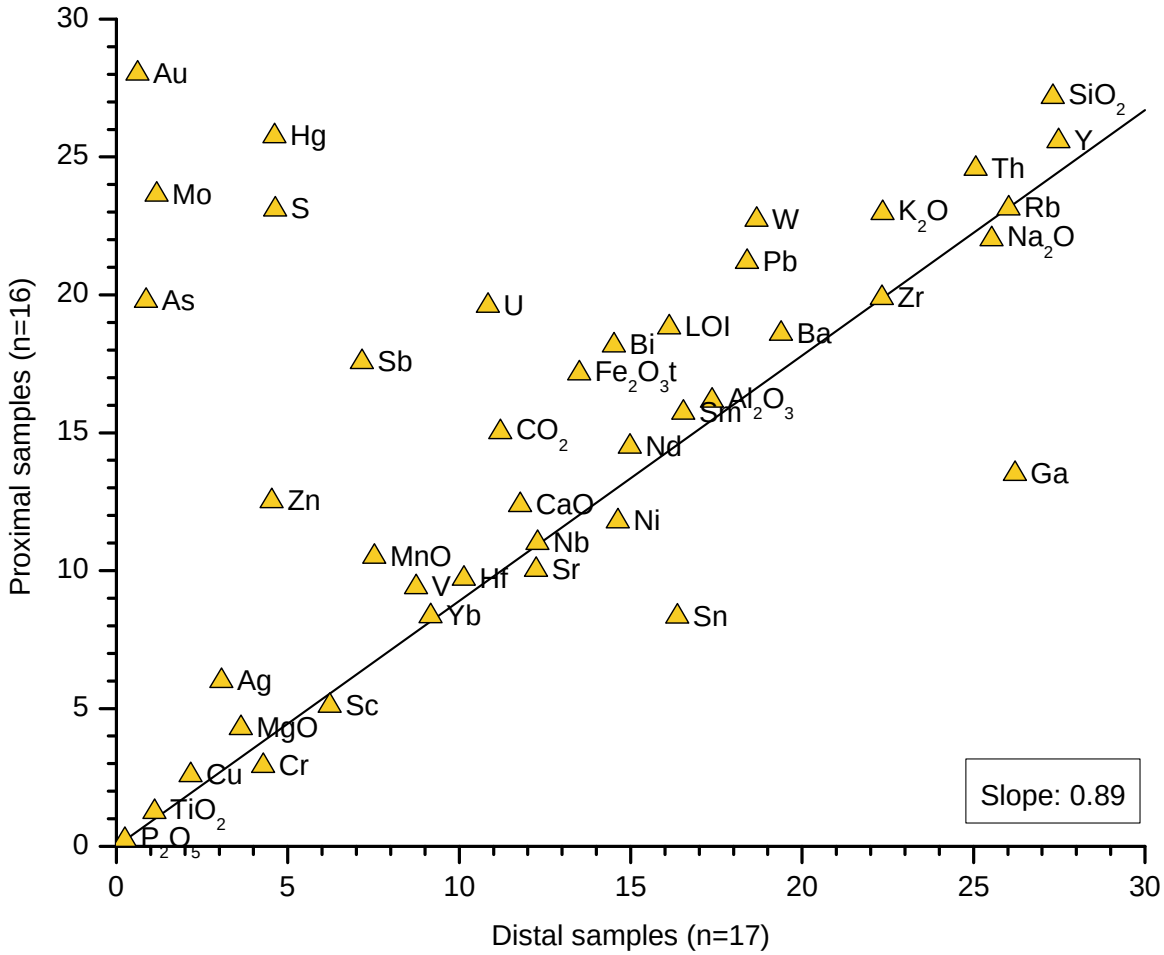


Figure 8.42 – Isocon diagram of the porphyritic Central Duparquet unit. Distal (least-altered) samples are located at distances $>$ 5 m or $>$ 15 m from D_2 shear faults and contacts (see text for explanation). Proximal (altered) samples are therefore located at distances $<$ 5 m or $<$ 15 m respectively.

mation. The scaling factors are given in Table 8.13 and the isocon diagram is presented in Figure 8.43.

Elemental variations indicate that Ni, Pb, Ga, Sn and Sr will have a tendency to be depleted and may distort the true trend of the unit. Additionally, Hg, Au, Ag, Bi, S, CO_2, As and LOI may also have a tendency to be enriched caused by a complete lack of Au-mineralization in the equigranular magnetite-bearing unit. This lack will only result in the enhancement of the Au-related signature in the proximal samples and therefore should not overly distort the general pattern. With these variations in mind, Figure 8.44 demonstrates the elemental variation of average proximal megaporphyritic samples and Figure 8.45 demonstrate the variation of the average lath syenite samples, both against the equigranular magnetite-bearing samples.

Table 8.13 – Scaling factors and identification of immobile elements for the porphyritic Beattie, megaporphyritic and lath syenite units against the equigranular magnetite-bearing unit.

Element	Scaling factor			Element	Scaling factor		
	Beattie	Megaporphyritic	Lath		Beattie	Megaporphyritic	Lath
SiO_2	0.45	0.45	0.45	**Hg**	2	0.2	50
Al_2O_3	1	1	1	**Mo**	5	0.5	10
Fe_2O_3t	3	4	4	**Nb**	1	1	1
CaO	6	4.5	4.5	**Nd**	0.1	0.1	0.15
MgO	5	5	5	**Ni**	3	0.6	3
Na_2O	5	5	4.5	**Pb**	0.5	0.6	0.6
K_2O	4	4	4	**Rb**	0.2	0.2	0.2
MnO	100	100	100	**Sb**	5.5	0.3	11
TiO_2	2	2	2	**Sc**	1.2	2	2
P_2O_5	1	1	1	**Sm**	0.95	1	1
LOI	5	8	5	**Sn**	5	5	5
CO_2	3	12	4	**Sr**	0.009	0.009	0.009
S	80	30	100	**Th**	1	1	0.9
Ag	20	30	20	**U**	2	2	2
As	0.5	0.015	1	**V**	0.2	0.1	0.07
Au	0.4	0.09	4.5	**W**	1	0.4	1.5
Ba	0.008	0.008	0.008	**Y**	0.8	0.78	0.6
Bi	4	22	20	**Yb**	2	2	2
Cu	0.1	1	0.1	**Zn**	0.1	0.1	0.1
Ga	1	1	1	**Zr**	0.06	0.06	0.06
Hf	1	1	1				
Immobile elements	P_2O_5, TiO_2, Nb, Zr						

Scaling factors for both diagrams are presented in Table 8.13.

The isocon diagram of the megaporphyritic unit reveals that Au is strongly associated with Sb, Mo, W, Hg, S and As (see Figure 8.44). This enrichment pattern is almost exact as the porphyritic Beattie syenite unit with the exception of Hg. A similar enrichment in Hg has been noted in the porphyritic Central Duparquet unit and has been hypothesized to be the result of slight differences in sulphidation states in the area caused by an increase in distance from the hydrothermal source. To this end, the megaporphyritic unit is only found in the eastern portions of the syenite and has a Ag/Au ratio (averaged proximal samples) of 0.73, which is the lowest ratio yet. As such, the progressive decrease in the Ag/Au ratio from west to east seems to be the result of increasing distance from the centre of the hydrothermal source. Elements demonstrating a pronounced depletion are Sr, Sn and Ba, all of which could be influenced by the equigranular magnetite-bearing unit.

Figure 8.45 demonstrates a pronounced enrichment in Au, Hg, CO_2, LOI and to some extent, Cu. It should be noted that the lath syenite unit is the least Au-mineralized of all the units (see Table 8.11) and also has the least amount of available samples. Consequently, the

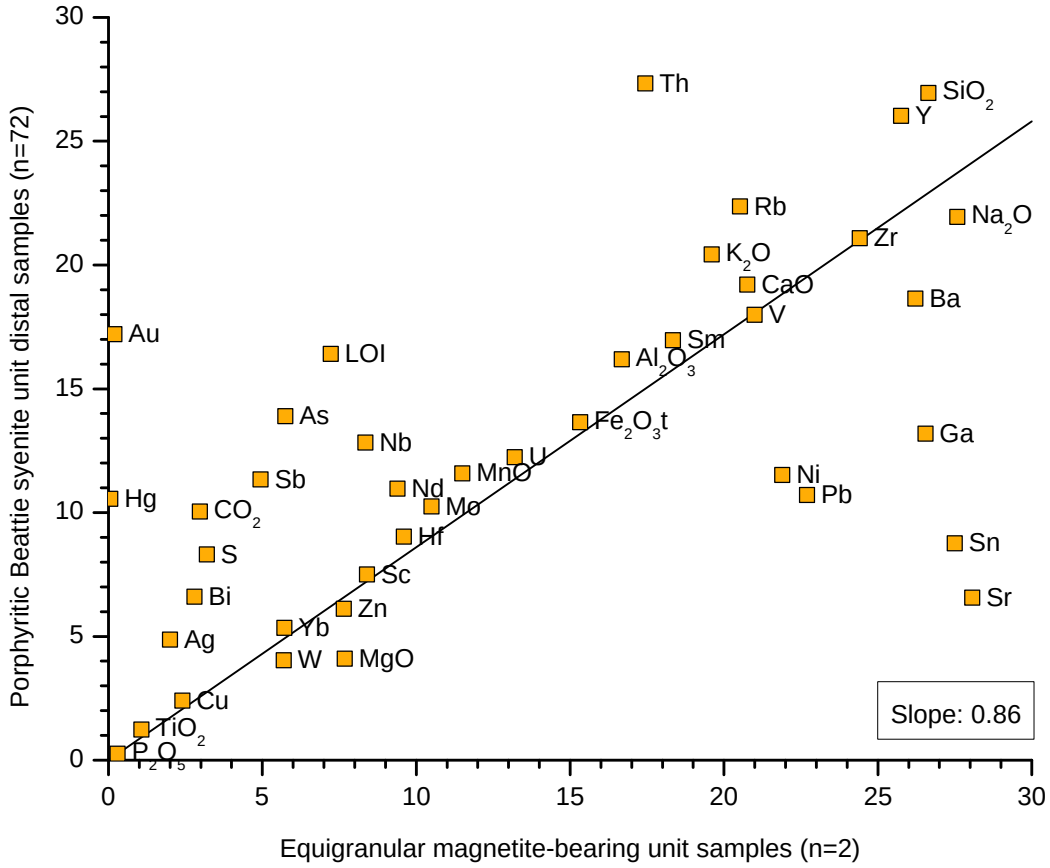


Figure 8.43 – Isocon diagram between distal porphyritic Beattie syenite and the equigranular magnetite-bearing units. Distal (least-altered) samples are located at distances > 5 m or > 15 m from D_2 shear faults and contacts (see text for explanation).

mineralization signature presented in by unit could be inaccurate. Elements demonstrating a depletion are Sr, Sn, Mo and Pb, all of which could be influenced by the chemical properties of the equigranular magnetite-bearing unit.

Another important feature to note is the progressive diminution of gold abundance when progressing eastwards. This feature is best illustrated in the porphyritic Beattie unit which spans the greatest length and covers the most area of all units. Gold concentration averages are summarized in Table 8.14.

Table 8.14 highlights an important distribution pattern in gold. Specifically, that gold abundances in proximal (Au-mineralized) samples decrease nearly 9 times (averaged) from the Donchester mine eastwards. An explanation for this phenomenon lies in the abundance of secondary D_2 shear faults, including the PDFZ, conjugate shear and extension fractures which dominate the western parts of the Beattie syenite. The D_2 deformation is responsible

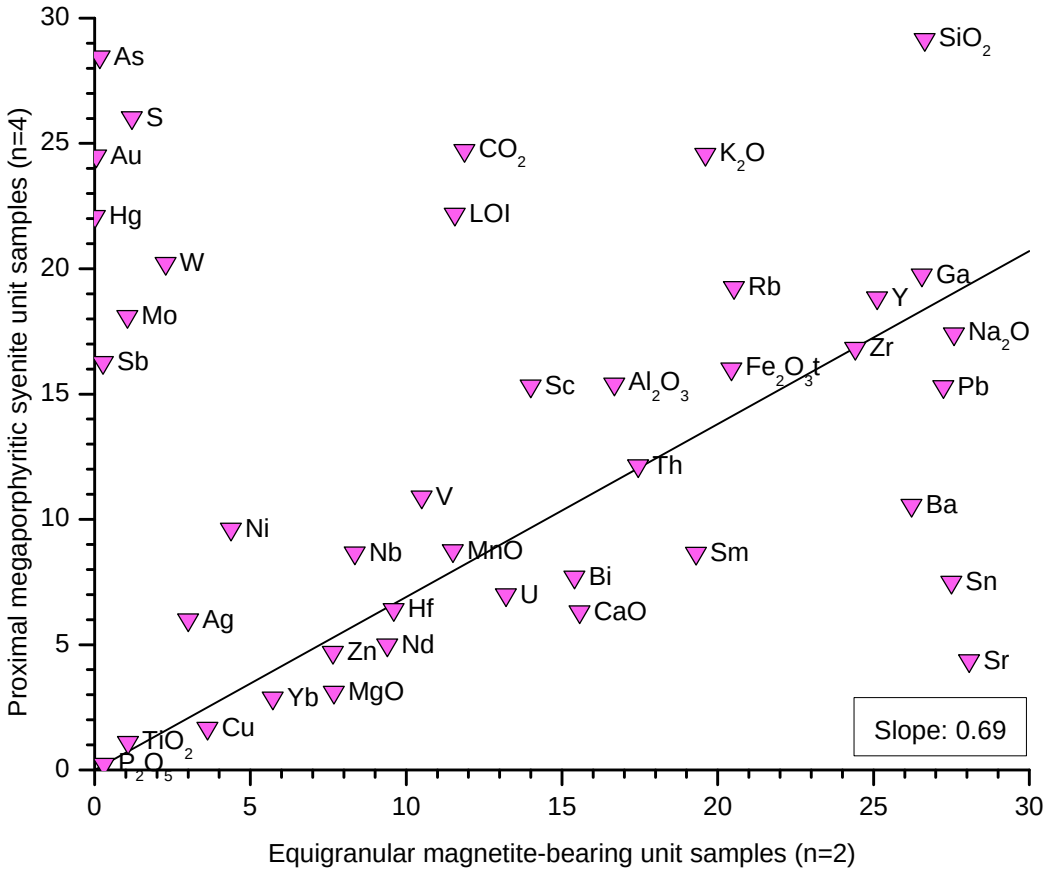


Figure 8.44 – Isocon diagram of the megaporphyritic unit against the equigranular magnetite-bearing unit. Proximal (altered) samples are located at distances < 5 m or < 15 m from D_2 shear faults and contacts (see text for explanation).

Table 8.14 – Average gold concentration in the porphyritic Beattie unit. Gold abundance is given in ppb. The division line used to differentiate between west and east samples is the abandoned mine shaft of the Donchester mine.

Samples	**West**		**East**	
Proximal	809.53	n=89	80.99	n=20
Distal	50.68	n=45	28.00	n=27
All	454.85	n=134	48.61	n=47
	n = number of samples			

for the creation of the PDFZ and numerous E-W striking shear faults (see Section 5.3). Complex interactions between the shear faults and the PDFZ, combined with several displacement episodes, resulted in the creation of the multitude of fractures observed in the western portions of the syenite (see Section 8.1.2) which turn permitted the channelling and subsequent precipitation of hydrothermal Au-enriched fluids. Progressing eastwards however, the abundance of shear zones and fractures decrease, caused by an increase in distance between the D_2 shear

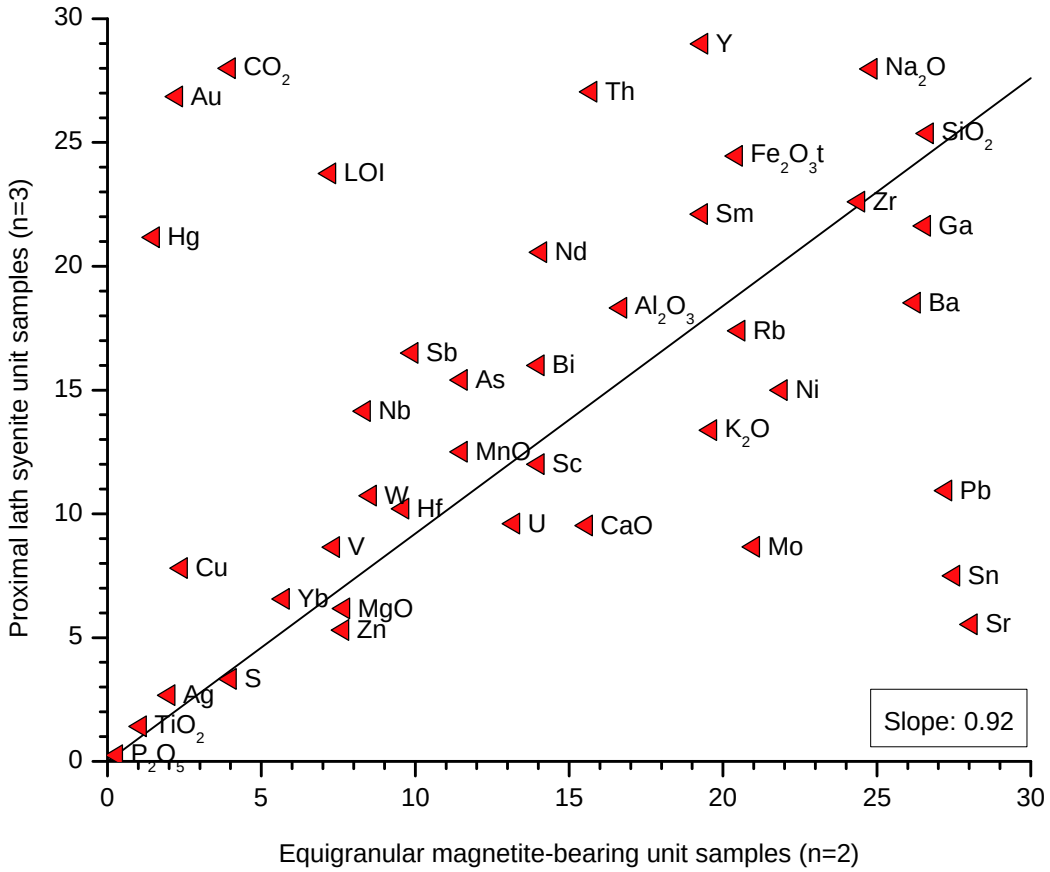


Figure 8.45 – Isocon diagram of the lath syenite unit against the equigranular magnetite-bearing unit. Proximal (altered) samples are located at distances < 5 m or < 15 m from D_2 shear faults and contacts (see text for explanation).

faults and the PDFZ, therefore resulting in a reduction of gold abundance.

To summarize, gold in the Beattie syenite is strongly associated with As, S, Ag, W, Sb and Mo. All the syenite units and country rocks demonstrate a similar signature which indicates that Au-hydrothermal fluids were pervasive throughout the Beattie area. Small elemental variations combined with a progressive decrease in the Ag/Au ratio from west to east seem to be the result of small differences in sulphidation caused by an increase in distance from the centre of the hydrothermal source. The abundance of gold is also structurally controlled rather than being directly associated with the intrusion of the syenitic pluton. This characteristic was demonstrated for both the Beattie syenite and the Deguisier Formation where gold was channelled and preferentially precipitated in the multiple fractures and shear zones. Therefore, the identification of D_2 faults and related features are of utmost importance to identify potential gold-bearing zones in the Beattie syenite.

8.2.2 Regional metamorphism to the greenschist facies

The NORMAT technique was employed to define and characterize the changes produced by regional metamorphism to the greenschist facies. This technique developed by Piché and Jébrak (2004) is used to calculate and characterize the corresponding metamorphic mineralogical assemblage. The technique employs major element data to produce a set of greenschist facies normative minerals without the need for petrographic observations. Certain restrictions apply to pelitic shales and rocks containing spinel, graphite and abundant sulphides. Fortunately, basalt protolith rocks of the area only contain trace amounts of minerals from the spinel group (i.e., magnetite at < 5.36 wt%). Rocks containing graphite and sulphides violate the technique's assumption that the sample's LOI is composed exclusively of H_2O and CO_2. This error can be avoided if C and S have been measured, otherwise the estimate of the carbonatization intensity as well as the calculated normative carbonate minerals can be erroneous, as extra assumptions and calculation steps are necessary. The following metamorphic calculation descriptions and alteration indices are summarized from Piché and Jébrak (2004).

The NORMAT technique begins by recalculating oxides values as completely anhydrous, which are then converted to cation mol%. Afterwards, metamorphic CO_2 and LOI (wt%) values are obtained by recalculating the original oxide total to 100% and subsequently applying the same multiplication factor to the original CO_2 and LOI values. Next, iron-free sulphides are calculated followed by aresenopyrite. Iron is then allowed to react with chalcocite, sphalerite and millerite yielding bornite and chalcopyrite, Fe-bearing sphalerite and pentlandite. At this stage pyrite is also calculated. Any Fe excess is then reacted with pyrite to form pyrrhotite. Next, carbonate minerals are calculated according to the metamorphic CO_2 value. Initial calcite is then allowed to react with siderite and magnesite, yielding ankerite and dolomite. Any excess CO_2 is calculated as rhodochrosite. Subsequently, silica-undersaturated minerals, such as forsterite, fayalite, anatase, titanite and stilpnomelane are calculated. As for leucite and nepheline, they are directly calculated as their greenschist facies equivalents; potassic to sodic cancrinite. Cancrinite is then allowed to react with silica to form feldspars. However, a side step is necessary to establish the relative proportion in which Ca is divided between

anorthite and clinopyroxene. The partition ratio (CaRatio) is given in the following equation:

$$CaRatio = \frac{VA/5}{(\frac{VA}{5} + \frac{VCpx}{4})/4} \tag{8.5}$$

VA or virtual anorthite and VCpx or virtual clinopyroxene are calculated based on original Ca and Si contents. Piché and Jébrak (2004) notes that the coefficients were empirically determined based on trial end error testing of a database containing $\sim$ 400 000 whole rock analyses. As such, this procedure eliminates the artificial migration of Ca from clinopyroxene to anorthite in weakly altered rocks, thereby calculating the excess aluminium. This excess Al is the allowed to react with albite, orthoclase and olivine, yielding hydrothermal paragonite, sericite and chlorite. Any remaining Al is then calculated as hydrothermal pyrophyllite. These hydrothermal minerals are then used to calculate the alteration indices (discussed below). The NORMAT calculation then establishes a metamorphic mineral assemblage to each sample. As such, the program automatically selects and performs the following mineral calculation sequences (Piché and Jébrak, 2004):

Assemblage 1:	Epidote $\rightarrow$ chlorite $\rightarrow$ paragonite, sericite $\rightarrow$ pyrophyllite
Assemblage 2:	Actinolite $\rightarrow$ epidote $\rightarrow$ calcite
Assemblage 3:	Epidote $\rightarrow$ actinolite $\rightarrow$ chlorite
Assemblage 4:	Chlorite $\rightarrow$ actinolite $\rightarrow$ talc

These reactions allow any remaining Ca, Fe, Mg and Al to be partitioned into metamorphic minerals. Additionally, any remaining olivine is then decomposed into cations. Consequently, unused Si and Mg result in the formation of serpentine, talc and brucite, Al and Si in pyrophyllite, Na or K and Al in alunite, Na, K and Al in halite, sylvite and diaspore. Any excess Ca is then used in calcite. Iron is reacted with pyrite to form pyrrhotite and any remaining Fe yields magnetite. Finally, excess Si is used in quartz.

The NORMAT technique also calculates alteration indices. A total of 6 indices are employed to characterize the different alteration styles. They are respectively: 1) fresh index (IFRAIS), 2) paragonite index (IPARA), 3) sericite index (ISER), 4) chlorite index (ICHLO), 5) pyrophyllite index (IPYRO), and 6) carbonate alteration index (IPAF). The first index,

IFRAIS, is computed using the following equation:

$$IFRAIS = 100 \times \frac{(Ab + Or + An + Cpx)}{(HChl + HSer + HPar + HPyr) + (Ab + Or + An + Cpx)} \tag{8.6}$$

where, HChl represents hydrothermal chlorite; HSer represents hydrothermal sericite; HPar represents hydrothermal paragonite, and HPyr represents hydrothermal pyrophyllite. With this equation an estimate of the extent of hydrothermal alteration can be obtained, whereby an IFRAIS value of 100% is presumably representative of a unaltered rock and an IFRAIS value of 0% is representative of a completely altered rock.

The remaining 4 indices serve to isolate normative hydrothermal paragonite (IPARA), sericite (ISER), chlorite (ICHLO) and pyrophyllite (IPYRO). They are calculated using the inversed IFRAIS Equation (8.6) such that:

$$IPARA = 100 \times \frac{HPar}{(HChl + HSer + HPar + HPyr) + (Ab + Or + An + Cpx)} \tag{8.7}$$

The other indices can also be calculated in the same manner.

The last index, IPAF measures the intensity of carbonate alteration. For samples analyzed for CO_2 this is simply done by combining CO_2 with CaO, MgO, FeO and MnO. These oxides are present as silicate minerals in a non-carbonatized rock (F variable), and combine with CO_2 to form calcite, dolomite, ankerite, magnesite, siderite and rhodochrosite in a carbonate rock (A variable). The resulting relationship is expressed by the following equation:

$$IPAF = 100 \times \frac{A}{(A + F)} \tag{8.8}$$

For analyses without measured CO_2, a different method is needed, whereby a ratio between the measured LOI and 2 normative LOI values are employed. The full method is explained in detail by Piché and Jébrak (2004).

Deguisier basalt

The normative mineralogy of the least-altered Deguisier basalt samples, as established in Chapter 7, as well as the indices have been calculated and are presented in Table 8.15.

Table 8.15 – NORMAT normative mineralogy of the least-altered basaltic samples. Normative mineralogy is presented in weight %.

Sample	D958053	D958056	D958103	D958057	2003031998	D958236	3258
Actinolite	—	9.65	9.91	4.51	10.18	1.35	—
Albite	26.15	22.89	16.23	10.62	32.46	14.83	14.76
Ankerite	—	—	—	—	—	—	—
Apatite	0.35	0.22	0.18	0.25	0.29	0.16	0.25
Calcite	4.50	0.27	0.38	—	0.05	0.56	2.10
Fe chlorite	18.85	10.38	11.92	18.55	11.01	14.60	16.87
Mg chlorite	11.96	13.41	11.86	17.56	10.50	13.65	14.41
Chromite	0.04	0.05	0.01	0.01	0.02	0.05	0.10
Dolomite	—	—	—	—	—	—	—
Epidote	12.50	21.44	23.15	25.38	16.16	30.39	24.41
Magnetite	1.52	0.82	1.04	0.88	1.38	0.00	1.64
Orthoclase	0.33	1.32	0.96	0.71	0.25	0.45	0.32
Paragonite	0.53	—	—	—	—	—	0.20
Pyrophyllite	—	0.23	0.24	0.34	0.20	0.13	—
Quartz	19.08	3.81	10.78	13.19	3.90	19.16	20.48
Sericite	0.01	—	—	—	—	—	—
Titanite	4.05	2.95	3.37	3.71	3.86	3.25	3.28
Talc	—	—	—	—	—	—	1.16
Tremolite	—	12.48	9.86	4.27	9.70	1.26	—
Pyrite	0.11	0.01	0.06	—	0.02	0.13	—
Pyrrhotite	—	0.01	0.01	—	0.01	—	—
Chalcopyrite	0.02	0.02	0.02	0.02	—	0.02	—
Sphalerite	0.01	0.01	0.01	0.01	—	0.01	—
Petlandite	0.01	0.01	0.01	—	0.02	0.02	—
Arsenopyrite	—	0.01	0.01	—	—	—	—
Total	100.00	100.00	100.00	100.00	100.00	100.00	100.00
IFRAIS	100.00	100.00	100.00	78.92	100.00	87.26	91.23
IPARA	—	—	—	19.75	—	12.37	8.59
ISER	—	—	—	1.32	—	0.38	0.19
ICHLO	—	—	—	—	—	—	—
IPYRO	—	—	—	—	—	—	—
IPAF	30.06	1.74	2.59	-1.37	-3.86	4.39	9.14

The resulting characteristic normative greenschist facies mineralogy is dominated by chlorite$_{tot}$ (21.50 - 40.47 wt%), albite (5.39 - 34.01 wt%), epidote (4.47 - 30.39 wt%) and quartz (3.81 - 31.35 wt%). The obtained normative mineralogy corresponds very closely to thin section observations done by Goutier and Lacroix (1992). Normative accessory minerals are actinolite (1.35 - 11.98 wt%), calcite (0.05 - 7.84 wt%), orthoclase (0.33 - 7.16 wt%) and titanite (2.89 - 6.59 wt%). Both actinolite and calcite are present in thin sections described by Goutier and Lacroix (1992), orthoclase however is not. It is possible that orthoclase is not visible as it is intermixed with plagioclase in the fine-grained feldspathic matrix. Another discrepancy is

Table 8.15 Continued

Sample	3261	3951	3691	3694	3287	D958309	D958310	3679
Actinolite	5.99	—	—	6.34	—	11.98	11.24	—
Albite	21.90	21.20	28.26	15.91	22.28	24.57	12.05	18.40
Ankerite	—	0.42	0.10	—	1.52	—	—	—
Apatite	0.25	0.33	0.30	0.34	0.33	0.41	0.39	0.32
Calcite	2.15	6.27	7.84	0.70	5.25	0.22	0.04	4.35
Fe chlorite	12.59	18.11	16.94	16.36	14.65	12.16	12.97	18.58
Mg chlorite	13.04	22.36	18.63	15.36	12.68	9.80	11.03	19.15
Chromite	0.13	0.09	0.09	0.09	0.08	0.01	0.01	—
Dolomite	—	0.52	0.11	—	1.31	—	—	—
Epidote	20.87	—	—	19.02	—	17.79	24.55	14.66
Magnetite	0.73	1.09	1.05	1.25	1.26	1.71	1.33	1.13
Orthoclase	1.07	0.73	1.34	0.52	8.95	0.51	0.19	0.26
Paragonite	—	0.41	1.29	—	5.74	—	—	0.62
Pyroplyllite	0.25	—	—	0.29	—	0.21	0.24	—
Quartz	11.93	24.33	20.10	14.04	19.74	6.61	11.96	18.29
Sericite	—	0.01	0.06	—	2.31	—	—	0.01
Titanite	2.89	4.10	3.85	3.77	3.89	4.23	4.39	4.20
Talc	—	—	—	—	—	—	—	—
Tremolite	6.20	—	—	5.95	—	9.66	9.56	—
Pyrite	—	—	—	—	—	—	—	—
Pyrrhotite	—	—	—	—	—	0.01	—	—
Chalcopyrite	—	0.02	0.02	0.02	—	0.02	0.02	0.02
Sphalerite	—	0.02	0.01	0.01	—	0.01	0.01	0.01
Petlandite	—	—	—	—	—	0.01	0.01	—
Arsenopyrite	—	—	—	—	—	—	—	—
Total	100.00	100.00	100.00	100.00	100.00	100.00	100.00	100.00
IFRAIS	100.00	95.75	100.00	92.32	100.00	100.00	100.00	95.38
IPARA	—	4.11	—	7.43	—	—	—	4.56
ISER	—	0.14	—	0.24	—	—	—	0.06
ICHLO	—	—	—	—	—	—	—	—
IPYRO	—	—	—	—	—	—	—	—
IPAF	6.93	46.08	46.25	1.01	50.32	1.64	0.22	23.11

noted by the absence of normative stilpnomelane. It could be that some of the normative K from orthoclase may be attributed to stilpnomelane. Nonetheless, the overall normative mineralogy of the basalt corresponds well to observations made in thin sections by Goutier and Lacroix (1992) and therefore match the sub- to greenschist facies mineralogical assemblage as expected.

Table 8.15 Continued

Sample	3292	3669	3668	3665	3666	3667
Actinolite	—	—	—	—	—	5.31
Albite	30.38	19.18	10.35	5.39	26.91	34.01
Ankerite	—	—	1.71	0.52	—	—
Apatite	0.39	0.40	0.36	0.39	0.35	0.32
Calcite	4.14	3.84	4.01	7.13	3.36	2.75
Fe chlorite	16.39	22.58	19.40	24.50	20.86	16.61
Mg chlorite	15.29	14.14	13.40	15.52	16.22	11.82
Chromite	0.07	0.05	0.09	0.06	0.08	0.11
Dolomite	—	—	1.18	0.33	—	—
Epidote	5.50	1.61	—	—	4.47	5.50
Magnetite	1.07	1.89	1.80	2.08	1.60	2.03
Orthoclase	3.95	7.16	6.67	0.71	0.51	5.53
Paragonite	0.49	0.32	5.94	7.14	0.60	0.00
Pyroplyllite	—	—	—	—	—	0.23
Quartz	17.29	22.07	26.91	31.35	20.62	7.94
Sericite	0.06	0.12	3.83	0.94	0.01	—
Titanite	4.94	6.59	4.32	3.91	4.37	4.03
Talc	—	—	—	—	—	—
Tremolite	—	—	—	—	—	3.78
Pyrite	—	—	—	—	—	—
Pyrrhotite	—	—	—	—	—	—
Chalcopyrite	0.02	0.03	0.03	0.02	0.02	0.02
Sphalerite	0.02	0.02	0.01	0.01	0.01	0.01
Petlandite	—	—	—	—	—	—
Arsenopyrite	—	—	—	—	—	—
Total	100.00	100.00	100.00	100.00	100.00	100.00
IFRAIS	93.11	75.08	81.17	90.50	74.85	100.00
IPARA	6.09	18.14	11.45	8.40	24.67	—
ISER	0.79	6.78	7.38	1.11	0.47	—
ICHLO	—	—	—	—	—	—
IPYRO	—	—	—	—	—	—
IPAF	30.95	19.76	42.08	46.53	24.04	13.38

Deguisier andesite to dacite

The NORMAT normative mineralogy of the least-altered andesitic to dacitic samples is presented in Table 8.16.

Table 8.16 – NORMAT normative mineralogy of the Deguisier andesite to dacite unit. Normative mineralogy is presented in weight %.

Sample	2003031903	D958224	D958195	D958198	D958228	D958227	D958226
Albite	4.55	34.47	46.64	54.24	12.88	25.64	21.80
Anatase	—	—	—	—	—	—	—
Ankerite	3.45	4.14	2.10	4.53	5.33	6.51	2.59
Apatite	0.74	0.78	0.76	0.88	0.86	0.94	1.29
Calcite	—	—	—	—	—	—	—
Fe chlorite	—	2.80	—	3.63	0.71	1.43	2.63
Mg chlorite	—	1.37	—	1.60	0.22	0.58	1.31
Chromite	—	0.01	0.01	0.01	0.01	0.01	0.01
Dolomite	7.51	2.02	0.90	2.00	1.64	2.64	1.29
Epidote	—	—	—	—	—	—	—
Magnesite	1.02	0.16	1.17	0.43	0.02	—	0.90
Magnetite	0.63	1.02	1.31	1.52	0.84	1.15	1.14
Orthoclase	15.62	5.29	6.58	3.69	8.91	8.73	9.66
Paragonite	3.37	8.97	6.19	1.67	11.98	12.19	14.51
Pyrophyllite	0.01	—	—	—	0.01	0.01	0.01
Quartz	47.35	34.53	27.84	21.95	45.51	32.90	31.30
Rhodochrosite	—	—	—	—	—	—	—
Stilpnomelane	0.32	—	—	—	—	—	—
Sericite	11.57	1.38	0.87	0.11	8.28	4.15	6.43
Siderite	0.47	0.32	2.73	0.98	0.07	—	1.81
Titanite	2.05	2.72	2.86	2.71	2.70	2.89	3.30
Pyrite	1.29	—	0.02	0.03	—	—	—
Pyrrhotite	—	—	—	—	—	—	—
Chalcopyrite	—	0.02	0.01	—	—	—	—
Sphalerite	—	0.01	0.01	0.01	0.01	0.01	0.01
Petlandite	—	—	—	—	—	—	—
Arsenopyrite	0.04	—	—	—	—	—	—
Total	100.00	100.00	100.00	100.00	100.00	100.00	100.00
IFRAIS	100.00	100.00	100.00	100.00	96.61	100.00	77.66
IPARA	—	—	—	—	2.01	—	15.48
ISER	—	—	—	—	1.39	—	6.86
ICHLO	—	—	—	—	—	—	—
IPYRO	—	—	—	—	—	—	—
IPAF	70.46	82.61	120.10	82.11	95.75	93.53	82.50

The normative greenschist facies mineralogy is dominated by quartz (16.22 - 60.37 wt%), albite (0.57 - 62.07 wt%), chlorite$_{tot}$ (0.93 - 26.80 wt%) paragonite (0.20 - 14.51 wt%) and orthoclase (2.00 - 15.62 wt%). This trend does not exactly reflect the mineralogy observed in thin section where chlorite and epidote are dominant minerals with concentrations of 18%$_m$ and 25%$_m$ respectively. Nonetheless, it is evident that normative paragonite along with sericite (0.01 - 16.96 wt%) are replacing chlorite and epidote. Furthermore, quartz only represents 5%$_m$ of the thin section, whereas normative quartz levels are much higher. Therefore as

Table 8.16 Continued

Sample	D958230	D958233	D958253	D958256	D958238	D958235	D958247
Albite	11.88	62.07	18.80	31.73	0.57	25.65	16.91
Anatase	—	—	—	0.14	—	—	—
Ankerite	6.03	1.10	3.31	—	2.74	—	7.41
Apatite	0.69	0.84	1.01	1.12	0.74	0.56	0.69
Calcite	—	1.87	0.45	—	1.07	0.94	—
Fe chlorite	—	8.17	11.29	8.66	4.05	11.61	—
Mg chlorite	—	2.74	6.89	3.30	1.63	15.19	—
Chromite	0.01	0.01	0.01	0.01	0.01	0.01	0.01
Dolomite	3.30	0.37	2.02	—	1.10	—	2.26
Epidote	—	—	—	—	—	5.93	—
Magnesite	0.36	—	—	0.41	—	—	—
Magnetite	1.15	1.15	1.44	1.07	0.67	0.26	1.12
Orthoclase	10.11	2.00	5.71	3.07	5.24	4.20	10.22
Paragonite	9.20	0.20	8.70	12.62	1.86	2.92	13.11
Pyrophyllite	0.01	—	0.01	0.01	0.01	—	0.01
Quartz	46.37	16.22	34.53	32.13	60.37	30.25	36.81
Rhodochrosite	—	—	—	—	—	—	0.26
Stilpnomelane	—	—	—	—	0.26	—	—
Sericite	7.83	0.01	2.64	1.22	16.96	0.48	7.92
Siderite	0.65	—	—	1.09	—	—	0.01
Titanite	2.30	3.21	3.11	3.33	2.16	1.99	3.19
Pyrite	0.10	—	0.02	0.05	0.51	—	0.04
Pyrrhotite	—	—	0.02	0.01	0.01	—	—
Chalcopyrite	0.01	0.02	0.02	0.01	0.01	—	—
Sphalerite	0.01	0.01	0.02	0.01	0.01	0.01	—
Petlandite	—	—	—	0.01	—	—	—
Arsenopyrite	—	—	—	—	0.03	—	—
Total	100.00	100.00	100.00	100.00	100.00	100.00	100.00
IFRAIS	100.00	100.00	78.73	52.09	80.30	55.80	100.00
IPARA	—	—	16.32	43.68	1.94	37.98	—
ISER	—	—	4.96	4.22	17.75	6.22	—
ICHLO	—	—	—	—	—	—	—
IPYRO	—	—	—	—	—	—	—
IPAF	104.01	50.64	50.20	25.32	71.57	10.35	103.05

hinted by the CIPW norm, quartz along with subordinate amounts of orthoclase are likely constituents of the fine-grained matrix. Accessory minerals are dominated by an assortment of carbonate minerals. They are, respectively, siderite (0.01 - 2.82 wt%), magnesite (0.02 - 1.61 wt%), dolomite (0.29 - 7.51 wt%) and ankerite (0.84 - 6.51 wt%). The andesite to dacite unit tends more in favour of an assemblage of carbonate minerals compared to the basalt. Whether this trend is actual or not cannot be verified due to the lack of thin sections.

Table 8.16 Continued

Sample	D958272	D958273	D958301
Albite	14.91	8.96	15.69
Anatase	—	—	—
Ankerite	6.22	2.53	0.84
Apatite	0.43	0.93	0.91
Calcite	—	—	—
Fe chlorite	—	—	0.71
Mg chlorite	—	—	0.25
Chromite	0.01	0.01	0.01
Dolomite	2.02	0.87	0.29
Epidote	—	—	—
Magnesite	0.84	0.97	1.61
Magnetite	1.79	1.21	1.69
Orthoclase	11.56	13.00	17.10
Paragonite	14.79	10.43	9.76
Pyrophyllite	0.01	0.01	0.01
Quartz	29.29	39.94	32.55
Rhodochrosite	—	—	—
Stilpnomelane	—	—	—
Sericite	11.47	15.14	10.63
Siderite	2.58	2.82	4.61
Titanite	4.03	3.15	3.28
Pyrite	0.01	0.03	0.04
Pyrrhotite	—	—	—
Chalcopyrite	0.02	0.01	0.01
Sphalerite	0.01	0.01	0.01
Petlandite	—	—	—
Arsenopyrite	0.01	—	—
Total	100.00	100.00	100.00
IFRAIS	95.28	70.80	68.06
IPARA	2.66	11.91	15.28
ISER	2.06	17.29	16.66
ICHLO	—	—	—
IPYRO	—	—	—
IPAF	104.55	107.54	95.20

Deguisier rhyolite

The resulting normative mineralogy of the rhyolite is presented in Table 8.17.

Table 8.17 – NORMAT normative mineralogy of the Deguisier rhyolite. Normative mineralogy is presented in weight %.

Sample	05-A	JEB-10-09	D958143	D958269	94-00033
Albite	25.74	40.15	13.70	11.53	17.68
Anatase	0.30	0.86	0.63	0.67	—
Ankerite	—	—	—	—	0.08
Apatite	0.85	1.04	0.91	0.81	0.02
Fe chlorite	0.59	1.36	—	—	—
Mg chlorite	0.26	0.40	—	—	—
Chromite	—	—	0.01	0.01	—
Dolomite	—	—	—	—	0.04
Magnesite	0.36	0.03	0.41	0.42	0.14
Magnetite	0.22	0.06	0.41	0.08	—
Orthoclase	15.40	11.04	17.32	11.51	9.57
Paragonite	7.25	7.88	4.83	11.23	11.23
Pyrophyllite	0.01	—	0.01	0.01	—
Quartz	42.50	34.78	54.10	50.85	54.65
Sericite	4.34	2.17	6.11	11.21	6.08
Siderite	0.82	0.11	1.46	0.94	0.30
Titanite	1.35	0.08	0.09	0.70	0.22
Pyrite	—	0.01	—	0.02	—
Chalcocite	—	—	0.01	—	—
Chalcopyrite	0.01	0.01	—	0.01	—
Total	100.00	100.00	100.00	100.00	100.00
IFRAIS	77.10	81.40	74.51	51.70	62.56
IPARA	14.33	14.58	11.25	24.17	24.29
ISER	8.57	4.01	14.23	24.13	13.15
ICHLO	—	—	—	—	—
IPYRO	—	—	—	—	—
IPAF	76.70	67.83	110.53	122.77	115.77

The bulk greenschist facies mineralogy of the rhyolite is composed of albite (11.53 - 40.15 wt%), orthoclase (9.57 - 17.32 wt%) and quartz (34.78 - 54.65 wt%). Closely following are paragonite (4.83 - 11.23 wt%) and sericite (2.17 - 11.21 wt%) in almost equal proportions. The calculated normative mineralogy is similar to observations obtained from a thin section. Paragonite would be in solid-solution with sericite as amorphous crystals, therefore being undistinguishable from one another. Accessory normative minerals are chlorite (0.59 - 1.76 wt%), siderite (0.11 - 1.46 wt%) and titanite (0.08 - 1.35 wt%). The rhyolite does not seem to be a suitable host for sulphides compared to both the basalt and andesite to dacite units. This observation is supplemented by the normative mineralogical assemblage containing abundances < 0.02 wt% norm pyrite.

Gabbro

The obtained metamorphic normative mineralogy of the least-altered gabbro samples is presented in Table 8.18.

Table 8.18 – NORMAT normative mineralogy of the gabbro. Normative mineralogy is presented in weight %.

Sample	D958257	3286
Actinolite	9.68	9.88
Albite	33.96	26.83
Apatite	0.36	0.27
Calcite	1.03	0.68
Fe chlorite	10.41	11.26
Mg chlorite	7.81	12.09
Chromite	0.04	0.13
Epidote	7.87	17.52
Magnetite	1.80	1.25
Orthoclase	8.52	1.46
Pyrophyllite	0.16	0.22
Quartz	7.37	4.67
Titanite	3.73	3.13
Tremolite	7.26	10.61
Total	100.00	100.00
IFRAIS	100.00	100.00
IPARA	—	—
ISER	—	—
ICHLO	—	—
IPYRO	—	—
IPAF	8.86	-0.14

The dominant greenschist facies minerals are chlorite$_{tot}$ (18.22 - 23.35 wt%), albite (26.83 - 33.96 wt%), epidote (7.87 - 17.52 wt%), tremolite (7.26 - 10.61 wt%) and actinolite (9.68 - 9.88 wt%). This composition is remarkably similar to that of the Deguisier basalt. Thin sections observations performed by Goutier and Lacroix (1992) also reveal a similar mineralogical assemblage. Accessory minerals are quartz (4.67 - 7.37 wt%), orthoclase (1.46 - 8.52 wt%) and calcite (0.68 - 1.03 wt%).

Beattie syenite

The NORMAT normative mineralogy of the least-altered porphyritic Beattie syenite, equigranular magnetite-bearing, porphyritic Central Duparquet, megaporphyritic and lath syenite unit samples are presented in Tables 8.19, 8.20, 8.22 and 8.23 respectively.

Table 8.19 – NORMAT normative mineralogy of the porphyritic Beattie syenite unit. Normative mineralogy is presented in weight %.

Sample	D958002	D958004	2004042805	D958179	D958051	D958215	D958221
Albite	6.23	8.45	31.74	7.84	20.18	13.61	40.17
Anatase	—	—	—	—	—	—	0.22
Ankerite	—	—	1.26	0.56	1.93	0.77	—
Apatite	0.65	0.74	0.22	0.56	0.62	0.65	0.53
Calcite	—	2.35	1.34	0.44	—	0.92	—
Fe chlorite	1.81	3.18	2.52	1.74	2.60	0.98	—
Mg chlorite	1.42	3.03	1.56	1.27	0.81	2.07	—
Chromite	0.01	0.01	—	0.01	0.01	0.01	0.01
Dolomite	—	—	0.78	0.41	0.60	1.64	—
Epidote	2.23	0.83	—	—	—	—	—
Magnesite	—	—	—	—	0.28	—	0.35
Magnetite	0.04	0.37	0.28	0.31	0.83	0.05	1.11
Orthoclase	64.93	69.96	34.45	64.59	51.14	56.35	40.03
Paragonite	—	—	6.60	—	2.68	1.65	3.27
Pyrophyllite	—	—	0.01	—	—	—	—
Quartz	19.17	7.95	11.48	18.68	9.37	10.23	7.36
Stilpnomelane	—	0.18	—	0.10	—	0.09	—
Sericite	0.04	0.04	7.17	0.03	6.78	6.85	3.26
Siderite	—	—	—	—	0.88	—	3.22
Titanite	0.96	1.07	0.56	0.92	1.19	1.22	0.45
Talc	—	0.18	—	—	—	—	—
Pyrite	2.34	1.40	0.03	2.40	0.08	2.76	—
Pyrrhotite	—	0.16	0.01	—	—	—	—
Chalcopyrite	—	—	—	—	—	—	—
Sphalerite	0.01	0.01	—	0.01	—	0.02	—
Molybdenite	0.01	—	—	—	—	0.01	—
Arsenopyrite	0.14	0.09	—	0.11	0.01	0.11	—
Total	100.00	100.00	100.00	100.00	100.00	100.00	100.00
IFRAIS	96.63	100.00	95.38	100.00	93.74	99.99	92.65
IPARA	0.29	—	2.22	—	1.77	—	3.68
ISER	3.08	—	2.41	—	4.49	0.01	3.67
ICHLO	—	—	—	—	—	—	—
IPYRO	—	—	—	—	—	—	—
IPAF	-19.87	48.31	77.96	56.35	75.13	75.99	110.90

Porphyritic Beattie syenite The normative bulk mineralogy of the porphyritic Beattie unit is composed of orthoclase (9.73 - 74.73 wt%), albite (2.37 - 67.25 wt%) and quartz (0.65 - 42.87 wt%). Such large quantities of quartz are contradictory of thin section observations where quartz was noted only to occur in veins with percentages of $< 15\%_m$ (see Chapter 6).

Accessory minerals are carbonate minerals, chlorite, sericite (0.02 - 18.15 wt%) and parag-

Table 8.19 Continued

Sample	JG-1332-01	2004042820	JG-1332-06	JG-1332-07	D958156	D958159	JG-1332-09
Albite	52.09	49.37	53.22	36.01	49.89	34.08	51.15
Anatase	—	—	—	—	—	0.30	—
Ankerite	0.54	0.56	0.43	1.07	4.36	—	—
Apatite	0.75	0.67	0.64	0.72	0.72	0.30	0.70
Calcite	1.75	1.48	2.42	5.70	0.97	—	2.31
Fe chlorite	5.94	5.92	6.05	2.20	1.24	2.78	5.30
Mg chlorite	4.54	5.15	4.07	1.71	0.43	0.59	3.88
Chromite	—	—	—	—	0.01	0.01	—
Dolomite	0.41	0.49	0.29	0.83	1.52	—	—
Epidote	—	—	—	—	—	—	1.63
Magnesite	—	—	—	—	—	0.17	—
Magnetite	0.80	0.58	0.62	0.15	0.85	0.40	1.09
Orthoclase	31.14	29.57	26.36	15.91	26.00	35.17	30.41
Paragonite	0.09	0.11	0.10	12.76	4.45	7.42	0.04
Pyrophyllite	—	—	—	0.01	—	0.01	—
Quartz	0.65	4.78	4.52	16.07	6.00	10.08	1.57
Stilpnomelane	—	—	—	—	—	—	—
Sericite	0.05	0.07	0.05	5.64	2.32	7.66	0.02
Siderite	—	—	—	—	—	0.78	—
Titanite	1.24	1.20	1.18	1.21	1.17	0.23	1.19
Talc	—	—	—	—	—	—	0.65
Pyrite	0.01	0.03	0.01	0.01	0.05	0.01	—
Pyrrhotite	—	—	—	0.01	—	—	0.04
Chalcopyrite	—	—	—	—	—	—	—
Sphalerite	0.01	0.01	0.01	—	0.01	—	0.01
Molybdenite	—	—	—	—	—	—	—
Arsenopyrite	—	—	—	—	—	—	—
Total	100.00	100.00	100.00	100.00	100.00	100.00	100.00
IFRAIS	95.47	100.00	100.00	100.00	100.00	78.99	100.00
IPARA	2.83	—	—	—	—	10.34	—
ISER	1.69	—	—	—	—	10.67	—
ICHLO	—	—	—	—	—	—	—
IPYRO	—	—	—	—	—	—	—
IPAF	19.01	38.38	44.77	90.83	89.33	41.44	17.01

onite (0.04 - 18.14 wt%). Paragonite in the norm should in fact be interpreted as sericite as chemical investigations of the major rock-forming minerals have demonstrated the presence of ferrian-muscovite in the porphyritic Beattie syenite unit.

Trace minerals common to the majority of samples are apatite, chromite, magnetite, titanite, pyrite and arsenopyrite, all observed in thin sections. However, magnetite in the norm should be interpreted as hematite. This modification stems from thin section observations where hematite is a much more common occurrence than magnetite.

The NORMAT mineralogy reveals that changes produced by hydrothermal alteration consist principally of sericite and carbonate minerals. Sulphides are also considered to be associated with hydrothermal alteration rather than regional metamorphism as per thin section and field observations. Mineralogical changes associated with regional metamorphism, deduced

Table 8.19 Continued

Sample	D958157	D958154	D958153	D958058	D958107	D958113	D958108
Albite	27.23	49.14	47.99	33.78	2.37	37.58	17.02
Anatase	—	—	—	—	—	—	—
Ankerite	2.09	4.83	3.05	1.87	4.04	1.89	4.47
Apatite	0.20	0.75	0.75	0.58	0.39	0.58	0.62
Calcite	0.32	—	0.68	—	0.49	0.19	—
Fe chlorite	4.56	0.54	4.82	2.23	0.88	3.48	—
Mg chlorite	1.43	0.48	2.01	1.48	0.68	1.01	—
Chromite	0.01	0.01	0.01	0.01	0.01	0.01	0.01
Dolomite	0.65	4.28	1.27	1.24	3.13	0.55	3.57
Epidote	—	—	—	—	—	—	—
Magnesite	—	0.06	—	0.31	—	—	0.22
Magnetite	0.70	0.87	0.98	0.57	0.77	0.56	0.78
Orthoclase	32.85	25.72	28.91	33.91	74.73	28.26	49.54
Paragonite	5.30	4.87	2.26	5.66	0.12	7.08	3.23
Pyrophyllite	0.01	—	—	0.01	—	0.01	0.01
Quartz	17.14	4.65	4.48	11.01	7.44	11.47	9.72
Stilpnomelane	—	—	—	—	—	—	—
Sericite	6.39	2.55	1.36	5.68	3.72	5.33	9.42
Siderite	—	0.06	—	0.47	—	—	0.27
Titanite	1.02	1.11	1.28	1.17	1.14	1.22	1.10
Talc	—	—	—	—	—	—	—
Pyrite	0.08	0.06	0.13	0.02	0.09	0.77	0.02
Pyrrhotite	0.01	—	0.01	—	—	0.01	—
Chalcopyrite	—	0.01	—	—	—	—	—
Sphalerite	0.01	—	—	0.01	—	0.01	0.01
Molybdenite	—	—	—	—	—	—	—
Arsenopyrite	—	—	—	—	—	0.01	—
Total	100.00	100.00	100.00	100.00	100.00	100.00	100.00
IFRAIS	90.32	100.00	100.00	93.12	100.00	89.93	100.00
IPARA	4.39	—	—	3.43	—	5.75	—
ISER	5.30	—	—	3.45	—	4.32	—
ICHLO	—	—	—	—	—	—	—
IPYRO	—	—	—	—	—	—	—
IPAF	61.28	93.64	68.85	74.78	91.71	64.23	102.11

from thin section observations combined with the calculated NORMAT mineralogical assemblage, are the addition of quartz, minor albite and carbonate minerals. All these minerals correspond with the Ab-Cb and Qtz-Ab-Cb veins, therefore suggesting that these veins are of metamorphic origin.

Table 8.19 Continued

Sample	2009048666	D958109	2009048667	D958075	D958119	D958117	D958116
Albite	41.88	27.10	41.34	45.65	9.39	27.29	25.79
Anatase	—	—	—	—	—	—	—
Ankerite	3.34	2.68	4.60	2.96	0.54	2.93	5.16
Apatite	0.30	0.62	0.66	0.94	0.04	0.60	0.61
Calcite	—	—	0.13	—	—	—	0.75
Fe chlorite	0.04	1.53	0.53	—	2.26	—	0.45
Mg chlorite	0.01	0.53	0.25	—	0.46	—	0.34
Chromite	—	0.01	—	0.01	0.01	0.01	0.01
Dolomite	1.24	0.94	2.18	1.03	0.11	0.90	3.92
Epidote	—	—	—	—	—	—	—
Magnesite	0.15	0.03	—	0.75	0.43	0.42	—
Magnetite	0.65	0.55	0.77	1.21	0.86	0.95	0.81
Orthoclase	37.19	45.58	34.27	9.73	47.67	46.67	20.36
Paragonite	5.26	3.99	5.63	9.00	3.57	3.11	8.20
Pyrophyllite	—	0.01	—	0.01	0.01	—	0.01
Quartz	3.70	8.15	3.72	20.63	13.66	9.07	26.02
Stilpnomelane	—	—	—	—	—	—	—
Sericite	4.68	6.71	4.67	1.92	18.15	5.32	6.48
Siderite	0.40	0.08	—	2.14	2.12	1.38	—
Titanite	0.99	1.18	1.12	2.85	0.69	1.05	0.98
Talc	—	—	—	—	—	—	—
Pyrite	0.15	0.31	0.10	1.09	0.01	0.26	0.08
Pyrrhotite	—	—	—	—	0.01	—	—
Chalcopyrite	—	—	—	0.01	—	—	—
Sphalerite	0.01	0.01	0.01	0.01	0.01	0.01	0.01
Molybdenite	—	—	—	—	—	—	—
Arsenopyrite	—	0.02	—	0.07	—	0.01	—
Total	100.00	100.00	100.00	100.00	100.00	100.00	100.00
IFRAIS	98.04	97.43	95.98	99.83	72.69	100.00	100.00
IPARA	1.04	0.96	2.20	0.14	4.49	—	—
ISER	0.92	1.61	1.82	0.03	22.82	—	—
ICHLO	—	—	—	—	—	—	—
IPYRO	—	—	—	—	—	—	—
IPAF	83.39	84.03	80.20	104.60	75.15	100.79	97.41

Table 8.19 Continued

Sample	D958114	D958115	D958190	D958223	2004042804	2009048663	D958252
Albite	36.53	26.20	29.44	30.25	17.64	30.61	21.16
Anatase	—	—	—	—	—	—	—
Ankerite	3.27	1.48	1.27	3.51	2.14	0.63	4.32
Apatite	0.73	0.70	0.67	0.69	0.59	0.04	0.77
Calcite	—	2.77	2.70	1.37	—	4.23	—
Fe chlorite	2.11	5.12	3.70	3.09	2.71	1.69	—
Mg chlorite	1.05	0.86	1.41	1.12	1.54	0.85	—
Chromite	0.01	0.01	0.01	0.01	0.01	—	0.01
Dolomite	1.62	0.25	0.49	1.27	1.22	0.31	1.70
Epidote	—	—	—	—	—	—	—
Magnesite	0.17	—	—	—	0.16	—	0.14
Magnetite	0.75	0.62	0.34	0.82	0.66	0.15	0.75
Orthoclase	27.58	27.19	20.66	35.47	57.22	42.41	9.96
Paragonite	8.12	8.27	12.72	5.02	1.45	4.14	10.40
Pyrophyllite	0.01	0.01	0.01	0.01	—	—	0.01
Quartz	9.94	16.61	16.35	9.81	8.38	7.75	42.87
Stilpnomelane	—	—	—	—	—	0.11	—
Sericite	6.13	8.58	8.93	5.89	4.70	5.73	4.90
Siderite	0.35	—	—	—	0.27	—	0.36
Titanite	1.29	1.23	1.28	1.52	0.96	0.64	2.62
Talc	—	—	—	—	—	—	—
Pyrite	0.31	0.07	—	0.15	0.32	0.66	—
Pyrrhotite	—	0.01	—	—	—	—	—
Chalcopyrite	0.01	—	0.01	0.01	—	—	—
Sphalerite	0.01	0.01	—	0.01	0.01	0.01	—
Molybdenite	—	—	—	—	—	—	—
Arsenopyrite	—	—	—	—	0.01	0.02	—
Total	100.00	100.00	100.00	100.00	100.00	100.00	100.00
IFRAIS	96.28	97.22	93.41	100.00	98.92	100.00	100.00
IPARA	2.12	1.37	3.87	—	0.25	—	—
ISER	1.60	1.42	2.72	—	0.82	—	—
ICHLO	—	—	—	—	—	—	—
IPYRO	—	—	—	—	—	—	—
IPAF	83.20	72.03	74.75	82.39	57.06	72.22	117.45

Table 8.19 Continued

Sample	D958229	D958239	D958264	D958254	JG-5099-02	2004042815	2004042814
Albite	56.96	41.39	46.16	43.38	22.73	46.81	43.32
Anatase	—	—	—	—	—	—	—
Ankerite	0.69	1.75	0.59	2.10	0.70	2.49	3.92
Apatite	0.63	0.09	0.04	0.22	0.32	0.75	0.60
Calcite	2.55	0.31	1.85	—	0.53	1.35	0.39
Fe chlorite	5.35	1.77	3.06	1.31	4.33	3.90	1.57
Mg chlorite	1.85	0.56	0.89	0.26	2.21	1.33	1.48
Chromite	0.01	0.01	0.01	0.01	—	—	—
Dolomite	0.24	0.55	0.17	0.42	0.36	0.85	3.69
Epidote	—	—	—	—	—	—	—
Magnesite	—	—	—	0.11	—	—	—
Magnetite	0.65	0.20	0.29	0.65	0.43	0.78	0.75
Orthoclase	25.56	15.19	25.30	29.57	52.71	25.84	26.34
Paragonite	0.15	18.14	6.84	4.45	2.40	3.69	4.48
Pyrophyllite	—	0.01	0.01	—	—	—	—
Quartz	4.07	12.82	10.49	12.91	6.69	8.86	9.52
Stilpnomelane	—	—	—	—	—	—	—
Sericite	0.07	6.66	3.75	3.03	5.57	2.04	2.72
Siderite	—	—	—	0.56	—	—	—
Titanite	1.20	0.51	0.50	1.00	0.97	1.24	1.13
Talc	—	—	—	—	—	—	—
Pyrite	0.01	0.03	0.06	—	0.03	0.06	0.07
Pyrrhotite	—	0.01	—	—	0.01	—	—
Chalcopyrite	—	—	—	—	—	—	—
Sphalerite	0.01	—	0.01	—	0.01	0.01	—
Molybdenite	—	—	—	—	—	—	—
Arsenopyrite	—	—	—	—	—	—	—
Total	100.00	100.00	100.00	100.00	100.00	100.00	100.00
IFRAIS	100.00	78.98	97.93	97.96	90.90	100.00	100.00
IPARA	—	15.38	1.34	1.21	2.74	—	—
ISER	—	5.64	0.73	0.83	6.36	—	—
ICHLO	—	—	—	—	—	—	—
IPYRO	—	—	—	—	—	—	—
IPAF	56.50	77.34	68.69	85.08	48.53	78.96	83.84

Table 8.19 Continued

Sample	D958259	2004042811	3958	2004042799	3280	3698	3284
Albite	62.14	52.33	14.76	67.25	34.41	44.96	57.78
Anatase	—	—	—	—	—	—	—
Ankerite	0.80	0.89	—	2.92	0.63	0.76	1.21
Apatite	0.21	0.64	0.25	0.73	0.63	0.76	0.85
Calcite	0.78	5.03	2.10	2.81	1.12	2.13	3.88
Fe chlorite	1.94	4.59	16.87	3.69	7.19	5.96	5.98
Mg chlorite	1.08	1.81	14.41	2.75	2.47	2.16	2.28
Chromite	0.01	—	0.10	0.09	0.14	0.09	0.09
Dolomite	0.44	0.35	—	2.17	0.22	0.28	0.46
Epidote	—	—	24.41	—	—	—	—
Magnesite	—	—	—	—	—	—	—
Magnetite	0.18	0.47	1.64	0.81	0.82	0.63	0.78
Orthoclase	11.38	9.08	0.32	5.74	35.52	25.05	18.26
Paragonite	9.90	9.32	0.20	2.16	1.34	5.52	2.48
Pyrophyllite	0.01	0.01	—	—	—	—	—
Quartz	8.07	12.67	20.48	7.20	12.94	8.62	5.18
Stilpnomelane	—	—	—	—	—	—	—
Sericite	1.81	1.62	—	0.19	1.38	3.07	0.78
Siderite	—	—	—	—	—	—	—
Titanite	1.10	1.17	3.28	1.48	1.18	—	—
Talc	—	—	1.16	—	—	—	—
Pyrite	0.14	—	—	—	—	—	—
Pyrrhotite	—	0.01	—	—	—	—	—
Chalcopyrite	—	—	—	0.01	—	—	—
Sphalerite	—	—	—	—	—	—	—
Molybdenite	—	—	—	—	—	—	—
Arsenopyrite	—	—	—	—	—	—	—
Total	100.00	100.00	100.00	100.00	100.00	100.00	100.00
IFRAIS	92.90	100.00	91.23	100.00	96.12	98.13	100.00
IPARA	6.00	—	8.59	—	1.91	1.20	—
ISER	1.10	—	0.19	—	1.97	0.67	—
ICHLO	—	—	—	—	—	—	—
IPYRO	—	—	—	—	—	—	—
IPAF	67.82	74.75	9.14	73.37	52.47	62.45	56.58

Table 8.20 – NORMAT mineralogy of the equigranular magnetite-bearing unit. Normative mineralogy is presented in weight %.

Sample	JG-1332-04	90-34316
Actinolite	0.98	3.39
Albite	51.58	48.91
Apatite	0.64	0.62
Calcite	1.27	0.31
Fe chlorite	1.58	3.43
Mg chlorite	1.20	2.59
Epidote	6.42	4.88
Magnetite	2.20	0.50
Orthoclase	29.27	29.48
Pyrophyllite	0.01	0.06
Quartz	0.04	2.13
Titanite	1.14	1.13
Talc	2.86	—
Tremolite	0.75	2.56
Pyrrhotite	0.06	—
Sphalerite	—	0.01
Total	100.00	100.00
IFRAIS	100.00	100.00
IPARA	—	—
ISER	—	—
ICHLO	—	—
IPYRO	—	—
IPAF	5.67	6.70

Equigranular magnetite-bearing Table 8.20 provides the normative greenschist facies mineralogy of the equigranular magnetite-bearing syenite unit. The corresponding mineralogy is dominated by albite (48.91 - 51.58 wt%) and orthoclase (29.27 - 29.48 wt%). Accessory normative minerals are chlorite, actinolite, epidote, magnetite, tremolite and titanite. Both the dominant norm mineralogy and thin section observations are in accord.

The accessory thin section mineralogy contains actinolite, epidote, titanite and magnetite as does the norm. However there is a lack of tremolite and only trace amounts of chlorite that were noted in thin sections as opposed to values given in the norm. Rather, Ca in tremolite might be associated with hornblende, combined with some of the normative Fe-chlorite as chemical analyses of chlorite revealed that it is clinochlore. Furthermore, normative talc was not observed in the unit.

The NORMAT mineralogy reveals that there was a complete lack of hydrothermal alteration, confirmed by an IFRAIS index of 100%. Therefore, all mineralogical changes are attributed to regional metamorphism. Specifically, actinolite, hornblende, calcite and epidote are the product of regional metamorphism to the greenschist facies.

Table 8.21 – NORMAT mineralogy of the porphyritic Central Duparquet unit. Normative mineralogy is presented in weight %.

Sample	2004042817	1990034318	2004042816	D958197	2009048662	2004042813
Albite	53.16	38.98	44.20	42.68	49.83	40.28
Anatase	—	—	—	—	—	—
Ankerite	3.63	2.90	3.57	3.88	4.22	4.58
Apatite	0.61	0.35	0.77	0.30	0.62	0.45
Calcite	1.31	—	0.26	0.46	—	—
Fe chlorite	2.04	0.76	1.27	1.80	0.44	1.32
Mg chlorite	0.78	0.67	0.70	0.79	0.40	0.88
Chromite	—	—	—	0.01	—	—
Dolomite	1.38	2.57	1.97	1.70	3.83	3.05
Magnesite	—	0.13	—	—	0.27	0.16
Magnetite	0.78	0.53	0.64	0.76	0.72	0.93
Orthoclase	20.79	30.96	26.34	30.29	13.01	32.73
Paragonite	5.21	5.36	6.70	6.39	12.97	5.37
Pyrophyllite	—	—	0.01	0.01	0.01	—
Quartz	7.05	11.20	8.15	5.30	8.82	4.21
Sericite	2.04	4.26	3.99	4.54	3.38	4.36
Siderite	—	0.15	—	—	0.29	0.24
Titanite	1.16	1.15	1.32	1.10	1.18	1.38
Pyrite	0.04	—	0.09	—	—	0.04
Chalcopyrite	—	—	—	—	—	0.01
Sphalerite	0.01	0.01	—	—	0.01	0.01
Arsenopyrite	—	—	—	—	—	—
Total	100.00	100.00	100.00	100.00	100.00	100.00
IFRAIS	100.00	100.00	100.00	100.00	100.00	95.45
IPARA	—	—	—	—	—	2.51
ISER	—	—	—	—	—	2.04
ICHLO	—	—	—	—	—	—
IPYRO	—	—	—	—	—	—
IPAF	83.33	92.13	87.54	87.35	97.40	85.19

Porphyritic Central Duparquet The bulk mineralogy of the porphyritic Central Duparquet unit is dominated by albite (23.86 - 55.03 wt%) and orthoclase (7.53 - 43.38 wt%) and quartz (4.21 - 18.79 wt%). The quantities of normative quartz are again contradictory of thin section observations where percentages are $< 2\%_m$ (see Table 8.1). This same discrepancy was noted with the NORMAT mineralogy of the porphyritic Beattie syenite unit.

Accessory minerals are sericite (1.15 - 10.40 wt%), paragonite (3.56 - 12.97 wt%), carbonate minerals and chlorite. All these minerals with the exception of paragonite have been confirmed though field, thin section observations or EMPA. Paragonite in the norm should in fact be interpreted as sericite as chemical investigations of the major rock-forming minerals have once again demonstrated the presence of muscovite varying to ferrian-muscovite in the unit.

Trace minerals are dominantly titanite, apatite, magnetite and pyrite. A portion of magnetite should however be attributed to hematite, as deduced from thin section observations.

Table 8.21 Continued

Sample	2004042812	D958248	D958249	2009048664	2009048665	2004042808
Albite	55.03	23.86	40.67	32.31	37.61	29.87
Anatase	—	—	—	0.09	0.09	0.32
Ankerite	3.07	0.45	2.03	—	—	—
Apatite	0.48	0.43	0.46	0.40	0.47	0.37
Calcite	1.86	—	—	—	—	—
Fe chlorite	1.59	1.01	0.14	2.33	3.70	3.99
Mg chlorite	1.09	0.48	0.07	0.77	0.57	0.90
Chromite	—	0.01	0.01	—	—	—
Dolomite	2.11	0.21	1.05	—	—	—
Magnesite	—	0.50	0.44	0.07	0.07	0.04
Magnetite	0.58	0.35	0.53	0.17	0.48	0.37
Orthoclase	7.53	33.65	30.39	43.38	39.08	41.66
Paragonite	8.40	7.37	8.10	4.76	3.73	4.01
Pyrophyllite	—	0.01	0.01	0.01	—	—
Quartz	16.10	18.79	7.76	8.34	9.10	12.61
Sericite	1.15	10.40	6.05	6.39	3.88	5.59
Siderite	—	1.05	0.86	0.21	0.45	0.19
Titanite	0.92	1.27	1.29	0.69	0.67	—
Pyrite	0.06	0.09	0.13	0.07	0.10	0.02
Chalcopyrite	—	—	—	—	—	—
Sphalerite	—	—	—	—	0.01	—
Arsenopyrite	—	0.05	—	—	—	—
Total	100.00	100.00	100.00	100.00	100.00	99.97
IFRAIS	100.00	77.95	94.01	84.25	86.60	83.01
IPARA	—	9.15	3.43	6.73	6.57	7.09
ISER	—	12.90	2.56	9.03	6.83	9.89
ICHLO	—	—	—	—	—	—
IPYRO	—	—	—	—	—	—
IPAF	79.99	79.10	98.28	9.16	52.21	26.26

The NORMAT alteration indices reveal that changes produced by hydrothermal alteration mainly consist of sericite and carbonate minerals. Similar changes were noted in the porphyritic Beattie syenite unit indicating that hydrothermal alteration affected a large area. Sulphides are also considered of hydrothermal origin as seen from both field and thin section observations. Mineralogical changes attributed with regional metamorphism, as deduced from thin section observations and NORMAT mineralogy consist again of quartz with minor albite and carbonate minerals found as Ab-Cb and Qtz-Ab-Cb veins.

Table 8.21 Continued

Sample	2004042809	D958303	2004042810	D958277
Albite	27.59	33.95	48.12	49.13
Anatase	0.31	0.02	—	—
Ankerite	—	—	3.01	2.53
Apatite	0.24	0.24	0.59	0.59
Calcite	—	—	—	—
Fe chlorite	0.70	—	0.92	0.10
Mg chlorite	0.22	—	0.81	0.07
Chromite	—	0.01	—	0.01
Dolomite	—	—	2.65	1.81
Magnesite	0.65	0.41	0.27	0.64
Magnetite	0.68	0.46	0.62	0.70
Orthoclase	30.28	37.01	22.61	22.66
Paragonite	6.21	3.56	6.44	6.37
Pyrophyllite	0.01	—	—	—
Quartz	23.95	17.86	9.12	10.09
Sericite	6.82	3.88	3.03	2.94
Siderite	2.08	1.47	0.31	0.90
Titanite	0.08	0.82	1.18	1.17
Pyrite	0.04	0.30	0.32	0.27
Chalcopyrite	0.01	—	—	—
Sphalerite	0.11	0.01	0.01	0.01
Arsenopyrite	—	—	—	—
Total	100.00	100.00	100.00	100.00
IFRAIS	80.88	90.73	100.00	100.00
IPARA	9.12	4.44	—	—
ISER	10.00	4.84	—	—
ICHLO	—	—	—	—
IPYRO	—	—	—	—
IPAF	82.27	115.88	81.29	98.94

Table 8.22 – NORMAT normative mineralogy of the megaporphyritic syenite unit. Normative mineralogy is presented in weight %.

Sample	2002025869	2004042806
Albite	23.18	48.11
Ankerite	0.04	2.14
Apatite	0.41	0.28
Fe chlorite	2.59	2.04
Mg chlorite	0.98	0.95
Dolomite	0.02	0.99
Magnesite	0.11	0.13
Magnetite	0.18	0.61
Orthoclase	37.20	25.61
Paragonite	5.84	4.33
Pyrophyllite	0.01	0.00
Quartz	18.48	11.28
Sericite	9.38	2.31
Siderite	0.29	0.27
Titanite	1.08	0.92
Pyrite	0.19	0.00
Total	100.00	100.00
IFRAIS	76.41	99.04
IPARA	9.06	0.63
ISER	14.53	0.34
ICHLO	—	—
IPYRO	—	—
IPAF	94.96	77.49

Megaporphyritic syenite The mineralogy of the megaporphyritic unit is dominated by albite (23.18 - 48.11 wt%), orthoclase (25.61 - 37.20 wt%) and quartz (11.28 - 18.48 wt%). This mineralogical assemblage is similar to that of the porphyritic Beattie and Central Duparquet units. Once again there is a discrepancy noted with the large abundance of quartz were in thin section the typical percentage does not exceed $1\%_m$. However, large veins filled with quartz have been noted in some of the thin sections.

Accessory minerals are normative paragonite (4.33 - 5.84 wt%), sericite (2.31 - 9.38 wt%), carbonate minerals and chlorite. Once again normative paragonite should be interpreted as sericite as chemical investigations of sericite in other units have yielded ferrian-muscovite. The remainder of the minerals were confirmed though thin section observations.

Normative trace minerals are apatite, magnetite, titanite and pyrite, all of which were confirmed from thin section observations. The only minor change proposed is the attribution of over half the weight % of magnetite to hematite.

The NORMAT mineralogy reveals once again that the changes produced by alteration consists of sericite and carbonate minerals. Pyrite is also associated with alteration as de-

duced from thin section observations. Minerals associated with regional metamorphism to the greenschist facies consist once again in the addition of quartz, minor albite and carbonate minerals.

Table 8.23 – NORMAT normative mineralogy of the lath syenite unit. Normative mineralogy is presented in weight %.

Sample	2003031914	2004042819
Albite	41.65	59.39
Ankerite	2.93	0.24
Apatite	0.71	0.55
Fe chlorite	—	6.21
Mg chlorite	—	2.26
Dolomite	1.97	0.09
Magnesite	1.42	0.11
Magnetite	1.12	0.63
Orthoclase	21.08	14.62
Paragonite	10.98	9.30
Pyrophyllite	0.01	0.01
Quartz	8.79	2.48
Sericite	5.56	2.29
Siderite	2.10	0.31
Titanite	1.61	1.46
Pyrite	0.03	0.02
Pyrrhotite	—	0.01
Chalcopyrite	0.02	0.02
Sphalerite	0.01	—
Total	100.00	100.00
IFRAIS	97.04	79.18
IPARA	1.97	16.71
ISER	1.00	4.11
ICHLO	—	—
IPYRO	—	—
IPAF	100.98	28.99

Lath syenite The dominant greenschist facies minerals are albite (41.65 - 59.39 wt%) and orthoclase (14.62 - 21.08 wt%). Accessory minerals are paragonite (9.30 - 10.98 wt%), quartz (2.48 - 8.79 wt%), sericite (2.29 - 5.56 wt%) and carbonate minerals (0.75 - 8.42 wt%). The greenschist facies mineralogy again contains much more quartz than anticipated. Such an abundance is also contrary to thin section observations which contained $< 1\%_m$ of quartz. However, at times numerous veins of quartz have been observed in thin sections. As for paragonite, it is to be interpreted as sericite as thin section observations combined with EMPA have confirmed the presence of ferrian-muscovite.

Normative trace minerals are apatite (0.55 - 0.71 wt%), magnetite (0.63 - 1.12 wt%), titanite (1.46 - 1.61 wt%), chlorite and sulphide minerals, all of which are within acceptable margins (deduced from thin section observations).

The NORMAT mineralogy reveals that sericite and a portion of carbonate minerals are the products of hydrothermal alteration. As such, the remaining mineralogical changes, mainly quartz, albite and some of the carbonate minerals, can be attributed to regional metamorphism.

The mineralogical homogeneities demonstrated by the majority of the units confirm that the hydrothermal alteration events in the Beattie syenite postdate the youngest intrusive phase. Therefore, Au-mineralization of the syenite and country rocks occurred after the emplacement of the syenite. Furthermore, both the hydrothermal alteration and metamorphism to the greenschist facies affected the whole Beattie area.

Chapter 9

Interpretations

The objective of this chapter is to integrate the petrological, mineralogical and geochemical findings presented in the previous chapters and use this information to establish a petrogenetic and postmagmatic alteration model of the Beattie area, with emphasis on the Beattie syenite. The following interpretations will proceed chronologically (from oldest to youngest). Additionally, sketches of the petrogenetic model of the Beattie area are presented in Figure 9.1.

Deguisier Formation, Kinojévis Group

The geological history of the Beattie area begins at 2720 - 2718 Ma (Zhang et al., 1993) with the eruption of the Deguisier Formation. Geochemical investigations using both major and rare earth elements indicate a volcanic island arc setting, while not entirely precluding a mid-oceanic ridge setting. Altogether, the formation reaches a thickness of approximately 4.3 km (post-deformation and metamorphism).

Outside the Beattie area, the Deguisier Formation is dominantly represented and begins with pillowed basalts likely erupted in a submarine environment. These basaltic flows are accompanied by thin bands of rhyolite which appear between the flows (see Figure 9.1a). The Deguisier Formation also is also rarely accompanied by bands of magnesian basalt from the 2723 - 2720 volcanic episode (previously known as the Stoughton-Roquemaure assemblage). These bands attain a maximum thickness of 370 m (post-deformation and metamorphism) and are primarily confined to the base of the Deguisier Formation (Goutier and Beausoleil, 2000).

In the Beattie area, the base is composed of pillowed basalts. These basalts again likely erupted in a submarine environment (see Figure 9.1b). Overlying the basalt are andesites to dacites which are massive to occasionally pillowed (see Figure 9.1c). This change could, but not necessarily, be the result of subaerial exposure caused by thickening of the volcanic arc. At the stratigraphic top are rhyolites (see Figure 9.1d) accompanied by additional andesites to dacites. Whether the rhyolite erupted in a submarine or subaerial environment and is the result of flow or a dome remains elusive pending additional research.

Lanaudière Formation, Kinojévis Group

Overlying the Deguisier is the Lanaudière Formation which has been U-Pb zircon dated at 2718 ±2 Ma (Zhang et al., 1993). In the Beattie area, rocks of this formation consist of volcanic submarine komatitic basalts and komatiites (see Figure 9.1e). The komatitic basalts have been described by Capus (1988) as either pillowed or as flow breccias whereas komatiites are massive, occasionally pillowed with a spinifex texture. Unfortunately, the lack of detailed observations and geochemical analyses prevents the attribution of a tectonic setting.

Gabbro

The next episode is characterized by the intrusion of gabbro constrained at an age between 2717 - 2716 Ma (this thesis). Field relationships indicate that the gabbro intrudes into both the Deguisier and Lanaudière Formations (see Figure 9.1e). Younger gabbro intrusions, as documented in the eastern portions of the Duparquet area, have been omitted from this discussion. Similarities between the gabbro and the Deguisier Formation are demonstrated both in REE and incompatible trace elements (see Section 7.6). As such, the gabbro seems related to the same magmatic source that gave rise to the Deguisier Formation. Similar investigations with the Lanaudière Formation have not been performed in the context of this thesis. Therefore, from both field and geochemical investigations, the gabbro is hypothesized to have intruded immediately post-chronously with respect to the Deguisier and Lanaudière Formations.

Hébécourt Formation, Blake River Group

After approximately 12 Ma of quiescence was the 2704 - 2695 Ma (Mercier-Langevin et al., 2011) volcanic episode, previously known as the Blake River assemblage. Rocks from this episode were initially located southeast of the Deguisier and Lanaudière Formations, separated by an unknown distance. The Blake River Group has been interpreted as a caldera cluster by Pearson and Daigneault (2009). However, the lack of volcaniclastic - pyroclastic deposits near the calderas (Goutier, pers. comm., 2011) led Rogers (2010) and Mercier-Langevin et al. (2011) to suggest a series of overlapping volcanoes on a submarine volcanic plain (see Figure 9.1f). The group consists of 4 major cycles of submarine volcanism and volcaniclastic sequences, of which the Hébécourt Formation (one of 9 formations) composes the base.

First shortening event

Between 2694 - 2692 Ma (Legault et al., 2005) was the first major shortening event (D_1) which resulted in the formation of large scale folds, tilting all stratigraphic groups to the current southern polarity (Goutier and Lacroix, 1992; Legault et al., 2005) (see Figure 9.1g). The shortening also produced some uplifting wherein erosion occurred and gave rise to the Porcupine and Kewagama Group sediments.

Quartz-feldspar porphyry

Following D_1 was a periodic, local N-S extensional period, between 2692 - 2680 Ma (Legault et al., 2005). This extension permitted the intrusion of dykes to masses of the QFP (see Figure 9.1h) dated at $2689.4\ ^{+3.2}_{-2.9}$ Ma (Mueller et al., 1996). The QFP has been structurally emplaced at shallow depths (Goutier and Lacroix, 1992).

Porcupine Group and Mont-Brun Formation, Kewagama Group

The periodic extensional period also created basins. These basins accumulated deep marine sediments, dated between $< 2687 \pm 2$ Ma (Ayer et al., 2005) and $> 2682 \pm 3$ Ma (Mortensen, 1993), possibly in a deep sea fan environment, with local variations in sediment type (see Figure 9.1i). Specifically, both the Porcupine (north) and Kewagama Groups (south) contain mudrocks and greywackes, but only the Porcupine Group contains a polymict conglomerate.

Field observations and hand-sample petrography reveal that conglomeratic lenses measure < 10 m in thickness (post-deformation and metamorphism). As such, the hypothesized initial thickness as estimated from the amount of elongation observed in the clasts would not have surpassed 20 - 25 m (provided that shortening was equal across the scales). Furthermore, no evidence of a regolith or paleosol was found. Consequently, such thin conglomeratic lenses combined with mudrocks and greywackes, and the absence of a regolith or palosol indicate a deep marine setting wherein the conglomerate and greywacke lenses were deposited and possibly reworked by turbiditic currents.

Beattie syenite

The N-S extensional period also permitted the intrusion of the Beattie syenite pluton, dated at 2682.9 ± 1.1 Ma (David et al., 2007) and 2681.5 ± 1.0 Ma (Mueller et al., 1996) (see Figure 9.1j). Geochemical investigations have determined that the Beattie syenite likely originated from an anhydrous crustal melt (see Section 7.7). The Beattie syenite is not only composed of a series of E-W elongated lens and dykes but also of five petrographically distinct comagmatic units.

The depth of intrusion of the Beattie syenite is hypothesized to be shallow, less than 10 km. Shallow plutons commonly intrude the country rocks in an irregular fashion. Such is the case for the Beattie syenite which exhibits dykes, offshoots and contains numerous small to large xenoliths. Perfect examples of dykes and offshoots of the porphyritic Beattie syenite unit dominate the SCB and NEB (see Figure 6.1 or accompanying geological map presented in Appendix B). Cooling in shallow plutons is typically rapid as the epizone is characterized by relatively cool (< 300 °C) rocks. However, in the case of the Beattie pluton, the porphyritic aspect upheld by the majority of the units and the aphanitic matrix reveals that the pluton was sharply undercooled, with the matrix initially forming a near vitrophyric texture. Further evidence is exhibited by the small size of the pluton and sharp contacts which are typical of shallow intrusions.

The Beattie syenite was likely injected via feeder zones and flowed laterally eastwards. The exact locations of the feeder zones were not observed, but are hypothesized to occur at the westernmost portions of the syenite. This hypothesis is weighed by a gradation from

undisturbed[1] country rocks through a zone of increasing density of syenitic dykes and tongues extending from the pluton, whereas the remainder of the syenite demonstrates a sharp contact with the country rocks. The intrusion of the syenite could have been facilitated by the competence contrast between the Deguisier Formation and the Porcupine sediments. The intrusion would have then flowed eastwards exploiting the regional stratigraphy, and possibly competence contrasts between the units of the Deguisier formation and the Porcupine sediments. The evidence of flow was determined by the E-W orientation of tabular feldspar phenocrysts of the widespread porphyritic Beattie syenite unit.

The Beattie pluton demonstrates a history of multiple comagmatic injections which directly translate to the petrographic units. Interestingly, the petrographic units are also spatially organized. Specifically, the western parts of the Beattie syenite contain the porphyritic Beattie unit and the equigranular magnetite-bearing unit. Progressing east is the porphyritic Central Duparquet and finally the megaporphyritic units (see accompanying geological map, Appendix B). The arrangement is hypothesized to be the result of an eastern migration of the injections. As such, the sequential emplacement of the units would have begun with the porphyritic Beattie unit which flowed eastwards. It was then followed by the intrusion of the equigranular magnetite-bearing unit prior to the complete cooling of the westernmost parts. As the injections progressed eastwards, the porphyritic Central Duparquet followed, where in the BDB it formed smaller shaped lenses since the porphyritic Beattie unit was almost completely crystallized. Further east, in the CDB, the porphyritic Beattie unit yields to the Central Duparquet unit along a 400 m transition. Subsequently, the megaporphyritc unit was injected into the mostly crystallized porphyritic Central Duparquet, as witnessed by the occasional gradationnal contact. The final injection stage consists of lath syenite dykes which transect every syenitic unit. The sharp contact of the dykes indicate that all the other syenitic units had extensively cooled. An early onset of the second shortening (D_2) event (see below) seems unlikely to have effected the intruding syenite, whereas displacements of the nearby PDFZ would have resulted in the formation of small phenocrysts of the porphyritic Beattie syenite unit, whereas further away from the PDFZ larger crystals could have formed. Detailed petrographic studies have in fact attributed the lack or small phenocryst size near the PDFZ to be the result of subsequent cataclasm and hydrothermal activity (see Chapter 8).

[1] disregarding subsequent deformation and regional metamorphism

The porphyritic aspect and aphanitic matrix of most of the petrographic units suggest that the Beattie syenite was sharply undercooled. In this case, the exsolution of the hydrous volatile phase quickly undercooled the syenite causing the widespread vitrophyric texture observed in the matrix, without significantly lowering the temperature of the system. This exsolution of the hydrous volatile phase was permitted by the shallow depth of the intrusion, where pressure changes can cause sufficient loss of hydrous volatiles to drive rapid undercooling (Lowenstern et al., 1997). Such dramatic pressure changes are only possible when plutons are <3 km deep and therefore further constraining the intrusion depth of the Beattie syenite. However, the cause of this pressure change such as from dome growth, an eruption or the creation of new dyke-conduits could not be determined due to subsequent erosion.

Latent heat in the Beattie syenite also resulted in the devitrification textures observed in most of the syenitic units. This is logical, since crystals in the matrix appear as slightly radiating fibrous crystals with a diffuse to sutured margin. Devitrification is interpreted to have occurred prior to hydrothermal alteration (see below) since hydrothermal minerals clearly cut the devitrified matrix. This heat would have also resulted in additional spinodal decomposition seen by the jagged, uneven and irregular exsolution textures exhibited by the feldspar phenocrysts. However, the effects of devitrification could have locally varied in extent; that in places, the feldspar phenocrysts possess a rather jagged transition from albite to orthoclase while elsewhere, igneous features such as the crypto-mesoperthite rims have been preserved.

Second shortening event, hydrothermal alteration and Au-mineralization

Almost immediately after the intrusion of the Beattie syenite was the onset of the second N-S shortening event (D_2) (see Figure 9.1k), accompanied by major hydrothermal alteration and accompanying Au-mineralization.

First and foremost, this period created the far-reaching PDFZ. Structural studies of the PDFZ reveals that it corresponds to a complex superposition of multiple faults which were active over several events (Goutier, 1996). Reverse dextral displacement by the PDFZ transported the Kewagama and Blake River Groups northwest (Goutier and Lacroix, 1992; Goutier, 1996), to overlap the Lanaudière Formation. Additionally, the fault zone contains lenses of spinifex-bearing altered komatiites from the Lanaudière Formation (Graham, 1954). Later on, the D_2 also created several large dextral strike-slip, E-W striking faults which transect most

lithologies. Displacement of these faults in turn effected the PDFZ (Goutier and Lacroix, 1992). However, these faults are not necessarily extensions of the PDFZ as they cover a broad age range. Specifically, some faults are older and some younger than the Duparquet Formation.

The large dextral strike-slip D_2 faults in turn created numerous, E-W trending, secondary shear faults. These shear faults are abundant in proximity of the PDFZ. In the syenite, shear faults are coated with tourmaline slikenfibers, implying a slow aseismic creep (Twiss and Moores, 1992). Furthermore, shear faults also produced a series of conjugate shear and extension fractures. The conjugate shear fractures generally strike E-W and dip at $\sim 45^{\circ}$ from each other. The exact chronology of the conjugate shear fractures could not be determined as they have interacted with each other. This interaction indicated prolonged activity caused by the slow, continuous creeping displacements of the shear faults, which were in turn affected by the displacement episodes of the PDFZ. Extension fractures strike N-S with most terminating by dying out or uncommonly terminating in a series of en-echelon fractures (see Section 6.3).

The creation of numerous faults permitted the channelling and infiltration of hydrothermal fluids. Their evolution is presented in Figure 9.2. It is well known that the PDFZ channelled primarily CO_2- and lesser amounts of H_2O-fluids in the Beattie area. Additionally detailed geochemical studies have demonstrated that the hydrothermal fluids were also enriched in K_2O, Mo, Rb, S, As, Ag, and Au (see Section 8.2.1). First, the influx of CO_2-fluids altered and replaced clinopyroxene, and produced disseminated carbonate minerals throughout the syenite. Lesser amounts of H_2O-fluids resulted in the alteration of clinopyroxene to chlorite which was subsequently dissolved, transported and precipitated in conjugate shear and extension fractures. Subsequently, K_2O combined with minor amounts of H_2O resulted in the formation ferrian-muscovite veins in the Beattie syenite. Sericitization occurred immediately after carbonatization as the veins replace carbonate minerals in clinopyroxene relicts, transect or have deformed disseminated carbonate minerals. The influx of sericite likely contributed to the alteration of carbonate minerals (currently observed) and the remobilization of chlorite. Finally, sulphur, arsenic, silver and gold occur as cryptocrystalline inclusions in, or as pyrite and arsenopyrite. Both sulphides appear as disseminated crystals in contact zones and in areas demonstrating repeat brittle deformation. Only rarely do the disseminated sulphide minerals appear as an irregular-shaped mass which overprint the syenite. Both pyrite and arsenopyrite do not interact with carbonate minerals, chlorite and sericite, indicating the termination of

chloritization and sericitization, and a pause for carbonatization. In hand sample sulphide mineral veins cut both small chlorite and sericite veins. Microscopically, the sulphides overprint both carbonate minerals and sericite, indicating that they are post-carbonatization and sericitization. The irregular-shaped masses of sulphide minerals are often accompanied by quartz, suggesting minor subsequent remobilization of the sulphide minerals.

A long standing question is: What is the relationship between Au-mineralization and the Beattie syenite? From geochemical investigations, it was demonstrated that gold was channelled by D_2 faults (see Section 8.2.1). Gold is therefore structurally controlled rather than being directly associated with plutonism. Along the PDFZ, Au-mineralization is more prevalent near bends in the fault (Robert, 2012). This increase in Au-mineralization can be explained by the distribution of strain where areas of lower strain represent the best candidates for the precipitation of gold. Strain distributions along fault bends demonstrate lower pressures in the bends and adjacent areas, whereas pressures are increased at the outer edges of the bend. As such, theoretical PDFZ strain models by Faure and Rafini (2009) demonstrate that the Beattie syenite, which occurs in a bend, is located in an area ($\sim$65 km^2) of low pressure. Looking on a finer scale, most of the ore was located in the Porcupine sediments (i.e., Beattie mine), in the Deguisier andesite to dacite (i.e., Donchester mine) as well as along contacts or fractures in the syenite (i.e., Beattie and Central Duparquet 2 mine). Ore in the Porcupine sediments is separated from the PDFZ by the Beattie syenite (see accompanying geological map, Appendix B). In this scenario the syenite, which is a competent cohesive body, would have taken much of the strain from the PDFZ resulting in even lower pressures in the Porcupine sediments, producing the perfect low pressure environment for gold precipitation. Ore contained in fractures in the Deguisier andesite to dacite could have formed in a similar fashion given that geochemical investigations have not effectively demonstrated that a higher Fe/Mg ratio is principally responsible (see Section 8.2.1). Consequently, the andesite to dacite's proximity to the PDFZ would have resulted numerous fractures. Given that the Au-mineralization in the Deguisier andesite to dacite rests principally between syenitic lens, it is possible that the syenite once again reduced strain by partially shielding them. Au-fluids would have then precipitated in the fractures, possibly helped by a slightly higher Fe/Mg ratio of 2.93 compared to the basalt which has a ratio of 1.46 (see Section 8.2.1). Finally, ore at the contacts and in the Beattie syenite could have also taken advantage of lower strain rates

to precipitate.

Duparquet Formation, Timiskaming Group

At $< 2679 \pm 3$ Ma (David et al., 2006) an episode of uplifting, permitting erosion (including the Beattie syenite) resulted in the creation of the Duparquet Formation sediments (see Figure 9.1l). The formation principally consists of a polymict conglomerate with extraformational clasts, ranging from cobbles to boulders. Conglomerate lens are much thicker and widespread compared to the older Porcupine Group ones. As such, the Duparquet sediments were probably deposited in a non-marine, fluvial or deltaic environment. This interpretation is in agreement with the observation of numerous erosional discordances as well as developed paleosols within the stratigraphic sequence in the AGB (Mueller et al., 1994; Ayer et al., 2005).

Regional metamorphism

Also synchronous with D_2 shortening was the onset of static regional metamorphism which lasted between 2677 - 2643 Ma (Powell et al., 1995). Regional metamorphism in the Beattie area corresponds to the greenschist facies, specifically the actinolite-epidote sub-facies. Detailed studies by Powell et al. (1995) yielded metamorphic conditions of 220 MPa and 250°C.

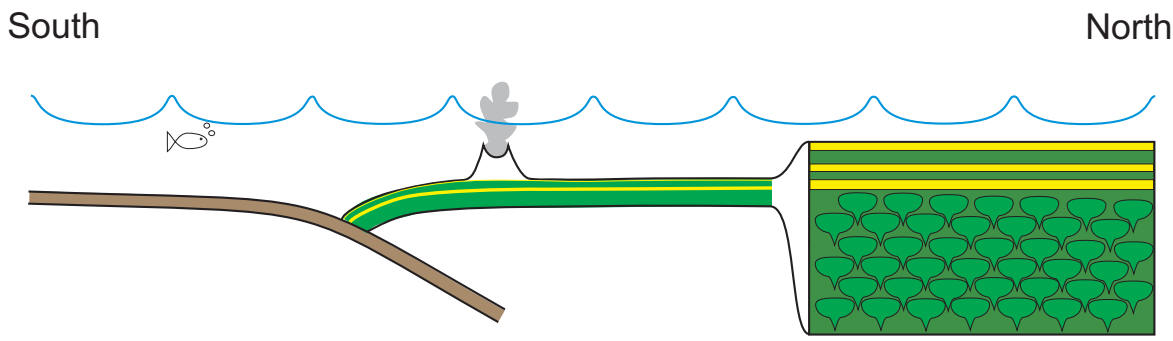
Regional metamorphism in the Beattie area is mineralogically denoted by chlorite and prehnite in the Deguisier basalt and andesite to dacite units (Goutier and Lacroix, 1992). As for the rhyolite, paragonite dominates, determined with NORMAT calculations (see Section 8.2.2). The greenschist mineralogical assemblage for sediments was not observed nor calculated.

In the Beattie syenite, the effects of metamorphism are best observed in the equigranular magnetite-bearing unit. Particularly, metamorphism resulted in the creation of epidote, porphyroblasts of hornblende and the alteration of clinopyroxene to actinolite with subordinate amounts of titanite and oxides. There is very little evidence of retrograde metamorphism. The only evidence is observed in small amounts of calcite replacing actinolite. As for the other units of the Beattie syenite, metamorphism is not as evident. Rather, metamorphic minerals are found in veins accompanied by CO_2-fluids from the PDFZ. At first the CO_2-fluids were accompanied by albite which transitioned to quartz over time (see Figure 9.2). Veins of albite and carbonate minerals occupy the central portions of sulphide mineral veins. Occasionally

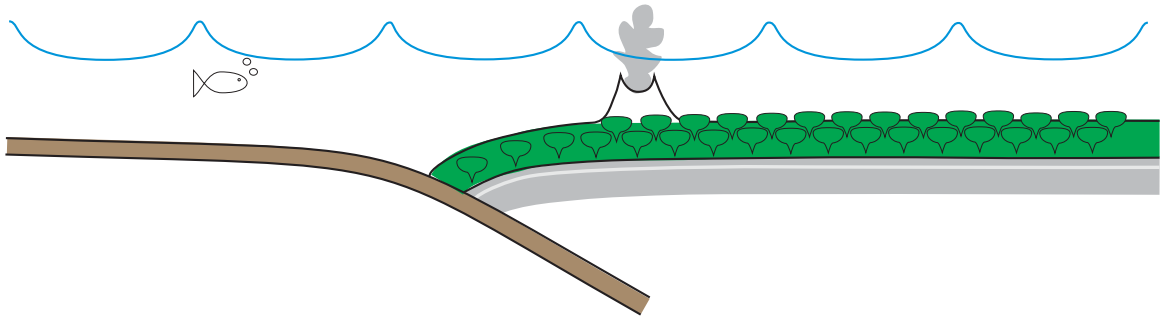
lesser amounts of quartz also occupy the centre of the veins. The albite and carbonate mineral veins are cut by quartz, albite and carbonate mineral veins. Finally, veins containing principally quartz with lesser amounts of carbonate minerals transect all veins. Occasionally, veins described above are at the centre of pre-existing chlorite-filled conjugate shear and extension fractures. Specifically, chlorite is often found at the outer margins of the vein with a mixture of the other minerals at the centre. Some chlorite dissolution, transportation and precipitation also occurred at this stage, observed by a few chlorite crystals at the vein-centre.

Third shortening event and hydrothermal mineralization

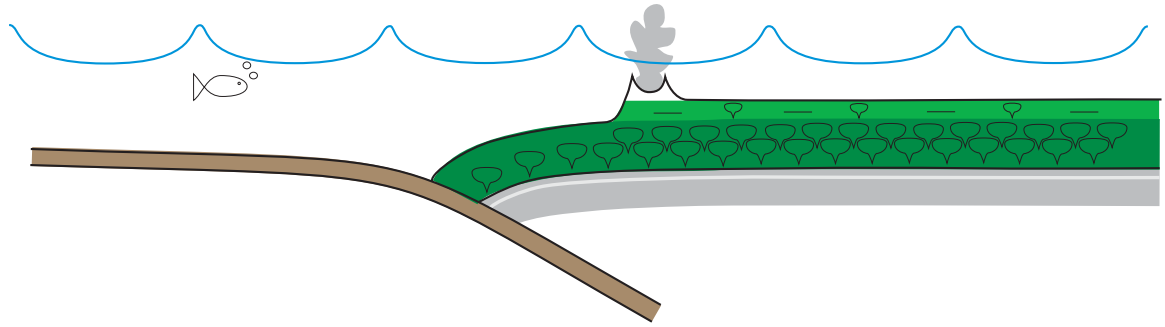
The last significant event in the petrogenesis of the Beattie area was another shortening event (D_3) which was accompanied by hydrothermal minerals. This last shortening event affected all rocks and structures as they are cut by numerous conjugate faults. These faults either strike NE-SW or NW-SE and are equally divided between a dextral or sinistral displacement. The faults are accompanied by quartz and carbonate mineral veins (see Figure 9.2). Larger 100 m long, 30 cm wide, NW-SE striking, quartz and carbonate minerals tension veins found in syenite and gabbro near D_3 faults may occasionally contain gold. The vein's arrival was quite late (i.e., syn-D_3) with an age between 2670 - 2671 Ma (Legault et al., 2005) as they are not deformed and support minimal alteration. Gold in these veins is in a free state and is accompanied by chalcopyrite, pyrite, tetrahedrite, arsenopyrite, sphalerite and galena.



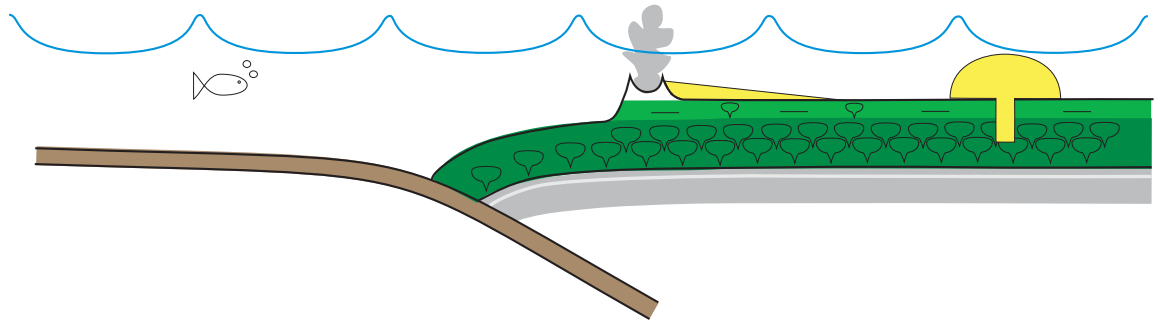
(a) 2720 - 2718 Ma: Beginning of the Deguisier Formation outside the Beattie area, likely erupted in a volcanic arc setting. This sequence is charaterized by pillowed basalts (green with pillows) and thin rhyolitic lens (yellow).



(b) 2720 - 2718 Ma: Continuation of submarine volcanism with the eruption of pillowed basalts (green with pillows) composing the stratigraphic base of the Beattie area. The basalts (dark grey) and thin rhyolite lens (pale grey) outside the Beattie area are underneath.

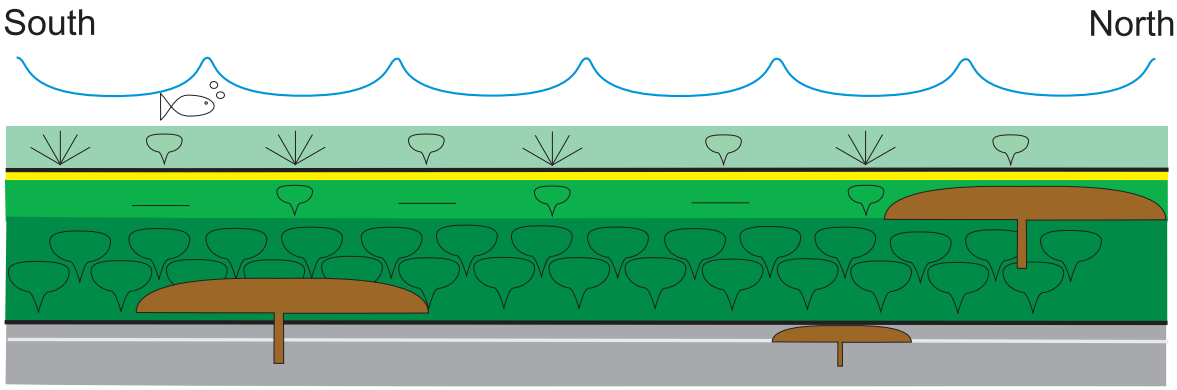


(c) 2720 - 2718 Ma: Eruption of pillowed to massive andesite to dacite (pale green with pillows and horizontal lines) overlaying pillowed basalts. Whether the andesite to dacite was erupted in a submarine or subaerial environment remains inconclusive.

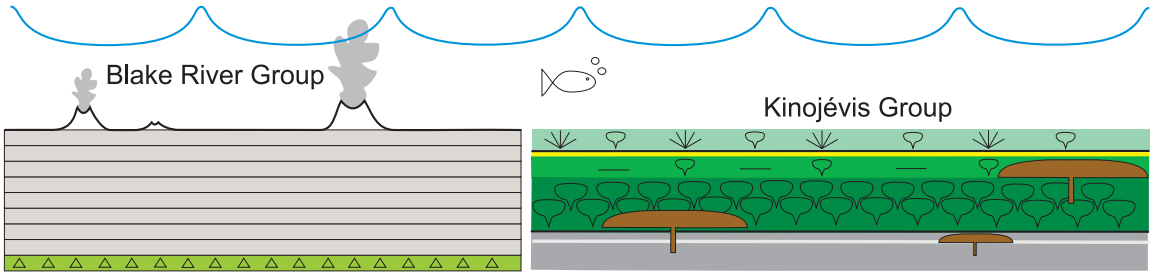


(d) 2720 - 2718 Ma: Eruption of rhyolite (uniform yellow). However, whether the rhyolites is the product of a volcanic flow (left) or dome (right) remains unclear.

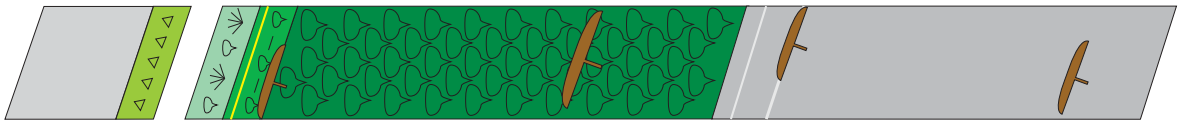
Figure 9.1 – First 4 sub-figures of the petrogenetic model of the Beattie area.



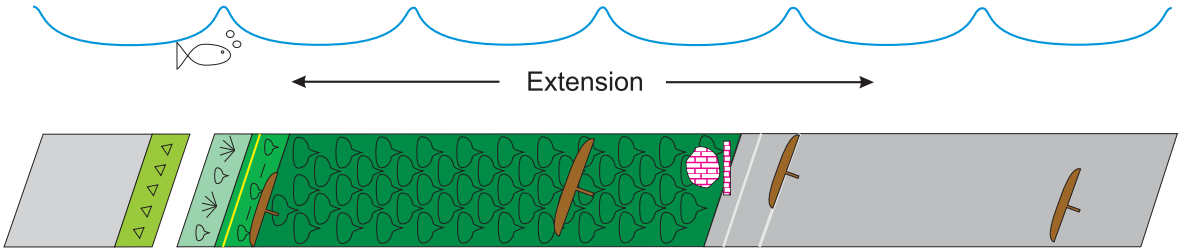
(e) 2718 - 2716 Ma: Eruption of the Lanaudière Formation (teal with pillows and radial lines), characterized by komatitic basalts as pillowed or flow breccias, and komatiites as massive, occasionally pillowed with a spinifex texture. Subsequently, the gabbro (uniform brown) intruded both in the Deguisier and Lanaudière Formations.



(f) 2703 - 2701 Ma: Eruption of the Blake River Group from a series of overlapping volcanoes located south of the Deguisier and Lanaudière Formations. The Hébécout Formation is at the base of the group (bright green with triangles) with the remaining formations in grey.

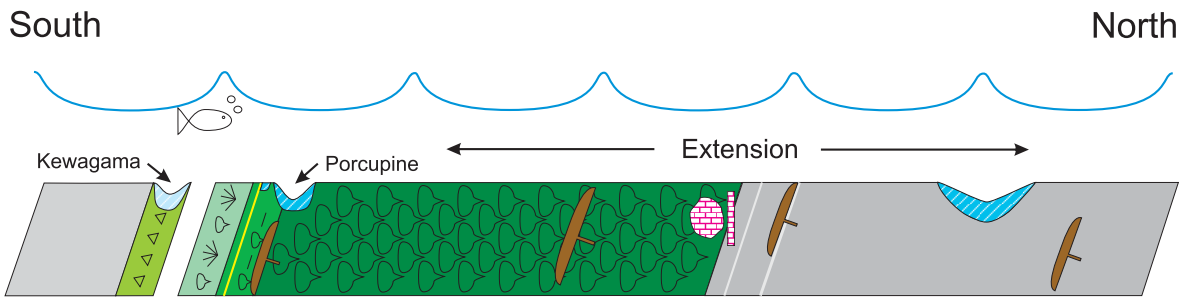


(g) 2694 - 2692 Ma: D_1 shortening event which produced large scale folds tilting all stratigraphic groups.

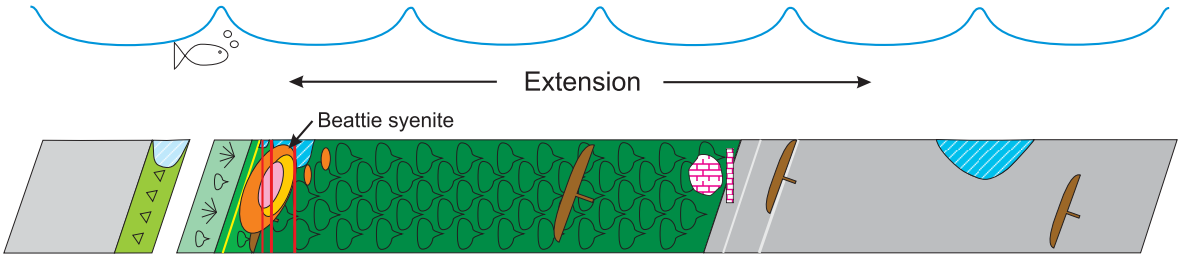


(h) 2692 - 2680 Ma: Extensional period with the intrusion of masses and dykes of the QFP (pink bricks) at 2689.4 Ma.

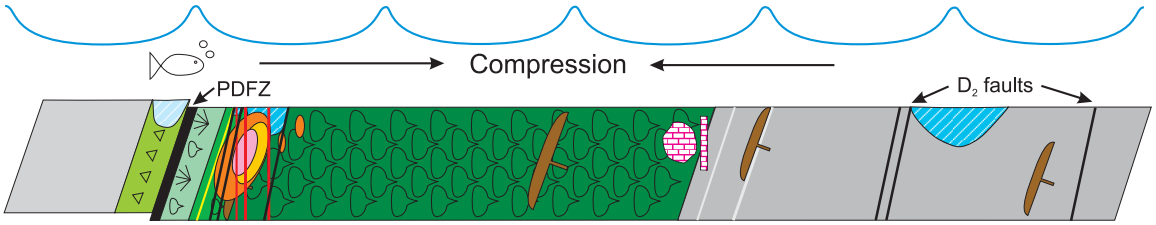
Figure 9.1 – Sub-figures 5 to 8 of the petrogenetic model of the Beattie area.



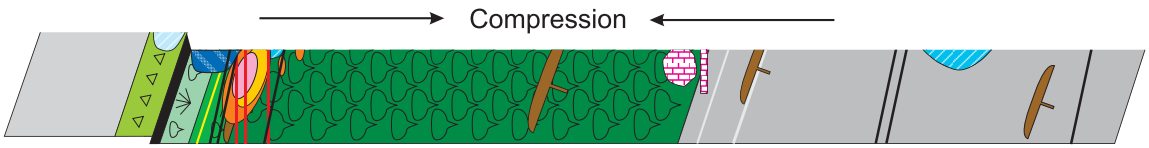
(i) 2686 - 2683 Ma: Creation of deep marine basins which accumulated the Porcupine sediments and the Kewagama Group sediments (blue and pale blue with diagonal lines).



(j) 2682.9 - 2681.5 Ma: Intrusion of the Beattie syenite. The syenite is the result of multiple comagmatic injections at shallow depth (< 10 km). The injections began in the Porcupine sediments and progressed eastwards (see accompanying geological map, Appendix B).



(k) ≤ 2680 Ma: Onset of the D_2 shortening event. This event created the PDFZ which in turn transported the Kewagama and Blake River Groups northwest to overlap the Lanaudière Formation. The D_2 event also created numerous E-W trending faults (black lines), permitting the infiltration and channelling of numerous hydrothermal fluids. The evolution of hydrothermal fluids is presented in Figure 9.2.



(l) < 2679 Ma: Uplifting, erosion and subsequent accumulation of the Duparquet Formation sediments (dark blue with white diagonal lines) in a non-marine, fluvial or deltaic environment.

Figure 9.1 – Petrogenetic model of the Beattie area. Schematic longitudinal sections are not to scale. Uniform grey colours are for units/formations located outside the limits of the study area.

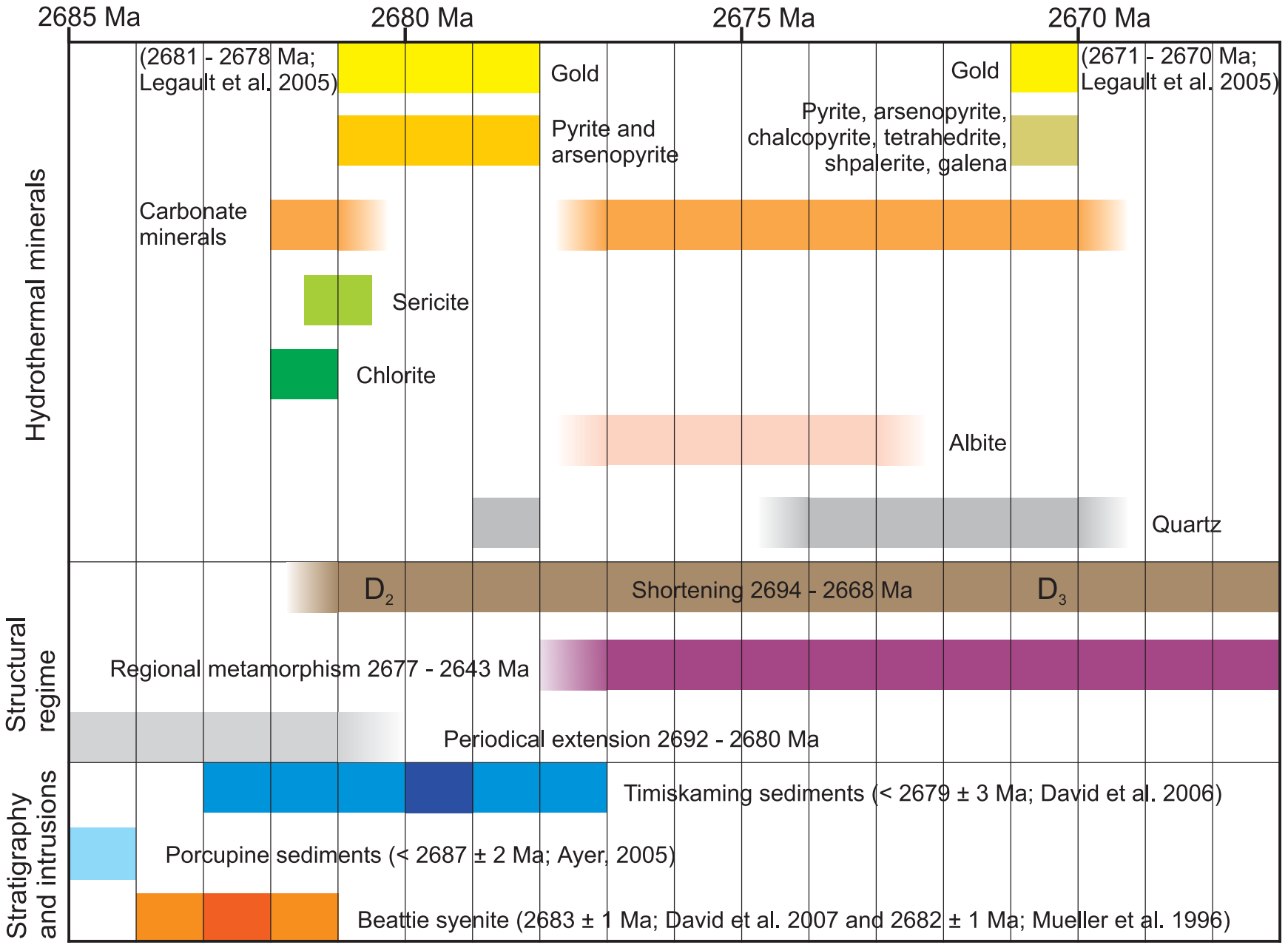


Figure 9.2 – Hydrothermal fluid evolution in the Beattie area after the intrusion of the Beattie syenite.

Chapter 10

Conclusion

The Archean Beattie syenite is composed of a series of syenitic lens that occur immediately north of the PDFZ in the town of Duparquet, approximately 32 km north of Rouyn-Noranda in the Abitibi Subprovince. The syenite was host to 4 gold mines which were in production from the early 1930s to the late 1950s, yielding a combined total of approximately 35 million grams of gold. Because of its strong association with gold mineralization, the Beattie syenite was the subject of intense study and exploration which provided a base for this thesis. However, after the closure of the mines, documentation of the syenite ceased. Consequently, this study produced an updated geological map of the area with the first incorporation of the five petrographic units. Additionally, this study described the petrological, mineralogical and geochemical properties of the Beattie syenite which led to a better understanding of the petrogenesis and the postmagmatic alteration of the rocks.

Petrological and mineralogical investigations resulted in the identification of 5 petrographic units. They are, chronologically:

1- The porphyritic Beattie syenite unit, composed of 2 - 10$\%_m$ of tabular sub- to anhedral feldspar phenocrysts (2 - 10 mm) set in a red feldspathic and aphanitic matrix.

2- The equigranular magnetite-bearing syenite unit which lacks or is composed of very few feldspar phenocrysts (2 - 10 mm) set in a fine-grained matrix. It is characterized by unaltered titanite, metamorphic epidote, actinolite and hornblende porphyroblasts.

3- The porphyritic Central Duparquet syenite which contains between 2 - 25$\%_m$ of coarse equant euhedral feldspar phenocrysts (5 - 16 mm) in a red or sometimes grey aphanitic matrix.

4- The megaporphyritic syenite unit, composed of very coarse alkali feldspar phenocrysts (1 - 6 cm) which often demonstrate a glomeroporphyritc texture and are set in a red aphanitic matrix.

5- The lath syenite unit which occurs as numerous thin dykes, on the order of a few meters in width, that cross-cut all other petrographic units. The lath dykes display a characteristic trachytoid texture defined by the preferential alignment of alkali feldspar laths (1 - 3 cm) in a grey or red aphanitic matrix.

The identification of the units combined with geochemical investigations led to the proposal of a petrogenetic model for both the Beattie syenite and country rocks. First, basalts to rhyolites of the Deguisier Formation (2720 - 2718 Ma) erupted, likely in a volcanic arc setting. Afterwards was the eruption of the Lanaudiére komatiites and komatitic basalts over the Deguisier Formation. Both formations were subsequently intruded by gabbro (2717 - 2716 Ma) which demonstrates chemical similarities with the Deguisier Formation. After a pause of 12 Ma, the 2704 - 2695 Ma (Mercier-Langevin et al., 2011) volcanic episode (Blake River assemblage) erupted further southeast. Afterwards was a first shortening event (D_1) which tilted all lithologies. This shortening was followed by an extensional period facilitating the intrusion of quartz feldspar porphyries (2689 Ma), the formation of basins permitting the accumulation of the Porcupine and Kewagama sediments ($<$ 2687 - $>$ 2682 Ma) and finally the intrusion of the Beattie syenite (2683 - 2682 Ma). The syenite was determined to have been injected at shallow depths ($<$ 3 km) and is the product of multiple injections that progressed eastwards, yielding the five comagmatic units. After the crystallization of the syenite was the onset of a second shortening event (D_2) which created the PDFZ, numerous E-W trending shear faults, and was accompanied by hydrothermal fluids. These fluids first consisted in the carbonatization and chloratization, followed by the sericitization of the syenite. Afterwards was the first Au-mineralization episode (2681 - 2678 Ma) where gold is found in disseminated pyrite and arsenopyrite. This Au-mineralization was channelled by D_2 shear faults and preferentially precipitated in zones of low strain. Synchronously with the second deformation episode was the accumulation of the Duparquet Formation sediments ($<$ 2679 Ma) and the onset of regional metamorphism to the greenschist facies (2677 - 2643 Ma). Regional metamorphism resulted in the influx of albite, carbonate minerals and quartz. Finally, a third shortening event (D_3) pro-

duced numerous strike-slip faults and was accompanied by a second Au-mineralization event (2671 - 2670 Ma), this time as free gold in quartz and carbonate mineral veins.

In the spirit of future research on the subject of the Beattie syenite, an isotopic study should give better constraints on the petrogenetic processes that led to the formation of five comagmatic units. Nd isotope data should help identify if any crustal contamination occurred. Furthermore, a 3D model of the syenite is now feasible with all drill core data that was made available in the course of this project. This model should help to track the distribution of the syenitic units and possibly identify other zones of interest (e.g., feeder zones, Au-mineralized zones, etc.). U-Pb zircon dating of all the units should also help better constrain the age of the syenite (since both obtained dates are from the megaporphyritic unit). The ages would also help to track the progression and rate of syenitic injections. Finally, an investigation of the Beattie syenite compared to the other intrusions along the PDFZ (e.g., Iris, Ludgate, Garrison, Pangea, etc.) could help identify if these intrusions support any relationship to a similar or different mantle reservoir.

Future research in the Beattie area would also include an isotopic study in an attempt to yield better constraints in petrogenetic processes and to cement the relationship between the Deguisier Formation and the gabbro. A detailed study of the Deguisier rhyolite is needed to ascertain whether the unit is the product of a volcanic flow or dome. U-Pb zircon dating of the Deguisier Formation would also help constrain an age. Furthermore, dating of the cycles and units would help track the progression and rate of formation of an Archean volcanic arc.

References

Anonymous (2010). Diamond drill hole log, Dumico project. Ministère des Ressources naturelles, Report GM 65358, pp. 149.

Archibald, F. R., Martin, F. J., and Koenen, A. T. (1935). The separation of pyrite from arsenopyrite in Beattie ore. Beattie research report.

Archibald, F. R., Martin, F. J., and Koenen, A. T. (1936a). The classification of syenite residue into sizes and the analyses of fractions. Beattie research report.

Archibald, F. R., Martin, F. J., and Koenen, A. T. (1936b). The separation of minerals from the Beattie concentrate and the relation of gold extraction to mineral content. Beattie research report.

Archibald, F. R., Martin, F. J., and Koenen, A. T. (1937). The elimination of arsenic in flotation tailings without sacrificing gold recovery. Beattie research report.

Archibald, F. R., Martin, F. J., and Koenen, A. T. (1939). Roasting of Beattie concentrate. *The Canadian Institute of Mining and Metallurgy*, 42:608–631.

Archibald, F. T. (2008). 2008 diamond drilling program, Dumico property. Ministère des Ressources naturelles, Report GM 64140, pp. 20.

Armbruster, T., Bonazzi, P., Akasaka, M., Bermanec, V., Chopin, C., Gieré, R., Heuss-Assibichler, S., Liebscher, A., Menchetti, S., Pan, Y., and Pasero, M. (2006). Recommended nomenclature of epidote-group minerals. *European Journal of Mineralogy*, 18:551–567.

Ayer, J. A., Amelin, Y., Corfu, F., Kamo, S. L., Ketchum, J. W. F., Kwok, K., and Trowell, N. (2002). Evolution of the southern Abitibi greenstone belt based on U-Pb geochronol-

ogy: Autochtonous volcanic construction followed by plutonism, regional deformation and sedimentation. *Precambrian Research*, 115:63–95.

Ayer, J. A., Goutier, J., Thurston, P., Dubé, B., and Kamber, B. (2010). Tectonic and Metallogenic Evolution of the Abitibi and Wawa Subprovinces. Ontario Geological Survey, Open file report 6260, pp. 424.

Ayer, J. A., Thurston, P. C., Bateman, R., Dubé, B., Gibson, H. L., Hamilton, M. A., Hathway, B., Hocker, S. M., Houlé, M. G., Hudak, G., Ispolatov, V. O., Lafrance, B., Lesher, C. M., MacDonald, P. J., Péloquin, A. S., Piercey, S. J., Reed, L. E., and Thompson, P. H. (2005). Overview of results from the greenstone architecture project: Discover Abitibi initiative. Ontario Geological Survey, Open file report 6154, pp. 146.

Bailey, S. W. (1988). Chlorites: Structures and crystal chemistry. In *Hydrous Phylosilicates (exclusive of micas)*, volume 19, pages 347–403. Mineralogical Society of America.

Banfield, A. F. (1940). *The Geology of Beattie Gold Mines (Québec) Limited, Duparquet, Québec, Canada*. PhD thesis, Northwestern University, Evanston, United States, pp. 205.

Bannerman, H. M. (1940). Lépine lake area, Destor Township, Abitibi county. Ministère des mines, Québec, Geological report RG-004 (A), pp. 35.

Bayliss, P. (1975). Nomenclature of trioctahedral chlorite. *Canadian mineralogist*, 13:178–180.

Beaudry, D. (1992). Analyse structurale des assemblages volcanosedimentaires au voisinage de la faille Porcupine - Destor, Abitibi, Québec. Master's thesis, Université du Québec a Chicoutimi, Chicoutimi, Canada, pp. 127.

Bevan, P. A. (2008). Technical report on Beattie-Donchester gold mine property, Duparquet township, Québec. Clifton Star Resources Inc., Report NI 43-101, pp. 80.

Bevan, P. A. (2011). Technical report on Donchester gold mine property, Duparquet township, Québec. Clifton Star Resources Inc., Report NI 43-101, pp. 76.

Bigot, L. (2012). Gold mineralizatio in the Archean Beattie syenite, Duparquet, Abitibi Belt, Québec, Canada. In *St. John, Association géologique du Canada, Association minéralogique du Canada, Program and Abstracts*, volume 35, page 11.

Bohlke, J. (1988). Carbonate-sulphide equilibria and stratabound disseminated epigenetic gold mineralization: a proposal based on examples from Alleghany, California. *Applied Geochemistry*, 3:499–516.

Boivin, P. (1974). *Pétrographie, stratigraphie et structure de la ceinture de schistes verts de Noranda dans les cantons de Hébécourt, de Duparquet et Destor, Québec, Canada.* PhD thesis, Université de Clermont, Clermont-Ferrand, France, pp. 133.

Buffam, B. (1927). Destor area, Abitibi County, Quebec. *Geological Survey of Canada*, pages 82–104.

Cameron, E. and Hattori, K. (1987). Archean gold mineralization and oxydized hydrothermal fluids. *Economic Geology*, 82:1177–1191.

Capus, G. (1988). Projet porcupine-est: Rapport de fin de saison. Cogema Canada limitée, Report GM 48562, pp. 173.

Chown, E., Harrap, R., and Moukhsil, A. (2002). The role of granitic intrusions in the evolution of the Abitibi belt, Canada. *Precambrian Research*, 115:291–310.

Colvine, A., Fyon, J., Heather, K., Marmont, S., Smith, P., and Troop, D. (1988). *Archean lode gold deposits.* Ministry of Northern development and mines. Ontario Geological Survey, Miscellaneous paper 139, pp. 136.

Cook, H. C., James, W. F., and Mawdsley, J. B. (2031). Geology and Ore Deposits of the Rouyn-Harricanaw Region, quebec. Geological Survey of Canada, Memoir 166, pp. 314.

Cox, K., Bell, J., and Pankhurst, R. (1979). *The interpretation of igneous rocks.* George, Allen and Unwin, London.

David, J., Davis, D. W., Dion, C., Goutier, J., Legault, M., and Roy, P. (2007). Datations U-Pb effectuées dans la Sous-province de l'Abitibi en 2005-2006. Ministère des Ressources naturelles et Faune, Québec, Report RP 2007-01, pp. 17.

David, J., Dion, C., Goutier, J., Roy, P., Bandyayera, D., Legault, M., and Rhéaume, P. (2006). Datations U-Pb effectuées dans la Sous-province de l'Abitibi à la suite des travaux

2004-2005. Ministère des Ressources naturelles et Faune, Québec, Report RP 2006-04, pp. 22.

Davidson, S. C. (1938). Geology of the Beattie mine. Private mine report.

Davidson, S. C. (1948). Beattie mine. The Canadian Institute of Mining and Metallurgy, Geological Division, In Structural Geology of Canadian Ore deposits, p. 692-701.

Davidson, S. C. and Banfield, A. F. (1944). Geology of the Beattie gold mine, Duparquet, Québec. *Economic Geology*, 39(8):299–315.

Davis, D. W. (2002). U-Pb geochronology of Archean metasedimentary rocks in the Pontiac and Abitibi subprovinces, Québec, constraints on timing, provenance and regional tectonics. *Precambrian Research*, 115:97–118.

Deer, W. A., Howie, R. A., and Zussman, J. (1992). *An introduction to the rock-forming minerals*. Pearson Prentice Hall, pp. 696.

Douglas, G. H., Wright, G. H., and Segsworth, W. E. (1924). Extension of the Porcupine gold belt into Québec. *Engineering and Mining Journal-Press*, 117(19):763–764.

Dupéré, M., Duplessis, C., and Gagné, C. (2011). Technical report mineral resource estimation Duperquet - Beattie property for Osisko Mining Corporation and Clifton Star Resources Inc. SGS Canada Inc., Report NI 43-101, pp. 109.

Eden, W. J. (1964). Earthflows at the Beattie mine, Québec, Canada. *Canadian Geotechnical Journal*, 1(2):104–114.

Eriksson, P. G., Altermann, W., Nelson, D. R., Mueller, W. U., and Catuneanu, O. (2004). *The Precambrian Earth: Tempos and Events*, volume 12 of *Elsevier B.V.* Developments in Precambrian Geology.

Faure, S. and Rafini, S. (2009). Modélisation des paléocontraintes le long de la Faille Destor-Porcupine: implication pour l'exploration aurifére. Forum technologique Consortium de recherche en exploration minérale (CONSORTEM) Divex, Presentation.

Feng, R. and Kerrich, R. (1992). Geochemical evolution of granitoids from the Archean Abitibi Southern Volcanic Zone and the Pontiac Subprovince, Superior Province, Canada: Implications for tectonic history and source regions. *Chemical Geology*, 98:23–70.

Gadoury, J. (1995). Rapport de forages propriété Central Duparquet. Exploration Fieldex Inc., Report GM 53555, pp. 93.

Gagnon, P. (1981). Rapport de géochimie d'humus et lithogéochimie: Projet d'Alembert. SOQUEM Inc., pp. 20.

Gélinas, L., Brooks, C., Perrault, G., Carignan, J., Trudel, P., and Grasso, F. (1976). Chemostratigraphic divisions within the Abitibi volcanic belt, Rouyn-Noranda district, Québec. Ministère des Richesses naturelles: Direction générale des mines, Report DVP 426, pp. 49.

Goutier, J. (1996). Géologie de la région de Duparquet. Ministère des Ressources naturelles du Québec et la section de l'Institut canadien des Mines, de la Métallurgie et du Pétrole, section de Rouyn-Noranda, In Métallogénie et évolution tectonique de la région de Rouyn-Noranda, edited by J. F. Couture et J. Goutier, Report MB 96-06, p. 41-44.

Goutier, J. and Beausoleil, C. (2000). Compilation géologique Duparquet. Ministère des Ressources naturelles et de la Faune, Québec, Carte géologique 32D11-200-0102.

Goutier, J. and Lacroix, S. (1992). Géologie du secteur de la faille Porcupine-Destor dans les cantons de Destor et Duparquet. Ministère des Ressources naturelles, Québec, Report MB 92-06, pp. 62.

Goutier, J. and Melançon, M. (2010). Compilation géologique de la Sous-province de l'Abitibi (version préléminaire. Ministère des Ressources naturelles et faune, Québec, Report RP 2010-04, pp. 3.

Goutier, J., Mercier-Langevin, P., McNicoll, V., and Ayer, J. (2010). The Abitibi subprovince: its evolution and its VMS deposits - an overview. In Wyche, S., editor, *Yilgarn - Superior workshop - Abstracts, Fifth International Archean Symposium*, number 20, pages 37–41. Geological Survey of Western Australia.

Graham, B. R. (1954). Parts of Hebecourt, Duparquet and Destor Townships, Abitibi-west county. Mineral Deposit Branch, Government of Québec, Geological Report 61, pp. 61.

Grant, J. A. (1986). The isocon diagram - a simple solution to Gresens' equation for metasomatic alteration. *Economic Geology*, 81:1976–1982.

Hallé, L. (1990). Campagne d'exploration 1989 - 1990: Projet Duparquet. Ressources minière Forbex Inc., Report GM 49711, pp. 71.

Harris, N. B. W., Pearce, J. A., and Tindle, A. G. (1986). Geochemical characteristics of collision-zone magmatism. *Geological Society, London, Special publications*, 19:67–81.

Henderson, P. (1984). *Rare earth element geochemistry.* Elsevier, Developments in Geochemistry 2.

Hodgson, C. J. (1993). Mesothermal lode-gold deposits. In Kirkham, R. V., Sinclair, W. D., Thrope, R. I., and Duke, J. M., editors, *Mineral deposit modeling*, volume 40, pages 635–678. Geological Survey of Canada.

Hopper, C. H. J. (1935). Geology of the Beattie mines. Private mine report.

Houlé, M. G., Ayer, J. A., Baldwin, G., Berger, B. R., Dinel, E., Fowler, A. D., Moulton, B., Saumur, B.-M., and Thurston, P. C. (2008). Field trip guidebook to the stratigraphy and volcanology of supracrustal assemblages hosting base metal and gold mineralization in the Abitibi greenstone belt, Timmins, Ontario. Ontario Geological Survey, Open file report 6225, pp. 84.

Houlé, M. G. and Lesher, C. M. (2010). Localization of komatiite-associated Ni-Cu-(PGE) mineralization in the Abitibi greenstone belt, Superior Porvince, Canada. In Wyche, S., editor, *Yilgarn - Superior workshop - Abstracts, Fifth International Archean Symposium*, number 20, pages 27 – 31. Geological Survey of Western Australia.

Irvine, T. N. and Baragar, W. R. A. (1971). A guide to the chemical classification of the common volcanic rocks. *Canadian Journal of Earth Sciences*, (8):523–548.

James, W. F. (1923). Duparquet map area, Québec. *Summary Report of the Geological Survey of Canada*, pages 75–96. map.

Jensen, L. (1976). A new cation plot for classifying subalkalic volcanic rocks. *Ontario division of mines, micellaneous paper 66*, pages 1–22.

Jiang, S.-Y., Wang, R.-C., Xu, X.-S., and Zhao, K.-D. (2005). Mobility of high field strength elements (HFSE) in magmatic-, metamorphic-, and submarine-hydrothermal systems. *Physics and chemistry of the Earth*, 30:1020–1029.

Jones, M. (1992). Variolotic basalts: Relations to Archean epigenetic gold deposits in the Abitibi Greenstone belt. Master's thesis, University of Ottawa, Ottawa, Canada, pp. 300.

Lacroix, S. and Landry, J. (1991). Géologie du secteur de la mine Duquesne: Region de Rouyn-Noranda. Ministère des Ressources naturelles et de la Faune, Québec, Report MB 91-06, pp. 36.

Lang, A. H. (1933). Gold prospecting rouyn-bell river region, Quebec. *Canadian Mining Journal*, 54(7):267–272.

Le Maitre, R. W., Bateman, P., Dudek, A., Keller, J., Lameyre Le Bas, M. J., Sabine, P. A., Schmid, R., Sorensen, H., Streckeisen, A., Wolley, A. R., and Zanettin, B. (1989). *A classification of igneous rocks and glossary of terms.* Blackwell, Oxford.

Leacke, B. E., Wooller, A. R., Arps, C. E. S., Birch, W. D., Gilbert, M. C., Grice, J. D., Hawthorne, F. C., Kato, A., Kisch, H., Krivovichev, V. G., Lintout, K., Laird, J., Mandarino, J. A., Maresch, W., Nickel, E. H., Rock, N. M. S., Schumacher, J. C., Smith, D. C., Stephenson, N. C. N., Ungaretti, L., Whittaker, E. J. W., and Youzhi, G. (1997). Nomenclature of amphiboles: report of the subcommittee on amphiboles of the international mineralogical association on new mineral and mineral names. *The Canadian Mineralogist*, 35:219–246.

Legault, M., Goutier, J., Beaudoin, G., and Aucoin, M. (2005). Synthèse métallogénique de la Faille de Porcupine-destor, Sous-province de l'Abitibi. Ministère des Ressources naturelles et de la Faune, Québec, Report ET 2005-01, pp. 35.

Legault, M. and Lalonde, A. (2009). Discrimination des syénites associées au gisements aurifères de la Sous-province de l'Abitibi, Québec, Canada. Ministère des Ressources naturelles et Faune, Québec, Report RP 2009-04, pp. 10.

Lenardic, A. (1998). On the partitioning of mantle helat loss below oceans and continents

over time and its relationship to the archaean paradox. *Geophysical Journal International*, 134:706–720.

Lowenstern, J. B., Clynne, M., and Bullen, T. D. (1997). Comagmatic A-tyoe granophyre and rhyolite from the Alid volcanic center, Eritrea, northeast Africa. *Journal of Petrology*, 38(12):1707–1721.

Macdonald, P. J., Piercey, S. J., and Hamilton, M. A. (2005). An intergrated study of intrusive rocks spatically associated with gold and base metal mineralization in the Abitibi greenstone belt, Timmins area and Clifford Township. Ontario Geological Survey, Discover the Abitibi initiative, Open file report 6160, pp. 190.

MacLean, W. H. and Barrett, T. J. (1993). Lithogeochemical techniques using immobile elements. *Journal of Geochemical Exploration*, 48:109–133.

McDonough, W. F. and Sun, S. S. (1995). The composition of the Earth. *Chemical geology*, 120:223–253.

McNicoll, V., Goutier, J., Dubé, B., Mercier-Langevin, P., Ross, P. S., Dion, C., Monecke, T., Legault, M., Percival, J., and Gibson, H. (in press). New U-Pb geochronology from the Blake River Group, Abitibi Subprovince, Québec: implications for geological interpretations and base metal exploration. *In press at Economic geology.*

Mercier-Langevin, P., Goutier, J., Ross, P.-S., McNicoll, V., Monecke, T., Dion, C., Dubé, B., Thurston, P., Bécu, V., Gibson, H., Hannington, M., and Galley, A. (2011). The Blake River Group of the Abitibi Greeenstone Belt and its unique VMS and gold-rich VMS endowment. Field Trip guidebook prepared for the Ottawa 2011 joint annual meeting of the Geological association of Canada - Mineralogical association of Canada - Society of Economic Geologists - Society for Geology applied to mineral deposits, pp. 72.

Middlemost, E. A. K. (1975). The basalt clan. *Earth Science Review*, 11:337–364.

Middlemost, E. A. K. (1989). Iron oxidation ratios, norms and the classification of volcanic rocks. *Chemical Geology*, 77:19–26.

Moorhouse, W. W. (1959). *The study of rocks in thin section.* Harper and Row, Publishers.

Morimoto, N. (1989). Nomenclature of pyroxenes. *Canadian Mineralogist*, 27:143 – 156.

Mortensen, J. K. (1993). U - Pb geochronology of the eastern Abitibi Subprovince. part 2: Noranda - Kirkland Lake area. *Canadian Journal of Earth Sciences*, 30:29–41.

Moulton, B. J. A., Fowler, A. D., Ayer, J. A., and Berger, B. R. (2011). Archean subqueous high-silica rhyolite coulées: Examples from the Kidd-Munro Assemblage in the Abitibi Subprovince. *Precambrian Research*, 189:389 – 403.

Mueller, W., Donaldson, J. A., and Doucet, P. (1994). Volcanic and tectono-plutonic influences on sedimentation in the Archean Kirkland basin, Abitibi greenstone belt, Canada. *Precambrian Research*, 68(3-4):201–230.

Mueller, W., Mortensen, J. K., Daigneault, R., and Chown, E. H. (1996). Docking evidence of Archean terranes: Evidence from the Abitibi greenstone belt, Quebec, Canada. *Tectonophysics*, 265:127–150.

Mullen, E. D. (1983). MnO/TiO2/P2O5/: a minor element discriminant for basaltic rocks of oceanic environments and its implications for petrogenesis. *Earth and Planetary Science Letters*, 62:53–62.

O'Neil, J., Carlson, R. W., Francis, D., and Stevenson, R. K. (2008). Neodymium-142 Evidence for Hadean mafic crust. *Science*, 321(5897):1828–1831.

O'Neill, J. J. (1933). The Beattie gold mines, Duparquet township, western Québec. *Québec Bureau of Mines, Annual Report*, C:3–28.

O'Neill, J. J. (1934a). Beattie-Galatea map-area, parts of Duparquet and Destor townships. *Québec Bureau of Mines, Annual Report*, C:75–109.

O'Neill, J. J. (1934b). Geology of the Beattie gold mine, Duparquet township, Québec. *Transactions of the Canadian Institute of Mining and Metallurgy and of the Mining Society of Nova Scotia*, 37:299–315.

Patry, S. (2005). Étude pétrographique, géochimique et métallogénique de la syénite de Duparquet, faille de Porcupine-Destor, sous-province de l'Abitibi. In *Halifax, Association*

géologique du Canada, Association minéralogique du Canada, Programme et Sommaires, volume 30, page 74.

Pearce, J., Harris, N., and Tindle, A. (1984). Trace element discrimination diagrams for the tectonic interpretation of granitic rocks. *Journal of Petrology*, 25:956–983.

Pearson, V. and Daigneault, R. (2009). An Archean megacaldera complex: The Blake River Group, Abitibi greenstone belt. *Precambrian Research*, 168:66–82.

Percival, J. A. (2007). Geology and metallogeny of the Superior Province. In *Mineral Deposits of Canada: A Synthesis of Major Deposit-Types, District Metallogeny, the Evolution of Geological Provinces, and Exploration Methods, Special publication*, number 5, pages 903–928. Geological Association of Canada, Mineral Deposits Division.

Percival, J. A. and Stott, G. M. (2010). Superior Province: overview, update and reflections. In *Yilgarn-Superior workshop, Fifth International Archean Symposium - Abstracts*, number 5, pages 4–6. Geological Survey of Western Australia.

Piché, M. and Jébrak, M. (2004). Normative minerals and alteration indices developed for mineral exploration. *Journal of Geochemical Exploration*, 82:59–77.

Pigeon, L. (2003). Mineralogy, petrology and petrogenesis of syenitic rocks of the Porcupine-Destor fault zone near Matheson, Ontario. Master's thesis, University of Ottawa, Ottawa, Canada, pp. 285.

Powell, W. G., Carmichael, D. M., and Hodgson, C. J. (1995). Conditions and timing of metamorphism in the southern Abitibi greenstone belt, Québec. *Canadian Journal of Earth Sciences*, 32:787–805.

Praisé, J. (1981). Rapport sommaire des traveaux effectués sur le groupe GR10-15: Projet Duparquet, Canton Duparquet, Québec. Ressources Gold Fields Canada Ltée, Report GM 39845, pp. 18.

Reider, M., Cavazzini, G., D'Yakonov, Y., Gottardi, G., Guggenheim, S., Koval, P. V., Muller, G., Neiva, A. M. R., Radoslovich, E. W., Robert, J.-L., Sassi, F. P., Takeda, H., Weiss, Z., and Wones, D. R. (1998). Nomenclature of Micas. *The Canadian Mineralogist*, 36:1–8.

Rioux, L. (2011). Technical report on the Duparquet properties (Beattie, Donchester and Central Duparquet. Osisko Mining Corporation Inc. and Clifton Star Resources Inc., Report GM 65858, pp. 13210.

Robert, F. (1997). Syenite-associated disseminated gold deposits along the Porcupine-Destor fault zone. In *Atypical gold deposits in the Abitibi belt*. Geological Association of Canada - Mineralogical association of Canada (GAC-MAC) Field trip guidebook, number B5, p. 29-51.

Robert, F. (2001). Syenite-associated disseminated gold deposits in the Abitibi greenstone belt, Canada. *Mineralium Deposita*, 36:503–516.

Robert, F. (2012). Intrusion-hosted gold deposits in the Abitibi. In *Short course; Intrusion related gold in the Abitibi: Theory and application to exploration*, pages 29–51. Society of economic geologists, London student chapter.

Rocheleau, M. (1980). *Stratigraphie et sédimentologie de l'Archéen dans la région de Rouyn, Abitibi, Québec*. PhD thesis, Université de Montréal, Montréal, Canada, pp. 313.

Rogers, R. (2010). Volcanology and metallogeny of a sector of the Blake River Group, Abitibi Subprovince, Québec and Ontario. Master's thesis, Institut national de la recherche scientifique, Québec, Canada, pp. 169.

Ropchan, J. C. (2000). Petrographic and Geochemical studies of the alteration zones associated with gold mineralization at the Holloway mine, Southwestern Abitibi Greenstone Belt, Canada. Master's thesis, University of Ottawa, Ottawa, Canada, pp. 141.

Ropchan, J. C., Luinstra, B., Fowler, A. D., Benn, K., Ayer, J. A., Berger, B., Dahn, R., Labine, R., and Amelin, Y. (2002). Host-rock and structural controls on the nature and timing of gold mineralization at the Holloway mine, Abitibi Subprovince, Ontario. *Economic geology*, 97:291 – 309.

Ross, P.-S. and Bédard, J. (2009). Magmatic affinity of modern and anciend subalkaline volcanic rocks determined from trace-element discriminant diagrams. *Canadian Journal of Earth Sciences*, 46:823 – 839.

Ross, P.-S., Percival, J. A., Mercier-Langevin, P., Goutier, J., McNicoll, V. J., and Dubé, B. (2007). Intermediate to mafic volcaniclastic units in the peripheral Blake River Group, Abitibi greenstone belt, quebec: origin and implications for volcanogenic massive sulphide exploration. Geological Survey of Canada, Current Research, v.2008-1, pp.18.

Roy, P. and Roy, F. (1998). Rapport des traveaux d'exploration effectués sur la propriété Duparquet en 1997. Exploration Maude Lake Ltée, Report GM 56356, pp. 57.

Schumacher, J. C. (1991). Empitical ferric iron corrections: necessity, assumptions, and effects on selected geothermobarometers. *Mineralogical magazine*, 55:3–18.

Shand, S. J. (1927). *The eruptive rocks*. John Wiley.

Stott, G. M., Corkery, M. T., Percival, J. A., Simard, M., and Goutier, J. (2010). Project units 98-006 and 98-007. a revised terrane subdivision of the Superior Province. In *Summary of field work and other activities*, number 6260, pages 244–253. Ontario geological survey.

Thompson, R. N. (1984). Dispatches from the basalt front; 1, experiments. *Proceedings of the Geologists' Association*, 95:249–262.

Thurston, P. C. (1994). Archean volcanic patterns. In Condie, K., editor, *Archean Crustal Evolution: Developments in Precambrian Geology*, number 11, pages 45–84. Elsevier.

Thurston, P. C., Ayer, J. A., Goutier, J., and Hamilton, M. A. (2008). Depositional gaps in Abitibi greenstone belt stratigraphy: A key to exploration for syngenetic mineralization. *Economic Geology*, 103(6):1097 – 1134.

Tuttle, J. (1939). The spiral stoping system as applied at the Beattie mine. *The Canadian Institute of Mining and Metallurgy*, 42:95–122.

Twiss, R. and Moores, E. (1992). *Structural geology*. W.H. Freeman and Company.

Wilson, M. E. (1914). *Kewagama Lake map area, Québec*. Geological Survey of Canada, Memoir number 39, pp. 134.

Wilson, M. E. (1918). *Timiskaming County, Québec*. Geological Survey of Canada, Memoir number 103, pp. 197.

Winter, J. (2001). *An introduction to igneous and metamorphic petrology.* Prentice Hall.

Zane, A. and Weiss, Z. (1998). A procedure for classifying rock-forming chlorites based on microprobe data. *Accademia Nazionale dei Lincei*, 9:51–56.

Zhang, Q., Machado, N., Ludden, N., Moore, D., and Anomynous (1993). Geotectonic constraints from U-Pb ages fro the Blake River group, the Kinojevis and the Normetal Mine area, Abitibi, Québec. In *Program with Abstracts - Geological Association of Canada; Mineralogical Association of Canada: Joint Annual Meeting*, volume 1993, page 114. Geological Association of Canada.

Appendix A

Error calculation

A.1 EMP errors

A mathematical approach to calculate the chemical formula of any given mineral can be obtained by the following function:

$$f(x_i) = \left(\frac{\alpha \left(\frac{x_i}{M_{wt}} \right)}{\sum_{j=1}^{n} \left(\frac{N_j}{M_{wt}} \right) x_j} \right) \tag{A.1}$$

Where x_i is the oxide calculated (in weight percent), α is the number of anions (O,OH,F), and M_{wt} is the molecular weight of the oxide concerned. For the Sum function, here all the detected oxides are included, where N_j is the number of oxygens for the corresponding oxide and x_j is the weight of the detected oxide (in weight percent). For the calculation of the respective errors we need to modify our equation (A.1). Of course, the only numbers that will have any associated errors are the ones to have been detected and measured:

$$f\left(\frac{\Delta x}{x_i}\right) = \left(\frac{\alpha \left(\frac{x_i \pm \Delta x_i}{M_{wt}} \right)}{\sum_{i=j}^{n} \left(\frac{N_j}{M_{wt}} \right) x_j \pm \Delta x_j} \right)$$

This equation can be expanded to:

$$f\left(\frac{\Delta x}{x_i}\right) = \left(\frac{\left(\frac{\alpha}{M_{wt}} x_i \pm \frac{\alpha}{M_{wt}} \Delta x_i \right)}{\sum_{j=1}^{n} \left(\frac{N_j}{M_{wt}} x_j \pm \frac{N_j}{M_{wt}} \Delta x_j \right)} \right) \tag{A.2}$$

Here we will simplify $(\frac{N_j}{M_{wt}} x_j)$ as S and $(\frac{N_j}{M_{wt}} \Delta x_j)$ as ΔS. Then, using the standard deviation

to calculate the error propagation, we obtain the following equation:

$$f(x_i \pm \Delta x) = \frac{\alpha}{M_{wt}} \left(\frac{x_i}{S} \pm \frac{x_i}{S} \sqrt{\left(\frac{\Delta x_i}{x_i}\right)^2 + \left(\frac{\Delta S}{S}\right)^2} \right) \tag{A.3}$$

For practical purposes, a calculation of a feldspar chemical formula is provided below with the inclusion of the respective errors. The following table provides the initial detected values and their associated errors.

Table A.1 – Measured weight percent of oxides in a feldspar

Oxide	Weight %	Error
SiO_2	66.76	0.47
TiO_2	0.00	0.00
Al_2O_3	20.13	0.14
FeO	0.37	0.02
MgO	0.00	0.00
BaO	0.29	0.03
CaO	0.70	0.02
Na_2O	6.91	0.10
K_2O	6.61	0.05

We will begin by calculating the chemical formula without the errors using equation (A.1). Here α will be equal to 8 (since there are 8 oxygens in the formula). The first step to calculate in this equation will be the $\sum$. Therefore,

$$\begin{aligned} \sum_{j=1}^{n} &= \left(\frac{N_{SiO_2}}{M_{SiO_2}}\right) x_{SiO_2} + \left(\frac{N_{TiO_2}}{M_{TiO_2}}\right) x_{TiO_2} + \left(\frac{N_{Al_2O_3}}{M_{Al_2O_3}}\right) x_{Al_2O_3} + ... \\ &= 3.02 \end{aligned} \tag{A.4}$$

Now we can simply calculate each normalized oxide for the chemical formula:

$$\begin{aligned} f(x) &= \frac{8(66.76/60.0848)}{3.02} \\ &= 2.95 \end{aligned}$$

This can be continued for each oxide of the feldspar listed in table A.1. A complete list of the calculated results are listed in table A.2. Obviously, the next step is to calculate the errors associated to each oxide. This can be done using the equation A.3. First, we will again

start by calculating Δ S, and is as follows:

$$\begin{aligned}\Delta S &= \sqrt{\sum_{i=j}^{n}\left(\frac{N}{M}\Delta x_i\right)^2} \\ &= \sqrt{\left(\frac{N_{SiO_2}}{M_{SiO_2}}\Delta x_{SiO_2}\right)^2+\left(\frac{N_{TiO_2}}{M_{TiO_2}}\Delta x_{TiO_2}\right)^2+\left(\frac{N_{Al_2O_3}}{M_{Al_2O_3}}\Delta x_{Al_2O_3}\right)^2+...} \\ &= 0.02\end{aligned} \tag{A.5}$$

Next, we can simply now calculate the individual errors for each oxide:

$$\begin{aligned}\Delta SiO_2 &= \left(\frac{8}{60.0848}\right)\left(\frac{66.76}{3.02}\right)\sqrt{\left(\frac{0.47}{66.76}\right)^2+\left(\frac{0.02}{3.02}\right)^2} \\ &= 0.03\end{aligned}$$

This can be expanded to calculate each and every oxide concerned. A complete list of errors can be viewed in the following table.

Table A.2 – Calculated chemical oxides for the feldspar formula

Oxide	Normalized	Error
SiO_2	2.95	0.03
TiO_2	0.00	0.00
Al_2O_3	1.05	0.01
FeO	0.01	0.00
MgO	0.00	0.00
BaO	0.01	0.00
CaO	0.03	0.00
Na_2O	0.59	0.01
K_2O	0.37	0.00

Therefore, our final chemical formula for our feldspar is:

$$(Na_{0.59\pm0.01}\ K_{0.37\pm0.00}\ Ca_{0.03\pm0.00}\ Ba_{0.01\pm0.00})(Si_{2.95\pm0.03}\ Al_{1.05\pm0.01}\ {Fe^{3+}}_{0.01\pm0.00})$$

Since feldspars are represented in terms of ternary weight percentages, we can also calculate the propagation of the errors on the ternary percentages. Therefore the formula to calculate

the various end-member percentages of feldspar (in weight %):

$$f(y_i) = \left(\frac{y_i W_f}{\sum (y_j W_f)}\right) 100 \tag{A.6}$$

Here y_i is the oxide belonging to an end-member of feldspar and W_f is the weight of the end-member of feldspar obtained form literature. As for the sum, y_j corresponds to each oxide of the end-members multiplied by their respective weight. Here again we will simplify $\sum (y_j W_f)$ as S. Using the same methods to obtain the error formulas as above, we obtain for the end-members of feldspar:

$$f(\Delta y_i) = \left(\frac{y_i W_f}{\sum (y_j W_f)}\right) \sqrt{\left(\frac{\Delta y_i W_f}{y_j W_f}\right)^2 + \left(\frac{\Delta S}{S}\right)^2} 100 \tag{A.7}$$

Using the same calculation methods as above we obtain the following results.

Feldspar	Percentage	Error
An	3.44	0.11
Ab	57.89	1.06
Or	38.67	0.52

Table A.3 – Ternary percentages and errors of each end-member of feldspar

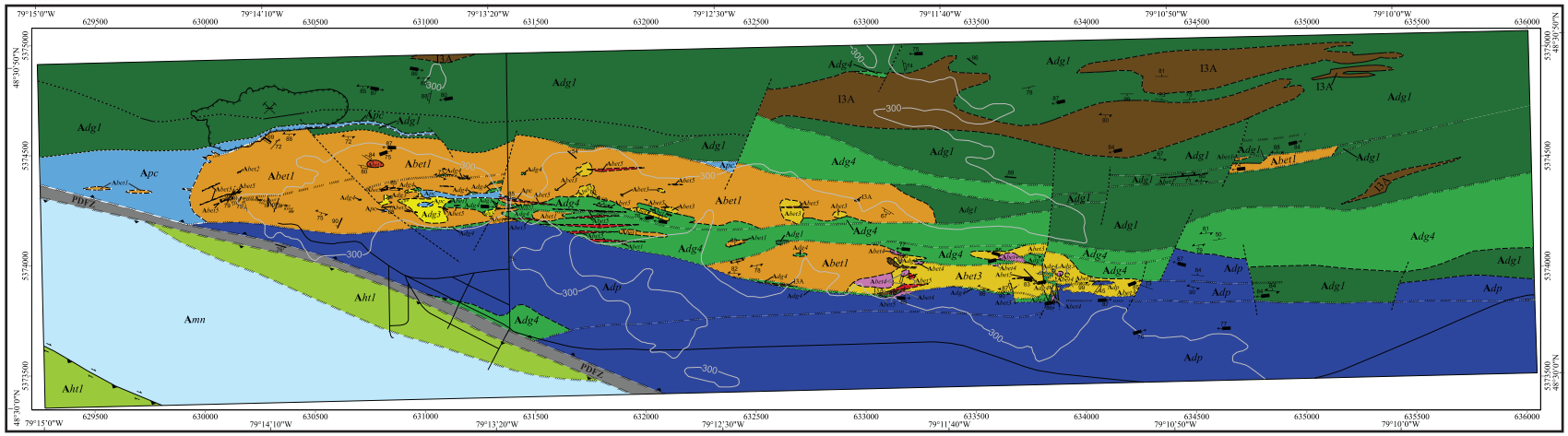
Appendix B

Geological and outcrop maps

The geological and outcrop maps of the Beattie syenite are presented here in vector format to permit viewing at full resolution. To obtain more recent data concerning this region, please consult the geomatic products of the Système d'information géominière du Québec (E-SIGEOM) at `http://www.mrn.gouv.qc.ca/english/products-services/mines.jsp`.

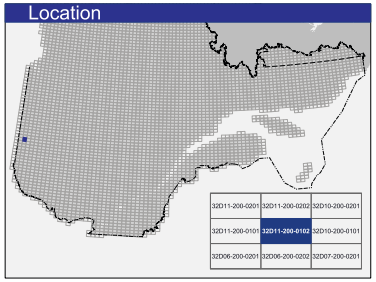
Geology - BEATTIE SYENITE

32D11-200-0102



32D11-200-0102

Location



Metadata

Geodetic reference surface: Ellipsoid GRS 80

Geodetic reference system: NAD 83 compatible with worldwide system WGS 84

Cartographic projection: Universal transverse mercator (UTM), zone 18

Base longitude: 79° 07' 30"

Base latitude: 0°

Frontières

- International border
- Interprovincial border
- Québec - Newfoundland and Labrador border (this border is not definitive)

0 250 500 1,000 1,500 2,000 Mètres

1/7 500

Sources

Data

Territory planning database (BDAT), scale 1/100 000

Organization

Ministère des Ressources naturelles

Production

Geology: Julie Bourdeau, Jean Goutier (2013)

References: Archibald, F.T. (2008) - GM 64140
Banfield, A.F. (1940) - Ph.D. thesis
Bevan, P.A. (2011) - Report NI 43-101
Capus, G. (1988) - GM 48562
Davidson, S. et Banfield, A.F. (1944) - Economic Geology Vol.39, No.8
Gadoury, J. (1995) - GM 53555
Gagnon, P. (1981) - SOQUEM Inc.
Goutier, J. et Lacroix, S. (1992) - MB 92-06
Graham, R.B. (1954) - RG 06
Hallé, L. (1990) - GM 49711
Legault, M. *et al.* (1995) - ET 2005-01
O'Neill, J.J. (1932) - Québec Bureau of Mines, Annual Report
Praisé, J.C. (1981) - GM 38945
Rioux, L. (2011) - GM 65856

Technical assistance: Claude Guérin

Production: University of Ottawa
Ministère des Ressources naturelles

Distribution: University of Ottawa
Ministère des Ressources naturelles

The present document does not have a legal scope
© Gouvernement du Québec, 1er trimester 2013

To obtain more recent data concerning this region, we suggest that you consult the geomatic products of the Système d'information géominière du Québec (SIGÉOM)

SIGÉOM Système d'information géominière du Québec

STRATIGRAPHIC LEGEND

ARCHEAN

Timiskaming Group

Duparquet Formation (<2679 ± 3 Ma; David et al., 2006)

- Adp — Polygenetic conglomerate, wacke and mudstone

Beattie Syenite (2683 ± 1 Ma; Mueller, 1996; 2682 ± 1Ma; David et al., 2007)

- Abet5 — Lath syenite, dykes with trachytic texture
- Abet4 — Megaporphyritic syenite, locally glomeroporphyritic texture
- Abet3 — Porphyritic Central Duparquet syenite, with equant feldspar phenocrysts
- Abet2 — Equigranular magnetite-bearing syenite
- Abet1 — Porphyritic Beattie syenite, locally cataclastic

Porcupine Group (< 2687 ± 2 Ma; Ayer et al., 2005)

- Apc — Greywacke, mudrock and polygenetic conglomerate

Kewagama Group

Mont-Brun Formation (< 2686 ± 4 Ma; Davis et al., 2002; > 2682 ± 3 Ma; Mortensen, 1993)

- Amn — Greywacke and mudrock

Blake River Group

Hébécourt Formation (2701 - 2703 Ma; Mercier-Langevin et al., 2011)

- Aht1 — Basalt

Kinojévis Goup

Deguisier Formation(2720 - 2718 Ma; Zhang et al., 1993)

- Adg3 — Rhyolite
- Adg4 — Andesite to dacite
- Adg1 — Basalt

LITHOLOGICAL LEGEND

ARCHEAN

- PDFZ — Porcupine-Destor fault zone
- I3A — Gabbro

The order of succession of the individual units in the lithological legend may not necessarily respect the order of superposition

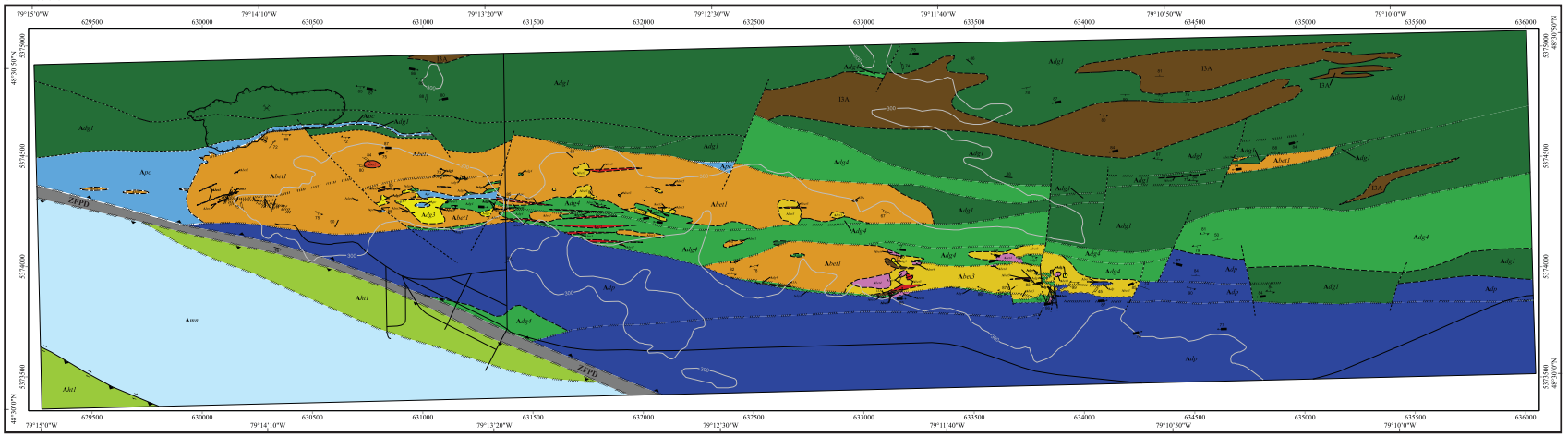
Symbols and abbreviations used in this map are described in the publication PRO 2000-08 from the Ministère des Ressources naturelles

uOttawa

Ressources naturelles Québec

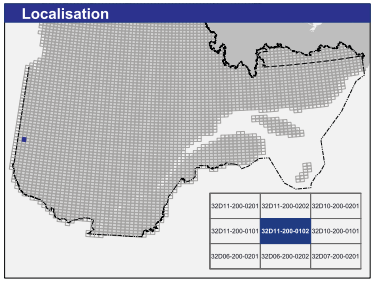
Géologie - SYÉNITE DE BEATTIE

32D11-200-0102



32D11-200-0102

Localisation



Métadonnées

Surface de référence géodésique: Elipsoide GRS 80

Système de référence géodésique: NAD 83 compatible avec le système mondial WGS 84

Projection cartographique: Mercator transverse universelle (MTU), fuseau 18

Longitude d'origine: 79° 07' 30"

Latitude d'origine: 0°

Frontières

- Frontière internationale
- Frontière interprovinciale ou interétatique
- Frontière Québec - Terre-Neuve-et-Labrador (cette frontière n'est pas definitive)

0 250 500 1,000 1,500 2,000 Mètres

1/7 500

Sources

Données

Base de données pour aménagement du territoire (BDAT) échelle 1/100 000

Organisme

Ministère des Ressources naturelles

Réalisation

Géologie: Julie Bourdeau, Jean Goutier (2013)

Références: Archibald, F.T. (2008) - GM 64140
Banfield, A.F. (1940) - Ph.D. thesis
Bevan, P.A. (2011) - Report NI 43-101
Capus, G. (1988) - GM 48562
Davidson, S. et Banfield, A.F. (1944) - Economic Geology Vol.39, No.8
Gadoury, J. (1995) - GM 53555
Gagnon, P. (1981) - SOQUEM Inc.
Goutier, J. et Lacroix, S. (1992) - MB 92-06
Graham, R.B. (1954) - RG 06
Hallé, L. (1990) - GM 49711
Legault, M. *et al.* (1995) - ET 2005-01
O'Neill, J.J. (1932) - Québec Bureau of Mines, Annual Report
Praisé, J.C. (1981) - GM 38945
Rioux, L. (2011) - GM 65856

Assistance technique: Claude Guérin

Production: Université d'Ottawa
Ministère des Ressources naturelles

Diffusion: Université d'Ottawa
Ministère des Ressources naturelles

Le présent document n'a aucune portée légale
© Gouvernement du Québec, 1er trimestre 2013

Pour obtenir les données les plus récentes concernant cette région, nous vous suggérons de consulter les produits géomatiques du Système d'information géominière du Québec (SIGEOM)

SIGÉOM
Système d'information géominière du Québec

LÉGENDE STRATIGRAPHIQUE

ARCHÉEN

Groupe de Timiskaming

Formation de Duparquet (<2679 ± 3 Ma; David et al., 2006)

Adp — Conglomérat polygénétique et grès lithique

Syénite de Beattie (2683 ± 1 Ma; Mueller, 1996; 2682 ± 1Ma; David et al., 2007)

Abet1 — Syénite à lattes, filons avec texture trachytique

Abet4 — Syénite mégaporphyrique et glomeroporphyritique à feldspath

Abet3 — Syénite porphyrique Central Duparquet, avec phénocristaux de feldspath équigranulaires

Abet2 — Syénite equigranulaire à magnétite

Abet1 — Syénite porphyrique Beattie, par endroit cataclastique

Groupe de Porcupine (< 2687 ± 2 Ma; Ayer et al., 2005)

Ajc — Grès, mudrock et conglomérat polygénetique

Groupe de Kewagama

Formation de Mont-Brun (< 2686 ± 4 Ma; Davis et al., 2002; > 2682 ± 3 Ma; Mortensen, 1993)

Amn — Grès et mudrocks déposés par courants turbiditiques

Groupe de Blake River

Formation d'Hébécourt (2701 - 2703 Ma; Mercier-Langevin et al., 2011)

Ahb1 — Basalte

Groupe de Kinojévis

Formation de Deguisier (2720 - 2718 Ma; Zhang et al., 1993)

Adj3 — Rhyolite

Adj4 — Andésite à dacite

Adj1 — Basalte

LÉGENDE LITHOLOGIQUE

ARCHÉEN

ZFPD — Zone de faille Porcupine-Destor

I3A — Gabbro

L'ordre de succession des subdivisions des unités de la légende ne respecte pas necessairement l'ordre du superposition

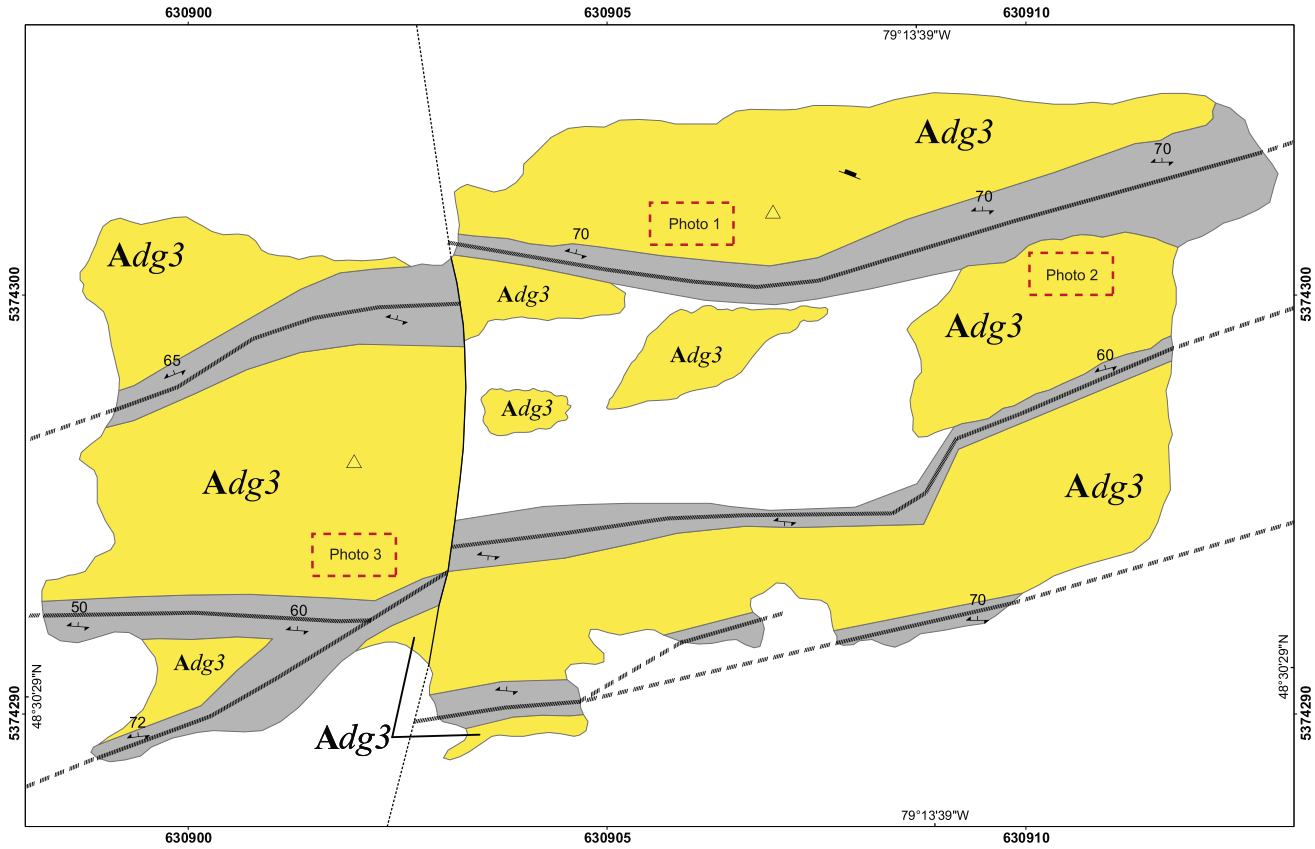
Les symboles et abréviations utilisés sur cette carte sont décrits dans la publication PRO 2000-08 du Ministère des Ressources naturelles

uOttawa

Ressources naturelles Québec

Affleurement Deguisier rhyolite - Deguisier rhyolite outcrop

JEB-09-10



PHOTOGRAPHS

Location of photographs approximate

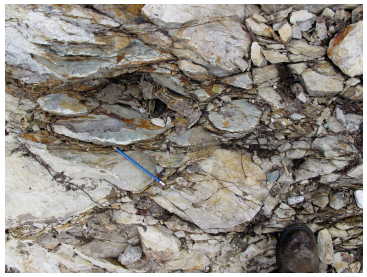


Photo 1 - Brecciated massive rhyolite withought amygdules.



Photo 2 - Anastamosing sericite filled fractures in the Deguisier rhyolite. Quartz-filled amygdules are near perpendicular to the sericite veins and occur in both the veins as well as in the undisturbed rhyolite. The particular arrangement of the arc-shaped sericite-filled fractures have been mistaken for pillow structures.

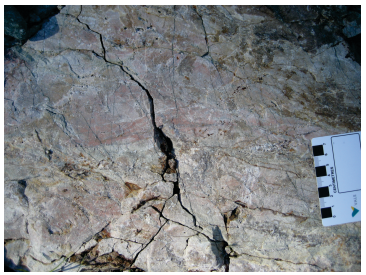
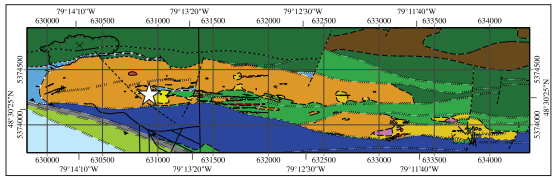


Photo 3 - Reddish-pink massive rhyolite without amygdules.

LOCATION



Full scale map and legend can be found in accompanying thesis

METADATA

Geodetic reference surface:	Ellipsoid GRS 80
Geodetic reference system:	NAD 83 compatible with with worldwide system WGS 84
Cartographic projection:	Universal transverse mercator (UTM), zone 18
Origin longitude:	79° 07' 30"
Origin latitude:	0°

3 1.5 0 3 Meters

1 / 20

PRODUCTION

Geology: Ludovic Bigot, Julie Bourdeau

References: Graham, R.B. (1954) - RG 061
O'Neill, J.J. (1932),
The Beattie gold mines Ltd.
Rioux, L. (2011) - GM 65856

Production: University of Ottawa
Ministère des Ressouces naturelles
Direction Generale de Géologie Québec

Distribution: University of Ottawa
Ministère des Ressources naturelles
Direction Générale de Géologie Québec

This present document does not have a legal scope

To obtain more recent data concerning this region, we suggest that you consult the geomatic products of the Système d'information géominière du Québec (SIGEOM)

STRATIGRAPHIC LEGEND

Deguisier Formation
(2720 - 2718 Ma; Zhang et al., 1993)

Adg3 — Rhyolite; heterogeneous, commonly massive and brecciated, rarely with visible microphenocrysts

LITHOLOGICAL LEGEND

Schist zone

STRUCTURAL AND OTHER SYMBOLS

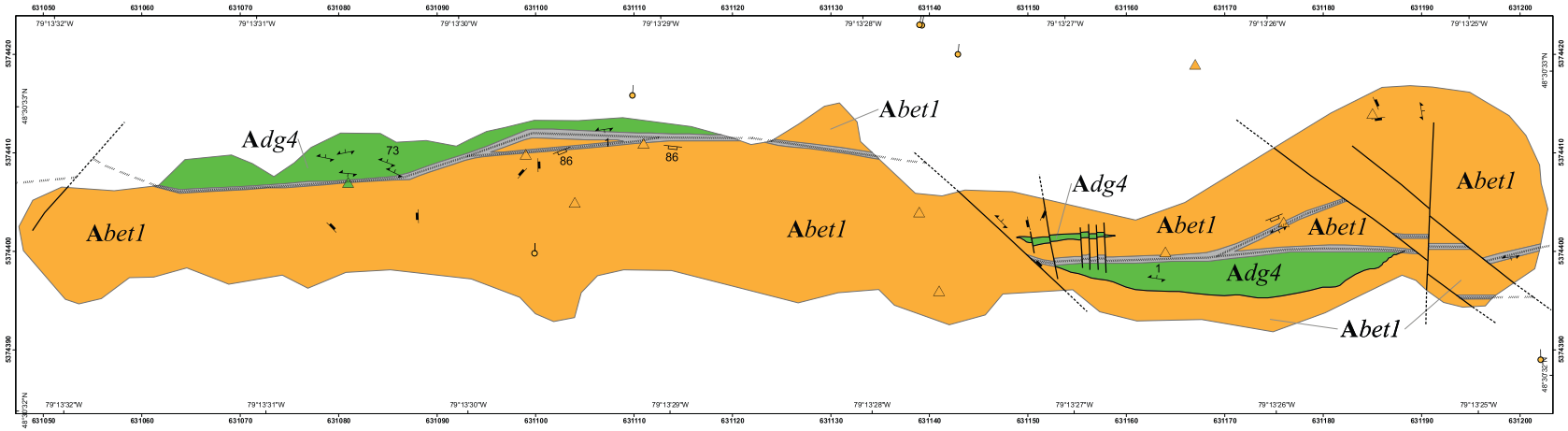
- Shearing
- Sericite vein
- Fault location certain
- Fault location inferred
- Shear zone certain
- Shear zone inferred
- Rhyolitic geochemical sample location

uOttawa

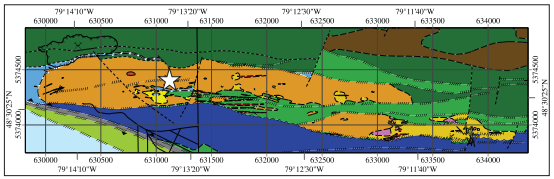
Ressources naturelles Québec

Outcrop East Beattie - Affleurement Beattie est

JG 5152



LOCATION



Full scale map and legend can be found in accompanying thesis

METADATA

Geodetic reference surface:	Ellipsoid GRS 80
Geodetic reference system:	NAD 83 compatible with with worldwide system WGS 84
Cartographic projection:	Universal transverse mercator (UTM), zone 18
Origin longitude:	79° 07' 30"
Origin latitude:	0°

PRODUCTION

Geology: Marc Bardoux, Julie Bourdeau

References: Bardoux, M. et al., (1990) - GM 49436
Graham, R.B. (1954) - RG 061
O'Neill, J.J. (1932),
The Beattie gold mines Ltd.
Rioux, L. (2011) - GM 65856

Production: University of Ottawa
Ministère des Ressouces naturelles
Direction Generale de Géologie Québec

Distribution: University of Ottawa
Ministère des ressources naturelles
Direction Générale de Géologie Québec

This present document does not have a legal scope

To obtain more recent data concerming this region, we suggest that you consult the geomatic products of the Système d'information géominière du Québec (SIGEOM)

SIGÉOM
Système d'information géominière du Québec

STRATIGRAPHIC LEGEND

ARCHEAN

Beattie syenite (2683 ± 1 Ma; Mueller, 1996; 2682 ± 1Ma; David et al., 2007)

Abet1 — Porphyritic Beattie syenite; 2 - 10 mm sub- to anhedral feldspar phenocrysts contained in a red aphanitic matrix, locally cataclastic

Deguisier Formation (2720 - 2718 Ma; Zhang et al., 1993)

Adg4 — Andesite to dacite; pillowed to massive volcanic flows occasionally amygdaloidal, distinguished from basalt on the basis of geochemistry

LITHOLOGICAL LEGEND

Schist zone

STRUCTURAL SYMBOLS

- Shearing
- Joint / Fracture
- Quartz vein
- Contact location certain
- Fault location certain
- Fault location inferred
- Shear zone certain
- Shear zone inferred

OTHER SYMBOLS

- Diamond drill hole: direction of hole (colour: First lithology logged)
- Syenitic geochemical sample location
- Andesitic or dacitic geochemical sample location

0 10 20 30 40 50 Meters

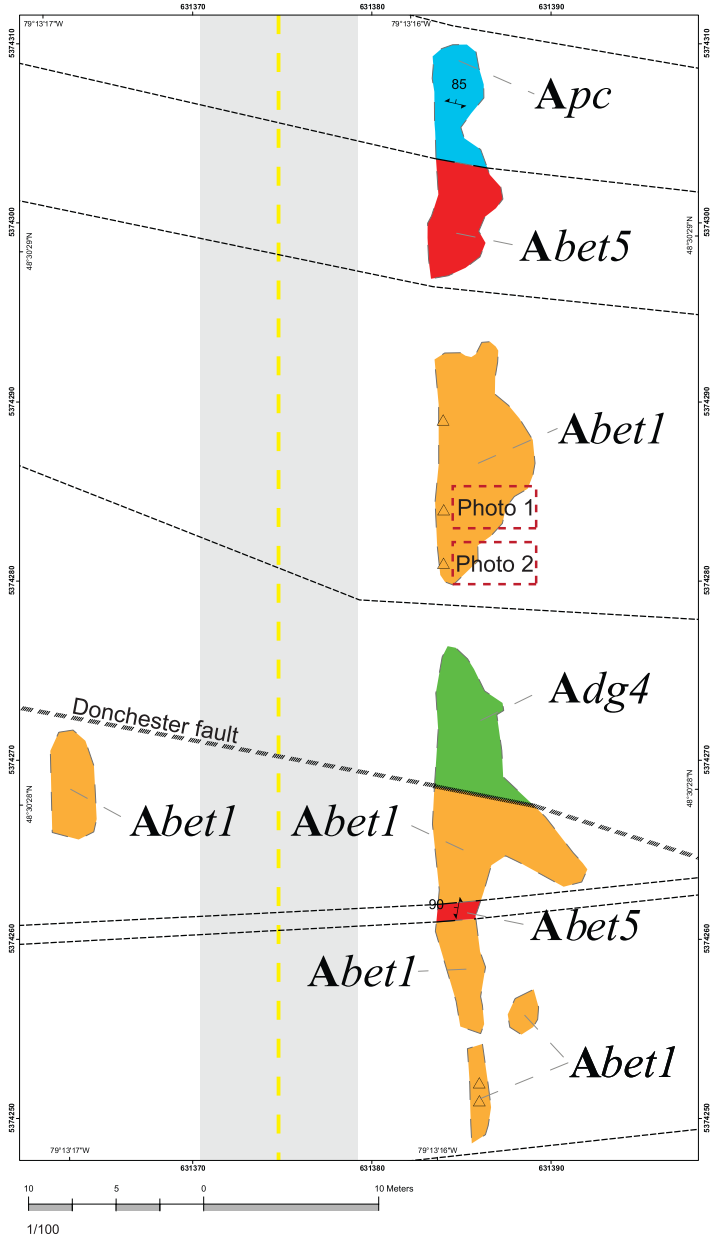
1 / 170

uOttawa

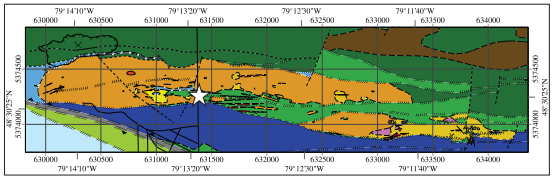
Ressources naturelles Québec

Affleurement à côté de la route QC-393 N - Outcrop next to QC-393 N road

JG 1027



LOCATION



Full scale map and legend can be found in accompanying thesis

METADATA

Geodetic reference surface: Ellipsoid GRS 80

Geodetic reference system: NAD 83 compatible with with worldwide system WGS 84

Cartographic projection: Universal transverse mercator (UTM), zone 18

Origin longitude: 79° 07' 30"

Origin latitude: 0°

PRODUCTION

Geology: Jean Goutier, Julie Bourdeau

References: Graham, R.B. (1954) - RG 061
Rioux, L. (2011) - GM 65856

Production: University of Ottawa
Ministère des Ressouces naturelles
Direction Generale de Géologie Québec

Distribution: University of Ottawa
Ministère des ressources naturelles
Direction Générale de Géologie Québec

This present document does not have a legal scope

To obtain more recent data concerning this region, we suggest that you consult the geomatic products of the Système d'information géominière du Québec (SIGEOM)

SIGÉOM
Système d'information géominière du Québec

STRATIGRAPHIC LEGEND

ARCHEAN

Beattie syenite (2683 ± 1 Ma; Mueller, 1996; 2682 ± 1Ma; David et al., 2007)

Abet5 — Lath syenite; dykes with 1 - 3 cm long feldspar laths demonstrating a trachytic texture

Abet1 — Porphyritic Beattie syenite; 2 - 10 mm sub- to anhedral feldspar phenocrysts contained in a red aphanitic matrix, locally cataclastic

Porcupine Group (< 2687 ± 2 Ma; Ayer et al. 2005)

Apc — Greywacke, mudrock and polygenetic conglomerate; elongated < 5 cm clasts of greenish chert, rhyolite and basalt

Deguisier Formation (2720 - 2718 Ma; Zhang et al., 1993)

Adg4 — Andesite to dacite; pillowed to massive volcanic flows occasionally amygdaloidal, distinguished from basalt on the basis of geochemistry

STRUCTURAL SYMBOLS

- Shearing
- Contact location certain
- Contact location inferred
- Shear zone certain
- Shear zone inferred

OTHER SYMBOLS

- Syenitic geochemical sample location
- Road QC-393 N to La Sarre

PHOTOGRAPHS

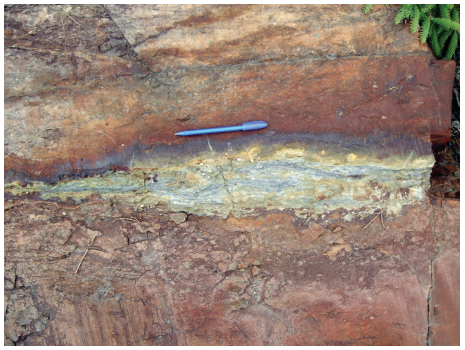


Photo 1 - Finely disseminated pyrite and arsenopyrite in Au-mineralized vein. This particular vein contains 1825 ppm Au and 667 ppm As.



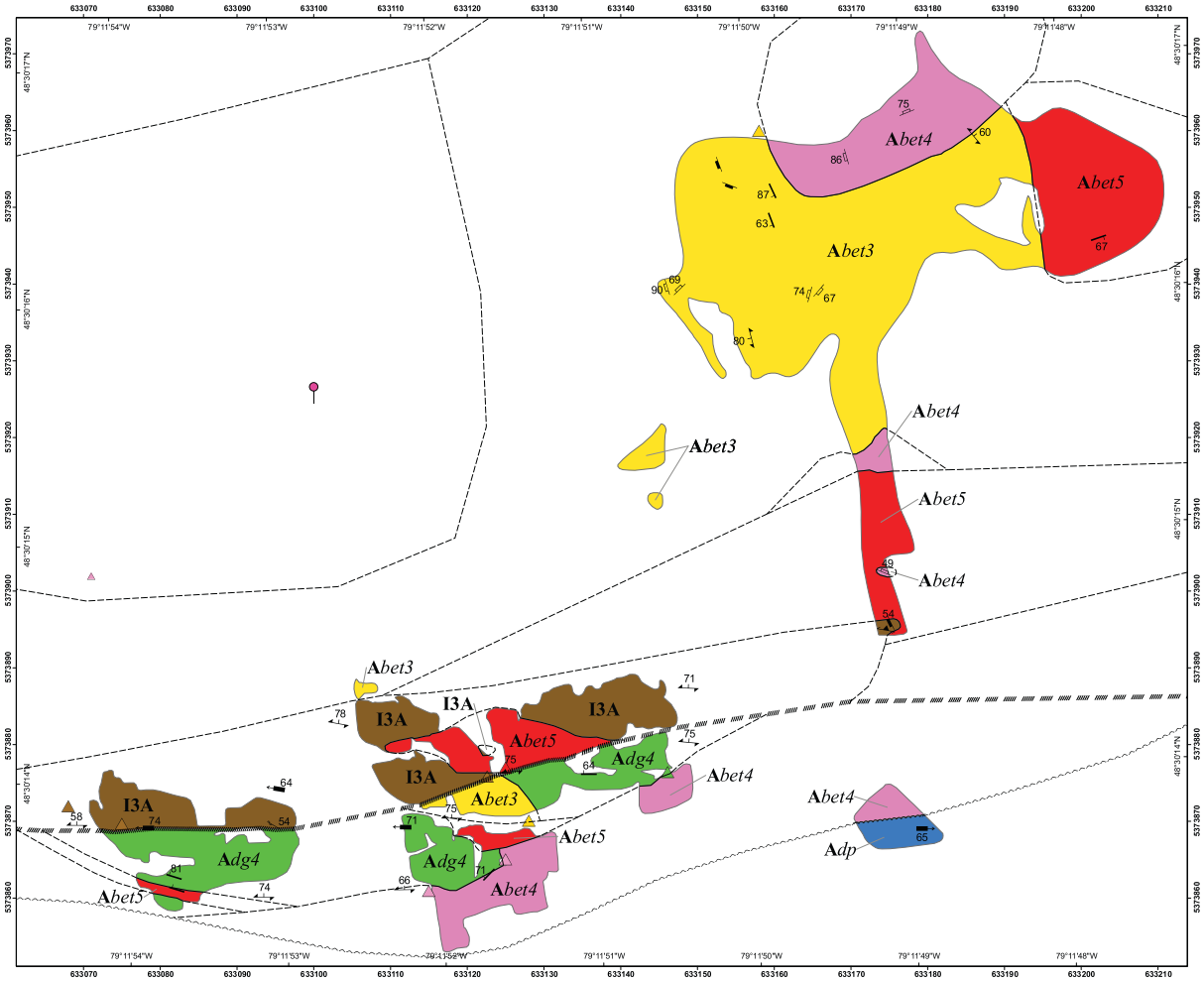
Photo 2 - Smaller Au-mineralized vein, a few meters south of photo 1. This particular vein contains 156 ppm Au and 905 ppm As.

uOttawa

Ressources naturelles Québec

Affleurement Central Duparquet - Central Duparquet outcrop

JG 5127, JG 5502, JG 5503



STRATIGRAPHIC LEGEND

ARCHEAN

Duparquet Formation (< 2679 ± 3 Ma; David et al., 2006)

- **Adp** — Polygenetic conglomerate, wacke and mudstone; extraformational clasts, including jasper and Beattie syenite clasts

Beattie syenite (2683 ± 1 Ma; Mueller, 1996; 2682 ± 1Ma; David et al., 2007)

- **Abet5** — Lath syenite; dykes with 1 - 3 cm long feldspar laths demonstrating a trachytic texture
- **Abet4** — Megaporphyritic syenite; phenocrysts up to 6 cm across in an aphanitic matrix, locally glomeroporphyritic texture
- **Abet3** — Porphyritic Central Duparquet syenite; 10 - 20 mm equant euhedral feldspar phenocrysts contained in a red or grey aphanitic matrix

Deguisier Formation (2720 - 2718 Ma; Zhang et al., 1993)

- **Adg4** — Andesite and dacite; pillowed to massive volcanic flows occasionally amygdaloidal, distinguished from basalt on the basis of geochemistry

LITHOLOGICAL LEGEND

- **I3A** — Gabbro; phaneritic and mesocratic

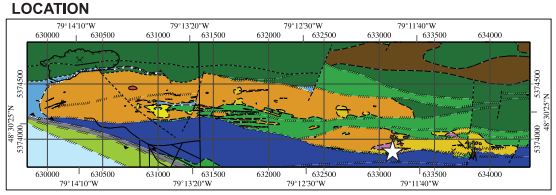
STRUCTURAL SYMBOLS

- Shearing
- Foliation
- Joint / Fracture
- Quartz or chlorite vein
- Fault striation
- Fault
- Schistosity
- Contact location certain
- Contact location inferred
- Shear zone certain
- Shear zone inferred
- Unconformable contact certain
- Unconformable contact inferred

OTHER SYMBOLS

- Diamond drill hole: direction of hole (colour: First lithology logged)
- Geochemical sample location (colour: lithology sampled)

LOCATION



Full scale map and legend can be found in accompanying thesis

METADATA

Geodetic reference surface:	Ellipsoid GRS 80
Geodetic reference system:	NAD 83 compatible with with worldwide system WGS 84
Cartographic projection:	Universal transverse mercator (UTM), zone 18
Origin longitude:	79° 07' 30"
Origin latitude:	0°

25 12.5 0 25 Meters

1/250

PRODUCTION

Geology: Jean Goutier, Julie Bourdeau

References: Bardoux, M. et al., (1990) - GM 49436
Graham, R.B. (1954) - RG 061
Rioux, L. (2011) - GM 65856

Production: University of Ottawa
Ministère des Ressouces naturelles
Direction Generale de Géologie Québec

Distribution: University of Ottawa
Ministère des Ressources naturelles
Direction Générale de Géologie Québec

This present document does not have a legal scope

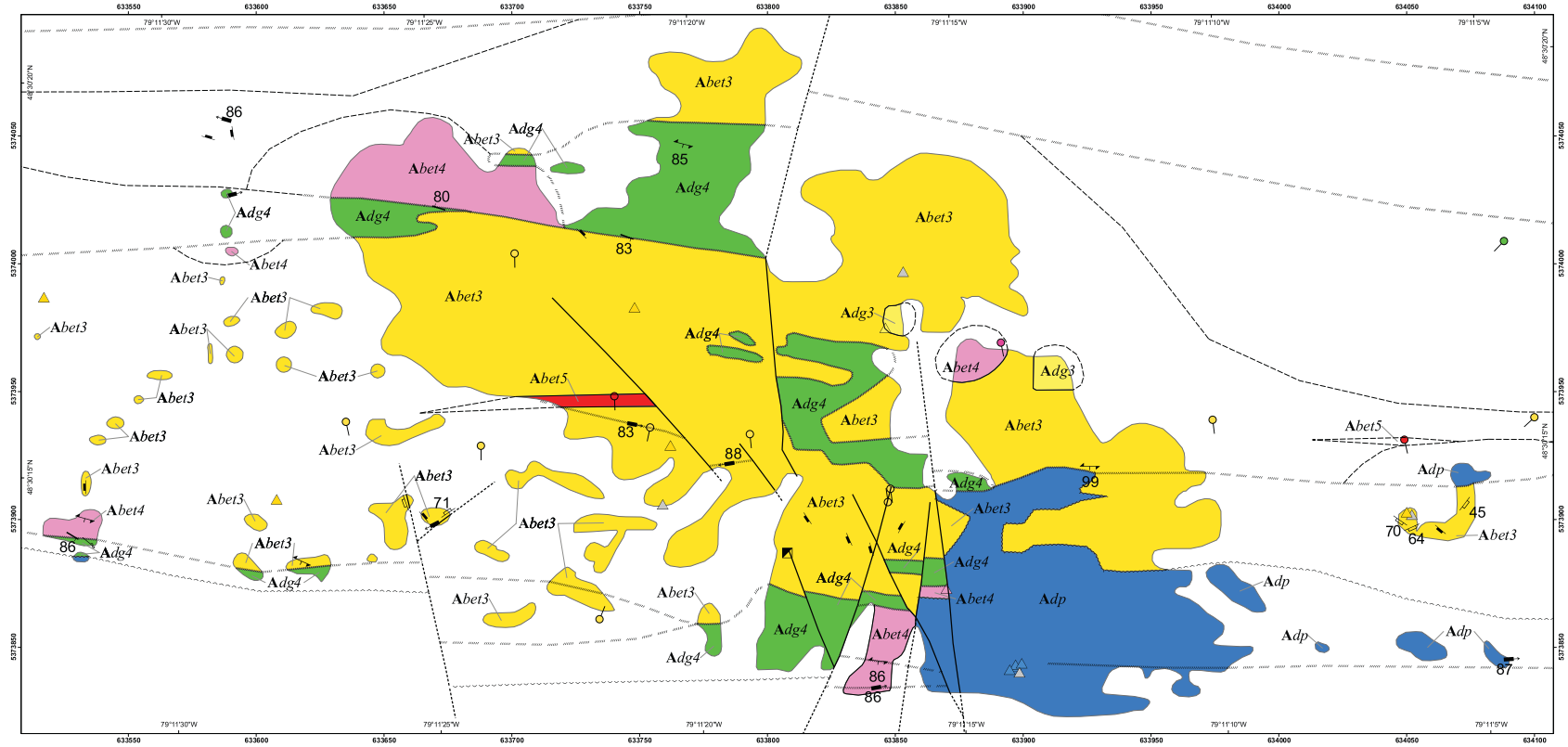
To obtain more recent data concerning this region, we suggest that you consult the geomatic products of the Système d'information géominière du Québec (SIGEOM)

SIGÉOM Système d'information géominière du Québec

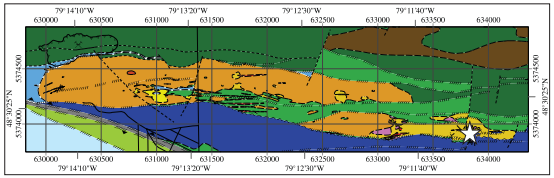
uOttawa

Ressources naturelles Québec

Affleurements de la discordance - Unconformity outcrops



LOCATION



Full scale map and legend can be found in accompanying thesis

METADATA

Geodetic reference surface:	Ellipsoid GRS 80
Geodetic reference system:	NAD 83 compatible with with worldwide system WGS 84
Cartographic projection:	Universal transverse mercator (UTM), zone 18
Origin longitude:	79° 07' 30"
Origin latitude:	0°

80 40 0 80 Meters

1/650

PRODUCTION

Geology: Jean Goutier, Julie Bourdeau

References: Graham, R.B. (1954) - RG 061
Rioux, L. (2011) - GM 65856

Production: University of Ottawa
Ministère des Ressouces naturelles
Direction Generale de Géologie Québec

Distribution: University of Ottawa
Ministère des Ressources naturelles
Direction Générale de Géologie Québec

This present document does not have a legal scope

To obtain more recent data concerning this region, we suggest that you consult the geomatic products of the Système d'information géominière du Québec (SIGEOM)

SIGÉOM
Système d'information géominière du Québec

uOttawa

Ressources naturelles Québec

STRATIGRAPHIC LEGEND

ARCHEAN

Duparquet Formation
(< 2679 ± 3 Ma; David et al., 2006)

- Adp — Polygenetic conglomerate, wacke and mudstone; extraformational clasts, including jasper and Beattie syenite clasts

Beattie syenite (2683 ± 1 Ma; Mueller, 1996; 2682 ± 1Ma; David et al., 2007)

- Abet5 — Lath syenite; dykes with 1 - 3 cm long feldspar laths demonstrating a trachytic texture
- Abet4 — Megaporphyritic syenite; phenocrysts up to 6 cm across in an aphanitic matrix, locally glomeroporphyritic texture
- Abet3 — Porphyritic Central Duparquet syenite; 10 - 20 mm equant euhedral feldspar phenocrysts contained in a red or grey aphanitic matrix

Deguisier Formation
(2720 - 2718 Ma; Zhang et al., 1993)

- Adg4 — Andesite and dacite; pillowed to massive volcanic flows occasionally amygdaloidal, distinguished from basalt on the basis of geochemistry

STRUCTURAL SYMBOLS

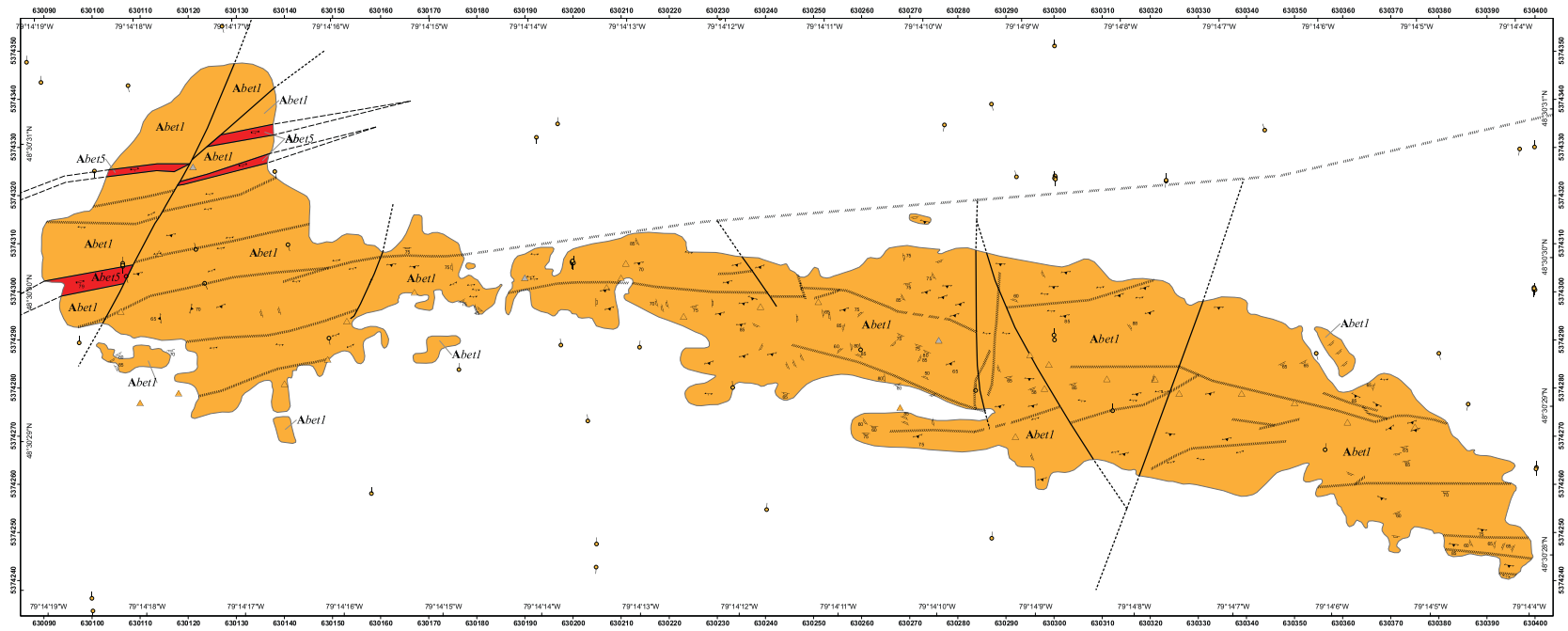
- Shearing
- Fault striation
- Joint / Fracture
- Fault
- Quartz or sericite vein
- Schistosity
- Contact location certain
- Contact location inferred
- Fault location certain
- Fault location inferred
- Shear zone certain
- Shear zone inferred
- Unconformable contact certain
- Unconformable contact inferred

OTHER SYMBOLS

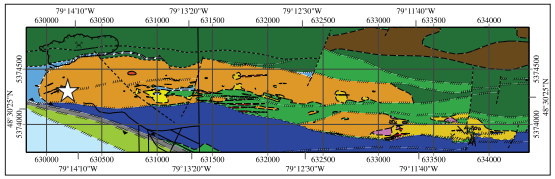
- Diamond drill hole: direction of hole (colour: First lithology logged)
- Geochemical sample location (colour: lithology sampled)
- Central Duparquet 1 mine shaft

South Beattie outcrop - Affleurement Beattie sud

JG 5500 - JG 5138



LOCATION



Full scale map and legend can be found in accompanying thesis

METADATA

Geodetic reference surface:	Ellipsoid GRS 80
Geodetic reference system:	NAD 83 compatible with with worldwide system WGS 84
Cartographic projection:	Universal transverse mercator (UTM), zone 18
Origin longitude:	79° 07' 30"
Origin latitude:	0°

0 12.5 25 50 75 100 Meters

1 / 750

PRODUCTION

Geology: Anomynous, Julie Bourdeau, Jean Goutier

References: Anomymous, Beattie gold mines Ltd. Contour plan of surface sampling
Anonymous, Beattie gold mines Ltd. Geological plan, Area 1
Graham, R.B. (1954) - RG 061
Rioux, L. (2011) - GM 65856

Production: University of Ottawa
Ministère des Ressources naturelles
Direction Générale de Géologie Québec

Distribution: University of Ottawa
Ministère des Ressources naturelles et
Direction Générale de Géologie Québec

This present document does not have a legal scope

To obtain more recent data concerning this region, we suggest that you consult the geomatic products of the Système d'information géominière du Québec (SIGEOM)

SIGÉOM
Système d'information géominière du Québec

STRATIGRAPHIC LEGEND

ARCHEAN

Beattie syenite (2683 ± 1 Ma; Mueller, 1996; 2682 ± 1Ma; David et al., 2007)

Abet5 — Lath syenite; dykes with 1 - 3 cm long feldspar laths demonstrating a trachytic texture

Abet1 — Porphyritic Beattie syenite; 2 - 10 mm sub- to anhedral feldspar phenocrysts contained in a red aphanitic matrix, locally cataclastic

STRUCTURAL SYMBOLS

- Lath dyke
- Fracture / Joint
- Shearing
- Foliation
- Contact location certain
- Contact location inferred
- Fault location certain
- Fault location inferred
- Shear zone certain
- Shear zone inferred

OTHER SYMBOLS

- Diamond drill hole: direction of hole
- Syenitic geochemical sample location
- Quartz vein geochemical sample location

uOttawa

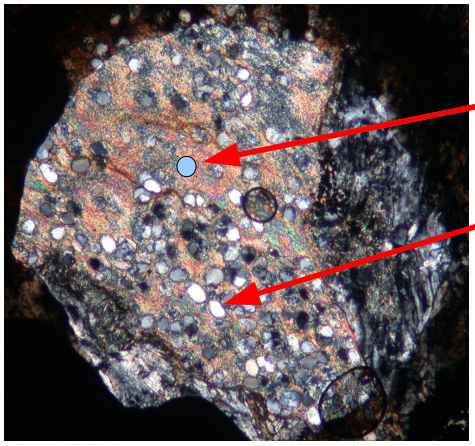
Ressources naturelles Québec

Appendix C

EMPA data

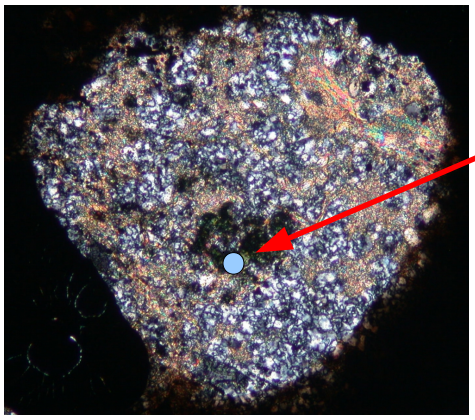
C.1 Mineral targets

JG – 94 – 5148 “48”

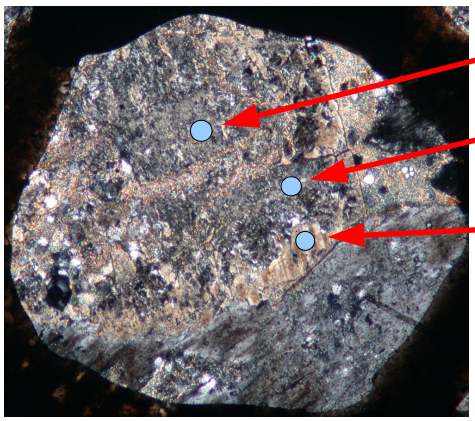


48-1-1 Sericite (C)

Albite (PC) [All albite in the sericite]



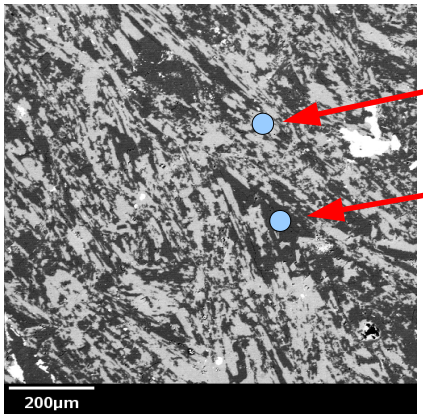
48-2-1 Chlorite (C) [Very Fe-rich]



48-3-1 K-feldspar (C) [At the centre]

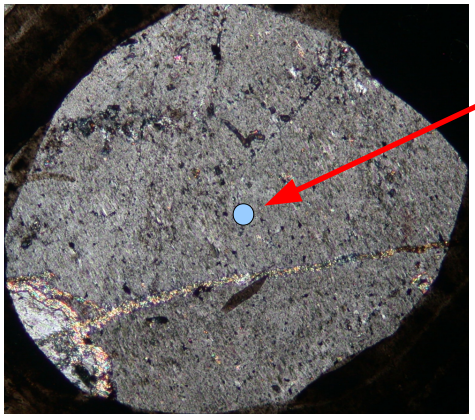
48-3-2 K-feldspar (C) [Outer part]

48-3-3 Albite (C) [Contact between k-feldspar and albite are very sharp. Definitely a later overgrowth]

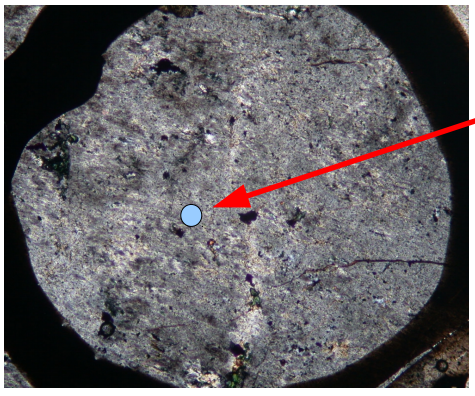


48-5-2 K-feldspar (C) [Very fine intermix]

48-5-1 Albite (C)

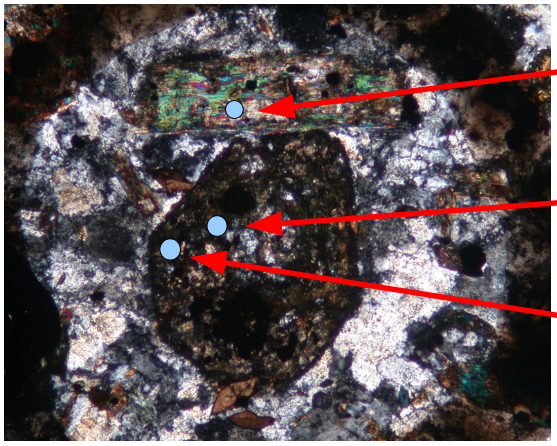


48-6-1 K-feldspar (C) [There is some Na exsolution]



48-8-1 K-feldspar (C)

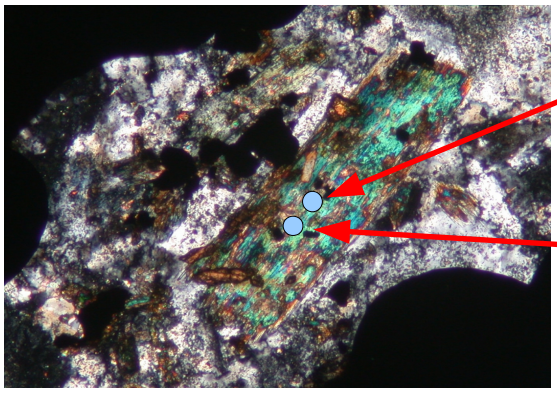
JG – 1332 – 04



JG-04-01 Amphibole (C)

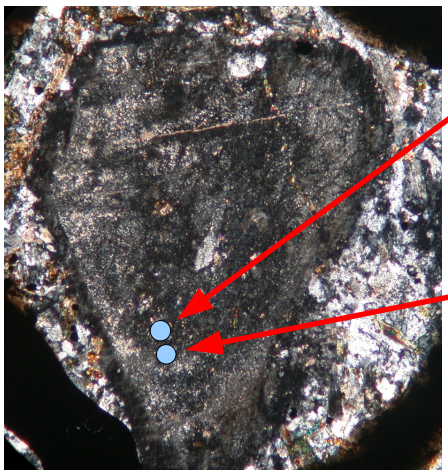
JG-04-02 Amphibole mixed with calcite (C)

JG-04-03 Amphibole (C)



JG-04-04 Amphibole (C)

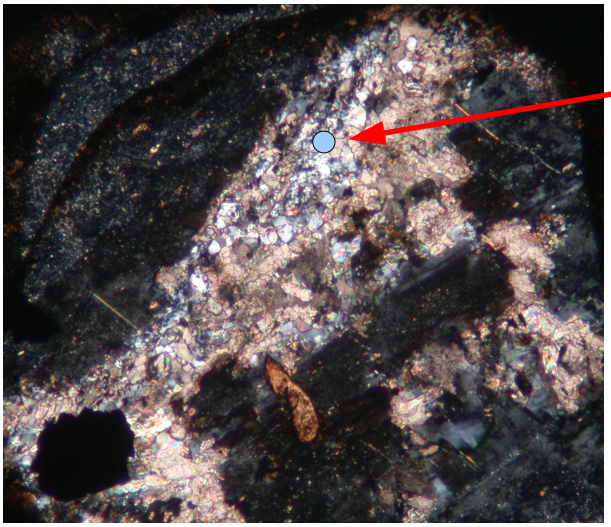
JG-04-05 Amphibole (C) Compositional difference, brighter in colour



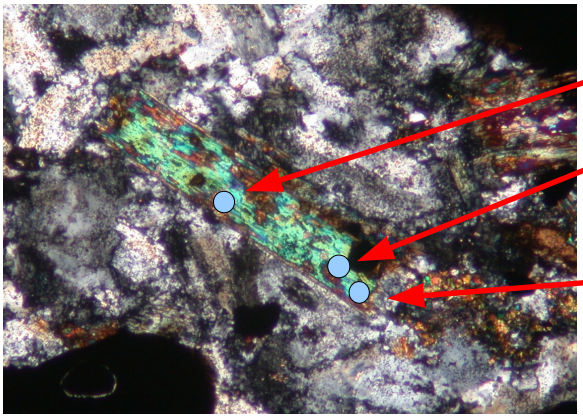
JG-04-07 K-feldpspar (C) Feldspar is albite at its centre

JG-04-06 Albite (C) Was burned, total+Al too high

JG-04-06 REP Albite (C)



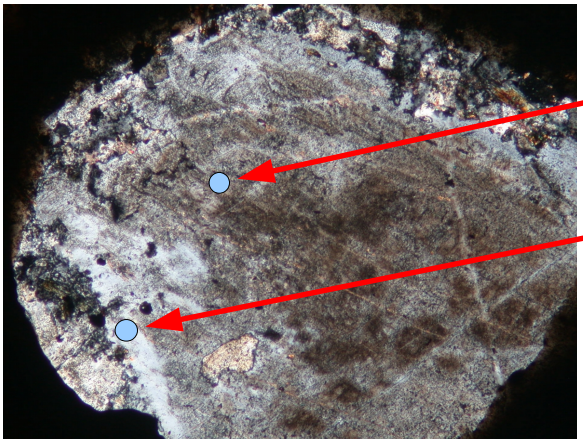
JG-04-08 Abltie (C) The albite is concentrated in the outer rim



JG-04-09 Amphibole (C)

JG-04-10 Amphibole (C) Brighter

JG-04-11 Amphibole (C) Darker

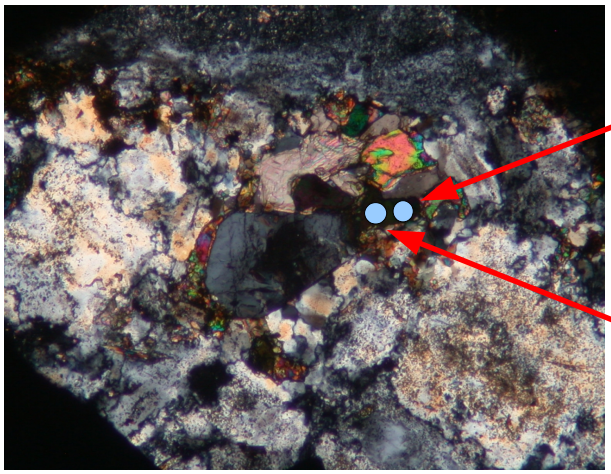


JG-04-12 K-feldspar (C) Rich in Ba, the border is less so

JG-04-13 Anorthoclase (C)

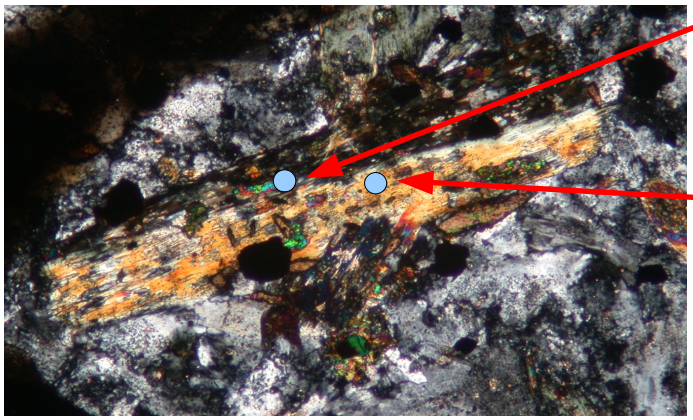


Same hybrid feldspar, a composite picture were taken



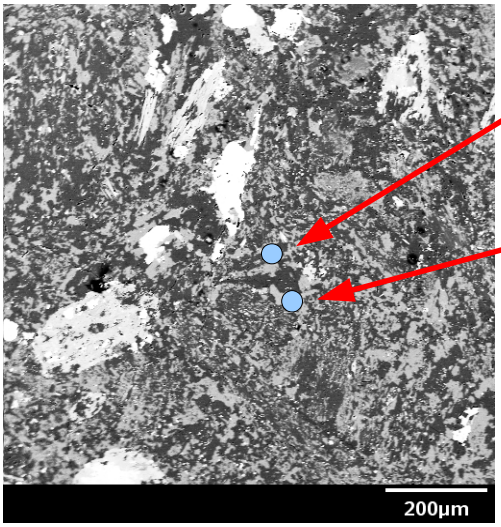
JG-04-17 Epidote (C) Brighter

JG-04-16 Epidote (C) Darker



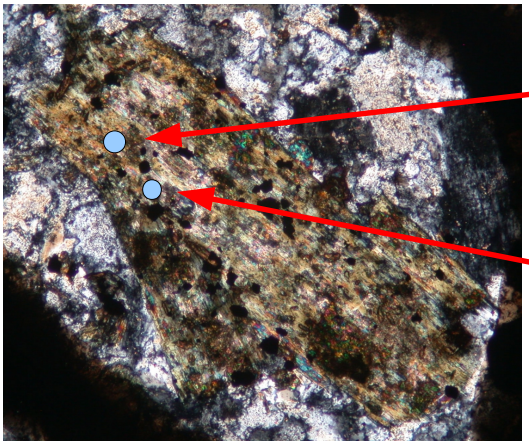
JG-04-15 Epidote (C) Very little REE Peak data

JG-04-14 Amphibole (C)



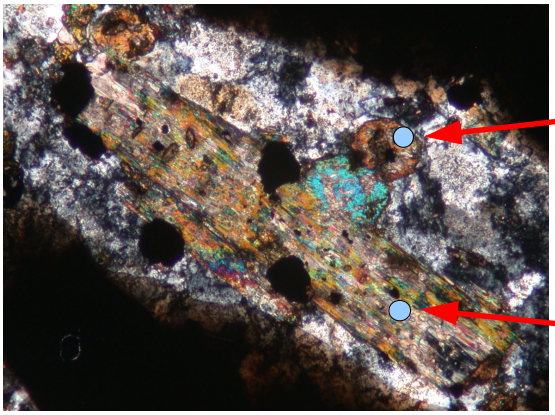
JG-04-19 Albite (C)

JG-04-20 K-feldspar (C)



JG-04-18 REP Amphibole (C)

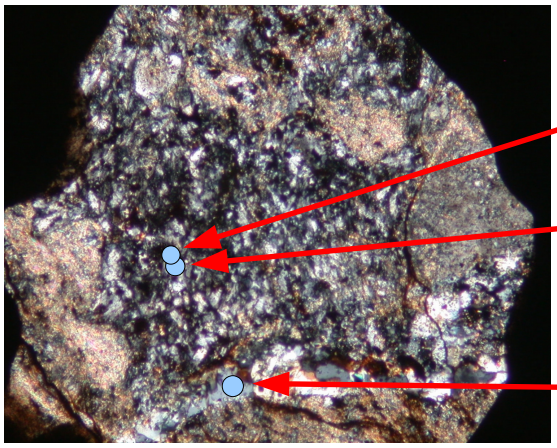
JG-04-18 Calcite (PC) Burned, Calcite is dominant in this crystal



JG-04-22 Amphibole (C)

JG-04-21 Amphibole (C)

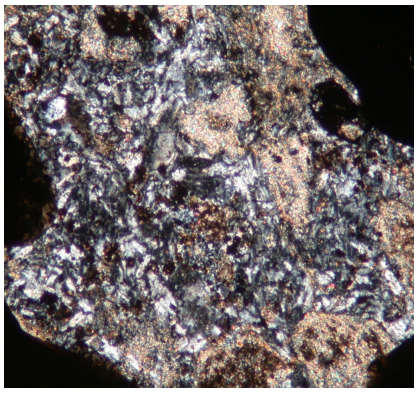
JG – 3002 – L



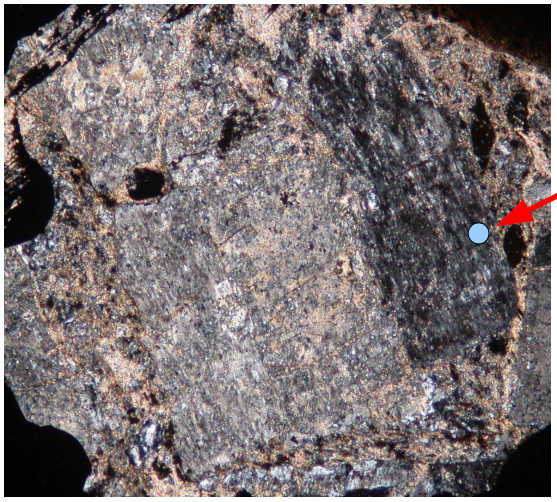
JG-3002-02 K-feldspar (C)

JG-3002-01 Albite (C) First analysis was a burn (this is a second one)

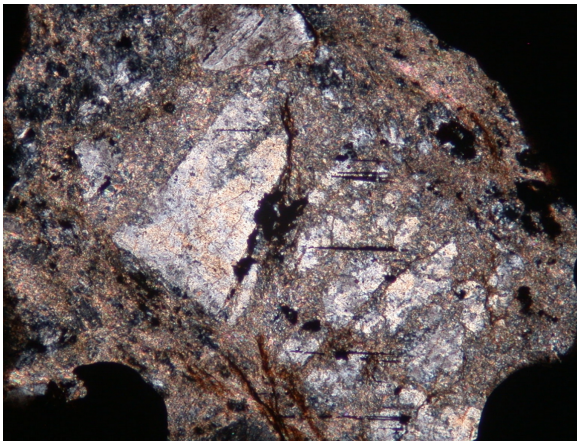
Quartz (PC)



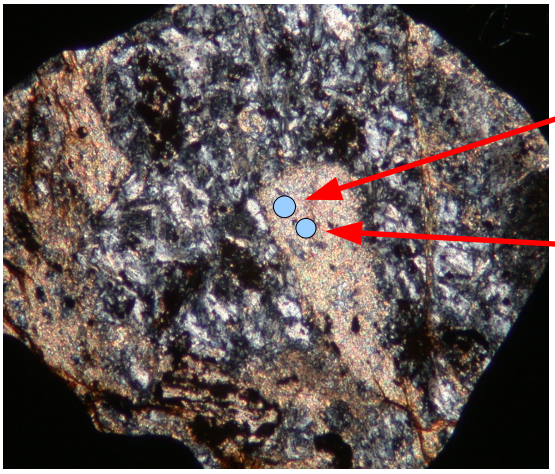
Picture only



JG-3002-03 K-feldspar (C)

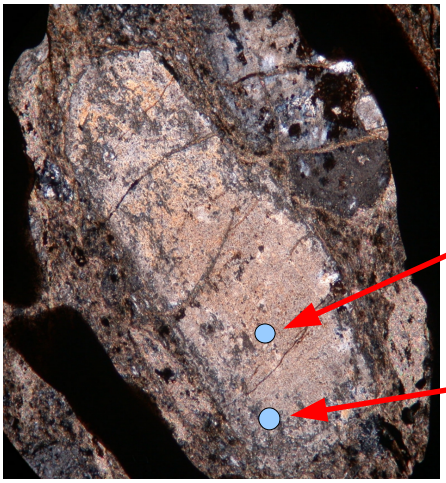


Very mixed
50% Albite
50% K-feldspar
Boundaries not clear at all



JG-3002-04 Sericite (C) Missing F

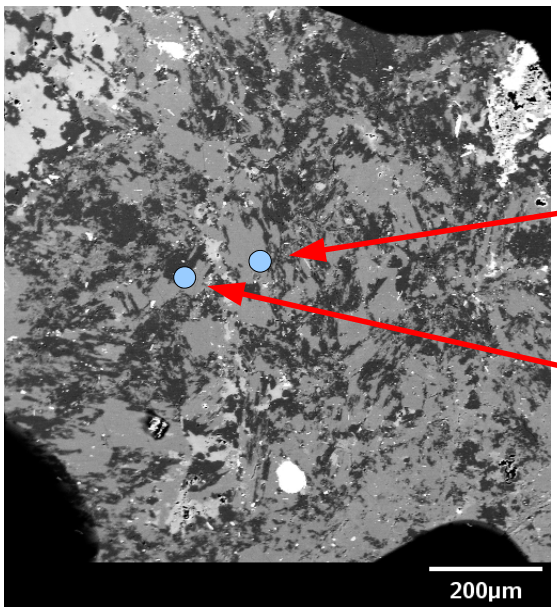
JG-3002-04 REP Sericite (C) With F



JG-3002-06 Albite (C)

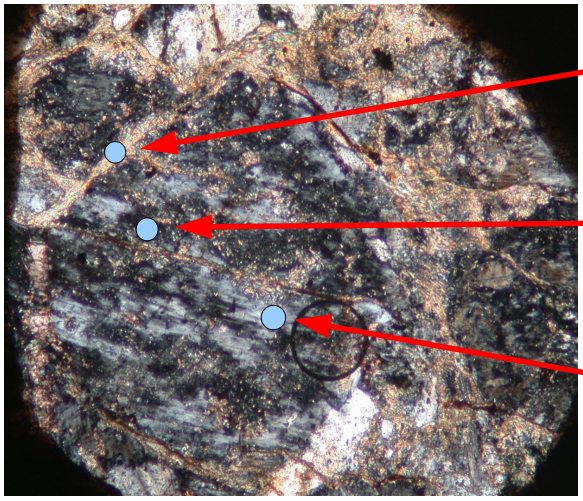
JG-3002-05 K-feldspar (C)

JG – 5099 – 02



JG-5099-02 K-feldspar (C)

JG-5099-01 Albite (C)

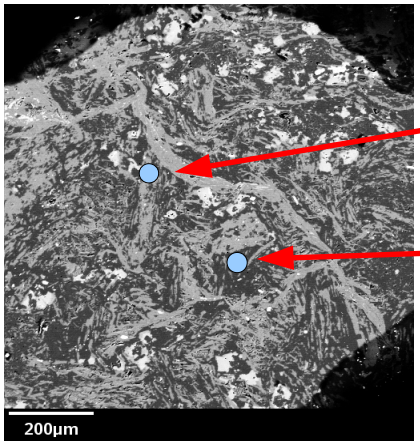


JG-5099-05 Sericite (C)

JG-5099-04 Albite (C)

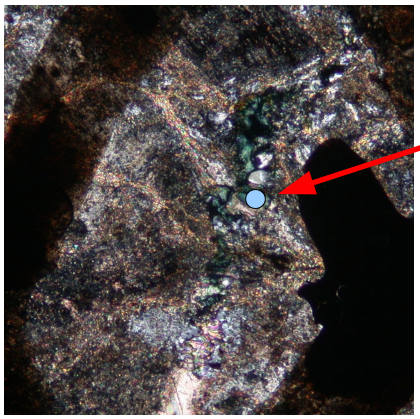
JG-5099-03 K-feldspar (C)

ZP – 04 – 002 “02”

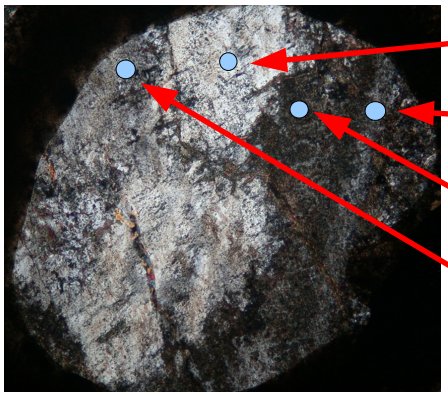


2-1-1 K-feldspar (C) [The matrix in a fine intermix of albite and k-feldspar]

2-1-2 Albite (C)



2-2-1 Chlorite (C)

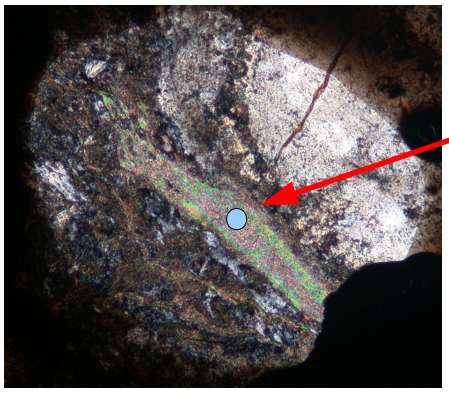


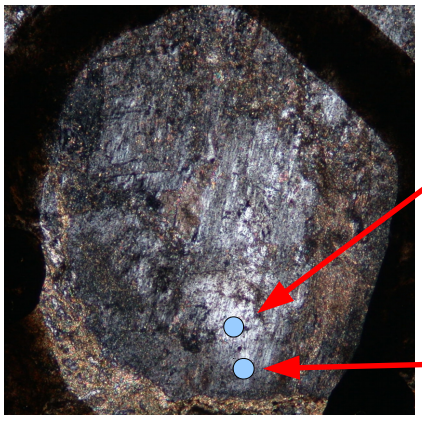
2-3-2 Albite (C) [Homogeneous]

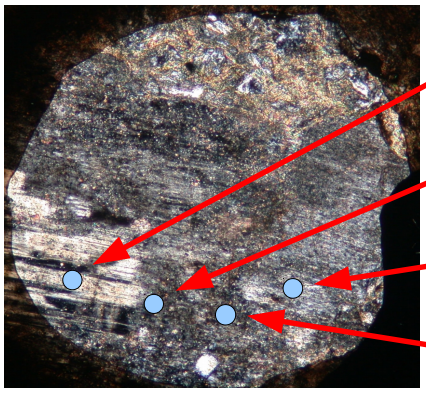
2-3-4 K-feldspar (C) [Slight change]

2-3-3 K-feldspar (C)

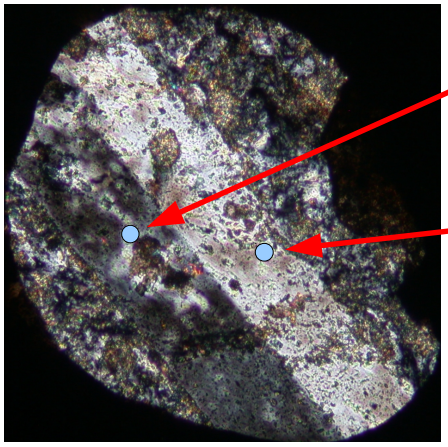
2-3-1 K-feldspar (C) [Interlaced with albite]


2-4-1 Sericite (C)


2-5-1 Albite (C)
2-5-2 K-feldspar (C)

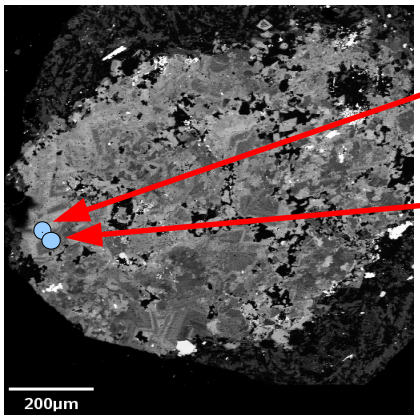

2-7-1 Albite (C)
2-7-2 K-feldspar (C)
2-7-4 K-feldspar (C)
2-7-3 Albite (C)

ZP – 04 – 021 “21”



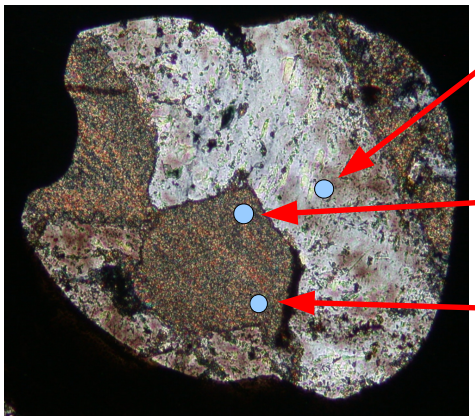
21-1-2 K-feldspar lath (C) [No Ba analysis]

21-1-1 K-feldspar lath (C) [With Ba analysis]



21-2-2 Ankerite (C) [Even richer in Fe]

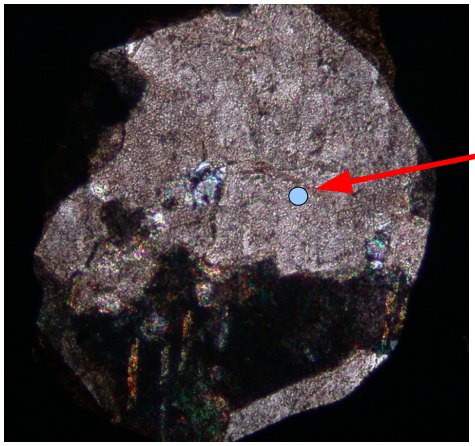
21-2-1 Ankerite (C) [Riche in Fe. Also zoned]



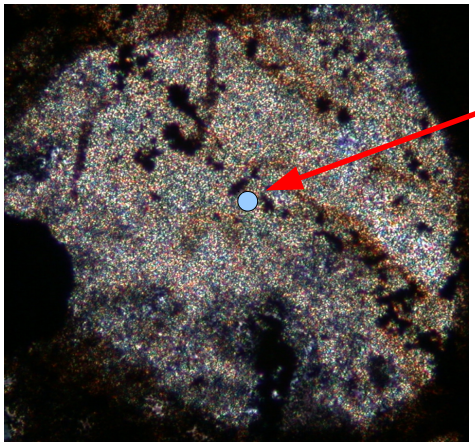
21-3-1 K-feldspar (C)

21-3-2 Sericite (C) [Rich in Fe, responsible for the colouration]

21-3-3 Sericite (C)

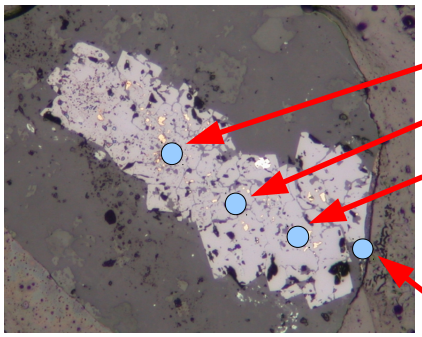


21-4-1 Calcite (C)



21-7-1 Sericite (C) [Rich in Fe, a little of Ba]

21-9-1 Albite (C) [K-feldspar present among the matrix, ratio K:Na - 3:1

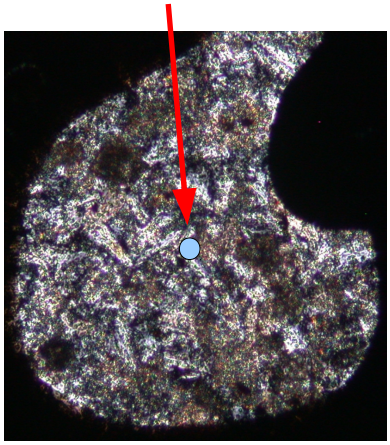


Galena

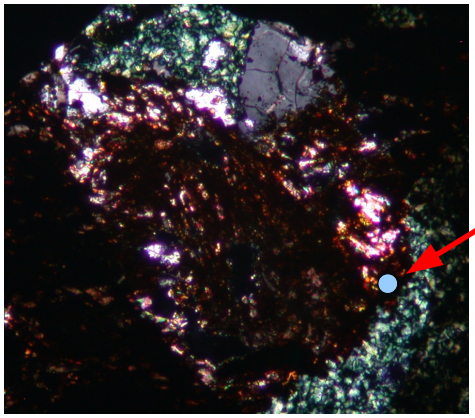
Magnetite

Chalcopyrite

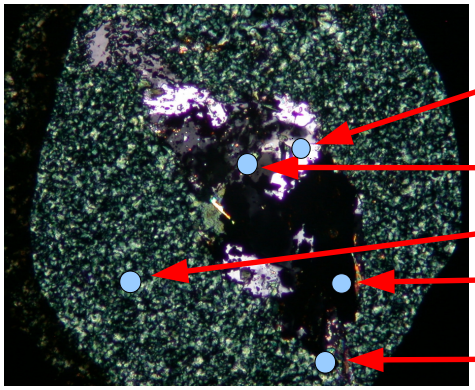
Barite



ZP – 04 – 042 “42”



42-1-1 Calcite (C) [Very faint to no zonation]



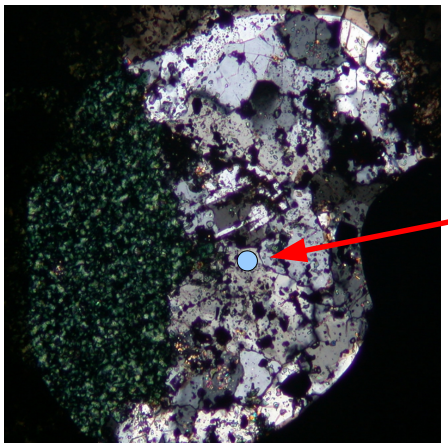
Quartz (PC)

42-2-2 Chlorite (C) [Rich in Fe]

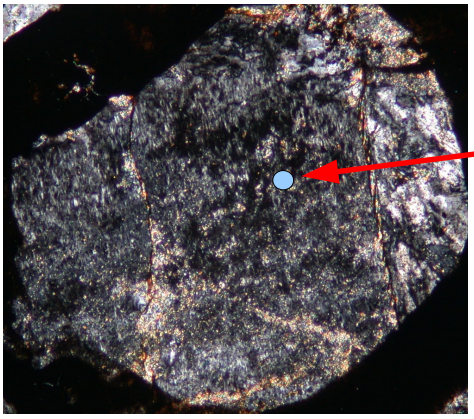
42-2-1 Chlorite (C)

Magnetite (PC)

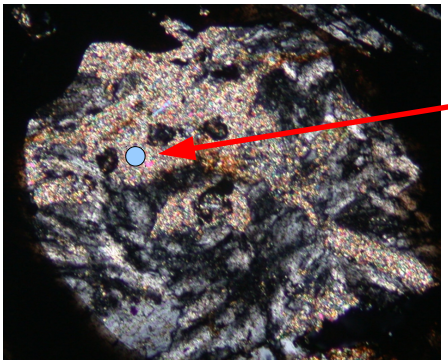
42-2-3 Muscovite (C)



42-3-1 Albite (C) [Very pure albite]



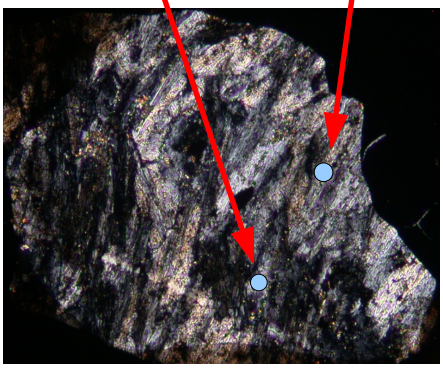
42-4-1 K-feldspar (C) [A little amount of Ba. Feldspar homogeneous]

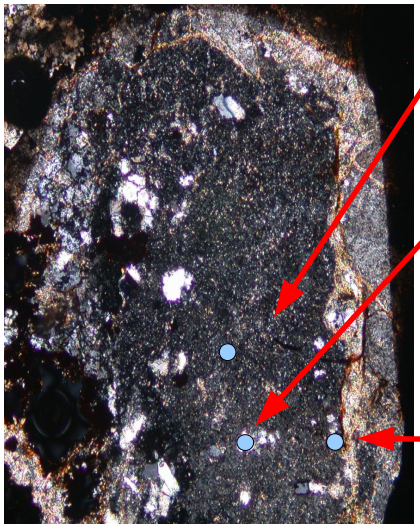


42-5-1 Sericite (C)

42-7-1
K-feldspar (C) [Lower in Ba compared to larger K-feldspars]

42-7-2
Albite (C)



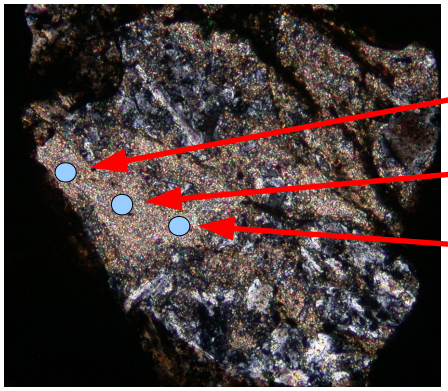


42-6-1 K-feldspar (C)

42-6-2
Quartz
(C)

42-6-3 K-feldspar
(C)

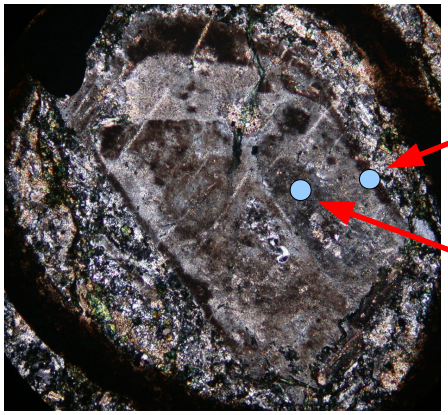
ZP – 04 – 047 “47”



47-1-3 Sericite (C)

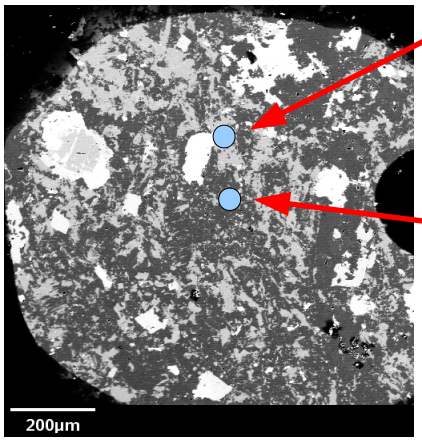
47-1-1 Sericite (C)

47-1-2 Sericite (C) [Extremely rich in K]



47-2-2 K-feldspar (C) [Composite image taken]

47-2-1 K-feldspar (C)

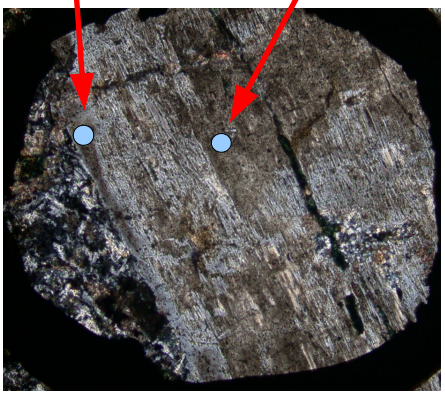


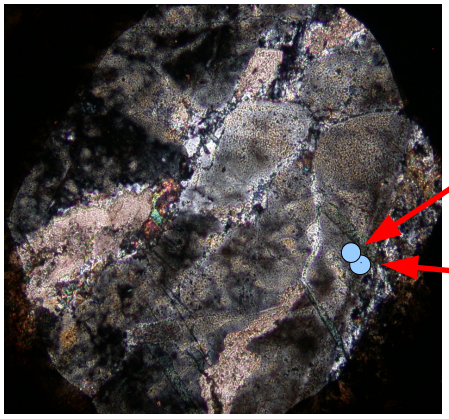
47-3-2 K-feldspar (C)

47-3-1 Albite (C)

47-4-2 K-feldspar (C)

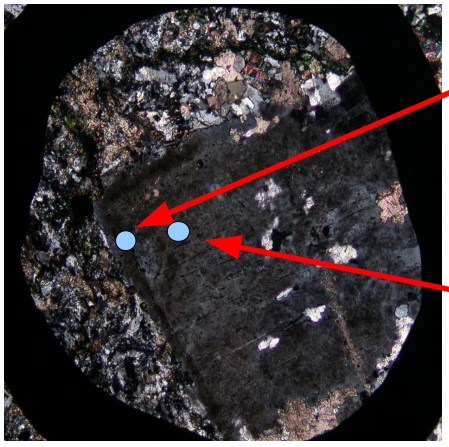
47-4-1 Albite (C)





47-5-1 K-feldspar (C)

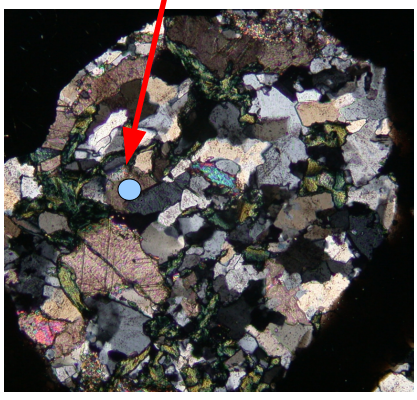
47-5-2 K-feldspar (C)



47-7-2 K-feldspar (C)
[More Ba at the surface]

47-7-1 K-feldspar (C)

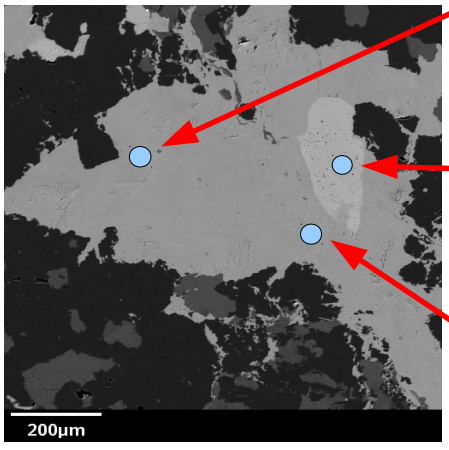
47-9-1 Ankerite (C)
[Presence of Sr, peak data obtained]



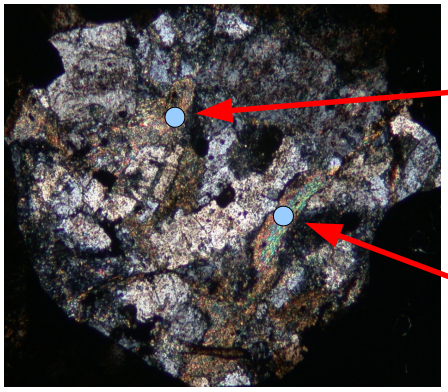
47-8-2 Chlorite (C)

Apatite (PC)

47-8-1 Chlorite (C)

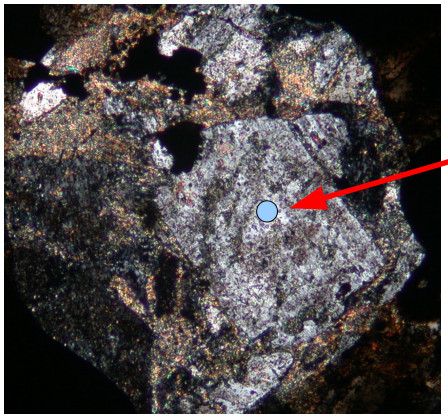


ZP – 04 – 052 “52”



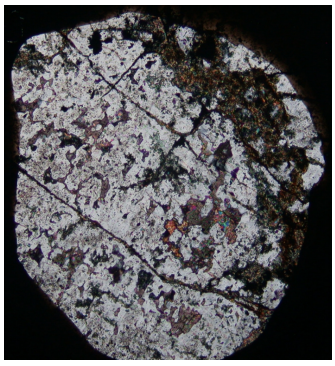
52-1-2 Sericite (C)

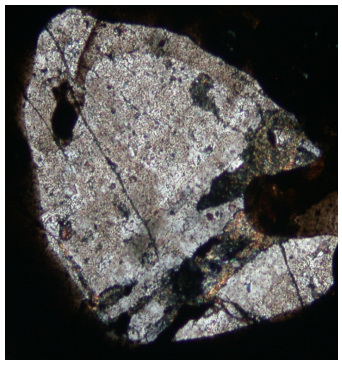
52-1-1 Sericite (C)

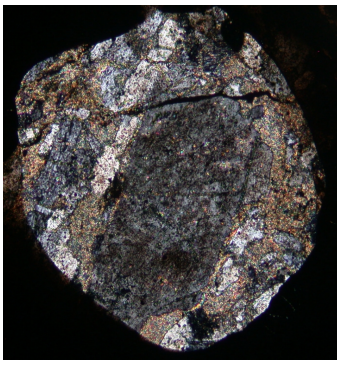


52-4-1 Albite (C) [Very homogeneous]

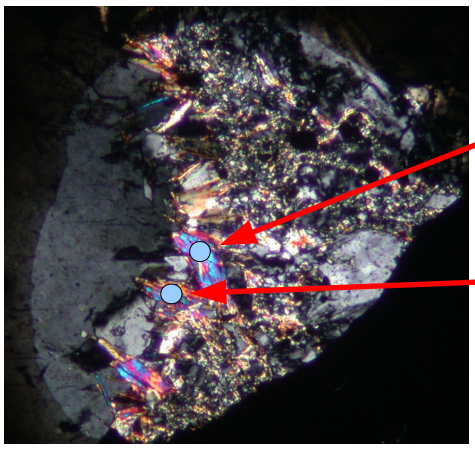
All three are albite. No zonations are seen (PC)





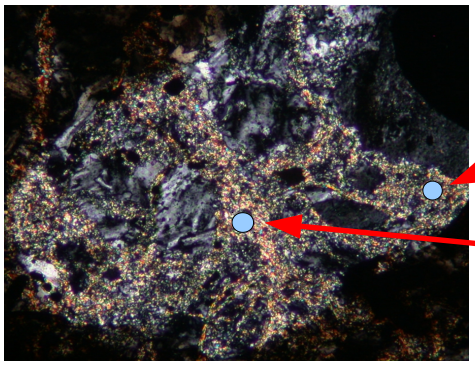


ZP – 04 – 056 “56”



56-1-1 Muscovite (C)
[Minimal Cr]

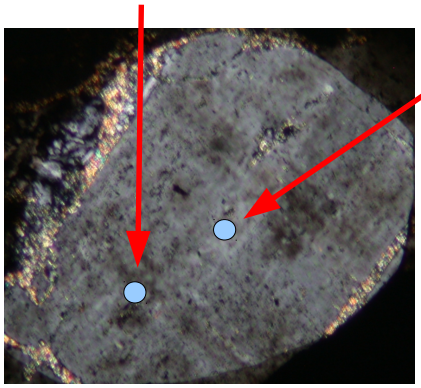
56-1-2 Muscovite (C)
[Minimal Cr]



56-2-2 Sericite (C)
[Rich in Fe]

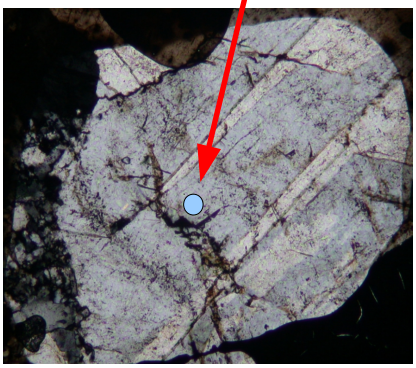
56-2-1 Sericite (C)
[Rich in Fe]

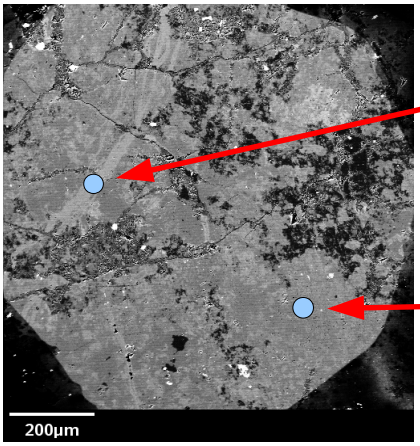
56-3-2 K-feldspar (C) [Slight zonation]



56-3-1
K-
feldspar

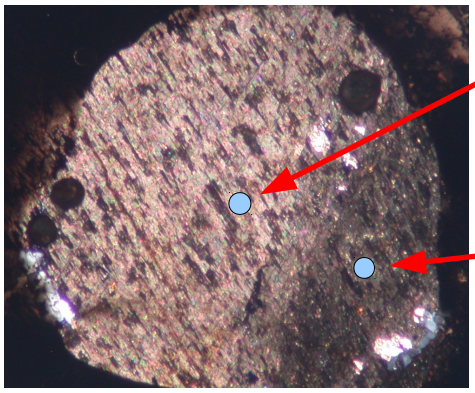
56-4-1 Albite (C)
[Pure albite]





56-5-2 K-feldspar (C) [Almost 2% Ba]

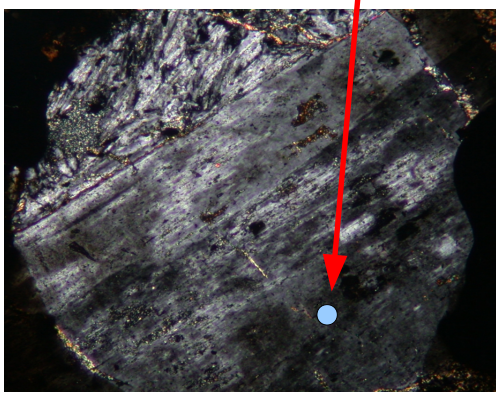
56-5-1 K-feldspar (C)



56-6-1 Siderite (C) [Very rich in Fe]

56-6-2 Siderite (C) [Very rich in Fe]

56-7-1 K-feldspar (C)

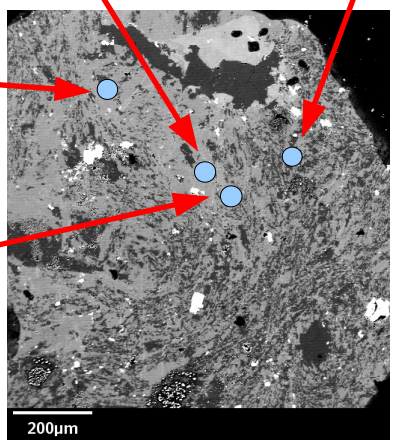


56-8-1 K-feldspar (C)

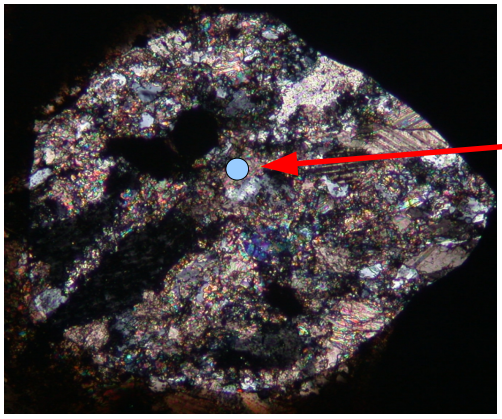
Quartz (PC)

Quartz (PC)

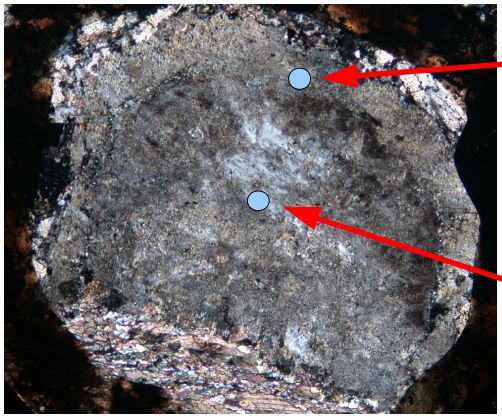
56-8-2 Quartz (C)



ZP – 04 – 058 “58”



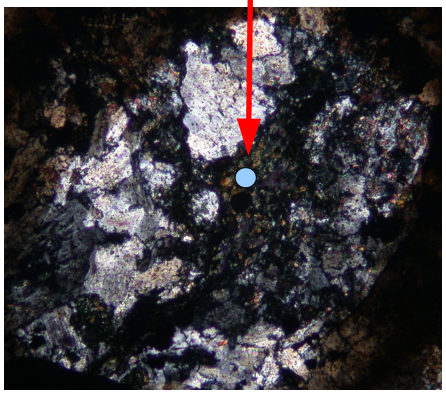
58-1-1 Calcite (C)



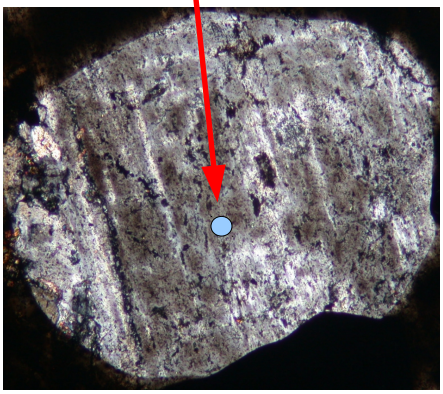
58-2-2 K-feldspar (C)

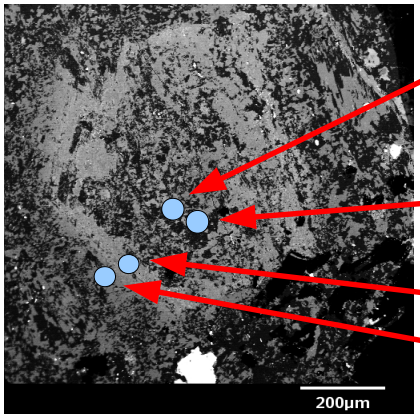
58-2-1 K-feldspar (C)

58-3-1 Chlorite (C)



58-4-1 K-feldspar (C)
[More albite at the centre]



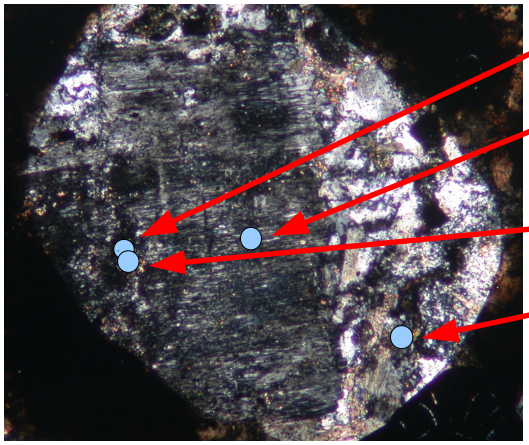


58-5-2 K-feldspar (C) [Gradation to the outer edge]

58-5-1 Albite (C) [Some very small k-feldspar blades, can't evade them 100%]

58-5-3 K-feldspar (C)

58-5-4 K-feldspar (C)



56-6-1 K-feldspar (C) [Very Ca rich]

56-6-3 Albite (C)

56-6-2 K-feldspar (C)

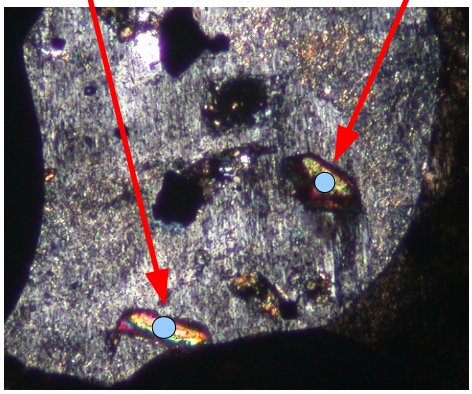
58-9-4 Calcite (C)

58-9-1 Albite (C) [Spot mode]

58-9-2 K-feldspar

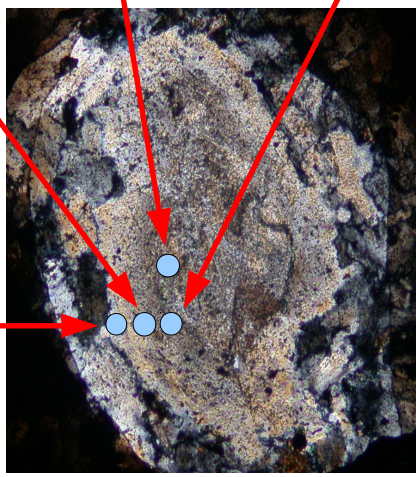
58-7-2 Titanite (C)

58-7-1 Titanite (C)



58-9-3 K-feldspar (C) [3% Ba]

58-9-4 K-feldspar (C) [1% Ba]



C.2 Raw data

For simplification purposes all analyses that were obtained at the microprobe have been included in the accompanying comment (with Foxit PDF reader) on this page. The author recommends Foxit PDF reader to extract the attached data on this page. 

Appendix D

Geochemistry data

A total of 505 geochemical analyses were obtained for this project. For simplification purposes, they have been compiled together and have been included in the accompanying comment (with Foxit PDF reader) on this page. The author recommends Foxit PDF reader to extract the attached data on this page. 

D.1 Choice of loss-on-ignition (LOI) cut-off

This section details the reasoning employed to decide on a LOI cut-off value for the Beattie syenite. LOI cut-off for other lithologies were subjected to the same procedure.

First, all geochemical samples were plotted on the TAS diagram developed by Cox et al. (1979) for plutonic rocks regardless of alteration. Included in the diagram and presented in Figure D.1 is the average of all data samples available.

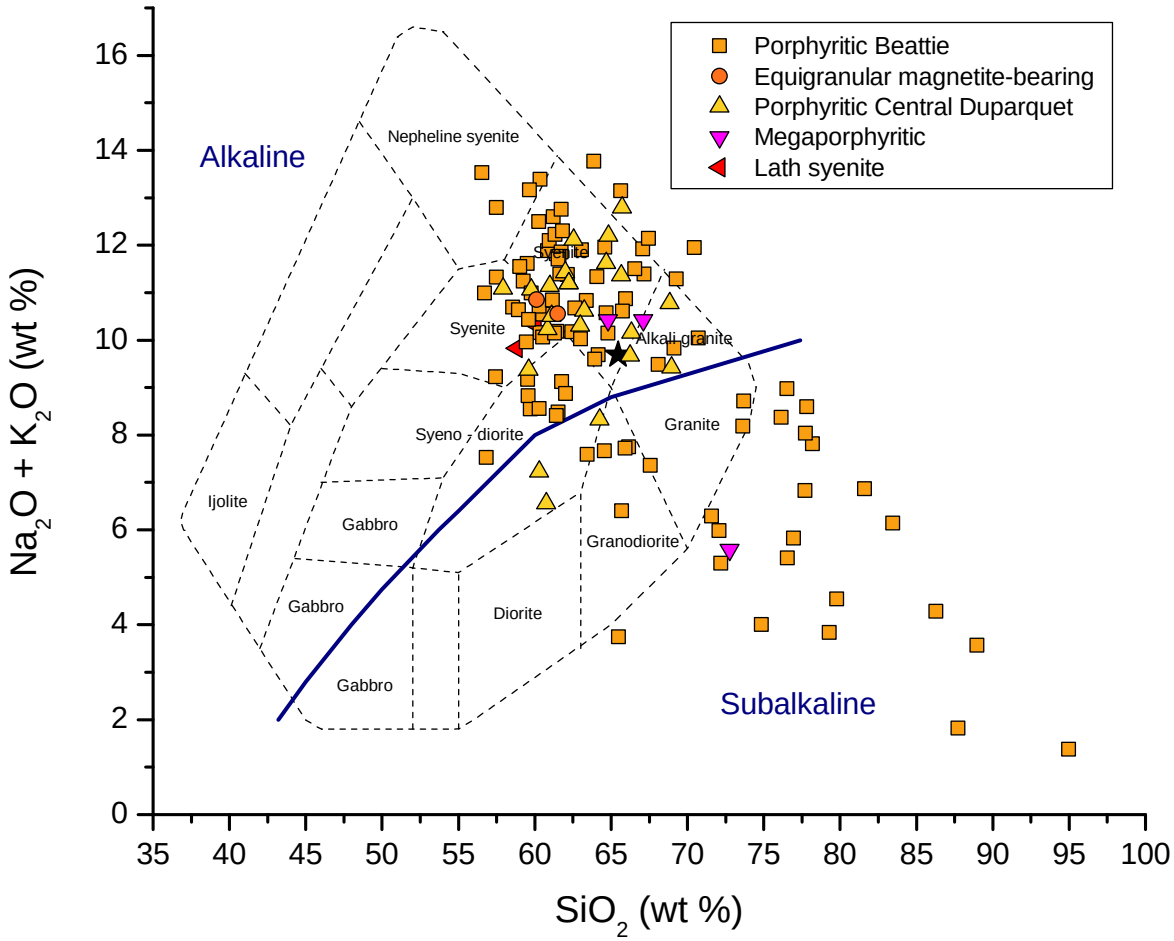


Figure D.1 – Analyses of all the Beattie syenite samples illustrated in the TAS classification scheme for plutonic rocks of Cox et al. (1979). Also included in the diagram is the dividing boundary between the alkaline and subalkaline rocks (blue line) of Irvine and Baragar (1971). The black star corresponds to the average of all data samples.

Now to explore the effects of an increasing LOI cut-off, Figures D.2, D.3, D.4 and D.5 demonstrate the remaining data at a LOI cut-off of 8%, 6%, 4% and 2% respectively by filtering out samples which fall outside of this LOI cut-off threshold. In addition, the average of all data samples for each specific cut-off is indicated in each diagram.

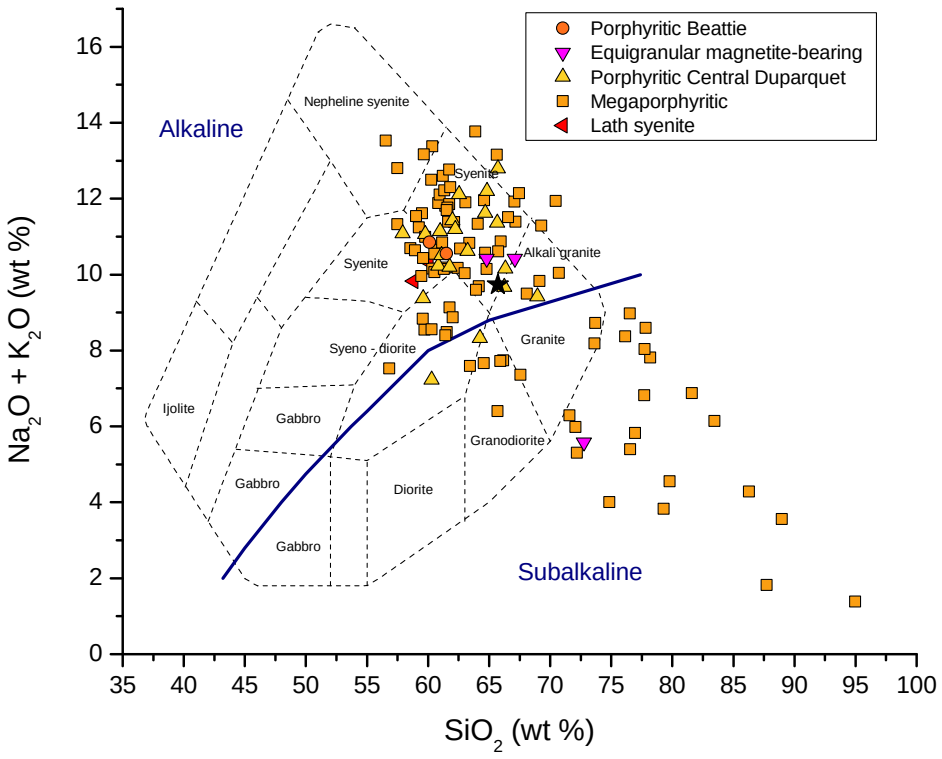


Figure D.2 – Analyses of the Beattie syenite samples with a LOI cut-off of 8%. The black star corresponds to the average of all data samples.

As expected, there is a clear decrease in the amount of data available with each decrement of LOI cut-off. The averages demonstrate an interesting trend towards subalkalinity. This trend is better illustrated in Figure D.6.

Figure D.6 illustrates that as the cut-off LOI is increased, the averages progressively then rapidly depart the syenitic field into the alkali granite field. For LOI cut-off values larger than 6%, the average remains in the syenitic field. Therefore, when choosing an optimal LOI cut-off, the criterion is such that the average of the data does not leave the syenitic field while retaining a statistically significant amount of data. Figure D.7 demonstrates that the number of samples sharply decreases at a LOI cut-off of 4% and again at 2%. Consequently, to maintain a statistically significant amount of data, the LOI cut-off cannot be lower than 4%. In conclusion, in the case of the Beattie syenite, one can choose a LOI between 6-7%.

Of course, as explained in Chapter 7, other factors (e.g., location of samples, sample origin, etc.) were considered in addition to the LOI cut-off for the characterization of altered samples.

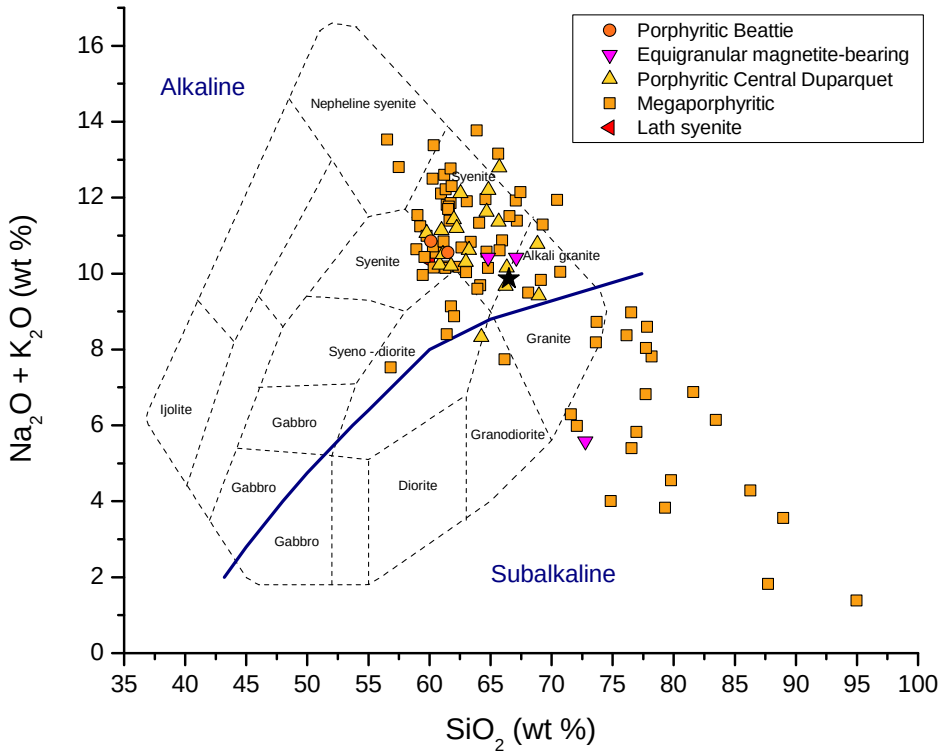


Figure D.3 – Analyses of the Beattie syenite samples with a LOI cut-off of 6%. The black star corresponds to the average of all data samples.

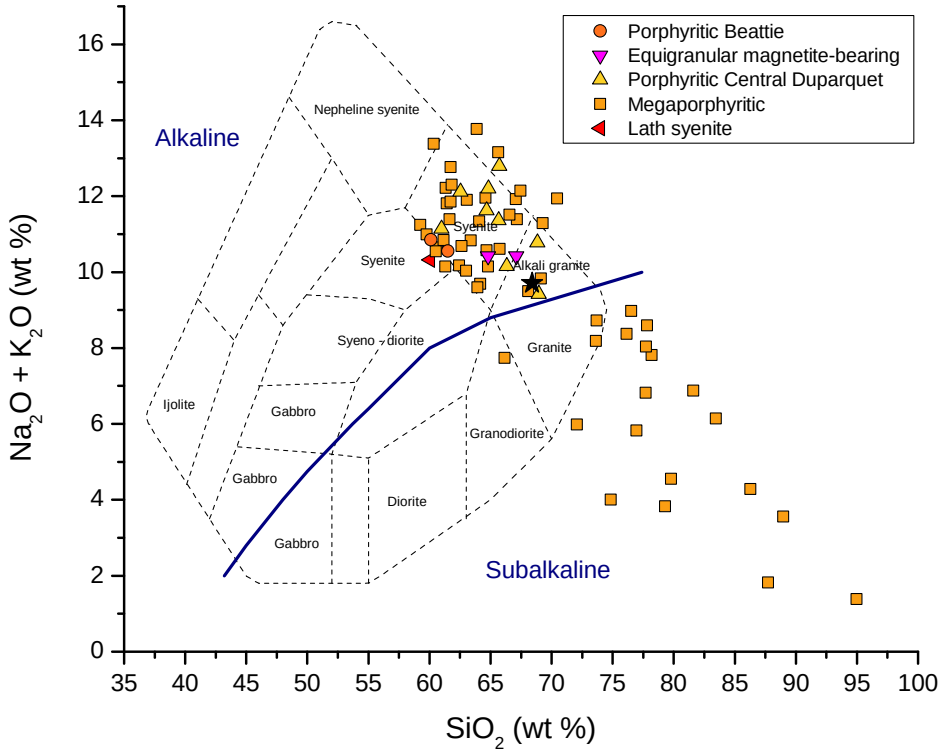


Figure D.4 – Analyses of the Beattie syenite samples with a LOI cut-off of 4%. The black star corresponds to the average of all data samples.

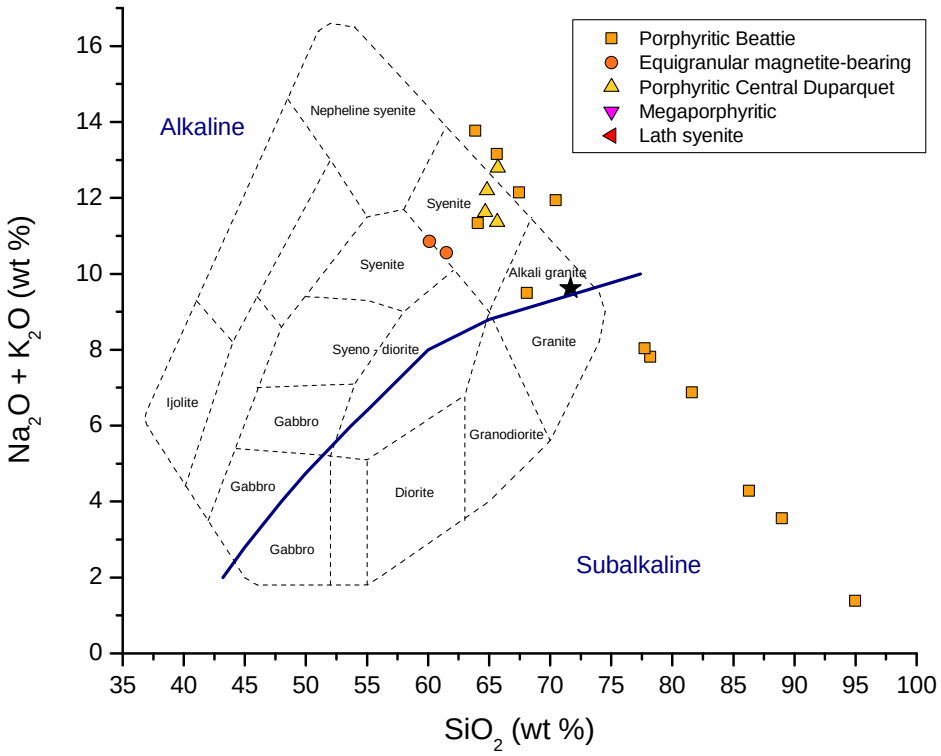


Figure D.5 – Analyses of the Beattie syenite samples with a LOI cut-off of 2%. The black star corresponds to the average of all data samples.

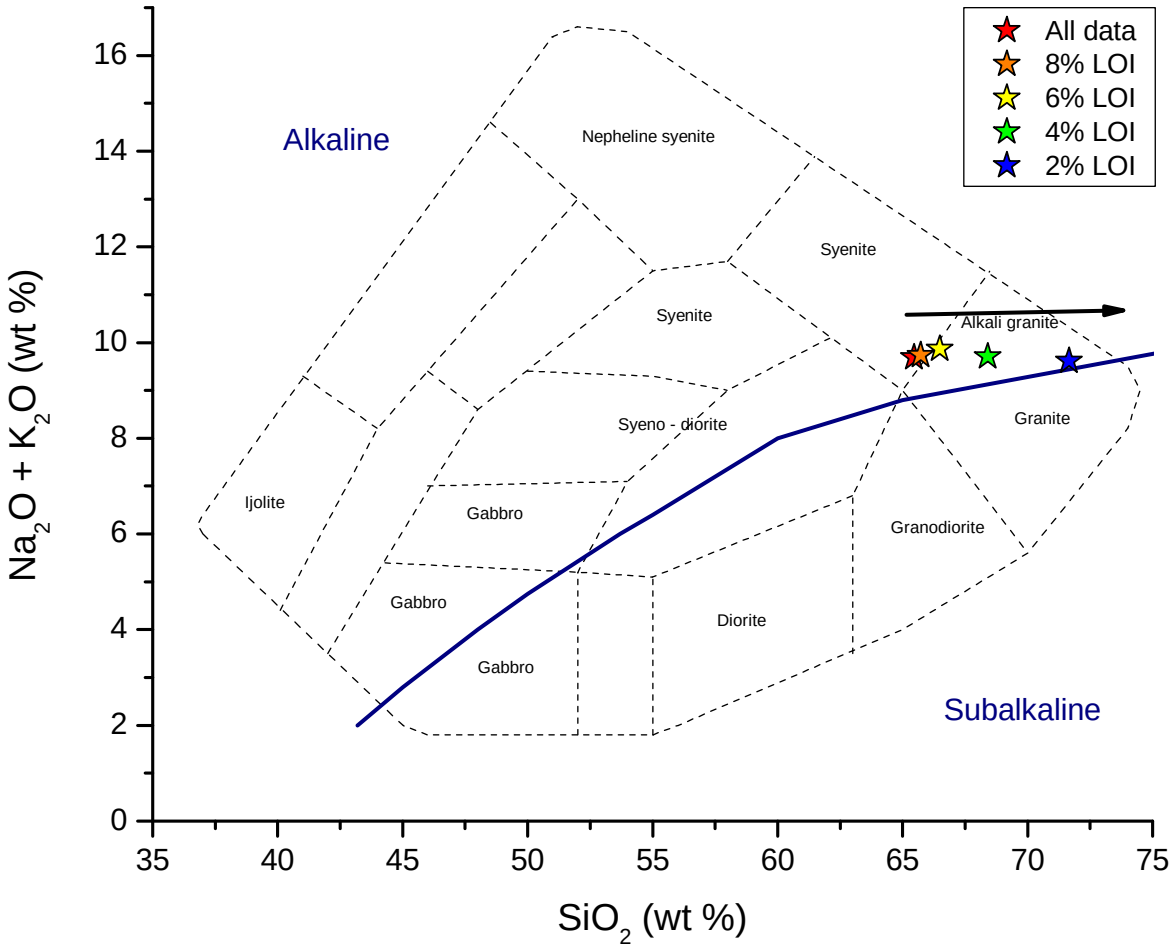


Figure D.6 – Averages for each step of increasing LOI cut-off for samples of the Beattie syenite. The black arrow corresponds to the trend illustrated by an increase in LOI cut-off.

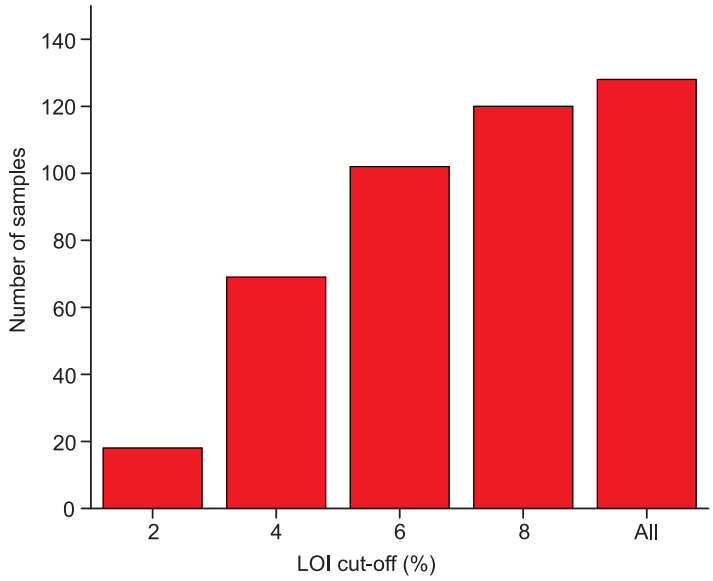


Figure D.7 – Number of Beattie syenite samples remaining after each LOI cut-off.